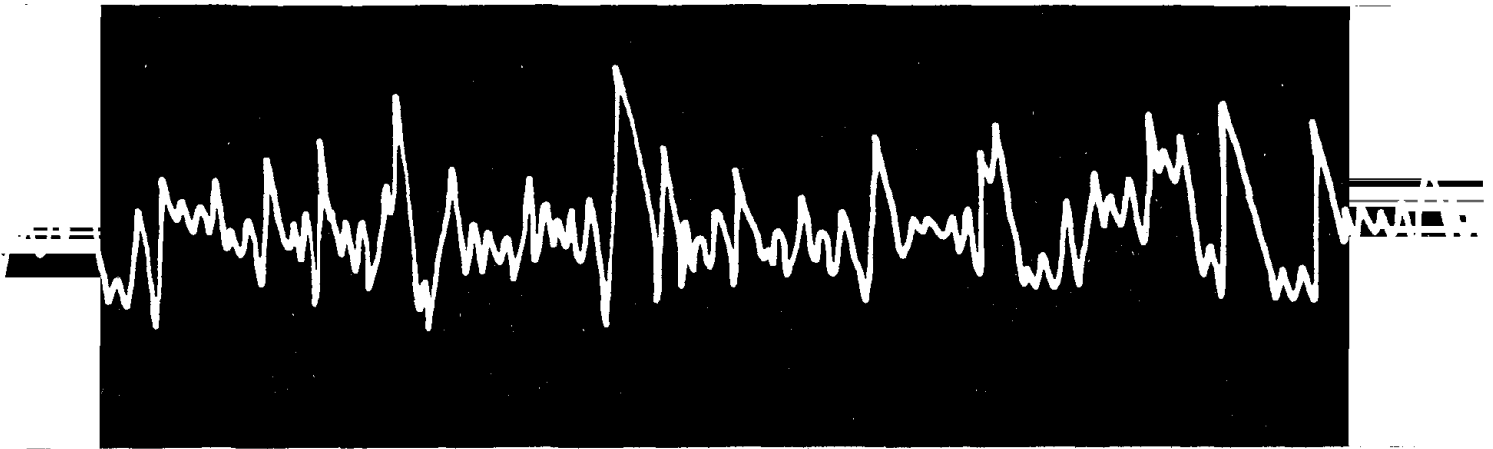


**PROCEEDINGS OF
THE SECOND INTERNATIONAL CONFERENCE ON
MICROZONATION
FOR SAFER CONSTRUCTION—RESEARCH AND APPLICATION**



VOLUME

II

Any opinions, findings, conclusions
or recommendations expressed in this
publication are those of the author(s)
and do not necessarily reflect the views
of the National Science Foundation.

Sponsored by:
National Science Foundation
UNESCO
American Society of Civil Engineers
Earthquake Engineering Research Institute
Seismological Society of America
Universities Council for Earthquake Engineering Research

SAN FRANCISCO, CALIFORNIA, U.S.A.

NOVEMBER 26-DECEMBER 1, 1978



REPORT DOCUMENTATION PAGE	1. REPORT NO. NSF/RA-780618	2.	3. Recipient's Accession No. PB301144
4. Title and Subtitle Microzonation for Safer Construction, Research and Application, Proceedings of the Second International Conference, Vol. 2, San Francisco (11/26/78-12/1/78)		5. Report Date December 1978	
7. Author(s)		6.	
9. Performing Organization Name and Address University of Washington at Seattle Seattle, Washington 98105		8. Performing Organization Rept. No.	
12. Sponsoring Organization Name and Address Engineering and Applied Science (EAS) National Science Foundation 1800 G Street, N.W. Washington, D.C. 20550		10. Project/Task/Work Unit No.	
15. Supplementary Notes		11. Contract(C) or Grant(G) No. (C) (G)PFR7723228	
16. Abstract (Limit: 200 words) Two conference sessions are reported. The first covers geology, seismology, geophysics and side effects. Seismic investigations of various regions in the world were presented together with earthquake prediction studies. Considerable attention was devoted to such theoretical aspects as peak horizontal and vertical accelerations, the relevancy of one dimensional shear models in predicting surface acceleration, and the theory of connectivity. The second session dealt with soil dynamics, soil structure interaction, and ground effects. Various aspects of liquefaction potential were presented. Studies of shear deformation in sandy soils by acoustic emission response and seismic shear strain induced in soil deposits were reported. Recent earthquake resistant design methods for different types of foundations in Japan were described. In general, each topic was prefaced by an abstract and an introduction followed by the methodology, results, conclusions and references.		13. Type of Report & Period Covered Proceedings 11/26/78 - 12/1/78	
17. Document Analysis a. Descriptors Geology Seismology Soil dynamics b. Identifiers/Open-Ended Terms Acoustic emission response Earthquake engineering c. COSATI Field/Group		14.	
18. Availability Statement NTIS		19. Security Class (This Report)	21. No. of Pages 516
		20. Security Class (This Page)	22. Price PC A22 ME A01

TABLE OF CONTENTS

VOLUME I

STATE-OF-THE-ART SESSION		Page
C. Kisslinger	Seismicity and Global Tectonics as a Framework for Microzonation	3
P. C. Jennings D. V. Helmberger	Strong-Motion Seismology	27
N. C. Donovan	Soil & Geologic Effects on Site Response	55
M. A. Sherif I. Ishibashi	Soil Dynamics Considerations for Microzonation . . .	81
A. S. Veletsos	Soil-Structure Interaction for Buildings during Earthquakes	111
L. S. Cluff	Geologic Considerations for Seismic Microzonation	135
V. J. Murphy	Geophysical Engineering Investigative Techniques for Site Characterization	153
J. R. Hutton D. S. Miletic	Social Aspects of Earthquakes	179
H. J. Lagorio E. E. Botsai	Urban Design and Earthquakes	193
K. V. Steinbrugge	Earthquake Insurance and Microzonation	203
N. S. Remmer	Government Responsibility in Microzonation	215

MICROZONATION SESSION

Progress on Seismic Zonation in the San Francisco Bay Region

E. E. Brabb R. D. Borchardt	1. Introduction and Summary	229
D. G. Herd	2. Neotectonic Framework of Central Coastal California and Its Implications to Microzonation of the San Francisco Bay Region	231
R. D. Borchardt J. F. Gibbs T. E. Fumal	3. Progress on Ground Motion Predictions for the San Francisco Bay Region, California	241
R. J. Archuleta W. B. Joyner D. M. Boore	4. A Methodology for Predicting Ground Motion at Specific Sites	255

T. L. Youd J. C. Tinsley D. M. Perkins E. J. King R. F. Preston	5. Liquefaction Potential Map of San Fernando Valley, California	267
D. K. Keefer G. F. Wieczorek E. L. Harp D. H. Tuel	6. Preliminary Assessment of Seismically Induced Landslide Susceptibility	279
S. T. Algermissen K. V. Steinbrugge	7. Earthquake Losses to Buildings in the San Francisco Bay Area	291
W. J. Kockelman E. E. Brabb	8. Examples of Seismic Zonation in the San Francisco Bay Region	303
J. B. Perkins	9. The Use of Earthquake and Related Information in Regional Planning--What We've Done and Where We're Going	315
W. G. Milne D. H. Weichert	The Sensitivity of Seismic Risk Maps to the Choice of Earthquake Parameters in the Georgia Strait Region of British Columbia	323
J. A. Fischer J. G. McWhorter	The Microzonation of New York State: Progress Report No. 2	329
J. Kuroiwa E. Deza H. Jaén J. Kogan	Microzonation Methods and Techniques Used in Peru	341
E. L. Harp R. C. Wilson G. F. Wieczorek D. K. Keefer	Landslides from the February 4, 1976 Guatemala Earthquake: Implications for Seismic Hazard Reduction in the Guatemala City Area	353
S. T. Mau C. S. Kao	A Risk Model for Seismic Zoning of Taiwan	367
H. K. Acharya	Ground Motion Attenuation in the Philippines	379
K. Moazami-Goudarzi H. Parhikhteh	A Quantitative Seismotectonic Study of the Iranian Plateau	391
N. Mândrescu	The Vrancea Earthquake of March 4, 1977 and the Seismic Microzonation of Bucharest	399
J. Petrovski	Need for Experimental Evidence in Development of Seismic Microzoning Methods	413
S. Hattori	A New Proposal of the Seismic Risk Map Based on the Maximum Earthquake Motions, the Ground Characteristics and the Temporal Variations of the Seismicity	421
E. Shima	Seismic Microzoning Map of Tokyo	433

S. Yoshikawa Y. T. Iwasaki M. Tai	Microzoning of Osaka Region	445
D. R. Packer L. S. Cluff D. P. Schwartz F. H. Swan, III I. M. Idriss	Auburn Dam - A Case History of Earthquake Evaluation for a Critical Facility	457
E. J. Bell D. T. Trexler J. W. Bell	Computer-Simulated Composite Earthquake Hazard Model for Reno, Nevada	471
A. S. Patwardhan D. D. Tillson R. L. Nowack	Zonation for Critical Facilities Based on Two-Level Earthquakes	485
W. W. Hays S. T. Algermissen R. D. Miller K. W. King	Preliminary Ground Response Maps for the Salt Lake City, Utah, Area	497
C. E. Glass	Application of Regionalized Variables to Micro- zonation	509
J. L. Alonso L. Urbina	A New Microzonation Technique for Design Purposes	523
A. S. Patwardhan L. S. Cluff	The Concept of Residual Risk in Earthquake Risk Assessments	535
S. Murakami K. Midorikawa	Land Use Technique for Microzonation	547
J. G. Anderson M. D. Trifunac	Application of Seismic Risk Procedures to Problems in Microzonation	559
B. A. Schell	Seismotectonic Microzoning for Earthquake Risk Reduction	571
A Report on the Miyagiken-oki, Japan, Earthquake of June 12, 1978		
	Abstract	587
H. Kobayashi K. Seo S. Midorikawa	I. Strong Ground Motions and Seismic Microzoning	588
Y. Yoshimi I. Tohno K. Tokimatsu	II. Geotechnical Aspects of Damage	600
T. Katayama	III. Damage to Lifeline Utility Systems (A) . . .	606
H. Shibata	IV. Damage to Lifeline Utility Systems (B) . . .	612

Index of Authors

VOLUME II

GEOLOGY, SEISMOLOGY, GEOPHYSICS AND SITE EFFECTS SESSION

B. A. Bolt	Fallacies in Current Ground Motion Prediction . . .	617
E. W. Hart	Zoning for the Hazard of Surface Fault Rupture in California	635
M. R. Ploessel	High-Resolution Geophysical Surveys, A Technique for Microzonation of the Continental Shelf	647
L. Esteva E. Bazán	Seismicity and Seismic Risk Related to Subduction Zones	657
W. D. Page W. U. Savage J. N. Alt L. S. Cluff D. Tocher	Seismic Hazards along the Makran Coast of Iran and Pakistan: The Importance of Regional Tectonics and Geologic Assessment	669
S. Kh. Negmatullaev G. S. Seleznyov D. W. Simpson C. Rojahn	Engineering and Seismological Observations at Dams	681
R. A. Wiggins G. A. Frazier J. Sweet R. Apsel	Modeling Strong Motions from Major Earthquakes . .	693
F. T. Wu	Prediction of Strong Ground Motion Using Small Earthquakes	701
T. Iwasaki T. Katayama K. Kawashima M. Saeki	Statistical Analysis of Strong-Motion Acceleration Records Obtained in Japan	705
A. F. Shakal M. N. Toksöz	Analysis of Source and Medium Effects on Strong Motion Observations	717
F. J. Sánchez-Sesma	Ground Motion Amplification due to Canyons of Arbitrary Shape	729
E. Mardiross	A Method for Assessment of Seismic Design Motions	739
A. M. Rogers W. W. Hays	Preliminary Evaluation of Site Transfer Functions Developed from Earthquakes and Nuclear Explosions	753
K. Kudo	The Contribution of Love Waves to Strong Ground Motions	765
I. S. Oweis	The Relevancy of One Dimensional Shear Models in Predicting Surface Acceleration	777

N. Goto Y. Ohta H. Kagami	Deep Shear Wave Velocity Measurement for Evaluation of 1-10 Sec Seismic Input Motions	793
K. Sadigh M. S. Power R. R. Youngs	Peak Horizontal and Vertical Accelerations, Velocities, and Displacements on Deep Soil Sites during Moderately Strong Earthquakes	801
F. J. Sabina I. Herrera R. England	Theory of Connectivity: Applications to Scattering of Seismic Waves. I. SH Wave Motion	813
S. Midorikawa H. Kobayashi	On Estimation of Strong Earthquake Motions with Regard to Fault Rupture	825

SOIL DYNAMICS, SOIL-STRUCTURE INTERACTION AND GROUND EFFECTS SESSION

W. D. L. Finn Y. P. Vaid S. K. Bhatia	Constant Volume Cyclic Simple Shear Testing	839
Y. Yoshimi K. Tokimatsu	Two-Dimensional Pore Pressure Changes in Sand Deposits during Earthquakes	853
A. S. Arya P. Nandakumaran V. K. Puri S. Mukerjee	Verification of Liquefaction Potential by Field Blast Tests	865
H. Dezfulian S. R. Prager	Use of Penetration Data for Evaluation of Liquefaction Potential	873
T. Iwasaki F. Tatsuoka K. Tokida S. Yasuda	A Practical Method for Assessing Soil Liquefaction Potential Based on Case Studies at Various Sites in Japan	885
K. Ishihara K. Ogawa	Liquefaction Susceptibility Map of Downtown Tokyo	897
J. Isenberg D. K. Vaughan	Three-Dimensional Nonlinear Analysis of Soil-Structure Interaction in a Nuclear Power Plant Containment Structure	911
E. Alarcón J. Domínguez A. Martín F. Paris	Boundary Methods in Soil-Structure Interaction	921
Y. Sugimura	Seismic Shear Strain Induced in Soil Deposits	933
R. D. Singh W. S. Gardner R. Dobry	Post Cyclic Loading Behavior of Soft Clays	945

S. Nemat-Nasser A. Shokoh	A New Approach for the Analysis of Liquefaction of Sand in Cyclic Shearing	957
K. Tanimoto M. Nishi T. Noda	A Study of Shear Deformation Process of Sandy Soils by the Observation of Acoustic Emission Response	971
W. P. Grant I. Arango D. N. Clayton	Geotechnical Data at Selected Strong Motion Accelerograph Sites	983
Y. Shioi T. Furuya M. Okahara	Recent Earthquake Resistant Design Methods for Different Types of Foundations in Japan	1001
W. F. Marcuson, III R. F. Ballard, Jr. S. S. Cooper	Comparison of Penetration Resistance Values to In Situ Shear Wave Velocities	1013
C. M. Duke G. C. Liang	Site Effects from Fourier Transforms	1025
A. M. Abdel-Ghaffar R. F. Scott	Dynamic Characteristics of an Earth Dam from Two Recorded Earthquake Motions	1037
B. Tucker J. King K. Aki J. Brune I. Nersesov W. Prothero G. Shpilker G. Self	A Preliminary Report on a Study of the Seismic Response of Three Sediment-Filled Valleys in the Garm Region of the USSR	1051
K. W. Campbell	Empirical Synthesis of Seismic Velocity Profiles from Geotechnical Data	1063
S. D. Werner H. S. Ts'ao	Effect of Local Site Conditions on Spectral Amplification Factors	1077
I. Lam C. F. Tsai G. R. Martin	Determination of Site Dependent Spectra Using Non-linear Analysis	1089
M. L. Traubenik J. E. Valera W. H. Roth	Effects of Soil Inertia Forces on Design of Buried Pipelines Crossing Faults	1105
C. B. Crouse B. E. Turner	Analysis of Ground Motion Spectra	1117

Index of Authors

VOLUME III

ENGINEERING MECHANICS AND STRUCTURAL DESIGN SESSION

G. C. Hart C. Rojahn	Selection of Buildings for Strong-Motion Instrumentation Using Zonation Information and Decision Theory	1135
V. V. Bertero S. A. Mahin	Need for a Comprehensive Approach in Establishing Design Earthquakes	1145
A. R. Chandrasekaran D. K. Paul	Velocity Response Spectra for Sites on Rock or Soil	1157
P. C. Chen J. H. Chen	Generation of Floor Response Spectra Directly from Free-Field Design Spectra	1169
T. Hisada Y. Ohsaki M. Watabe T. Ohta	Design Spectra for Stiff Structures on Rock	1187
A. H. Hadjian	On the Correlation of the Components of Strong Ground Motion	1199
T. Iwasaki K. Kawashima	Seismic Analysis of a Highway Bridge Utilizing Strong-Motion Acceleration Records	1211
G. C. Delfosse J. C. Miranda	Buildings on Isolators for Earthquake Protection	1223
W. J. Hall J. R. Morgan N. M. Newmark	Traveling Seismic Waves and Structural Response	1235
R. V. Whitman	Effective Peak Acceleration	1247
B. Mohraz M. L. Eskijian	A Study of Earthquake Response Spectra for Offshore Platforms	1257
J. Petrovski	Influence of Soil-Structure Interaction Effects on Dynamic Response of Large Panel Prefabricated Buildings	1269

OFFSHORE MICROZONATION SESSION

I. M. Idriss L. S. Cluff A. S. Patwardhan	Microzonation of Offshore Areas - An Overview	1281
A. S. Patwardhan	Factors Influencing Seismic Exposure Evaluation for Offshore Areas	1291
R. G. Bea M. R. Akky	Seismic Exposure and Reliability Considerations in Offshore Platform Design	1307

J. A. Fischer C. T. Spiker	Preliminary Microzonation of the Baltimore Canyon Lease Area	1329
L. A. Selzer R. T. Eguchi T. K. Hasselman	Seismic Risk Evaluation of Southern California Coastal Region	1341
J. R. Benjamin F. A. Webster C. Kircher	The Uncertainty in Seismic Loading and Response Criteria	1369
D. Nair J. B. Weidler R. A. Hayes	Inelastic Seismic Design Considerations for Offshore Platforms	1383
H. Kappler G. I. Schuëller	The Influence of Microzonation on the Reliability- Based Design of Offshore Structures	1399
B. J. Watt R. C. Byrd	Aseismic Design Considerations for Concrete Gravity Platforms	1409
Y. Moriwaki E. H. Doyle	Site Effects on Microzonation in Offshore Areas . .	1433
H. J. Swanger D. M. Boore	Importance of Surface Waves in Strong Ground Motion in the Period Range of 1 to 10 Seconds	1447
J. Kallaby W. W. Mitchell	Guidelines for Design of Offshore Structures for Earthquake Environment	1459

URBAN PLANNING, SOCIO-ECONOMICS AND GOVERNMENT RESPONSIBILITY SESSION

R. A. Olson	The Policy and Administrative Implications of Seismic Microzonation: Toward Logic or Confusion	1475
M. Abolafia A. L. Kafka	Toward a Measure of Socio-Seismicity	1489
E. Kuribayashi T. Tazaki	An Evaluation Study on the Distribution of Property Losses Caused by Earthquakes	1499
H. C. Cochrane	Potential for Inflated Building Costs after Disaster	1511
R. Themptander	Earthquake and Insurance	1525
D. R. Nichols R. A. Matthews	The U.S. Geological Survey's Role in Geologic- Related Hazards Warning	1531

Index of Authors



GEOLOGY, SEISMOLOGY, GEOPHYSICS AND

SITE EFFECTS SESSION

FALLACIES IN CURRENT GROUND MOTION PREDICTION

by

Bruce A. Bolt^I

ABSTRACT

A number of methods of predicting future earthquake intensities at a site or in a region appear to contain serious fallacious arguments. The ways that fallacies in strong motion evaluations arise are discussed and the place of observational tests is stressed. A number of general fallacies occur because of dubious assumptions on probability laws, peak acceleration, earthquake magnitude, faulting models, and the neglect of seismic surface waves. As an example, justification of important soils engineering effects calls on significant deviation from the perfect elasticity model used commonly in seismology. Yet procedures from the former studies have been transferred to the later case with little verification. The particular case of incorrect regression of intensity I_{mm} with peak acceleration A is analyzed. A more adequate regression law is

$$\log A = -0.340 + 0.313 I_{mm} ,$$

for which the intensity is assumed to have an error distribution with variance 0.25.

INTRODUCTION

There are several reasons why I think a critical look at current practices in estimating the seismic intensity and risk at a site is now an important matter for seismologists and engineers.

To begin with, the last decade has seen a great increase in the development of strong motion seismology. The stimulus has come from the engineering side, but more recently seismologists are playing a much greater role. During this time the observational base of the subject has improved, particularly with the large suite of records obtained in the 1971 San Fernando earthquake in California, but also in the recording of strong ground motions from assorted earthquakes and varying geological conditions in other parts of the world. It is natural that in the early stages of a developing subject there will be confusions and workers with diverse backgrounds will introduce terminologies and procedures not readily understandable by those from other disciplines. This situation gives rise to some muddledom and conceptual discussions which are rather woolly. A better understanding by all, in which a sounder grasp is reached, requires critical analysis of the whole subject, using the powerful elementary concepts of mechanics and scientific method. The search for fallacious reasoning in current practice of microzonation and site evaluations seems a worthwhile part of this analysis.

But there are more immediate practical reasons also. Never before has there been so great a demand for answers to questions on likely earthquake motions than at the present time. The demand comes from the public

I Professor of Seismology, University of California, Berkeley, California.

at large, from developers, from regulatory agencies, and above all from the engineering profession which must respond to design questions in a variety of circumstances and under severe architectural and economic constraints. In such circumstances it is understandable that practical pressures lead to rule-of-thumb and "black-box" methodologies that often involve rules based on unspecified assumptions. A common form is the use of computer programs which give the user no specific knowledge of inbuilt algorithms and premises. This situation is made more serious by the development of proprietary interests in the methodologies. Seismologists and engineers, as well as regulatory bodies, cannot be expected to abandon readily methods which they have clung to for many years and precedents which they feel must be justified under post facto criticism. It is natural to feel that prestige is at stake and that, further, a change in past positions will lead to radical modifications of the whole way of proceeding - an appalling conclusion.

Another reason for a critique is simply that, as scientists, we must continually discuss the bases of our predictions, try to develop more thorough-going theories, and continually compare the conclusions of these theories with the new data which come to hand. In the last decade, I have been personally involved in a wide variety of studies of strong ground motion, ranging from requirements for the Alaska pipeline to nuclear siting and the checking of hospital and dam safety (1,2). I have been struck by the probing questions asked by the engineers involved in these projects and the difficulties in giving useful seismological responses. Happily, the situation is improving to some extent, but many problems remain on which much research has to be done. Nevertheless, both seismologists and engineers have an obligation to point out inconsistencies in the arguments now used and, if possible, suggest sounder rules. In what follows I can take up only a few of the arguments used in predictions of earthquake intensity and draw attention to certain problems with them. The list is not intended to be complete and, in the short space available, it is not possible to refer to all published treatments of the various points. The main aim is to highlight certain general difficulties in the subject at the present time, rather than analyze specific ones in detail - a procedure which is much more suitable in special research papers.

ARGUMENTS AND CONCLUSIONS ON INTENSITY

Predictions on earthquake intensity at a site, whether deterministic or probabilistic, must be made for engineering and planning purposes, whether or not we can prove everything that is asserted. The fact that we cannot offer a proof for each point in the argument does nothing whatever to show that the ground motion prediction is false. Thus, if the critic in a nuclear regulatory agency hearing demonstrates that the ground motion assessment for the site has not been proved, he cannot go on to imply that the assessment must be false. Indeed, the critic would then himself be committing a most serious fallacy - the fallacy of ignoring the point. If the assessment of ground motion is to be shown to be false, then the critic must offer a disproof of it; the fact that a full proof, in the logical sense, cannot be offered at that time is not enough. The criticism does, of course, reduce the probability of the assessment to some extent and may open the way for a sounder treatment.

Let us consider the case of a microzonation of a city. Microzonation based on, say, the recording of microseisms at sites around the city or

surficial soil properties might take the form of a map which is presented to the authorities as a basis for zoning (see Figure 1). Now I happen to believe that some of the justifications for this type of microzonation are invalid arguments, that is, ones in which the conclusions do not follow from the kind of measurements on which they are based. In other words, the arguments commit a fallacy. However this may be, the fact that the argument is invalid by no means shows that the prediction on the distribution of intensity across the city in a future earthquake will be found to be false. (Of course, the earthquake may show that it is quite different, also, as in the case of Bucharest in the 1976 Romanian earthquake (3).) It is easy enough to see from experience and basic physical principles that something is likely to be the case, but when asked to prove it in a strict way, we cannot do it. Rather, it is easy to fall into fallacious arguments in the course of making the attempt. What is important is that arguments on microzonation and site response be written down clearly with all assumptions stated so that critics can draw attention to the difficulties.

So far as possible, because assertions concerning future strong ground motion cannot usually be proved in any formal way, it is better to treat these opinions as hypotheses which have certain probabilities. Then these hypotheses can be tested by examining their consequences when earthquakes actually occur. These tests of strong ground motion prediction can be obtained, of course, outside the region of one's immediate interest which is one reason why studies of foreign earthquakes are of such importance to the whole subject. Yet even when such tests become available, there is a tendency to turn a blind eye to exceptions to the predicted ground motions and to welcome whatever appears to be a confirmation. A case in point is the widespread use of simple curves which correlate maximum ground acceleration with the magnitude of an earthquake (4). Many measurements from strong motion instruments now indicate that high peak accelerations occur in quite small magnitude earthquakes at near distances. Such observations must be faced up to, and either found to be expected exceptions to the rule, according to a theoretical model, or admissible data points which must be incorporated into an overall reassessment of the problem of scaling intensities with earthquake size and distance (5,6).

Of course, the criticism of established procedures is open to being labeled as "destructive." But the cleaning up of false positions is an essential stage in the development of strong motion seismology, and in the long run, is welcomed by all. The critic, of course, for his part, must be prepared to recognize that what seems to be an exception might not really be an exception at all. Thus, the peak vertical acceleration of 1.2g recorded in the Gazli earthquake in May 17, 1976, in the U.S.S.R., might not really be an exception to the distribution of vertical accelerations recorded in California (7). The explanation might be in terms of a different focal mechanism, for example. In the criticism that follows I try not only to point out the difficulties in some current procedures, but also indicate sounder approaches.

FALLACIES IN ARGUMENTS BY ANALOGY

It is generally accepted that the most reliable method of ground motion prediction is to use a value of a parameter from an identical case which has already occurred. In practice, although there is never an exact repetition, a great deal can be gained by making detailed comparisons

between the problem at hand and analogous cases. For example, the intensity distribution in Utah can be estimated from similar geological and seismological situations that have occurred in California and in other parts of the world.

It should be remarked that it is not necessary for an analogy to be complete for the inferences drawn from it to be highly reliable even though such arguments are often dismissed out-of-hand. Indeed, it can be shown that, where there are a great many common properties, the probability of the similarity of another measured property will be very high.

If p is a hypothesis which on data H entails consequences $q_1, q_2, \dots, q_n, \dots$, and if the initial probability of P on data H , $P(p|H)$, is non-zero, then it can be proved that

$$\lim_{n \rightarrow \infty} (P(q_{n+1}|q_1, q_2 \dots q_n H)) = 1. \quad (1)$$

This result may be applied to argument by analogy in the following way.

A previous earthquake x is to be compared with a design earthquake y , each of which has n observable properties x_n, y_n that are identical. We assume that the properties of x and y that are dissimilar are enumerable.

Suppose that x has the property x_{n+1} that may or may not belong to y . Consider the hypothesis p that after the dissimilarities between x and y have been enumerated, the remaining properties of x and y are identical. (Note $P(p|H)$ may be unlikely; we require it only to be non-zero.)

Then, if q_i is the result that property x is observed identical to property y_i , then p entails q_i for all i . Further, from the assumptions regarding x and y , it follows that tests $q_1, q_2 \dots q_n$ have been successful. Thus, from (1), the probability of q_{i+1} is high.

It follows that, as the number of observed identical properties of the observed and design earthquakes x and y increases, the probability that a predicted property (i.e., seismic parameter) of y is similar to an observed property of x approaches certainty. It is thus perfectly proper to weight heavily intensity observations from selected earthquakes at other times and places when considering prudent parameters for a specific site. It is a common fallacy to allow a theoretical development, based on numerous assumptions, undue weight compared with such empirical evidence.

An illustration is the unwillingness of regulatory groups to give strong weight to the observed intensities in the 1906 San Francisco earthquake when assessing ground motions for sites affected by waves from similar sources. The evidence from the 1906 earthquake ($M_S = 8-1/4$) is that no especially severe intensity of ground shaking occurred along the fault rupture. In an important paper, Louderback (8) discussed in detail the distribution of intensities in the near field of the 1906 seismic source (the San Andreas fault rupture). Louderback argued that (particularly in strike-slip faulting) because of the mean depth of the radiating source (5-10 km, say), the intensity of shaking near to a surface fault rupture is not a sharp maximum but rather there is a broad zone in which the highest intensities depend mainly on the nature of the ground and affected structures. He noted that the seismic intensity along the San

Andreas fault rupture in 1906, so far as buildings were concerned, and leaving aside the ground breakage along the fault rupture, was about VII to VIII (Modified Mercalli Scale).

My own inferences from the reports of intensity in the 1906 earthquake are, in the light of present theoretical and observations knowledge, two-fold. First, the broad average intensity in the 1906 earthquake within 10 km of the San Andreas fault would correspond to MM VIII-IX (or about 0.5g maximum peak acceleration in the frequency range 5-10 Hz). The pockets of highest observed damage in 1906 were associated with weak structures often at distances of tens of kilometers from the fault, usually where special soil conditions could be responsible for the effects. Secondly, it is fallacious to extrapolate remote measurements of intensity of ground motion to the surface faulting using essentially linear regression curves. The maximum intensity of shaking from both strike-slip and dip-slip faulting does not occur at the surface rupture, although the physical reasons are probably different in each case.

FALLACIES IN THE USE OF MAGNITUDE AS A SCALING PARAMETER

At the present juncture, probably few seismologists or earthquake engineers would be prepared to justify the use of magnitude (or moment) as the single or even dominant seismic parameter in predicting the overall seismic intensity at a site. The evidence from strong-motion records is that peak accelerations can range by factors of two and three (in the frequency band 1 to 10 Hz) for earthquakes of the same magnitude; some earthquakes of quite small magnitude, such as the magnitude 4.5 Ancona, Italy earthquakes in June 1972 and the Melindy Ranch (magnitude 4.7) earthquake of September 4, 1972, had peak accelerations exceeding 0.6g. The epicentral distances were 5 and 9 km, approximately.

The finding that magnitude is not a robust scaling factor for ground motion leaves many intensity attenuation curves (9,10), which are based on magnitude alone, without firm support. There are, however, aspects of earthquakes which are closely dependent on the magnitude parameter. These are, in particular, the meizoseismal area and the duration of the shaking (11). Both of these parameters are ultimately concerned with the dimensions of the wave generation surface and, in particular, in strike-slip faulting, the length of the fault rupture. Thus, a long, thin earthquake source, like that of 1906 in California, produces a very elongated meizoseismal area. The magnitude of a strike-slip earthquake affects duration much more than it affects peak acceleration, because the larger the magnitude the greater the length of ruptured fault and hence the more extended the area from which the seismic waves are progressively emitted.

The intensity of shaking is, of course, both mitigated and changed in character as time goes on. The further the site is away from the ruptured fault the more on the average will the wave amplitudes decay, the higher frequencies being attenuated more severely than the lower ones. If San Francisco were subjected to shaking from a magnitude 8 earthquake on the San Andreas fault, for example, the highest amplitudes of the high-frequency seismic waves would come from the part of the fault which ruptured adjacent to the site. As the rupture extended along the San Andreas fault north and south for hundreds of kilometers, the waves reaching San Francisco would change their frequency content markedly, with more and more a shift to longer periods. Most structures would, therefore, be subjected to loadings

which are moving further away from the main frequency band of engineering response.

Of the source parameters presently defined, perhaps stress drop is the most satisfactory to describe the local intensity of shaking. The increments of stress drop on the radiating fault adjacent to the site will be decisive in producing the highest pulses of high frequency energy. Further, unlike magnitude or moment, the stress drops are local, not global, phenomena and depend on the local properties and stress conditions of the rock. If it is accepted that stress drop is the dominant parameter to scale high frequency spectra at a local site, then a consequence appears to be that the relevant scaling, after certain minimum values are reached, is not dominantly related to the length of the fault nor to the ultimate magnitude. Thus, in my mind, values of acceleration recorded in the near field in the 1940 El Centro, 1966 Parkfield, 1967 Koyuna, and 1973 Managua earthquakes should be given considerable weight in estimating the expected acceleration values near to a strike-slip fault source of much larger magnitude earthquakes.

FALLACIES IN PROBABILITY ESTIMATION

In evaluating the probability of predicted seismic site parameters, two important considerations are sometimes overlooked. First, a methodology commonly followed nowadays requires the joint assertion of a number of propositions. These propositions are often not statistically independent but are assumed related to each other in some way (such as the common but perhaps ill-founded view (see below) that the peak acceleration is related to the fault rupture length). Secondly, in calculating the joint probability, the product rule must be used correctly. In application, the rule is liable to become: the probability of the conjunction of two propositions on given data is the product of their separate probabilities on those same data. This is false when there is a dependence between them.

As an illustration, let us consider just four propositions that are proposed to hold at the same time during the lifetime of a structure.

- a = a peak acceleration (or spectral scale parameter) will occur greater than a.
- m = an earthquake of magnitude (or moment) will occur greater than m.
- d = a fault rupture will occur within distance d of the site.
- r = a transfer parameter (reciprocal attenuation index, focussing, etc.) will pertain greater than r.

Then the joint probability of these four events is (with an order that allows for the main dependencies)

$$P(amdr|H) = P(d|H) P(m|dH) P(r|mdH) P(a|rmdH). \quad (2)$$

With only these four factors, and even allowing odds as large as 10 per cent for each, the probability of the joint occurrence of all four assertions is of order 10^{-4} . Those who insist on "conservative" (high) values for a, m, and r and (low) values of d often produce quite remote probabilities for the joint occurrence. Any judgment on risk that does not treat the situation in this way must be suspect.

INCORRECT REGRESSION MODELS

Two correlations between empirical strong-motion parameters have come to play a central role in the forecasting of seismic intensities. The first is a regression of the magnitude M of an earthquake on the logarithm of the length of fault rupture L of the form

$$M = a + b \log L . \quad (3)$$

$\log L$ has also been regressed on M and quite wrongly used to predict a magnitude, given a fault rupture length (11). Even when, however, the correct regression (1) has been used to predict a probable size of an earthquake at a site near to an active fault, a fallacy of a different type has been incorporated in the analysis in most cases. The fallacy is that the usual least-squares fitting of a and b in (1) assumes that all error resides in the measurement of magnitude and that the observations of L are error-free, despite disclaimers by geologists. A correct regression scheme involves the simultaneous assumption of random variation in both the dependent and independent variables, although the scatter in the measurements of surface faulting is probably the greater. Appropriate statistical models are available (12).

A similar regression model arises in correlations of peak acceleration A (cm sec^{-2}) with the maximum Modified Mercalli Intensity I_{mm} of the earthquake in question. Three linear solutions (6,13,14) with somewhat different data sets are, in order:

$$\log A = 0.26 + 0.24 I_{mm} , \quad (4)$$

$$\log A = -0.041 + 0.308 I_{mm} , \quad (5)$$

$$\log A = 0.014 + 0.30 I_{mm} . \quad (6)$$

In all these fits, no formal account is taken of the effect of the variance in the statistical distribution of the observed intensity. While the whole question of estimation of intensity is now under substantial review, it is clearly possible from the published felt reports and descriptions of damage of each earthquake to produce a frequency distribution of elements in the intensity scale. As an example, such an assessment has been done for this study in the case of 36 U.S. earthquakes listed in Table 1, all of which have peak accelerations recorded by instruments in the meizoseismal zone. An example of the frequency distribution obtained is shown in Figure 2 for the Kern County earthquake of July 21, 1952. (The variable widths of the histogram rectangles reflects the adopted method of allocating weights to each element in the intensity scale, but the details are not of importance to the present argument.) What can be seen from Figure 2 is that the various elements, given their allocated weights, range from a low of VI to a high IX. The central tendency is not strong, but a value (in Arabic numerals) of about 8.6 might be chosen as a representative "maximum" intensity for this particular earthquake. (We take the upper quartile line rather than the actual highest element which is often abnormal given the whole body of observations.) It can also be seen from the distribution of Figure 2 that a standard error yielding $\sigma^2 = 0.25$ (intensity units) is a reasonable value to indicate the scatter about the adopted value. Such estimates of upper tendency and of variance are probably precise enough for the present purpose, but the question of sensitivity needs more detailed work. The method illustrated in Figure 2 yielded "maximum" intensities and peak accelerations listed in

Table 1. These values were fitted to a linear form like (4), (5), and (6) on the assumption that the ratio of the standard deviations of the two variables are constant. In this case, the slope b is given by

$$b = \frac{\sum x_i y_i}{\sum x_i^2 - (n-1)\sigma^2},$$

where x is the intensity and y the log acceleration, measured about the mean values. The data used are shown as crosses in Figure 3. Regressions were then made for $\sigma^2 = 0$ and $\sigma^2 = 0.25$ for all intensity values. The latter assumption is not exact but serves as an illustration of the effect of allowing for errors in the independent variable. The two least-squares lines obtained are shown in Figure 3. There is a substantial difference in slope between the error-free (EF) and error (E) lines. The numerical results are

$$\log A = 0.160 + 0.245 I_{mm}, \quad (\sigma^2 = 0) \quad (7)$$

$$\log A = -0.340 + 0.313 I_{mm}. \quad (\sigma^2 = 0.25) \quad (8)$$

For comparison, in Figure 3 is shown the fits by Neumann (13), and Trifunac and Brady (14). These two solutions are surprisingly so close as to preclude two lines being shown in the figure. It is not suggested that the statistical model defined by equation (6) is the most satisfactory one for the present work. Mark prefers (11) the use of a bi-variate normal population as a suitable approximation. The actual form of the probability distribution will depend upon the distributions obtained from appropriate weighting of the intensity data.

TENABILITY OF VERTICAL PROPAGATING WAVE TESTS

For a decade or more, soils engineers, with few exceptions, have steadfastly developed models for testing wave propagation through surficial layers which assume that the incident seismic waves travel vertically upwards. The theoretical justification is the significantly lower velocities of the soils compared with the underlying rock structure and the predicted motions have been checked against strong motion records from a limited number of sites where information is available on the soil and rock velocities. Such special programs are justified by the finding that the elastic properties of soils are not limited to those normally assumed in seismology, i.e., perfect and isotropic elasticity, homogeneous layering, and infinitesimal Hookian stress-strain relations. Recently, however, the same methods, validly developed for special soils applications, have been carried over to predictions of strong ground motions in situations where the seismological assumptions hold to a close approximation. Yet even in such geological conditions where a well-tested and highly-developed elastic theory is available, the assumption of vertically propagating waves has proved to have an adhesive quality.

Among the questions that have now been raised concerning the assumption of vertical wave propagation for site evaluation, two are perhaps most important. First, in the near field of the earthquake source, it has been observed and theoretically predicted that in certain directions a wave pulse will spread outwards associated with the relaxation of the double couple of forces at the fault. A pulse of this kind was recorded at station 2 in the 1966 Parkfield earthquake and at the Pacoima station in the 1971 San Fernando earthquake (see last section for further discussion). These pulses consist predominantly of SH motions which reach the surface obliquely from

the fault surface. Their periods are relatively long, giving wave lengths of the order of many hundreds of meters which are much greater than the thickness of the surficial soil layers usually considered in the upward traveling wave models. In the treatment of such pulses, simple geometric ray theory is unsatisfactory, and arguments which depend on sharp upward refraction through thin surface soil layers can, at the best, be crude approximations.

More serious criticism of the model is the omission of surface waves. Surface waves of both Love and Rayleigh type have been observed for many geological conditions by both regular seismographs in the far field and strong motion instruments in the near field (15). They have been shown to exist for frequency ranges of engineering interest, namely from frequencies of about five Hertz to periods of many seconds in appropriate circumstances. A recent informative study of the development of surface waves from the fault source of the 1971 San Fernando earthquake, across profiles of strong motion accelerometers in the Los Angeles area, has been given by Hanks (15). For small structures the effect of surface waves traveling in the surficial layers may not be of great engineering importance, but for large structures, such as long bridges and large nuclear reactors, this is not the case. For example, foundation mats of some of the most recently proposed nuclear reactors have dimensions of 150 meters, which are close to the quarter wavelengths of surface waves which are likely to be present near to the source of earthquakes. Structural engineers have commenced to consider these effects (16) and the literature contains numerous seismological discussions. It should be kept in mind that even for a single layer of unconsolidated alluvium over an elastic half-space the wave patterns associated with Rayleigh waves may be rather complicated. In one calculation (17), in which the alluvium thickness was taken as 100 meters, it was shown that a complicated dispersion pattern containing the fundamental first and second high Rayleigh modes might be expected. It was found that in the frequency diagram all of the modes passed very steeply through the region of dominantly vertical motion; hence, most of the surface displacements would be horizontal, except at the highest frequencies.

ASSUMPTIONS ON RISK ESTIMATION

A resilient but ill-founded assumption is that earthquakes in a region occur in an independent manner so that a Poisson distribution is a suitable one for summarizing their occurrence. This assumption of independence of events is contrary to the general physical model of earthquake genesis which assumes that the crust is slowly straining so that, as time goes on, the likelihood of another large earthquake becomes greater. Similarly, in after-shock sequences, it is assumed physically that as the sequence progresses less strain is available and hence the likelihood of another earthquake decreases.

Most recent risk mapping based on probabilistic models in the United States (17) has assumed the Poisson law. The question whether this assumption gives rise to adequate estimates of risk, even though it violates the physical assumptions, has not been much explored. Yet there are alternative statistical treatments in the theory of point processes which adequately represent the situation. One of these is the Hazard function $h(t)$. Let q be the statement "an earthquake occurs in $(t, t+dt)$ " and p be "the last earthquake was at $t = 0$." Then

$$h(t) dt = P (q | p) \quad (9)$$

and, therefore

$$\begin{aligned} h(t) &= f(t) / (1 - F(t)) \\ &= - \frac{d}{dt} (\ln (1 - F(t))). \end{aligned} \quad (10)$$

The Hazard function in its classical form above fails to take account of two important aspects of the memory problem. First, it is not so much the last event which is of interest as the origin of the interval, but that ($p =$) "an event of consequence occurred at $t = 0$." The treatment of this is expressed in terms of the auto-intensity probability function

$$h_0(t) dt = P (q | p) . \quad (11)$$

The second problem is that in any seismicity study the risk depends not only on the time sequence but on the size M of the previous earthquakes. We therefore require a joint probability $H(t, M)$ which incorporates the fundamental notion of the Hazard function with the probability law for statement s that "the earthquake has magnitude M ." On the assumption of independence, we can write

$$\begin{aligned} H(t, m) &= P (q \text{ and } s | p) \\ &= h(t) dt \cdot P (M > m) . \end{aligned} \quad (12)$$

For non-independence, the marginal distribution becomes rather complicated.

SIMPLISTIC FAULT SOURCE MODELS

Working mainly with western U.S. earthquakes, it is easy to fall into an unquestioned position that the source of damaging earthquakes is the rupture of a single fault. Indeed, many large historical earthquakes in California and Nevada have been clearly the consequence of the sudden dislocation of a shallow fault of simple geometry with offsets quite evident at the surface. Yet there is much evidence that this earthquake source mechanism is not universal; crustal ruptures may be rather widespread and many stranded. Case histories may be cited from the Fairview Peak-Dixie Valley earthquakes of 1954, from Japan, New Zealand, and Italy. One illustration is the Friuli earthquakes in 1976 in northern Italy. Based upon the structural geology and well-located aftershocks (see Figure 4), the inference is that slip occurred on many thrust faults in the hypocentral region.

Adoption of the multiple fault-slip model may lead to radical changes in some of the methodology now in vogue for the prediction of strong ground motion or microzonation of a region. For example, the use of a fault length formula such as equation (3) would be fallacious.

Finally, it may be worthwhile pointing out again that the fault source model, whether simple or complex, does not lend itself to the present chain of reasoning which uses the peak horizontal ground acceleration as the key scaling parameter for design spectra. As was mentioned above, there is seismological evidence that near to a rupturing fault a pulse of approximately one second duration propagates outwards and affects structures on the surface. This pulse, however, may not have the largest accelerations in the record, although it may be associated with the greatest kinetic energy.

It has been pointed out from studies of the damaged Olive View Hospital in California in the 1971 San Fernando earthquake (17) that failures in that structure apparently occurred during the long duration pulse that can be seen in the Pacoima velocity record about three seconds after the instrument triggered. The hospital structure was forced out of its elastic range of response by this motion with significant damage to the supporting columns of the lower floors. The subsequent strong ground motion, which was of higher frequency and contained a peak acceleration greater than 1.0g, then shook the damaged building about its new configuration without further significant inelastic displacements.

The lesson is that a line of argument which is intended to be cautious in design, if based solely upon the large values of acceleration at high frequencies, may miss its goal and there may be no assurance of sufficient structural resistance. As more near-field seismograms come to hand, there will be an opportunity for rigorous testing of the present arguments on intensity and microzonation and the elimination of prejudicial fallacies.

ACKNOWLEDGMENTS

Mr. Mark Rovetta worked up the intensity reevaluations associated with Figures 2 and 3. This study was supported by NSF AEN74-21548 and NSF PFR78-02650.

BIBLIOGRAPHY

1. Bolt, B.A., R.G. Johnston, J. Lefter, and M.A. Sozen, (1975). "The Study of Earthquake Questions Related to VA Hospital Facilities," Bull. Seism. Soc. Am., 65, 937-950.
2. Donovan, N.C., B.A. Bolt, and R.V. Whitman, (1976). "Development of Expectancy Maps and Risk Analysis," ASCE Convention, Preprint 2805, 1-19.
3. Berg, G.V., B.A. Bolt and others, (1977). "Earthquake in Romania, March 4, 1977," Newsletter EERI, 11, 1-41.
4. Esteva, L., and E. Rosenblueth, (1964). "Spectra of Earthquakes at Moderate and Large Distances," Soc. Mex. de Ing. Sismica, 2, 1-18.
5. Seekins, L.C., and T.C. Hanks, (1978). "Strong-Motion Accelerograms of the Oroville Aftershocks and Peak Acceleration Data," Bull. Seism. Soc. Am., 68, 677-690.
6. Murphy, J.R., and L.J. O'Brien, (1978). "Analysis of a Worldwide Strong Motion Data Sample to Develop an Improved Correlation Between Peak Acceleration Seismic Intensity and Other Physical Parameters," Nuclear Regulatory Commission Report NUREG-0402.
7. Bolt, B.A., and R. Hansen, (1977). "The Uplift of Objects in Earthquakes," Bull. Seism. Soc. Am., 67, 1415-1427.
8. Louderback, G.D., (1942). "Faults and Earthquakes," Bull. Seism. Soc. Am., 32, 305-330.
9. Schnabel, P.B., and H.B. Seed, (1973). "Accelerations in Rock for Earthquakes in the Western United States," Bull. Seism. Soc. Am., 63, 501-528.

10. Geller, R.J., (1976). "Scaling Relations for Earthquake Source Parameters and Magnitudes," Bull. Seism. Soc. Am., 66, 1501-1523.
11. Mark, R.K., (1977). "Application of Linear Statistical Models of Earthquake Magnitude versus Fault-Length in Estimating Maximum Expectable Earthquakes," Geology, 5, 464-466.
12. Bolt, B.A., (1978). "Incomplete Formulations of the Regression of Earthquake Magnitude with Surface Fault Rupture Length," Geology, 6, 233-235.
13. Neumann, F., (1954). "Earthquake Intensity and Related Ground Motion," Univ. Press, Seattle, Washington, 77 pp.
14. Trifunac, M.D., and A.G. Brady, (1975). "On the Correlation of Seismic Intensity Scales with Peaks of Recorded Strong Ground Motion," Bull. Seism. Soc. Am., 65, 139-162.
15. Hanks, T.C., (1975). "Strong Ground Motion of the San Fernando, California, Earthquake," Bull. Seism. Soc. Am., 65, 193-235.
16. Wolf, J.P., (1976). "Soil-Structure Interaction with Separation of Base Mat from Soil (Lifting-Off), Nuclear Engineering and Design, 38, 357-384.
17. Mooney, H.M., and B.A. Bolt, (1966). "Dispersive Characteristics of The First Three Rayleigh Modes for a Single Surface Layer," Bull. Seism. Soc. Am., 56, 43-67.
18. Algermissen, S.T., and D.M. Perkins, (1976). "A Probabilistic Estimate of Maximum Acceleration in Rock in the Contiguous United States," U.S. Geological Survey Open File Report 76-416.
19. Bartole, R., and others, (1976). "Earthquake Catalogue of Friuli-Venezia Giulia Region - From Roman Epoch up to 1976," Bollet. di Geofis. Teor. et Applic., XIX, 72, 300-334.
20. Bertero, V.V., S.A. Mahin, and R.A. Herrera, (1978). "Aseismic Design Implications of Near-Fault San Fernando Earthquake Records," Earthquake Eng. and Struct. Dyn., 6, 31-42.

TABLE 1. Revised Acceleration-Intensity Data

<u>Earthquake</u>	<u>Date</u>	<u>Max.Acc.(xg)</u>	<u>Upper Intensity</u>
Long Beach	03/10/33	0.15	8.4
Los Angeles	10/02/33	0.07	7.5
Ferndale	07/06/34	0.16	5.9
El Centro	12/30/34	0.18	7.6
Helena, Mont.	10/31/35	0.15	8.5
Ferndale	02/06/37	0.04	7.0
Ferndale	09/11/38	0.13	6.8
El Centro	05/18/40	0.29	9.8
Santa Barbara	06/30/41	0.21	7.8
Ferndale	10/03/41	0.12	6.9
Los Angeles	11/14/41	0.14	8.6
Hollister	03/09/49	0.18	7.0
Seattle, Wash.	04/13/49	0.24	8.5
El Centro	01/23/51	0.03	6.7
Ferndale	10/07/51	0.12	7.0
Kern County	07/21/52	0.19	8.6
Ferndale	09/22/52	0.07	6.0
San Luis Obispo	11/21/52	0.05	7.0
El Centro	06/13/53	0.03	6.9
Taft	01/12/54	0.07	6.3
Hollister	04/25/54	0.05	7.2
El Centro	11/12/54	0.03	5.8
Eureka	12/21/54	0.12	7.3
El Centro	12/16/55	0.01	6.2
Port Hueneme	03/18/57	0.08	7.3
San Francisco	03/22/57	0.07	7.5
Hollister	01/19/60	0.05	6.6
Ferndale	06/05/60	0.05	6.4
Hollister	04/08/61	0.13	7.3
Olympia, Wash.	04/29/65	0.07	8.4
Parkfield	06/27/66	0.51	7.5
El Centro	08/07/66	0.02	6.4
Eureka	12/10/67	0.21	6.3
Borrego Mtn.	04/08/68	0.10	7.4
Lytle Creek	09/12/70	0.04	7.4
San Fernando	02/09/71	1.25	10.9

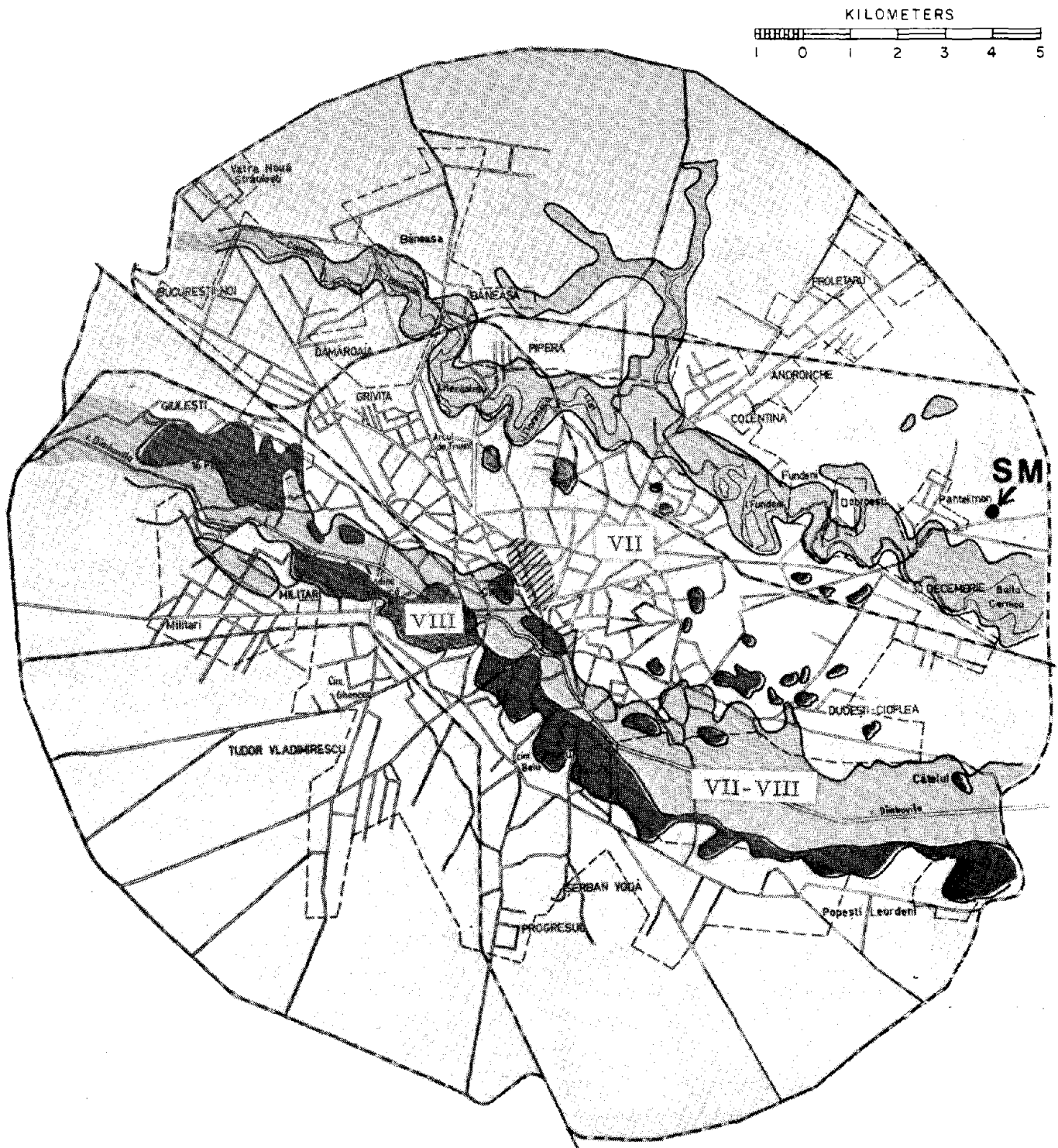


FIG. 1. Three microzonation levels for Bucharest before March 4, 1977 earthquake. Hatched area shows area of most damage; SM is site of accelerogram record.

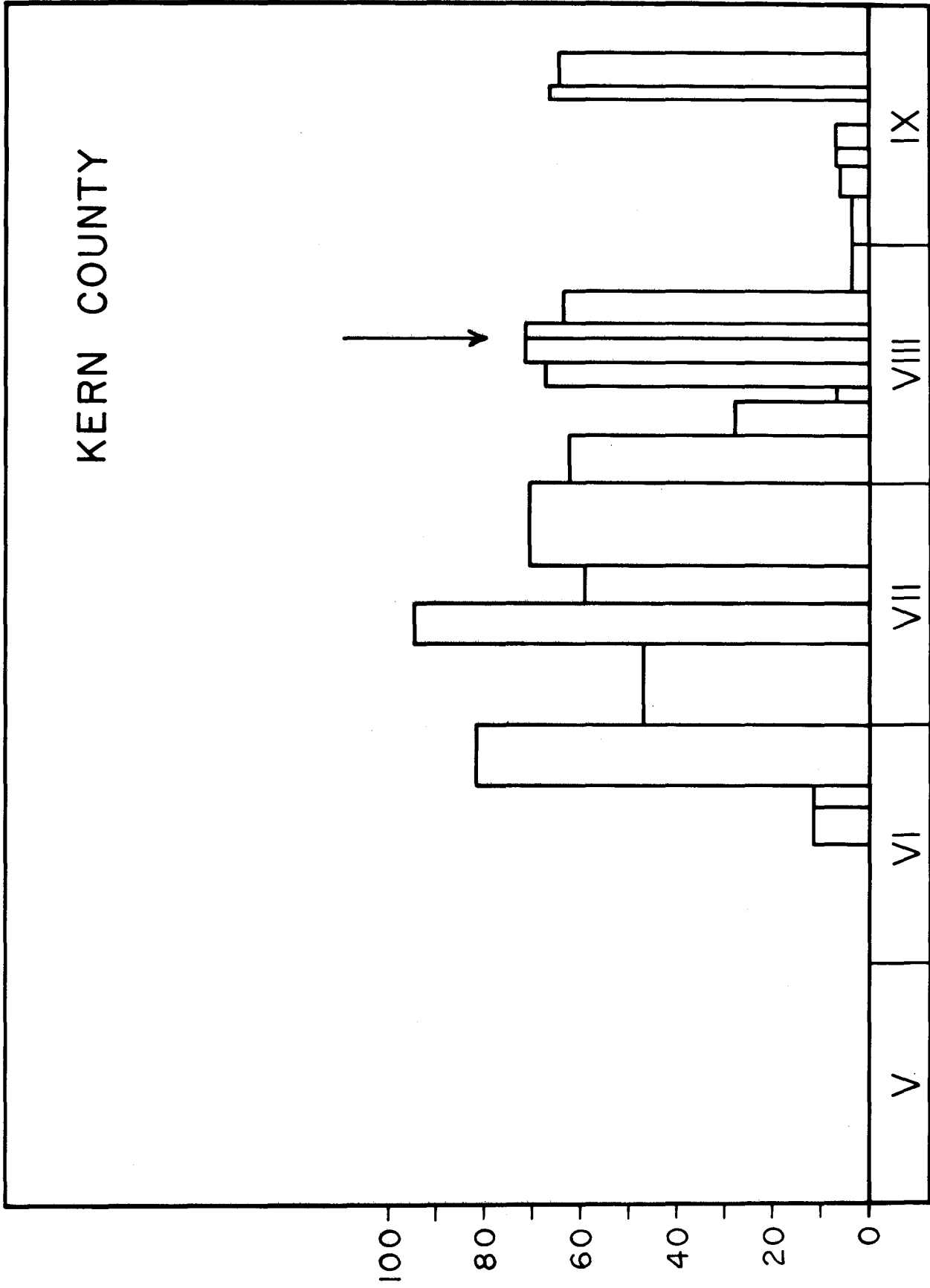


FIG. 2. Frequency histogram for intensity reports of modified Mercalli intensity, Kern County earthquake, July 21, 1953.

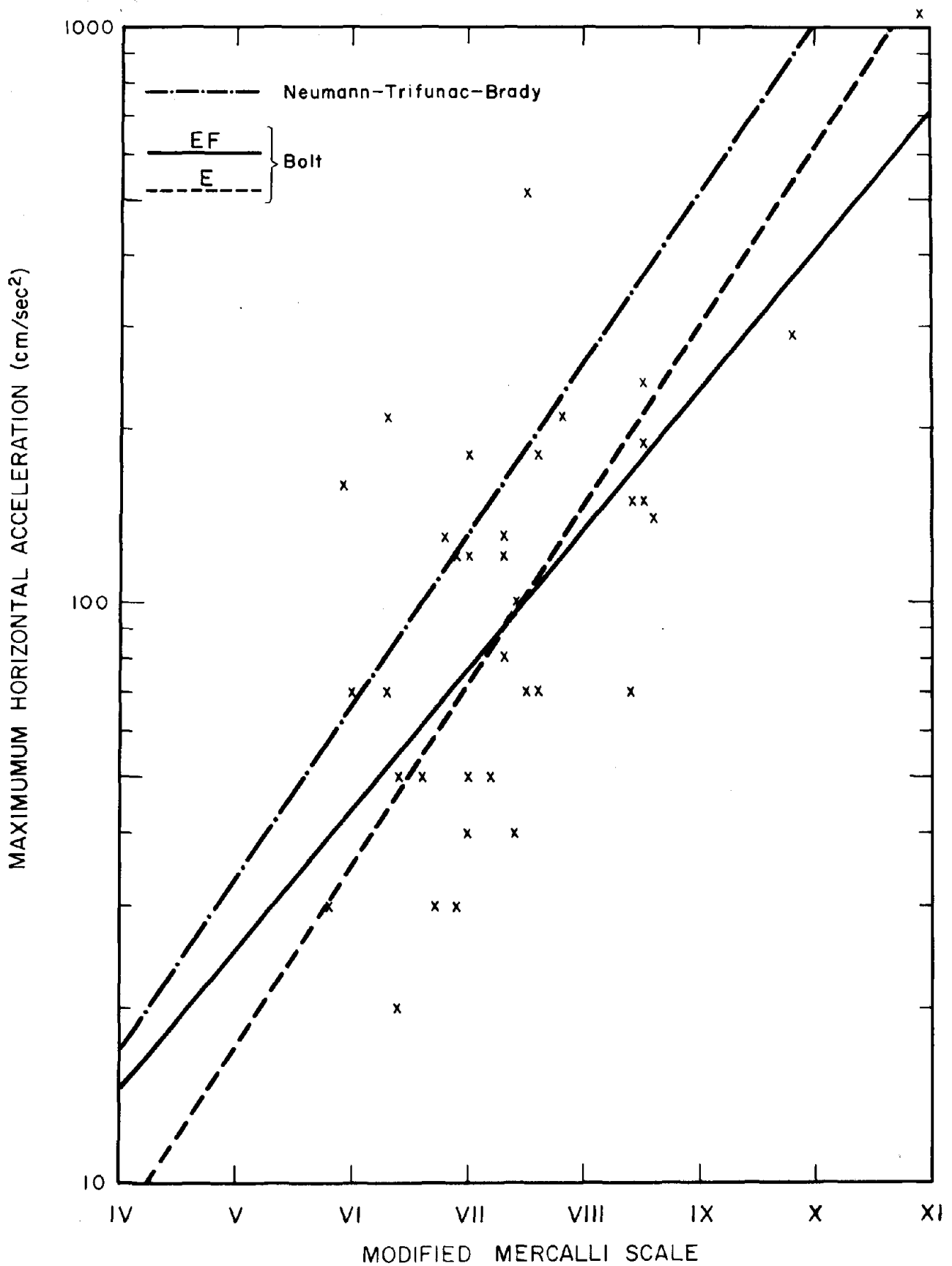


FIG. 3. Regression lines and data crosses for present study.

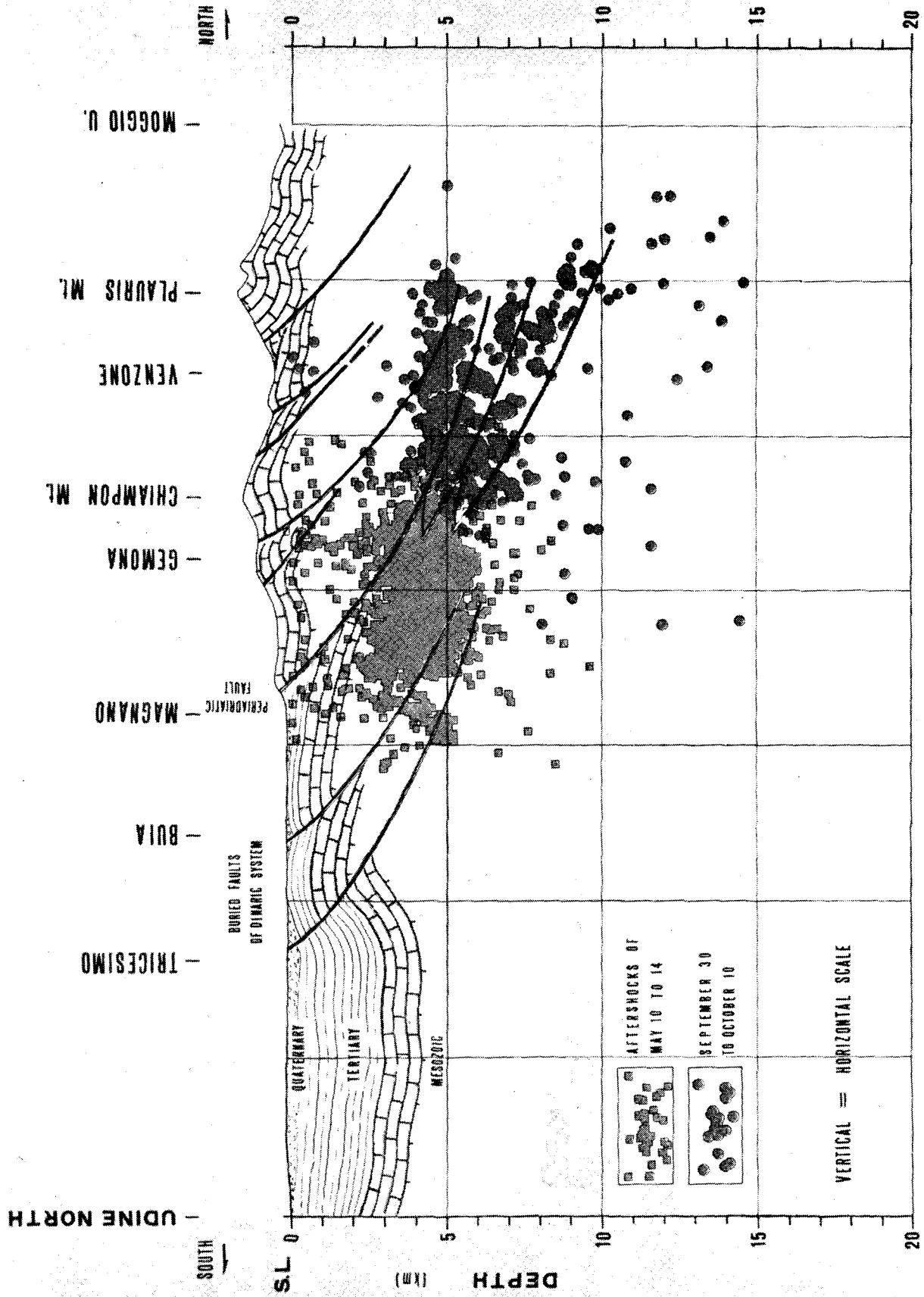


FIG. 4. Crustal cross section and aftershocks of Friuli earthquake, Italy, May 6, 1976.

INTENTIONALLY BLANK

634

ZONING FOR THE HAZARD OF SURFACE FAULT RUPTURE IN CALIFORNIA

by

Earl W. Hart¹

ABSTRACT

Under provisions of the Alquist-Priolo Special Studies Zones Act of 1972, the State of California establishes regulatory zones in order to mitigate the hazard of surface fault rupture. The regulatory zones are delineated to encompass traces of the San Andreas and other hazardous faults. Regulation of most proposed development projects within the zones is carried out by affected cities and counties. In most cases, geologic site-investigations are required prior to development and structures for human occupancy cannot be sited astride active faults that are identified. The investigative reports are reviewed by local government for adequacy and subsequently filed with the State Geologist. Although the fault-rupture hazard is generally considered to be the most readily mitigated geologic hazard, accurate location and evaluation of faults appear to be more difficult than initially anticipated.

INTRODUCTION

Surface fault rupture generally has been viewed by geologists as the most easily avoidable of the several geologic hazards. This view is based on the well-defined features and observed historic rupture along the San Andreas and other highly active faults. Thus, following the 1971 San Fernando earthquake and associated fault ruptures in southern California, the State Legislature passed the Alquist-Priolo Special Studies Zones Act in 1972. Under this Act, zones are established to regulate development near the traces of potentially hazardous faults. This is the only law of its kind in the United States.

ALQUIST-PRIOLO SPECIAL STUDIES ZONES ACT

This Act, also known as Chapter 7.5 of Division 2 of the Public Resources Code, was signed into law in 1972 and amended in 1974, 1975 (twice) and 1976. Responsibilities for carrying out the Act are shared among state agencies and local governments. Simply stated, the State Geologist is responsible for delineating Special Studies Zones; cities and counties affected by the zones must regulate certain development "projects" in which structures for human occupancy are planned within the zones; and the State Mining and Geology Board establishes specific "Policies and Criteria" to guide the cities and counties in their implementation of the law. The specific requirements and functions of the Act are identified in table 1 and the full text of the law is given in Appendix A. The Policies and Criteria, which have the affect of law, are summarized in table 2. Most important of the latter are the definition of an "active fault" and the Specific Criteria.

¹Senior Geologist, Supervisor of Fault Zoning Program, California Division of Mines, San Francisco, California.

Preceding page blank
Thank James F. Davis and Charles W. Jennings who reviewed this manuscript and provided useful comments.

Table 1. Summary of responsibilities and implied functions under the Alquist-Priolo Special Studies Zones Act.

State Geologist

1. Delineates Special Studies Zones; compiles and issues maps.
 - a. Preliminary Review Maps.
 - b. Official Maps.
2. Reviews new data.
 - a. Revises existing maps.
 - b. Compiles new maps.
3. Approves requests for waivers initiated by cities and counties.

State Mining and Geology Board

1. Formulates policies and criteria to guide cities and counties.
2. Serves as Appeal Board.

Seismic Safety Commission

1. Advises the State Geologist and the State Mining and Geology Board.

Cities and Counties

1. Regulates "project" developments within Special Studies Zones.
 - a. Determines need for site investigations.
 - b. Reviews investigative reports.
 - c. Submits reports to State Geologist for file.
 - d. May initiate waiver request.
 2. Approves permits for "projects".
 3. Collects fees to cover administrative costs.
-

Table 2. Summary of policies and criteria adopted by the State Mining and Geology Board. (See Appendix B, Ref. 2 for full text.)

Policies

1. Suggests methods relating to review of Preliminary Maps prior to issuance of Official Maps.
2. Defines active fault (equals potential hazard) as a fault that has had surface displacement during Holocene time (last 11,000 years).

Specific Criteria

1. No structures for human occupancy are permitted on the trace of an active fault. (Unless proven otherwise, the area within 50 feet of an active fault is presumed to be underlain by an active fault).
2. Requires geologic report directed at the problem of potential surface faulting for all projects defined by the Act (Section 2621.6).
3. Requires that geologic reports be submitted to State Geologist for open file.
4. Requires cities and counties to review geologic reports for adequacy.
5. Permits cities and counties to establish standards more restrictive than the policies and criteria.
6. Defines (a) "project", (b) structure for human occupancy, and (c) new real estate development.

STATE PROGRAM FOR ZONING FAULTS

Section 2622 of the Alquist-Priolo Special Studies Zones Act requires that the State Geologist shall do the following:

1. "Delineate...appropriately wide special studies zones to encompass all potentially and recently active traces of the San Andreas, Calaveras, Hayward, and San Jacinto Faults, and such other faults or segments thereof, as he deems sufficiently active and well-defined as to constitute a potential hazard to structures from surface faulting or fault creep."
2. Compile maps of Special Studies Zones and submit such maps to affected cities, counties, and state agencies for their review and comment. Following appropriate reviews, the State Geologist must provide Official Maps to the affected cities, counties, and state agencies.
3. Continually review new geologic and seismic data in order to revise the Special Studies Zones or delineate additional zones.

As required under the Act, the State Geologist (Chief of the California Division of Mines and Geology) initiated a program early in 1973 to delineate Special Studies Zones to encompass traces of potentially and recently active traces of the San Andreas, Calaveras, Hayward, and San Jacinto faults and to compile and distribute maps of these zones. A project team, headed by this writer, was established within the Division to develop and conduct a program for delineation of the zones.

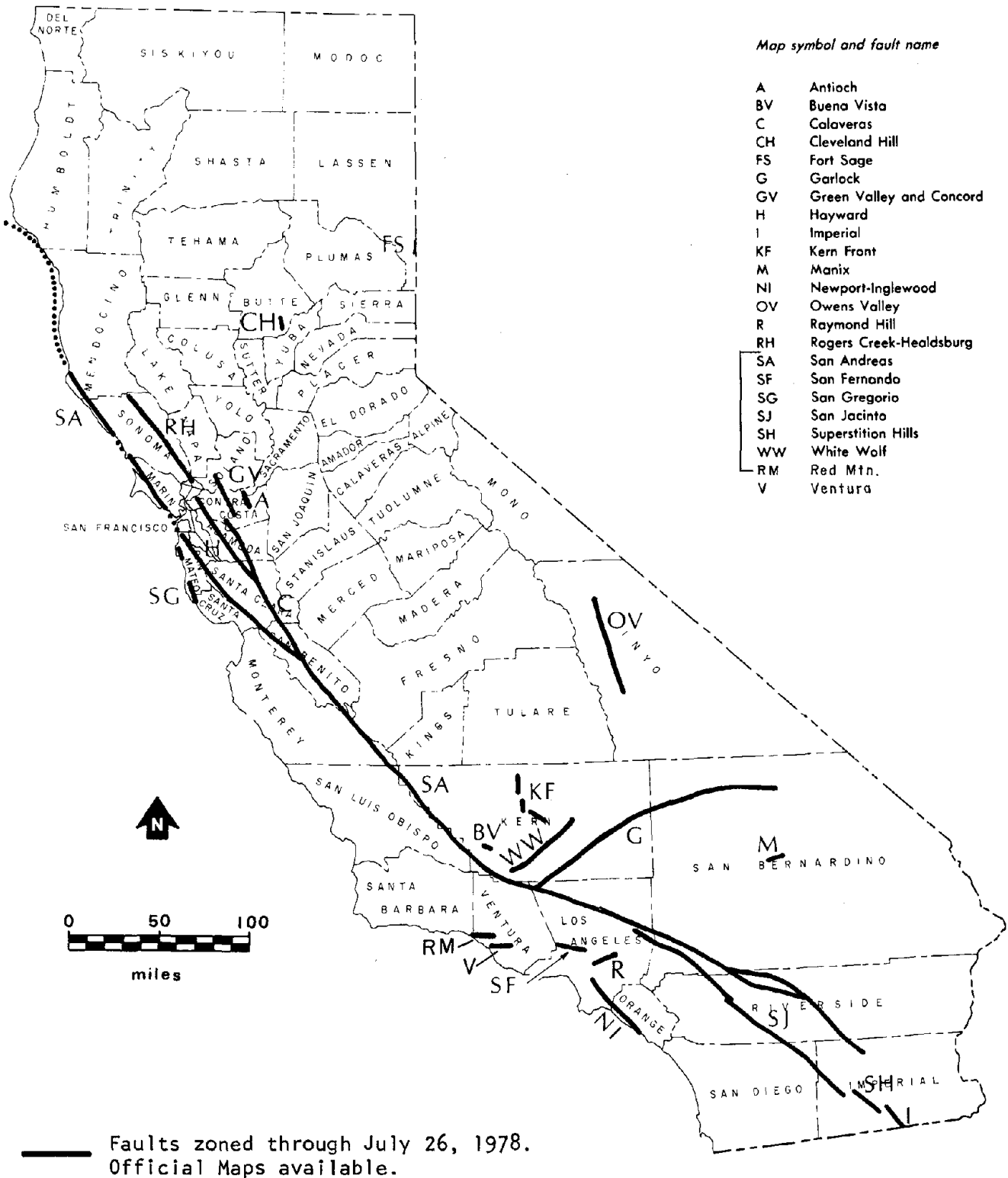
Initially, 175 maps of Special Studies Zones were delineated for the four named faults. These zone maps, issued as Preliminary Review Maps, were distributed for review by local and state government agencies on December 31, 1973. Following prescribed 90-day review and revision periods, Official Maps were issued on July 1, 1974. At that time, the Special Studies Zones became effective and implementation was required by the affected cities and counties. Official Maps of new and revised zones also were issued in 1976, 1977 and 1978, following similar formal review, for other faults considered "sufficiently active and well-defined."

As of July 26, 1978, a total of 263 Official Maps of Special Studies Zones had been issued for the faults identified in figure 1. An index map identifying the zone maps issued is provided in Special Publication 42, which is revised periodically (3). Additional faults will be zoned and some existing zones will be revised in the future. Approximately 24 counties and 64 cities are affected by the existing zones.

Definitions

In order for the State Geologist to carry out his mandate to issue zone maps, certain terms identified in Section 2622 of the Act had to be defined:

A fault is defined as a fracture or zone of closely associated fractures along which rocks on one side have been displaced with respect to those on the other side. A fault trace is the line formed by the intersection of a fault and the earth's surface. It is also the representation of a fault as depicted on a map, including maps of Special Studies Zones.



NOTE: Other potentially active faults may be zoned in the future, and some of the existing zones may be revised when warranted by new fault data.

Figure 1. Potentially active faults in California zoned for special studies under the Alquist-Priolo Special Studies Zones Act of 1972.

An active fault is defined by the State Mining and Geology Board in their Policies and Criteria (3) as one which has "had surface displacement within Holocene time (about the last 11,000 years)." The Board's definition of an active fault "is intended to represent minimum criteria only," and local jurisdictions "may wish to impose more restrictive definitions requiring a longer time period of demonstrated absence of displacement for critical structures." This definition provides specific guidance for the site investigations required by local government. It also serves as a basis for other definitions and policies of the State Geologist.

Because the Alquist-Priolo Act requires the State Geologist to establish Special Studies Zones to encompass all "potentially and recently active" traces of the San Andreas, Calaveras, Hayward, and San Jacinto faults, additional definitions were needed. Faults were defined as potentially active, and were zoned, if they showed evidence of surface displacement during Quaternary time (last 2 to 3 million years). Exceptions were made for certain Quaternary faults presumed to be inactive based on direct geologic evidence of inactivity during all of Holocene time or longer. The term recently active was not defined, as it was considered to be roughly equivalent to "potentially active."

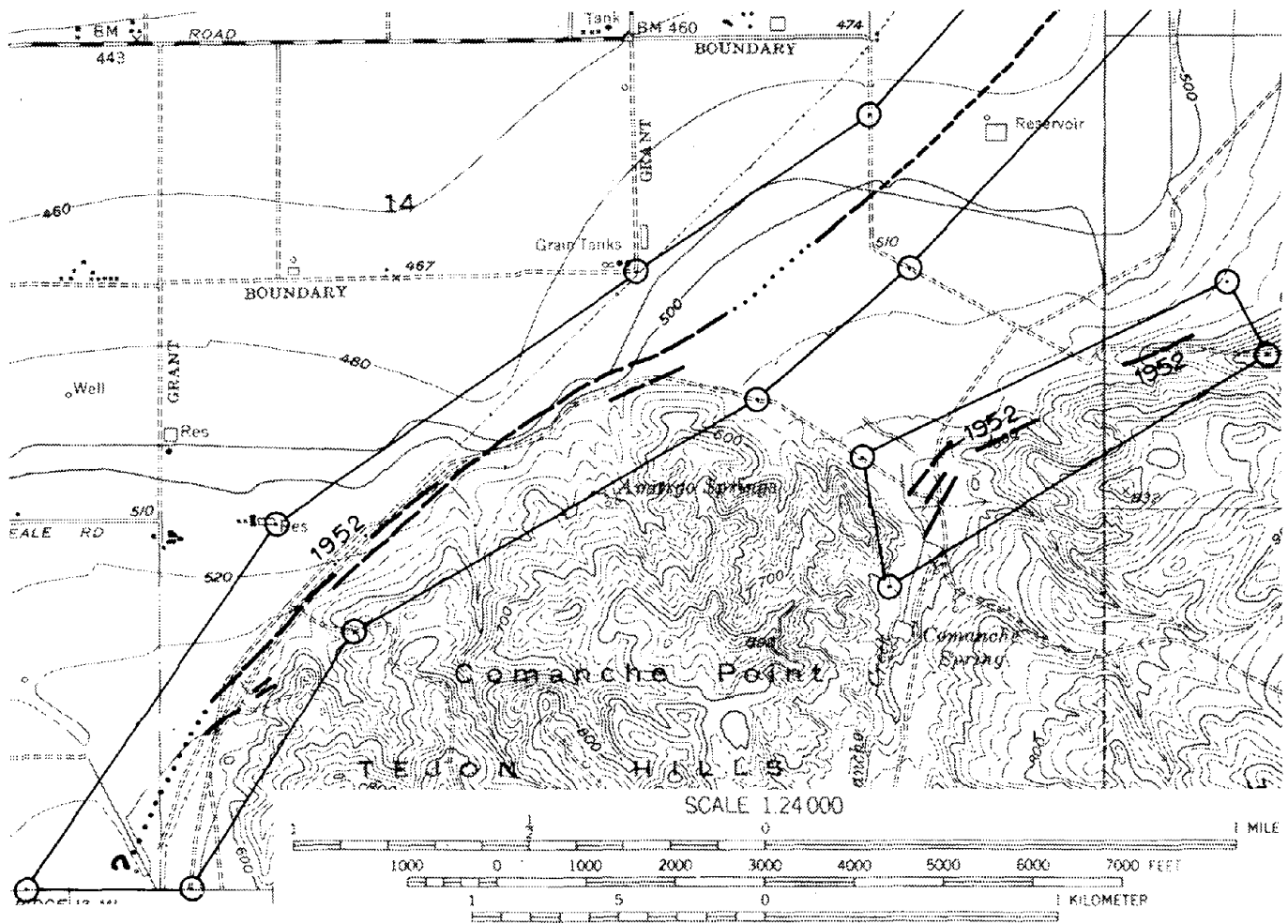
A major objective of the Division's continuing fault evaluation program is to evaluate the hundreds of remaining potentially active faults in California for zoning consideration. However, there are so many potentially active (i.e. Quaternary) faults in the State (6) that it would not be meaningful to zone all of them. In late 1975, a policy decision was made by the State Geologist to zone only those potentially active faults that had a relatively high potential for ground rupture. To facilitate this, the terms "sufficiently active" and "well-defined," from Section 2622 of the Act, were defined to apply to faults other than the four named ones. These two terms constitute the present criteria used by the State Geologist in determining if a given fault should be zoned under the Alquist-Priolo Act.

Sufficiently active. A fault is deemed sufficiently active if there is evidence of Holocene surface displacement along one or more of its segments or branches. This evidence may be directly observable or inferred and it need not be present everywhere along a fault to qualify that fault for zoning.

Well-defined. A fault is considered well-defined if its trace is clearly detectable by a trained geologist as a physical feature at or just below the ground surface. The fault may be identified by direct observation or by indirect methods (e.g. geomorphic evidence or geophysical techniques). The critical consideration is that the fault, or some part of it, can be located with sufficient precision and confidence in the field so as to indicate that the required site-specific investigations would meet with some success.

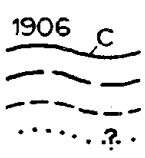
Determining if a fault is sufficiently active and well-defined is a matter of judgment. However, these definitions provide workable guidelines for establishing Special Studies Zones under the Act. More precise meanings of these terms should develop as more is learned about the techniques of evaluating the hazard of surface faulting.

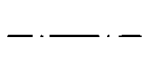
The evaluation of faults for zoning purposes is done with the realization that not all active faults can be identified. Furthermore,



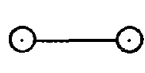
MAP EXPLANATION

Potentially Active Faults


 Faults considered to have been active during Quaternary time; solid line where accurately located, long dash where approximately located, short dash where inferred, dotted where concealed; query (?) indicates additional uncertainty. Evidence of historic offset indicated by year of earthquake-associated event or C for displacement caused by creep or possible creep.


 Aerial photo lineaments (not field checked); based on youthful geomorphic and other features believed to be the results of Quaternary faulting.

Special Studies Zone Boundaries


 These are delineated as straight-line segments that connect encircled turning points so as to define special studies zone segments.


 Seaward projection of zone boundary.

Figure 2. Example of Special Studies Zones map and explanation of map symbols.

certain faults considered to be active (e.g. because of known seismic activity at depth) are so poorly defined at the surface that zoning is impractical. Although the Official Maps of Special Studies Zones indicate that "potentially active" (i.e. Quaternary) faults are zoned under the Alquist-Priolo Special Studies Zones Act, it is emphasized that only those potentially active faults that meet the criteria of "sufficiently active and well-defined" are actually zoned.

Delineating the Special Studies Zones

Special Studies Zones are delineated on topographic base maps of the U.S. Geological Survey at a scale of 1:24,000 (1 inch equals 2,000 feet). The zone boundaries are straight-line segments defined by turning points (figure 2). Most of the turning points are intended to coincide with locatable features on the ground (e.g. bench marks, roads, streams).

Locations of Special Studies Zone boundaries are controlled by the position of fault traces shown on the Official Maps of Special Studies Zones. With few exceptions, the faults shown on the early Special Studies Zones maps were not field checked during the compilation of these maps. However, all faults zoned since 1976 have been field-checked to verify that they do meet the criteria of sufficiently active and well-defined. Zone boundaries on early maps were positioned about 660 feet (200 meters) away from the fault traces to accommodate imprecise locations of the faults and possible existence of active branches. Later zones are narrower and some zone boundaries have been positioned as close as 200 to 300 feet from the identified traces.

FAULT EVALUATION PROGRAM

This is a 10-year program, initiated in early 1976 and designed to evaluate those "other" faults identified in the Act as "sufficiently active and well-defined" (see definitions above). The need for this program is based on the recognition that effective future zoning could not rely solely on limited fault data of others. Justification of this program is discussed in more detail in California Division of Mines and Geology Special Publication 47 (2).

In order to evaluate the potentially active faults in California, the state is divided into 10 regions, and one region is evaluated each year. Evaluations for the first two years of this program have been completed and the results are summarized by Hart and others (4, 5). Based on field and aerial photographic interpretations, as well as the work of others, recommendations were made to establish new zones for segments of 6 faults and to revise existing zones for segments of 2 others. Perhaps more important is the large number of potentially active (Quaternary) faults that were not recommended for zoning because the criteria of "sufficiently active and well-defined" were not satisfied. It is recognized, however, that some of the faults not recommended for zoning may be active, at least at depth (as indicated by recorded seismicity), and future surface faulting is possible. Although public safety is of primary concern to the State Geologist, he also recognizes the difficulties in evaluating certain active faults. This is particularly true with regard to reverse faults in the Transverse Ranges where historic surface rupture has been complex and distributed over wide zones (6). Also, traces of such faults tend to be quickly obscured by debris shed from the rising mountain ranges.

IMPLEMENTATION BY CITIES AND COUNTIES

Upon issue of the Official Maps of Special Studies Zones, local jurisdictions are required to regulate certain development "projects" within the delineated zones (see Section 2621.6 of Appendix A). Specific procedures must be established to screen development permits and to notify developers if a geologic investigation is required for the development site. If an investigation is required, this must be done by a Registered Geologist (California) (table 2). The ensuing report is submitted to the city or county for review as to its adequacy. A review must be made by a Registered Geologist who may set his own minimum standards or may use guidelines provided by the State (3). Ultimately, a permit is issued (or denied) on the basis of the investigation and proposed structures are sited so as to avoid active faults that may have been identified. A copy of the investigative report is then filed with the State Geologist.

The decisions regarding the location and recency of faulting and the level of risk acceptable often are difficult to make and may be shared by the investigating geologist with local government and even the developer. Some side effects have developed as a result of the Alquist-Priolo Special Studies Zones Act that were not anticipated when the law was passed (e.g. with regard to insurance, loans, property sales). Also, there is a tendency by some individuals to assume that all seismic hazards are confined within the Special Studies Zones and at least one state law (school construction) was amended as a consequence. Although individuals and government agencies are learning to implement the new law, it is quite apparent that identifying and avoiding hazardous faults is not a simple task.

SITE-INVESTIGATIONS FOR SURFACE FAULT RUPTURE

Many references exist on the methods and rationale for identifying and evaluating faults in terms of recency and some references are specifically directed at the problem of surface fault rupture. In spite of this, there seems to be some disagreement and uncertainty among geologists as to how specific sites should be investigated under the various geologic conditions that exist. In order to evaluate this problem, the investigative reports filed with the State Geologist through 1977 were systematically reviewed to determine the methods used to investigate faults and what the state of the art is for fault investigations in California. The results are summarized by region and for three periods of time in table 3.

Several observations can be made based on the tabulated data. Most obvious is that significant contrasts in the methods used to investigate sites exist between northern and southern California. This is particularly true for the number of investigations using trenching, boreholes, and geophysical methods. The decreasing use of trenching and magnetic methods employed in northern California during the 1974-1977 period also is revealed by table 3. The reasons for this are not completely clear, although the reliance on geophysical methods (especially magnetic profiling) has been discouraged by the State Division of Mines and Geology and others. For example, guidelines issued in 1975 (as CDMG Note 49 and later reprinted (3)) may have had some effect on the use of the inconclusive geophysical methods. In spite of these efforts, a number of geologists continue to use geophysics to evaluate faults, apparently because the methods are rapid and non-destructive and in the belief that the absence of a geophysical anomaly

Table 3. Statistical summary of methods used to evaluate the hazard of surface fault rupture for site investigation reports filed with the California State Geologist under the Alquist-Priolo Special Studies Zones Act. All reports were reviewed and accepted by cities and counties prior to being filed. The number of reports evaluated are shown in parentheses.¹

Method ¹¹	<u>Percentage of site-investigations using each method</u>								
	<u>N. Calif.</u>			<u>S. Calif.</u>			<u>Total Calif.</u>		
	<u>74-75</u> <u>(76)</u>	<u>75-76</u> <u>(116)</u>	<u>76-77</u> <u>(166)</u>	<u>74-75</u> <u>(42)</u>	<u>75-76</u> <u>(71)</u>	<u>76-77</u> <u>(115)</u>	<u>74-75</u> <u>(118)</u>	<u>75-76</u> <u>(187)</u>	<u>76-77</u> <u>(281)</u>
Trenching	63%	58%	54%	86%	83%	88%	71%	67%	68%
Pits	4	4	4	2	8	7	3	6	5
Boreholes	28	34	27	2	10	7	19	25	17
Geophysical	61	48	44	0	6	4	39	32	28
Seis. refraction	38	45	35	0	3	1	25	29	21
Magnetic	40	12	15	0	3	3	26	9	10
Elec. resistivity	1	1	1	0	0	0	1	1	1
Other	3	0	0	0	0	1	2	0	1
None of the above	12	14	14	10	7	6	11	11	11
¹¹¹ Active faults identified	-	-	14%	-	-	16%	-	-	15%

¹Compiled by E.W. Hart; assisted by D.L. Wagner, W.Y.C. Lo, and J.G. Moreno.

¹¹Literature review, interpretation of aerial photographs, and field mapping methods are not given; data for these methods either are not considered representative or are not useful, based on reports of the 1974-75 period. A partial analysis of 1974-75 reports for northern and southern California, respectively, indicated 93% and 74% of the investigations did literature review and 66% and 38% did air photo interpretation.

¹¹¹Not determined for 1974-75 and 1975-76 periods.

demonstrates the absence of an active fault. Clearly, the data in table 3 indicate that standards vary from place to place in California.

A more subjective evaluation of the reports on file raised serious questions regarding 1) the appropriateness of investigative methods for certain sites, 2) the lack of documentation and general report quality, and 3) the validity of the conclusions reached regarding the existence or absence of active faults at the investigated sites.

Even though many of the reports on file with the State Geologist are inadequate in some respects, many provide useful new information that necessitates revision of existing Special Studies Zones for some faults. The most useful data are provided by trench excavations in alluvium and careful logging -- information not previously available to us. A good example of new data is provided near Hemet in Riverside County, California, where more than 50 site investigations have utilized deep trenching as the principal investigative tool (figure 3). These trenches revealed that: 1) the traces of the Casa Loma fault are not always located where they are shown on earlier maps and 2) the so-called Park Hill fault (a ground water barrier) apparently does not exist as a surface fault and presumably is not a fault-rupture hazard. Based on these data, a deletion of the zone established for the Park Hill fault is relatively

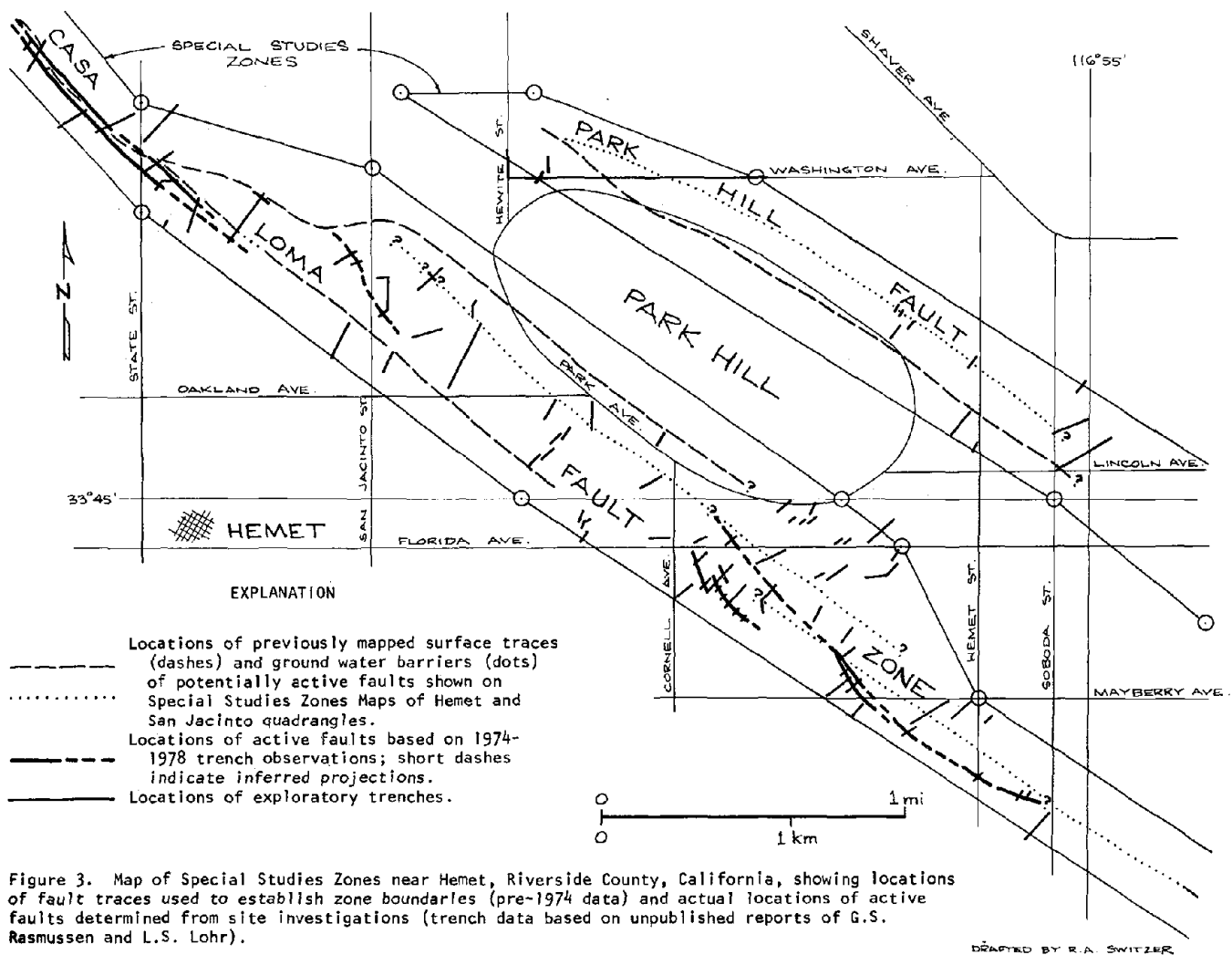


Figure 3. Map of Special Studies Zones near Hemet, Riverside County, California, showing locations of fault traces used to establish zone boundaries (pre-1974 data) and actual locations of active faults determined from site investigations (trench data based on unpublished reports of G.S. Rasmussen and L.S. Lohr).

uncomplicated. However, revising the zone boundaries for the Casa Loma fault will be rather difficult in some areas due to the proven existence of discontinuous and multiple fault strands in Holocene alluvium. Additional uncertainties in revising the Casa Loma zone is caused by the realization that 1) some faults may have been overlooked or misidentified in one of the trenches; 2) the area is subject to non-tectonic subsidence which may be the cause of some ground rupture, and 3) some of the unfaulted alluvium is so young that some fault strands may be obscured by recent erosion and sedimentation.

CONCLUSIONS

Based on accumulated experience, it is apparent that: 1) the abundance and complexity of Quaternary faults are much greater than formerly believed; 2) the evaluation of faults in terms of recency of activity and precise location generally is very difficult, both with regard to zoning and to site development; 3) the revision of Special Studies Zones is a delicate procedure that must be based on information clearly superior to the information used to establish the zone. California's practical experience with regard to zoning faults for the hazard of surface rupture should be of value to other governments contemplating the establishment of seismic zones.

REFERENCES

1. Barrows, A.G., Kahle, J.E., Weber, F.H. Jr., Saul, R.B., and Morton, D.M., 1975, Surface effects map of San Fernando earthquake area in San Fernando, California, Earthquake of 9 February 1971: California Division of Mines and Geology Bulletin 196, pl. 3.
2. California Division of Mines and Geology, 1976, Active fault mapping and evaluation program -- 10-year program to implement Alquist-Priolo Special Studies Zones Act: California Division of Mines and Geology Special Publication 47, 42 p.
3. Hart, E.W., 1977 (Revised), Fault hazard zones in California: California Division of Mines and Geology Special Publication 42, 24 p., plus Supplements nos. 2 and 3.
4. Hart, E.W., Bortugno, E.J., and Smith, T.C., 1977, Summary report -- Fault Evaluation Program, 1976 area (Western Transverse Ranges): California Division of Mines and Geology Open File Report OFR 77-8SF, 13 p., 2 pl.
5. Hart, E.W., Smith, D.P., and Smith, T.C., 1978, Summary report -- Fault Evaluation Program, 1977 area (Los Angeles basin region): California Division of Mines and Geology Open File Report OFR 78-10 SF, 16 p., 1 pl.
6. Jennings, C.W., 1975, Fault map of California with locations of volcanoes, thermal springs, and thermal wells: California Division of Mines and Geology Geologic Data Map 1.

Appendix A

ALQUIST-PRIOLO SPECIAL STUDIES ZONES ACT

Excerpts from California Public Resources Code

DIVISION 2. GEOLOGY, MINES AND MINING
CHAPTER 7.5. SPECIAL STUDIES ZONES

2621. This chapter shall be known and may be cited as the Alquist-Priolo Special Studies Zones Act.

2621.5. It is the purpose of this chapter to provide for the adoption and administration of zoning laws, ordinances, rules, and regulations by cities and counties in implementation of the general plan that is in effect in any city or county. The Legislature declares that the provisions of this chapter are intended to provide policies and criteria to assist cities, counties, and state agencies in the exercise of their responsibility to provide for the public safety in hazardous fault zones.

This chapter is applicable to any project, as defined in Section 2621.6, upon issuance of the official special studies zones maps to affected local jurisdictions, but does not apply to any development or structure in existence prior to the effective date of the amendment of this section at the 1975-76 Regular Session of the Legislature.

2621.6. (a) As used in this chapter, "project" means

(1) Any new real estate development which contemplates the eventual construction of structures for human occupancy, subject to the Subdivision Map Act (commencing with Section 66410 of the Government Code).

(2) Any new real estate development for which a tentative tract map has not been approved.

(3) Any structure for human occupancy, other than a single-family wood frame dwelling not exceeding two stories.

(4) Any single-family wood frame dwelling which is built or located as part of a development of four or more such dwellings constructed by a single person, individual, partnership, corporation, or other organization. No geologic report shall be required with respect to such single-family wood frame dwelling if the dwelling is located within a new real estate development, as described in paragraph (1) or (2) of this subdivision, for which development a geologic report has been either approved or waived pursuant to Section 2623.

(b) For the purposes of this chapter, a mobilehome whose body width exceeds eight feet shall be considered to be a single-family wood frame dwelling not exceeding two stories.

2621.7. This chapter, except Section 2621.9, shall not apply to the conversion of an existing apartment complex into a condominium. This chapter shall apply to projects which are located within a delineated special studies zone.

2621.8. This chapter shall not apply to alterations or additions to any structure within a special studies zone the value of which does not exceed 50 percent of the value of the structure.

2621.9. A person who is acting as an agent for a seller of real property which is located within a delineated special studies zone, or the seller if he is acting without an agent, shall disclose to any prospective purchaser the fact that the property is located within a delineated special studies zone.

2622. In order to assist cities and counties in their planning, zoning, and building-regulation functions, the State Geologist shall delineate, by December 31, 1973, appropriately wide special studies zones to encompass all potentially and recently active traces of the San Andreas, Calaveras, Hayward, and San Jacinto Faults, and such other faults, or segments thereof, as he deems

sufficiently active and well-defined as to constitute a potential hazard to structures from surface faulting or fault creep. Such special studies zones shall ordinarily be one-quarter mile or less in width, except in circumstances which may require the State Geologist to designate a wider zone.

Pursuant to this section, the State Geologist shall compile maps delineating the special studies zones and shall submit such maps to all affected cities, counties, and state agencies, not later than December 31, 1973, for review and comment. Concerned jurisdictions and agencies shall submit all such comments to the State Mining and Geology Board for review and consideration within 90 days. Within 90 days of such review, the State Geologist shall provide copies of the official maps to concerned state agencies and to each city or county having jurisdiction over lands lying within any such zone.

The State Geologist shall continually review new geologic and seismic data and shall revise the special studies zones or delineate additional special studies zones when warranted by new information. The State Geologist shall submit all revised maps and additional maps to all affected cities, counties, and state agencies for their review and comment. Concerned jurisdictions and agencies shall submit all such comments to the State Mining and Geology Board for review and consideration within 90 days. Within 90 days of such review, the State Geologist shall provide copies of the revised and additional official maps to concerned state agencies and to each city or county having jurisdiction over lands lying within any such zone.

2623. The approval of a project by a city or county shall be in accordance with policies and criteria established by the State Mining and Geology Board and the findings of the State Geologist. In the development of such policies and criteria, the State Mining and Geology Board shall seek the comment and advice of affected cities, counties, and state agencies. Cities and counties shall require, prior to the approval of a project, a geologic report defining and delineating any hazard of surface fault rupture. If the city or county finds that no undue hazard of this kind exists, the geologic report on such hazard may be waived, with approval of the State Geologist.

After a report has been approved or a waiver granted, subsequent geologic reports shall not be required, provided that new geologic data warranting further investigations is not recorded.

2624. Nothing in this chapter is intended to prevent cities and counties from establishing policies and criteria which are stricter than those established by this chapter or by the State Mining and Geology Board, nor from imposing and collecting fees in addition to those required under this chapter.

2625. (a) Each applicant for approval of a project may be charged a reasonable fee by the city or county having jurisdiction over the project.

(b) Such fees shall be set in an amount sufficient to meet, but not to exceed, the costs to the city or county of administering and complying with the provisions of this chapter.

(c) The geologic report required by Section 2623 shall be in sufficient detail to meet the criteria and policies established by the State Mining and Geology Board for individual parcels of land.

2630. In carrying out the provisions of this chapter, the State Geologist and the board shall be advised by the Seismic Safety Commission.

HIGH-RESOLUTION GEOPHYSICAL SURVEYS,
A TECHNIQUE FOR MICROZONATION OF THE CONTINENTAL SHELF

by

Michael R. Ploessel^I

ABSTRACT

A high-resolution geophysical survey is a necessary component of the studies for microzonation of areas on the continental shelf. The shallow geology of the continental shelves cannot be adequately understood without high-resolution seismic data. High-resolution survey instruments include side-scan sonar, Fathometer, tuned transducers, boomers and sparkers. These instruments provide a map view of the seafloor, as well as subbottom data along the line of survey. Tuned transducers and boomers provide information to depths of 100 to 500 feet below the seafloor and can resolve individual layers 1 to 3 feet thick. Faults with as little as 1 to 2 feet of throw (vertical offset) can be identified on the records. Sparkers provide data to depths in excess of 3000 feet below the seafloor, but can only resolve individual layers about 25 feet apart. However, faults with as little as 10 feet of throw can be identified from sparker records. High-resolution geophysical data, particularly from boomer systems, also provide an indication of the characteristics of seafloor materials. Although geophysical data are not a substitute for sampling of materials, very soft, unconsolidated sediments commonly can be distinguished from denser sediment and from rock. High-resolution geophysical data has already been obtained for large portions of the United States Continental Shelves.

INTRODUCTION

High-resolution geophysical survey techniques combined with traditional marine geologic and seismologic research techniques make microzonation of the continental shelves of the world possible. The basic data needed for microzonation of the continental shelf is similar to that needed onshore. Microzonation of an area cannot be adequately completed without a thorough understanding of the geologic environment. In the marine environment, one of the techniques necessary to adequately understand the geologic environment is a high-resolution geophysical survey.

Geologic data needed for microzonation include the location of active and potentially active faults, the characteristics of the seafloor and subbottom earth materials, and the location submarine landslides and similar features. When this geologic data is utilized in conjunction with historic seismicity data. The magnitude of earthquakes that could affect an area can be estimated along with the potential effects of such events.

I Senior Engineering Geologist, McClelland Engineers, Inc. 5450
Ralston St., Ventura, California 93003.

Microzonation of the continental shelves of the world has been hampered in the past by an inadequate knowledge of the geology of the shelves. This is particularly true of knowledge of the geology at and immediately below the seafloor, the information most needed for microzonation studies. Since the early 1940's, reasonably accurate water depth recorders have been operated on research vessels to map the seafloor topography. In addition, petroleum companies have explored the deep geology of the continental shelves through the use of "deep seismic systems." In general, seafloor topography and the deep geology are not adequate to determine the geology of the shallow sediments. Within the past ten to fifteen years, high-resolution geophysical equipment, capable of clearly delineating the seafloor and shallow subbottom geology, has been developed and is commercially available. The most widely used of these instruments are side-scan sonar, Fathometer, tuned transducers, boomers, and sparkers. Each of the various types of sources operate at different frequencies. Basically, instruments with higher frequencies (shorter wavelengths) have greater resolution. In this paper, the term "resolution" refers to the distance that can be resolved between distinct acoustic interfaces in order that they may be displayed as distinct reflections on a seismic record.

HIGH-RESOLUTION GEOPHYSICAL SYSTEMS

All of the high-resolution acoustic (seismic) systems described here operate on the principle whereby transmitted seismic energy incident upon an acoustic interface is reflected from that interface. The reflections from the acoustic interfaces are displayed graphically. Generally, the acoustic interfaces displayed on the subbottom profiles correspond to physical interfaces, such as bedding planes, unconformities, faults, the top of hard rock, boundaries of gas zones and similar interfaces. A complete description of these systems is beyond the scope of this paper, the reader is referred to Parkinson (3), Klein (2), Sieck and Self (4), and Van Overeem (6) for additional discussion of the various systems and additional references.

Side-Scan Sonar System

Side-scan sonar systems provide graphic records that show a two dimensional (map) view of the seafloor topography and objects on the seafloor. These records are analogous to low-angle, oblique aerial photographs. Side-scan sonar transducers transmit pulses of about 100 kilohertz. This relatively high-frequency signal is reflected entirely from the seafloor, and no subbottom information is obtained. The width of the area covered by a side-scan sonar record can be adjusted to range from a few feet to 2600 feet. Figure 1 is a side-scan sonar record showing Tertiary sedimentary bedrock exposed at the seafloor.

Fathometer

Fathometers are traditional water depth recorders. They usually operate at frequencies of about 40 or 200 kilohertz. Because of this high frequency, no subbottom penetration is obtained. However, the

high frequency provides resolution of less than one foot. Figure 2 is a Fathometer record.

Tuned Transducer Systems

Tuned transducers are often operated as precision depth recorders and subbottom profiling systems. The commercially available systems usually operate at 3.5 or 7 kilohertz. The transmitted pulse has a wavelength of less than 1 foot and allows resolution of fine detail on the seafloor and in the shallow subsurface. A considerable amount of the energy from these sources is reflected from the seafloor, but subbottom penetration up to 300 feet below the seafloor can be obtained in thick sections of soft, unconsolidated sediments. Typical subbottom penetration is 30 to 100 feet. In soft sediments, faults with throws (vertical offset) of as little as 1 to 2 feet can be resolved with tuned transducer records (Figure 3).

Boomer Systems

Boomers have electromechanical sources that generate broad-spectrum, relatively clean acoustic pulses. The output pulse usually ranges from 200 to 10 kilohertz. These instruments provide considerably greater penetration than tuned transducers at only slightly lower resolution. Boomers can provide subbottom penetration in excess of 500 feet in areas of soft sediment. Typical penetration is 100 to 300 feet. Resolution of boomer type instruments is about 1.5 to 3 feet. Faults with as little as 1.5 to 2 feet of throw can be defined on the records (Figures 4 and 5).

Sparker Systems

Sparkers provide deeper penetration below the seafloor than tuned transducer or boomer systems, but have noticeably lower resolution. Energy output of the sparker is commonly 3 to 15 kilojoules. The frequency of the output pulse is broadband, ranging from about 10 to 500 kilohertz. The sparker source creates the sound pulse by electrical discharge between electrodes and a metal cage. Subbottom penetration is generally 1000 to 3000 feet. A typical high-resolution sparker has a resolution of about 25 feet, but faults with as little as 10 feet or less of throw can be determined (Figures 6 and 8).

SURVEY GRIDS

The line spacing or survey grid necessary for microzonation depends on the nature of the geology in the area to be surveyed. In areas of simple geology, the primary lines could be spaced as far as two miles apart, with tie lines perpendicular to the primary lines, 6 miles apart. In areas of complex geology, such as offshore southern California or Alaska, considerably closer line spacing is required. Primary lines spaced at one-half mile with tie lines 1.5 miles apart should generally prove adequate.

DATA COST AND AVAILABILITY

The initial cost of obtaining high-resolution geophysical data is highly variable and depends on a great number of factors, including the number and types of instruments used in the survey, navigation difficulties, the size of the boat needed, weather, and so on. As a general rule, however, high-resolution geophysical data can be acquired in 1978 dollars for approximately \$100 to \$200 per line-mile.

Although the initial cost of obtaining high-resolution geophysical data is relatively high, there are many areas of the Continental Shelf where this data has been acquired for various reasons and is presently available for relative low cost. For example, the U.S. Geological Survey requires that high-resolution geophysical surveys be performed over all areas proposed to be leased for offshore oil exploration and production. This data is available to the public for only the cost of reproduction. Various governmental agencies have also obtained high-resolution geophysical data for a variety of purposes. In the United States this data is also available for the cost of reproduction. Many private geophysical contracting firms have performed speculative proprietary surveys over large areas to be sold to mineral exploration companies. Several years after acquisition, much of this data is considered to have relatively low value. It can then be acquired at relatively low cost. A list of firms that may have such data is in The Geophysical Directory (5). In the United States, data are available for virtually all areas which have been subjected to petroleum exploration. This includes a great portion of the United States Continental Shelf.

The cost of interpretation of high-resolution data could range from \$10 to \$100 a line-mile, depending on number of systems run, complexity of geology and so on. High-resolution seismic data is most effectively utilized when interpreted by qualified, experienced geologists and geophysicists (1, 4).

GEOLOGIC FEATURES MAPPABLE FROM HIGH-RESOLUTION SEISMIC DATA

High-resolution seismic data can clearly delineate seafloor and shallow subbottom geologic features important to effective microzonation. Not only can the location of shallow faults be determined, but the data is often of sufficient quality to determine if the faults have been recently active. Figures 3, 5, and 6, show faults that reach the seafloor. There is a rather strong fault-line scarp at approximately fix mark 216 on Figures 5 and 6. To determine the recency of activity, it would be necessary to date the sediments that are faulted. To do this the sediments must be sampled and dated. Figure 4 shows a fault that clearly has been inactive during the Holocene, although the fault does offset older Quaternary sediments.

Some of the characteristics of earth materials can be inferred from high-resolution data alone. Very soft unconsolidated or very hard, dense material can usually be distinguished. Positive identification of sediment or rock type and age, however, can only be made by direct sampling and analysis. Tuned transducers only obtain the depth of penetration

shown in Figure 3 in soft, unconsolidated sediment. A soil boring in the area of Figure 3 revealed these sediments to be soft, unconsolidated clay. The usefulness of samples is greatly extended by high-resolution data because the distribution, depth and thicknesses of sedimentary units which have been identified by sampling can be determined. Figure 7 is a boomer record inferred to be unconsolidated sediment overlying steeply dipping sedimentary bedrock. Samples from a soil boring confirmed this as Quaternary sediment over Tertiary bedrock. Figure 8 is a sparker record of Tertiary sediment over volcanic rock. The volcanic rock is "acoustic basement" and there is no coherent return of the seismic signal from these rocks. Again, to determine the type of rock appearing as acoustic basement on the records, it was necessary to sample the rock. However, data from one well chosen sample station, can be extrapolated with the seismic data over a large area.

Many other geologic features that must be delineated to accomplish microzonation can be seen on high-resolution data. Submarine landslides, clearly distinguished on the data (Figure 8), are one of these features.

CONCLUSION

A high-resolution geophysical survey is only one component necessary for microzonation of an area on the continental shelf. Such surveys are however, a necessary component. Historic seismicity data is not sufficient to accomplish microzonation. Without an adequate understanding of the geology of the area, complete microzonation cannot be done. A complete and thorough understanding the shallow subsurface geology of the continental shelf can only be accomplished with high-resolution geophysical survey techniques.

REFERENCES

1. Davidson, Linda, 1976, Obstacles to interpretation: Spring Symposium of Geophysical Society of Houston, 28 p.
2. Klein, Marty, 1976, Side-scan sonar: Spring Symposium of Geophysical Society of Houston, 11 p.
3. Parkinson, L. E., 1976, Tuned transducers, boomers, and graphic recorders: Spring Symposium of Geophysical Society of Houston, 26 p.
4. Sieck, H. C., and Self, G. W., 1977, Analysis of high-resolution seismic data in Seismic Stratigraphy - applications to hydrocarbon exploration: Am Assoc. Petroleum Geologists, Tulsa, Oklahoma, p.353-385.
5. The Geophysical Directory, Inc., 1977, The geophysical directory: Houston, Texas, 459 p.
6. Van Overeem, A. J. A., 1978, Shallow-penetration high-resolution subbottom profiling: Marine Geotechnology, v. 3, p. 61-84.

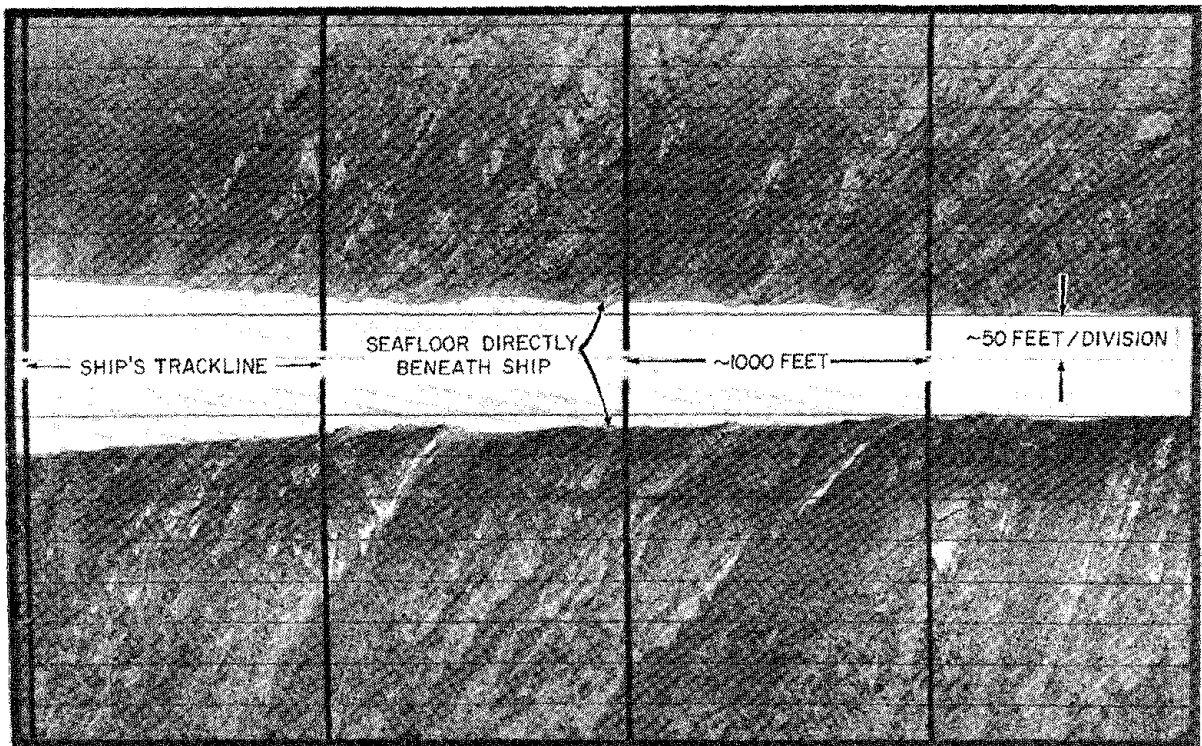


Figure 1: Side-scan sonar record showing folded sedimentary rocks exposed at the seafloor.

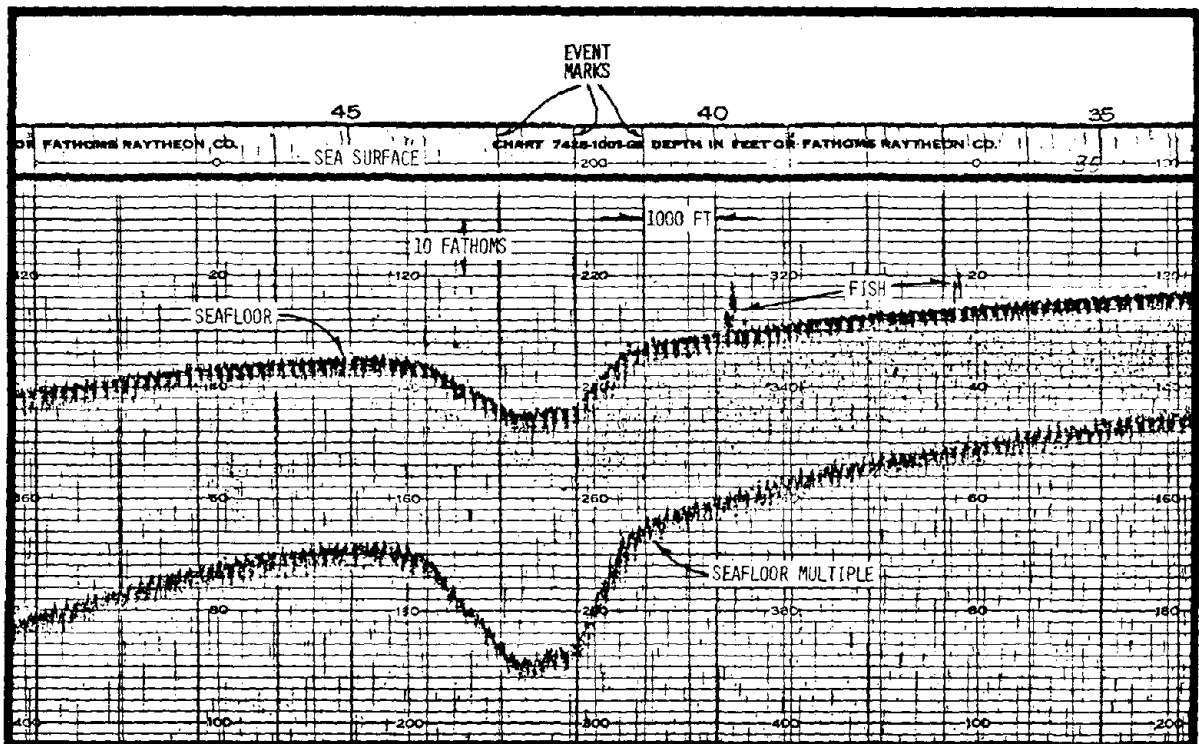


Figure 2: Fathometer record showing seafloor. Note approximately one-half mile wide channel and fish in the water column.

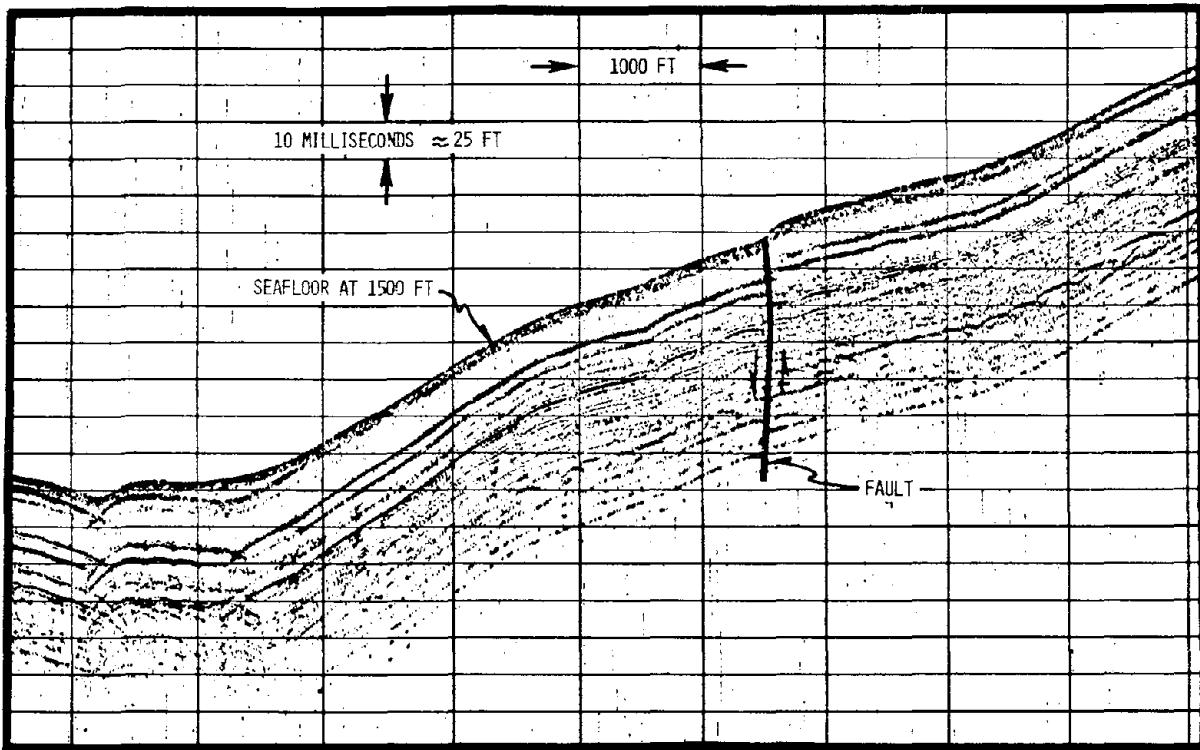


Figure 3: Tuned transducer record of soft, unconsolidated sediments on the upper continental slope. A minor scarp at the seafloor indicates recent activity of the fault.

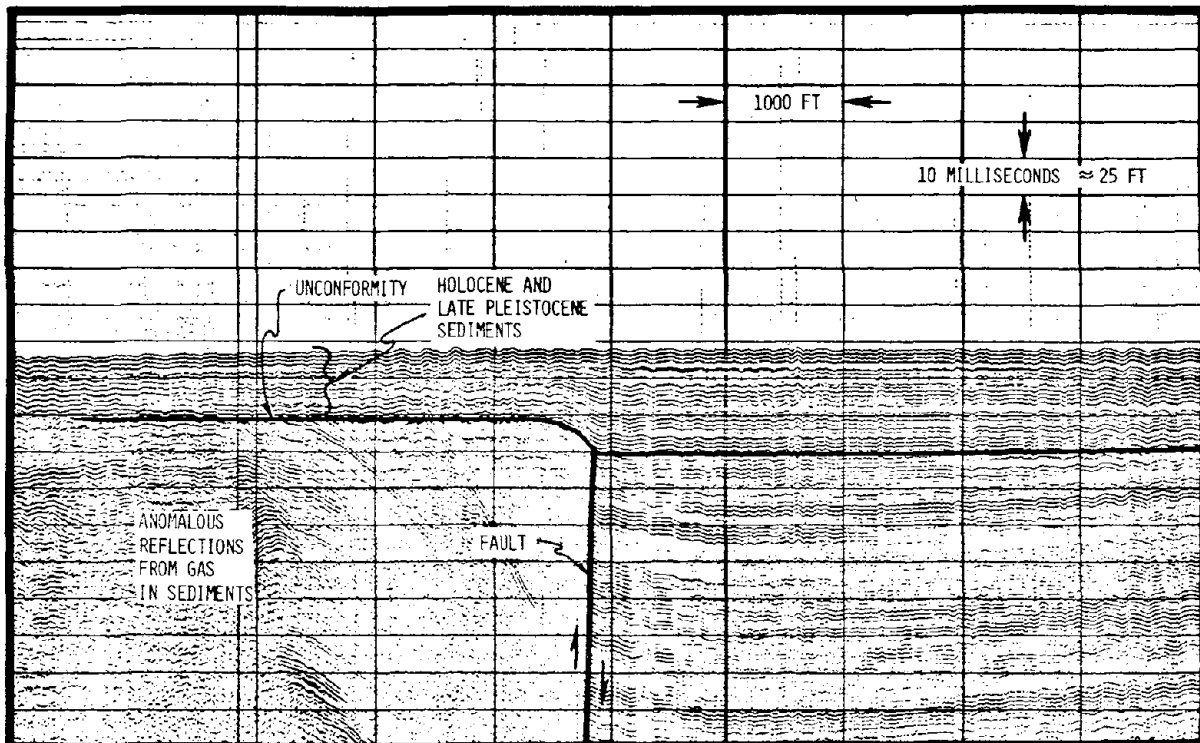


Figure 4: Boomer record (Acoustipulse) showing a fault offshore southern California. Pleistocene and older sediments are faulted but Holocene sediments are not offset. The fault is thus considered inactive.

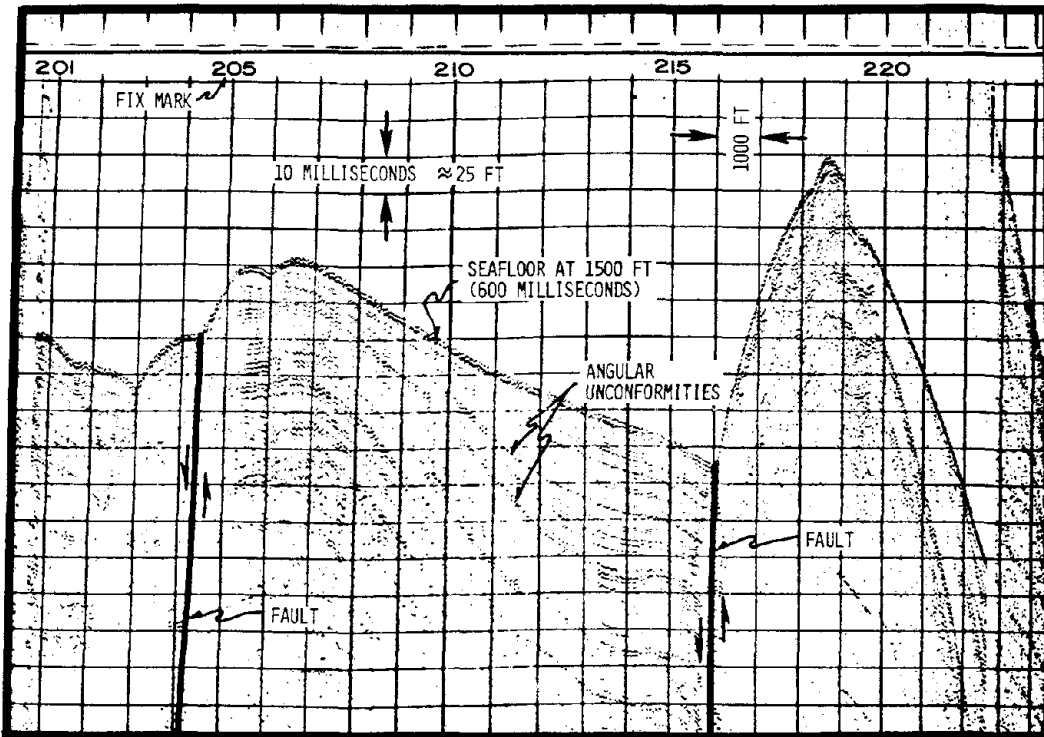


Figure 5: Boomer (Acoustipulse) record showing fault and fault-line scarp. Figure 6 is a sparker record of the same area.

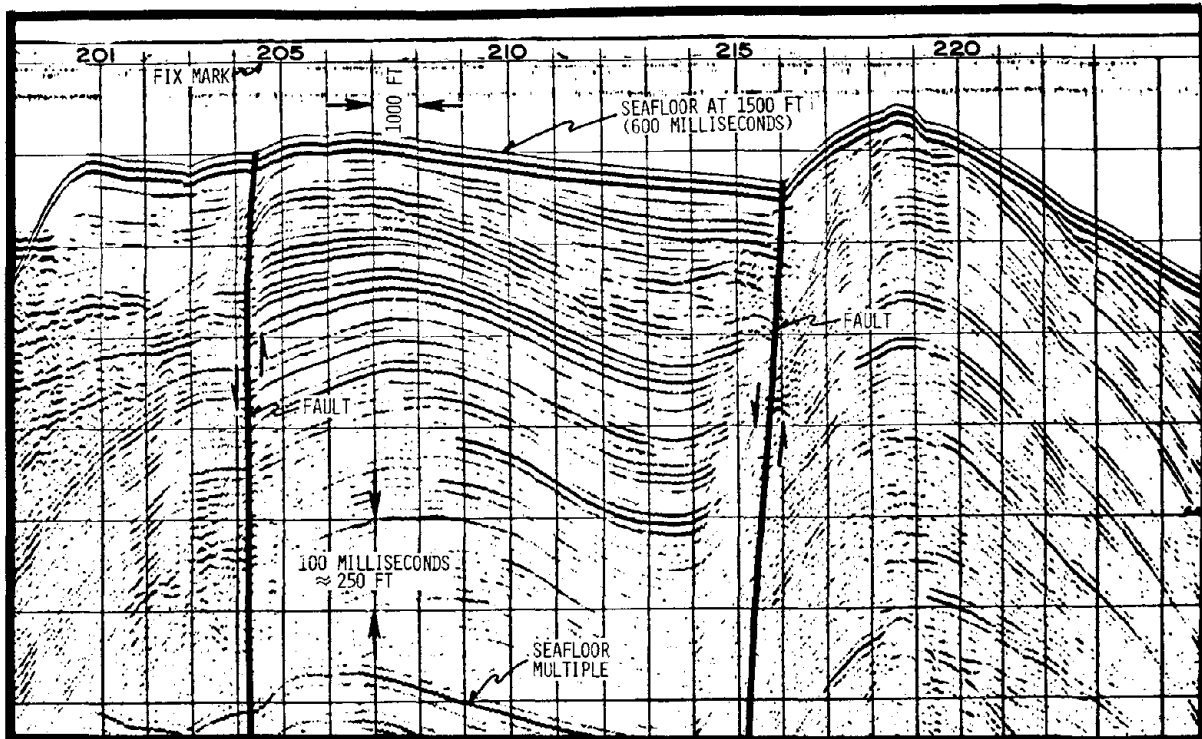


Figure 6: Sparker (10 kilojoules) record showing fault. Figure 5 is a boomer record of the same area. The sparker obtains much greater penetration but less resolution.

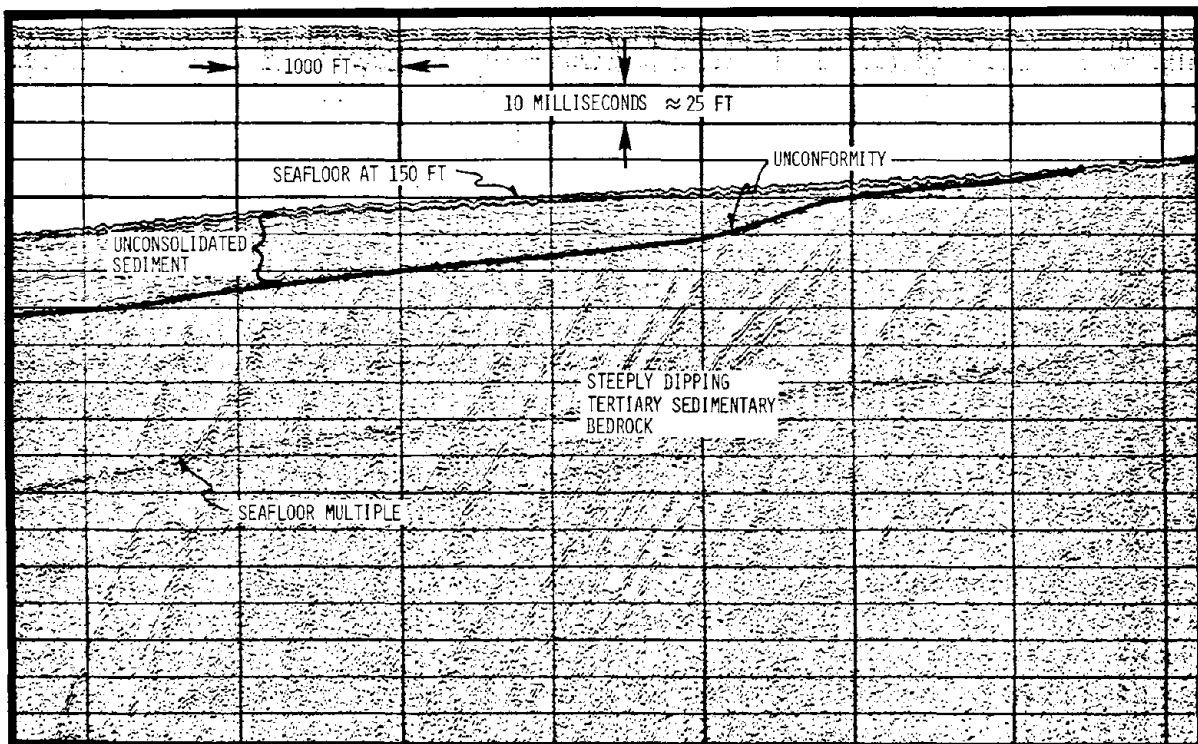


Figure 7: Boomer (Acoustipulse) record of unconsolidated (Quaternary) sediments overlying steeply dipping Tertiary sedimentary bedrock.

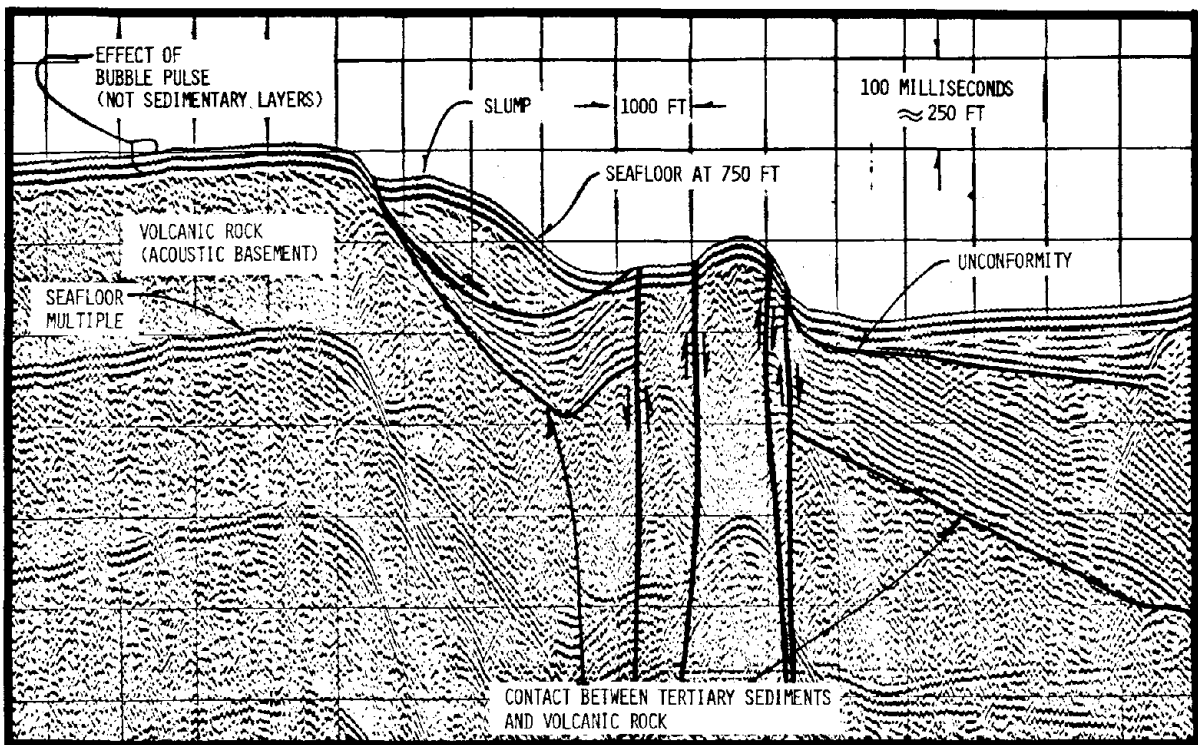


Figure 8: Sparker (10 kilojoules) record from the Outer Banks, offshore southern California. A slump more than 250 ft thick and one quarter mile long occurred at contact between Tertiary sediments and volcanic rock. Several faults reach the seafloor and may have experienced recent activity.

INTENTIONALLY BLANK

656

SEISMICITY AND SEISMIC RISK RELATED TO SUBDUCTION ZONES

by

L. Esteva^I and E. Bazán^I

ABSTRACT

A criterion is presented for estimation of intensity-recurrence relations at sites near subduction zones. Intensities are expressed in terms of engineering parameters (peak ground acceleration or velocity, ordinates of response spectra) for firm ground and standard flat topography. Recurrence relations for intensities are obtained from those corresponding to magnitudes of earthquakes generated at given volumes of the earth's crust (local seismicity), through use of attenuation expressions relating magnitude, intensity and focal distance. A formulation based on the concepts of bayesian statistics is adopted for the assessment of local seismicity at given earthquake sources, by probabilistic analysis of statistical information concerning seismic activity at those sources and at others having similar geotectonic characteristics.

INTRODUCTION

Determination of seismic design parameters for structures requires estimating probability distributions of maximum values of certain variables measuring ground motion intensity (such as peak ground acceleration or velocity), which can be correlated with structural response. Due to lack of direct instrumental information at given sites, such distributions must be determined from magnitudes of past earthquakes, models of local seismicity, and expressions relating intensity with magnitude and site-to-source distance.

This paper deals with the assessment of local seismicity in subduction zones; i.e., with the formulation of stochastic process models concerning occurrence times, magnitudes and hypocentral coordinates of earthquakes, and with the estimation of parameters of such models. The criterion adopted involves definition of local seismicity in terms of the rate of occurrence of earthquakes with magnitudes greater than given values, in a unit volume of the earth's crust (1). The analysis proposed takes into account statistical data and geological evidence in the zone of interest as well as available information of other regions with similar geological characteristics. Evaluation of the associated uncertainties is accomplished through application of Bayes' theorem, which serves to obtain probability distributions of alternative hypotheses concerning the characteristics and parameters of the random process model used to represent local seismicity of earthquake sources near a given site.

Seismic activity of subduction zones (fig 1) takes place at both, subducting plate and continental block, as well as at their interface. Local seismicity varies with depth and distance to the trench line. This paper

^I Research Professor. Instituto de Ingeniería, UNAM, Ciudad Universitaria,

Preceding page blank

studies spatial variation of seismicity at a segment of the subduction zone of Cocos plate under the Mexican Southern coast. Use is made of statistical information from this zone and from other subduction zones in the Circum-pacific Belt. Seismological data covering magnitudes greater than 6 from 1953 to 1965, and greater than 7 from 1917 to 1964, were obtained from Rothé (2) and Duda (3) respectively.

The criterion presented is applied to the estimation of seismic risk at the projected site for a dam near the southern coast of Mexico (see fig 2).

BAYESIAN ESTIMATION OF LOCAL SEISMICITY

Occurrence of earthquakes with magnitudes greater than of equal to M generated at a given seismic source will be represented by a Poisson process with mean rate $\lambda(M)$ per unit volume and per unit time. Hence, estimation of local seismicity will consist in determining λ for several values of M . According to Esteva (1), $\lambda(M)$ is expressed as follows:

$$\lambda(M) = \alpha(e^{-\beta M} - e^{-\beta M_1}) \quad \text{for } M < M_1$$

$$= 0 \quad \text{for } M \geq M_1 \quad (1)$$

where α , β and M_1 are parameters to be determined. M_1 is an upper bound to the magnitudes that can be generated at the source under study. Ideally, estimation of these parameters should be based on direct statistical information of the seismic source of interest; however seismological records cover only a very short time interval and hence they are insufficient for making precise estimates of α , β and, especially, M_1 . Because of this lack of direct data the information of other zones with similar geotectonic characteristics is very valuable. Use of this information enhances the extent of available data, although at the expense of introducing additional uncertainties about the differences between seismicities of zones considered similar. This is consistent with the conventional practice of estimating maximum magnitudes at a given source by extrapolating observations made at similar sources.

As mentioned above, interest of this paper is centered on a segment of the subduction zone of Cocos plate under the southern coast of Mexico. Nine auxiliary regions were considered with similar geotectonic characteristics (see Table 1). Estimates of α , β and M_1 for each auxiliary region are very uncertain if based exclusively on statistical data from that same region. This uncertainty can be largely reduced if estimates are based on the overall information for all auxiliary regions, in conjunction with a reasonable assumption concerning the probability distribution of possible deviations between local seismicities of all auxiliary regions. Uncertainty in α , β and M_1 for a randomly chosen region, among those considered similar according their geotectonic features, comprises two portions: that stemming from actual inter-zone variability, and that tied to the estimation process starting from statistical evidence. The latter results from the estimation criteria adopted, while the former depends on comparisons of geotectonic features of the zones (dimensions, rates of deformation, etc). For instance, the extreme hypothesis that all regions of Table 1 have the same values of α , β and M_1 , leads to important uncertainty reductions, as data of all zones are included in the same population. The largest uncertainties result under

the assumption that the seismicity of each zone is defined by a vector of random parameters, independent of those corresponding to the other zones, but belonging to the same population. Even in the last case use of statistical information of auxiliary zones may drastically reduce uncertainty in seismicity estimates.

Initial distribution of M_1 for each auxiliary zone

As mentioned above, M_1 is the maximum feasible magnitude at a given seismic source. Recent studies (4, 5) have shown that near field ground motion is more precisely correlated with seismic moment and stress drop than with magnitude. Thus use of the latter quantities, may be advantageous when trying to predict seismic intensities from local parameters. Besides, physical and mechanical characteristics of potential seismic sources, can be better used for predicting bounds to seismic moments and stress drops than to magnitudes. Assuming that the failure mechanism in an earthquake source consists in relative slip between contact surfaces in the rupture zone, and given a hypothesis about the shape of that zone, cracking theory can be used to express seismic moment M_0 as $\Omega A^{3/2} \Delta\sigma$ (6, 7), where Ω depends on the shape of the rupture interface, A is the corresponding area and $\Delta\sigma$ is the mean shear stress drop. Kanamori (8) used the former relationship to determine stress drops for some earthquakes and found values within a narrow band about 30 bars. However because statistical information about focal parameters consists mainly of data about earthquake magnitude most engineering work on intensity attenuation expressions has been based on the latter parameter. Such expressions are used herein, considering, in addition, that available statistics are expressed in terms of magnitudes and focal coordinates.

For each of the nine auxiliary zones, a beta type bayesian initial distribution $f_{M_1}^*(\cdot)$ of M_1 was assumed:

$$f_{M_1}^*(m) = \Gamma(p)\Gamma(q)x^p(1-x)^q/\Gamma(p+q+1) \quad (2)$$

Here, $x = (m - m_a)/(m_b - m_a)$, $\Gamma(\cdot)$ is the gamma function, with parameters p and q related as follows with mean \bar{m} and variance $\text{Var}(M_1)$ of the bayesian distribution of M_1 :

$$\frac{\bar{m} - m_a}{m_b - m_a} = \frac{p}{p+q} \quad ; \quad \frac{\text{Var}(M_1)}{(m_b - m_a)^2} = \frac{pq}{(p+q)^2 (p+q+1)}$$

The lower bound m_a of feasible values of M_1 , was taken equal to the maximum value observed in each zone; the upper bound m_b was considered equal to q for all zones. The mean value \bar{m} was based on indirect estimations of maximum observed seismic moments, and on maximum expected values taking into account the dimensions of the respective seismic source, and correlations between seismic moment and magnitude (9). From the uncertainty in estimates based on geophysical data, it was assumed that M_1 had a 50 per cent probability of lying between $m_a + 0.8(\bar{m} - m_a)$ and $m_b - 0.8(\bar{m}_b - \bar{m})$. This condition fully determines p and q for each auxiliary region. However, in region 9 M_1 was considered uniformly distributed between m_a and m_b , because there $\bar{m} < m_a$.

Initial distribution of α and β in auxiliary zones

Due to lack of adequate criteria for estimating α and β (eq 1) from geophysical information, the following formulations is based exclusively on statistical data of each region. Only earthquakes with focal depth lower than 300 km were taken into account, because deeper earthquakes have no significant contribution to seismic risk at the surface.

Two sets of statistical data are available for each region, namely n' earthquakes with magnitudes $m_j \geq M_0'$ ($j = 1, n'$; $M_0' = 6$) during time interval t' (13 years) and n'' with magnitudes $m_k \geq M_0''$ ($k = 1, n''$; $M_0'' = 7$) during time interval t'' (35 years). Each earthquake is only in one set, as t' and t'' do not overlap. According to Bayes' theorem, if no information other than a statistical sample is available, the probability density function of α , β and M_1 , given the statistical information, is proportional to the likelihood of that information. Under the assumption that earthquakes occur according to a Poisson process, this likelihood is:

$$p = e^{-(\lambda_0' t' + \lambda_0'' t'')} (abt')^{n'} e^{-b(\sum_j m_j + \sum_k m_k)} (abt'')^{n''} \quad (3)$$

where $\lambda_0' = e^{-bM_0'} - e^{-bm}$, $\lambda_0'' = e^{-bM_0''} - e^{-bm}$, $0 \leq a \leq \infty$, $0 \leq b \leq 3.46$. In eq 3, a , b and m are specific values of the uncertain parameters α , β and M_1 . The bound 3.46 is needed to ensure that the amount of energy liberated per unit time is finite (10).

Elimination of terms that do not depend on a , b , and m turns eq 3 into the following:

$$p(a, b, m) = C(ab)^n e^{-a\gamma - b\mu} \quad (4)$$

where C is a normalization constant, $n = n' + n''$, $\gamma = t'(e^{-bM_0'} - e^{-bm}) + t''(e^{-bM_0''} - e^{-bm})$, $\mu = \sum_{j=1}^{n'} m_j + \sum_{k=1}^{n''} m_k$.

If C satisfies $\int_a \int_b p(a, b, m) db da = 1$, eq 4 gives the conditional probability distribution of α and β given the statistical evidence and given $M_1 = m$, i.e., for the i -th zone,

$$f_i'(a, b | m) = C_i (ab)^{n_i} e^{-a\gamma_i - b\mu_i} \quad (5)$$

The joint probability distribution of α , β and M_1 for the i -th region is:

$$f_i'(a, b, m) = f_i'(m) f_i'(a, b | m) \quad (6)$$

where $f_i'(m)$ and $f_i'(a, b | m)$ are given by eqs 2 and 5, respectively.

Initial and posterior distributions of α , β and M_1 in the zone of interest

Because the nine auxiliary regions are equally similar to the zone of interest, the initial probability function of α , β and M_1 in this zone was

taken as $f'(a,b,m) = \frac{1}{9} \sum_{i=1}^9 f_i^*(a,b,m)$, where $f_i^*(a,b,m) = f_i'(m) f_i'(a/w_i, b|m) / w_i$; w_i = area of zone of interest/area of auxiliary region in i (see Table 1).

Application of Bayes' theorem with the likelihood function given by eq 4 leads to the following expression for the posterior distribution of α , β and M_1 :

$$f''(a,b,m) = k \sum_i f_i^*(a,b,m) (ab)^{n_i^*} e^{-a\gamma^* - b\mu^*} \quad (7)$$

where n^* , γ^* and μ^* are defined as in eq 4, but with data of the zone of interest; k is determined by the condition $\int_a \int_b \int_m f''(a,b,m) da db dm = 1$.

Algebraic transformations lead to eq 8:

$$f''(a,b,m) = k \sum_{i=1}^9 C_i f_i'(m) (ab)^{\bar{n}_i} e^{-a\bar{\gamma}_i - b\bar{\mu}_i / w_i^{n_i+1}} \quad (8)$$

Here, $\bar{\gamma}_i = \gamma^* + \gamma_i / w_i$, $\bar{n}_i = n_i + n^*$, $\bar{\mu}_i = \mu_i + \mu^*$ and γ_i , n_i and μ_i were defined in eq 4.

Expected value of local seismicity

The expected value of local seismicity is given as follows:

$$E[\lambda(M)] = \int_m \int_b \int_a f''(a,b,m) \lambda(M|a,b,m) da db dm \quad (9)$$

Here, $f''(a,b,m)$ is given by eq 8 and $\lambda(M|a,b,m)$ must be calculated with eq 1. Values of $E[\lambda(M)]$ determined by means of the above procedure for the selected segment of subduction zone are shown in fig 3. A comparison with statistical data can be appreciated in the same figure.

Adoption of the form of eq 1 for local seismicity of each auxiliary region does not necessarily lead to an expression of the same form for $E[\lambda(M)]$; however, as fig 3 shows, negligible errors (lower than 0.5 per cent) are obtained if the latter function is given by eq 10 with $\tilde{\alpha} = 368,000$, $\tilde{\beta} = 1.95$ and $\tilde{M}_1 = 1.84$.

$$E[\lambda(M)] \doteq \tilde{\lambda}(M) = \tilde{\alpha} (e^{-\tilde{\beta}M} - e^{-\tilde{\beta}\tilde{M}_1}) \quad (10)$$

SPATIAL VARIABILITY OF LOCAL SEISMICITY

The procedure presented in the foregoing sections gives a bayesian estimation of local seismicity averaged throughout all the subduction zone. However, seismic risk estimates are sensitive to values of local seismicity averaged over much smaller volumes of the earth's crust; hence the need to develop criteria for probabilistic inference of possible patterns of space variability throughout subduction zones. Such variability depends on the magnitude interval under consideration.

A typical section of a subduction zone, divided into 90 cells, is shown in fig 4. The dimensions are those of the Cocos plate. The problem consists in determining the probability $p_i(M)$ that an earthquake known to have been generated somewhere in the zone originated precisely at cell i . The p_i 's are

stochastically dependent, because $\sum_{i=1}^9 p_i(M) = 1$; nevertheless, the correlation is small, as the number of terms in the addition is high. Moreover, the following derivations are based on marginal distributions of each $p_i(M)$, rather than on their joint distribution of the p_i 's.

Initial distribution of $p_i(M)$

The subduction zone segment of interest was divided into three subzones (fig 2). Each subzone was in turn subdivided into 90 cells (fig 4). An uncertain $p_i(M)$ was supposed to correspond to each cell. In order to assign initial probability distributions to the p_i 's each auxiliary region was divided into two to five subzones (the larger the length of the region the larger the number of subzones); each subzone was in turn subdivided into 90 cells following the same pattern of the zone of interest, 26 auxiliary subzones were defined in this manner.

Let n_j be the number of earthquakes with magnitude $M \geq M_0$ generated at subzone i . If r_{ij} of those earthquakes were generated at cell j , the likelihood of Z_{ij} (probability that an earthquake generated at subzone i originated at cell j) has the form of a beta distribution with the following mean and coefficient of variation (11)

$$\bar{Z}_{ij} = (r_{ij} + 1) / (n_{ij} + 2) \quad (11)$$

$$V_{ij} = \{(n_j - r_{ij} + 1) / [(r_{ij} + 1)(n_j + 3)]\}^{1/2} \quad (12)$$

In order to satisfy the condition $\sum \bar{Z}_{ij} = 1$, it is necessary that $\bar{Z}_{ij} = (r_{ij} + 1) / (n_j + k)$ where k is the total number of cells in which subzone j was divided; hence, this equation was used instead of eq 11. The expression for V_{ij} remains unchanged. These equations provide estimates of \bar{Z}_{ij} and V_{ij} for each cell i of each subzone j . These estimates define initial mean and variance of the bayesian distribution of $p_i(M)$:

$$E[p_i(M)] = E[\bar{Z}_{ij}] = \frac{1}{\ell} \sum_{j=1}^{\ell} \bar{Z}_{ij} \quad (13)$$

$$\sigma^2[p_i(M)] = E[\sigma_{ij}^2] + \sigma^2[\bar{Z}_{ij}] = \frac{1}{\ell} \sum_{j=1}^{\ell} \sigma_{ij}^2 + \frac{1}{\ell-1} \left\{ \sum_{j=1}^{\ell} \bar{Z}_{ij}^2 - \ell E^2[p_i(M)] \right\} \quad (14)$$

where $\sigma_{ij} = \bar{Z}_{ij} V_{ij}$, and ℓ stands for the number of subzones.

Because $0 \leq p_i(M) \leq 1.0$, the distribution of $p_i(M)$ can be taken as beta with mean and variance given by eqs 13 and 14. This is equivalent to assuming r_i fictitious earthquakes generated at cell i of a subzone out of n_i generated at the whole subzone, where n_i and r_i are related with the moments of the initial bayesian distribution of $p_i(M)$ as follows:

$$n_i = E[p_i(M)] \{1 - E[p_i(M)]\} / \sigma^2[p_i(M)] - 3 \quad (15)$$

$$r_i = E[p_i(M)] (n_i + 2) - 1 \quad (16)$$

Posterior distribution of $p_i(M)$

Let the initial probability distribution of $p_i(M)$ at a cell of the subzone of interest be beta with parameters n_i' , r_i' . If statistical data show that r_i earthquakes with magnitude greater than or equal to M were generated at the mentioned cell, out of n earthquakes in the same magnitude range generated at the subzone, then, according to Bayes' theorem, the posterior distribution of $p_i(M)$ is also of the beta family, with mean and coefficient of variation given by:

$$E''[p_i(M)] = (r_i'' + 1)/(n_i'' + 2) \quad (17)$$

$$V''[p_i(M)] = \left\{ (n_i'' - r_i'' + 1) / [(r_i'' + 1)(n_i'' + 3)] \right\}^{1/2} \quad (18)$$

where $r_i'' = r_i' + r_i$; $n_i'' = n_i' + n$.

Statistical data include earthquakes with unknown focal depth between 0 and 70 km. These earthquakes were put in ten additional fictitious cells. The values of $p_i(M)$ for these cells were determined as for real ones; later those values were distributed to cells lying between 0 and 70 km. Finally, posterior means of $p_i(M)$ were normalized so that $\sum_{i=1}^{90} E[p_i(M)] = 1$.

The described procedure was applied for $M = 6$ and $M = 7$. The results obtained are given in Table 2, for subzone A of fig 2. It was assumed that $p_i(M) = p_i(6)$ for $M < 6$, $p_i(M) = p_i(7)$ for $M > 7$ and that $p_i(M)$ varies linearly for $6 < M < 7$. The latter assumption can be improved by computing $p_i(M)$ for other values of M .

REGIONAL SEISMICITY

The final goal of local seismicity assessment is the estimation of regional seismicity. This can be made for instance in terms of recurrence periods $v(Y)$ of given intensities Y . Values of $v(Y)$ are obtained by integrating the contributions of local seismicity of nearby sources, and hence they reflect bayesian uncertainties tied to those seismicities. Thus,

$$v(Y) = \int_{Vol} p_i(M) \tilde{\lambda} [M(Y,R)] dVol \quad (19)$$

where $\tilde{\lambda}(M)$ is given by eq 10, and M is the value of magnitude that gives place to intensity Y at a site distant R from the source whose contribution is being considered. The integration process requires the use of attenuation relations between M , R and Y (1). Here expressions derived by Esteva and Villaverde (12) for peak accelerations and velocities were used to obtain their respective recurrence periods at the site of interest, with coordinates $100^\circ W$ and $17.97^\circ N$. The results of applying eq 19 have to be corrected in order to account for the dispersion in the attenuation relations. This was accomplished by means of an analytical procedure proposed by Esteva (1). Final results are shown in fig 6; they do not include local effects of stratigraphy and topography.

CONCLUDING REMARKS

A criterion has been derived and implemented for the assessment of local seismicity related with subduction zones. The criterion is a particularization of the philosophy of bayesian analysis of seismicity. The formulation presented herein allows coordinated analysis of information arising from available statistics and geotectonic evidence. It deals with overall seismic activity throughout subduction zones as well as with the spatial distribution of that activity.

ACKNOWLEDGEMENTS

Statistical data used in this work were selected and revised by S.K. Sing, who also surveyed and interpreted the geophysical information.

REFERENCES

1. Esteva, L (1976), "Seismicity" Chapter 6 of Seismic Risk and Engineering Decisions, edit. por C. Lomnitz y E. Rosenblueth, Elsevier, Amsterdam.
2. Rothé, J.P (1969), The seismicity of the earth 1953-1965, UNESCO.
3. Duda, S.J (1965), "Secular seismic energy release in the circum-Pacific belt", Tectonophysic, vol 2.
4. Brune, J. N (1968), "Seismic moment, seismicity and rate of slip along major fault zones", J. Geophys. Res., 73.
5. Berril, J. B (1975), "A study of high-frequency strong ground motion from the San Fernando earthquake", Ph D thesis, California Institute of Technology, Pasadena, Cal.
6. Keilis-Borok, V.I (1959), "On estimation of the displacement in a earthquake source and of source dimensions", Ann, Geofis (Rome) 12.
7. Starr, A. T (1928), "Slip in a crystal and rupture in a solid due to shear", Cambridge Phil. Soc. Proc. 24.
8. Kanamori, H. and Anderson, D.L (1969), "Theoretical basis of some empirical relations in seismology", Bull. Seism. Soc. Am. 59.
9. Chinnery, M. A. and North, R. G (1975), "The frequency of very large earthquakes", Science, V. 190, No 4220.
10. Rosenblueth, E (1969), Seismicity and earthquake simulation. Report on NSF-UCEER Conf. on Earthq. Engrg. Res., Pasadena, Cal.
11. Raiffa, H. and Schlaifer, R (1961), Applied Statistical Decision Theory, The MIT Press, Cambridge.
12. Esteva, L. and Villaverde, R (1973), "Seismic risk, design spectra and structural reliability", Proc. World Conf. Earthquake Eng., Rome.

Table 1. Auxiliary regions

Region i	Location	Coordinates	m_a	\bar{m}	m_b	length (km)	ϕ ($^{\circ}\text{C}$)	area(1.) (km^2)	$w_i(2)$
1	Southern Chile	33°S-45°S 60°W-90°W	8.30	8.5	9.0	1130	25	242000	0.786
2	Center Chile	27°S-33°S 60°W-90°W	8.30	8.6	9.0	670	10	378000	0.505
3	Northern Chile and Southern Peru	15°S-27°S 60°W-90°W	8.10	8.5	9.0	1450	27	285000	0.668
4	Peru and Ecuador	2°S-15°S 60°W-90°W	8.00	8.6	9.0	1440	10	818000	0.233
5	Central America	8°N-15.5°N 83.5°W-94°W	7.90	8.3	9.0	1160	43	125000	1.528
6	Alaska	50°N-64°N 142.1°W-164°W	8.50	8.5	9.0	1330	20	366000	0.520
7	Aleutians	50°N-60°N 165.1°E-160°W	8.25	8.5	9.0	2330	27	459000	0.417
8	Kamchatka	48°N-55°N 155°E-165°E	8.30	8.5	9.0	1040	19	302000	0.630
9	Kuriles	42°N-48°N 145°E-155°E	8.70	8.4	9.0	890	28	169000	1.127

(1) area = $100 L \cot \phi$; ϕ is defined in fig 1.

(2) w_i = area of region of interest/area of region i.

Table 2. Expected values of $p_i(M)$ for subzone A of fig 2.for $M = 6$

987	2111	1653	1714	1328	2514	1021	947	948	947
953	1267	2184	7456	1479	1974	983	1016	948	947
953	1214	2284	3321	1571	995	982	1072	1018	947
883	806	678	1026	1374	1229	962	856	833	881
814	814	969	1042	1321	877	938	873	814	848
814	814	851	852	1098	1985	875	814	814	814
814	814	883	931	979	983	913	875	814	848
814	814	814	814	869	848	845	848	875	814
814	814	814	814	814	836	844	814	844	873

for $M = 7$

1132	1316	1450	1228	1382	1311	1152	1132	1135	1135
1132	1414	1718	1539	1433	1311	1152	1132	1135	1135
1132	1669	1615	1807	1593	1405	1152	1132	1135	1135
1101	1021	1644	1060	1505	1219	1112	1104	1043	1043
950	950	1021	950	1087	950	1079	950	950	950
950	950	950	1056	1017	1076	950	1020	950	950
950	950	985	950	1019	950	1018	987	985	950
950	950	950	950	1019	1020	950	1020	984	985
950	950	950	950	950	950	950	985	984	984

These values must be multiplied by 10^{-5}

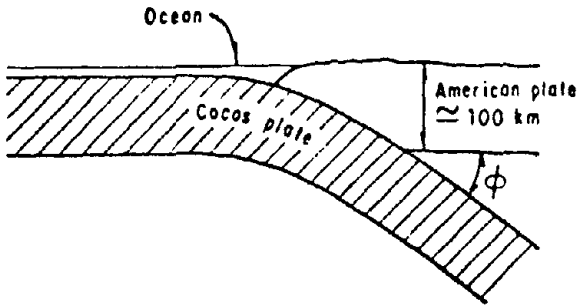


Fig 1. Schematic cross section of Cocos plate as it subducts underneath American plate

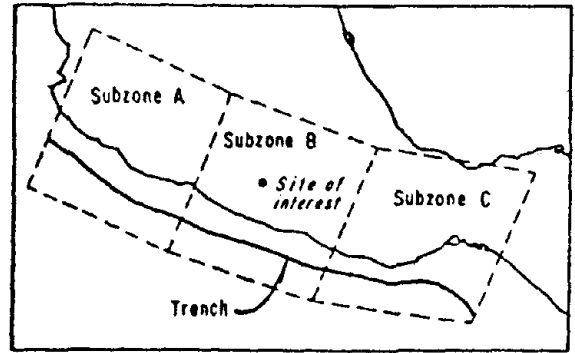


Fig 2. Cocos plate subduction zone in southern Mexico

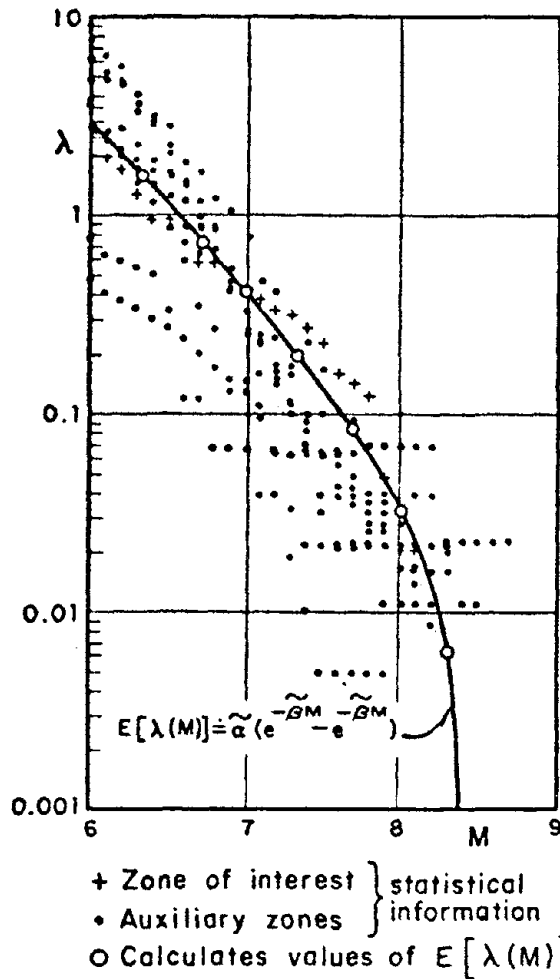


Fig 3. Comparison of $E[\lambda(M)]$ with statistical information

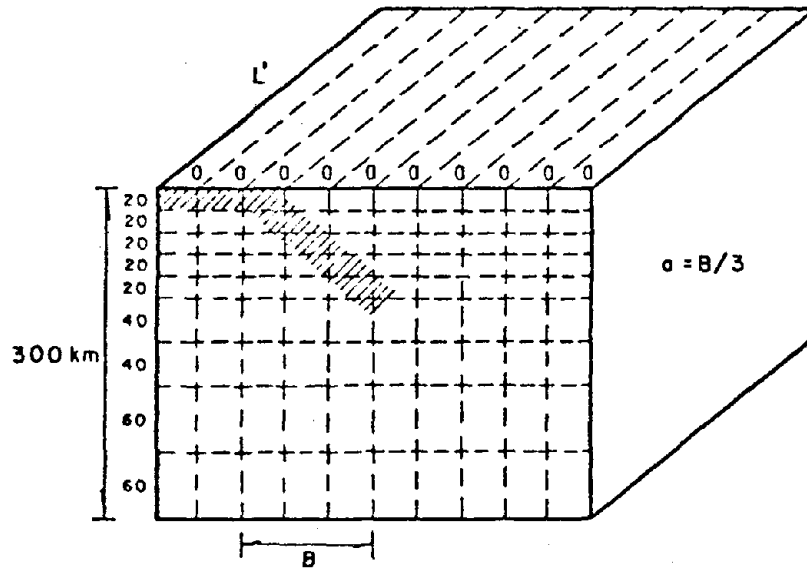


Fig 4. Subdivision of the subduction zone into cells for study of spatial variability of local seismicity

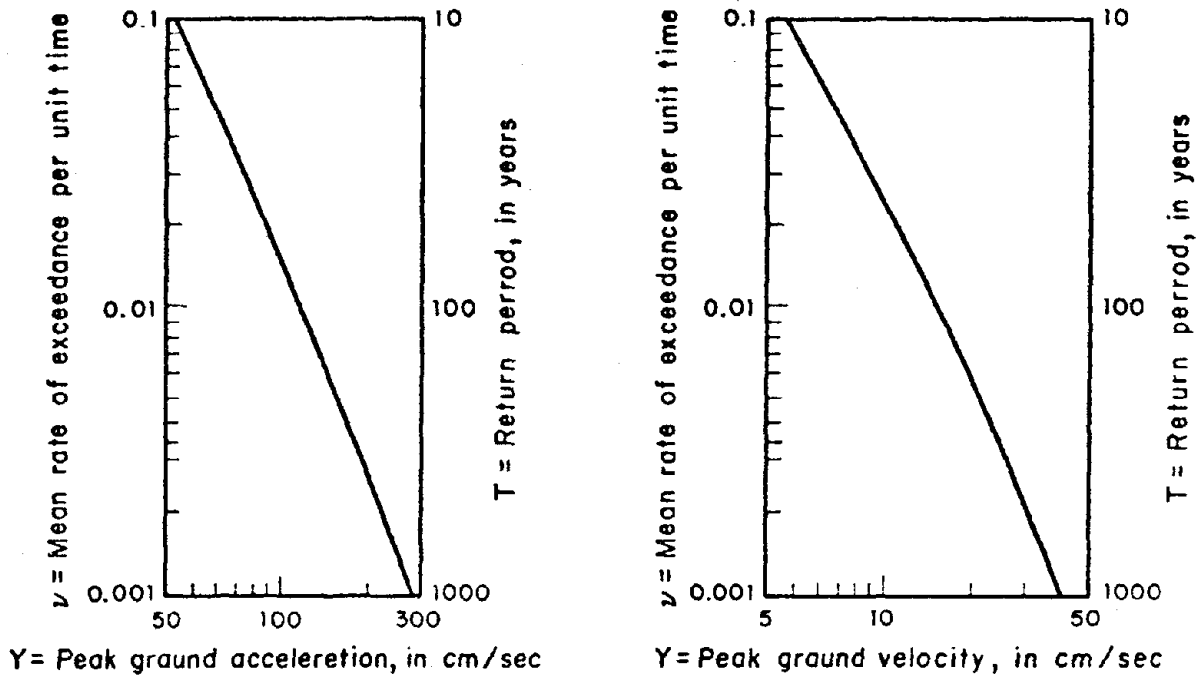


Fig 5. Intensity recurrence relations

SEISMIC HAZARDS ALONG THE MAKRAN COAST OF IRAN AND PAKISTAN:
THE IMPORTANCE OF REGIONAL TECTONICS AND GEOLOGIC ASSESSMENT

By
W. D. Page^I, W. U. Savage^{II}, J. N. Alt^{III},
L. S. Cluff^{IV}, and D. Tocher^V

ABSTRACT

The available record of historical seismicity along the Makran coast of Iran and Pakistan is limited and indicates scattered seismic activity east of the Iran-Pakistan border. If only the Iranian portion of the Makran coast is considered, the seismic hazard, based on interpretation of the historical record, may be incorrectly assessed as low. A more accurate analysis of the seismic hazard must include consideration of the regional tectonic framework in combination with the historical record of seismicity and geologic evidence of tectonic activity.

An assessment of the regional geology and tectonics along the Makran coast indicates two tectonic regions. The west Makran coast is characterized by Quaternary units displaced by thrust faults of the Zendan fault system. The south Makran coast lies shoreward of an active subduction zone characterized by a trench, an emerging coast, deformed sedimentary rock, and active volcanoes inland from the coast. The 27 November 1945 earthquake (M_s 8.3) near Pasni, Pakistan, is related to the near-coast subduction zone and field investigations have documented 1 to 3 m uplift of the coast at Ormara, Pakistan. The coast at Ormara has raised marine terraces and beaches, and similar raised terraces are found on the headlands along the entire Makran coast from Karachi, Pakistan, to Jask, Iran. At Konarak, Iran, where raised beaches were examined in some detail, nine terraces were observed. The two lowest terraces at Konarak occur as small remnants, and radiocarbon dates indicate they are Holocene in age.

Quaternary faults of the Zendan fault system are estimated to have earthquakes of magnitudes as large as 7.5. The raised marine terraces and other geologic evidence of the subduction zone indicate that the emergence of the Makran coast is probably associated with major earthquakes and that major earthquakes can be expected in the future along the entire active coastline from Karachi to Jask. This example illustrates the importance of assessing the tectonic framework and the regional geology and reevaluating the locations of historical earthquakes in the region as part of a realistic assessment of seismic hazards.

-
- I Project Geologist, Woodward-Clyde Consultants, San Francisco, California
 - II Senior Project Seismologist, Woodward-Clyde Consultants, San Francisco, California
 - III Project Geologist, Woodward-Clyde Consultants, San Francisco, California
 - IV Chief Geologist, Woodward-Clyde Consultants, San Francisco, California
 - V Chief Seismologist, Woodward-Clyde Consultants, San Francisco, California

INTRODUCTION

Modernization and industrialization of Iran is proceeding at a rapid pace and extending into regions of the country that have formerly been inhospitable desert with few scattered villages. The southern coast of Iran, south and east of Bandar Abbas to the Pakistan border, is one of these regions. As plans for development are made and various structures and facilities built, evaluation of seismic risk for major installations becomes desirable. If only the historical and instrumental seismic data are used for this evaluation, the risk would be incorrectly assessed because the instrumental seismic record in this region shows only a few small earthquakes, mostly located near Bandar Abbas and along the Pakistan border.

If the geologic record is examined and related to the probable plate tectonic model for the region, it is apparent that large earthquakes could occur here in the future. The area of study along the coast can be divided geologically and tectonically into two parts, the west Makran coast along the Strait of Hormuz from 50 km east of Bandar Abbas to Jask, and the main Makran coast along the Gulf of Oman and the Indian Ocean from Jask, Iran, to Karachi, Pakistan.

This paper summarizes the data and extends the interpretations presented in other studies on the Makran coast (1, 2). It discusses the seismic record in the area, presents a tectonic model, examines Quaternary faulting along the west Makran coast, and evaluates the uplift of the Makran coast. A comparison is also made between geologic similarities of the Pakistan part of the Makran coast, where the 1945 Pasni, Pakistan, earthquake (M_s 8.3) occurred, and the Iranian portion of the Makran coast.

The field work was done as part of a siting study by Woodward-Clyde Consultants for the Atomic Energy Organization of Iran. Six weeks from May to July 1975 were spent in the field. The authors wish to thank the geologists who worked on parts of the study for their assistance and critical discussion of the problem, particularly Gary Anttonen, Shakir Zuberi, Tom Freeman, Mike Perkins, and Paul Guptil. We also wish to acknowledge George Plafker for his discussions and contributions in the field.

SEISMICITY OF THE MAKRAN REGION

The instrumental seismic record of the Makran region (Fig. 1) is characterized by scattered, infrequent earthquakes in the period of record, May 1926 through April 1977. By contrast, in the Zagros Mountains to the northwest, moderate to large earthquakes are common, particularly along the eastern Zagros front. To the east of the Makran area, moderate earthquakes are scattered along the Owens fracture zone and inland along or near the Ornach Nal and Chaman fault belts (Fig. 2).

The Iranian segment of the Makran coast and Makran ranges has had only one third the number of earthquakes that the Pakistani segment has had. These earthquakes are concentrated in two places: east of Bandar Abbas, and near the Pakistan border. The two largest earthquakes in the region, the November 27, 1945 earthquake (M_s 8.3) and the August 5, 1947 earthquake (M_s 7.3), occurred near Pasni, Pakistan. The small number of earthquakes and their wide variation in reported focal depths (near zero

to more than 100 km) does not support any clear correlation with geologic structures in the Makran region. Jacob and Quittmeyer (3), however, show the depths of the earthquakes increase inland from the coast to a depth of 80 km.

REGIONAL STRUCTURES

Southern coastal Iran can be divided into three structurally distinct regions: The Zagros Mountains, which lie between the Persian Gulf and the Iranian Plateau; the west Makran coastal zone, which lies along the coast of the Strait of Hormuz from east of Bandar Abbas to Jask; and the Makran ranges, which lie between the Gulf of Oman and the Jaz Murian Depression.

The Zagros Mountains trend northwest and consist of broad anticlines that are locally pierced by salt diapirs. The valleys between the anticlines are narrow synclines that locally contain thrust faults. The structures progress from broad gentle anticlines along the Persian Gulf to a discontinuous series of low-angle thrusts and overturned folds to the more continuous, main Zagros thrust along the mountain front (4). The main Zagros thrust bifurcates at its southeastern end and appears to continue southward and southeastward into the Makran ranges as two major fault systems: the Zendan fault system along the west Makran coast, and the Jaz Murian system along the southern margin of the Jaz Murian Depression (Fig. 2).

The Makran ranges have two distinct structural trends. The west Makran coastal zone is a narrow strip, approximately 30 km wide, of north-trending folds and faults lying between the Strait of Hormuz and the north-trending Zendan fault system. The main Makran range east of the Zendan fault system has east-trending faults and folds extending from the Jaz Murian Depression to the Gulf of Oman.

Folding along the west Makran coast is characterized by broad, dish-shaped synclines separated by narrow, sharply defined anticlines that have steeply dipping flanks. The anticlinal folds are from 20 to 70 km long. High-angle, east-dipping reverse faults associated with overturned beds are common on the western anticlinal limbs.

The Zendan fault system extends more than 250 km, from the termination of the main Zagros thrust on the north to the coastal mountains west of Jask (Fig. 2). It is characterized by east-dipping faults produced by tangential compression and overthrusting toward the west. The fault system is relatively linear from its intersection with the main Zagros thrust to north of Senderk, approximately 50 km southeast of Minab. This segment of the fault system consists of only two or three main traces striking approximately N20°W. Fault traces in the southern part of this system are less linear, which could reflect lower-angle thrusting than that along the northern segment. Branch faults east of the main thrust zone appear to change in strike and parallel the east-west structural trends of the main segment of the Makran ranges.

The older rocks in west Makran region are the most strongly deformed, indicating deformation has been continuous since Pliocene or early Quaternary. Older Quaternary alluvium, which was deposited across the folded and eroded Tertiary strata with a marked angular unconformity, is faulted and deformed.

Folds in the Makran ranges east of the Zendan fault system generally parallel the southeasterly and east-west trends of the Makran ranges. Overturning toward the south associated with north-dipping thrust faults is common along the southern flanks of these structures (4). Ahmed (5) describes similar structural relationships in the eastern Makran ranges of Pakistan. Faults at the western end of the Jaz Murian Depression and along its southern border also exhibit evidence of Quaternary activity (1).

QUATERNARY FAULTING IN THE WEST MAKRAN AREA

The Zendan fault system has had late Quaternary displacement (1, 6). Fault scarps in the late Quaternary alluvial fans along and north of the Senderk River, approximately 45 km southeast of Minab, indicate uplift of eastern blocks relative to the western blocks. Holocene displacement (7000 to 1250 yr BP) occurs 40 km north north of Minab (6). This faulting is also compressional in nature, but with the southwestern block overthrust to the northeast. Quaternary fault activity along the system is less pronounced south of Senderk, but scarps suggest late Quaternary faulting involving uplift and overthrusting from the east.

Several smaller faults, found 20 km west of the main Zendan fault zone in an area southeast of Kuhestak displace Quaternary alluvium. These are east-dipping reverse faults found in the steeply overturned, western limbs of anticlines. They include the 8-km-long Zeyarat fault, and the 20-km-long Labani fault.

UPLIFT OF THE MAKRAN COAST

Raised Quaternary beaches and marine terraces along the Makran coast from Jask, Iran, to Karachi, Pakistan indicate a tectonically emerging coast (7, 8) related to earthquakes (9). The coast is marked by a series of prominent headlands separated by low areas. The headlands are generally flat topped or stepped by marine terraces. Some terraces are 1 to 2 km wide and 10 to 15 km long. The wave-cut terraces are locally tilted, and small faults having a few meters displacement cut some terraces. Landward from and between the headlands are low coastal plains characterized by accretionary beaches, lagoonal deposits, and tombolos.

NOVEMBER 27, 1945, EARTHQUAKE, M_s 8.3

The November 27, 1945 earthquake near Pasni, Pakistan is believed typical of the seismic events along the Makran coast, including the seismically quiet Iranian sector of the coast. The published locations of this earthquake were as far as 200 km apart, so the earthquake has been studied and relocated to near Pasni, Pakistan (Fig. 1) The intensity of the shock may have reached XI, on the modified Mercalli scale, at Pasni and Ormara. Many one-story buildings there, constructed of unreinforced masonry (sun-dried brick) and dressed stone and mud mortar, collapsed or were seriously damaged during the earthquake. The intensity of the earthquake at Karachi had decreased to not more than IV or V, and at Jiwani to not more than IV (1, 9).

Approximately 2 m uplift of the coast occurred at Ormara (1, 9). The Ormara area is characterized by a steep, rocky headland that is connected to the mainland by a low tombolo. Pre-1945 beaches and wave cut

platforms are now 1 to 3 m above highest tide and the tombolo broadened several hundred meters. Moreover, the Ormara headland and vicinity had been uplifted prior to the 1945 earthquake, indicating that uplift has continued throughout the late Quaternary, or longer (1, 9).

RAISED BEACHES IN IRAN

The highest, most extensive sequence of raised beaches in Iran is present on the Konarak headland, an area that is similar to the Ormara headland. The nine terraces preserved on the south side of Konarak headland, which is connected to the mainland by a tombolo, have been described (1, 7, 9) and the conclusions are presented here. Shallow-water, marine deposits of late Quaternary age form terraces and overlie siltstone bedrock of Tertiary age with an angular unconformity. Some terraces are continuous for several kilometers, whereas others are preserved as only scattered remnants. The terraces are marked by wave-cut platforms and wave-cut cliffs. With increasing elevation, the terraces show an increase in dissection and weathering, and shells in the deposits show increasing recrystallization.

The two lowest terraces occur as small remnants along the southeast side of the headland. The third and most extensive terrace covers most of the southeast part of the headland. The deposits of the third terrace consist of about 4 m of limey sands and silts having numerous shells. Uranium series dates on the shells range from 138,000 to 156,000 years old, and indicate this terrace is Sangamon in age (9). The fourth through ninth terraces are older but have not been dated.

LONG TERM AVERAGE RATES OF UPLIFT

Calculating the amounts of uplift and rates at a particular place requires estimates of the relative (eustatic) position of sea level during the Quaternary at that place. Calculations of Sangamon high sea level stand (approximately 125,000 years ago) at plus 6 m (10) used in this study are based on the late Pleistocene sea levels recorded from Barbados (11) and New Guinea (12). Clark's (13) curve of the Holocene rise of sea level along the Makran coast is used for Holocene sea level estimates [see (9) for a more complete discussion].

At Konarak, the best Holocene data, shells in situ from raised lagoonal deposits associated with the lowest terrace, give a Holocene rate of uplift the same as the post-Sangamon rate, suggesting the actual tectonic rate is 0.01 to 0.02 cm/yr (9). There is no post-Sangamon rate for comparison, but the headland and associated raised terraces are higher than at Konarak (14). This could indicate a faster long-term average rate of tectonic uplift for the Ormara area. At Jask, the post-Sangamon uplift rate is zero (9).

The long-term average uplift rate appears to increase from Jask on the west to Ormara on the east. This reflects different amounts of uplift at different places on the coast, a fact supported by the tilting and faulting and discontinuous remnants of the pre-Holocene terraces seen all along the coast. In general, the terraces increase in number and elevation from one at Jask to nine at Konarak up to 100 m in elevation, and an unknown number at Ormara up to 500 m in elevation.

PLATE TECTONIC MODEL

The plate tectonic model (Fig. 2) used in this report was described by Page and others (1) and is from Stonely (15), White and Klitgord (16), and Farhoudi and Karig (17). In the proposed model, the Afro-Arabian plate is moving northeastward with respect to the Eurasian plate and underthrusting beneath it. The Zagros thrust zone connects with the north-trending Zendan fault system, which in turn connects with a subduction zone off the south Makran coast.

The northern part of the Zendan fault system apparently connects to the east end of the Zagros thrust and the western end of the subduction zone off the south Makran coast. Stonely (15) characterizes the Zendan fault system as a right-slip fault. Field reconnaissance during this study, however, revealed no positive evidence of right slip along this structure. Surface features associated with the fault system indicate overthrusting from the east, suggesting a more easterly direction of movement for the Arabian plate than that postulated by Stonely. However, the Zendan fault system could have a strong component of right slip obscured by thrust displacement.

The postulated active subduction zone off the Makran coast extends from the Zendan fault system to the Owens fracture zone and the Chaman fault. Evidence for this subduction zone consists of 1) active andesitic volcanoes north of the Jaz Murian Depression and 350 km north of the trench in the Gulf of Oman (3); 2) an accretionary sequence of turbidite deposits constituting the Makran ranges which are being squeezed between subducting oceanic lithosphere on the south and the Eurasian continental lithosphere on the north (17); 3) seismic events that increase in depth inland from the coast (3); and 4) raised beaches between Jask, Iran, and Karachi, Pakistan (7), which indicate episodic uplift of the continental margin along the southern Makran coast (1, 9). The active fault system trending along the southern edge of the Jaz Murian Depression is not a plate boundary in the proposed model, but is related to the subduction zone (1).

EVALUATION OF SEISMIC HAZARD

In spite of the low seismicity known from the historical and instrumental record, the geologic evidence and the tectonic setting indicate that the coastal area of Iran from 50 km east of Bandar Abbas to the Pakistan border is tectonically active and, therefore, is an area of significant seismic hazard.

Along the west Makran coast, numerous faults, including faults in the Zendan fault system, have displaced Quaternary alluvial units in the west Makran region. These Quaternary units have not been dated (other than locally by reconnaissance work of Vita-Finzi (8)), nor has the faulting been studied in enough detail to assess the degree of activity. However, lengths of the faults studied for this report can be used to estimate maximum earthquake magnitudes. Using the curves of Patwardhan and others (2) the Zendan fault system (200 ± km long) is estimated to have a maximum earthquake magnitude of 7.5, the Labani fault (20 km long) a maximum magnitude of 6.5, and the Zeyarat fault (8 km long) a maximum magnitude of 6.0. Three earthquakes, magnitudes 5.3, 5.6, and 6.25 (Fig. 1), have occurred in the northern area of the Zendan fault and tend

to confirm the estimates of magnitude based on fault length; however, magnitude/fault length relationships alone are generally inadequate to confidently assess earthquake magnitude and further comparisons of other parameters are needed to give more reliable estimates.

Along the Makran coast, major earthquakes can be expected. If the 1945 Pasni earthquake is typical, and assuming no aseismic uplift in this area, then uplift along the Makran coast can occur as discrete increments along different parts of the coast at different times. The lower two terraces at Konarak may have formed this way. Using the calculated uplift rate at Ormara of 0.1 to 0.2 cm/yr, and an uplift of 2 m for the Pasni-Ormara earthquake, then the recurrence interval of such an earthquake along this particular part of the coast is 1000 to 2000 years. At Konarak, where the uplift rate is slower (0.02 to 0.1 cm/yr), the recurrence interval of a Pasni-Ormara-type earthquake would be 2000 to 10,000 years. Assuming the Pasni earthquake reflects a strain release along the coast from Pasni to east of Ormara, a distance of 125 km, and measuring the length of the coastal subduction zone of 850 km, the recurrence interval for a similar magnitude 8+ earthquake somewhere along the Makran coast is approximately 125 to 250 years. Because the terraces increase in elevation and number toward the east, the east end of the coast appears more likely to have more frequent and larger magnitude earthquakes than the west end.

This analysis of the regional geology, tectonics and plate tectonic model, local detailed geologic studies, and evaluation of seismicity of the Makran region in Iran underscores the need to incorporate all these disciplines before a reasonable assessment of seismic hazard can be made: it must be kept in mind that a lack of seismicity in an area is not necessarily an indication of low seismic hazard.

REFERENCES

1. Page, W. D., Anttonen, G., and Savage, W. U., 1978 (in press) The Makran coast of Iran, a possible seismic gap: U.S. Geological Survey, Open-File Report.
2. Patwardhan, A. S., Tocher, D., and Savage, E. D., 1975, Relationships between earthquake magnitude and length of rupture surface based on aftershock zones (abs): Geological Society of America Abstracts with Programs, v. 7, no. 3, p. 419.
3. Jacob, K. H., and Quittmeyer, R. C., 1978, The Makran region of Pakistan and Iran--trench-arc system with active plate subduction: manuscript in press.
4. Iranian Oil Operating Companies (IOOC), 1969, Geologic map of southwest Iran: Geological and Exploration Division, Tehran, scale 1:1,000,000.
5. Ahmed, S. S., 1969, Tertiary geology of part of South Makran, Baluchistan, West Pakistan: American Association of Petroleum Geologists Bulletin, v. 53, no. 7, p. 1480-1449.
6. Vita-Finzi, C., and Ghorashi, M., 1978, A recent faulting episode in the Iranian Makran: Tectonophysics, v. 44, no. 5, p. T21-T25.

7. Little, R. D., 1972, Terraces of the Makran coast of Iran and parts of West Pakistan: University of Southern California, M.A. thesis, 151 p.
8. Vita-Finzi, C., 1975, Quaternary deposits in the Iranian Makran: *Geographical Journal*, v. 141, p. 415-420.
9. Page, W. D., Alt, J. D., Cluff, L. S., and Plafker, G., 1978 (in press), Evidence for the recurrence of large magnitude earthquakes along the Makran coast of Iran and Pakistan: *Tectonophysics*.
10. Broecker, W. S., and van Donk, J., 1970, Insolation changes, ice volumes and the O^{18} record in deep-sea cores: *Review of Geophysics and Space Physics*, v. 8, p. 169-198.
11. Steinen, R. P., Harrison, R. S., and Matthews, R. K., 1973, Eustatic low stand of sea level between 125,000 and 105,000 B.P.--evidence from the subsurface of Barbados, West Indies: *Geological Society of America Bulletin*, v. 84, p. 63-70.
12. Bloom, A. L., Broecker, W. S., Chappell, J. M. A., Matthews, R. K., and Mesolella, K. J., 1974, Quaternary sea level fluctuations on a tectonic coast--new $^{230}\text{Th}/^{234}\text{U}$ dates from the Huon Peninsula, New Guinea: *Quaternary Research*, v. 4, p. 185-205.
13. Clark, J. A., 1977, Global sea level changes since the last glacial maximum and sea level constraints on the ice sheet disintegration history: University of Colorado, Ph.D. thesis, 150 p.
14. Photographic Survey Corporation, 1958, Reconnaissance geology of part of West Pakistan--a Colombo plan cooperative project: Photographic Survey Corporation, Toronto, Canada, Geological Maps 3 to 5.
15. Stonely, R., 1974, Evolution of the continental margins bounding a former southern Tethys, *in* Burk, C. A., and Drake, C. L. (eds.), *The geology of continental margins*: Springer-Verlag, New York, p. 889-903.
16. White, R. S., and Klitgord, K., 1976, Sediment deformation and plate tectonics in the Gulf of Oman: *Earth and Planetary Science Letters*, v. 32, p. 199-209.
17. Farhoudi, G., and Karig, D. E., 1977, The Makran of Iran and Pakistan as an active arc system: *Geology*, v. 5, p. 664-668.

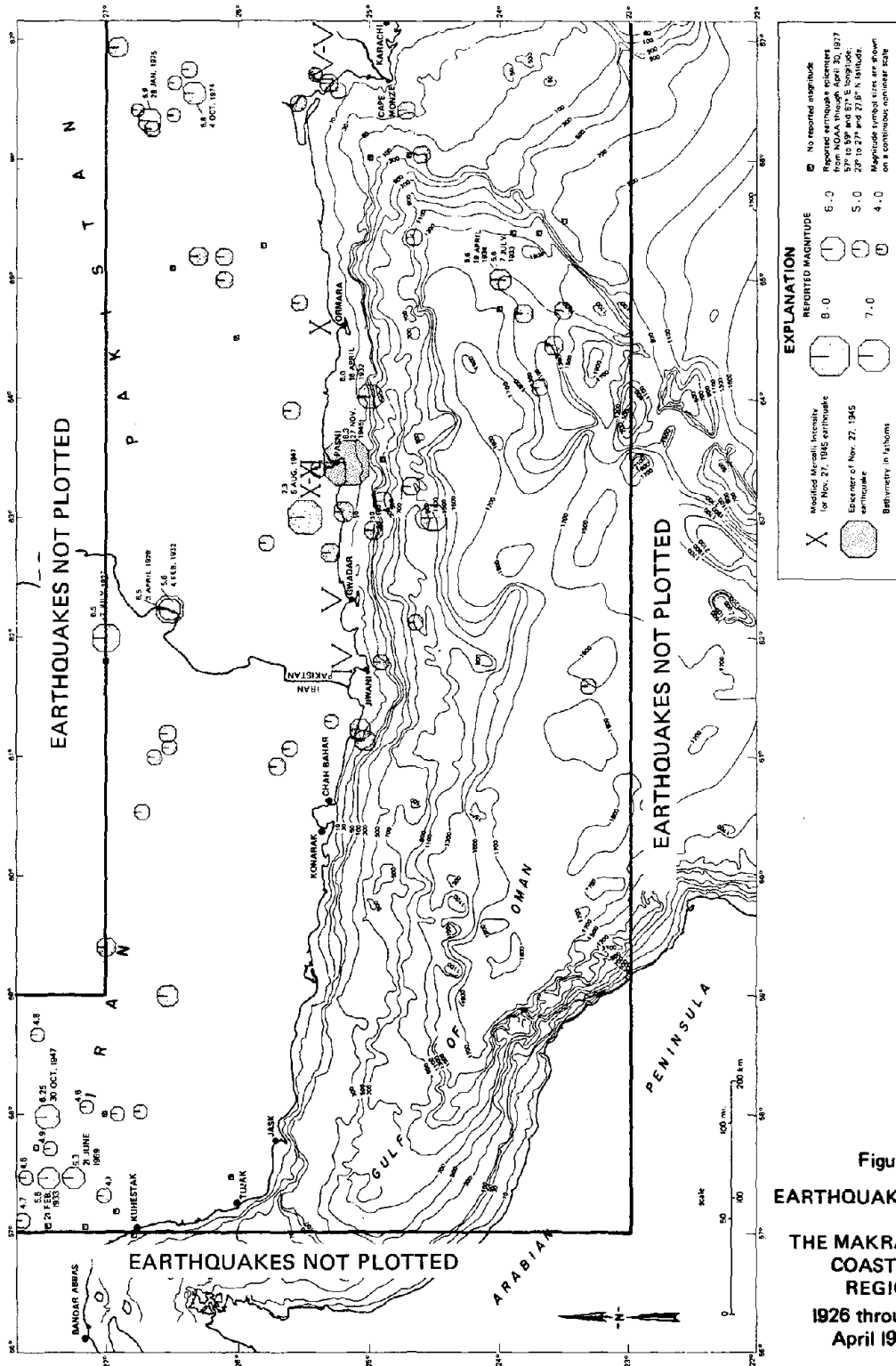


Figure 1
EARTHQUAKES
OF
THE MAKRAN
COASTAL
REGION
1926 through
April 1977)

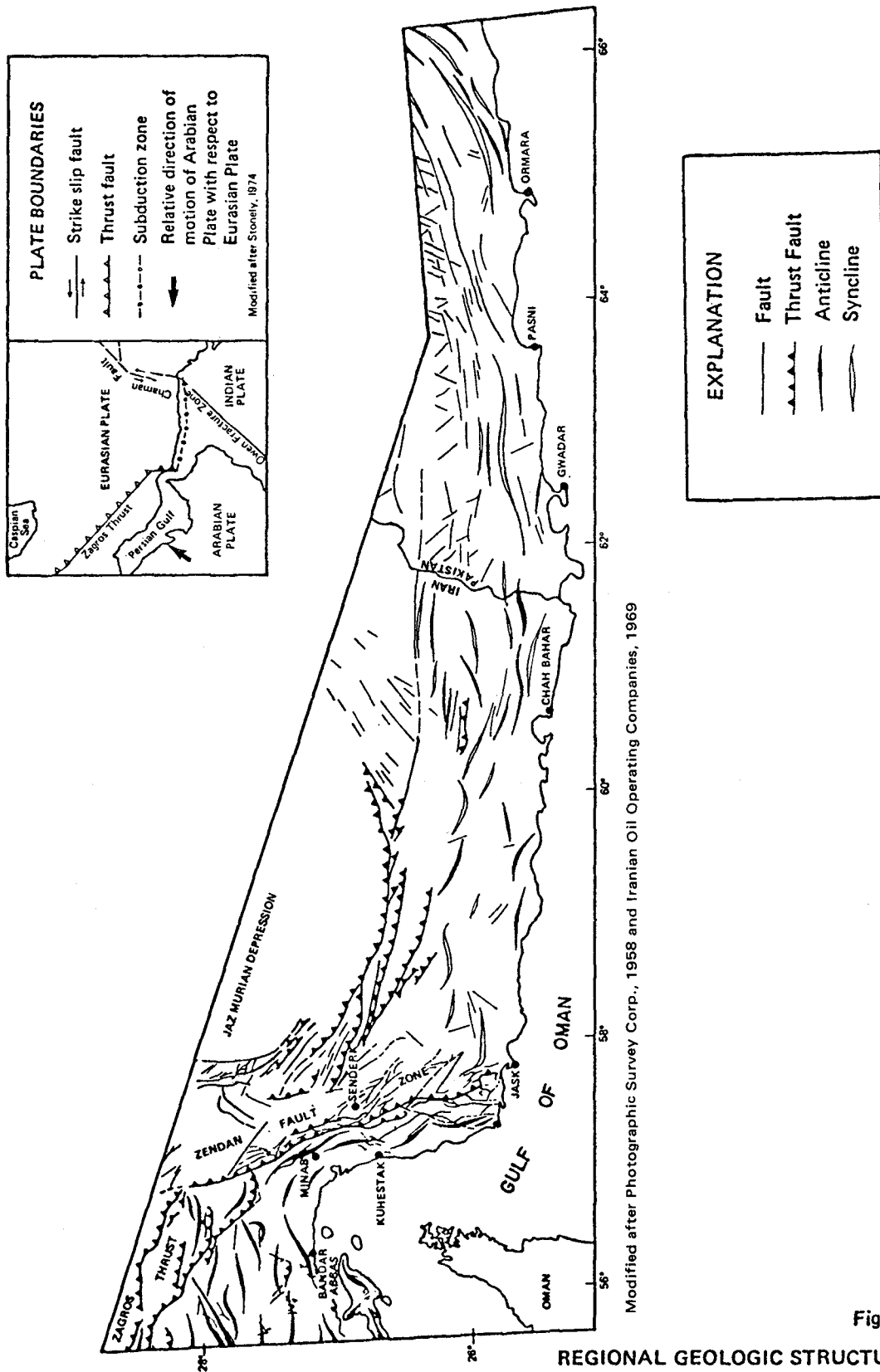


Figure 2

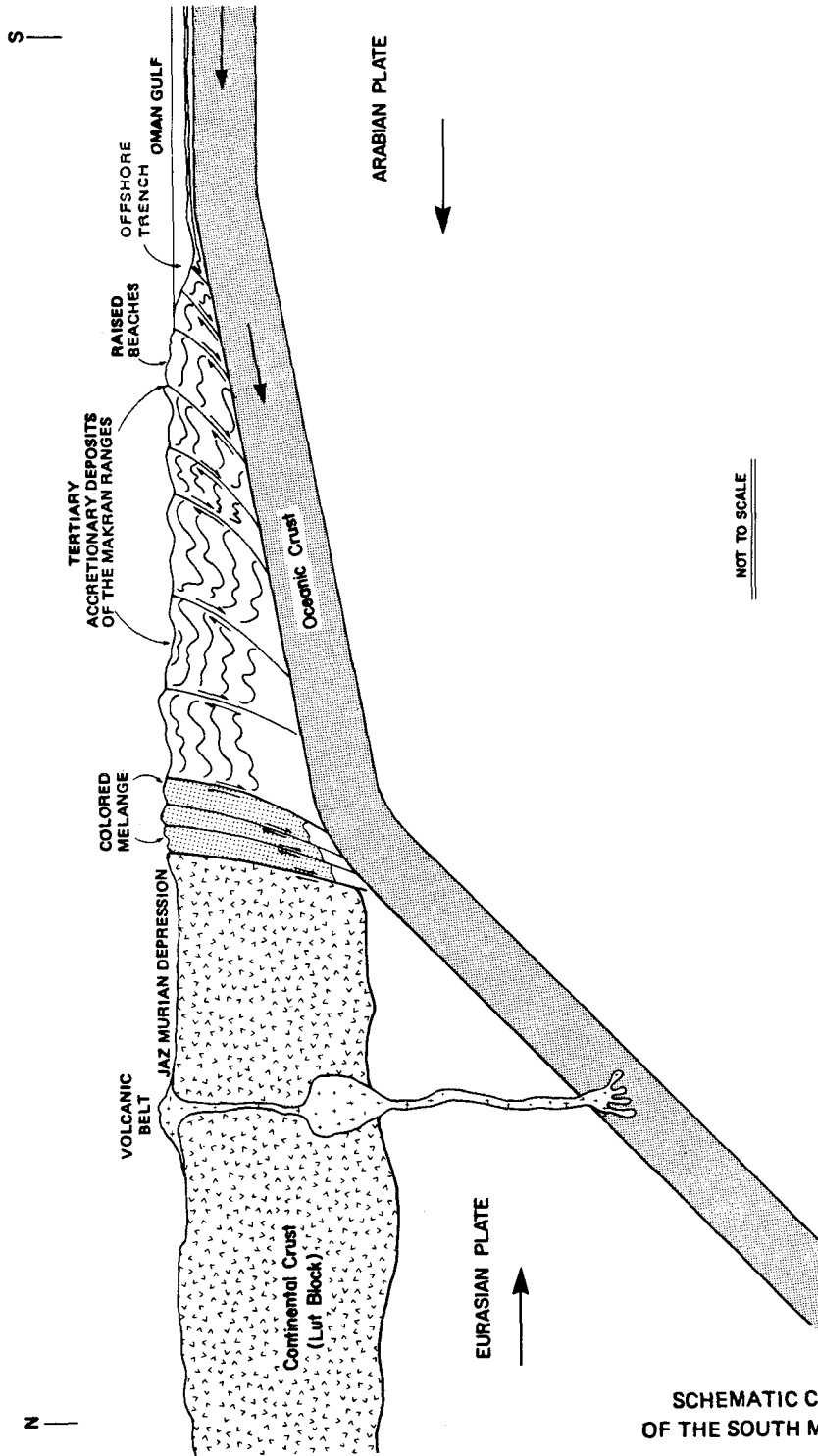


Figure 3
SCHEMATIC CROSS-SECTION
OF THE SOUTH MAKRAN COAST

Modified after Farhoudi and Karig, 1977

INTENTIONALLY BLANK

ENGINEERING AND SEISMOLOGICAL OBSERVATIONS AT DAMS

by

S. Kh. Negmatullaev^I, G. S. Seleznyov^{II}, D. W. Simpson^{III} and C. Rojahn^{IV}

ABSTRACT

Seismological studies related to dams must investigate the pre-impounding seismic regime and monitor any changes in seismicity during and after filling of the reservoir. Engineering seismological studies must investigate the kinematics of ground motion in and around the dam during earthquakes, the dynamic stresses and pore pressure within the body of the dam and any residual deformation. Depending on the size of the dam and seismic hazard, three levels of investigation are recommended:

- 1) For dams less than 100 meters high in areas of low seismicity, continuous operation of 1 to 3 seismograph stations in the reservoir region and 1 or 2 strong-motion instruments on or near the dam.
- 2) For dams more than 100 meters high in areas of moderate to high seismicity, continuous operation of 4 to 6 seismograph stations around the reservoir and 4 to 6 sets of instruments for measuring strong-motion, stress, pore pressure and residual deformation within the dam.
- 3) For dams of special interest, such as the 315 meter high earth-fill Nurek Dam in Tadjikistan, continuous operation of more than 6 seismograph stations around the reservoir including at least 5 years of pre-impounding monitoring; and a more complete complex of instruments for measuring strong-motion and stress deformation conditions within the dam.

INTRODUCTION

In order to satisfy increased demands for hydroelectric power, irrigation, flood control and water supply, the number of large reservoirs, especially those with very high dams, has increased rapidly over the last two decades. There are now more than 400 dams higher than 100 meters of which 93 have heights greater than 150 meters (1). The highest dams are: Ragoun (USSR, 340 m), Nurek (USSR, 317 m), Grande Dixence (Switzerland, 285 m), Inguri (USSR, 272 m), Rossella (Italy, 265 m), Vajont (Italy, 261 m), Mica (Canada, 242 m), Sayano-Shushenskoe (USSR, 242 m), Mauvoisin (Switzerland, 236 m) and Oroville (USA, 236 m). These dams produce reservoirs with capacities (for the largest dams) from 10 to 169 km³. About half of these reservoirs are located in seismically active regions. These unique structures demand special attention, not only during the planning and construction stages, but also during utilization.

-
- I Institute Director, Institute of Seismoresistant Construction and Seismology, Dushanbe, Tadjikistan, USSR.
- II Chief, Department of Hydrotechnical Structures, Institute of Seismoresistant Construction and Seismology, Dushanbe, Tadjikistan, USSR.
- III Research Associate, Lamont-Doherty Geological Observatory of Columbia University, Palisades, New York 10964.
- IV Research Civil Engineer, U.S. Geological Survey, Menlo Park,

Preceding page blank

Large dams must be constructed to withstand the strongest earthquake shaking expected at the site. This requires information on both the expected maximum earthquake and the response of the dam to this ground shaking. In the design of most critical engineering structures, seismic risk is evaluated assuming that future seismicity can be estimated from the seismic history of the area. This assumes that the structure is passive and has no effect on the local seismicity. With dams and large reservoirs this may not be true. The impounding of large reservoirs has, in a number of cases, severely modified the local seismic regime (1, 2). Estimates of seismic risk for large dams must, therefore, include the effect of natural seismicity and also the potential for induced seismicity.

To insure the seismic safety of a large dam requires the integration of geological, seismological and engineering studies of the reservoir area, the dam site and the dam structure. These studies, and a close coordination between them, must extend throughout the planning, construction and utilization of the project. In the following, we will discuss some of the techniques and instrumentation required for monitoring the seismic safety of a dam, with special reference to existing and proposed studies at the Nurek Dam in Tadzhikistan, USSR.

SEISMOLOGICAL OBSERVATIONS

Seismicity studies at reservoirs, as with any large engineering structure, must include studies of regional seismicity in order to estimate the maximum expected earthquake for which the structures must be designed. In the early planning stages for a large dam project, estimates must be made of the seismic risk. This requires a knowledge of the regional seismicity, active geological structures and historical earthquake activity within the region. From these data, standard techniques are used to estimate the expected size and location of the maximum natural earthquake. Unlike other types of structures, however, studies of seismicity at large reservoirs must also take into consideration the effect which the reservoir may have on changing the seismic regime (1).

The initial basis for evaluating the seismic requirements for a dam is the regional seismicity. In most areas of moderate to high seismicity, such information is available from regional or national seismograph networks. These provide an indication of the general level of seismicity in the project area. Early in the planning stages for the dam, special studies should be initiated, increasing the number of stations and improving the coverage of the reservoir area. If there is seismicity near the reservoir, seismological and geological information should be integrated to identify the extent of active or potentially active faults. As the time of impounding approaches, the station coverage should be further increased to provide detailed observations during the initial filling cycles.

How many stations are required will depend on a number of factors, including the background level of seismicity, the size of the dam and reservoir, the potential for induced seismicity and the hazard posed to populated areas (5). For any large dam, 1 to 3 sensitive seismograph stations should be included in the standard monitoring equipment for the project. For dams more than 100 meters high in areas of moderate to high seismicity, 4 to 6 stations should begin operation at least 5 years prior to first impounding and continue to operate throughout the lifetime of the

dam. These stations should be located within an area, centered on the reservoir, with a diameter of less than twice the maximum dimension of the reservoir.

For those dams which are of special interest, either because of their size or specific seismic hazards, a temporary network of stations should supplement the long-term observations during, and for 5 years following, the first filling of the reservoir. This network, consisting of 6 to 10 stations, should be located in the immediate vicinity of the reservoir, with special emphasis near areas of active faulting and near the deepest part of the reservoir.

Studies of reservoirs with potential for induced seismicity require monitoring of both temporal and spatial changes in seismicity. In order to positively identify changes in the seismic regime caused by filling of a reservoir, it is necessary to have stable observations of seismicity over many years. At most of the reservoirs where large induced earthquakes have occurred (e.g., Kariba, Koyna, Kremasta, Hoover, Hsinfengkiang) (1, 2), networks of seismograph stations were installed only after the onset of increased seismicity, so that it has been difficult to compare pre- and post-impounding seismicity and to define the exact nature of changes caused by the reservoir.

When induced or natural earthquakes occur near a reservoir, it is important to be able to locate hypocenters with sufficient accuracy to associate activity with specific faults. Migration of activity and changes in the level of activity associated with variations in water level in the reservoir may be important in predicting future patterns of seismic activity. A dense network of high-magnification stations close to the reservoir is necessary to provide the accuracy and detection of microearthquakes required for such studies.

As an example of a combination of regional, local and intensive seismicity surveys for observation at a large reservoir where induced seismicity is occurring, we will use the case of Nurek Reservoir on the Vakhsh River in Tadjikistan (3). When completed in 1979, the earth-fill Nurek Dam will be 315 meters high and impound a reservoir volume of 10.5 km^3 . The reservoir first filled to 100 meters in 1972 and the second stage of filling, to 200 meters, was in 1976 (Figure 1).

The southern part of Tadjikistan is a region of moderate to high seismicity. Instrumental observations of seismicity began in Tadjikistan in 1920. Since 1955, regional seismic stations have operated around the reservoir, and the catalog of earthquakes greater than magnitude 2.5 is complete from 1955. The maximum expected earthquake for the area has been estimated as magnitude 6.5 (3).

As shown in Figure 1, there have been pronounced increases in seismic activity during the first two stages of filling of the reservoir. Before filling, approximately 10 earthquakes per year greater than magnitude 1.5 occurred within 10 km of the reservoir. During the early filling stages, this number rose to more than 100 per year. The largest earthquakes following impounding were two of magnitude 4.5 near the southwest end of the reservoir, at the end of the first stage of filling in 1972 (4).

When the dam began filling in 1971, there were five stations within 40 km of the reservoir operated by the Tadjik Institute of Seismoresistant Construction and Seismology and four additional stations were added before 1976. In 1975, as part of a joint Soviet-American program in earthquake prediction, a radio-telemetered network of 10 stations was installed around the reservoir. Figure 2 shows the location of the two sets of stations. The combined network of Soviet and American stations is well-suited for studying both temporal and spatial variations in seismicity. The Soviet stations have provided a stable and complete catalog of earthquakes for the 10-15 year period prior to and during filling of the reservoir. Each of the Soviet stations is manned and operates independently, recording three components of ground motion at magnifications of 10,000-20,000. Because of the relatively wide spacing between stations, the location accuracy is not high, but the temporal stability provides a clear indication of the changes in seismicity caused by filling of the reservoir (Figure 1).

The stations of the American network installed in 1975 operate unattended, continuously telemetering data to a central recording location. Station magnifications are 200,000-500,000. The network is concentrated near the central part of the reservoir, where most of the induced seismicity is occurring. Within this area, location accuracy has improved by an order of magnitude and the detection threshold has decreased by 2 magnitude units.

Figure 1 shows that increased seismicity at Nurek is closely related to times of rapid change in water level (e.g., November 1972, March 1975, August 1976). There are also indications that the level of seismicity is also related to the rate at which the water level is changed. Thus, it is possible that careful control of the way in which the water level is changed can be used to control the level of seismic activity. In order to monitor such controlled changes in seismicity, or to observe changes in microearthquake activity preceding larger natural or induced earthquakes, a sensitive network of seismograph stations is required in the immediate reservoir area.

ENGINEERING INVESTIGATIONS

Many of the parameters necessary to study the seismic response of a large dam are included in the standard observations for the control and monitoring of the dam structure. These "static" observations include the monitoring of residual deformation (settlement and displacement), stress, pore pressure (especially in the core, in the upstream face and in the foundation), filtration rates through the dam and water levels upstream and downstream from the dam. These observations, some obtained by passive measurement and some through active experiments, are traditional and well known, and will not be discussed here. Usually, the extent to which these static observations are made depends on the size and importance of the structure.

When dams are constructed in seismic regions, these static observations must be supplemented with equipment for monitoring "dynamic" processes (5, 6, 7), especially the kinematic parameters of motion: displacement, velocity and acceleration. A detailed study of the dynamic processes taking place in dams during earthquakes also requires observation of

the dynamic deformation, stresses and pore pressure within the dam and its foundation. Such observations can lead to improved design techniques and predictions of the behavior of specific structures during severe ground shaking.

Following is a general description of proposed instrumentation for monitoring "dynamic" processes in Nurek Dam. The proposed schemes have been recommended by the Tadjik Institute of Seismoresistant Construction and Seismology. They are based on experience gained from studies of other large dams in the Soviet Union (6, 7).

The earth-fill Nurek Dam will have a height of 315 meters and a crest length of 700 meters; it will extend 1500 meters along the river channel (Figure 3). The body of the dam consists of a central water-resistant core, transition zones, supporting prisms of gravel and rockfill on the upstream and downstream faces. The gradients of the slopes are 1:2.25 for the upstream face and 1:2.20 for the downstream face. The dam will form a reservoir with a total capacity of 10.5 km³ and an area of 100 km², which will extend 70 km upstream from the dam. Annual variations in water level will be 50 to 60 meters (a volume of 4.5 km³).

Shown in Figure 3 is the proposed system for measuring kinematic parameters in the dam. The system will consist of 29 measuring points (13 permanent and 16 temporary); its purpose is to record the movement of the foundation, the walls of the canyon and the body of the structure during small and strongly felt earthquakes. The thirteen measuring points designed for long-term use are equipped with apparatus for recording strong and destructive earthquakes. The other 16 measuring points are to be used for short-term experiments (3 to 5 years). Their purpose is to obtain data for special projects such as the study of spatial variations in the vibration of the body of the dam, variations in the dynamic behavior of the rock canyon and/or the interaction of the structure with the rock foundation.

Shown in Figure 4 is a proposed system for observing dynamic stresses in the core and downstream prism, which is the most stressed element within the body of an earth-fill dam. The three-component dynamic stress cells are to be located at three levels with a total of 5 measuring points in the prism and 2 in the central core.

Also shown in Figure 4 are proposed locations for pore pressure measurements in the core of the dam and in the water-saturated upper prism. The instruments are to be located at the levels of the main viewing galleries, i.e., at 1/2 and 3/4 of the height of the dam.

Strainmeters for measuring residual deformations during earthquakes are proposed at 5 points along the transverse profile (maximum section) of the dam (Figure 4). These observations will be made at the crest on both slopes and in the viewing galleries at approximately 1/2 and 3/4 of the dam height.

Continuous observations will also be made of the variations in water level upstream and downstream of the dam. Locations of the proposed gauges are shown in Figure 4. The range of these observations must include variations in the reservoir level during normal use and also take into

account possible disturbances as the result of a strongly felt earthquake (e.g., seiches, increased filtration).

For monitoring and control of the dam structure, it is proposed that the following 24 channels of data be continuously recorded at a central site: residual displacements at the crest and on the slopes (6 channels); acceleration of the foundation and crest at the maximum section (6 channels); pore pressure in the upper prism and in the central core at 2 levels (4 channels); water level upstream and downstream of the dam (2 channels); and dynamic stress at one point in the core and at one point in the lower prism (6 channels).

The extent of instrumentation for measuring the dynamic response of Nurek Dam is based on the fact that the dam is unusually large and is located in a moderately active seismic zone. The degree to which smaller dams should be instrumented depends on the relative size and type of dam as well as the expected level and occurrence of seismic activity. A survey of instrumented dams in the U.S. (8) suggests that most instrumented dams fall into one of the following two categories: 1) dams where 1 or 2 strong-motion accelerographs have been installed to record site response; and 2) dams where 4 to 6 strong-motion accelerographs have been installed to measure site response and structural response. It is assumed that the extent of instrumentation at each of these dams is dependent upon the availability of funding, size and type of dam and extent of expected seismic activity. Considering such factors in general as well as experience with dam instrumentation in the USSR, the following instrumentation schemes are recommended: 1) for dams less than 100 meters high in areas of low seismicity 1 or 2 strong-motion instruments near and/or beneath the dam; 2) for dams more than 100 meters high in areas of moderate to high seismicity, 4 to 6 sets of instruments for measuring strong-motion on and near the dam as well as stress, pore pressure and residual deformation within the dam; and 3) for dams of special interest such as the 315 meter high earth-fill Nurek Dam, a more complete complex of instruments for measuring strong-motion and stress deformation conditions within the dam.

ACKNOWLEDGEMENTS

This work is supported in part by National Science Foundation Grants ENV 77-01092, AEN 75-22996, U.S. Geological Survey Contract 14-08-0001-15279 and Earth Science Section, National Science Foundation Grant GA 43650. We wish to thank Michael Hamburger for assistance in translation.

Lamont-Doherty Geological Observatory Contribution Number 2713.

BIBLIOGRAPHY

- (1) Simpson, D.W., 1976. Seismicity changes associated with reservoir loading; In "Induced Seismicity", edited by W.G. Milne, Eng. Geol., 10(2-4), 123-150.
- (2) Gupta, H.K. and B.K. Rastogi, 1976. Dams and Earthquakes, Elsevier, Amsterdam, 229 pp.

- (3) Negmatullaev, S.Kh. (ed.), 1975. Induced Seismicity near Nurek Reservoir; Donish Publishing House, Dushanbe, 88 pp. [in Russian].
- (4) Soboleva, O. and U.A. Mamadaliev, 1976. The influence of the Nurek Reservoir on local earthquake activity; Eng. Geol., 10, 293-305.
- (5) Bolt, B.A. and D.E. Hudson, 1975. Seismic instrumentation of dams; J. Geotechnical Engineering Division, Proc. Amer. Soc. Civil Engineers, 10, 1095-1104.
- (6) Sagdiev, T.G., R.S. Shuser and G.S. Seleznyov, 1966. On the establishment of engineering-seismological observations at dams; Eng. Seismol., No. 3-4, Donish Publishing House, Dushanbe, pp. 82-86 [in Russian].
- (7) Sagdiev, T.G., G.S. Seleznyov and U.L. Zaslavckii, 1968. Questions on the Organization of Engineering-Seismological Surveys at Dams; Donish Publishing House, Dushanbe, 41 pp. [in Russian].
- (8) Western Hemisphere Strong Motion Accelerograph Station List, 1976; USGS Open File Report N77-374, 1977, 112 pp.

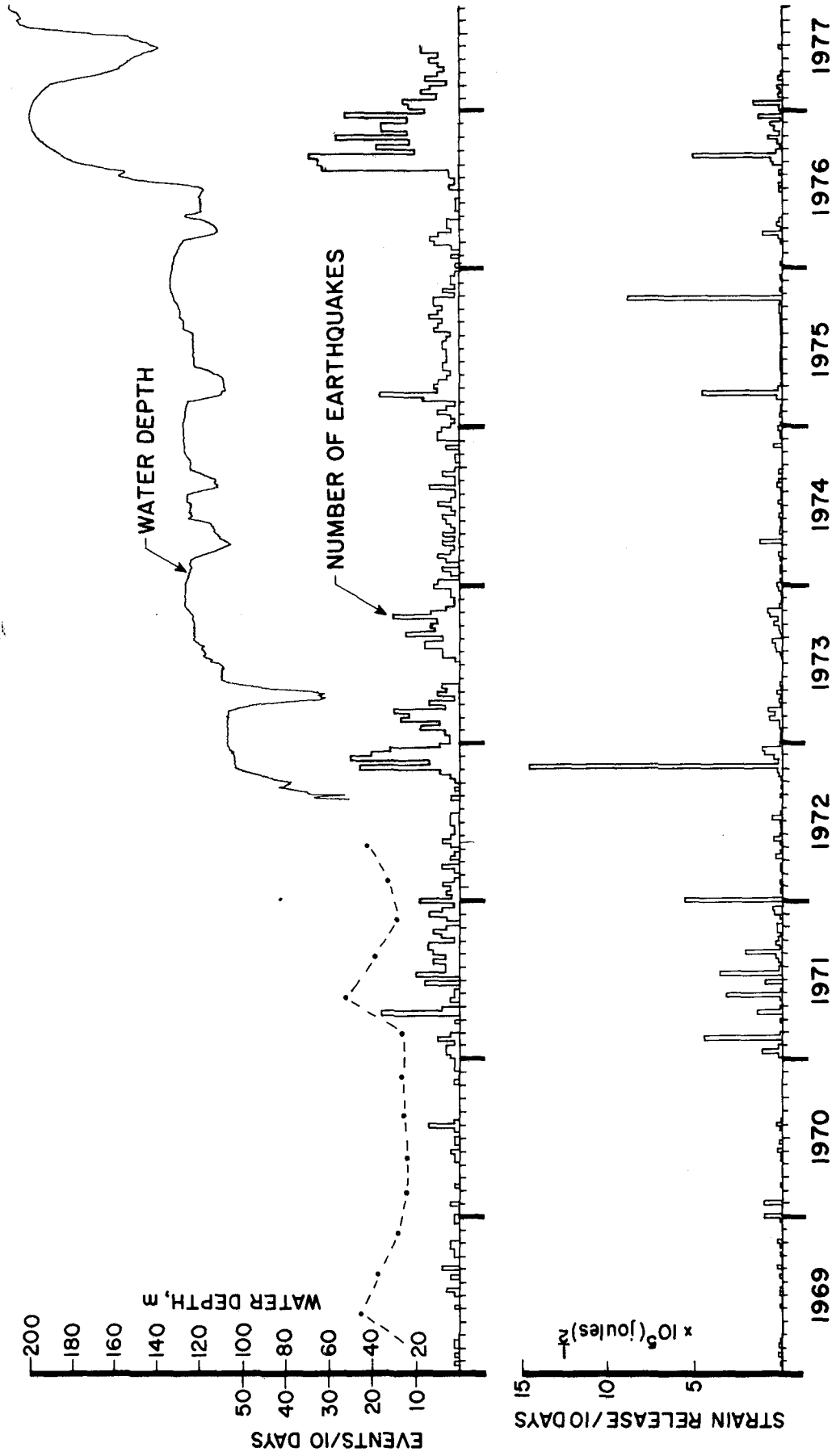


Figure 1: Water level, number of earthquakes per ten days and strain release per ten days for earthquakes within 10 km of Nurek Reservoir.

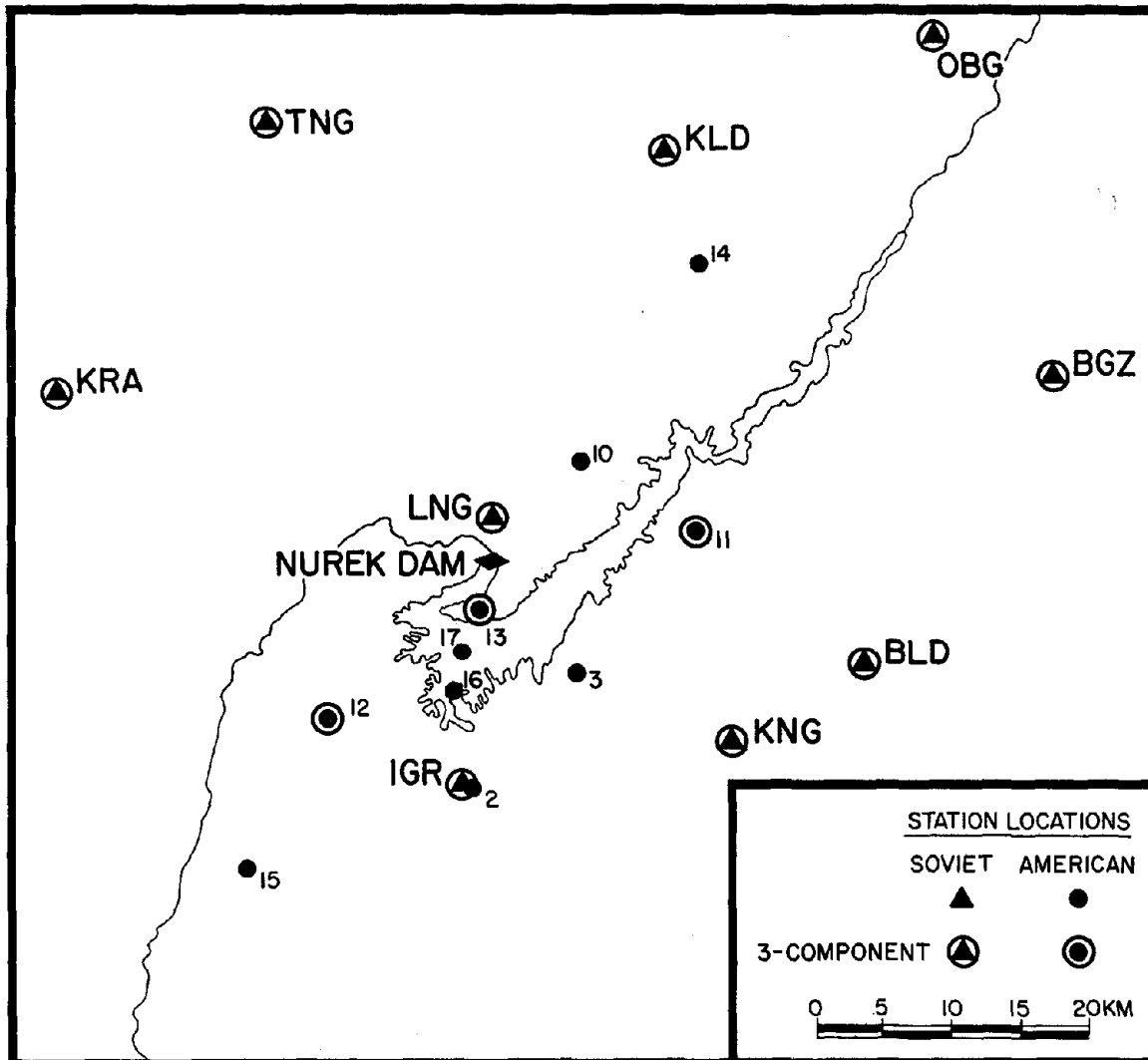


Figure 2: Seismograph stations in the vicinity of Nurek Reservoir.

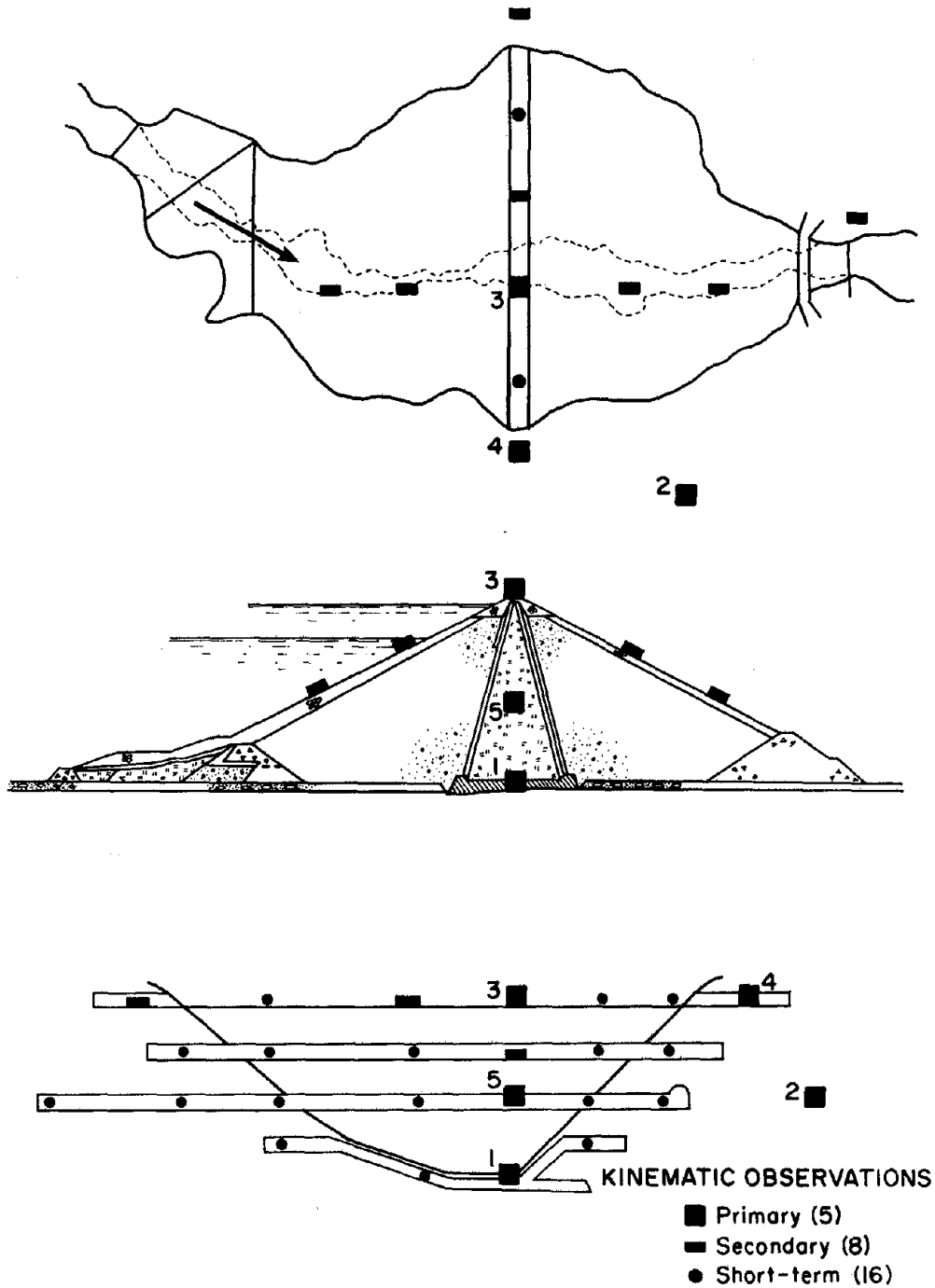


Figure 3: Plan view, transverse section and longitudinal section of Nurek Dam showing proposed system for measuring strong-motion.

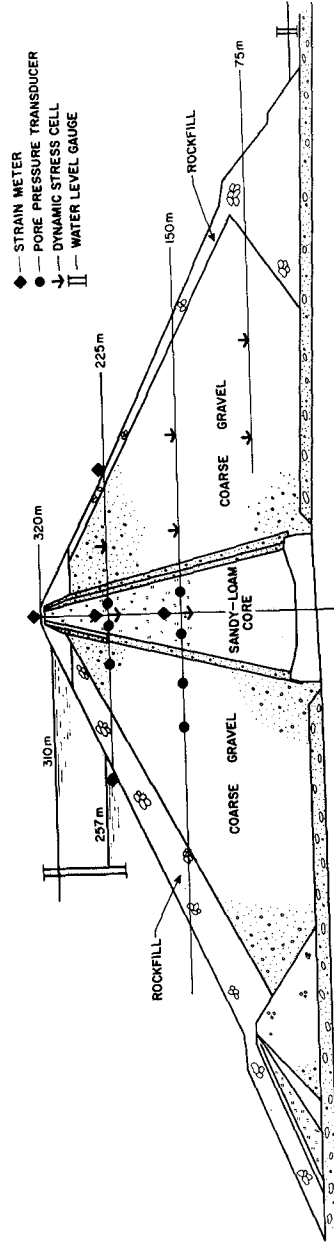


Figure 4: Transverse section of Nurek Dam showing proposed system for measuring dynamic stress and pore pressure.

INTENTIONALLY BLANK

MODELING STRONG MOTIONS FROM MAJOR EARTHQUAKES

by

R. A. Wiggins^I, G. A. Frazier^I, J. Sweet^I, and R. Apsel^I

ABSTRACT

We have implemented a set of programs for computing strong motion synthetic seismograms for hypothetical earthquake ruptures. The modeling procedure consists of three parts: a) characterization of the fault slip at each point on the rupture surface, b) synthesis of Green's functions of the wave propagation from points on the rupture surface to receivers, and c) convolution of the Green's functions with the rupture motion. The slip function incorporates a very rapid initial displacement to simulate observed slip behavior near the crack tip. The Green's functions computed are the complete response for a point dislocation in a layered viscoelastic halfspace over the frequency range from 0.02 to 20 Hz. We assume that the rupture spreads from the hypocenter at some fraction of the shear velocity and that the rupture remains coherent only for short distances. Parameter studies indicate that high frequency radiation is strongly controlled by the motion at the crack tip while low frequency radiation is controlled by the magnitude and duration of the total slip. In addition, rupture propagation strongly focuses high frequency radiation. Other relevant earthquake processes include rupture coherence or lack of coherence, propagation paths and wave types, and wave attenuation with distance.

INTRODUCTION

The traditional method for assigning seismic risk is based on averaging and scaling response spectra from past earthquakes. Such scaling is based on the magnitude of the earthquake and the distance from the fault to a receiver or site. We have extended this procedure by using a simple model of earthquake rupture in an idealized earth to predict ground motion. This model includes parameters describing fault geometry, slip characteristics and geologic structure. Field observations, laboratory measurements, and recordings from past earthquakes are used to establish values for the parameters. The procedure makes use of several lengthy computer codes to implement the earthquake model. The combined computer procedures then serve to predict the motion for a specific location from a hypothetical rupture.

The elements of the computer model can be visualized from Figure 1. The model answers the following questions: How does rupture propagate across the fault surface? What is the nature of slip at each point on the fault surface? And, how does the seismic energy propagate from the fault surface to the receiver?

The following section describes the computer model in more detail and the final section describes the results of validation studies.

^I

Preceding page blank sociates, P. O. Box 1083, Del Mar, CA 92014.

COMPUTER MODEL

1. Fracture Simulation

A three-dimensional finite element code (SWIS) was used in conjunction with analytical solutions and laboratory experiments to provide information on how fault slip occurs during an earthquake (1). Experiments performed on compressed rock specimens indicate that shear fracture occurs when the shear stress exceeds some limiting value in the neighborhood of one kbar. (The actual failure strength depends on rock composition, loading range, the presence of cracks, confining pressure, and interspersed fluid.) The fracture strength of rocks can then be related to the maximum velocity of particles on the fault surface near the crack tip.

The physics of spontaneous shear fracture is contained in our characterization of fault slip. The following parameters are pertinent:

- (a) Rupture Velocity: The rupture initiates at a point on the fault surface and spreads at a velocity which is taken as a fraction of the local shear-wave velocity. Sensitivity studies have been performed with rupture velocity varying from 50 percent to 90 percent of the shear wave velocity, the upper limit being set at the Rayleigh-wave velocity according to fracture mechanics. The shape of the resulting rupture fronts is illustrated in Figure 2. A low velocity near the top of the fault surfaces distort the circular wave fronts.
- (b) Dynamic Stress Drop: Large particle accelerations occur at points on the fault where new crack surface is being produced due to stress concentrations. Immediately following the production of new crack surface, a portion of the stress concentration is relieved and the shear stress drops rapidly to a lower value. This effect is characterized in the slip function by a peak in the slip velocity at rupture initiation. This rapid slip, which can be related to dynamic stress drop using simplified mechanics, occurs for a brief interval of time while the crack extends a few tens of meters.
- (c) Static Stress Drop: The static stress drop is a measure of the average difference in shear stress before and after an earthquake. The average final offset on the fault is linearly related to the static stress drop when the rupture area is held constant. After the initial peak, the slip velocity drops to a uniform value consistent with the static stress drop and rise time.
- (d) Rise Time: Rise time is a measure of the duration of fault slip at a single point. SWIS calculations indicate that the "rise time" is controlled by the time it takes for information from non-sliding portions on the fault surface to propagate to points where sliding is occurring. On the average, the "rise time" appears to be the time it takes for the shear-wave velocity to traverse the fault width.

- (e) Spatial Variations: In an actual earthquake, slip characteristics inevitably vary in some complex manner over the fault surface. In an effort to minimize the number of earthquake parameters, the same slip function is used for all points on the rupture surface.

The time history of slip at each point is specified by the above parameters. Their graphical relationship is illustrated in Figure 3.

2. Wave Propagation

An analytical code (PROSE) has been developed to propagate seismic waves in a horizontally layered, viscoelastic earth. The method accurately synthesizes the multiplicity of waves that arise in a layered medium over the frequency range from 0.02 to 20. Hz. Green's functions are obtained for wave contributions that result from rapid slip over small fault segments which are distributed over the surface of impending rupture. Several hundred of these Green's functions are obtained for a single earthquake to insure accurate simulation of the seismic energy that radiates from all portions of the rupture surface.

The SH-wave Green's functions for the Imperial Valley crustal structure are shown in Figure 4. The functions illustrate the SH motion that would be detected at a variety of distances from point dislocations placed at five depths. Notice that the shallow sources excite long period surface waves and are much more complex than the deeper sources. The principal arrival from the deeper sources is the direct body wave. The source at depth 5 km is located just above a layer boundary. The critical reflection is located at about 12 km. Beyond 12 km, a head wave can be seen separating from the reflected wave.

3. Ground Motion

The fault slip, based on calculations by SWIS, is combined with the wave propagation produced by PROSE to produce synthetic earthquake motions using a convolution code (FALTUNG) (see Figure 5). The prescription of fault slip is convolved, both in time and space over the rupture surface, with the elementary solutions from PROSE to produce synthetic ground motion at selected points on the earth's surface over the frequency range from 0.02 to 20. Hz.

VALIDATION STUDIES

The range of validity of the computer model has been tested by simulating three past earthquakes — Brawley (1976), Imperial Valley (1940) and Parkfield (1966). For all three earthquakes, best fits are obtained for a rupture velocity of 90 percent of the shear-wave velocity, a dynamic stress drop of 0.5 kbars and "rise time" set to the travel-time for shear waves to traverse the smallest fault dimension.

Brawley — Ground motions are modeled at an epicentral distance of 33 km using a 1.8 km-square rupture surface at a hypocentral depth of 7 km. A sufficiently good match is obtained between computed (2) and recorded ground motion to validate both the computer model and the geologic model for Imperial Valley. Sensitivity studies indicate that an adequate match with recorded signals depends critically on the size and depth of the rupture.

Figure 6 illustrates the effect of the fault size on the signal. Coherent rupture across a finite fault surface has the effect of filtering out high frequencies. On the other hand, the effect of depth (Figure 7) is to modify the ratio of late arriving surface waves to the initial body wave.

Imperial Valley — Ground motions are computed at the El Centro recording station using a bilateral rupture which initiates 12.3 km to the southeast of the recording station. This rupture extends over a length of 48 km and a width of 12 km. Although an adequate fit to the response spectra is obtained by a linear bilateral rupture, the fit to the coda is improved by use of a rupture propagating along the crooked path of the mapped surface break.

Parkfield — Comparisons of the observed and computed response spectra show excellent agreement for the horizontal components of Stations 5, 8, and 12, using a 32 km long rupture with a width of 9 km (see Figure 8 for a comparison for Station 5). The computed vertical components are uniformly high in the mid-frequency range but give good fits near the extreme frequencies of 0.02 and 20. Hz. Station 2 is so close to the fault that most of its response depends on local rupture properties which are not resolved in this study. The geologic structure on the N.E. side of the fault is not the same as on the S.W. side; nevertheless the fit to the Temblor Station is good.

A sample of computed synthetic seismograms are shown in Figure 9. These seismograms have the total appearance of strong motion recordings of real earthquakes.

CONCLUSION

As discussed above, some aspects of fault slip may be complicated beyond our ability to understand in detail; however, rather uncomplicated characterizations can be used which explain earthquake data over a broad range of frequencies. Our studies indicate that high and low frequency seismic behavior is dependent on very different aspects of the earthquake model. Fault proximity, rupture depth and rupture velocity have major effects on both low and high frequencies. The total size of the rupture surface, the static stress drop and the rise time or slip duration affect only the low frequency radiation. The dynamic stress drop and geologic structure at the receiver affects high frequencies. Hence a picture merges in which large high-frequency radiation comes from a fairly limited region on the fault and is strongly dependent on the rupture strength of the medium and the location and geology of the site.

Based on these studies we conclude that our computer models can provide useful estimates of the frequency content of site specific ground motions for earthquake design purposes.

REFERENCES

1. Archuleta, Ralph J., and Gerald Frazier, 1978. Three-dimensional numerical simulations of dynamic faulting in a half-space: Bull. Seis. Soc. Am. 68, 541-572.
2. Heaton, Thomas H., and Donald V. Helmberger, 1977. Predictability of strong ground motion in the Imperial Valley: Modeling the M 4.9, November 4, 1976, Brawley Earthquake: Bull. Seis. Soc. Am. 68, 31-48.

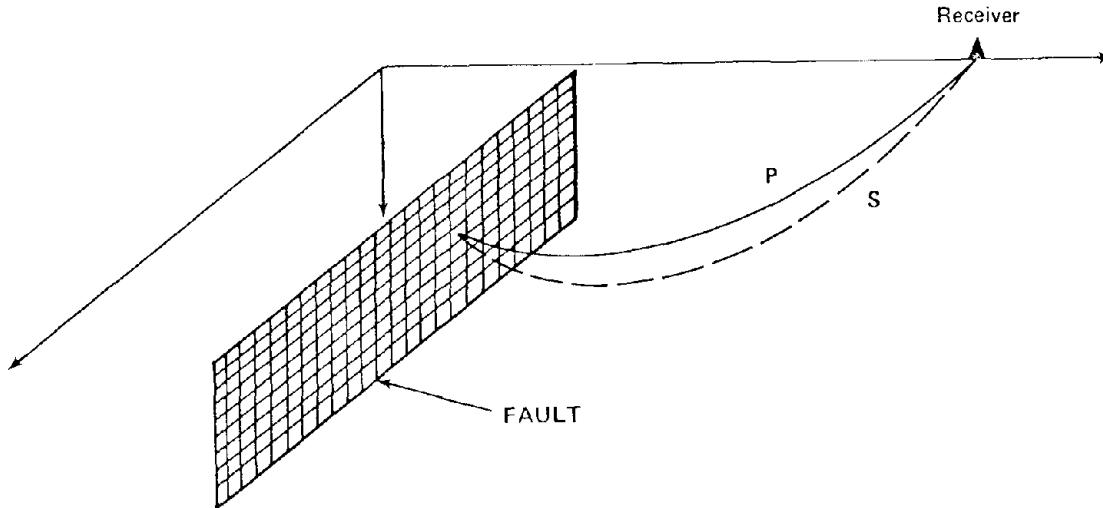
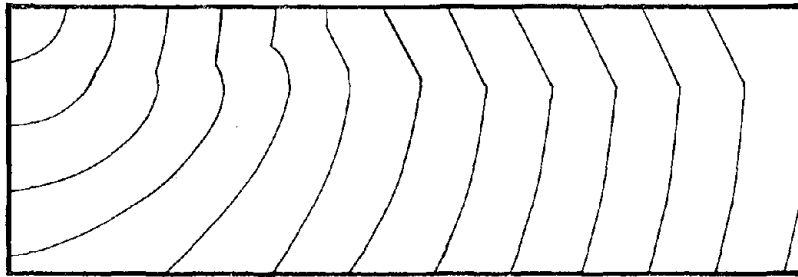
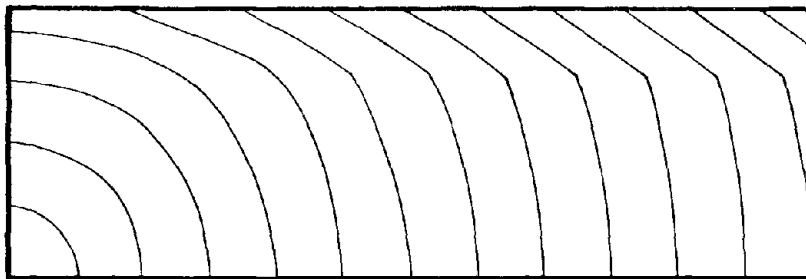


Fig. 1 - The earthquake model computation includes a) distribution of rupture, b) fault slip vs. time and c) propagation to receiver.



RUPTURE FRONTS



RUPTURE FRONTS

Fig. 2 - Propagation of rupture fronts for a hypocenter located in the lower and upper left corner of the fault segment.

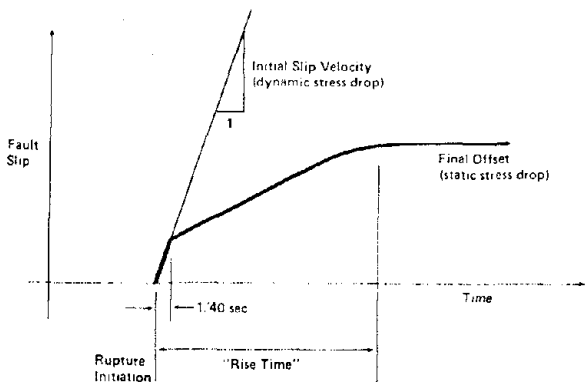


FIG. 3 - CHARACTERIZATION OF FAULT SLIP VS TIME.

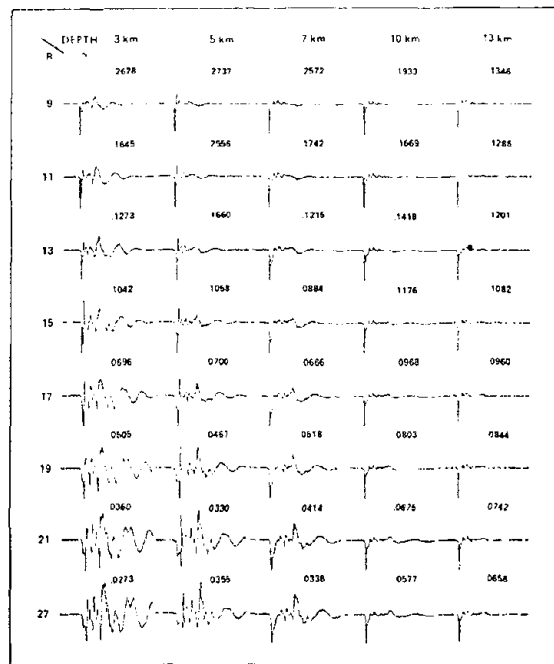


FIG. 4 - COMPUTED DISPLACEMENTS FOR SURFACE RECEIVERS LOCATED AT SEVERAL DISTANCES FROM BURIED STRIKE-SLIP DISLOCATIONS.

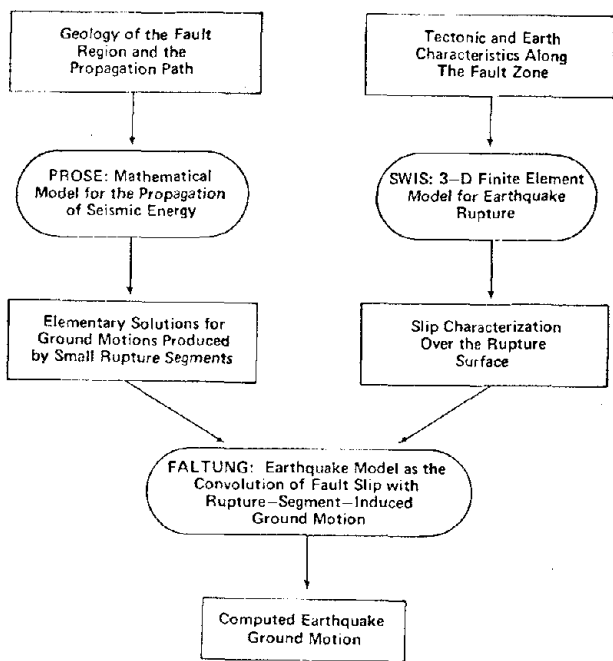


FIG. 5 - PROCEDURE FOR MODELING SITE SPECIFIC EARTHQUAKE GROUND MOTIONS (SISPEQ).

BRAWLEY EARTHQUAKE
SIZE OF RUPTURE

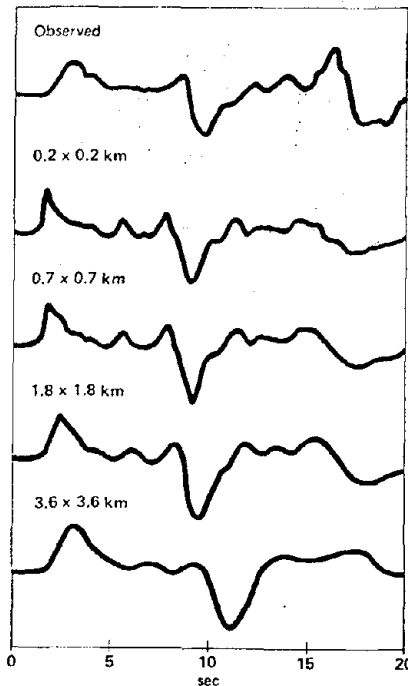


FIG. 6 - INCREASING THE SIZE OF THE FAULT SURFACE ENHANCES LOW FREQUENCIES. THE BEST FIT IS A 1.8 x 1.8 KM FAULT.

BRAWLEY EARTHQUAKE
DEPTH OF RUPTURE

PARKFIELD
STATION 5
COMPUTATION

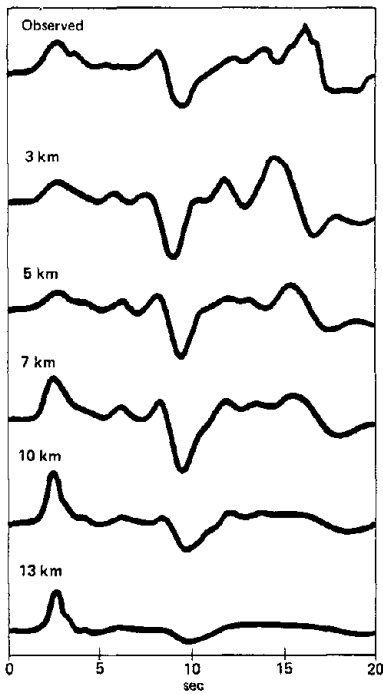


FIG. 7 - DEEP RUPTURE ENHANCES THE RATIO OF THE FIRST MOTION BODY WAVE TO THE LATER ARRIVING SURFACE WAVES. THE BEST FIT IS 7 KM DEPTH.

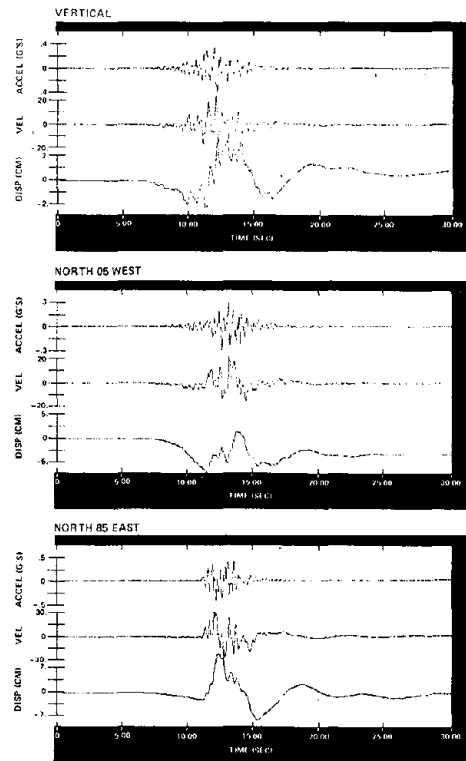


FIG. 9 - COMPUTED ACCELERATIONS, VELOCITIES AND DISPLACEMENTS FOR THE THREE COMPONENTS AT PARKFIELD STATION 5.

PARKFIELD STATION 5

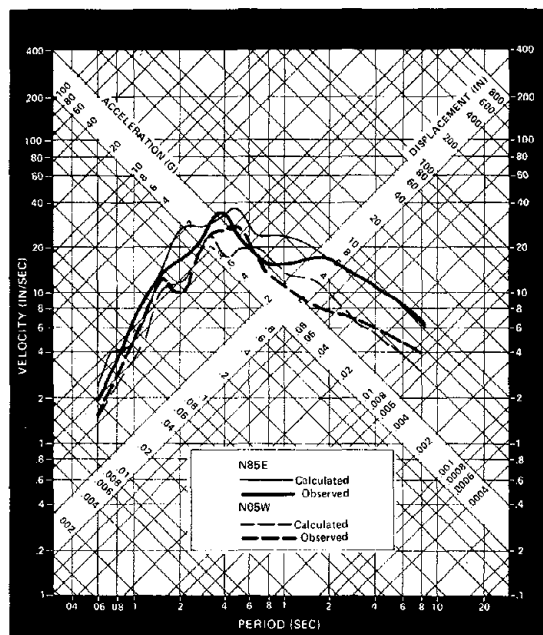


FIG. 8 - COMPARISON OF COMPUTED AND OBSERVED RESPONSE SPECTRA FOR PARKFIELD STATION 5 HORIZONTAL COMPONENTS.

700

INTENTIONALLY BLANK

PREDICTION OF STRONG GROUND MOTION
USING SMALL EARTHQUAKES

Francis T. Wu
Dept. of Geological Sciences
State University of New York
Binghamton, New York 13901

Abstract

A method is proposed here to use seismograms obtained from small earthquakes along an active fault to generate strong motion seismograms at a site.

Introduction

Strong motion seismograms are difficult to obtain, especially for a specific site. Actual strong motion records from a particular earthquake at a certain site is certainly the best estimate of strong motion at the site from a similar earthquake in the future, but it cannot easily be used with great confidence for that site for an earthquake with different source parameter, nor could it easily be used to predict strong motion used for different sites for different earthquakes. Purely theoretical computation is not yet comprehensive enough to include non-parallel, heterogeneous medium.

Operationally, the strong motion at a site can be considered as the convolution of source, path and site functions and attempts have been made to estimate the site and path functions (e.g., Duke and Mal, 1975). With the recent interest in strong motion array studies it may well be possible to know all three factors as functions of observable parameters such as geometry and geology of a fault, the material properties along the path and at the site, so that strong motion at a site can be predicted reasonably accurately. In the meantime, other methods of ground motion prediction have to be found.

Here a hybrid method is proposed. The method is based on the following considerations: (1) Small earthquakes, with their small fault dimensions and short time durations, generate accelerograms that can be scaled to yield Green's function or impulse response for the particular source-site pair. (2) For strong motion from a large earthquake on a fault at the site where small earthquakes on the same fault have been recorded, we may assume reasonable source spatial and temporal variations and sum the appropriate Green's functions weighted by the source function.

The theoretical basis related to this method has been discussed in papers by Burridge and Knopoff (1964), Langston and HelMBERGER (1975), Backus and Mulcahy (1976), Stump and Johnson (1977) and Hartzell et al. (1978).

The emphasis in this proposed method is the utilization of small magnitude ($1 < M < 4$) events to obtain empirical Green's functions. This method is made practical by the availability of a digital-cassette recording and relatively large dynamic-range instruments.

Preceding page blank

Method

There are two main problems involved in the proposed method, namely, the scaling of displacement from small earthquakes to reduce it to that of a unit excitation and the summation of elementary sources to produce simulated displacement from a large earthquake.

From Burridge and Knopoff (1964), the displacement at a point from a shear dislocation source can be written as

$$u_i(\vec{x}, t) = \int_{S'} d\vec{x}' \int_{-\infty}^{\infty} m_{kj}(\vec{x}', t') g_{ij,k}(\vec{x}, t; \vec{x}', t') dt' \quad (1)$$

where m_{kj} is the moment tensor density and can be expressed as

$$m_{kj} = \mu [n_k(\vec{x}') S_j(\vec{x}', t') + n_j S_k(\vec{x}', t')]$$

In these and the following equations, $\vec{x} = (x_1, x_2, x_3)$, t is time, prime refers to source coordinates, S_j is the dislocation specified at every point on the fault surface S' , and $\vec{n} = (n_1, n_2, n_3)$ is the unit normal to the fault surface. g_{ij} is the Green's function representing the displacement in the i th direction due to a point force in the j th direction with $\delta(t)$ as source time function. $g_{ij,k}$ denote differentiation with respect to source coordinates x'_k .

Considering an earthquake with source dimension much smaller than the wave lengths of interest, then the source can be approximated as a point and equation (1) can be written as a convolution integral (Stump and Johnson, 1977):

$$\bar{u}_i(\vec{x}, t; \vec{\xi}') = g_{ij,k}(\vec{x}, t; \vec{\xi}', 0) \otimes m_{jk}(\vec{\xi}, t)$$

where $\vec{x} - \vec{\xi}$ is the source location, and \otimes denotes convolution.

In frequency domain, we can then write

$$U_i(\vec{x}, f; \vec{\xi}) = G_{ij,k}(\vec{x}, \vec{f}; \vec{\xi}) M_{jk}(\vec{\xi}, f)$$

where f = frequency. In the first problem, we need to normalize U_i to that from a unit impulse. This can be approximately obtained by assuming a simple and yet reasonable structure between the source and the receiver to obtain g_{ij} and G_{ij} . Then m_{jk} or M_{jk} can be obtained by trial and error or inversion (Langston and HelMBERGER, 1975; Stump and Johnson, 1977). In order to obtain M_{jk} we need at least six components (for example, two three-component stations); but if we can make certain assumptions about the source--in the case of the San Andreas fault in Northern California, pure

strike-slip faulting may be assumed--then the number of independent records required can be decreased. The location of the earthquake, however, has to be accurately known, so that earthquakes not on the fault of interest will not be used; thus a conventional seismic network for locating microearthquakes could be used, or if there are enough stations of the kind needed in this work in the area, location can be performed also.

It should be remarked here that the intent of the procedure discussed above is not to fit the seismograms in every detail but to obtain a relative scaling of the sources.

By recording a large number of small earthquakes from the same fault, a library of $U_i(\vec{x}, t; \vec{\xi})$ can be established. Because of the non-uniform distribution of small earthquakes, interpolations have to be made. Hartzell et al. (1978) have demonstrated that theoretical Green's functions can be interpolated with satisfactory results.

Once the library of the \bar{U}_i 's is established, then the displacement field from a large earthquake can be calculated by using Hartzell et al. (1978):

$$u_i(\vec{x}, t) = \int_{S'} d\vec{x}' S(\vec{x}') \int_{-\infty}^{\infty} \bar{u}_i(\vec{x}, t; \vec{x}', t') f(\vec{x}', t') dt'$$

$$\approx \sum_n S_n(\vec{n}') S_n(\vec{x}') \bar{u}_{in}(\vec{x}, t; \vec{x}', \theta)$$

$$\theta f_n(\vec{x}', t)$$

where S_n = area of the element such that $\sum_n S_n$ equals the total fault area. $f(\vec{x}', t')$ and $S(\vec{x}')$ together specify the source of spatial and temporal variations and include factors such as rupture propagation velocity, variation of displacement along the fault, and stop-and-start nature of the source. By assuming various combinations of S' , $S(\vec{x}')$, and $f(\vec{x}', t')$ we can simulate earthquakes of various magnitudes, fault lengths and characteristics.

Discussion

This proposed method aims at incorporating correct path and site functions which are difficult to compute theoretically, not knowing the structure precisely nor ways to handle them mathematically, in the calculation of strong ground motion at a site. It will also enable one to calculate the motions from earthquakes with various fault parameters, such as fault length, rupture propagation velocity, amount of slip and the source time function; multiple event type of earthquakes can be simulated also by specifying appropriate $S(\vec{x})$ and $f(\vec{x}, t)$.

Although there has been a large collection of data at large distance ranges recorded on film with velocity transducers, those are not usable for the present purpose because of the lack of precise calibration and the

limited dynamic range. The feasibility of recording small accelerations, (down to tens of μg) has been proven (F. T. Wu, unpublished data), thus this proposed method is within reach. However, the Green's function library for a particular site will take a period of time to collect; if a fault is presently active and populated with small earthquakes, then this method is appropriate. Especially, for large important structures with long planning time, it is possible to obtain data within a few years.

Acknowledgments

This research is supported by a NSF/PFRA grant, ENV6-23897. Discussions with Dr. L. R. Johnson were helpful.

References

- Backus, G. and M. Mulcahy (1976). Moment tensors and other phenomenological descriptions of seismic sources--I. Continuous displacements, *Geophys. J.* 46, 341-61.
- Burridge, R. and L. Knopoff (1964). Body force equivalents for seismic dislocations, *Bull. Seism. Soc. Am.*, 54, 1875-1888.
- Duke, C. M. and A. K. Mal, (1975). A model for analysis of body and surface waves in strong ground motion, 6th World Conference on Earthquake Engineering, 77-24.
- Hartzell, S. H., G. A. Frazier and J. N. Brune. Earthquake modeling in a homogeneous half-space, *Bull Seism. Soc. Am.*, 68, 301-16.
- Langston, C. A. and D. V. Helmberger (1975). A procedure for modeling shallow dislocation sources, *Geophys. J.*, 42, 117-30.
- Stump, B. W. and L. R. Johnson (1977). The determinations of source properties by the linear inversion of seismograms, *Bull. Seism. Soc. Am.*, 67, 1489-1502.

STATISTICAL ANALYSIS OF STRONG-MOTION ACCELERATION RECORDS
OBTAINED IN JAPAN

by

T. Iwasaki^I, T. Katayama^{II}, K. Kawashima^{III} and M. Saeki^{IV}

ABSTRACT

This paper presents the results of multiple regression analysis of 301 strong-motion acceleration records, and also shows the results of a quantification analysis of average response accelerations obtained from 277-component horizontal acceleration records. From the analysis done, empirical formulas which can statistically estimate maximum horizontal acceleration, duration of major motion, and number of zero-crossing in terms of earthquake magnitude, epicentral distance, and subsoil condition, are proposed. Frequency characteristics of horizontal motions and ratios of vertical to horizontal accelerations are averagedly evaluated depending on subsoil conditions. Furthermore, various average response spectrum curves for a linear single-degree-of-freedom system are proposed in terms of earthquake magnitude, epicentral distance, and subsoil condition.

INTRODUCTION

In establishing reasonable criteria for earthquake resistant design of structures, it seems essential to properly evaluate characteristics of ground motions and structural behavior during strong earthquakes. A number of strong motion accelerographs are installed at various engineering structures and on neighboring grounds in Japan to grasp dynamic properties of ground motions and structural responses.

Although there will be a number of factors which affect characteristics of ground motions, it seems probable that three principal factors might be earthquake magnitude, geographical situation of the focal area of an concerned earthquake related to the structural site, and subsoil condition at the site. In this study characteristic variables of ground accelerations are statistically analyzed in terms of these three factors.

The results are utilized as basic materials in standard design seismic forces and seismic loads of "New Criteria of Earthquake Resistant Design (Draft)," (1, 2) proposed by the Ministry of Construction in March, 1977.

OBSERVATION OF STRONG-MOTION EARTHQUAKES AT ENGINEERING STRUCTURES IN JAPAN

In Japan the observation of strong-motion earthquakes for engineering structures was initiated when SMAC-type accelerographs were developed in 1953. The observation network has gradually progressed with experiences of severe structural damages due to the Niigata Earthquake of 1964 and the

-
- I Public Works Research Institute, Ministry of Construction, Chiba, Japan
 - II Associate Professor, Institute of Industrial Science, University of Tokyo, Tokyo, Japan
 - III Public Works Research Institute, Ministry of Construction, Chiba, Japan
 - IV Consulting Engineer, Japan Engineering Consultants, Tokyo, Japan

Tokachi-oki Earthquake of 1968. As of March, 1978, the number of SMAC accelerographs installed on various structures and neighboring grounds is over 1200 totally. It is believed, however, that the same number of accelerographs are necessitated in order to obtain enough strong records for major earthquakes which might take place at any areas of this country.

In addition to the stations with SMAC-type accelerographs, there are a number of stations where electromagnetic-type seismographs are equipped. Moreover, dynamic behavior of subsoils during earthquakes is also being measured using downhole seismometers at several points as well as standard seismometer and SMAC accelerograph measurements on the surface. Records obtained from these field measurement programs have been published periodically by institutions concerned (3).

ANALYSIS OF ACCELERATION RECORDS

A statistical analysis of measured acceleration records was attempted to quantitatively express characteristic variables of ground motions as functions of seismic conditions and subsoil properties at the observation point. In the present analysis were employed those records which were obtained during earthquakes with the Richter magnitude of 5.0 or higher and the hypocentral depth of 60 km or shallower, and which include at least one record with the maximum acceleration of 50 gals or higher for an earthquake. Records with the maximum acceleration less than 10 gals were excluded. The total number of the records used is 301 (the number of components treated is $3 \times 301 = 903$) for 51 earthquakes. Factors considered in the analysis are as follows:

- (1) Seismic properties: Richter magnitude M , epicentral distance Δ (km)
- (2) Subsoil conditions: Observation stations are classified into the following four groups depending on subsoil conditions.
 - 1st Group: Rock
 - 2nd Group: Diluvium
 - 3rd Group: Alluvium (Except 4th Group)
 - 4th Group: Soft Alluvium
- (3) Characteristic variables of acceleration records:
 - (a) Absolute maximum horizontal acceleration (larger value of two perpendicular horizontal motions) : $H_{\max}(\text{gals})$
 - (b) Period of vibration at the time when acceleration becomes H_{\max} : $T_1(\text{sec})$
 - (c) Duration of major motion : $T_d(\text{sec})$
 - (d) Ratio of vertical to horizontal accelerations : $v = V_{\max}/H_{\max}$
 - (e) Number of zero-crossing during the time interval of T_d : N_z
 - (f) Mean period during the time interval of T_d : $T_m = 2T_d/N_z$

The procedure for determining the above characteristic variables are illustrated in Fig. 1. Each of the characteristics values (expressed as X below) was assumed to be represented by the following two types of expressions:

$$\text{Type-1 : } X = a_1 \cdot 10^{b_1 M} \cdot \Delta c_1 \quad (1)$$

$$\text{Type-2 : } X = a_2 + b_2 M + c_2 \Delta \quad (2)$$

where a_1 , b_1 , c_1 ; a_2 , b_2 , c_2 are constants for each characteristic value, and are depending on subsoil conditions.

The analysis was conducted for five different cases, namely four groups of subsoil conditions plus the average subsoils including the entire data. In determining the expressions for H_{\max} , only eq. (1) was investigated and the term of Δ in eq. (1) was substituted by $(\Delta + \Delta_0)$, where Δ_0 was taken as 0, 10, 20, 30 and 40 km.

Table 1 indicates the distribution of 301 records used in the analysis. Table 2 shows formulated regression equations and correlation coefficients, which are obtained from the analysis based on the multiple regression analysis. In the table are shown the results of three characteristic values H_{\max} , T_d and N_z in which multiple correlation coefficients are greater than 0.5. Since correlation coefficients for expressions of Type-1 were generally greater than those for Type-2, the results for only Type-1 are shown in the table. Although the correlation coefficient was the highest in the cases of $\Delta_0=10$ km among the five cases analyzed, H_{\max} for the case of $\Delta_0=0$ is expressed in Table 2. Fig. 2 illustrates H_{\max} for $\Delta_0=0$ as functions of M and Δ , for the case of the average subsoils.

As for the other three characteristic values T_1 , v and T_m , the multiple correlation coefficients are found to be less than 0.5. This means that there is no distinct relation among those values and M and Δ . For these variables the mean values and the standard deviations are evaluated depending on subsoil conditions, and are listed in Table 3.

The results of the analysis described in the above may be summarized as follows:

- (1) The maximum horizontal acceleration (H_{\max}), the duration of major motion (T_d), and the number of zero-crossing (N_z) can be approximately expressed as functions of earthquake magnitude and epicentral distance.
- (2) The duration of major motions (T_d) defined in Fig. 1 gets longer as the earthquake magnitude (M) becomes greater and as the epicentral distance (Δ) becomes longer.
- (3) The relation between the number of zero-crossing (N_z) and the epicentral distance (Δ) is considerably affected by subsoil conditions. The value of N_z increases with the increase in Δ for harder grounds. It seems that N_z is not affected by Δ but M , for softer grounds. The number of repetitions of major motions which can be approximately $N_z/2$, is 30 to 100 for the various subsoil conditions.
- (4) The period of vibration (T_1) at the time of H_{\max} , the ratio of vertical to horizontal accelerations (v), and the mean period of vibration (T_m) during the major motion are not clearly related with M and Δ . The following two points, however, can be seen.
 - (a) The mean values of T_1 and T_b get longer as subsoils become softer. This tendency is obvious for soft alluvial grounds. The ratio of T_1 to T_m is 1.20 to 1.26, and the ratio is almost constant, irrespectively of subsoil conditions.

- (b) The mean value of v being 0.32 to 0.34 is not strongly affected by subsoil conditions. Since the standard deviation is 0.15 to 0.21, the vertical acceleration can be assumed to be the half of the horizontal acceleration for the designing purpose.

ANALYSIS OF EARTHQUAKE RESPONSE SPECTRA

The Port and Harbour Research Institute, the Ministry of Transport and the Public Works Research Institute, the Ministry of Construction have been conducting response spectrum analysis for major ground motions obtained at various grounds during moderate to strong earthquakes (4,5,6). In the present analysis the results of the response spectra done at the two Institutes for 277 horizontal components of ground motions, which were triggered during 68 earthquakes with the Richter magnitude between 4.5 and 7.9 and the hypocentral depth of 60 km or shallower, are employed.

Factors considered in the analysis are as follows:

- (1) Seismic properties: Earthquake magnitude on the Richter scale (M), and epicentral distance (Δ in km)
- (2) Subsoil conditions: Observations sites are classified into four groups in the same manner as shown in the previous section.
- (3) Characteristic variables of acceleration records and their response spectral values:
 - (i) Maximum horizontal acceleration (two perpendicular components for one record): A_{\max} (gals)
 - (ii) Absolute response acceleration: S_A (gals), which is computed from digitized values of triggered records by assuming a linear viscously damped single-degree-of-freedom system with the natural periods of T ($=0.1, 0.15, 0.2, 0.25, 0.3, 0.35, 0.4, 0.5, 0.6, 0.7, 0.8, 0.9, 1, 1.5, 2, 2.5, 3,$ and 4 seconds) and the damping ratio of h ($=5\%$ of critical).

In the analysis the following are assumed.

- (a) A quantification analysis can be applied to the estimation of S_A in terms of earthquake magnitude (M), epicentral distance (Δ), and subsoil conditions (S), by employing an expression as

$$\log_{10} \bar{S}_A = C(M) + C(\Delta) + C(S) \quad (3)$$

where \bar{S}_A : Estimated value of S_A (gals),

$C(M)$, $C(\Delta)$, and $C(S)$: Weighting functions depending on M , Δ , and S , respectively.

- (b) A quantification analysis can be also applied to the estimation of A_{\max} in terms of the three factors in the above, by assuming an expression of

$$\log_{10} \bar{A}_{\max} = C'(M) + C'(\Delta) + C'(S)$$

where \bar{A}_{\max} : Estimated value of A_{\max} (gals)

$C'(M)$, $C'(\Delta)$, and $C'(S)$: Weighting functions depending on M , Δ , and S , respectively.

Classification of 277 components employed in the analysis is shown in Tables 4 and 5. Magnitudes in the tables are irregularly divided into five groups with consideration of scattering of the data used and also convenience of practical application of the results.

Table 6 shows the results of the quantification analysis for S_A , and lists the weighting functions $C(M)$, $C(\Delta)$, and $C(S)$ in Eq. (3), ranges of the three functions, and the multiple correlation coefficients. Furthermore, Figs. 3 and 4 illustrate the response spectral curves ($T-S_A$ relation) which can be obtained from Table 6. In these figures, the maximum values of ground acceleration (A_{max}) which are also estimated from the quantification analysis are tabulated. From the two informations, the acceleration magnification factor $\beta (= S_A/A_{max})$ can be evaluated. The values of A_{max} shown here, however, may not be used for the estimation of the absolute maximum horizontal accelerations (H_{max}), but for the estimation of β . For estimating H_{max} , the results described in the previous section can be employed.

Degrees of the effects of the three factors (M , Δ , and S) on \bar{S}_A are shown in Fig. 5, by indicating the variation of the ranges of $C(M)$, $C(\Delta)$, and $C(S)$ with T .

From the analysis shown in the above, the following can be indicated.

- (1) As for the effects of subsoil conditions on S_A , the effect of rock ground is considerably different from those of the other three subsoils. Values of S_A for rock are smaller than those for the other subsoils, except for natural periods shorter than 0.3 seconds. For the range of comparatively longer periods, the values of S_A tend to become larger for softer subsoils.
- (2) The shapes of $T-S_A$ curves do not change much with the variations of M and Δ . It is understood that for the range of longer natural periods the values of β will increase as M gets greater, and as Δ gets longer.
- (3) Among the effects of the three factors, earthquake magnitude ($M=4.5$ to 7.9), epicentral distance ($\Delta = 6 - 405$ km), and subsoil condition (rock to soft alluvium), the effects of M are found to be the greatest for the entire range of natural periods. The effects of Δ are close to those of M for the shorter period range, and become small for the longer period range. The effects of subsoil condition are slightly smaller comparing with those of M and Δ , for the entire period range. This may be reasonable by the fact that the ranges of M and Δ are both considerably large. It should be noted, however, that for the range of the periods between 0.5 and 2 seconds the effects of subsoils become rather great.

CONCLUSIONS

The following remarks may be pointed out as the conclusions of the statistical analysis of strong motion records obtained in Japan.

- (1) The absolute maximum horizontal acceleration, the duration of major motions, and the number of zero-crossings can be approximately evaluated as functions of the earthquake magnitude, the epicentral distance, and subsoil condition.
- (2) The mean value of the ratio of vertical to horizontal accelerations is found to be around $1/3$. The ratio may be conservatively taken as $1/2$, for the design purpose.
- (3) Response spectral curves by which structural response accelerations can be averagedly estimated in terms of earthquake magnitude, epicentral distance, and subsoil conditions, are proposed. Among the three

factors of the earthquake magnitude (M), the epicentral distance (Δ), and the subsoil condition (S), which affect the response acceleration, the effects of M are the greatest. The effects of Δ are close to those of M for the range of shorter natural periods, and get smaller for the range of longer natural periods. The effects of subsoil conditions are generally small, but become comparatively large for the range of natural periods between 0.5 and 2 seconds. It is remarkable that response accelerations for the range of the natural periods between 0.5 and 2 seconds get larger as subsoils become softer.

ACKNOWLEDGMENTS

This study has been performed as one of comprehensive research projects done in the Aseismic Technology Development Committee which was established at the Technology Center for National Land Development with a commission from the Public Works Research Institute, Ministry of Construction. The authors express their thankful appreciation to Professor Shunzo Okamoto (President of Saitama University and the Chairmal of the Committee), Professor Keizaburo Kubo (Chairman of the Subcommittee on Seismic Forces and Subsoils). The authors also thank Messrs. Susumu Wakabayashi and Ken-ichi Tokida, Ground Vibration Section of the Public Works Research Institute for their strenuous efforts in processing a great deal of strong-motion records.

REFERENCES

- 1) Ministry of Construction, "New Criteria of Earthquake Resistant Design (Draft)," March, 1977 (In Japanese); and Masamitsu Ohashi, Kiyoshi Nakano, "A proposal for Earthquake Resistant Design Methods," Ninth Joint Meeting, U.S.-Japan Panel on Wind and Seismic Effects, U.J.N.R., Tokyo, Japan, May, 1977.
- 2) Public Works Research Institute, "Report on Research and Development of Aseismic Technology," March, 1977 (In Japanese).
- 3) E. Kuribayashi, H. Tsuchida and M. Watabe, "On the Maintenance of the Strong-Motion Accelerograph and the Data Processing of the Records," Seventh Joint Meeting, U.S.-Japan Panel on Wind and Seismic Effects, U.J.N.R., May, 1975.
- 4) M. Ohashi, T. Iwasaki, S. Wakabayashi and K. Tokida, "Statistical Analysis of Strong-Motion Acceleration Records," Ninth Joint Meeting, U.S.-Japan Panel on Wind and Seismic Effects, U.J.N.R., Tokyo, May, 1977.
- 5) T. Iwasaki and T. Katayama, "Statistical Analysis of Strong-Motion Earthquake Response Spectra," Japan-U.S. Seminar on Earthquake Engineering Research with Emphasis on Lifeline Systems, Tokyo, Japan, Nov., 1976.
- 6) H. Tsuchida, T. Yamada, E. Kurata and K. Sudo, "Annual Report on Strong-Motion Earthquake Records in Japanese Ports." Technical Note of Port and Harbour Research Institute, Vol. 55 (1968), Vol.62 (1968), Vol.64 (1969), Vol.80 (1969), Vol.98 (1970), Vol.100 (1970), Vol.116 (1971), Vol.136 (1972), Vol.160 (1973), Vol.181 (1974), Vol.202 (1975).

Table 1. Classification of 301 Strong-Motion Records Analyzed

Magnitude M	Subsoil Condition	Epicentral Distance Δ (km)				Total	
		20<Δ	20≤Δ<60	60≤Δ<120	120≤Δ<200		
5.0≤M<6.0	Rock	2	3			5	
	Dil.	3	12	3		18	
	All.	4	16	5	2	29	
	Soft All.	2	5	7	1	15	
6.0≤M<6.5	Rock		3	6	3	13	
	Dil.		7	8	2	18	
	All.		12	13	8	34	
	Soft All.		3	6	6	16	
6.5≤M<7.0	Rock		1	2	1	4	
	Dil.		1	6	6	13	
	All.	1	5	10	10	27	
	Soft All.		1	4	9	18	
7.0≤M<7.5	Rock			1		4	
	Dil.				2	14	
	All.			2	2	16	
	Soft All.			1	1	7	
7.5≤M<7.9	Rock				1	3	
	Dil.			3	8	11	
	All.			2	16	24	
	Soft All.			1	11	12	
Total		12	69	74	64	82	301

Note. 1) Numbers of records for four subsoil conditions are 29 for rock, 74 for diluvium, 130 for alluvium, and 68 for soft alluvium.

Table 2. Regression Equations for H_{max}, T_d and N_z

Characteristic Value	Subsoil Condition	Empirical Equations	Partial Correlation Coefficient		Multiple Correlation Coefficient r
			Magnitude M	Epicentral Distance Δ	
H _{max} (gals)	Rock	H _{max} = 28.5 x 10 ^{0.207M} Δ ^{-0.598}	0.33	-0.47	0.48
	Dil.	H _{max} = 13.2 x 10 ^{0.330M} Δ ^{-0.806}	0.50	-0.59	0.59
	All.	H _{max} = 32.1 x 10 ^{0.254M} Δ ^{-0.757}	0.47	-0.61	0.61
	Soft All.	H _{max} = 6.5 x 10 ^{0.423M} Δ ^{-0.977}	0.65	-0.72	0.72
T _d (sec)	Total	H _{max} = 18.4 x 10 ^{0.302M} Δ ^{-0.800}	0.51	-0.62	0.62
	Rock	T _d = 3.89 x 10 ⁻⁴ x 10 ^{0.466M} Δ ^{0.589}	0.59	0.40	0.89
	Dil.	T _d = 1.37 x 10 ⁻² x 10 ^{0.262M} Δ ^{0.485}	0.29	0.26	0.71
	All.	T _d = 2.75 x 10 ⁻² x 10 ^{0.291M} Δ ^{0.265}	0.37	0.17	0.61
N _z	Soft All.	T _d = 2.28 x 10 ⁻¹ x 10 ^{0.199M} Δ ^{0.233}	0.25	0.16	0.52
	Total	T _d = 2.08 x 10 ⁻² x 10 ^{0.274M} Δ ^{0.394}	0.32	0.23	0.65
	Rock	N _z = 1.43 x 10 ⁻² x 10 ^{0.410M} Δ ^{0.444}	0.41	0.22	0.75
	Dil.	N _z = 4.23 x 10 ⁻¹ x 10 ^{0.097M} Δ ^{0.681}	0.11	0.35	0.66
N _z	All.	N _z = 6.28 x 10 ⁻¹ x 10 ^{0.272M} Δ ^{0.0313}	0.39	0.02	0.54
	Soft All.	N _z = 4.05 x 10 ^{0.190M} Δ ^{-0.0646}	0.22	-0.04	0.29
	Total	N _z = 4.68 x 10 ⁻¹ x 10 ^{0.243M} Δ ^{0.195}	0.30	0.12	0.54

Table 4. Classification of 277 Components for the Response Spectrum Analysis

Magnitude M	Subsoil Condition	Epicentral Distance Δ (km)				Total
		Δ < 20	20 ≤ Δ < 60	60 ≤ Δ < 120	120 ≤ Δ < 200	
4.5 ≤ M < 5.4	Rock	6	4			10
	Dil.	4	10			14
	All.	12	8	2		30
5.4 ≤ M < 6.1	Soft All.	6				6
	Rock		4	2		6
	Dil.	4	4	4		12
6.1 ≤ M < 6.8	All.	2	12	6		20
	Soft All.	4	2	4		10
	Rock		4	6		10
6.8 ≤ M < 7.5	Dil.		4	4	2	10
	All.	4	32	22	8	68
	Soft All.		6	4	2	14
7.5 ≤ M < 7.9	Rock				2	2
	Dil.			6	2	8
	All.	2	6	4	2	14
Soft All.			2	10	12	
Total		42	92	72	32	277

Note: 1) Numbers of components for four subsoil conditions are 39 for rock, 52 for diluvium, 140 for alluvium, and 46 for soft alluvium.

Table 3. Averages and Standard Deviations of T₁, v, and T_M

	Subsoil Condition		
	Rock	Diluvium	Soft Alluvium
T ₁ (sec)	Average	0.43	0.49
	S.D.	0.39	0.30
v	Average	0.33	0.34
	S.D.	0.18	0.18
T _M (sec)	Average	0.34	0.39
	S.D.	0.22	0.22
T ₁ /T _M	1.20	1.26	1.23

Table 5. Classification of 277 Components and Mean Values in Each Category

Factor	Category	Number of Components	Mean Value	
			Peak Ground Acc. A _{max} (gals)	Epicentral Distance L (km)
Magnitude (M)	I 4.5 ≤ M < 5.4	60	66.0	5.0
	II 5.4 ≤ M < 6.1	48	67.5	5.8
	III 6.1 ≤ M < 6.8	102	63.6	6.3
	IV 6.8 ≤ M < 7.5	29	58.1	7.1
	V 7.5 ≤ M < 7.9	38	112.4	7.7
Epicentral Distance (Δ)	I 645 < 20km	42	110.6	5.3
	II 205Δ < 60km	92	68.2	5.8
	III 605Δ < 120km	72	59.1	6.2
	IV 1205Δ < 200km	39	56.2	7.0
	V 2005Δ < 405km	32	71.3	7.3
Subsoil Conditions (S)	I Rock	39	59.9	6.2
	II Diluvium	52	69.4	6.2
	III Alluvium	140	73.2	6.1
	IV Soft Alluvium	46	75.1	6.4
Total	-	277	70.9	6.2

Table 6. Estimation of Average Response Acceleration S_A ($\log_{10} S_A = C(M)+C(D)+C(S)$) for Systems with Natural Period of T and Damping Ratio of 0.05

Natural Period	C (M)					C (D)					C (S)					Multi-Correlation Coefficient, r	Range of C (M)	Range of C (D)	Range of C (S)
	Category of Earthquake Magnitude					Category of Epicentral Distance (km)					Category of Subsoil Condition								
	I	II	III	IV	V	I	II	III	IV	V	I	II	III	IV					
T_1	$4.5 \leq M < 5.4$	$5.4 \leq M < 6.1$	$6.1 \leq M < 6.8$	$6.8 \leq M < 7.5$	$7.5 \leq M \leq 7.9$	$6 \leq D < 20$	$20 \leq D < 60$	$60 \leq D < 120$	$120 \leq D < 200$	$200 \leq D \leq 405$	Rock	Diluvium	Alluvium	Soft Alluvium					
0.1	-0.66	-0.56	-0.53	-0.40	0	0.71	0.43	0.31	0.00	0	2.10	2.03	2.08	2.03	0.56	0.66	0.71	0.08	
0.15	-0.65	-0.56	-0.53	-0.35	0	0.69	0.48	0.33	0.00	0	2.19	2.11	2.15	2.10	0.53	0.65	0.69	0.10	
0.2	-0.73	-0.55	-0.54	-0.30	0	0.74	0.51	0.32	0.02	0	2.23	2.17	2.21	2.11	0.54	0.73	0.74	0.12	
0.25	-0.77	-0.60	-0.55	-0.27	0	0.84	0.56	0.37	0.08	0	2.13	2.11	2.16	2.11	0.55	0.77	0.84	0.05	
0.3	-0.79	-0.57	-0.55	-0.26	0	0.82	0.55	0.35	0.11	0	2.04	2.11	2.17	2.12	0.56	0.79	0.82	0.13	
0.35	-0.79	-0.56	-0.52	-0.23	0	0.76	0.48	0.33	0.10	0	1.97	2.10	2.17	2.15	0.55	0.79	0.76	0.20	
0.4	-0.82	-0.57	-0.51	-0.25	0	0.74	0.48	0.28	0.12	0	1.92	2.09	2.16	2.16	0.57	0.82	0.74	0.24	
0.5	-0.97	-0.63	-0.51	-0.23	0	0.80	0.46	0.20	0.13	0	1.88	2.05	2.15	2.19	0.63	0.97	0.80	0.31	
0.6	-1.05	-0.61	-0.49	-0.21	0	0.77	0.45	0.16	0.12	0	1.79	2.00	2.13	2.20	0.67	1.05	0.77	0.41	
0.7	-1.14	-0.65	-0.50	-0.19	0	0.83	0.47	0.19	0.14	0	1.70	1.95	2.07	2.17	0.70	1.14	0.83	0.47	
0.8	-1.17	-0.67	-0.53	-0.23	0	0.77	0.44	0.19	0.11	0	1.68	1.96	2.06	2.16	0.68	1.17	0.77	0.48	
0.9	-1.17	-0.67	-0.55	-0.24	0	0.71	0.38	0.17	0.08	0	1.67	1.96	2.05	2.13	0.67	1.17	0.71	0.47	
1	-1.19	-0.69	-0.55	-0.20	0	0.66	0.33	0.15	0.06	0	1.64	1.95	2.03	2.10	0.67	1.19	0.66	0.46	
1.5	-1.30	-0.86	-0.69	-0.27	0	0.64	0.34	0.16	0.00	0	1.52	1.75	1.84	1.93	0.72	1.30	0.64	0.41	
2	-1.22	-0.83	-0.67	-0.23	0	0.56	0.30	0.11	-0.03	0	1.39	1.57	1.64	1.66	0.71	1.22	0.60	0.27	
2.5	-1.23	-0.87	-0.74	-0.39	0	0.54	0.29	0.13	-0.02	0	1.34	1.51	1.55	1.52	0.70	1.23	0.57	0.21	
3	-1.18	-0.86	-0.71	-0.41	0	0.51	0.25	0.13	-0.06	0	1.27	1.42	1.45	1.42	0.69	1.18	0.58	0.18	
4	-1.15	-0.84	-0.73	-0.40	0	0.45	0.21	0.10	-0.10	0	1.19	1.31	1.38	1.28	0.68	1.15	0.55	0.19	

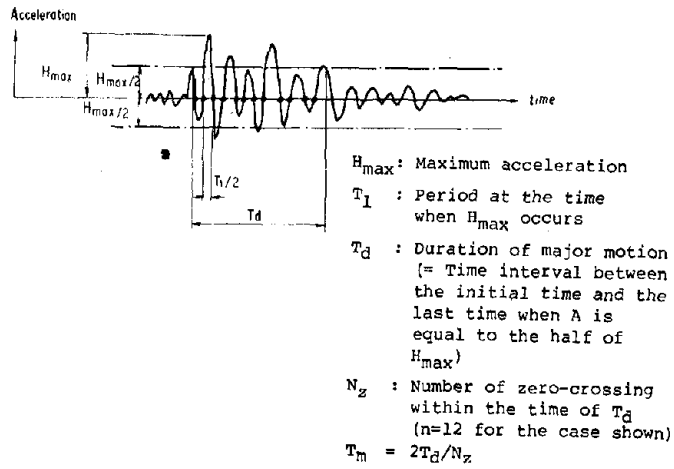


Fig. 1 Definitions of T_l , T_d , N_z , and T_m

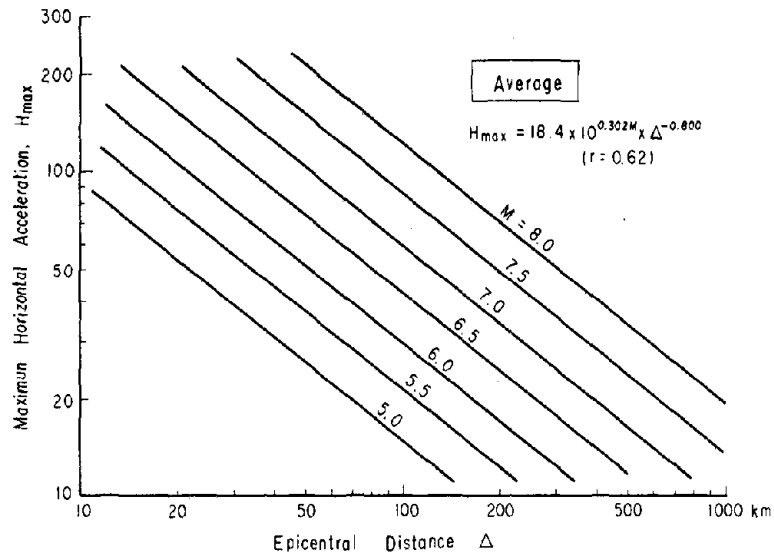


Fig. 2 Epicentral Distance versus Maximum Horizontal Acceleration for Average Subsoils

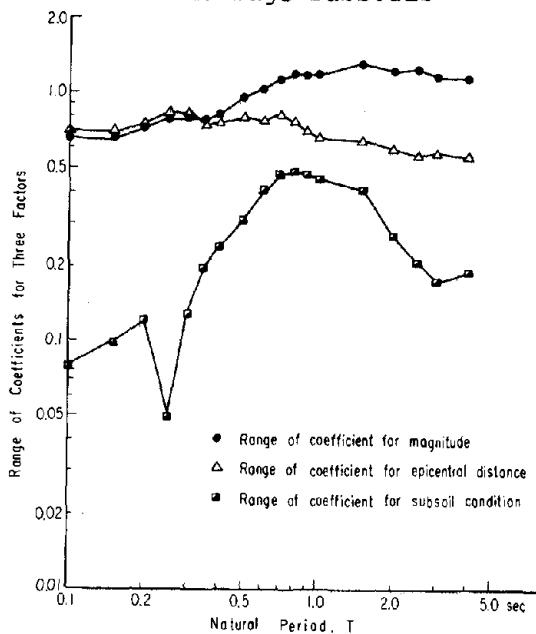


Fig. 5 Natural Period Versus Ranges of Coefficients for Three Factors (Magnitude, Epicentral Distance, and Subsoil Condition)

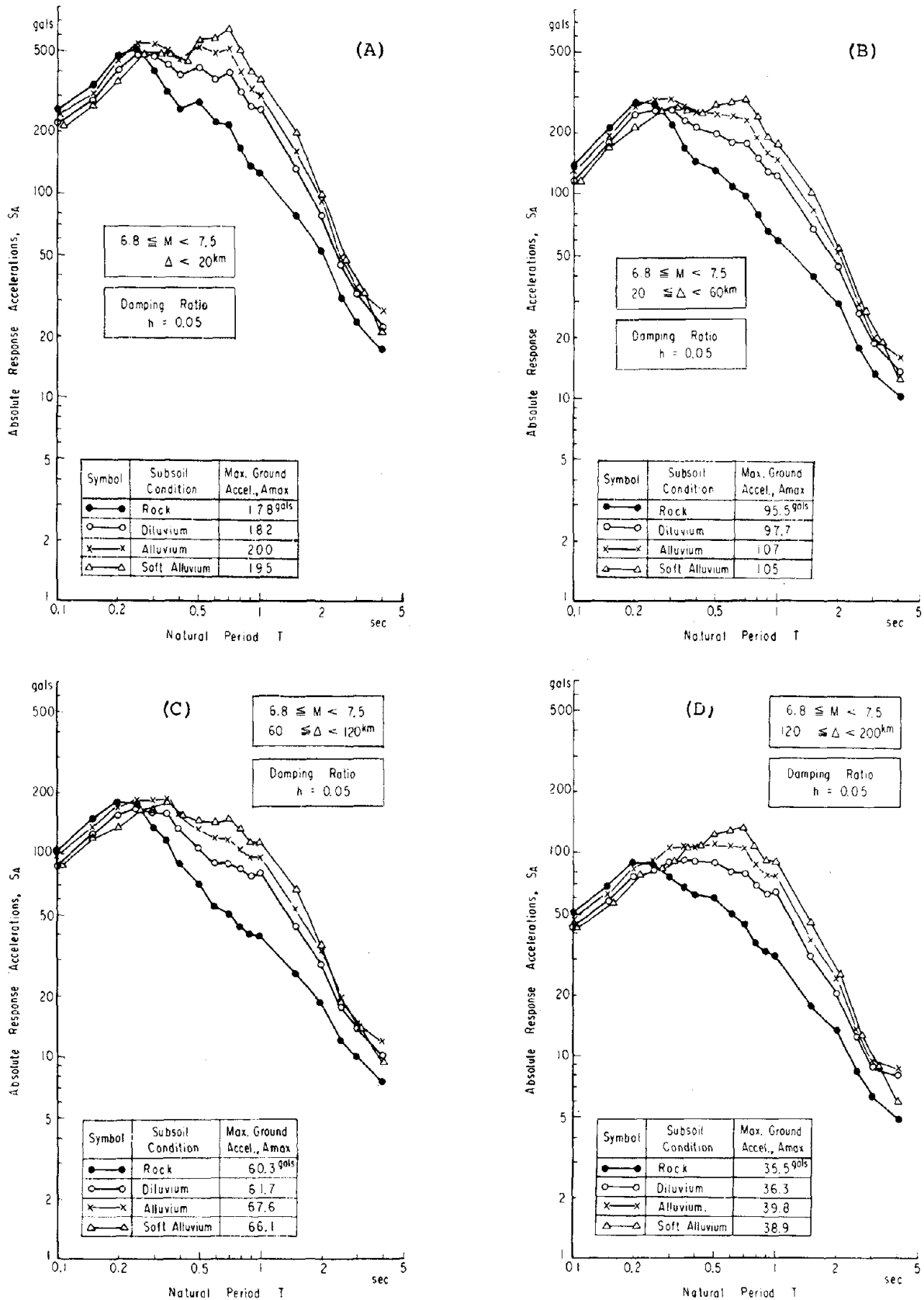


Fig. 3 (A) ~ (D) Response Spectrum Curves for Maximum Response Accelerations in Case of $6.8 \leq M < 7.5$

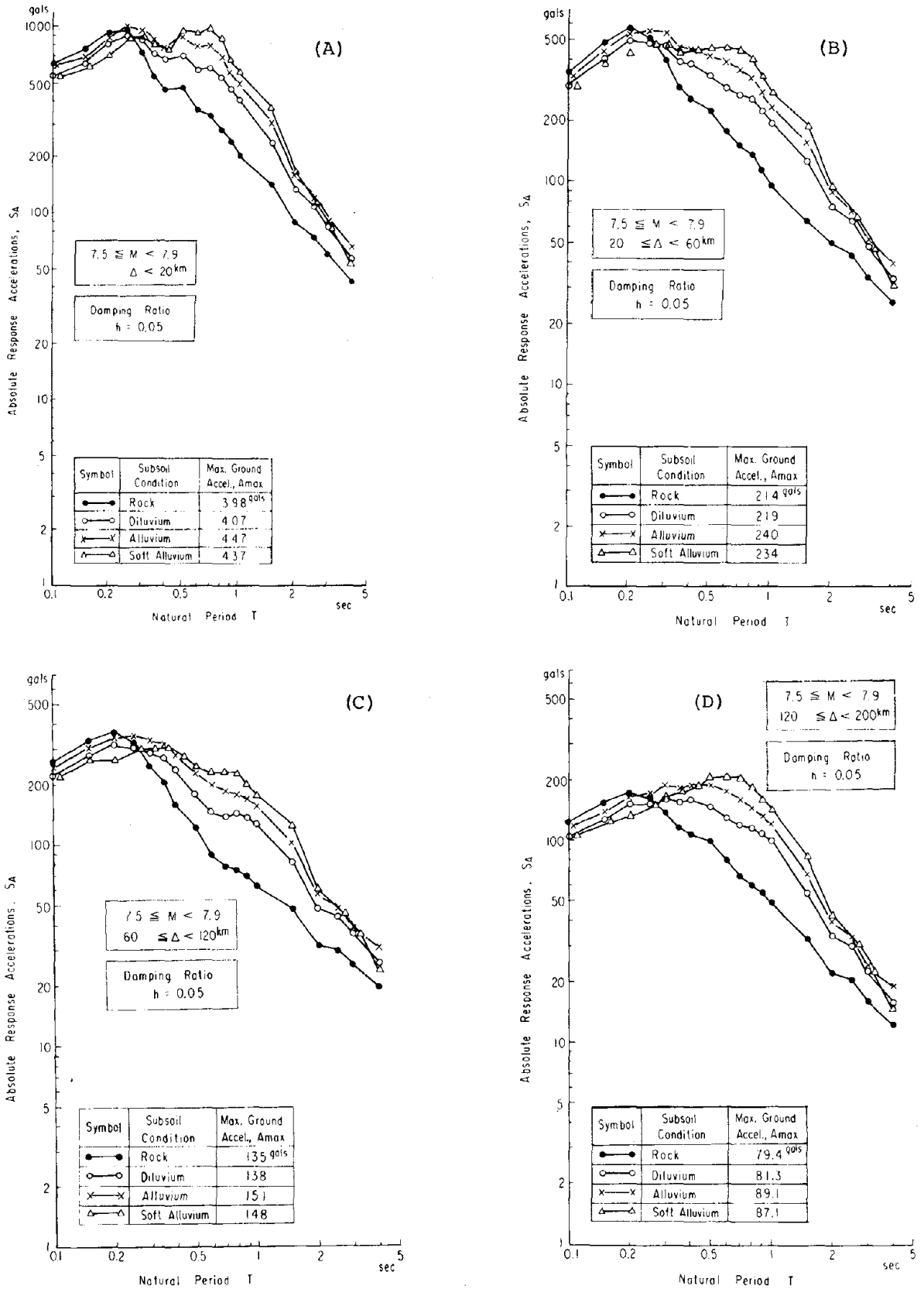


Fig. 4 (A) ~ (D) Response Spectrum Curves for Maximum Response Accelerations in Case of 7.5 ≤ M ≤ 7.9

ANALYSIS OF SOURCE AND MEDIUM
EFFECTS ON STRONG MOTION OBSERVATIONS

by

A. F. Shakal^I and M. N. Toksöz^{II}

ABSTRACT

The influence of the medium and source on recorded strong ground motion is studied through the analysis of accelerograms and theoretical modeling. The causes of the variations of ground motion at nearby sites are investigated by calculating the spectra, spectral ratio, and coherency for records from the San Fernando and Kern County earthquakes. The results show that the ground motion is coherent at low frequencies, but the coherency drops off at higher frequencies - between 1 and 10 Hz, depending on station spacing and site characteristics. The Pasadena and Lake Hughes area strong motion records from the San Fernando earthquake are re-examined to investigate the effects of local geology on the amplification of ground motion and the frequency dependence of this amplification. At the low frequencies in the pass band of the Wood-Anderson instrument, the strong motion shows effects of the sediment layering similar to those seen by Gutenberg. At the higher frequencies to which the acceleration is most sensitive, the shallow sedimentary layers have the greatest effect. Theoretical seismograms are calculated for a finite propagating source and the variation of these with azimuth is demonstrated.

INTRODUCTION

The strong motion records obtained from the San Fernando earthquake have provided the opportunity for detailed study of the variations of strong ground motion. Two particular aspects of these variations which have emerged from the subsequent analysis of these data are studied in this paper. First, the strong motion observations show significant variations between sites which are clearly not attributable to the effects of the source. Second, the sediment amplification effects on strong motion have been found to be apparently different from the amplification observed for small earthquake response.

In this paper, the strong motion variations at nearby sites are studied through spectral analysis of the recorded strong motion, considering in particular the frequency and site dependence of these variations. The sediment amplification effects on strong motion are re-examined considering the frequency dependence of the amplification and the frequency response of the recording instruments. Finally, the variations in the strong motion which may be expected simply due to the azimuthal dependence of the radiation from the source are considered.

I Graduate Student, Department of Earth and Planetary Sciences, Massachusetts Institute of Technology, Cambridge, Massachusetts.

II Professor, Department of Earth and Planetary Sciences, Massachusetts Institute of Technology, Cambridge, Massachusetts.

COHERENCY OF STRONG MOTION BETWEEN NEARBY SITES

The study of the variations in recorded strong motion is approached through analysis of the spectra, the spectral ratio, and the coherency at nearby stations. The coherency is an estimate of the correlation between two records as a function of frequency (1). The spectral ratio relates the amplitude of a frequency component in one record to that in the other without regard to phasing. Thus the spectral ratio and the coherency, sensitive to phasing, are complementary. The spectral ratio is often called the empirical transfer function in soil-structure interaction studies (2,3).

The coherency is defined as the smoothed cross power spectrum normalized by the product of the smoothed individual amplitude spectra

$$C_{xy}(f) = \frac{P_{xy}(f)}{[P_{xx}(f)P_{yy}(f)]^{1/2}}$$

As an example, Figure 1 shows the estimate of the coherency between the records from the San Fernando earthquake at Millikan and Atheneum in Pasadena, less than .5 km apart. The spectra are smoothed by tapering the covariance functions in the time domain; the bandwidth of that smoothing operator in the frequency domain is indicated in the figure. The coherency spectrum for these two records drops rapidly around 3 Hz. In general, we find that the width of this band of coherence narrows as the intersite distance increases, but is quite variable.

As an example at two closer stations, a similar analysis for the Hollywood Storage stations in Los Angeles is shown in Figure 2. HSB is in the basement of the Hollywood Storage building, HSL is about 100 ft from the building in a neighboring lot. Fortunately, records from both the San Fernando and Kern County earthquakes were obtained at both these stations, and so the between-station comparison can be made for two very different records. The spectra and the coherency for these stations are shown in Figure 2, for both the San Fernando and Kern County earthquakes. In the San Fernando records, there is a net loss at high frequencies in the building record, apparent both in the records and the amplitude spectra. The coherency is nearly unity out to 8 or 10 Hz. Crouse and Jennings (2) studied these records in terms of soil-structure interaction. The lower coherency values (i.e., reduced correlation) at about 2 and 5 Hz are at the frequencies that estimates of the theoretical building transfer function (2,3) are minimum. Thus these lows are consistent with their conclusion that soil-structure interaction influenced the basement record. The Kern County records have much less high frequency content than the San Fernando records, being recorded about 120 km from the source, as opposed to about 35 km. The coherency is high out to about 5 Hz. The spectra show that the building record once again has suffered a loss at the higher frequencies, and the difference is again roughly a factor of two. This is better shown by the ratios of the amplitude spectra, which are also shown in Figure 2. The spectral ratios are quite similar despite the different source mechanisms and the direction and distance of the two earthquakes. This appears to be a real site-to-site repeatable variation. The spectral ratios are near unity for low frequency, and near .5 for frequencies above about 5 Hz. Crouse and Jennings (2) found that the predictions from theoretical struc-

tural models were in general agreement with the observed spectra up to about 5 Hz, beyond which the theoretical model was unable to predict satisfactorily the filtering out of the higher frequencies by the building. At these higher frequencies scattering may be important. Considering the building resting on (or imbedded in) the surface of a half space, for wavelengths much longer than the building dimension, $\lambda \gg L$, the entire surface of the half space moves as one, and the waves recorded at the building should be little different from those recorded at any other point on the surface. For wavelengths near the dimension of the building, $\lambda \sim L$, complex interaction and coupling between P and S waves occurs. For wavelengths much shorter than the building dimension, $\lambda \ll L$, the wavefield at the building will be independent of that at the free-field station many wavelengths away. At these high frequencies, even if both energy spectra were the same, the ratio of the two amplitude spectra would be expected to be less than one, being controlled by the ratio of the effective elastic moduli of the building near the recording device to that at the free field station.

Seismic body waves in the low velocity near-surface layers propagate nearly vertically because of the bending of the rays. As an example Figure 3 shows the computed S-wave ray paths emerging at the Castaic site from a range of incidence angles at depth. Castaic is a site about 30 km to the northwest of San Fernando, chosen as an example simply because relatively deep velocity estimates are available for the structure under the site (4). The incidence angle in the upper layers is nearly vertical regardless of the incidence angle at depth. The cross-phase spectra for the records at the Hollywood Storage stations were computed for both the San Fernando and Kern County earthquakes and they indicate no major propagation in the horizontal direction.

FREQUENCY DEPENDENCE OF AMPLIFICATION DUE TO SEDIMENT LAYERING

In 1957, Gutenberg (6) studied seismograms from small earthquakes recorded at various locations in the Pasadena area and found a real correlation of amplification with geology. He observed strong amplification and increased duration in seismograms obtained over deep sediment as compared to those obtained at the CIT Seismological Laboratory, on basement. After the San Fernando earthquake Hudson (7) analyzed the strong motion records from this area to determine if the same effects Gutenberg saw for small earthquakes were observed for strong motion. He found that the strong motion records (see Figure 5) do not show a strong effect of the sediment under the stations on the amplitude of the acceleration. Hudson quite reasonably concluded that the local distribution of ground shaking predicted on the basis of small earthquake studies may not correspond very well with the distribution during a damaging earthquake. Because of the importance of this apparent discrepancy to microzonation, we have re-examined this problem considering the frequency dependence of amplification due to sediment layering and the frequency response of the recording instruments.

A major difference between the experiment of Gutenberg and the strong motion data from the San Fernando earthquake is the recording instrument. Gutenberg recorded with the low frequency Wood-Anderson instrument, the San Fernando data is recorded on accelerometers and seismoscopes. The response of these instruments is shown in Figure 4. The accelerometer responds most strongly to the higher frequencies, where the Wood-Anderson is down by a factor of ten from its maximum at about 1 Hz. (The difference between the accelerometer response and the acceleration is negligible below 15 Hz.)

The effect of the low pass band of the Wood-Anderson can be seen in Figure 5, where the acceleration records have been passed through the Wood-Anderson instrument response, and plotted for comparison (Kanamori and Jennings (8) made similar computations in M_L estimation). The acceleration records are all roughly similar except that the SL record is higher frequency. On the other hand, in the Wood-Anderson records, the SL record has been considerably reduced because its higher frequencies are outside the preferred band of the instrument. The Wood-Anderson records are in better agreement with Gutenberg's results. The duration at SL is less than that at ATH or MLK by a factor of 3 or 4. In amplitude, one component at SL is similar to those at ATH and MLK, the other is lower by a factor of perhaps 2 or 3. All of Gutenberg's results are based on single component records. If only one component of the San Fernando strong motion had been recorded, the resulting amplification ratio would lie within these extremes, depending on orientation. Gutenberg found a duration factor of about 4 and an amplification factor varying from 1 to 6 for ATH relative to SL. Therefore, the computed Wood-Anderson seismograms show a duration increase over the sediment at ATH roughly the same as Gutenberg's, and an amplification similar, but somewhat less than that seen by Gutenberg. Seismoscope recordings were obtained during the San Fernando earthquake (Morrill (9)) from several of the same sites at which Gutenberg made his recordings. Although the frequency and duration of the strong motion cannot be obtained from these records, the limited amplitude analysis possible yields a similar conclusion. The amplification that they show is similar to but less than that found by Gutenberg, particularly for sediment depths of 800 ft or greater. It is important to note, however, that the EW (roughly transverse) strong motion at SL is anomalously large compared to the records at the other bedrock stations MtW and WHS. Forming amplification ratios relative to SL is very sensitive to the SL record. If amplification ratios are formed relative to MtW the results are quite consistent with those of Gutenberg. It is difficult to establish at this point whether the lower amplification factors relative to SL are caused by strong motion being less amplified by sediment due, for example, to nonlinear response, or whether they are due to an anomalous record at SL, due to its proximity to an outcrop boundary trending along the azimuth to the epicenter.

Another example of the differences in amplification as seen on acceleration records and Wood-Anderson records, we consider the records at the Lake Hughes array, shown in Figure 6. These were all recorded in instrument shelters or 1-story buildings and so should be free of building effects. The acceleration records show roughly similar amplitude and duration except for LH12, which is large. LH9 apparently triggered late. According to the USGS station list (10), LH1 is on about 300m of alluvium over granitics, LH4 is on weathered granite, LH9 is on gneiss, and LH12 is on thin alluvium over conglomerate. The Wood-Anderson seismograms computed from the acceleration records are shown for comparison. They show quite clearly the sediment layer amplification at LH1 where the amplitude is 2 or 3 times that at LH4 or LH9. LH12, whose acceleration record is high amplitude, does not have a proportionately high amplitude Wood-Anderson record because of its high frequency, roughly 6 Hz, where the Wood-Anderson response is down by a factor of 3. This 6 Hz amplification in the acceleration record could arise from an alluvial layer of perhaps 60 to 80 ft.

To consider in greater detail what is occurring in the amplification, Figure 7 shows theoretical layered medium seismograms passed through the Wood-Anderson and accelerometer instrument responses. We consider a sediment layer of 15 and 90 meter thickness (50 and 300 ft) over basement corresponding

to the upper crust of Kanamori and Hadley (5). The sediment layer has a velocity of .5 km/sec (1600 ft/sec), and a shear Q of 20. For simplicity, we consider SH waves, incident from the halfspace at 30 deg. The two input time functions are shown in the figure, their spectra peak at 2 and 7 Hz, respectively.

The Wood-Anderson record over the thick layer is amplified relative to that over the thin layer because of the passband of the instrument and the low frequency response of the layer. Similarly, the accelerometer shows amplification at high frequency in the record over the thin layer. The deep layering causes increased amplitudes and duration in the Wood-Anderson record but not the acceleration because the high frequencies to which acceleration is sensitive are attenuated by the Q in the layer. The layer is only 1/5 of a wavelength thick at 1 Hz, while it is 2 wavelengths thick at 10 Hz. In sum, the Wood-Anderson pass band tends to reflect deeper sediment layering, as seen by Gutenberg, while acceleration records are influenced to a large extent by the shallow layering and do not show the deep layering well.

SOURCE RADIATION EFFECTS

The analysis of strong motion observations must include allowance for differences in source radiation if the station spacing is not small relative to the distance to the fault. As an example, Figure 8 shows velocity seismograms computed for stations varying in azimuth around a rectangular strike-slip fault. The stations are equispaced and located a constant distance from the fault. The seismograms were computed using the analytic solution of Madariaga (11) for the Haskell source. For simplicity, they were corrected for the free surface by doubling, since the incidence angles are in a range where, for strike-slip faulting, this is a reasonable approximation (Anderson (12)). It can be seen that there are strong variations in both the amplitude and frequency content of the computed strong motion, even for stations a constant distance from the fault.

CONCLUSIONS

Variations of strong ground motion at nearby sites are strongly dependent on frequency. Comparisons of spectra and coherency between sites shows that the strong motion is coherent at low frequencies, but the coherency drops off at higher frequencies. At high frequencies, the effects of attenuation and of scattering due to near surface heterogeneities and buildings are substantial.

The amplification effects of the site due to local geology are also dependent on frequency. Thus such effects when measured by a Wood-Anderson seismograph or by a strong-motion accelerometer appear to be different. Theoretical calculations made using different thicknesses of low velocity sedimentary layers show strong dependence of the amplitude of the surface motion on the peak frequency of the incident pulse. Theoretical seismograms for a finite propagating source predict significant variations in strong motion levels even at a constant distance from the fault.

ACKNOWLEDGEMENTS

This work was supported by the U.S. Geological Survey under contract No. 14-08-0001-16756. The use of the facilities of the Applied Seismology

Group, Lincoln Laboratory, is gratefully acknowledged. The acceleration data used in this study are from the CIT-EERL Strong Motion Data Processing program.

BIBLIOGRAPHY

- 1 Jenkins, G.M. and D.G. Watts (1968) Spectral Analysis and Its Applications, Holden-Day, Inc., San Francisco, 525 pp.
- 2 Crouse, C.B. and P.C. Jennings (1975) Soil-structure interaction during the San Fernando earthquake, BSSA, vol. 65, 13-36.
- 3 Hradilek, P.J. and J.E. Luco (1970) Dynamic soil-structure interaction, IDIEM Informa Tecnico no. 14, Universidad de Chile, Santiago.
- 4 Duke, C.M., J. Johnson, Y. Kharraz, K. Campbell, and N. Malpiede (1973) Subsurface site conditions in the San Fernando earthquake area, in San Fernando, California, Earthquake of February 9, 1971, vol. 3, U.S. Dept. Commerce.
- 5 Kanamori, H. and D. Hadley (1975) Crustal structure and temporal velocity change in southern California, Pure Appl. Geophys., vol. 113, 257-280.
- 6 Gutenberg, B. (1957) Effects of ground on earthquake motion, BSSA, vol. 47, 221-250.
- 7 Hudson, D.E. (1972) Local distribution of strong earthquake ground motions, BSSA, vol. 62, 1765-1786.
- 8 Kanamori, H. and P.C. Jennings (1978) Determination of local magnitude, M_L , from strong motion accelerograms, BSSA, vol. 68, 471-485.
- 9 Morrill, B.J. (1971) Seismoscope results - San Fernando earthquake of 9 February 1971. in Strong-Motion Instrumental Data on the San Fernando Earthquake of Feb. 9, 1971, D.E. Hudson, ed., CIT-EERL rept.
- 10 United States Geological Survey, Western Hemisphere Strong-Motion Accelerograph Station List - 1976, Open File Rept. 77-374, 112 pp.
- 11 Madariaga, R. (1978) The dynamic field of Haskell's rectangular dislocation fault model, BSSA, in press.
- 12 Anderson, J.G. (1976) Motions near a rupturing fault: evaluation of effects due to the free surface, Geophys. J.R. Astr. Soc., vol. 46, 575-593.

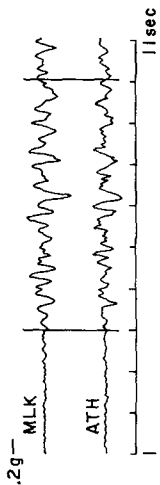
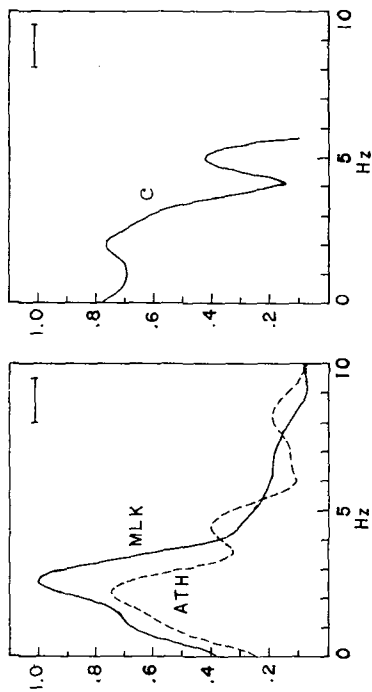
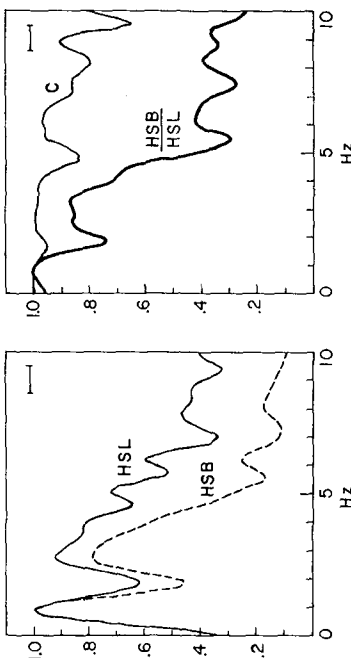


Figure 1. Normalized amplitude spectra and coherency for the EW San Fernando records at MLK and ATH. Spectra and coherency are of the high amplitude portion of the record within the cursors.



San Fernando



Kern County

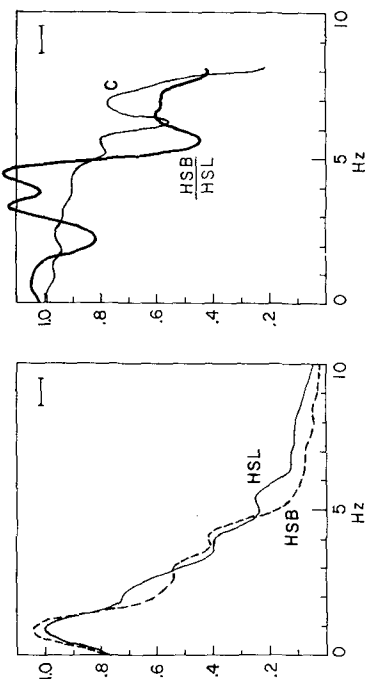
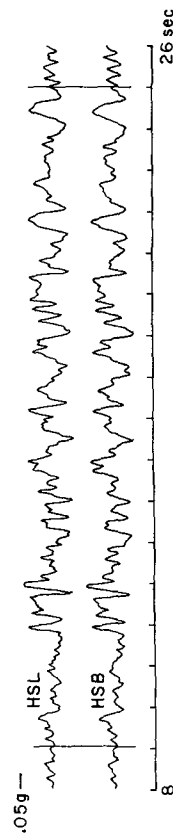
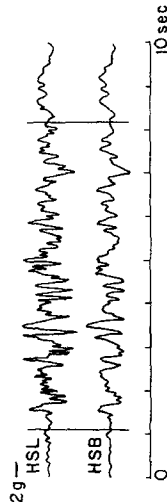


Figure 2. Normalized amplitude spectra, coherency and spectral ratio for the San Fernando and Kern County records at the Hollywood Storage stations, EW components.



CASTAIC

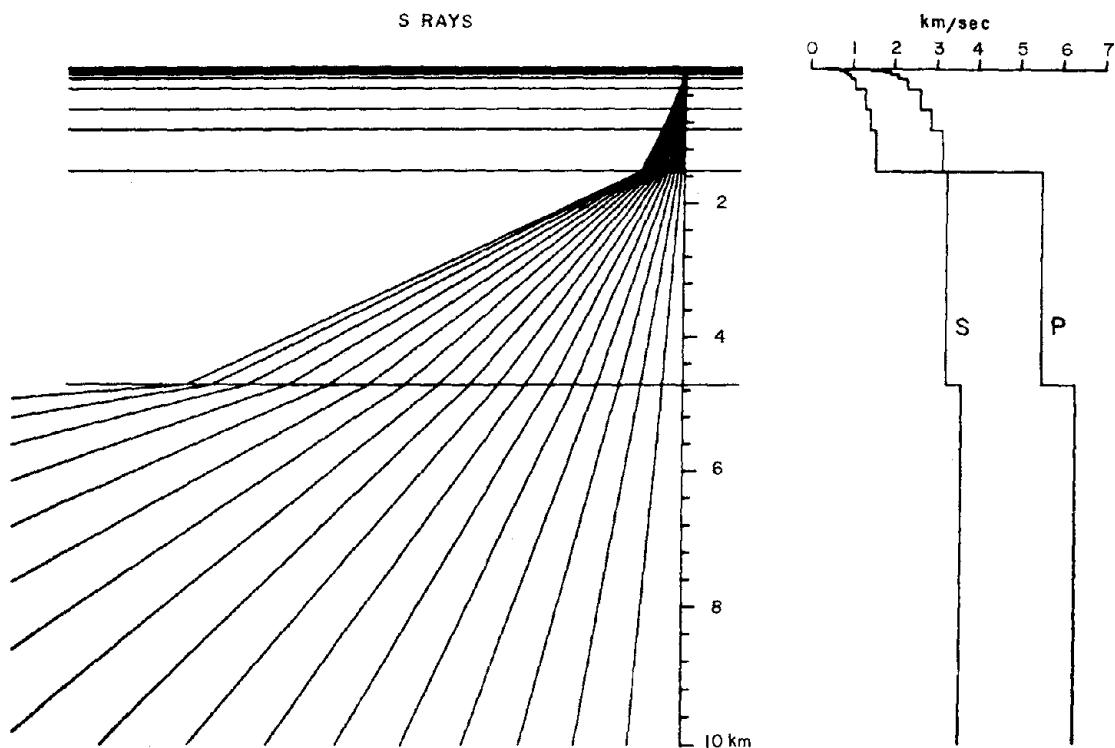


Figure 3. S-wave ray paths for the Castaic site. Velocity structure of Duke et al. (4) over basement corresponding to the upper crust of Kanamori and Hadley (5).

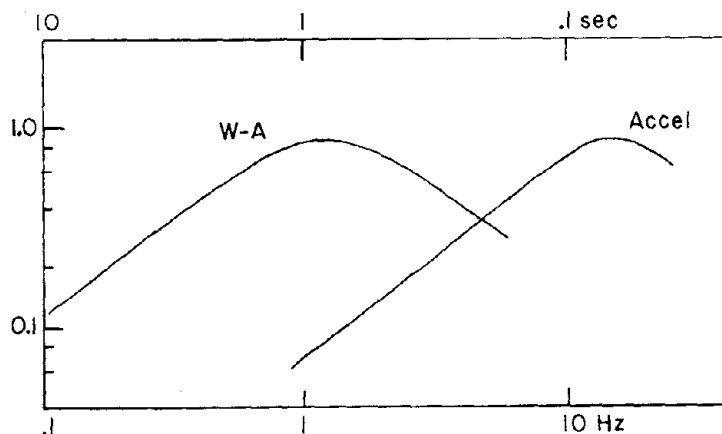
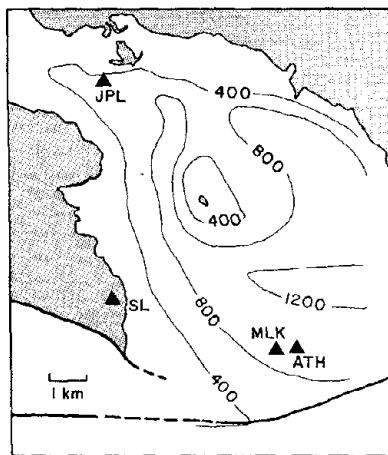
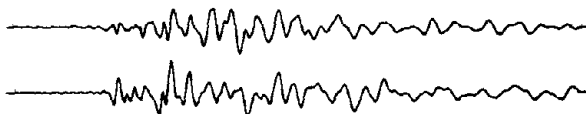
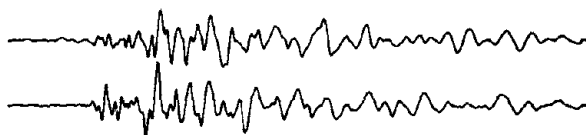
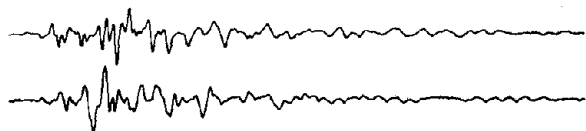
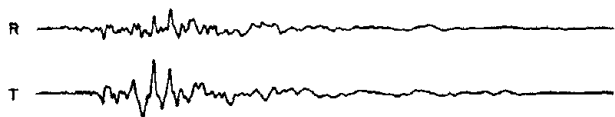


Figure 4. Normalized velocity response of the Wood-Anderson seismograph and the accelerometer. The response of the seismoscope is nearly identical to that of the Wood-Anderson, but with less damping.

SAN FERNANDO
AT
PASADENA STATIONS



WOOD-ANDERSON



25 m 1 sec

ACCELEROMETER



.2g 1 sec

Figure 5. Pasadena area acceleration records from the San Fernando earthquake and the synthetic Wood-Anderson records computed from them, radial and transverse components. Geologic map showing exposed basement and contours of sediment depth (in feet) after Gutenberg(6).

LAKE HUGHES ARRAY

N21E COMPS

WOOD-ANDERSON

ACCELEROMETER

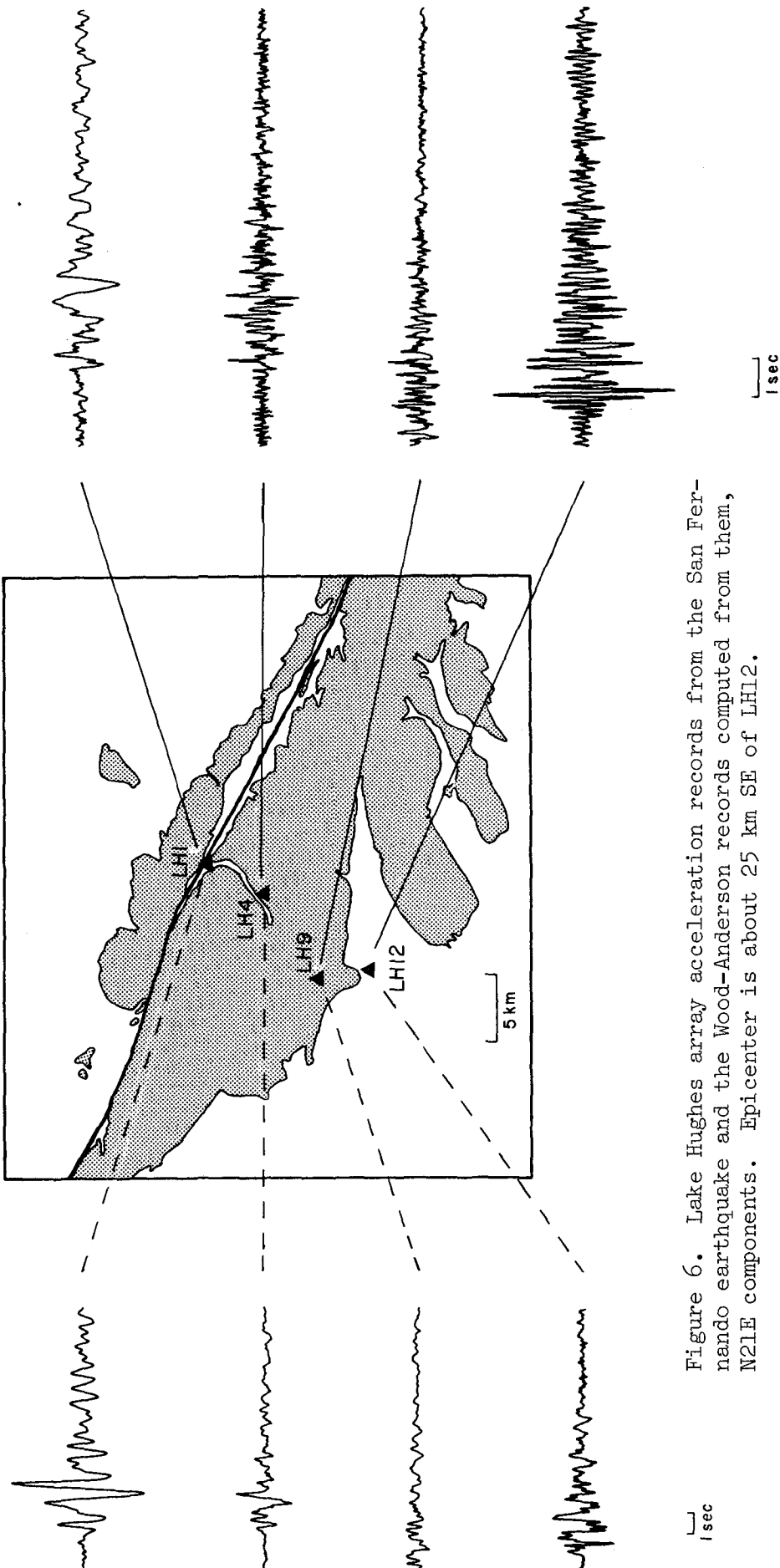
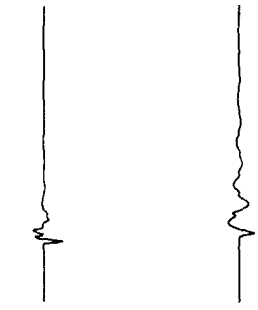


Figure 6. Lake Hughes array acceleration records from the San Fernando earthquake and the Wood-Anderson records computed from them, N21E components. Epicenter is about 25 km SE of LH12.

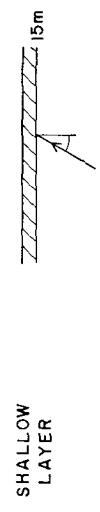
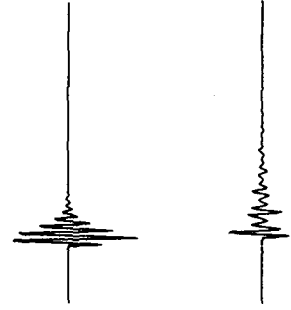
ACCELEROMETER

WOOD-ANDERSON

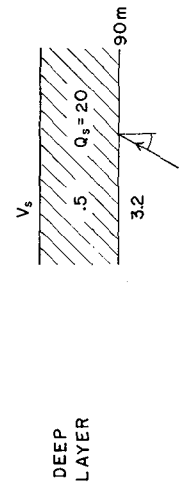
LOW FREQUENCY WAVELET



HIGH FREQUENCY WAVELET



SHALLOW LAYER



DEEP LAYER

SHALLOW

DEEP

1 sec

Figure 7. Computed Wood-Anderson and accelerometer records for a layer over halfspace for the velocity source functions shown.

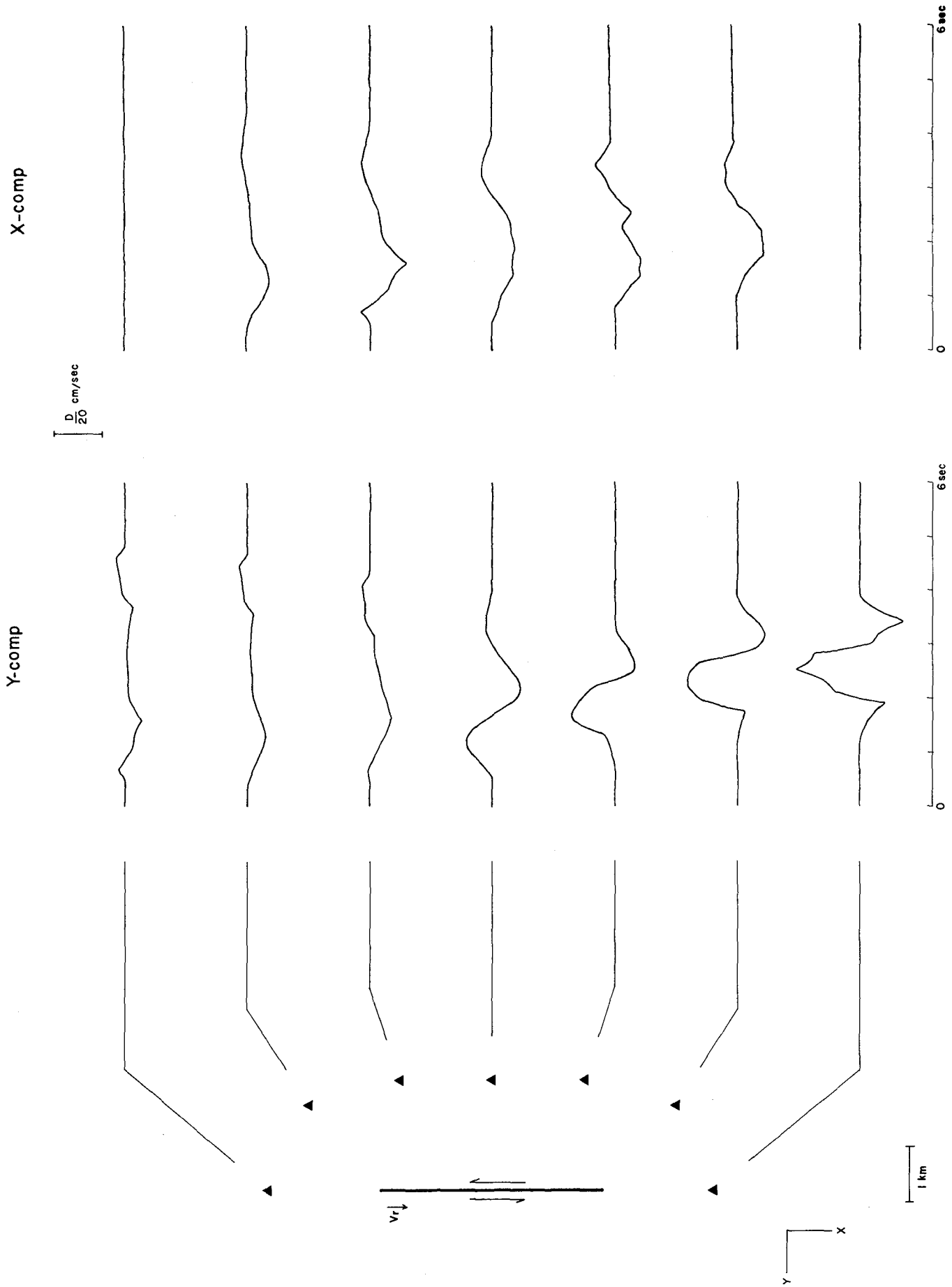


Figure 8. Computed velocity seismograms for points around a rectangular strike-slip fault. Fault is 4 by 2 km, 1 km below the plane of the stations. V_p , V_s , V_{rupt} are 5.5, 3.4, and 2.2 km/sec, rise time = .9 sec.

GROUND MOTION AMPLIFICATION DUE TO
CANYONS OF ARBITRARY SHAPE

by

Francisco J. Sánchez-Sesma¹

ABSTRACT

A method is presented to compute the scattering and diffraction of plane seismic waves by a canyon of arbitrary shape. The problem is formulated in terms of Fredholm integral equations of the first kind in which the integration path is defined outside the boundary, thus obtaining kernels which are regular. A class of discretization schemes using line source solutions is employed. Boundary conditions are satisfied in the least-squares sense. Semi-analytic line-source solutions are used for incident P or SV waves. Numerical results are presented for amplification spectra for semi-circular canyons. Extensions and possible applications are discussed.

INTRODUCTION

In the last few years the influence of local conditions on ground-motion has attracted the interest of numerous researchers. The construction of important structures, such as nuclear reactors or large dams, has enhanced this interest. In several regions, spatial distribution of seismic damage has been explained by the influence of local soil conditions and topographic features (1-3). The subject has been treated in the literature as scattering and diffraction of elastic waves by irregularities on the surface of an elastic half-space.

For semi-cylindrical and semi-elliptical canyons analytical solutions have been obtained for horizontally polarized incident plane SH waves (4,5). These solutions have been extended to deal with semi-cylindrical and semi-elliptical alluvial valleys (6,7). The SH-waves diffraction due to canyons of arbitrary shape has been formulated in terms of a Fredholm integral equation of the second kind and applied to the study of topographic effects at Pacoima Canyon (8). Another approach assumes periodicity of surface shape and discretizes integral equations to obtain ground motion amplifications for incident P, SV, or SH waves (9). This method is restricted to small slopes. For acoustic media an exact solution has been obtained for a semi-spherical valley and a semi-cylindrical canyon (10). Only vertically incident waves were considered in detail. A procedure has been proposed for P and SV waves which employs a least-squares criterion to satisfy free boundary conditions on the canyon and half-space surface (11). An alternative method has been developed for the solution of SH-waves diffraction by arbitrarily shaped canyons (12). This method makes use of

¹ Associate Professor of Engineering, Instituto de Ingeniería, Universidad Nacional Autónoma de México, México 20, D.F., México.

an integral representation of scattered and diffracted waves as a single-layer potential in which the integration path is outside the boundary, thus obtaining a regular kernel. This idea has been applied by De Mey to the solution of Laplace's interior problem (13) and has been proposed in a slightly different form for solving plane elastostatic problems (14). The method has been successfully extended for treating diffraction of SH waves caused by arbitrarily shaped alluvial valleys (15).

In the present paper the method is extended to incident P or SV waves in a two-dimensional problem. It is well known that incidence of P or SV waves at a given angle on a free surface generates both types of waves. The diffracted field is represented with the aid of single-layer potentials in which the integration paths are chosen outside the canyon's boundary, getting similarly regular kernels. Inclusion of traction-free boundary conditions leads to a system of Fredholm integral equations of the first kind. A class of discretization schemes using solutions of buried line sources in an elastic half-space is employed. Numerical results are obtained in the least-squares sense.

Solutions of buried line sources are obtained using the single-frequency method developed by Aki and Larner (16) and recently applied by Bouchon and Aki for modeling seismic-source wave fields (17). Spatial periodicity of sources is assumed and an approximate semi-analytical representation is obtained.

Questions arise regarding completeness of the set of sources and convergence of the method. We will not deal with these questions in this paper but it can probably be shown, using Herrera's theory of connectivity (18,19), that the set of concentrated sources is complete. The argument would be similar to one used in developing bases for some related problems (20). The same theory (18,19) can probably be used to show that the solution, using the least-square criterion, converges to the exact as the number of sources tends to infinity. These ideas are related to a procedure proposed by Millar (21), who described conditions for the validity of the Rayleigh hypothesis in scattering of acoustic waves.

PROBLEM FORMULATION

To formulate the problem for the propagation of harmonic P or SV waves let us consider the usual potentials ϕ and ψ (22). These potentials satisfy the Helmholtz equation

$$\frac{\partial^2 \phi}{\partial x^2} + \frac{\partial^2 \phi}{\partial y^2} + k_p^2 \phi = 0 \quad (1)$$

$$\frac{\partial^2 \psi}{\partial x^2} + \frac{\partial^2 \psi}{\partial y^2} + k_s^2 \psi = 0 \quad (2)$$

where $k_p = \omega/\alpha =$ P-wave number, $\alpha = \sqrt{(\lambda+2\mu)/\rho} =$ P-wave speed, $\lambda =$ Lamé constant, $\mu =$ shear modulus, $\rho =$ mass density, $\omega =$ circular frequency, $k_s = \omega/\beta =$ S-wave number, $\beta = \sqrt{\mu/\rho} =$ S-wave speed.

Displacements u_x and u_y in terms of ϕ and ψ are given by

$$u_x = \frac{\partial \phi}{\partial x} - \frac{\partial \psi}{\partial y} \quad \text{and} \quad u_y = \frac{\partial \phi}{\partial y} + \frac{\partial \psi}{\partial x} \quad (3)$$

The stress components can be written as

$$\left. \begin{aligned} \sigma_x &= (\lambda + 2\mu) \frac{\partial u_x}{\partial x} + \lambda \frac{\partial u_y}{\partial y} \\ \sigma_y &= \lambda \frac{\partial u_x}{\partial x} + (\lambda + 2\mu) \frac{\partial u_y}{\partial y} \\ \tau_{xy} &= \mu \left(\frac{\partial u_x}{\partial y} + \frac{\partial u_y}{\partial x} \right) \end{aligned} \right\} \quad (4)$$

The traction-free boundary condition implies that at the free surface

$$\left. \begin{aligned} t_x &= \sigma_x \cos \theta - \tau_{xy} \sin \theta = 0 \\ t_y &= \tau_{xy} \sin \theta - \sigma_y \cos \theta = 0 \end{aligned} \right\} \quad (5)$$

where t_x , t_y = traction components in x , y directions respectively, θ = angle measured counterclockwise from the x -axis to vector n , n = vector normal to the free surface (Fig. 1).

The potentials $\phi(0)$ and $\psi(0)$ of the free-field solution for incidence of harmonic P or SV plane waves, omitting the time factor $\exp(i\omega t)$, can be written as

$$\left. \begin{aligned} \phi(0) &= A_1 \exp[-ik_p(x \cos e - y \sin e)] + A_2 \exp[-ik_p(x \cos e + y \sin e)] \\ \psi(0) &= B_1 \exp[-ik_s(x \cos f - y \sin f)] + B_2 \exp[-ik_s(x \cos f + y \sin f)] \end{aligned} \right\} \quad (6)$$

where A_1 , B_1 = amplitudes of incident P, SV waves, A_2 , B_2 = amplitudes of reflected, P, SV waves, and e, f = angles of incidence and reflection (Fig. 2). For incident P waves it is clear that $B_1 = 0$. In order to obtain free boundary conditions at $y = 0$, amplitudes of reflected waves are put in the form

$$\left. \begin{aligned} \frac{A_2}{A_1} &= \frac{4 \tan e \tan f - (\tan^2 f - 1)^2}{4 \tan e \tan f + (\tan^2 f - 1)^2} \\ \frac{B_2}{A_1} &= -\frac{4 \tan e (\tan^2 f - 1)}{4 \tan e \tan f + (\tan^2 f - 1)^2} \end{aligned} \right\} \quad (7)$$

Similarly, for incident SV waves ($A_1 = 0$) we obtain

$$\left. \begin{aligned} \frac{A_2}{B_1} &= \frac{4 \tan f (\tan^2 f - 1)}{4 \tan e \tan f + (\tan^2 f - 1)^2} \\ \frac{B_2}{B_1} &= \frac{4 \tan e \tan f - (\tan^2 f - 1)^2}{4 \tan e \tan f + (\tan^2 f - 1)^2} \end{aligned} \right\} \quad (8)$$

The relation between f and e is given by $\cos f = (\beta/\alpha) \cos e$.

Assume that the solution including waves diffracted by the canyon has the form

$$\tilde{u} = \tilde{u}^{(0)} + \tilde{u}^{(d)} \quad (9)$$

where $u = [u_x, u_y]^T$, $u^{(0)} = [u_x^{(0)}, u_y^{(0)}]^T$, $u^{(d)} = [u_x^{(d)}, u_y^{(d)}]^T$, $u_x^{(0)}$, $u_y^{(0)}$ = displacements in the free-field solution in terms of $\phi^{(0)}$ and $\psi^{(0)}$, and $u_x^{(d)}$, $u_y^{(d)}$ = displacements due to diffracted waves in terms of diffracted potentials $\phi^{(d)}$ and $\psi^{(d)}$. Assume, extending the ideas of the SH-case (12), that we can write

$$\phi^{(d)}(P) = \int_{C_1} g(Q) \phi_1(P, Q) dS_Q + \int_{C_2} h(Q) \phi_2(P, Q) dS_Q \quad (10)$$

$$\psi^{(d)}(P) = \int_{C_1} g(Q) \psi_1(P, Q) dS_Q + \int_{C_2} h(Q) \psi_2(P, Q) dS_Q \quad (11)$$

where $P \in E \cup \partial E$, $Q \in C_1$ or $Q \in C_2$ (Fig. 3), $g(\cdot)$, $h(\cdot)$ = single-layer densities, an unknown functions to be determined, ϕ_1 and ψ_1 = potentials for a buried line source of P waves, and ϕ_2 and ψ_2 = potentials for a buried line source of SV waves.

As an illustration, express the potentials for the line source of P waves as (23, 24).

$$\phi_1 = \pi i \{ H_0^{(2)}(k_P r_1) - H_0^{(2)}(k_P r_2) \} + \int_{-\infty}^{\infty} A(k) \exp[-i y \nu] \exp[-i(x-x_0)k] dk \quad (12)$$

$$\psi_1 = \int_{-\infty}^{\infty} B(k) \exp[-i y \gamma] \exp[-i(x-x_0)k] dk \quad (13)$$

where $\nu = \sqrt{k_P^2 - k^2}$, $\text{Im}(\nu) < 0$, $\gamma = \sqrt{k_S^2 - k^2}$, $\text{Im}(\gamma) < 0$,

$$r_1 = [(x - x_0)^2 + (y - y_0)^2]^{1/2},$$

$$r_2 = [(x - x_0)^2 + (y + y_0)^2]^{1/2},$$

x, y = coordinates of point P

x_0, y_0 = coordinates of source at point Q,

$$A(k) = \frac{4ik^2\gamma}{F(k)} \exp[-i y_0 \nu], \quad B(k) = \frac{2ik(2k^2 - k_S^2)}{F(k)} \exp[-i y_0 \nu],$$

$F(k) = (2k^2 - k_S^2)^2 + 4k^2 \nu \gamma$ = Rayleigh function, and

$H_0^{(2)}(\cdot)$ = Hankel function of the second kind.

In order to evaluate the integrals in equations 12 and 13 (and similarly for potentials due to the SV source) approximately, we assume spatial

periodicity for the integral part of potentials and consider the frequency ω a complex number with a small negative imaginary part. In this way we obtain a series representation and the singularities from the real k -axis are removed. This procedure is due to Aki and Larner (16). Details can be found in Bouchon and Aki (17).

Substituting equations 10 and 11 into equations 3 and taking into account equation 9, we obtain

$$\underline{u}(P) = \underline{u}^{(0)}(P) + \int_{C_1} g(Q) \underline{u}^{(1)}(P, Q) dS_Q + \int_{C_2} h(Q) \underline{u}^{(2)}(P, Q) dS_Q \quad (14)$$

where $P \in E \cup \partial E$, $\underline{u}^{(1)}(P, Q)$, $\underline{u}^{(2)}(P, Q)$ = displacement vectors at point P due to a unit line source of P and SV waves respectively, located at point Q .

We may write a similar expression for the traction vector $\underline{t} = [t_x, t_y]^T$. For $P \in \partial E$, the canyon's boundary, equations 5 leads to

$$\int_{C_1} g(Q) \underline{t}^{(1)}(P, Q) dS_Q + \int_{C_2} h(Q) \underline{t}^{(2)}(P, Q) dS_Q = -\underline{t}^{(0)}(P), \quad P \in \partial E \quad (15)$$

Expression 15 constitutes a system of Fredholm integral equations of the first kind. We will solve the system in the least-squares sense requiring that the mean square error

$$\int_{\partial E} |\underline{t}^{(d)}(P) + \underline{t}^{(0)}(P)|^2 dS_P \quad (16)$$

be a minimum. In expression 16, $\underline{t}^{(d)}$ = traction vector due to diffracted waves.

NUMERICAL SOLUTION

Let $g(\cdot)$ and $h(\cdot)$ be of the form

$$g(Q) = \sum_{m=1}^M a_m \delta(|Q - Q_m|) \quad Q, Q_m \in C_1 \quad (17)$$

$$h(Q) = \sum_{n=1}^N b_n \delta(|Q - Q_n|) \quad Q, Q_n \in C_2 \quad (18)$$

where M = number of sources of P waves with amplitude a_m at points $Q_m \in C_1$, N = number of sources of SV waves with amplitude b_n at points $Q_n \in C_2$, and $\delta(\cdot)$ = Dirac's delta function. Thus equations 14 and 15 can be written as

$$\underline{u}(P) = \underline{u}^{(0)}(P) + \sum_{m=1}^M a_m \underline{u}^{(1)}(P, Q_m) + \sum_{n=1}^N b_n \underline{u}^{(2)}(P, Q_n) \quad (19)$$

and

$$\sum_{m=1}^M a_m \underline{t}^{(1)}(P, Q_m) + \sum_{n=1}^N b_n \underline{t}^{(2)}(P, Q_n) = -\underline{t}^{(0)}(P) \quad (20)$$

Imposing equation 20 at L points P_ℓ on the boundary of the canyon we obtain

$$\sum_{m=1}^M a_m \tilde{t}^{(1)}(P_\ell, Q_m) + \sum_{n=1}^N b_n \tilde{t}^{(2)}(P_\ell, Q_n) = -\tilde{t}^{(0)}(P_\ell), \quad \ell=1,2,\dots,L \quad (21)$$

Equation 21 represents a linear system of $2L$ equations with $M+N$ unknowns, which is solved in the least squares sense multiplying first the system by the transpose conjugate of the coefficients matrix. This procedure is the discrete equivalence of obtaining a minimum for the mean square error in expression 16. Once the system is solved, equation 19 leads to displacements in all points of region E and its boundary.

RESULTS

Figures 4 and 5 show amplitudes of normalized horizontal and vertical displacements on a semi-cylindrical canyon under incident plane P and SV waves with incident wave-length $\Lambda = 4\pi a$, where a = half-width of the canyon for three different incidence angles $\theta_0 = 0^\circ, 30^\circ, 60^\circ$ ($\theta_0 = 90^\circ - e$ for incident P waves and $\theta_0 = 90^\circ - e$ for incident SV waves). In all cases 15 sources and 50 collocation points on the boundary were taken. Curves C_1 and C_2 were circles with radii $0.6a$ and $0.7a$ respectively. The Poisson relation, $\lambda = \mu$, has been assumed.

General trends on amplification noted previously (2,4,5,9,11,12) also show up for semi-cylindrical canyon under incidence of plane P or SV waves; that is, for the frequencies covered here, there are reductions at the bottom for vertical incidence. The barrier effect is also noticeable; for the wave-length studied, there is about 100 per cent amplification in horizontal motion at one border of the canyon for incident P waves with 60° incidence angle. The SV case gives similar results.

CONCLUSIONS

A method has been presented to compute the scattering and diffraction of plane seismic waves by arbitrarily shaped canyons. The problem is formulated in terms of a system of Fredholm integral equations of the first kind in which the integration paths are curves differ from the canyon's boundary in order to get regular kernels. Line-source discretization and the least-squares criterion simplify numerical treatment and lead to stable, accurate solutions.

Amplitude reductions at the bottom were found for vertical incidence. There are large amplifications for oblique incidence. This barrier effect should be taken into account in bridge or reservoir design where large differences in support motion can take place.

Although results are limited to the frequencies studied, they also show that the method appears to be a useful tool to deal with some scattering problems. For instance, it can be applied to solve scattering by buried alluvial valleys or tunnels.

ACKNOWLEDGEMENTS

The writer thanks E. Rosenblueth and S. K. Singh for their constructive criticism. The assistance of J. A. Esquivel is greatly appreciated.

REFERENCES

1. Rosenblueth, E, "Soil and rock mechanics in earthquake engineering", *Proc International Symposium on Dynamical Methods in Soil and Rock Mechanics (DMSR 77)*, Karlsruhe, Germany (sep 12-16, 1977)
2. Ruiz, S, "Influencia de las condiciones locales en las características de los sismos", *Instituto de Ingeniería, UNAM, Mexico*, 387 (1977)
3. Hudson, D E, "Local distribution of strong earthquake motion", *Bull Seism Soc Am*, 62 (1972), 1765-1786
4. Trifunac, M D, "Scattering of plane SH waves by a semi-cylindrical canyon", *Earthq Engrg and Structl Dyn*, 1 (1973), 267-281
5. Wong, H L y Trifunac, M D, "Scattering of plane SH waves by a semi-elliptical canyon", *Earthq Engrg and Structl Dyn*, 3 (1973), 157-169
6. Trifunac, M D, "Surface motion of a semi-cylindrical alluvial valley for incident plane SH-waves", *Bull Seism Soc Am*, 61, 6 (1971), 1755-1770
7. Wong, H L, and Trifunac, M D, "Surface motion of a semi-elliptical alluvial valley for incident plane SH waves", *Bull Seism Soc Am*, 64, 5 (1974), 1389-1408
8. Wong, H L, and Jennings, P C, "Effects of canyon topography on strong ground motion", *Bull Seism Soc Am*, 65, 5 (1975), 1239-1257
9. Bouchon, M, "Effect of topography on surface motion", *Bull Seism Soc Am*, 63, 3 (1973), 615-632
10. Singh, S K, and Sabina, F J, "Ground-motion amplification by topographic depressions for incident P wave under acoustic approximation", *Bull Seism Soc Am*, 67, 2 (1977), 345-352
11. Ruiz, S E, and Esteva, L, "Efecto de la topografía en los movimientos del suelo provocados por ondas planas P y SV", en *Evaluación del riesgo-efectos locales, etapa I*, Instituto de Ingeniería, UNAM, Mexico (mar 1978)
12. Sánchez-Sesma, F J, and Rosenblueth, E, "Ground motion at canyons of arbitrary shape under incident SH waves", submitted to be published in *Earthq Engrg and Structl Dyn* (1978)
13. De Mey, G, "Integral equations for potential problems with the source function not located on the boundary", *J Computers & Structures*, 8, 1 (1978), 113-115

14. Heise, U, "Numerical properties of integral equations in which the given boundary values and the sought solutions are defined on different curves", *J Computers & Structures*, 8, 2 (1978), 199-205
15. Sánchez-Sesma, F J, and Esquivel, J A, "Ground motion on alluvial valleys under incident plane SH waves", presented at the *Twelfth International Symposium on Mathematical Geophysics*, Caracas, Venezuela (Aug 14-24, 1978)
16. Aki, K, and Larner, K L, "Surface motion of a layered medium having an irregular interface due to incident plane SH waves", *J Geophys Res*, 75, 5 (1970), 933-954
17. Bouchon, M, and Aki, K, "Discrete wave-number representation of seismic-source wave fields", *Bull Seism Soc Am*, 67, 2 (1977), 259-277
18. Herrera, I, "General variational principles applicable to the hybrid element method", *Proc National Academy of Sciences, USA*, 74 (1977), 2595-2597
19. Herrera, I, "Theory of connectivity for formally symmetric operators", *Proc National Academy of Sciences, USA*, 74 (1977), 4722-4725
20. Herrera, I, and Sabina, F J, "Connectivity as an alternative to boundary integral equations. Construction of bases", *Proc National Academy of Sciences, USA*, 75 (1978), 2059-2063
21. Millar, R F, "The Rayleigh hypothesis and a related least-squares solution of scattering problems for periodic surfaces and other scatterers", *Radio Science*, 8 (1973), 785-796
22. Ewing, W M, Jardetzky, W S, and Press, F, *Elastic waves in layered media*, McGraw-Hill Book Co, New York (1957)
23. Lamb, H, "On the propagation of tremors at the surface of an elastic solid", *Phil Trans Roy Soc London, Ser A* 203 (1904), 1-42
24. Lapwood, E R, "The disturbance due to a line source in a semi-infinite elastic medium", *Phil Trans Roy Soc London, Ser A*, 242 (1949), 63-100

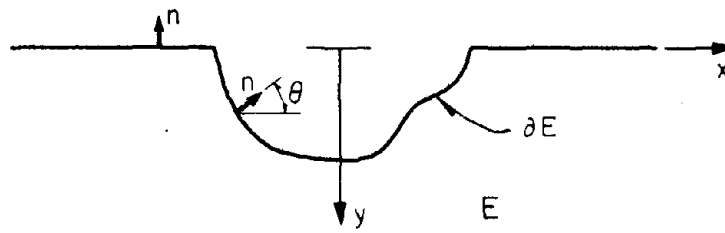


Fig 1. Canyon geometry

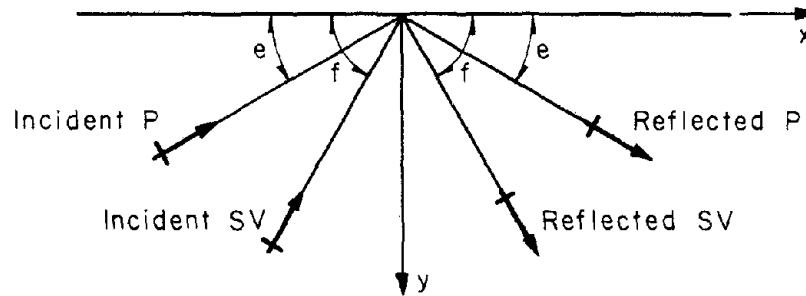
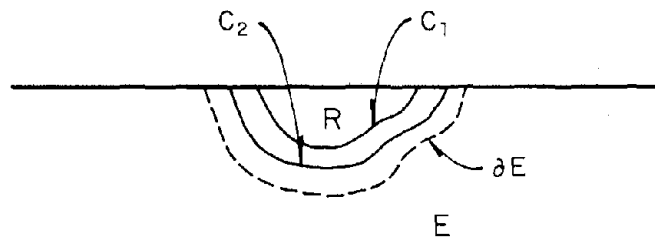


Fig 2. Incident and reflected waves on the free surface

Fig 3. Definition of regions R and E and curves C_1 , C_2 , and ∂E

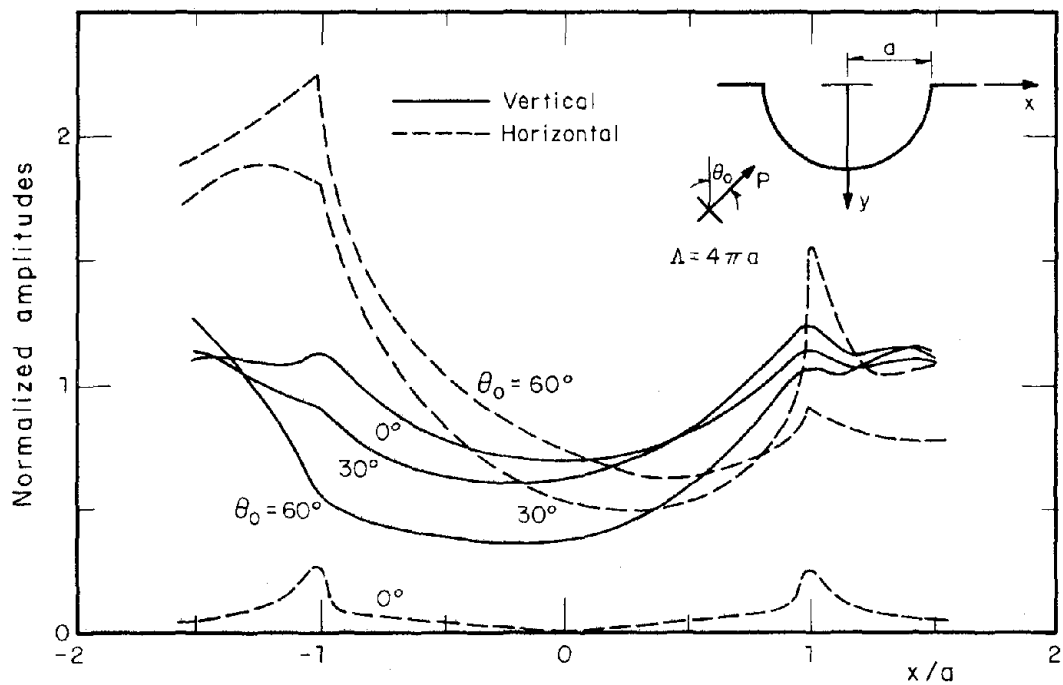


Fig 4. Normalized amplitudes of horizontal and vertical displacements on a semi-cylindrical canyon under incident plane P waves ; wave-length $\Lambda = 4\pi a$

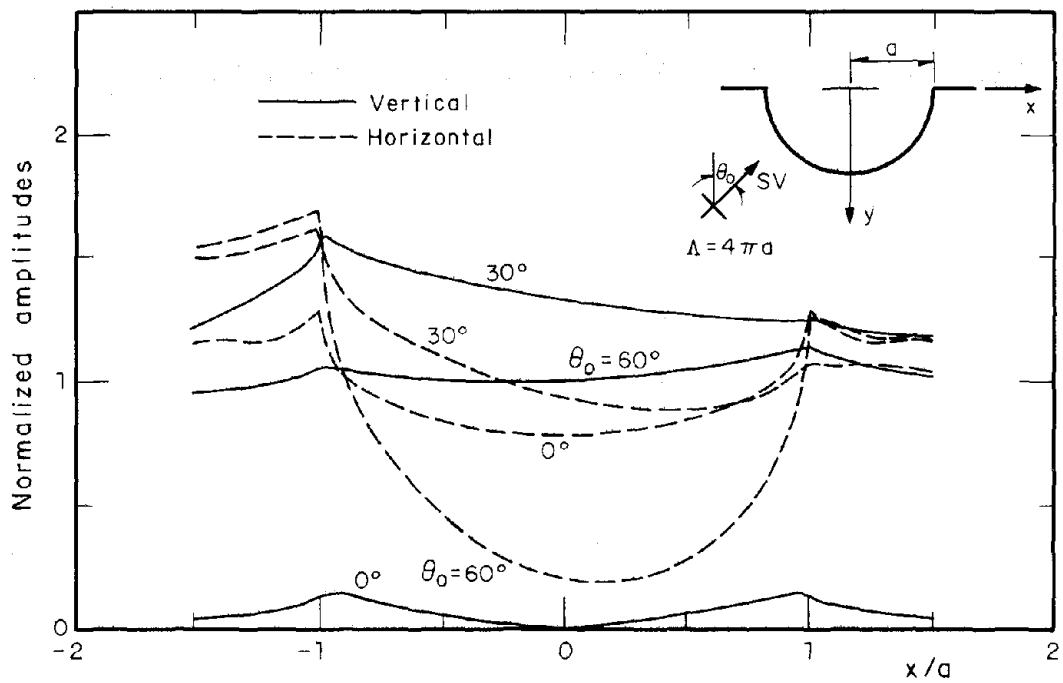


Fig 5. Normalized amplitudes of horizontal and vertical displacements on a semi-cylindrical canyon under incident plane SV waves ; wave-length $\Lambda = 4\pi a$

A METHOD FOR ASSESSMENT OF SEISMIC DESIGN MOTIONS

by

E. Mardiross^I, P HD , D.I.C., A.C.G.I., B.Sc(Eng.)

ABSTRACT

The present paper seeks to highlight an approach to modify recorded accelograms to suit a particular situation: accounting for the local site conditions. Considerable progress has been made in recent years in setting up a number of strong motion instruments in all over the world which could provide useful data, but until enough data becomes available designers will have to follow the following approach in establishing design criteria for structures and for microzoning purposes.

INTRODUCTION

Assessment of ground motion characteristics of the design earthquake for sites threatened by seismic ground motion is a major issue in dynamic analysis of engineering structures. The El Centro 1940 accelogram has been widely used by earthquake engineers as a seismic design motion for earthquake proof design in many countries where strong ground motion data are not available. Comparison of the latest recorded data in many countries with the El Centro record show considerable differences, both in frequency characteristics and amplitudes of the motion.

The new method of analysis which will be presented in this chapter is based on a combination of approaches discussed in (5) in order to arrive at the bedrock motion. The major new features introduced are:

- a) Use of scaling factor to scale the time coordinates of the bedrock motion.
- b) Use of maximum bedrock velocity as a criterion for prediction of bedrock motion.
- c) Computation of surface motion from the estimated bedrock motion, using the theory developed by the author (5).

BASIC INFORMATION

As a first step, the site soil and bedrock conditions must be determined and the potential earthquake magnitude established. Additional information, such as the predominant period of bedrock motion, duration of bedrock shaking and maximum velocity at the bedrock surface, is also necessary.

I Formerly Graduate Research Engineer, University of London, Imperial College, London.

THE POTENTIAL EARTHQUAKE MAGNITUDE

To start with, the design earthquake magnitude can be determined by the following two methods:

- a) Assuming that during the lifetime of the structure there will be a major event (Say $M = 6.5$) in the area.
- b) Use of past experience, i.e. a thorough review of both the seismicity and the geology of the area.

Approach (b) is very important but not enough. Gaps during the observation period are often the reason for such maps to cause seismological surprises. Therefore, potentiality of the future earthquake must be taken into account.

PREDOMINANT PERIOD OF THE BEDROCK MOTION

Predominant periods of the bedrock motions, using data from stations on or near granitic rock, are related to Magnitude by Gutenberg and Richter (2) by the equation:

$$\log T_{pb} = - 1.1. + 0.1M \quad (1)$$

where M is Richter magnitude and T_{pb} is predominant period of the bedrock. (1) is only valid for epicentral distances $\leq \sim 50\text{km}$.

The assessment of the predominant period of the bedrock motion may be carried out with the aid of Gutenberg-Richter formula, supplemented by data from small earthquakes or strong explosions. The results obtained from strong explosions, though not very good, will provide some idea.

PREDICTION OF MAXIMUM BEDROCK VELOCITY

The next stage of the method requires the estimation of maximum bedrock velocity at the bedrock formation of the proposed site. Amplitude of maximum bedrock velocity is chosen because it is less sensitive to effects, such as fracture propagation, as the fault ruptures.

The assessment of maximum bedrock velocity at a given epicentral distance can be done by means of a local attenuation equation. In the absence of one, the following attenuation equation can be used to describe the variation of expected maximum velocity with earthquake magnitude and epicentral distance:

$$v = 32 e^M / (R + 25)^{1.7} \quad (2)$$

where v is the maximum velocity in cm/sec. on hard ground or weathered rock, M is the Richter magnitude of the earthquake and R is the epicentral distance in kilometres (on the basis of the American events) (4). The values obtained for v for a given M and R should be checked against other similar formulae; attenuation of peak velocity

is not only highly dependent on the area, but also on the location of the proposed site w.r.t. the epicentre of potential earthquake. The two points A and B shown in fig. 1, although possessing the same epicentral distance, will have different arrival patterns, therefore - different motions.

ASSESSMENT OF DURATION OF BEDROCK MOTION.

Finally, calculate the duration of bedrock motion for the design earthquake using the equation given by (1).

METHOD OF ANALYSIS

The general method of analysis for assessment of the surface motion characteristics involves the following four steps:

- (a) Choose a number of existing strong motion records with different frequency characteristics. Try to include records made under similar conditions to yours, if possible.
- (b) Multiply the time and acceleration coordinates of the chosen records by the following factors, respectively:

$$t_f \quad (3)$$

$$A_f \quad (4)$$

where t_f is the time factor by which the time coordinate of the chosen accelogram should be multiplied to give the new required predominant period. t_f is obtained by computer runs using "SPECTRA"⁺. Figs. 2 and 3 present the results of the analysis for Golden Gate S80E adjusted by t_f values of 2 and 3 to give new predominant periods of 0.25 and 0.4 seconds, respectively. The value of A_f is determined from the relation:

$$A_f^* = \frac{2\pi}{T_{pb}} \cdot \frac{V_b}{A_s} \quad (5)$$

where V_b is the maximum estimated bedrock velocity, A_s is the peak acceleration of the chosen accelogram, T_{pb} is the predominant period of the adjusted accelogram.

- (c) Adjust the duration of shaking of the strong portion of the records to the value calculated for the design earthquake.

* This is a first approximation to A_f . Its true value is obtained by trial and error.

+ A computer program for computation of response spectra (5).

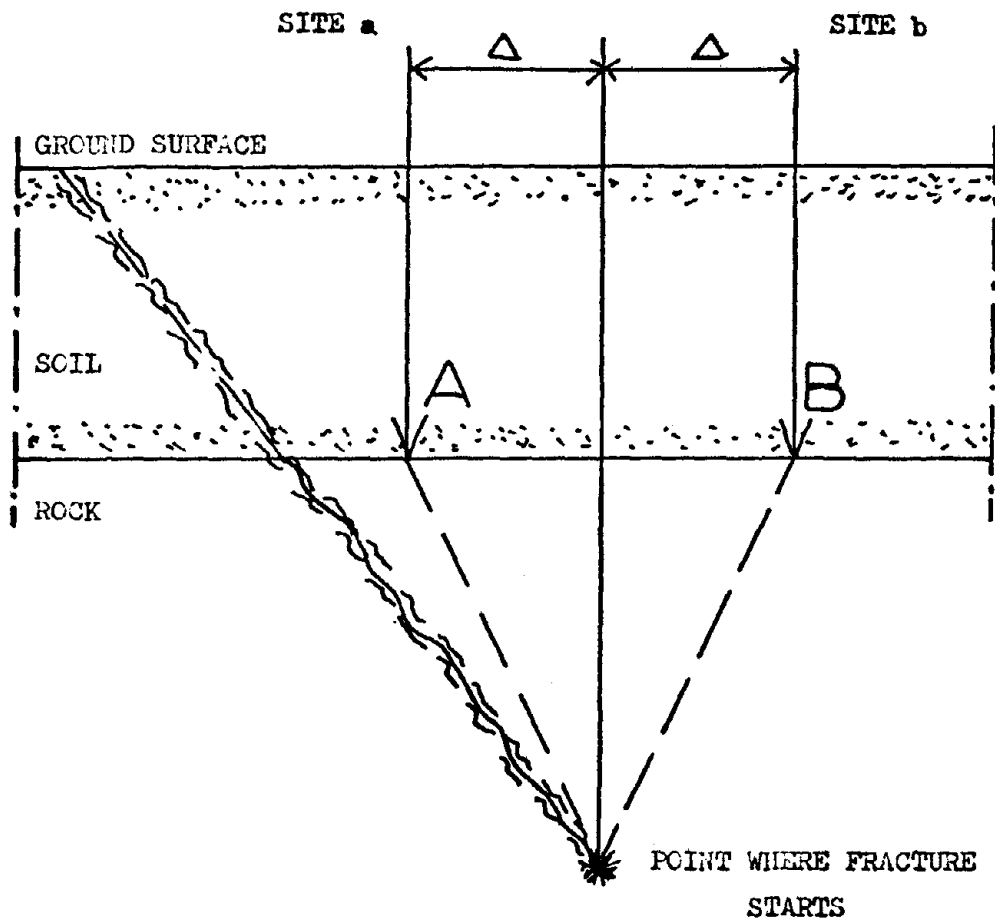


FIG. 1 LOCATION OF PROPOSED SITE W.R.T. THE EPICENTRE OF POTENTIAL EARTHQUAKE.

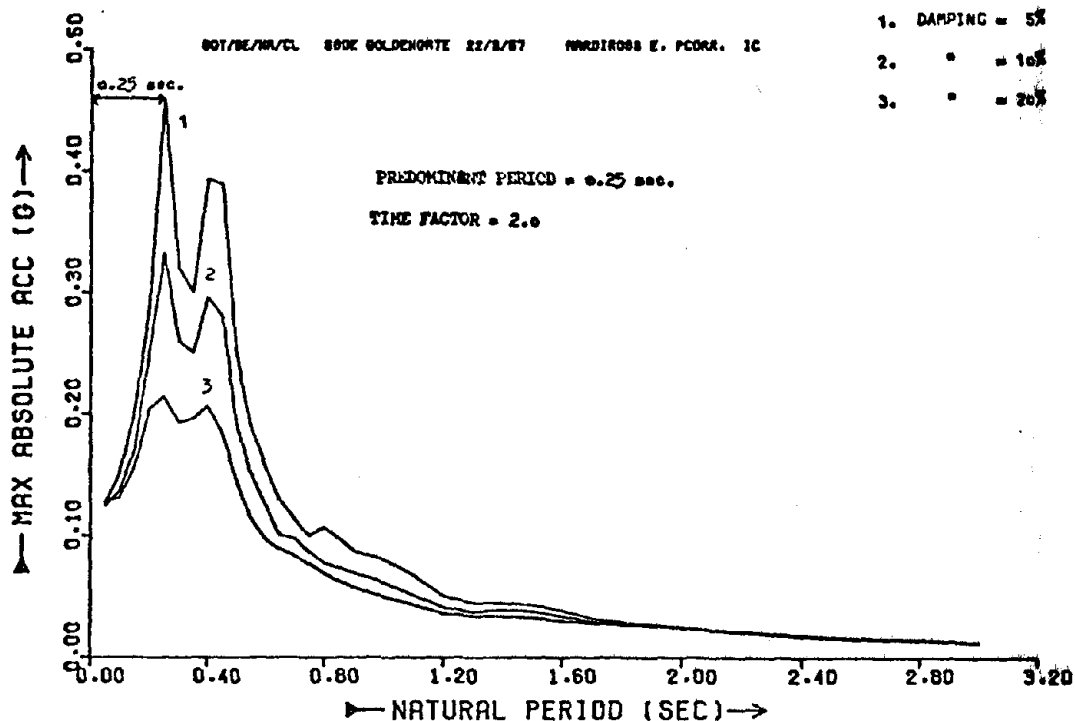


FIG. 2 COMPUTED ACCELERATION RESPONSE SPECTRA FOR TIME FACTOR = 2.0

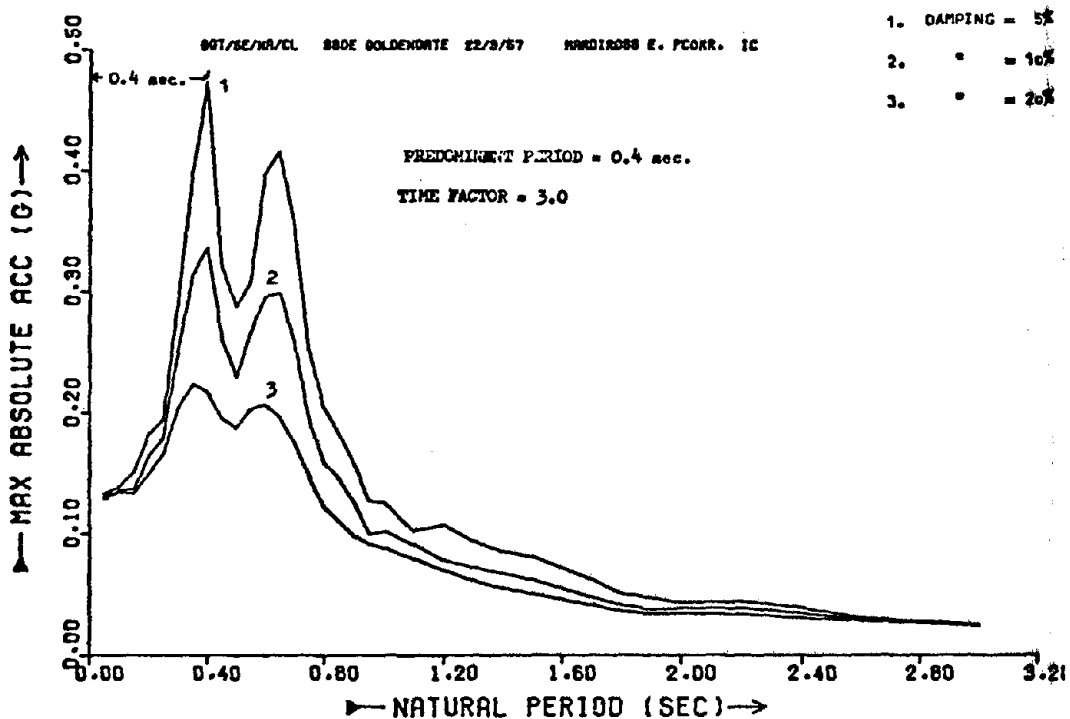


FIG. 3 COMPUTED ACCELERATION RESPONSE SPECTRA FOR TIME FACTOR = 3.0

- (d) Use the computer program "EARTHQUAKE" (5) to evaluate the effect of local soil conditions upon the bedrock motion, employing the dynamic properties of soil and bedrock.

DESIGN SPECTRUM OR TIME HISTORIES AND SEISMIC MICROZONING

With the four steps discussed in the above section one can calculate design spectrum. It is important to examine the validity of the proposed method of analysis for a building site in a highly seismic region. It is assumed that an earthquake of magnitude 6.9 is likely to occur at an epicentral distance of 40km. (with a focal depth ≤ 20 km) from a proposed building site, marked "A" shown in fig. 4, underlain by 40m of medium sand with shear wave velocity of 300 m/sec. followed by a very deep formation of shale with shear wave velocity of 3800 m/sec. Densities of the medium sand and the shale are 2000 kg/m³ and 2100 kg/m³, respectively. Hysteretic damping ratios of the sand was assumed to be 0.02. Calculate the following:

- a) Design velocity and acceleration response spectrum or Design time histories.
- b) Strength of the potential earthquake motion "S" at the proposed site.
- c) Suggest procedures for seismic microzoning of the region.

In the light of the previous discussion regarding the method of analysis, there are three parameters to be computed. Computed values of these parameters for $M = 6.9$ and epicentral distance $R = 40$ km. are the design values of maximum bedrock velocity equal to 30 cm/sec., predominant period of bedrock motion equal to 0.4 sec. and duration of bedrock shaking equal to 14.0 sec. The next step in arriving at response spectrum or time histories is to select a number of accelograms from "rock sample" or "hard ground" and adjust these motions by appropriate values calculated from 3 and 4.

The velocity and acceleration design spectrum and the design time histories for site A, based on two bedrock motions, i.e. Golden Gate S80E and San Fernando S16E* adjusted by $t_f = 3.0$, $A_f = 2.050$ and $t_f = 1.0$, $A_f = 0.280$ having accounted for the potential changes, which may result from variations in local soil conditions using "EARTHQUAKE", are presented in figs. 5 - 6 a,b,c,d. Obviously, the more bedrock motions are included the more ground surface spectrum and time histories will be obtained. Therefore, one should design for all the calculated spectrum, in this case two. It is much more meaningful to base the design on the characteristics of the individual spectrum rather than on the characteristics of an overall average.

* This accelogram as available in the Dept. of Civil Eng. of Imperial College possess duration of shaking slightly below 14.0 sec.

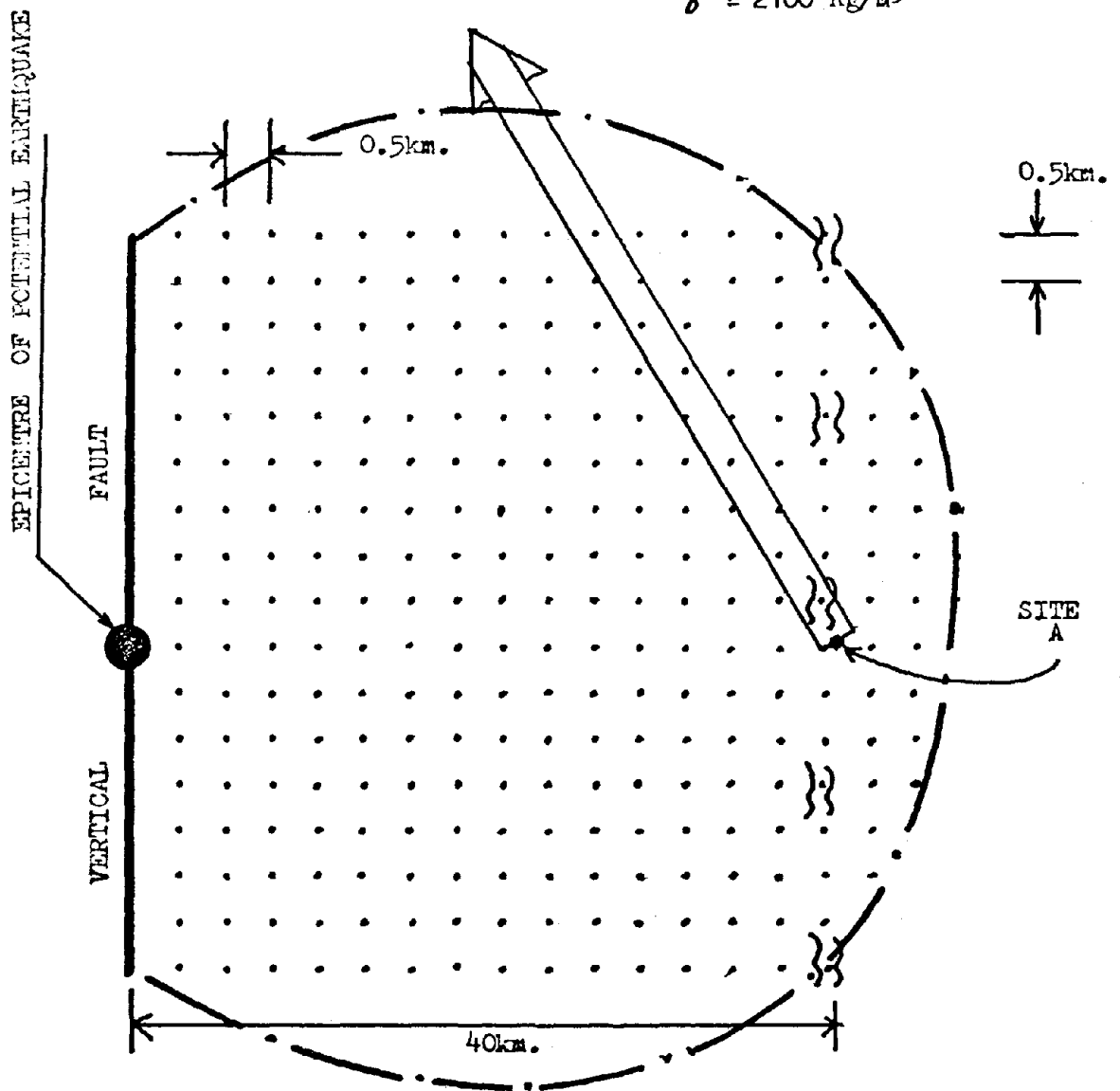
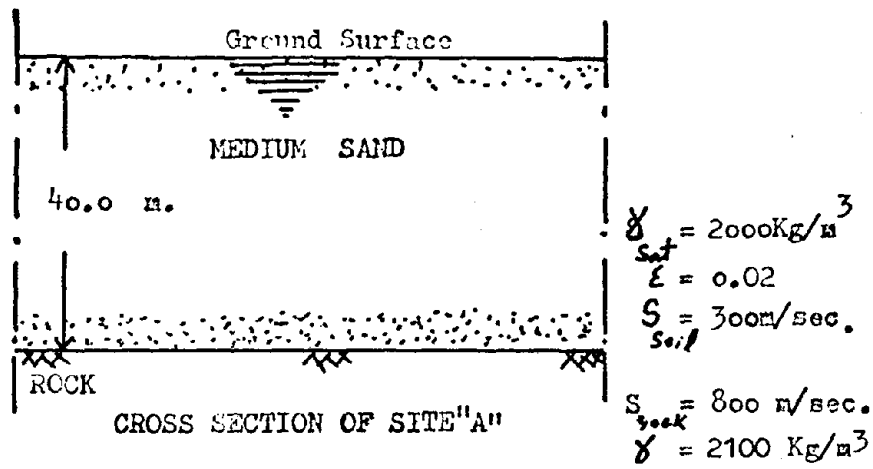


FIG. 4 SELECTED AREA FOR SEISMIC MICROZONING

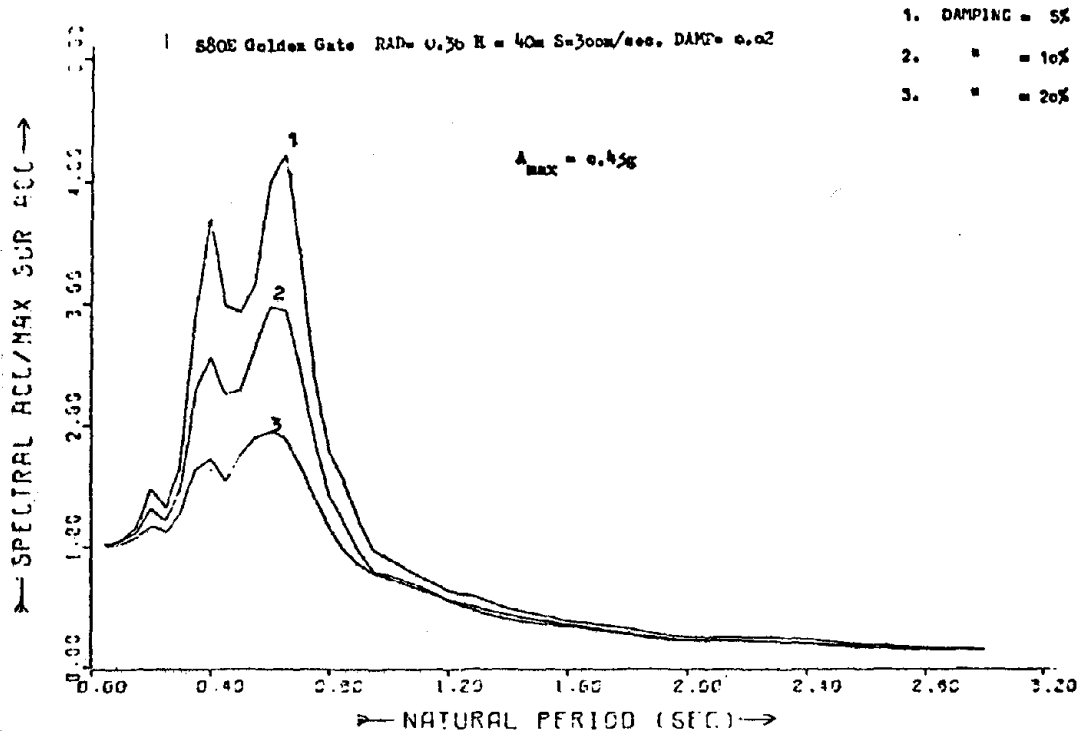


FIG. 5. COMPUTED GROUND SURFACE ACCELERATION RESPONSE SPECTRA AT SITE A.

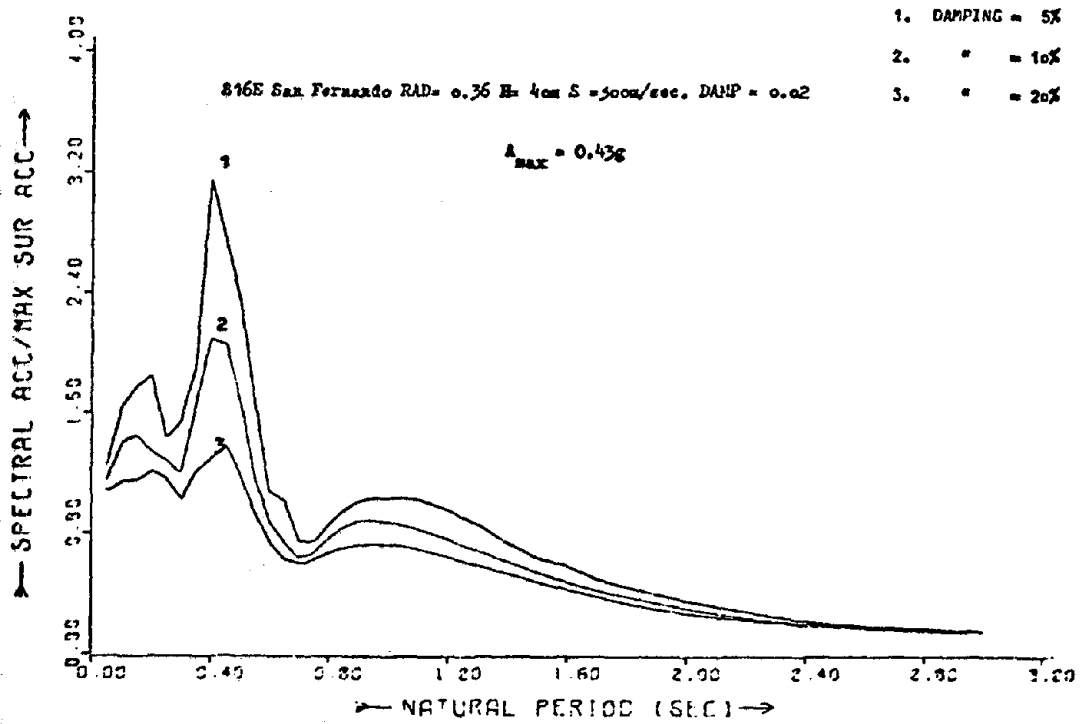


FIG. 6. COMPUTED GROUND SURFACE ACCELERATION RESPONSE SPECTRA AT SITE A.

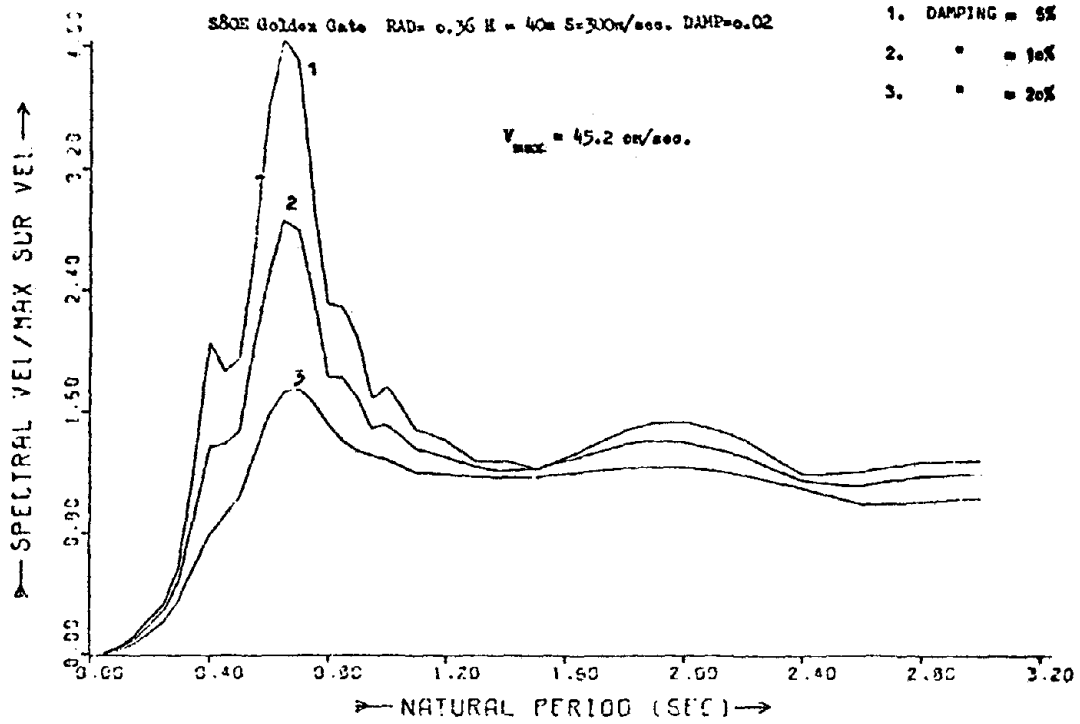


FIG. 5b COMPUTED GROUND SURFACE VELOCITY RESPONSE SPECTRA AT SITE A.

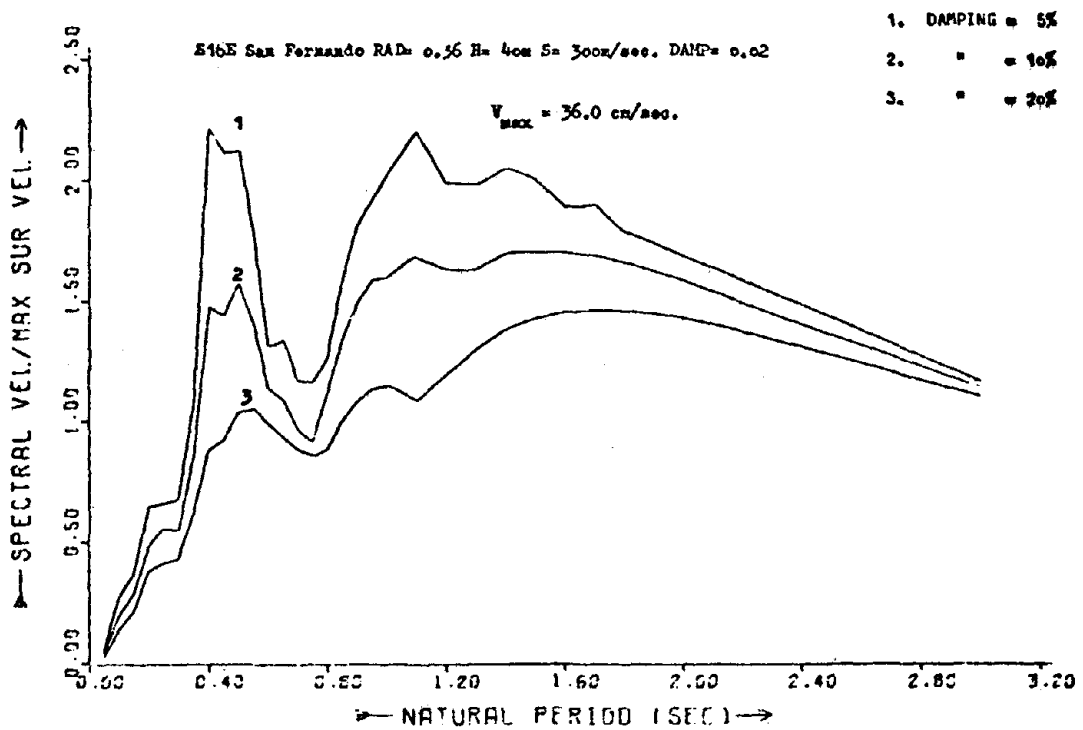


FIG. 6a COMPUTED GROUND SURFACE VELOCITY RESPONSE SPECTRA AT SITE A.

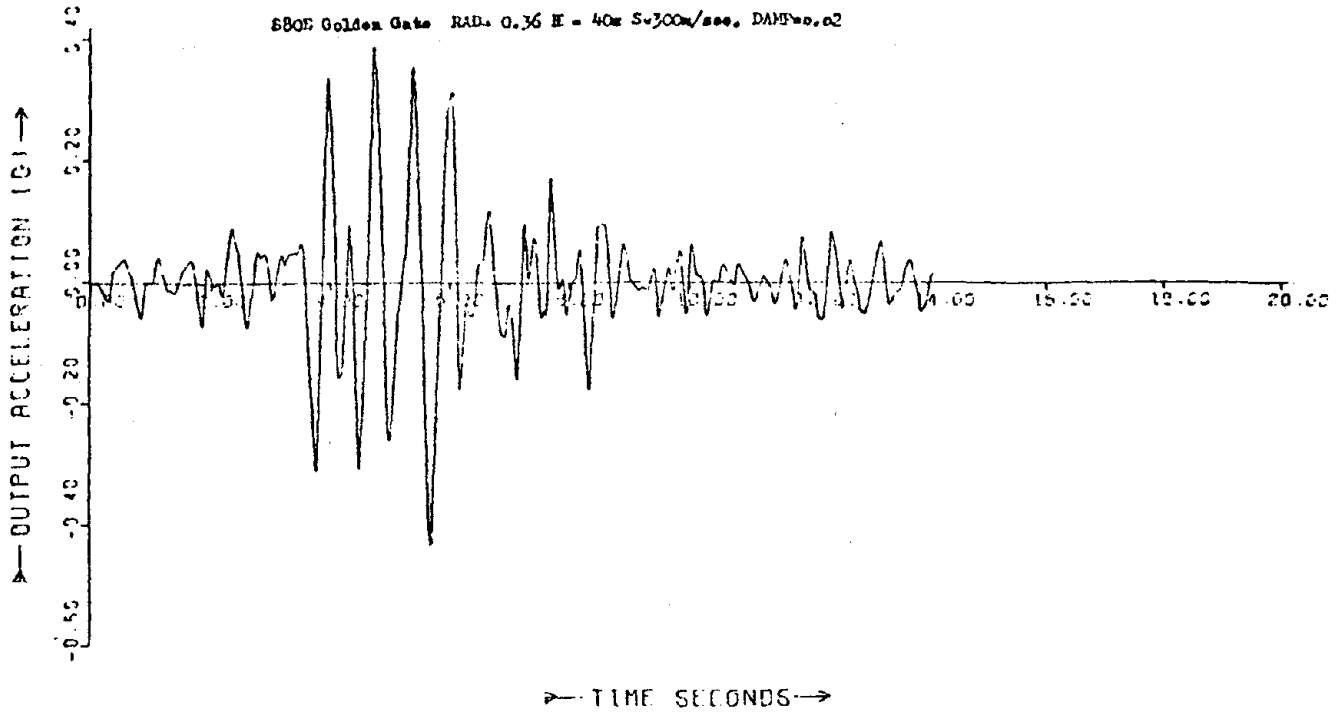


FIG. 5a COMPUTED GROUND SURFACE ACCELERATION TIME HISTORY AT SITE A.

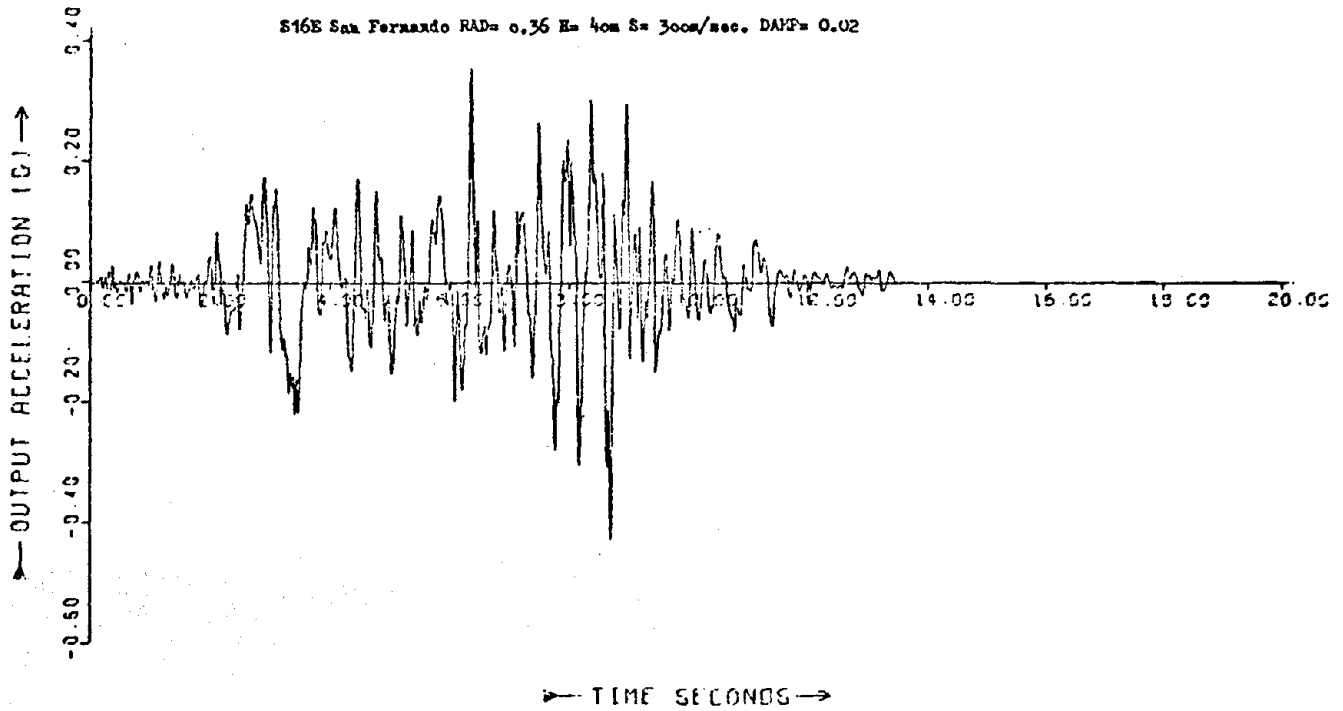


FIG. 6a COMPUTED GROUND SURFACE ACCELERATION TIME HISTORY AT SITE A.

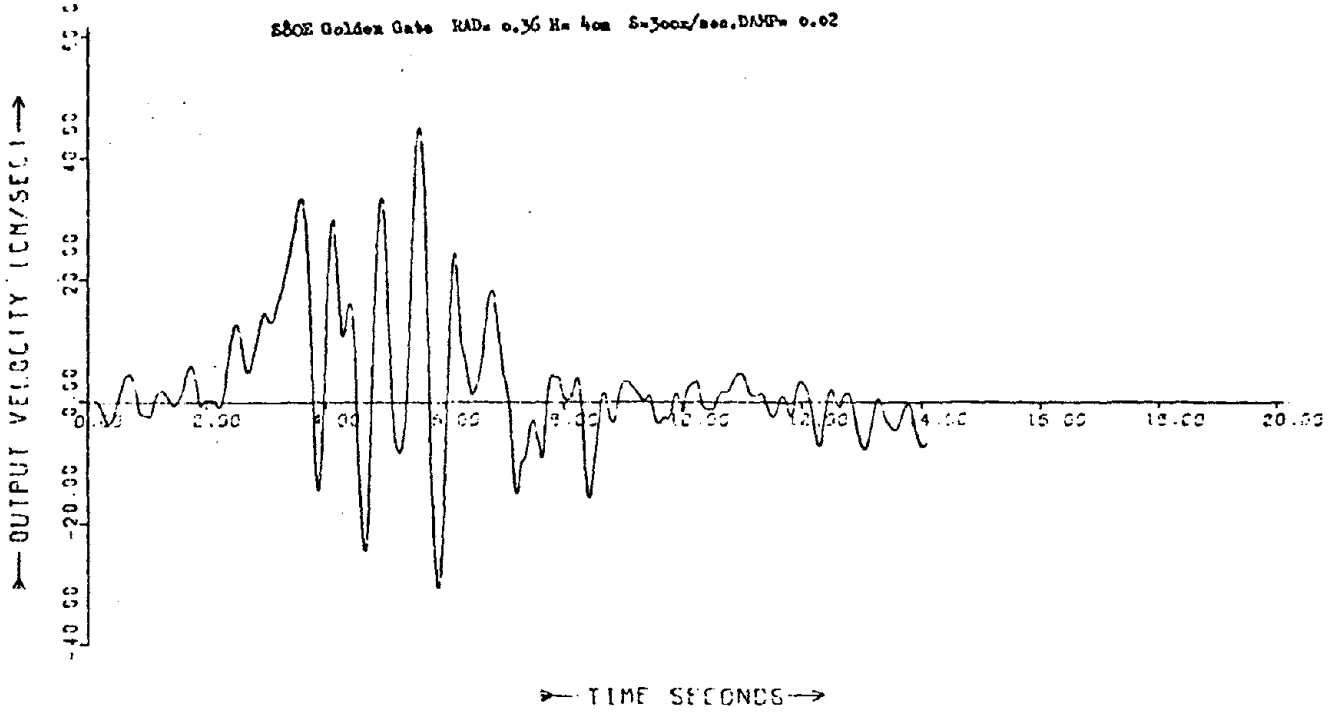


FIG. 54 COMPUTED GROUND SURFACE VELOCITY TIME HISTORY AT SITE A.

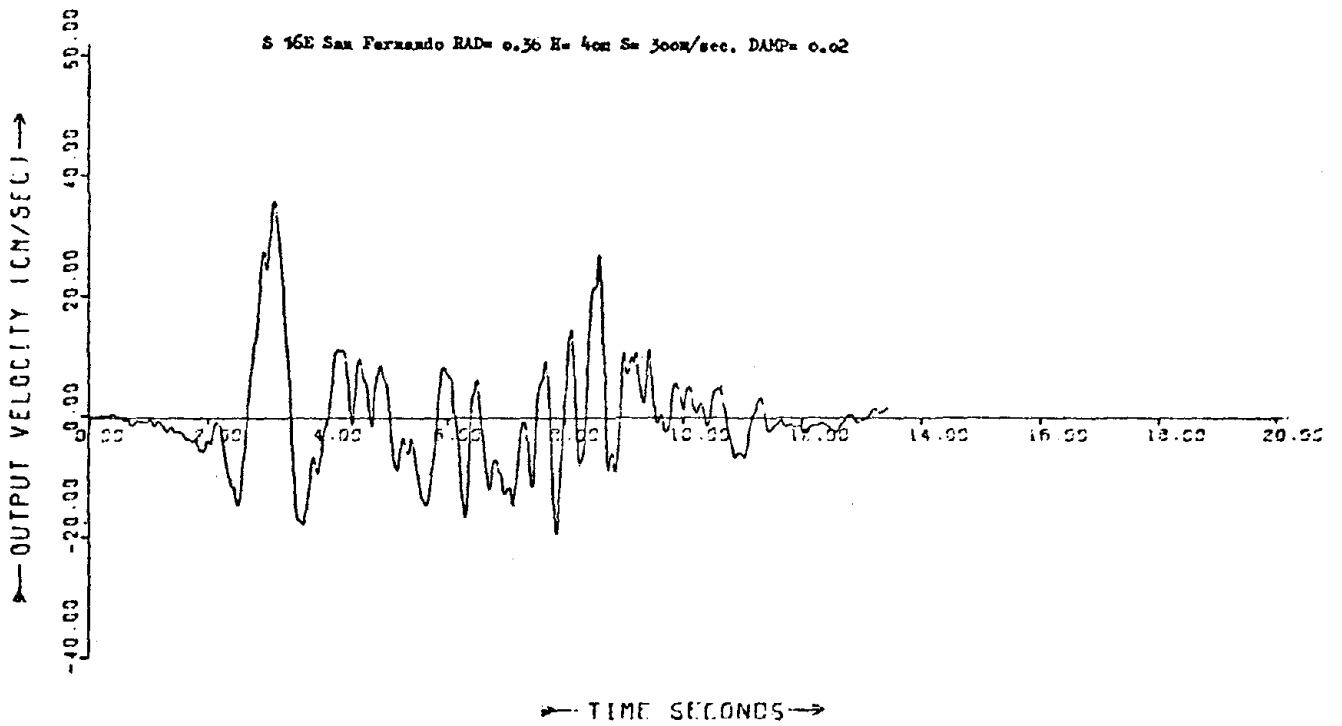


FIG. 55 COMPUTED GROUND SURFACE VELOCITY TIME HISTORY AT SITE A.

A PARAMETER AS A MEASURE OF SEVERITY OF GROUND SHAKING

Consider an element of soil, mass "m" at the surface of an overburden. The kinetic energy which will be available for damage at time "t" while the velocity is $v(t)$ is:

$$E_{\text{Kinetic}} = \frac{1}{2}mv^2(t) \quad (6)$$

or the total kinetic energy available to be fed into structures located on the deposit over a time interval " T_{dur} " where T_{dur} is the length of shaking is:

$$E_{\text{kinetic}} = 0.5.m. \sum_{t=0}^{T_{\text{dur}}} v^2(t) \delta t \quad (7.3)$$

Equation (7.3) is written as:

$$S = \frac{E_{\text{kinetic}}}{m} = 0.5 \sum_{t=0}^{T_{\text{dur}}} v^2(t) \delta t \quad (7.4)$$

where "S" is the total energy available for damage per unit mass of soil. The quantity "S" is called strength of earthquake motion and is a measure of total energy which would be supplied to structures located on the site, i.e. a measure of intensity of ground shaking. The advantage of this new parameter to describe the severity of ground shaking to the "old" ones, such as Spectrum intensity defined by Housner, is this: this new parameter includes duration of shaking, whereas that of Housner does not. The role played by the duration of ground shaking on structural damage is explained in (5).

The computed values of the more useful parameter "S", are 890 and 510 (cm/sec.)².

It is important to note that the predicted design parameters given in this section, as well as the computed acceleration and velocity time histories, could be used for seismic microzonation of the region for several design magnitudes and epicentral or source distances. The capability of the method used for seismic microzonation purposes permits the expected values of the design parameters to be calculated exactly on each grid point shown in fig. 4. Variations in design earthquake magnitude and epicentral or source distance on calculated design parameters could easily be assessed and the errors associated with such variations computed.

CONCLUSIONS

Based on the study reported in this paper it may be concluded that:

- (a) The new method of analysis presented in this chapter provides a useful means of calculating the design spectrum, the design motion time histories and the strength of the design earthquake at a particular site in many seismic parts of the world where no strong-motion data is available.

- (b) The main features of the bedrock motion should not be estimated from Modified Mercalli (MMI), defined in 1931 or Medvedev Sponheuer and Karnik (MSK) defined in 1964, intensity scales. These scales are not only objective scales but are designed for non-specialist designed buildings. Do not consider tall structures, prefabricated structures and long distance effect, etc. Approximate correlations of maximum bedrock velocity, duration of bedrock shaking and predominant period of bedrock motion with MMI or MSK would, therefore, only provide very rough estimates under certain conditions and be completely misleading under others. Instead the approach (a) is proposed.
- (c) The recommendations made and the new method of analysis presented would result in a considerable amount of savings in the total cost of the proposed projects. In particular, the new method allows a clear demonstration of the importance of taking into account the influence of local soil conditions on potential seismic motions.

REFERENCES

1. Dobry, R., Idriss, I.M., Chang, C.Y. and Ng, E., "Influence of Magnitude, Site Conditions and Distance on Significant Duration of Earthquakes", preprints of the Sixth World Conf. on Earthquake Eng., New Delhi, Theme 2, paper No. 23, (1976).
2. Gulenkerg, B. and Richter, C., "Earthquake Magnitude, Intensity, Energy and Acceleration", Bull. Seism. Soc. Am., 46, PP.105 - 146, (1956).
3. Housner, G.W., "Intensity of Ground Motion During Strong Earthquakes", Calif. Inst. of Technology, Earthquake Research Lab., Aug., (1952).
4. Lominity, C. and Rosengluetts, E., "Seismic Risk and Engineering Decisions", Elsevier, (1976).
5. Mardiross, E., "Response of Soil Deposits on the Deformable Bedrock During Earthquakes and the consequent Pore-Water Pressure Dissipation", PhD Thesis, University of London, (1978).

752

INTENTIONALLY BLANK

PRELIMINARY EVALUATION OF SITE TRANSFER FUNCTIONS
DEVELOPED FROM EARTHQUAKES AND NUCLEAR EXPLOSIONS

by

A. M. Rogers^I and W. W. Hays^I

ABSTRACT

Ground motion produced by the 1971 San Fernando earthquake was compared to that accompanying Nevada Test Site nuclear explosions, using recordings of both events at several common stations in the San Fernando Valley-Pasadena area of California. Similar trends in ground response were observed for both sources. Those differences in the nuclear and earthquake ratios that were observed are tentatively explained by changes in wave propagation at the rock sites due to the proximity of the earthquake source relative to the nuclear source. The known dispersion in such observations, however, would also account for significant portions of the observed variations.

INTRODUCTION

Sites in the San Fernando Valley-Pasadena area of California were occupied with three-component, broadband, L-7 seismographs to record Nevada Test Site nuclear explosions. These sites together with other station locations in the Los Angeles region will ultimately be used to establish the geographic variation in the ground shaking hazard and the relationship between the hazard and the geologic characteristics of the site. If it can be demonstrated that site response induced by nuclear events is nearly equal to that produced by earthquakes, the task of determining and mapping site response in Los Angeles will be greatly facilitated. Such maps could ultimately be of great value in city planning, in preparation for future earthquake disasters, and to building engineers. The primary analysis requirements for the overall study are (1) to determine how accurately the ground shaking hazard inferred from low-strain ground motions reflects the principal characteristics of ground response under high-strain ground motion conditions and (2) to determine if wave propagation effects at sites near the source cause significant ground response characteristics that are absent in the ground motion records recorded hundreds of kilometers from the source. The purpose of this paper is to present a preliminary assessment of ground motion data recorded at common sites in the San Fernando Valley-Pasadena area from nuclear explosions and from the 1971 San Fernando earthquake.

ANALYSIS TECHNIQUES

A broadband magnetic-tape-recording seismograph (1) was used to record velocity seismograms of Nevada Test Site explosions. The analog tapes were digitized and processed (2) to obtain pseudo-relative velocity

I Geophysicist, U.S. Geological Survey, P.O. Box 25046, Denver Federal Center, Denver, Colorado 80225

(PSRV) spectra, Fourier spectra, and acceleration, velocity, and displacement time histories. In this paper, the results are presented in terms of the ratios of PSRV spectra of the whole time history, a representation that can be related to the response of buildings. By taking ratios of spectra for sites underlain by alluvium to sites underlain by rock (when the distance between the two sites is small relative to the distance to the source), the approximate sedimentary transfer function is obtained. Although all three components of the ground motion data have been analyzed in this manner, only the arithmetic mean of the two horizontal components at each period are presented in this paper. Portions of the spectra contaminated by noise were not used. For the nuclear explosions the noise level was determined by computing spectra from a time segment prior to the arrival of the seismic signal. The criterion used in the analysis was that the spectral value at each period was used only if the signal-to-noise ratio was at least two. The San Francisco earthquake data were examined for contamination by comparing spectral values at periods of interest to the mean spectral level in the period range 0.06–0.09 seconds. Spectral values at periods of interest were rejected if they were not at least twice this mean level.

COMPARISON OF RATIOS RELATIVE TO THE GRIFFITH PARK ROCK SITE

Figure 1 shows the location of the recording stations used in this

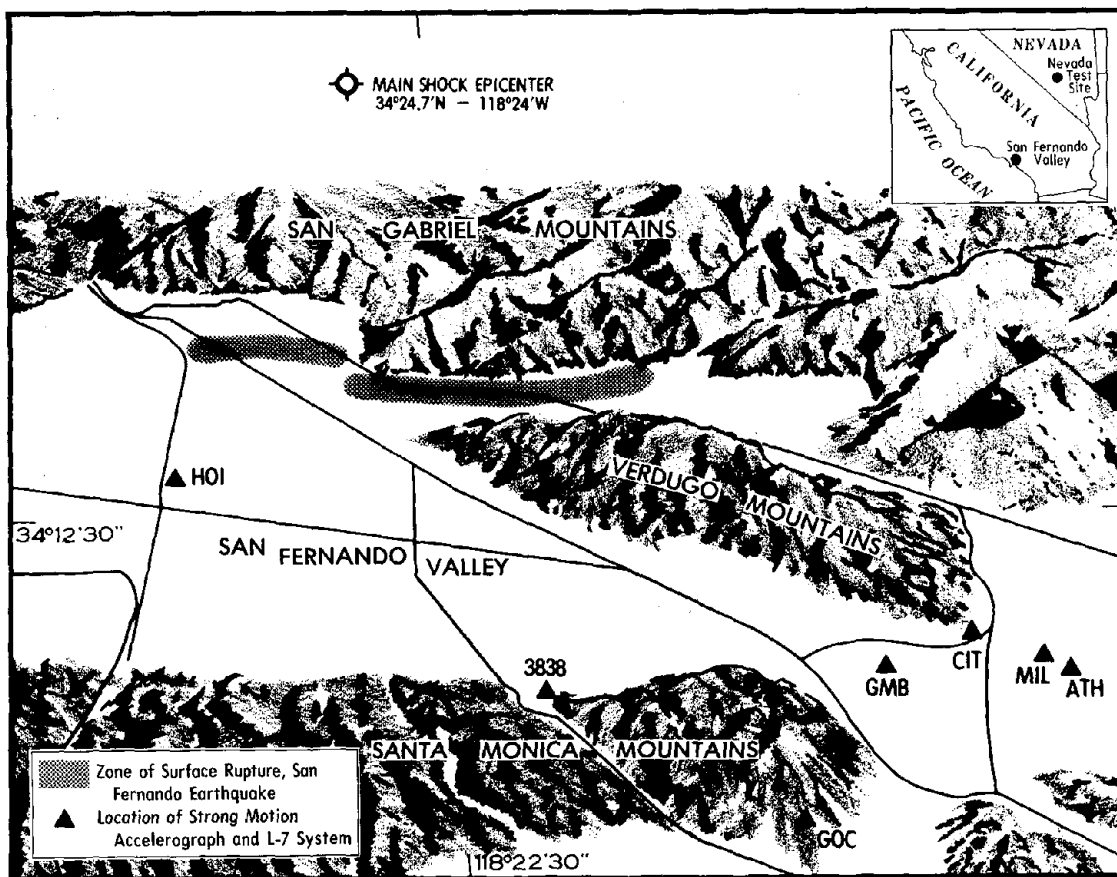


Figure 1.--Map showing 1971 earthquake epicenter, surface ruptures, and station locations.

study, the epicenter of the San Fernando earthquake, and the zone of surface faulting. Values of the peak ground acceleration and velocity recorded at each station, distance to the epicenter, and the azimuth from the epicenter to each station are given in table 1.

STATION NAME	ABBREV.	DISTANCE (KM.)	AZIMUTH FROM EPICENTER TO STATION	PEAK ACCEL. (g)	PEAK VEL. (cm/s)
HOLIDAY INN	HOI	20	197	0.27	30
GLENDAL MUNI. BLDG.	GMB	32	154	0.28	28
3838 LANKERSHIME	3838	30	172	0.18	15
ATHENAEUM	ATH	37	140	0.11	14
MILLIKAN LIB.	MIL	37	140	0.22	16
CALIF. INST. TECH.	CIT	34	144	0.19	12
GRIFFITH PARK	GOC	33	164	0.18	20

Table 1.--Station data giving azimuth and distance from the earthquake epicenter to the station and the peak acceleration and velocity on the strong motion records.

The spectral ratios (nuclear and earthquake) for three sedimentary sites are shown in figure 2, relative to the reference crystalline rock

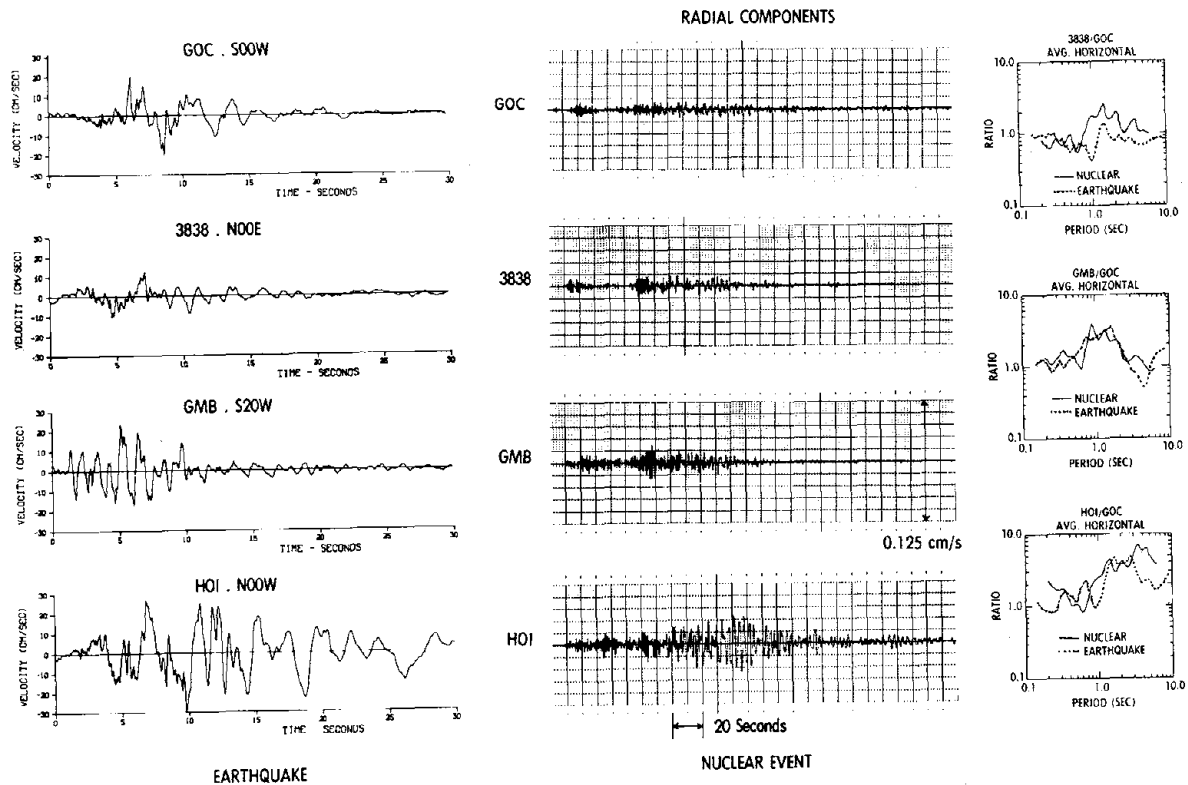


Figure 2.--Graphs showing earthquake time histories, nuclear event time histories, and nuclear and earthquake spectral ratios at common sites. Ratios are relative to rock site GOC.

site, Griffith Park (GOC). One time-history component is also shown for each station for both nuclear event and earthquake. Station Holiday Inn (HOI) is underlain by intermediate-depth alluvium (270 m) and deep sedimentary rock (4.2 km); station Glendale Municipal Building (GMB) is underlain by shallow alluvium (91 m) and shallow sedimentary rock (1.5 km); and station 3838 Lankershime (3838) is underlain by shallow sedimentary rock (<0.6 km?). All of these sites, including the reference rock site, are located at approximately the same azimuth and distance from the source region of the San Fernando earthquake; therefore, differences in spectral ratios due to source and path effects are minimal. The data show that average spectral amplitudes at sites underlain by alluvium in the thin (<100 m) to intermediate (100-500 m) thickness range are larger on alluvium than on rock and that the nuclear data broadly duplicate the earthquake data. However, some deviation does occur at the long periods for the HOI and 3838 sites. Discussion of the possible causes of these deviations follows.

Examination of the strong motion displacement time histories computed by Hanks (3) for the San Fernando earthquake indicates that surface waves developed locally, principally at sites underlain by a thick sedimentary section. The earthquake velocity records (fig. 2) for stations GOC, GMB, and 3838 show very little surface wave development, and most of the energy arrived at these sites within the first 10-15 seconds. As a consequence, the long-period earthquake spectral ratios approached 1 for periods greater than 1-2 seconds at stations GMB and 3838. In contrast, greater surface wave development occurred at station HOI, and the long-period earthquake spectral ratio (HOI/GOC) was consequently high relative to the other two sites.

On the other hand, the Nevada Test Site explosions produced ground motions in the San Fernando Valley-Pasadena region that were well dispersed. Significant surface waves were recorded at sites underlain both by basement rock and sedimentary rock. These surface waves were also modified by the local geologic structure, but because the waves were not primarily generated locally by incident body waves, they were present to some degree at all sites. The nuclear long-period ratios are relatively high owing to the persistence of surface wave energy propagating over several hundred kilometers that is modified locally at sites underlain by sediments. On the other hand, energy produced by nearby earthquakes that is incident at sedimentary sites may not have developed significant surface waves (from locally incident body waves) because the sedimentary travel path is too short or too heterogeneous. While this mechanism could produce differences in long-period earthquake and nuclear data at sites underlain by rock or sediments, in this case the most significant differences occur at a site underlain by rock. Although these results indicate that some discrepancies may be encountered when using ground motion data from distant nuclear explosions to predict strong motion site response for nearby earthquakes, these data show that the spectral ratios agree at most periods within a factor of 2.

In assessing the validity of the spectral ratio method for nuclear explosions and earthquakes, one must maintain some perspective on the goals. The expectation is that the method will produce mean amplification

values across several period bands that will closely approximate the values derived from the other data set. These mean values will be derived from several events recorded at a group of sites underlain by similar geologic conditions. However, because of the inherent variability in ground motion data (11), one cannot expect that a single ground motion recording, at a pair of sites, from either a nuclear explosion or an earthquake, will produce a precise transfer function. In estimating site-specific transfer functions, the most important requirement is to obtain an ensemble of ground motion data for pairs of stations that demonstrates the repeatability of the mean transfer function and establishes the approximate standard error of estimate. From the regression of nuclear PSRV data with yield for a single period and a single station, it is known (12) that the standard deviation of PSRV data at each period is about a factor of 1.6. Ratios of PSRV data will, therefore, exhibit even higher dispersion. Of course, differences in spectral ratios that occur across broad-period bands can be considered to be more significant statistically than differences that occur at a single period. Thus, for the case of the spectral ratios depicted in figure 2, some of the observed variability can be attributed to the inherent dispersion that is observed in earthquake and nuclear-explosion ground motion data.

COMPARISON OF RATIOS RELATIVE TO THE CALIFORNIA INSTITUTE OF TECHNOLOGY ROCK SITE

The time histories recorded at stations Athenaeum (ATH), Millikan Library (MIL), and the Seismological Laboratory (CIT), all at the California Institute of Technology, are shown in figure 3. The spectral ratios

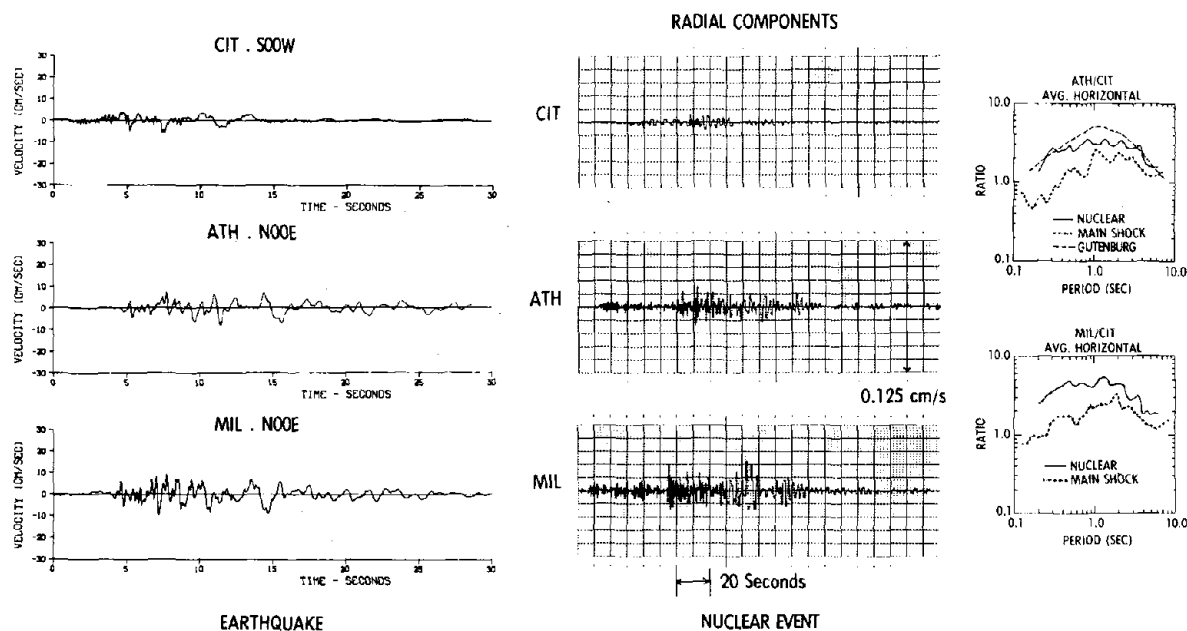


Figure 3.--Graphs showing earthquake time histories, nuclear event time histories, and nuclear and earthquake spectral ratios at common sites. Ratios are relative to rock site CIT.

relative to CIT are also shown and indicate a striking difference, at the short periods, between the ratios based on nuclear explosions and those derived from the San Fernando earthquake. The ratios based on nuclear explosion data are consistently higher than the ratios based on earthquake data. It should also be noted that the earthquake ratios are greater than 1 for periods greater than 0.3-0.4 second, indicating that in this case ground response on soils will be greater than on rock for periods longer than 0.4 second, and lower for periods shorter than 0.4 second. Hudson (4) first noted that ground motions for these two soil sites might be lower than on rock. On the other hand, the nuclear ground response data imply that ground motions will be larger on soil than on rock for periods greater than at least 0.2 seconds.

The ATH and MIL sites, which are about 500 m apart, are both underlain by 270 m of alluvium over crystalline rock, the same rock that underlies CIT. One would expect both MIL and ATH to exhibit a similar ground response relative to CIT because they are nearby and are underlain by the same geology. Thus, the similarity of the earthquake spectral ratios at MIL and ATH and the corresponding similarity of the nuclear spectral ratios verifies that the ground response is reproducible. There is also good agreement between the transfer function derived by Gutenberg (5) for the ATH site using earthquake data and the transfer function based on nuclear explosion data. Two sites have been occupied that indicate good agreement between Gutenberg's method (5) and the methods of this study (6). This agreement also supports the premise that the relative ground response derived from the nuclear data is reproducible and that the site transfer function is closely related to low-strain earthquake ground response.

Given that the ground motion data are accurate, an explanation is required for the striking difference, especially at the short periods, between the spectral ratios based on nuclear explosion and earthquake data. The nuclear explosion-based ratios imply consistently higher ground motion levels than the earthquake-based ratios. One possible explanation is that nonlinear effects are present in the strong motion data and absent in the nuclear explosion data. The nonlinear effects (7) would act to reduce the observed ground motion levels for periods less than 1-2 seconds at the alluvium (ATH, MIL) sites, but not at the rock site (CIT). Several facts, however, indicate that this mechanism is not a likely possibility. First, the strain levels from the San Fernando earthquake are not high at these sites, the peak strain being estimated as

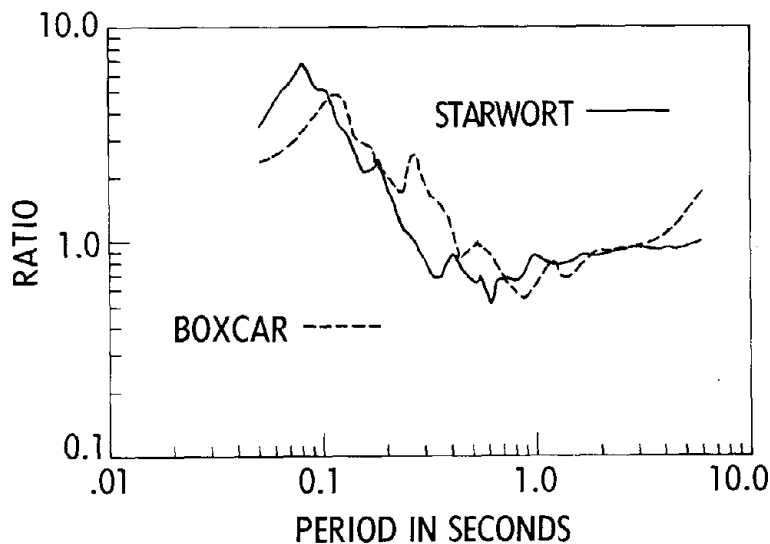
$$\frac{\partial u}{\partial x} = \frac{1}{v} \frac{\partial u}{\partial t} \cong 7 \times 10^{-4}$$

Where v (wave velocity) \cong 270 m/sec (8),

$$\frac{\partial u}{\partial t} = \text{ground velocity} \cong 0.2 \text{ m/sec}$$

Strains of this magnitude would be expected to produce at most, a change in relative ground response less than 20-30 percent (9), whereas the observed differences in ground response are several hundred percent. Second, no

strain-dependent effects are apparent in the ground response data for the GMB and HOI sites, which are closer to the epicenter than CIT and experienced particle velocities about twice the level observed in Pasadena. Third, spectral ratios of ground motion recorded at locations on the Nevada Test Site provide data to evaluate strain effects. Figure 4 compares ground motion ratios (alluvium/welded tuff) for two nearby nuclear explosions recorded at common sites on the Nevada Test Site. The peak ground motion parameters and strains produced at the sites are also shown in the figure. A velocity of 180 m/s (13) was used to estimate the strains at the site underlain by 6 m of alluvium. Thus, although the ground motion levels and strains are greater than an order of magnitude apart and are comparable to those recorded in Pasadena, the ratios shown are similar. This result, although limited, is evidence that ground response observed at low strain levels can be extrapolated to higher strain levels. The data also indicate that peak acceleration on alluvium are greater than on consolidated sediments for this level of ground shaking and these sediment thicknesses.



EVENT	STATION	PEAK VELOCITY (cm/s)	PEAK ACCELERATION (g)	ESTIMATED STRAIN
BOXCAR	ALLUVIUM	24.3	0.54	1.4×10^{-3}
	WELDED TUFF	24.8	0.24	—
STARWORT	ALLUVIUM	1.5	0.037	8.3×10^{-5}
	WELDED TUFF	1.5	0.018	—

Figure 4.--Graph comparing spectral ratios for two nuclear events. The recording sites, on the Nevada Test Site, are 20 m apart.

Examination of the GOC/CIT ratio shown in figure 5 for the earthquake

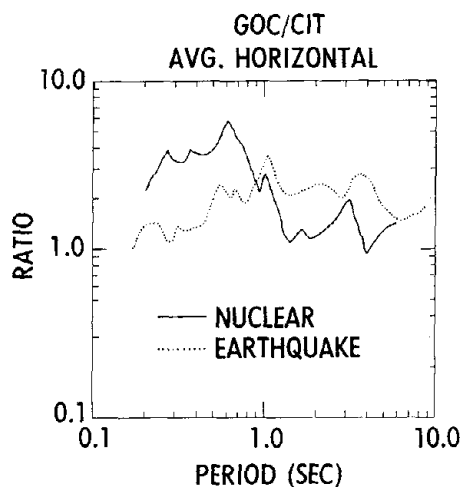


Figure 4.--Graph comparing spectral ratios for two nuclear events. The recording sites, on the Nevada Test Site, are 20 m apart.

indicates that of these two rock sites GOC recorded the largest amplitudes. Hanks (3) has shown that larger amplitudes were generated at azimuths to the south than at other azimuths, and this fact would explain the higher observed amplitudes at GOC. On this basis one might attempt to remove the azimuthal dependence in the GOC/CIT ratio by assuming the ratio averages about 1 at long periods. In this case the nuclear ratio, shown in figure 5, would match the earthquake ratio at long periods ($T > 1$ second), but would display an even greater difference at the short periods than that shown in figure 5. Because we accept the validity of the GOC nuclear and earthquake data on the basis of the comparison shown in figure 2, and we accept the ATH and MIL earthquake data on the basis of the comparisons shown in figure 3, the results seem to indicate anomalously large CIT earthquake amplitudes at periods less than one second relative to ATH-MIL. This result is both curious and difficult to explain.

Differences in wave propagation path from the source to the site can produce focusing effects (10) (including topographic effects suggested by Hudson (4) for the CIT site), which can be highly azimuth and distance dependent. Gutenberg (5), however, did not find a significant azimuthal effect for any of the earthquakes and sites that he studied, including ATH and CIT. This fact alone does not preclude the possibility of path effects, however, because it is possible that the right combination of azimuth and distance was not sampled by Gutenberg's data.

Another possible explanation of the observed differences is the presence of noise contamination in the strong motion record due to building vibrations that were excited during the earthquake, but not during the nuclear explosion. In a two-story building, however, vibrations with periods as long as 1 second do not seem likely.

Finally, path propagation effects not related to focusing may play a part in producing relatively high CIT short-period motions. Consider the fact that station CIT is located at the southeastern margin of a northwest-trending salient of crystalline rock (the Verdugo Mountains-San Rafael Hills) that is almost intersected on the northwest by the rupture surface. While a portion of the short-period energy recorded at CIT likely traversed deep horizons and arrived from below, it is possible that significant portions of short-period energy also traveled along more direct near-surface paths. Propagation of near-surface body and surface wave phases, for instance, may have been induced by the "breakout" of the fault surface near the northern terminus of the Verdugo Mountains. While these waves would undergo about a factor of 4 ($Q=150$) material attenuation over the 20 km between the rupture and CIT, attenuation of about a factor of 20 ($Q=50$) would occur between CIT and the stations ATH and MIL, because this 4.5 km travel path occurs totally in alluvium. Assuming this analysis can be extended to estimate the fraction of horizontal-to-vertical traveling earthquake amplitudes required at CIT to produce the observed effects and taking into account path attenuation and site response, the results of this analysis indicate that the horizontal traveling earthquake amplitudes at CIT are at least 30% of the total recorded amplitude, but may be as large as 50% of the total. Whether or not it is reasonable to expect a percentage of horizontal traveling amplitude this large is questionable and may only be resolved by analytical modeling. Further, the observed peak acceleration at the site (0.19 g) is not anomalous compared to Schnabel and Seed (14) acceleration vs. distance curves which indicate expected acceleration of about 0.2-0.3 g; however, a change in the peak acceleration of 30% could easily be masked by the normal scatter in such data. In conclusion it is uncertain which of the mechanisms discussed leads to the observed differences between CIT and ATH-MIL. It is possible, of course, that all of the factors play some role.

CONCLUSIONS

1) Average spectral ratios at sites underlain by thin-to-intermediate thickness alluvium indicate that for both nuclear and earthquake ground motions, spectral amplitudes on alluvium are greater than on rock (sedimentary or crystalline) across most of the period range of engineering significance. Also, long-period amplification at a site underlain by intermediate-thickness alluvium was observed to be higher than that at a site underlain by thin alluvium.

2) The general agreement between long-period earthquake and nuclear spectral ratios at alluvium sites indicates that surface waves develop with similar amplification characteristics for both nearby and distant sources at these sites. In one case, the lack of agreement at long periods between earthquake and nuclear spectral ratios for a site underlain by shallow sedimentary rock suggests that surface-wave development at this site reflects some wave-propagation differences for near and distant sources. This effect produces slightly conservative ground shaking response estimates at long periods.

3) Short-period earthquake energy recorded at CIT appears anomalously high relative to ATH and MIL, and this observation is possibly also related to travel-path effects. If correct, this result does not indicate that the site response estimate derived from the nuclear data at the two alluvial sites is in error, but suggests that estimation of actual ground shaking levels at sites near earthquake epicenters should incorporate complex source and travel-path geometry effects in addition to site response.

4) Because of the complexity of predicting source and travel path effects using present technology, prediction of mean site response using nuclear event ground motions may have to incorporate some additional variance related to unknown source and propagation effects to correctly represent expected earthquake-induced site response.

ACKNOWLEDGMENTS

The authors would like to thank R. Archuleta, D. Boore, R. McGuire, and D. Perkins for their helpful reviews and discussions of this paper. We also thank P. Covington for help in the data processing and K. King and G. Sembera who significantly aided in completing the field work.

REFERENCES

1. Navarro, R., and Wuollet, G. M., 1972, The L-7 velocity seismograph shaking-table results: U.S. Dept. Commerce, Natl. Oceanic Atmospheric Admin., Tech. Rept. ERL 254-ESL 26, 48 pp.
2. Park, R. B., and Hays, W. W., 1977, Use of a hybrid computer in engineering seismology research, U.S. Geol. Survey Jour. Research 5, 651-661.
3. Hanks, T. C., 1975, Strong ground motion of the San Fernando, California earthquake: Ground displacements, Bull. Seism. Soc. Am. 65, 105-225.
4. Hudson, D. E., 1972, Local distribution of strong earthquake ground motions, Bull. Seism. Soc. Am. 62, 1765-1786.
5. Gutenberg, B., 1957, Effects of ground on earthquake motion, Bull. Seism. Soc. Am. 47, 221-250.
6. Rogers, A. M., Tinsley, J. C., Hays, W. W., and King, K. W., 1978, Evaluation of the relation between near-surface geologic units and ground response in the vicinity of Long Beach, California, submitted to Bull. Seism. Soc. Am.
7. Joyner, W. B., and Chen, A. T. F., 1975, Calculation of nonlinear ground response in earthquakes, Bull. Seism. Soc. Am. 65, 1315-1336.
8. Eguich, R. T., Campbell, K. W., Duke, C. M., Chow, A. W., and Paternina, J., 1976, Shear velocities and near-surface geologies at accelerograph sites that recorded the San Fernando earthquake, Univ. California, Los Angeles, School of Engineering and Applied Sciences, UCLA-ENG-7653, 63 pp.

9. Seed, H. B., and Idriss, I. M., 1970, Soil moduli and damping factors for dynamic response analyses, Univ. of California, Berkeley, Rept. No. EERC70-10, 15 pp.
10. Environmental Research Corporation, 1974, Prediction of ground motion characteristics of underground nuclear detonations, available from U.S. Natl. Tech. Inf. Svc., Springfield, Va., as AEC Rept. NVO-1163-239.
11. Hays, W. W., 1978, A general procedure for estimating earthquake ground motions, The Institution of Mechanical Engineers, Proc. of Conference on Engineering Design for Earthquake Environments, London, England, 71-79.
12. Lynch, R. D., 1970, Single station analysis of PSRV data from Pahute mesa events, available from U.S. Natl. Tech. Inf. Svc., Springfield, Va., as AEC Rept. NVO-1163-130.
13. Murphy, J. R., Davis, A. H., and Weaver, N. L., 1971, Amplification of seismic body waves by low-velocity surface waves, Bull. Seism. Soc. Am. 61, 109-145.
14. Schnabel, P. B., and Seed, H. B., 1973, Accelerations in rock for earthquakes in the western United States, Bull. Seism. Soc. Am. 63, 501-516.

764

INTENTIONALLY BLANK

THE CONTRIBUTION OF LOVE WAVES TO STRONG GROUND MOTIONS

by

Kazuyoshi KUDO

ABSTRACT

Love waves whose characteristics are mostly controlled by thick (2-3km) sedimentary layers, were calculated using normal mode theory for given fault parameters of the Off-Izu-Peninsula earthquake (1974), the North-Izu earthquake (1930) and the Saitama earthquake (1931). These were compared with the transversely polarized displacements observed at Hongo, Tokyo. Good agreement between synthetic and observed seismograms was obtained in both amplitude and phase in the period range from 5 to 10 or more seconds. Far field expressions derived from normal mode theory are sufficient for the prediction of Love waves when kr is larger than 10, where k and r are wave number and epicentral distance, respectively. For waves with periods greater than about 10 seconds, this condition is fulfilled for epicentral distances larger than 40km for the structure in and around Tokyo. A point force approximation is adequate but a slight improvement is obtained by evaluating a fault of finite vertical extent.

INTRODUCTION

There is an urgent need to determine the characteristics of strong ground motion due to earthquakes in the period range from one to ten or more seconds, because of the increasing number of high-rise buildings and large scale structures.

Long-period strong-motion seismographs have been operating at the University of Tokyo, Hongo (Tokyo), since the beginning of this century. A few seismograms of great earthquakes, such as the Kanto earthquake of 1923, are overloaded but some complete records of large earthquakes are available. Among them, there are some seismograms where the amplitude is constant for a long time (1 to 2 minutes) with nearly constant period (7 to 10 seconds). Generally speaking, the longer the natural period of a building is, the smaller damping constant. Therefore, these earthquake ground motions are especially dangerous for such buildings, if their natural period matches that of the ground motions. The study of the generation and wave-types of these earthquake ground motions is important for anti-seismic designing.

Seismograms of the Off-Izu-Peninsula earthquake of 1974 ($M=6.9$), the North-Izu earthquake of 1930 ($M=7.0$) and the Saitama earthquake of 1931 ($M=7.0$) recorded at the University of Tokyo are analyzed in the following. The predominant displacement amplitudes at Tokyo due to these earthquakes are shown to be Love waves mostly controlled by thick sedimentary layers. The source parameters of the earthquakes have been determined by other authors. We will examine to what extent we can obtain agreement between observed and synthetic seismograms adopting the excitation theory of surface waves (Ben-Menahem, 1961; Ben-Menahem and Harkrider, 1964; Haskell, 1964; Harkrider, 1964, 1970; Saito, 1967), without any modification of the given source parameters as far as is possible.

Assistant of Earthquake Research Institute, University of Tokyo, Tokyo, Japan.

Preceding page blank

EXCITATION THEORY OF SURFACE WAVES

Theoretical amplitude spectra of surface waves from various types of sources at depth in layered media have been given by Harkrider(1964,1970), Haskell(1964), Saito(1967) and others. In the present paper, the expressions and notations by Harkrider are adopted. Far field spectral displacement amplitudes of horizontal Love and Rayleigh waves for a point double couple force, can be written as

$$U(\omega) = S(\omega) k \chi(\theta, h) E \exp[-i(kr+3\pi/4)] / \sqrt{2\pi r}$$

where $S(\omega)$ =spectral source function, $k(=\omega/C)$ =Love or Rayleigh wave number, θ =azimuthal angle measured counterclockwise from the strike direction to the station, h =focal depth and r =epicentral distance. The complex radiation pattern functions of Love and Rayleigh waves are

$$\chi_L(\theta, h) = i(\cos\lambda\cos\delta\sin\theta - \sin\lambda\cos2\delta\cos\theta)G(h) + (1/2\sin\lambda\sin2\delta\sin2\theta + \cos\lambda\sin\delta\cos2\theta)V(h)$$

and

$$\chi_R(\theta, h) = 1/2\sin\lambda\sin2\delta B(h) - i(\sin\lambda\cos2\delta\sin\theta + \cos\lambda\cos\delta\cos\theta)C(h) + (\cos\lambda\sin\delta\sin2\theta - 1/2\sin\lambda\sin2\delta\cos2\theta)A(h)$$

where λ =slip angle measured counterclockwise from a horizontal line to the strike and δ =dip angle measured downward from the negative dip direction. The quantities $V(h)$, $G(h)$, $A(h)$, $B(h)$ and $C(h)$ are given as

$$V(h) = [\dot{v}_s(h)/\dot{v}_o], \quad G(h) = 1/\mu_s [\tau_{Ls}^*(h)/(\dot{v}_o/C_L)],$$

and

$$A(h) = -[\dot{u}_s^*(h)/\dot{w}_o], \quad B(h) = -(3-4\beta_s^2/\alpha_s^2)[\dot{u}_s^*(h)/\dot{w}_o] - 2/(\rho_s \alpha_s^2) [\sigma_{Rs}^*(h)/(\dot{w}_o/C_R)]$$

and

$$C(h) = -1/\mu_s [\tau_{Rs}(h)/(\dot{w}_o/C_R)]$$

where the quantities in the right hand of the above equations are identical to Haskell(1953). Subscript s means the source layer. The amplitude factors are

$$E_L = A_L k_L^{-1/2}, \quad A_L = [2C_L U_L \int_0^\infty \rho [\dot{v}(z)/\dot{v}_o]^2 dz]^{-1}$$

and

$$E_R = -[\dot{u}_o^*/\dot{w}_o] A_R k_R^{-1/2}, \quad A_R = [2C_R U_R \int_0^\infty \rho \{[\dot{u}^*(z)/\dot{w}_o]^2 + [\dot{w}(z)/\dot{w}_o]^2\} dz]^{-1}$$

In the following, the time function of the force is assumed to be a simple ramp function. The expressions for a propagating fault have been given by Ben-Menahem(1961) as $\exp(-iX)\sin X/X$ for a unilateral fault if $r \gg L$, where $X = \omega L/2(1/V - \cos\theta/C)$. The corresponding effect for a symmetric bilateral and bidirectional fault may be written as $1/2[\exp(-iX)\sin X/X + \exp(-iY)\sin Y/Y]$, where $X = \omega L/4(1/V - \cos\theta/C)$, $Y = \omega L/4(1/V + \cos\theta/C)$. L , V and C are fault length, rupture velocity and phase velocity at angular frequency ω , respectively (Aki, 1966).

If we restrict our discussion for kr larger than 10, the far-field approximation is adequate.

OFF-IZU-PENINSULA EARTHQUAKE

RECORDS AT TOKYO

A large earthquake ($M=6.9$) occurred on May 9th of 1974 in the southern end of the Izu-Peninsula. Omori long-period strong-motion seismographs recorded the ground motion well at the Earthquake Research Institute ($35.72^{\circ}\text{N}; 139.72^{\circ}\text{E}$). The epicenter, focal depth and origin time are $34.62^{\circ}\text{N}; 138.81^{\circ}\text{E}$, 10km and $08^{\text{h}}33^{\text{m}}27.8^{\text{s}}$ (J.S.T.), respectively (Matsuzaki, 1975). The epicentral distance is 150km and the seismic intensity at Tokyo was III (Japanese scale).

The locations of epicenter and station are shown in Figure 1. The recorded seismograms and the seismograph constants are shown in Figure 2 and Table 1, respectively. They are reproduced from Iwata et al (1974). Digitizing of the records was done on a SMAC-READER which gave computer cards directly as out-put. Digitization points were taken at every 0.1mm which corresponds to a 0.2sec time interval. The distortions of wave form due to the finiteness of arm length were removed and the data were interpolated to equal time intervals (0.25sec) using a spline function (Saito, 1973).

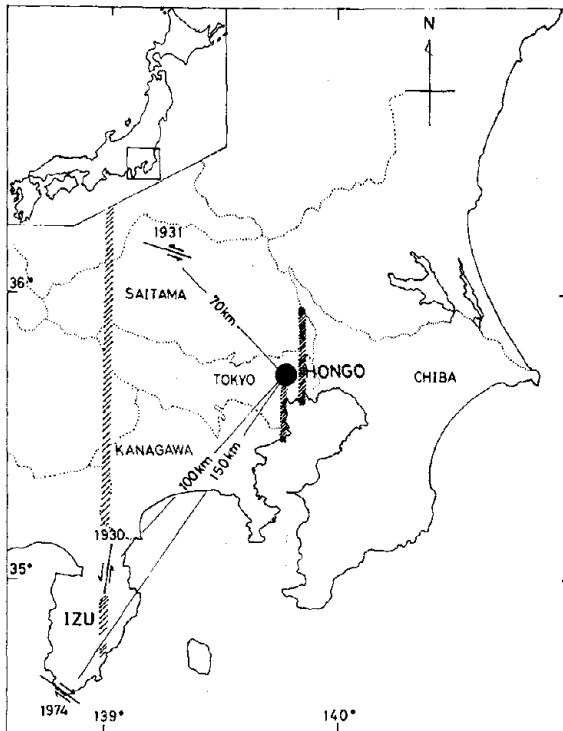


Fig. 1. Map indicating the epicenters of the Off-Izu-Peninsula earthquake of 1974, the North-Izu earthquake of 1930 and the Saitama earthquake of 1931, and the location of the recording site. Hatched lines show the locations of seismic profiles.

Real displacement of ground motion was acquired by the Fourier transform method (F.F.T.). In the computation, a Hamming spectral window having cut-off frequencies at 0.04 and 1.0 Hz was used. The upper two traces in Figure 3 show the displacement of the NS and EW components thus obtained. Lower traces in the figure show the displacements parallel and perpendicular to the wave propagation direction. As the amplitude of the transversely polarized wave is about two times larger than the radial one, we will discuss only this wave in what follows.

TABLE 1. Seismograph characteristics

Component	Natural period (sec)	Magnification	Damping Const. (h)	Paper speed (mm/min)
EW	19.9	1.34	0.23	30.0
NS	31.0	1.44	0.18	30.0

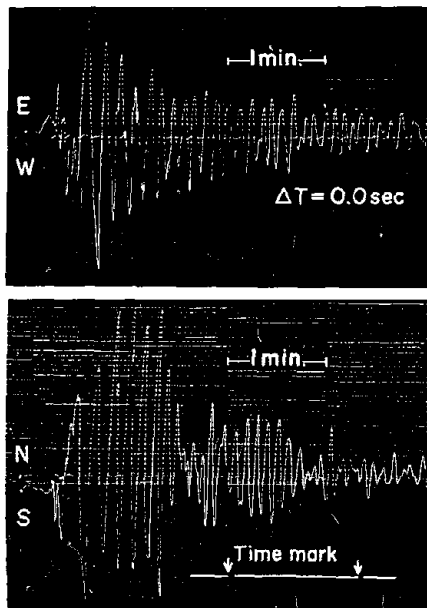


Fig. 2. Seismograms of the Off-Izu-Peninsula earthquake recorded at Tokyo, reproduced from Iwata et al (1974).

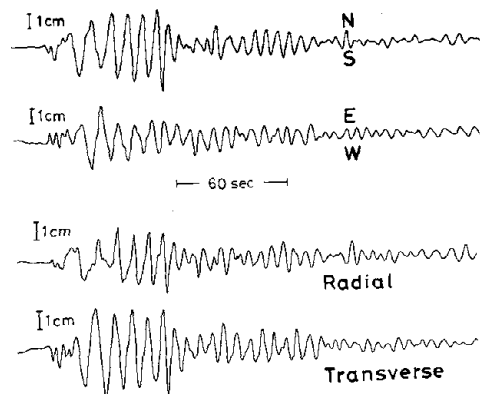


Fig. 3. Seismograms after the instrumental responses were removed (upper two traces), rotated into radial and transverse components (lower two traces).

UNDERGROUND STRUCTURE AND GROUP VELOCITY DISPERSION

The primary intention of the present analyses is to identify the wave type of the major amplitudes of the observed seismograms. For this work, it is suitable to obtain group velocities of each wave group. A moving-window multiple-filter method (e.g. Dziewonski et al, 1969) is adopted to obtain the group velocity dispersion curve. The power densities of the incoming wave, as functions of time (group velocity) and frequency, are contoured, as shown in Figure 4. The numbers on the contours show values relative to the peak value in decibels. Clear dispersion is found, and we are able to assume that the transversely polarized wave mainly consists of Love waves.

The dispersion characteristics are determined by the structure in which the waves propagate. We do not have a seismic cross section containing both source and station, nevertheless the structure in the Izu-Peninsula (source) and in and around Tokyo (station) are known independently. Hotta et al (1964) obtained a seismic cross section of central Japan including the Izu-Peninsula by the observation of P-waves generated by explosions. Corresponding S-wave velocities were determined by assuming Poisson's ratio to be 0.25 in each

layer (Model 1); Shima et al (1976a,b,c) obtained several P- and S-wave velocity structure models of Tokyo through the observation of seismic waves generated by explosions. Among them, two models were chosen (Model 2 and Model 3). The locations of seismic refraction profiles are shown by hatched lines in Figure 1. The constants of each model are shown in Table 2. Dispersion curves of Love wave group velocity (fundamental mode only) for these models were computed according to Haskell(1953), and were compared with the observed group velocity (solid circles) as shown in Figure 5. Although the dispersive characteristics of the observed group velocities are rather different from the computed values, the difference in the case of Model 3 is small compared with the other models. These discrepancies notwithstanding, we generate syntheses according to the excitation theory of Love waves for the three structural models.

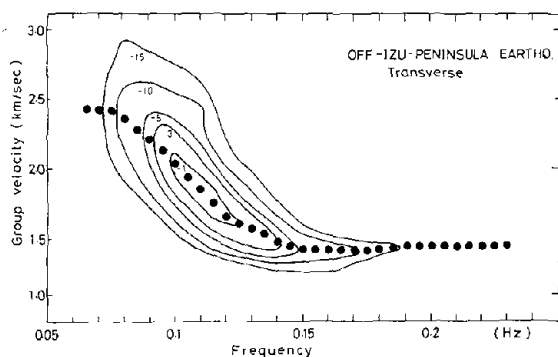


Fig. 4. Contour plot of power spectral density of the Off-Izu-Peninsula earthquake against group velocity and frequency. Numbers on the contours show values relative to the peak value in decibels. Chain of solid circles shows a ridge of the contour.

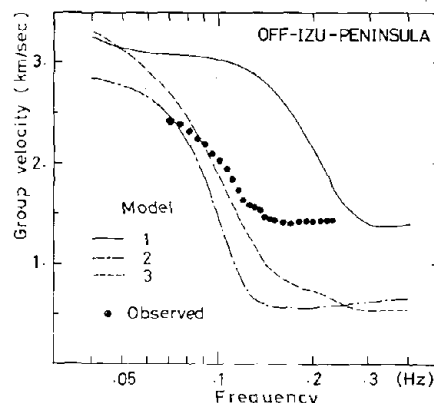


Fig. 5. Dispersion Curves of group velocity of fundamental mode Love waves, for three models, plotted against observed data (solid circles).

TABLE 2. Structure models based on seismic profiles

Model 1				
Layer	α (km/sec)	β (km/sec)	ρ (g/cm ³)	Thickness(km)
1	2.83	1.6	2.4	1.5
2	6.0	3.4	2.65	22.5
3	6.82	3.7	2.88	6.0
4	7.8	4.4	3.3	∞

Model 2				
Layer	α (km/sec)	β (km/sec)	ρ (g/cm ³)	Thickness(km)
1	1.8	0.7	2.0	1.0
2	2.5	1.5	2.3	1.6
3	5.5	3.0	2.5	∞

Model 3				
Layer	α (km/sec)	β (km/sec)	ρ (g/cm ³)	Thickness(km)
1	1.6	0.58	1.8	0.2
2	1.8	0.7	2.0	0.47
3	2.5	1.5	2.3	1.84
4	5.3	3.0	2.5	3.5
5	6.0	3.4	2.6	∞

SYNTHESIS

Matsuzaki(1976) obtained the source parameters of this earthquake as follows; strike=N50°W, slip angle=14°(right lateral), dip angle=76°, fault length=20km, fault width=10km, focal depth(h)=10km, mode of rupture=bilateral, rupture velocity=2.5km/sec, rise time=1sec, seismic moment=6.6x10²⁵dyne-cm,

Amplitude spectra of Love waves were calculated for three structures adopting the above source model. They were also computed for a focal depth of 6.0km holding the other source parameters constant. The spectra are shown in Figure 6. The synthetic amplitude spectrum for Model 3 for focal depth 6.0km (thick broken line in Figure 6) is somewhat larger than the observed spectrum but it resembles the major amplitudes of the record fairly well. The other cases are in poor agreement. From the view point of application to earthquake engineering, it is interesting that the major amplitude spectrum is roughly matched by the fundamental mode Love wave in the structure beneath the observation point.

The phase characteristics of the waves are also important from the same point of view. It is convenient for this work to obtain synthetic seismograms by means of the inverse Fourier transform (e.g. Kanamori,1970a,b). A Hamming spectral window having cut-off frequencies at 0.04 and 0.25 Hz was used for the computation. Synthetic seismograms of fundamental mode Love waves thus obtained are shown in Figure 7 together with the observed seismogram. Synthetic Love waves for all structure model are inconsistent with the observed seismogram, even though the case of Model 3 gave good agreement in its amplitude spectrum. None of the computed dispersion curves match the observed one. Therefore, there may be some factor beyond the scope of this study that causes the synthetic Love waves to be out of keeping with the observed ones. However, none of the structure models may be appropriate, because the seismic cross sections reveal only small parts of the path from source to station(see Figure 1). Groups velocities of surface waves reflect the average structure from source to station when an interface between a surface layer and a semi-infinite medium has dip, or when a surface layer has some vertical boundaries (Sato, 1959, 1966).

Is it possible to obtain a better synthesis if we introduce a structure whose group velocity dispersion curve agrees with the observed one?

IMPROVEMENT AND DISCUSSION

A new three layered model was proposed as follows. The observed group velocity at low frequencies is closest to the dispersion curve of Model 2, so the S-wave velocity of underlying semi-infinite medium was assumed to be 3.0km/sec. since it tends to 1.45km/sec at high frequencies (above 0.2Hz), the S-wave velocity of the uppermost layer was assumed to be 1.5km/sec. The S-wave velocity of intermediate layer was arbitrarily assumed to be 2.5km/sec. Densities corresponding to the 1st, 2nd, and 3rd layers were assumed to be 2.3, 2.6 and 2.7g/cm³, respectively. Several dispersion curves were computed varying the thickness of the first and second layers, and compared with the observed group velocity. The resulting dispersion curve and layer parameters are shown in Figure 8.

Synthetic amplitude spectra and seismograms were calculated again adopting this new model (Model A). A synthetic amplitude spectrum showing adequate agreement was obtained for a focal depth of 7.5km as shown in Figure 9. A slight improvement is obtained by taking into account the fault width, which is represented by point forces distributed continuously

on a vertical fault plane (Harkrider, 1964), as shown in Figure 9. In this calculation, the homogeneous point forces are distributed from 4 to 14km in depth every 0.5km. Excellent agreement between observed and synthetic seismograms was obtained in both amplitude and phase, except for the beginning of the S-arrival and the coda.

The underground structure Model A is not unique and another model may be equally acceptable. However, if we could model other earthquakes of similar path by Model A, it might be possible to predict the Love waves of future earthquakes which occur in and around the Izu-Peninsula, even though Model A does not reflect the real seismic cross section.

The disagreement in low frequencies may be caused by our adoption of the far field expression. However, short period waves less than around 10sec are the most important from an earthquake engineering point of view. Under this restriction, the far field expression is applicable for epicentral distance larger than 40 km, since the wave number $k(=\omega/C)$ at a period of 10sec is around 0.25(cycle/km) except for Model 1. An interpretation of short period waves less than 5sec as appeared at the beginning of the S-arrival is our next problem.

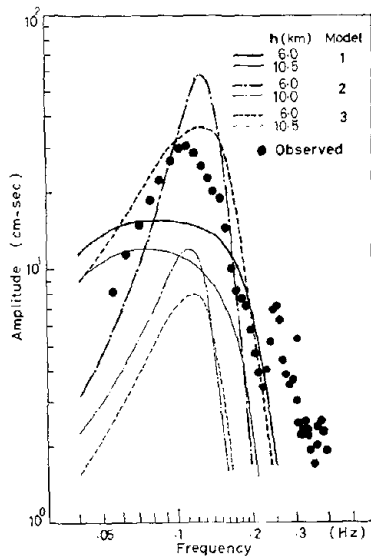


Fig. 6. Synthetic amplitude spectra of Love waves for six cases compared with the observed amplitude spectrum of the Off-Izu-Peninsula earthquake.

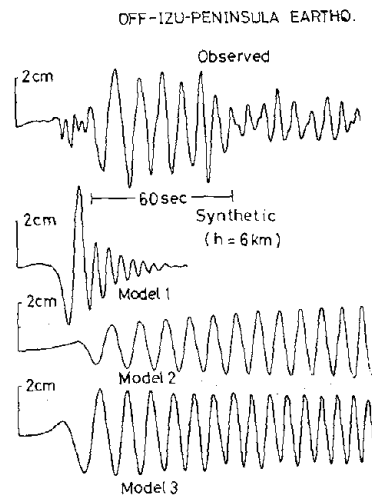


Fig. 7. Wave forms of synthesized Love waves for three models having focal depth 6.0km, compared with the observed transverse wave.

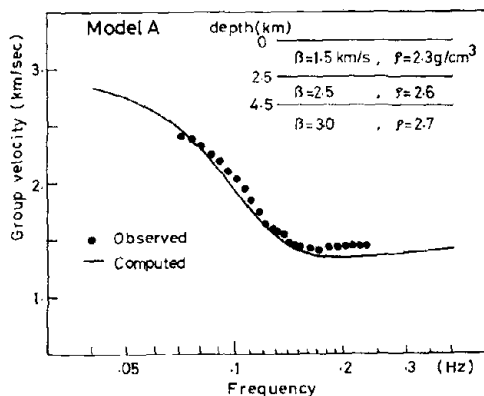


Fig. 8. Structure model and its group velocity dispersion curve of fundamental mode Love waves compared with the observed data.

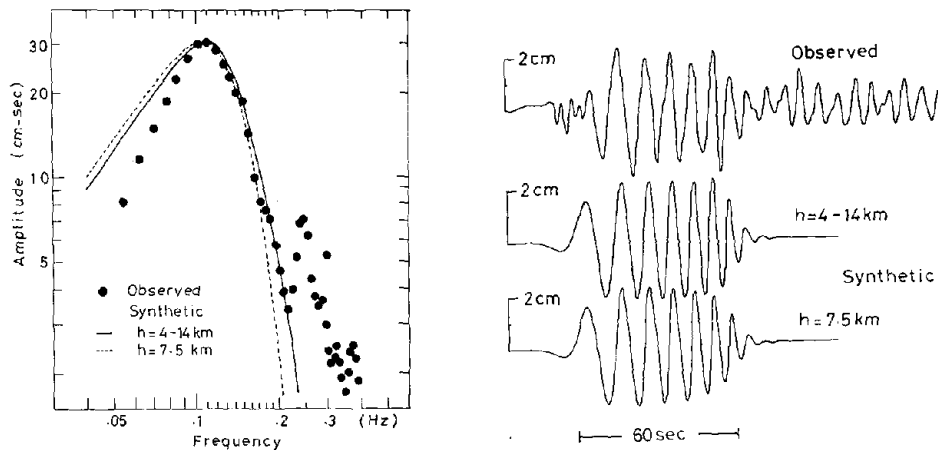


Fig. 9. Synthetic amplitude spectra and wave forms calculated by adopting Model A (see Figure 8). The solid curve shows the amplitude spectrum obtained through integrating homogeneous point forces distributed from 4 to 14 km on a vertical fault plane. The dashed curve is obtained from a point force at 7.5 km depth.

OTHER EXAMPLES

NORTH-IZU EARTHQUAKE OF 1930

A large earthquake ($M=7.0$) occurred on November 26, 1930, in the northern part of the Izu-Peninsula as shown in Figure 1. A general description of this earthquake is given by Richter(1958).

Omori long period strong-motion seismographs (Table 3) were operating at Hongo(Tokyo) and recorded the ground motion due to this earthquake well. Tanaka and Yoshizawa(1977) derived the real ground motion from the records. The transversely polarized wave is shown in Figure 10. The wave propagation path is almost the same as the case of the preceding section, but the epicentral distance is different (Figure 1). Accordingly, the underground structure of Model A should be adequate for synthesis of this earthquake, if a flat layering assumption is valid.

Source parameters of this earthquake were selected by referring to Ichikawa(1971), Geller(1976), and Abe(1978) as follows; strike= $N9^{\circ}E$, slip angle= 180° (left lateral), dip angle= 90° , fault length= 22km , fault width= 11km , rupture velocity= 2.0km/sec , rise time= 1.7sec , seismic moment= $2.7 \times 10^{26}\text{dyne-cm}$. Azimuthal angle and epicentral distance are 148° and 100km , respectively. Synthetic Love waves were computed for three cases of rupture; the first is that the rupture starts from the southern end of the fault and propagates north unilaterally, the second is that rupture propagation is in the opposite direction, and the third is that the rupture starts from the center of the fault and propagates bilaterally. The depth to the top of the fault was set at 5km . Synthetic Love waves thus obtained are shown in Figure 10 together with the observed seismogram. According to Imamura(1931), this earthquake is characterized by multiple shocks, at least four events. The fourth event, 7.5sec after the first event was the major shock. The beginning of the observed wave in Figure 10 corresponds to the P-arrival of the first shock. Then the timing of the synthetic seismogram is set corresponding to the P-arrival of the fourth shock. Synthetic Love waves for the first case of rupture match the record fairly well.

Roughly speaking, our flat layering model is adequate. However, an appropriate structure should be introduced for precise analysis, since the correspondence between synthesis and observation becomes weak in later phases.

TABLE 3. Seismograph characteristics that recorded the ground motions of the North-Izu and Saitama earthquake at Hongo

Component	Natural period(sec)	Magnification	Damping ratio(ν)
N13°W, S13°E	33	1.5	1.5
N77°E, S77°W	47	1.5	1.8

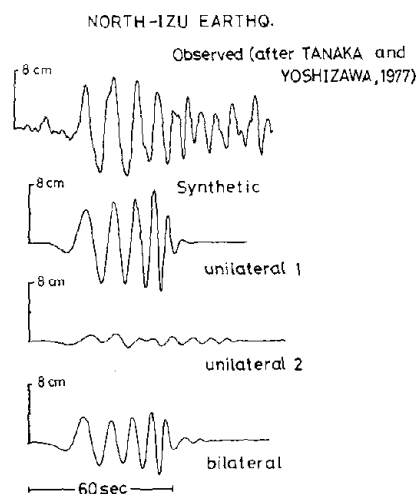


Fig.10. The transversely polarized wave of North-Izu earthquake of 1930 obtained from the seismograms recorded at Hongo, Tokyo and synthetic Love waves for three models of rupture propagation.

SAITAMA EARTHQUAKE OF 1931

The Saitama earthquake ($M=7.0$) occurred on September 21, 1931, in the northwestern part of Saitama Prefecture, as shown in Figure 1. The propagation path to Hongo is different from the preceding cases. Figure 11 shows the seismograms recorded by the same seismograph (Table 3) as the North-Izu earthquake at Hongo, Tokyo. The transversely polarized real displacement and its power amplitudes as functions of group velocity and frequency are obtained in the same way as in the preceding section. A significant dispersion of group velocity is also found in this case, but it is not as simple as in the preceding cases (Figure 12). Since one branch of the observed dispersion curve seems to match Model 2 as shown in Figure 13, we adopt Model 2 for generating the synthetic Love waves.

Abe(1974) determined the source parameters of this earthquake as follows; dip direction=N196°E, slip angle=5°(left lateral), dip angle=80°, fault length=20km, fault width=10km, mode of rupture=bilateral, rupture velocity=2.3km/sec, rise time=2sec, seismic moment= 6.8×10^{25} dyne-cm, focal depth=1km.

The amplitude spectrum and Love wave seismogram were synthesized adopting the above source model. However, they are much larger than the observed ones. Further calculations were done with the depth to the top of the fault at 3 and 5km, holding the fault width constant. They are compared with the observed amplitude spectrum and transversely polarized displacement in Figure 14. The synthesis for 5km depth matches the observed seismogram fairly well, though the consistency is poor compared with the case of the

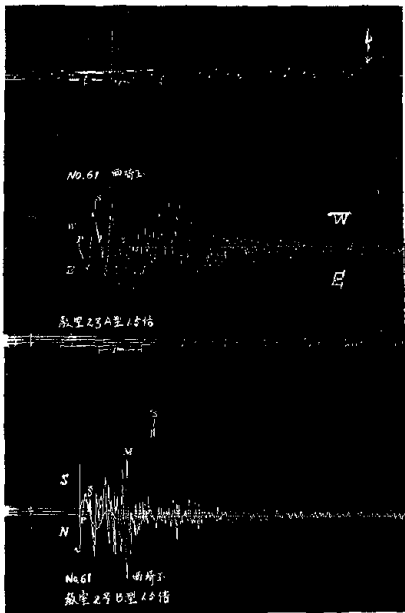


Fig.11. Seismograms of the Saitama earthquake of 1931 recorded at Hongo, Tokyo.

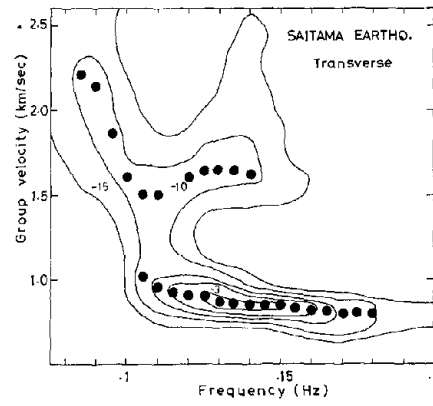


Fig.12. Contour plot of power density of the Saitama earthquake against group velocity and frequency.

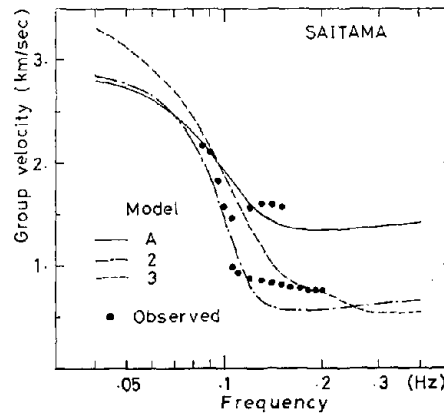


Fig.13. Group velocity dispersion curves of fundamental mode Love waves plotted against observed data.

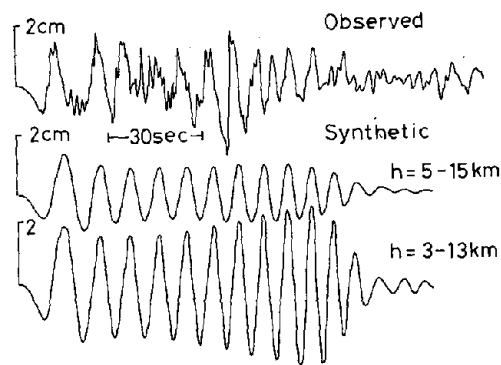
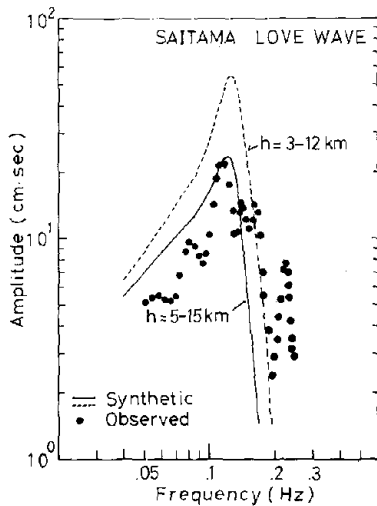


Fig.14. Comparison between observed transverse wave and synthetic Love waves of the Saitama earthquake, 1931.

Off-Izu-Peninsula and North-Izu earthquake.

The discrepancy of focal depth with Abe's(1974) model is not resolved at present; however one possibility is that our flat layering model is not suitable for a precise analysis of this earthquake. In fact, basement rocks are exposed in the source region, while the greater portion of the propagation path is covered with thick sedimentary layers. A similar problem is discussed in Heaton and HelMBERGER(1977).

CONCLUDING REMARKS

The transversely polarized displacements of three earthquakes observed at Hongo, Tokyo, mainly consist of fundamental mode Love waves. This is confirmed by adequate agreement between recorded and synthetic seismograms in both time and frequency domain through normal mode theory.

A flat layering assumption is valid if its group velocity dispersion curve fits the observed group velocity.

The most important conclusion from the viewpoint of earthquake engineering is that strong excitation of Love waves is expected when thick sedimentary layers exist in and the focal depth is shallow, even though the epicentral distance is small.

According to Kawasaki(1978), the agreement between the wave forms obtained by normal mode and exact ray theory is excellent even at close distances except for the head wave portion. Then normal mode theory is appropriate for estimating the displacements due to Love waves excited by shallow earthquake, from the viewpoint of computational economy.

Higher modes of Love waves have not been discussed in the present paper. However, they must be taken into account in any study of the generation of short period waves, which is important for ordinary buildings. A detailed structure model is needed to accomplish such a study.

ACKNOWLEDGEMENT

I wish to express my sincere thanks to Dr. Paul Somerville who kindly read the manuscript and made valuable suggestions, and Profs. Etsuzo Shima and Ryosuke Sato who gave me advice during the course of this study. I am also grateful to Drs. Teiji Tanaka and Shizuyo Yoshizawa, and Earthquake Prediction Observation Center of Earthquake Research Institute for providing valuable data and original records. Dr. Ichiro Kawasaki kindly showed me his works before publication. I am indebted to Dr. Kunihiko Shimazaki for his comments at the Danwa Kai (monthly meeting of Earthquake Research Institute).

REFERENCES

- Abe, K., Seismic displacement and ground motion near a fault: The saitama earthquake of September 21, 1931, J. Geophys. Res., 79, 4393-4399, 1974.
- Abe, K., Dislocation, source dimensions and stresses associated with earthquakes in the Izu Peninsula, Japan, 1978(preprint).
- Aki, K., Generation and propagation of G-waves from the Niigata earthquake of June 16, 1964, 2. Estimation of earthquake moment, released energy, and stress-strain drop from G-wave spectrum, Bull. Earthq.Res.Inst., 44, 73-88, 1964.
- Ben-Menahem, A., Radiation of seismic surface waves from finite moving sources, Bull. Seismol. Soc.Amer., 51, 401-435, 1961
- Ben-Menahem, A. and D.G. Harkrider, Radiation patterns of seismic surface waves from buried dipolar point sources in a flat stratified earth,

- J. Geophys. Res., 69, 2605-2620, 1964.
- Dziewonski, A., S. Bloch and M. Landisman, A technique for the analysis of transient seismic signals, Bull. Seismol. Soc. Amer., 59, 427-444, 1969.
- Geller, R. J., Scaling relations for earthquake source parameters and magnitudes, Bull. Seismol. Soc. Amer., 66, 1501-1523, 1976.
- Harkrider, D. G., Surface waves in multilayered elastic media. I. Rayleigh and Love waves from buried sources in a multilayered elastic half-space; Bull. Seismol. Soc. Amer., 54, 627-679, 1964.
- Harkrider, D. G., Surface waves in multilayered elastic media. Part II. Higher mode spectra and spectral ratio from point sources in plane layered earth models, Bull. Seismol. Soc. Amer., 60, 1937-1987, 1970.
- Haskell, N. A., The dispersion of surface waves on multilayered media, Bull. Seismol. Soc. Amer., 43, 17-34, 1953.
- Haskell, N. A., Radiation pattern of surface waves from point sources in a multi-layered medium, Bull. Seismol. Soc. Amer., 54, 377-393, 1964.
- Heaton, T. H. and D. V. Helmburger, A study of the strong ground motion of the Borrego Mountain, California, earthquake, Bull. Seismol. Soc. Amer., 67, 315-330, 1977.
- Hotta, H., S. Murauchi, T. Usami, E. Shima, Y. Motoya, and T. Asanuma, Crustal structure in Central Japan along longitudinal line 139°E as derived from explosion-seismic observations, Part 2, Crustal structure, Bull. Earthq. Res. Inst., 42, 533-541, 1964.
- Ichikawa, M., Reanalyses of mechanism of earthquakes which occurred in and around near Japan, and statistical studies on the nodal plane solutions obtained, 1926-1968, Geophys. Mag., 35, 207-274, 1971.
- Imamura, M., Seismometric study of the recent destructive N. Idu earthquake, Bull. Earthq. Res. Inst., 9, 36-49, 1931.
- Iwata, T., I. Karakama, M. Watanabe, and T. Watanabe, Seismograms of Izu-Hanto-Oki earthquake of 1974 obtained at the Tokyo and Tsukuba Seismological station, Special Bull. Earthq. Res. Inst., 14, 17-22, 1974.
- Kanamori, H., Synthesis of long-period surface waves and its application to earthquake of Oct. 13, 1963, J. Geophys. Res., 75, 5011-5027, 1970a.
- Kanamori, H., The Alaska earthquake of 1964: radiation of long period surface waves and source mechanism., J. Geophys. Res., 75, 5029-5040, 1970b.
- Kawasaki, I., The near-field Love wave by the exact ray method, 1978, in press.
- Matsuzaki, T., The focal process of the Off-Izu-Peninsular earthquake of May 9, 1974, Master thesis, Faculty of Science, Univ. of Tokyo, 1975.
- Richter, C. F., Elementary seismology, W. H. Freeman, San Francisco, 1958.
- Saito, M., Excitation of free oscillation and surface waves by a point source in a vertically heterogeneous earth, J. Geophys. Res., 72, 3689-3699, 1967.
- Saito, M., Subroutine package for time series analysis, Geotechnics, 9, 1974.
- Sato, R., On the determination of crustal structure by the dispersion curves of surface waves (III), Zisin, 12, 191-201, 1959.
- Sato, R., Group velocity in a layered medium with varying thickness, Zisin, 19, 147-148, 1966.
- Shima, E. et al, On base rock of Tokyo, Bull. Earthq. Res. Inst., 51, 1-11, 1976a.
- Shima, E. et al, On base rock of Tokyo II, B. E. R. I., 51, 45-61, 1976b.
- Shima, E. et al, Base rock of southern part of Tokyo, read at annual meeting of Seis. Soc. of Japan, 1976c.
- Tanaka, T. and S. Yoshizawa, Characteristics of strong earthquake ground motions in the period range from 1 to 20 second, *Shizen-Saigai-Kagaku Sōgo Symposium Kōenronbun-Shū*, 341-342, 1977.

THE RELEVANCY OF ONE-DIMENSIONAL SHEAR
MODELS IN PREDICTING SURFACE ACCELERATION

by

Issa S. Oweis^I

ABSTRACT

A simple shear beam model was established based on detailed analyses of cases covering various soil profiles from 15 sites. Profiles were excited by rock motions of various intensities and frequency content. The model was then applied to compare with recorded data. It is concluded that a) amplification occurs for low intensity rock motions in virtually all soil profiles; b) for high intensity rock motion, soils tend to attenuate rock motion and, c) profiles with large fundamental period tend to attenuate rock motion. Such profiles may be soft profiles or deep dense profiles. It is shown that these observations are in qualitative agreement with observational data but quantitatively, discrepancies may exist increasing in significance with increasing stiffness of the profiles.

INTRODUCTION

Site response analyses are being used in the United States to evaluate the effect of soil overburden on rock motion generated by earthquakes. In performing the analysis, the soil profile is modelled as horizontal layers with infinite lateral extent and ground motions are assumed to be the result of vertically propagating shear waves. The soil column is assumed to vibrate essentially as a shear beam subjected to base rock earthquake motion. The rock motion is required as input to the analysis and is usually characterized by peak acceleration, frequency content and duration. The response of the soil deposit is calculated utilizing the lumped mass approach (e.g. 8, 15, 24) or a continuous solution (wave propagation) approach (e.g. 6, 15, 16). The continuous solution approach allows the specification of earthquake rock motions at either of two locations (see Fig. 1): a) the soil rock interface at the bottom of the profile or b) a hypothetical rock outcrop near the site. The soil density ρ , shear modulus G and shear wave velocity V are functions of depth. The symbols S , I and O stand for soil surface, soil rock interface and rock outcrop, respectively. Accelerations at the rock interface are theoretically less than at the rock outcrop depending on the stiffness of the soil profile and underlying rock as illustrated in Fig. 2. Nonlinearity of the soil is accounted for by employing an equivalent linear model (8, 16) or employing a non linear stress strain relationship (24). Performing a site response analysis requires the definition of several parameters regarding the soil profile and input motion (5, 7).

In the types of analyses described above, it is assumed that the ground motion is primarily influenced by local site conditions and that ground motion is the result of shear wave propagation. The one dimensional and horizontal layering may be a simplification, but it is a reasonable assumption

^I Associate, Joseph S. Ward International, Inc., Caldwell, New Jersey

for many sites. Justifications for the theory are the reported modes of surface waves having some similarity to the modes of a shear beam model (30), and reported successful applications to several sites (7, 26). Significant discrepancies have been indicated in applying the theory to other than deep soft sites (5). It is believed that where the earthquake source is nearby, the assumption of the condition of vertically propagating shear waves may no longer be valid and for firm sites near the zone of energy release, ground motion is believed to be controlled primarily by source mechanism (17). Near fault ground motions in the 1971 San Fernando earthquake were characterized by long duration acceleration pulses which are believed to be directly related to the faulting process and are not a result of local geologic conditions (2). This type of ground motion is also believed to be typical of only firm sites close to the fault zone (12). An epicentral distance or distance to the closest point of fault rupture less than one-half the estimated length of rupture has been used as a criterion to distinguish earthquake data reflecting primary effects existing only very near the source (10). A statistical evaluation of recorded ground accelerations on rock and soil sites shaken by an earthquake with a magnitude of about 6.5 suggests little difference between the mean values of peak acceleration developed on rock or sites with stiff soil conditions (20). Site effects for other soils are more significant as shown in Fig. 3. Based on the mean relationships, site effects get more pronounced with decreasing stiffness of the soil, and smaller accelerations are amplified for the three soil categories. The same conclusion can be drawn from the site compatible response spectra (21) shown in Fig. 4. The site effects are reflected more clearly in Fig. 4 than in Fig. 3. The results summarized in Fig. 3 and 4 are consistent with an earlier observation (17) that with increasing stiffness, the soil would become rock-like and the soil profile would become an extension of the underlying rock.

The primary purpose of this paper is to assess the applicability of the shear wave propagation theory for the three soil categories in Fig. 3. In order to accomplish this, a simplified model, based on many detailed response analyses, is constructed to predict surface acceleration. The mean relationship for rock acceleration, given in Ref. 20 for an earthquake magnitude of about 6.5, was used for the input rock motion. The Frequency Content of the rock motion was characterized by the average response spectrum for rock shown in Fig. 4 but scaled down to correspond to 10% spectral damping, using ratios implied in Ref. 11. The resulting spectrum is shown in Fig. 5. The abscissa in Fig. 5 is the ratio T/T_p where T is the period and T_p is the predominant period of rock motion defined as the period at which the peak occurs in the response spectrum. Published relationships (18) were used to estimate T_p for a magnitude 6.5 earthquake.

ANALYTICAL MODEL

Figure 1 shows a generalized soil profile with rock outcrop. Assuming that normal modes of vibrations do exist for the soil profile, then the absolute acceleration $a(Z,t)$ at an arbitrary level Z (defined above rock as shown in Fig. 6) at time t is:

$$a(Z,t) = \sum_{i=1}^{\infty} \psi_i Y_i (Z) A_i (t) \quad \text{Eq. 1}$$

where $A_i(t)$ = absolute acceleration response of one degree of freedom system having the period and damping ratio of mode i , and subjected to the base acceleration $a_I(t)$.

$Y_i(Z)$ = normalized modal shape i

ψ_i = modal participation factor of mode i defined for the case $Y_i(H) = 1.0$.

Figure 6 shows the three modal shapes $Y_1(Z)$, $Y_2(Z)$ and $Y_3(Z)$ for the special case of uniform layer.

If the frequencies of the modes are well separated as is usually the case for many soil profiles subjected to shear, the root mean square (RMS) can provide good approximation for acceleration at the surface. In practice, a finite number of modes is usually considered and from Eq. 1

$$a(H,t) = \sum_{i=1}^m \psi_i^2 Sa_i^2 \quad \text{Eq. 2}$$

where Sa_i is the maximum value of A_i .

Considering a two mode approximation, the corresponding surface acceleration is:

$$a(H,t) = \psi_1 Sa_1 \sqrt{1 + \left(\frac{\psi_2}{\psi_1}\right)^2 \left(\frac{Sa_2}{Sa_1}\right)^2} \quad \text{Eq. 3}$$

The participation factor ψ_1 based on data listed in Table 1 may range from 1.28 to 1.61. The ratio ψ_2/ψ_1 may vary from 0.37 to 0.6. Using average values of 1.5 and 0.5 for ψ_1 and ψ_2/ψ_1 respectively, Eq. 3 reduces to

$$a_s = 0.75 Sa_1 \sqrt{4 + \left(\frac{Sa_2}{Sa_1}\right)^2} \quad \text{Eq. 4}$$

where a_s : surface acceleration

Sa_1, Sa_2 : absolute acceleration response spectra of rock input at interface $a_I(t)$ corresponding to the mode i having a period T_i . Sa_1 and Sa_2 correspond to the first and second modes, respectively.

Correlation of Surface Acceleration with Spectral Accelerations

A study was made to develop a correlation between calculated surface acceleration from detailed response analyses and the acceleration predicted from Eq. 4.

One hundred and thirty-four cases were analyzed in which a_s was available from runs of program SHAKE (16) and the fundamental period T_s was that associated with strain compatible soil profiles provided by SHAKE. The cases covered 15 sites with a range of different soil conditions. Eleven sites (Sites I through XI) were analyzed for correlation and the four remaining

sites (Sites XII through XV) were used to verify the correlation. Data on the cases studied are summarized in Table 2. Depth to rock varied from 40 feet to more than 500 feet, with small strain shear wave velocities varying from 300 fps to 2800 fps. The actual number of cases used in the correlation was one hundred twenty-seven. Site V was not included because of untypical extreme softness and high damping. The profiles were excited by a variety of rock accelerograms having peak accelerations from 0.02 g to 0.7 g.

The accelerograms used included recorded and artificial motions and in all cases the absolute acceleration response spectrum S_a vs. T was available for a spectral damping ratio = 0.1. To compute S_{a1} and S_{a2} , the available response spectrum of the input rock motion was used in each case in the manner shown in Fig. 7. S_{a1}/a_I was obtained at a period $T_1 = T_s$, while S_{a2}/a_I was taken as an eye average of S_a/a_I for the range of period between $T_2 = 0.3T_1$ and $T_2 = 0.5T_1$. The selection of this range for T_2 was based on the data summarized in Table 1.

In 29 cases, in which the rock input motion for SHAKE had been specified at the rock outcrop (point O in Fig. 1) instead of the rock interface (point I), the input response spectrum was scaled down by the ratio a_I/a_0 , prior to obtaining S_{a1} and S_{a2} . This ratio a_I/a_0 , which represents a correction for rock flexibility, was obtained from Fig. 2. The curve in Fig. 2 is based on wave propagation considerations (13) and the data points are from 21 cases where a_I was calculated as part of the SHAKE run.

Figure 8 shows the values of a_s computed from program SHAKE to those predicted by Eq. 4. Figure 8 suggests that Eq. 4 underpredicts the surface acceleration for S_{a1} less than about 0.1 g. For higher values of S_{a1} , Eq. 4 overpredicted the surface acceleration. Based on Fig. 8 the average relationship for surface acceleration is

$$a_s = 0.32 (S_{a1})^{0.61} \sqrt{4 + \left(\frac{S_{a2}}{S_{a1}}\right)^2} \quad \text{Eq. 5}$$

Application of Eq. 5 to the 127 cases of Fig. 8 resulted in the histogram shown in Fig. 9. The average value (a_s predicted/ a_s SHAKE) is nearly 1.0 and the standard deviation is 0.19. Seventy-two percent of the cases fall within mean plus and minus one standard deviation. In seventy-two percent of the cases the error is 20 percent or less. In 81 percent of the cases the error is 30 percent or less.

Equation 5 was applied to five cases from sites XII, XIII, XIV and XV and for one published case for the state building site (8). In all the five cases selected for verification, the error was 25 percent or less.

Evaluation of the Site Period T_s

Application of Eq. 5 requires the site period (T_s) to be known. Unfortunately, the site period is not known at the outset since it can vary significantly depending on the induced seismic shear strains and therefore on the characteristics of the base excitation (14, 19, 23). Several simple rules or procedures have been published for the estimate of site period of varied soils (e.g. 9, 13, 14, 25, 28). The purpose here is to present a procedure for a simple application of Eq. 5.

A meaningful estimate of T_s should be based on soil stiffness which is compatible with seismic strains (or shear stresses). Shear stresses induced in a soil profile as a result of underlying rock motion are primarily dependent on the spectral acceleration S_{a1} (14). It can be expected, therefore, that the site period be reasonably correlated with S_{a1} . The correlation was made between the spectral acceleration S_{a1} and the ratio T_s/T_i where T_i is the period calculated based on the initial (small strain) shear wave velocities. The mean relationship is described by Eq. 6 and Eq. 7, where S_{a1} is expressed in percent gravity.

For stiff sites and deep dense sand and gravel

$$\frac{T_s}{T_i} \approx 0.986 (S_{a1})^{.1929} \approx (S_{a1})^{0.193}; S_{a1} > 1 \quad \text{Eq. 6}$$

For soft to stiff sites

$$\frac{T_s}{T_i} \approx 1.41 (S_{a1})^{.167} \quad S_{a1} > 0.5 \quad \text{Eq. 7}$$

The cases from all 15 sites in Table 2 were used in establishing the above relationships. Application of these relationships to all the cases indicates an adequate correlation as illustrated in Fig. 10. For most of the cases, the site period was always greater than base rock motion predominant period T_p . Based on this, a relationship was established between S_{a1}/a_I and the ratio T/T_p ,

$$\frac{S_{a1}}{a_I} \approx 2.173 \frac{T}{T_p}^{-0.86} \quad \text{Eq. 8}$$

For $T = T_s$, substitution of Eq. 8 in Eq. 6 and 7 yields the following relationships.

For stiff sites or deep dense cohesionless soil profiles

$$T_s = 1.122 a_I^{0.1654} (T_p)^{0.142} (T_i)^{0.857} \quad T_s > T_p \quad \text{Eq. 9}$$

For soft to medium clay and sand layers

$$T_s = 1.512 (a_I)^{0.146} (T_p)^{0.126} (T_i)^{0.874} \quad T_s > T_p \quad \text{Eq. 10}$$

In Eq. 9 and 10, a_I is expressed in percent gravity, T_p and T_i and T_s in seconds. For very low values of T_p and very high values of T_i , Eq. 9 and 10 may result in values of T_s slightly less than T_i . In such situations, T_s shall be set equal to T_i . The correlations are applicable for a_I greater than or equal to 2% g. Applications of Eq. 9 and 10 to all the cases indicate a satisfactory correlation as illustrated in Fig. 11. Equations 9 and 10 are applicable where the anticipated T_s is greater than T_p . For stiff short profiles whose T_s may be less than T_p , an iterative procedure should be used to establish T_s using an appropriate response spectrum. The procedure would be: a) assume a reasonable value of T_s ; b) obtain a value for S_{a1}/a_I from response spectrum; c) calculate a new value of T_s/T_i from Eq. 6

and d) iterate until Step c coincides with Step a. An improved T_s value is used in each iteration.

The initial period T_1 can be calculated with good accuracy knowing the initial shear wave velocities of soil profile and the successive application of the two layer solution (4). Figure 12 shows the initial period T_1 for the sites used in this study plotted vs. profile thickness. Three curves are drawn: the lower curve is for a dense sand gravel deposit, the upper curve for profile of normally consolidated clays, the middle dashed line is the average of both extremes. Closed form solutions (4) were used to calculate the periods for the upper and lower curves. It is apparent that all cases involving stiff soil sites and deep dense cohesionless soil sites fall below the average line while the soft to medium sites fall above this average line. Site V plots well above the average and the upper curve because the profile is untypically soft.

APPLICATION OF THE MODEL TO SPECIFIC CASES

Equations 5, 9, and 10 and Fig. 12 were used to predict surface accelerations for cases where surface accelerations were recorded and/or estimated by detailed analysis and where sufficient data are provided to classify the site. A summary of the cases and the parameters used for the calculations are given in Table 3. Despite the approximate nature of the relationships used in the calculations, satisfactory agreement is indicated with results from detailed analysis. This justifies the application of the derived model to attempt to predict the relationship shown in Fig. 3. The largest discrepancy is for the Oakland City Hall site if the soil profile is assumed to be stiff and only 100 ft thick. Better agreement with recorded acceleration is indicated if a 1000 ft profile is assumed. The profile at Oakland City Hall consists of 100 ft of stiff soil underlain by hard clay. As suggested by Eq. 5, the surface accelerations depend on spectral acceleration and therefore on the site period. Large errors in estimating the period can therefore produce significant errors in calculating acceleration, especially if period errors are on the low side. The site period is controlled by the surface layer provided that the lower layer or layers are considerably stiffer than the surface layer. This is illustrated in Fig. 13 which was derived from the closed form solution of a two-layered system (4). The relationships in Fig. 13 indicate that as the soil becomes stiffer (layer A) the contribution of rock (layer B) with a velocity of 2500 fps to the period of the system becomes more significant. An underestimate of the period would result in an analytically stiffer profile and in most cases larger amplification of rock motion. Figure 13 suggests that analyses for stiff sites can be expected to be more sensitive to assumption or rock properties compared to other sites. Response spectra are usually smoother and less erratic in the long period range. Softer sites can therefore be less sensitive to errors in estimating T_s , and for the same T_p , less sensitive to the choice of rock motion accelerogram used in the analysis.

GENERAL APPLICATION OF THE MODEL

The derived model was applied to the results shown in Fig. 3 by making the following assumptions:

1) The range of thickness for the three soil categories were assumed as follows:

Stiff sites	50' - 150'
Deep cohesionless soils	250' - 500'
Soft to medium stiff clay and sand	100' - 500'

2) Deep cohesionless soils were assumed to be dense.

3) All rock accelerations were assumed to apply at rock outcrop. Interface accelerations a_1 were obtained by reducing outcrop values as suggested by Fig. 2. Outcrop rock accelerations for soft to medium sites were reduced by 20%. Outcrop rock accelerations for stiff sites and deep cohesionless soil sites were reduced by 30%.

Based on the above assumptions and using the response spectrum in Fig. 5, surface accelerations were calculated in the manner described earlier. The ratios of the calculated surface acceleration on soil divided by the rock acceleration at outcrop for the three site categories are shown in Fig. 14, 15, and 16. The mean relationships based on recorded motion are shown for comparison.

The trend predicted by theory compares well with the trend based on recorded data for soft to medium stiff soils and deep cohesionless soil. The agreement is not as good for stiff soils. For the same level of rock acceleration, discrepancies are the largest for stiff sites. Furthermore, discrepancies are consistently larger for smaller rock accelerations. The soil rock profile excited by a low level of rock acceleration is stiffer than the same profile excited by larger rock accelerations. Considering the assumptions made in applying the model and the approximations in the model itself, the discrepancies in surface accelerations suggested by the derived model and hence by the shear beam theory for the cases analyzed are less than one might expect considering the simplification to the problem inherent in the theory.

As indicated by Fig. 14, 15, and 16, comparisons are shown for rock accelerations up to 0.3 g. For higher rock accelerations for sites near the zone of energy release, the model would predict attenuation of rock motion for stiff and other conditions which is consistent with the extension of the recorded data base given in Ref. 20. However, as indicated earlier, near fault motions may be primarily controlled by source mechanism. The physical phenomenon involved may be quite different from simply a vertical propagation of shear wave. The validity of the one dimensional shear model has been judged based on comparison of peak accelerations (or other response parameters) and frequency contents (8).

CONCLUSIONS

An analytical model based on detailed ground response analyses suggests the following.

1. The trend of rock acceleration vs. surface acceleration on different soils for sites greater in distance than about 20 km from zone of energy release and for a magnitude 6.5 earthquake is on the average adequately predicted by the one dimensional shear wave propagation theory, especially for other than stiff sites. Low intensity rock motions are amplified regardless of soil conditions. Amplification decreases with increasing intensity of rock motion. Soft to medium stiff soils and deep cohesionless soils are more

effective in attenuating rock motion. Amplification for low intensity motion in soft to medium stiff soil is more compared to other soils.

2. Application of the derived model to estimate the relationships in Ref. 20 suggests that the shear wave propagation theory may provide a conservative estimate of the surface acceleration for a given rock acceleration. Conservatism in predictions can be anticipated to increase with decreasing site period.

3. Application of the derived model to specific cases and simple analysis suggests that the theoretical response of stiff sites compared to other sites may be more sensitive to assumptions on the stiffness of underlying rock and the character of input rock motion.

4. Based on reported evidence, surface motion for firm sites near the zone of energy release is predominantly influenced by source mechanisms. The shear wave propagation theory may, for some reason, provide satisfactory predictions of surface accelerations for such sites. Significant discrepancies, however, may exist in predicted vs. recorded frequency content of motion.

5. Based on this study, the site period appears to be a useful parameter to characterize the soil stiffness.

ACKNOWLEDGMENTS

The early part of this work was made while the author was with Woodward Clyde Consultants, to whom the author is grateful. The author thanks Dr. Edward Nowatzki for reviewing the paper, Mr. John Portelli for helping with the illustrations, and Mrs. Joanne Sorensen for typing the paper.

REFERENCES

1. Ambraseys, N. N., "A Note on the Response of an Elastic Overburden of Varying Rigidity to an Arbitrary Ground Motion," *Bull. Seis. Soc. Am.* 49 (1959).
2. Bertero, V. V., S. A. Mahin, and R. A. Herrera, "Aseismic Design Implications of Near-Fault San Fernando Earthquake Records," *Int. J. Earthq. Engng. Struct. Dyn.*, Vol. 6, 1978.
3. Dobry, R., R. V. Whitman, and J. M. Roesset, "Soil Properties and the One-Dimensional Theory of Earthquake Amplification," Research Report R71-18, Dept. of Civil Engineering, MIT, Cambridge, Mass., 1971.
4. Dobry, R., I. Oweis, and A. Urzua, "Simplified Procedures for Estimating the Fundamental Period of a Soil Profile," *Bull. Seis. Soc. Am.*, 66, 1976.
5. Donovan, N. C., "Site Response Procedures for Major Buildings," Dames and Moore Publication EE73-1, ASCE National Structural Engineering Meeting, April 1973.

6. Donovan, N. C. and P. B. Matthiesen, "Effects of Site Conditions of Ground Motions during Earthquakes," State-of-the Art Symposium, EERI, San Francisco, Cal., February 1968.
7. Idriss, I. M., and H. B. Seed, "Effect of Local Geologic and Soil Conditions on Damage Potential During Earthquakes," Paper prepared for Presentation at 2nd International Congress of the International Association of Engineering Geology, Sao Paulo, Brazil, August 1974.
8. Idriss, I. M., and Seed, H. B., "An Analysis of Ground Motion during the 1957 San Francisco Earthquake," Bull. Seis. Soc. Am., 58, 1968.
9. International Association of Earthquake Engineering, "Earthquake Resistant Regulations, a World List," I.A.E.E., Tokyo, Japan.
10. McGuire, R. K., "Seismic Design Spectra and Mapping Procedures Using Hazard Analysis Based Directly on Oscillator Response," Int. J. Earthq. Engng. Struct. Dyn., Vol. 5, 1977.
11. Newmark, N. M., J. A. Blume, and K. K. Kapur, "Seismic Design Spectra for Nuclear Power Plants," J. Power Div., ASCE, Vol. 99, 1973.
12. Newmark, N. M., and E. Rosenblueth, "Fundamentals of Earthquake Engineering," Prentice-Hall, Englewood Cliffs, N.J., 1971.
13. Ohsaki, Y., "The Effect of Local Soil Condition upon Earthquake Damage," State-of-the-Art Lecture, Proc., Specialty Sessions on Soil Dynamics, 7th International Conference on Soil Mechanics and Foundation Engineering, Mexico, 1969.
14. Oweis, I., and R. Dobry, "Establishment of Equivalent Linear Model and Site Period of a Soil Profile," presented at the 1st Caribbean Conference on Earthquake Engineering, Port-of-Spain, Trinidad, January 1978.
15. Roessett, J. M., and R. V. Whitman, "Theoretical Background for Amplification Studies," Research Report No. R69-15, Soils Publication No. 231, Dept. of Civil Engineering, MIT, Cambridge, Mass., 1969.
16. Schnabel, P. B., J. Lysmer, and H. B. Seed, "SHAKE: a Computer Program for Earthquake Response Analysis of Horizontally Layered Sites," Earthquake Engineering Research Center, Report No. EERC72-12, Univ. of California, Berkeley, 1972.
17. Scott, R., "A Comparative Study of Strong Ground Motion," Proc. of the 4th European Symposium on Earthquake Engineering, London, September 1972.
18. Seed, H. B., I. M. Idriss, and F. W. Kiefer, "Characteristics of Rock Motions during Earthquakes," Earthquake Engineering Research Center, Report No. EERC68-5, Univ. of California, 1968.
19. Seed, H. B., and I. M. Idriss, "Influence of Soil Conditions on Building Damage Potential during Earthquakes," J. Struct. Div., ASCE, February 1971.

20. Seed, H. B., R. Murarka, J. Lysmer, and I. M. Idriss, "Relationships between Maximum Acceleration, Maximum Velocity, Distance from Source and Local Site Conditions for Moderately Strong Earthquakes," Earthquake Engineering Research Center, Report No. EERC75-17, Univ. of California, Berkeley, 1975.
21. Seed, H. B., C. Ugas, and J. Lysmer, "Site Dependent Spectra for Earthquake-Resistant Design," Earthquake Engineering Research Center, Report No. EERC74-12, Univ. of California, Berkeley, 1974.
22. Seed, H. B., R. V. Whitman, H. Dezfulian, R. Dobry, and I. M. Idriss, "Soil Conditions and Building Damage in 1967 Caracas Earthquake," J. SMFD, ASCE, No. SM8, August 1972.
23. Taylor, P. W., "Discussion: Earthquake Design Formula Considering Local Soil Conditions," J. Struct. Div., ASCE, June 1972.
24. Taylor, P. W., and T. J. Larkin, "Seismic Response of Nonlinear Soil Media," J. Geot. Div., ASCE, No. GT3, March 1978.
25. Tezcan, S. S., "Earthquake Design Formula Considering Local Soil Conditions," J. Struct. Div., ASCE, September 1971.
26. Tezcan, S. S., H. B. Seed, R. V. Whitman, N. Serff, J. T. Christian, H. T. Durgunoglu and M. Yegian, "Resonant Period Effects in the Gediz, Turkey Earthquake of 1970," Int. J. Earthq. Engng. Struct. Dyn., Vol. 5, 1977.
27. Tsai, N. C., and G. W. Housner, "Calculations of Surface Motions of a Layered Half-space," Bull. Seis. Soc. Am., 60, 1970.
28. Uniform Building Code Standards, 1976 Edition.
29. Velera, J. E., and N. Donovan, "Soil Liquefaction, A Review," J. Geot. Div., ASCE, Vol. 103, No. GT6, June 1977.
30. Whitman, R. V., "Geotechnical Engineering Aspects," 1975 Seminar, Geotechnical and Structural Aspects of Earthquake Engineering, ASCE National Capital Section, 1975.

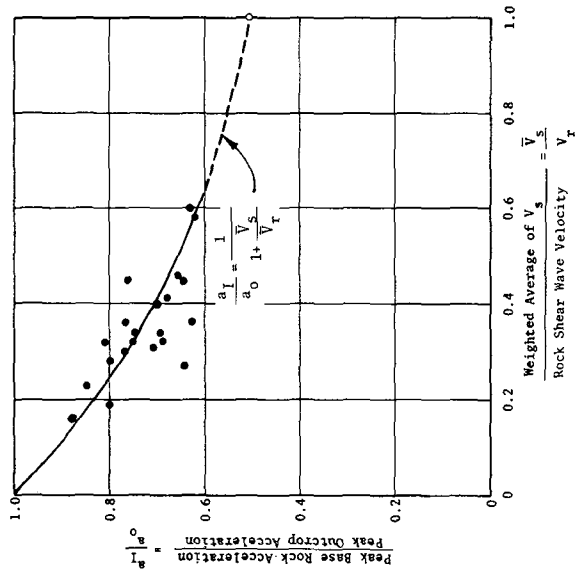


FIGURE 2. REDUCTION OF PEAK ACCELERATION DUE TO ROCK FLEXIBILITY (14)

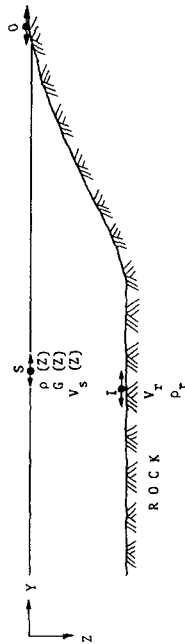


FIGURE 1. GENERALIZED SOIL PROFILE WITH ROCK OUTCROP

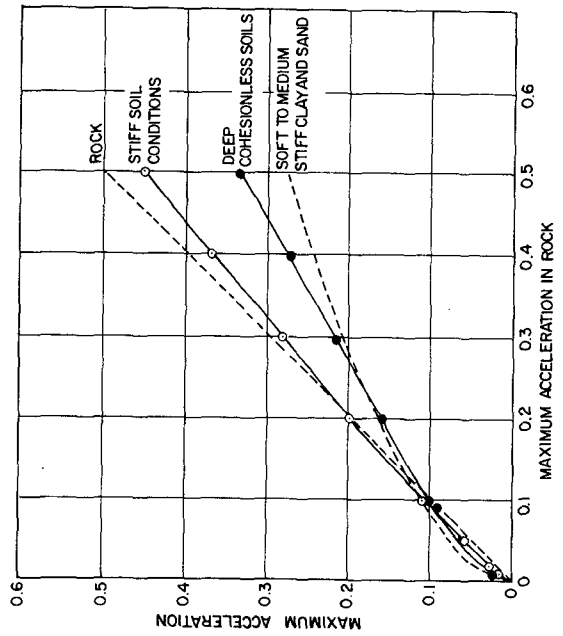


FIGURE 3 - APPROXIMATE RELATIONSHIPS BETWEEN MAXIMUM ACCELERATIONS ON ROCK AND OTHER LOCAL SITE CONDITIONS (20)

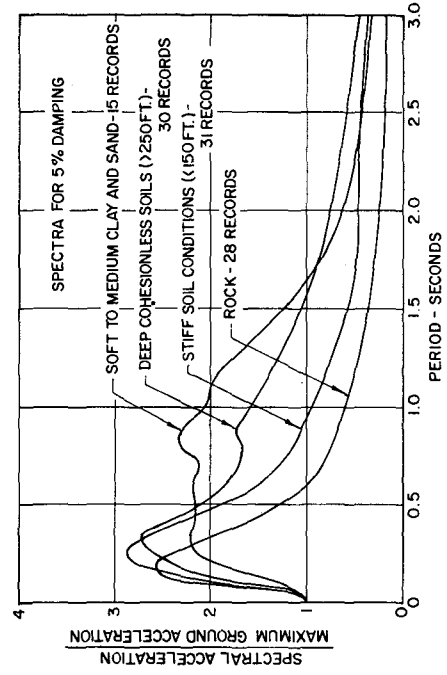


FIGURE 4 - AVERAGE ACCELERATION SPECTRA FOR DIFFERENT SITE CONDITIONS (21)

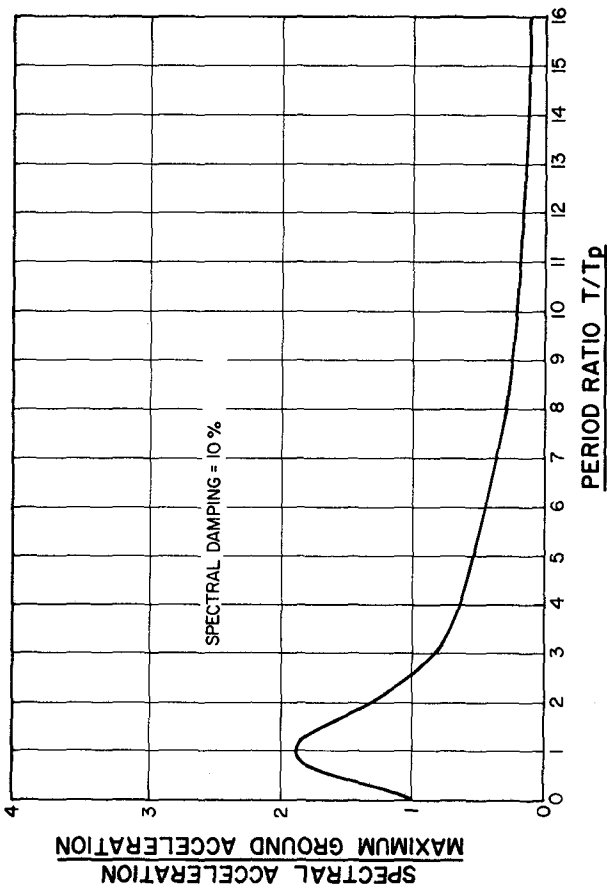


FIGURE 5-AVERAGE ROCK ACCELERATION SPECTRUM USED

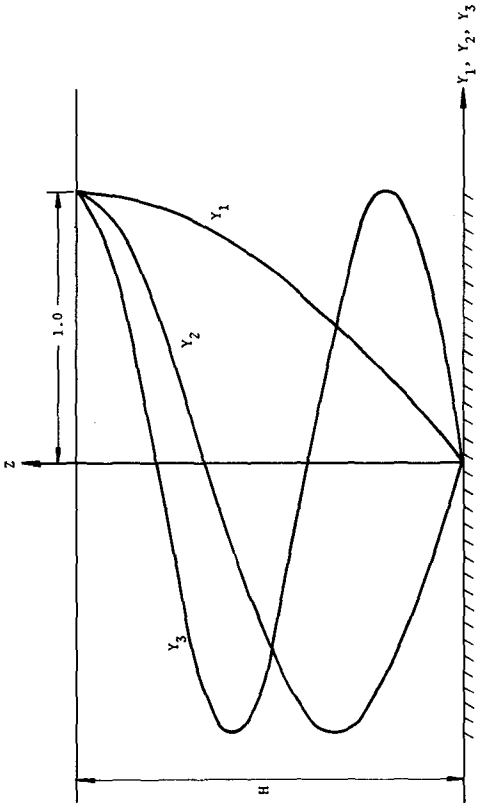


FIGURE 6. MODAL SHAPES FOR UNIFORM LAYER ON ROCK

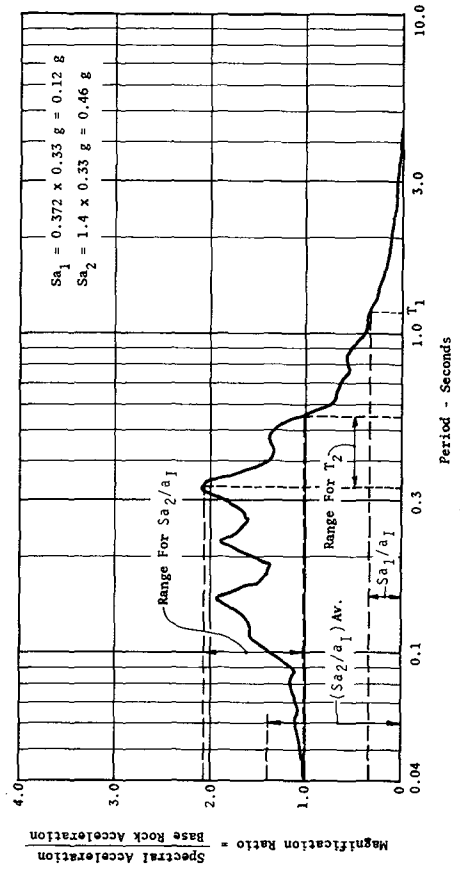
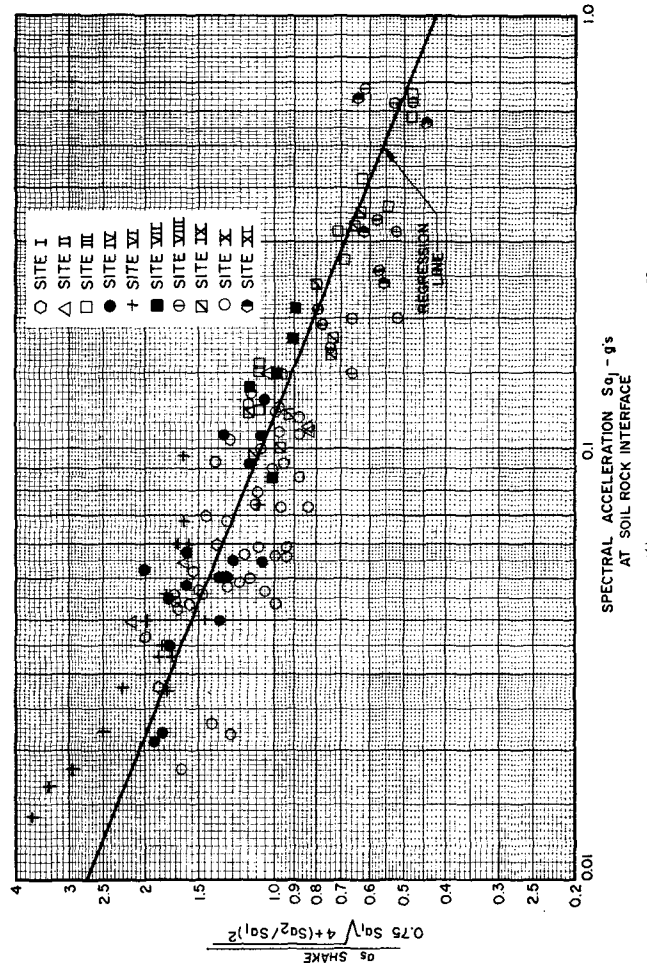


FIGURE 7. SELECTION OF S_{a1} and S_{a2} FOR A TYPICAL CASE (PEAK ACCELERATION $a_1 = 0.33g$; PREDOMINANT PERIOD $T_p = 0.32$ sec.)



SPECTRAL ACCELERATION $S_{a0} - g's$ AT SOIL ROCK INTERFACE

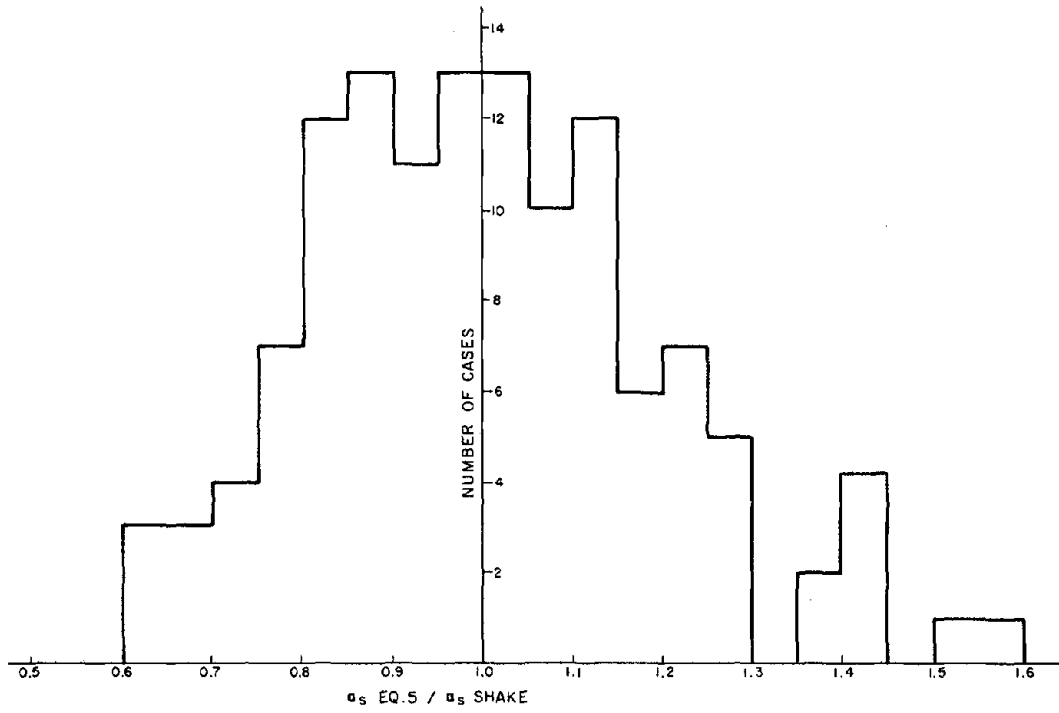


FIGURE 9 - EVALUATION OF EQ. 5

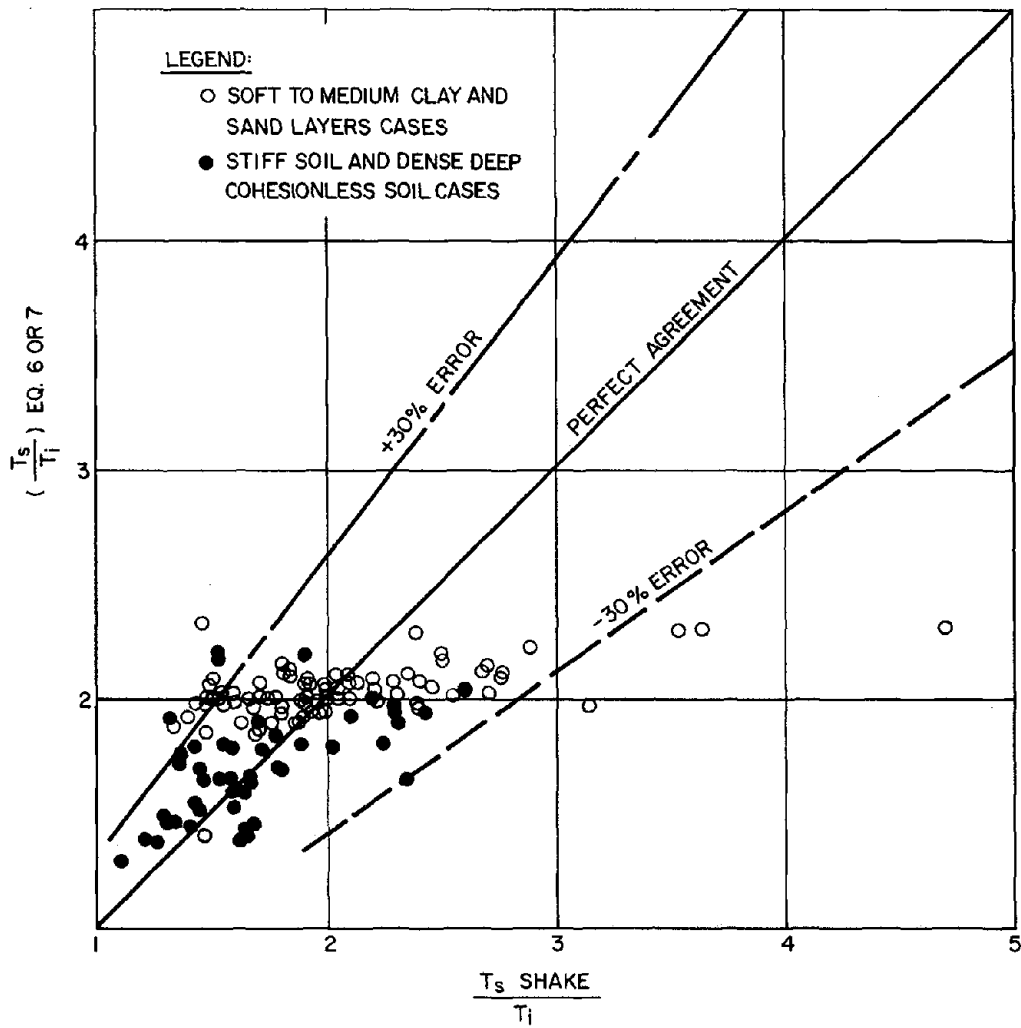


FIGURE 10 - EVALUATION OF EQ. 6 & 7

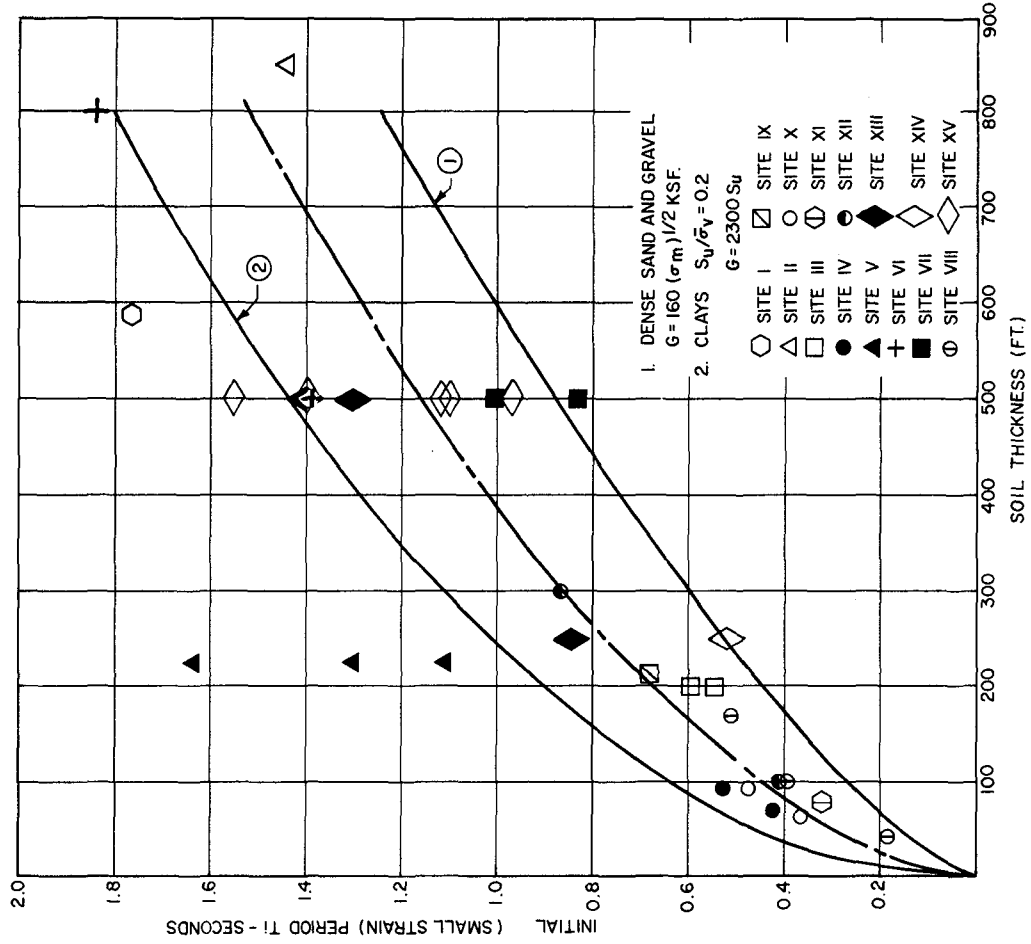


FIGURE 12 - INITIAL PERIOD FOR SITES STUDIED

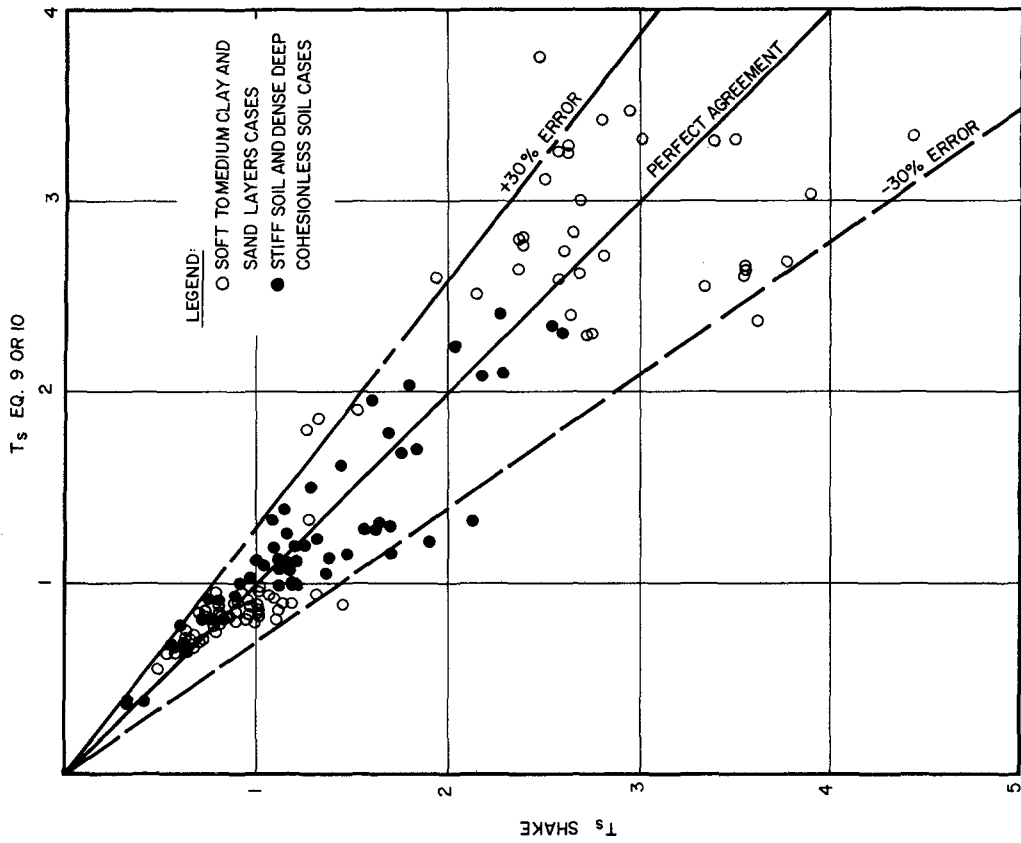


FIGURE 11 - EVALUATION OF EQ. 9 & 10

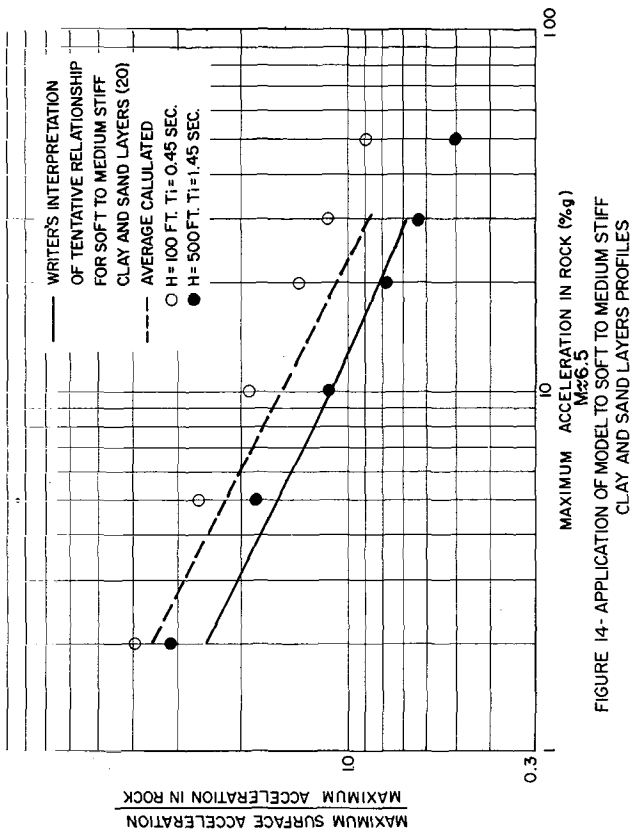


FIGURE 14- APPLICATION OF MODEL TO SOFT TO MEDIUM STIFF CLAY AND SAND LAYERS PROFILES

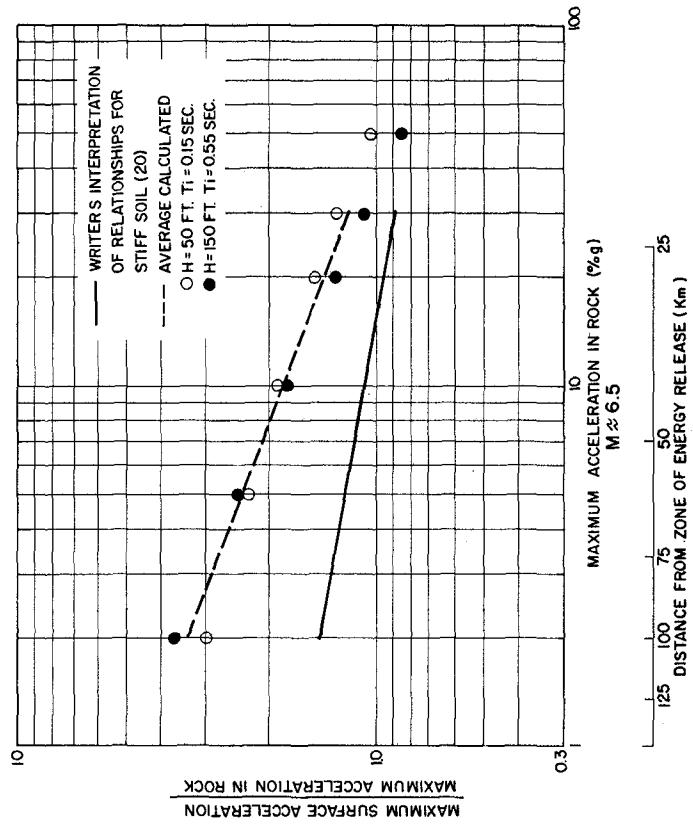


FIGURE 16- APPLICATION OF MODEL TO STIFF SOIL PROFILES

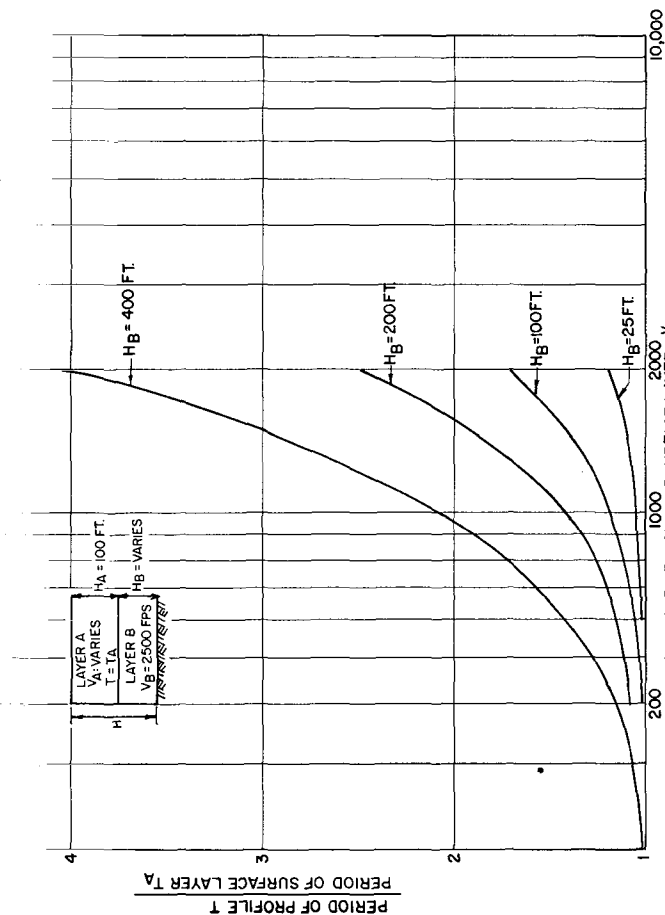


FIGURE 13- EFFECT OF ROCK FLEXIBILITY ON PERIOD CALCULATIONS

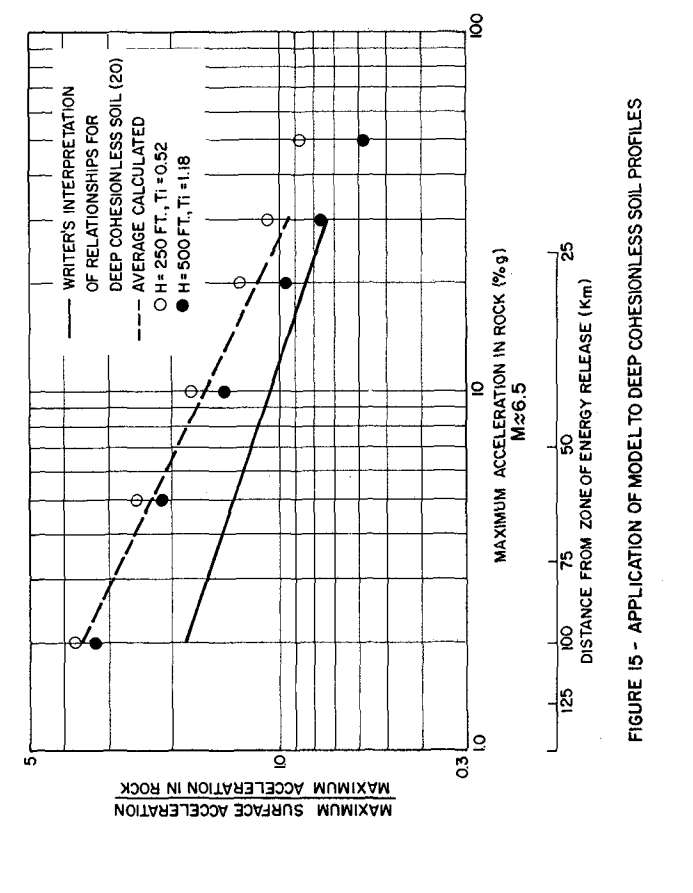


FIGURE 15 - APPLICATION OF MODEL TO DEEP COHESIONLESS SOIL PROFILES

TABLE 1
PERIODS AND PARTICIPATION FACTORS
OF FIRST AND SECOND MODES

SOIL PROFILE	PERIOD FIRST MODE T_1	PARTICIPATION FACTOR FIRST MODE ψ_1	T_2/T_1	ψ_2/ψ_1
Uniform Layer	--	1.28	0.33	0.33
$V = V_0 Z^{0.25}$ (3)	--	--	0.37	--
$V = V_0 Z^{0.5}$ (3)	--	1.60	0.43	0.60
$G = \text{min} Z$	--	--	0.34-0.44	--
45' clay (Union Bay, Seattle) (27)	0.4	1.44-1.47	0.46-0.49	0.42-0.43
5.6 Meters of Alluvium over 19.6 Meters of Dalwium (Rocky Station) (3)	0.4	1.53-1.61	0.46-0.49	0.46-0.48
Site X of this Paper (120' Profile)	0.9	1.46	0.44	0.4
Site II of this Paper	1.6-2.5	1.4	0.35-0.37	0.4-0.54

TABLE 2 - SUMMARY OF CASES STUDIED

SITE NO.	DEPTH TO ROCK H (ft)	NO. OF CASES USED	NO. OF ACCELEROGRAMS USED	RANGE OF ROCK ACCELERATION USED % g	RANGE OF PREDOMINANT PERIODS USED FOR INPUT MOTION	RANGE OF CALCULATED SITE PERIOD T_s BY PROGRAM SHAKE	RANGE OF CALCULATED SURFACE ACCELERATION BY PROGRAM SHAKE % g
I	588	9	3	17-40	0.2-0.48	2.57-3.49	18.9-25.2
II	850	6	4	10-50	0.22-0.64	1.61-2.54	21.0-34.0
III	200	9	3	20-70	0.13-0.5	0.81-2.14	25.4-59.2
IV	145-170	19	3	2-5	0.18-0.96	0.56-1.07	9.1-19.9
V	500-800	18	8	13-50	0.14-0.64	2.07-4.93	10.1-19.5
VI	500	18	8	3-22	0.12-0.64	2.63-4.42	12.3-36.0
VII	500	13	2	30-60	0.25-0.4	1.09-1.68	37.0-85.0
VIII	42-70	3	2	17-65	0.28-0.4	0.28-1.12	20.7-72.0
IX	91-123	35	4	8.33-39	0.15-0.45	0.598-1.64	14.3-50.7
X	100-400	3	2	2-15	0.18-0.64	0.48-1.32	6.0-26.4
XI	250-500	9	3	45-60	0.16	0.56-1.46	13.0-17.1
XII	350	5	2	40-55	0.23-0.3	1.28-3.87	16.3-45.0
XIII	500	5	2	53-85	0.34-0.4	0.88-1.36	29.0-54.0
XIV	500	5	2	28	0.134	1.61-2.6	17.0-21.0

SITE

- I 25' OF LOOSE SAND UNDERLAIN BY 75' OF SOFT TO FIRM CLAY OVERLYING 488' OF MEDIUM DENSE TO DENSE SAND
- II 50' OF STIFF CLAY OVERLYING 800' OF DENSE SAND AND GRAVEL
- III 33' OF SAND AND FIRM CLAY LAYERS OVERLYING 12' OF STIFF SILTY CLAY UNDERLAIN BY 21' OF DENSE CLAYEY SAND OVER 25' OF HARD SILTY CLAY
- IV SOFT FILL UNDERLAIN BY 25 TO 50' OF SOFT CLAY OVER 20'-40' OF DENSE SAND AND 25'-50' OF WEATHERED ROCK
- V 225' OF SOFT TO FIRM CLAY, OCCASIONAL THIN LAYERS OF SANDY SILT
- VI 28' OF SOFT CLAY UNDERLAIN BY 287' OF SAND, SILT AND STIFF CLAY LAYERS OVERLYING 185' TO 485' OF HARD CLAYEY SILT
- VII 8' OF FIRM CLAY UNDERLAIN BY DENSE SANDY GRAVEL DOWN TO ROCK
- VIII SAND AND CLAY LAYERS VARYING IN THICKNESS DOWN TO ROCK
- IX 20' OF LOOSE SANDY FILL OVERLYING SILTY SAND AND SILTY CLAY LAYERS DOWN TO ROCK
- X SOFT FILL 0-25' UNDERLAIN BY 25 TO 50' OF SOFT CLAY OVERLYING 20 TO 40' OF DENSE SAND AND GRAVEL
- XI 21' OF DENSE SANDY FILL AND SILTY SAND OVERLYING 56' OF FIRM TO STIFF SILTY CLAY
- XII STIFF CLAY UNDERLAIN BY DENSE SAND AND GRAVEL
- XIII MEDIUM STIFF CLAY AND FEW SAND LAYERS
- XIV STIFF CLAY AND DENSE SAND LAYERS
- XV DENSE SAND AND GRAVEL

TABLE 3 - APPLICATION OF MODEL TO SPECIFIC CASES

CASE	SOIL THICKNESS (ft)	CLASSIFICATION	ACCELEROGRAM FOR ROCK MOTION USED	T_p	T_i (FIG. 12)	a_i %	T_s (EQ. 9 OR 10)	S_{a1} %	S_{a2} %	a_s (EQ. 5)	a_s DE-TAILED ANALYSIS	a_s RE-CORDED
State Building Site (8)	200	Stiff to deep cohesionless soil	Golden Gate	0.12	0.55	10.3	0.73	3.12	9.0	13.5	11.2	10.5
Southern Pacific Building (8)	285	Soft to medium stiff	Golden Gate	0.12	0.9	8.3	1.44	0.8	2.8	6.8	6.5	5.0
Oakland City Hall (8)	1000	Stiff over hard clay	Golden Gate	0.12	1.5	4.5	1.51	0.4	1.35	4.3	4.4	4.5
Tofas Factory (26)	100	Stiff	Golden Gate	0.35	0.35	4.5	0.43	2.5	8.6	13.4		
	400	Soft to medium	San Onofre of 1971 San Fernando Earthquake	0.12	1.15	2	1.45	2.0	3.0	7.36	6.6	-
Carcas (22)	590	Deep dense sand and gravel	Taft	0.3	1.1	3	1.25	1.8	4.0	8.3	6.5	-

DEEP SHEAR WAVE VELOCITY MEASUREMENT FOR EVALUATION
OF 1-10 SEC SEISMIC INPUT MOTIONS

by

N.Goto^I, Y.Ohta^{II} and H.Kagami^{III}

ABSTRACT

Deep shear wave velocity loggings were planned at two sites in Tokyo area from the earthquake engineering point of view, and actually carried out down to 3500 m and 2300 m temporarily using earthquake observation wells. The purpose of these surveys is to elucidate experimentally the relation of detailed deep site structure to ground motions with 1-10 sec period during an earthquake.

Shear waves are produced by means of ordinary small explosions and specially designed SH wave generator. A set of three component seismometers was installed in a capsule having a clamping device to the borehole wall. Sequent measurements were conducted in different depths to the bottom at intervals of 100-500 m.

The velocity structures completely agree with the known data such as sonic logs, density distributions, geologic sections and so on.

Engineering seismological importance of shear wave measurement for thick soil deposits is stressed upon rough estimations of amplification between ground surface and bedrock.

INTRODUCTION

To know the underground structure near by the seismic observation station is essentially important for determining precise earthquake epicenters and for understanding vibration and propagating characteristics of seismic waves. P wave velocities, from the view point of oil exploration, have been precisely investigated as deep as several kilometers since the last two decades. But, for S wave velocities, which are more important in engineering seismology, the measurable depth has been generally very limited at most 100-200 meters due to their difficulties in experiment.

The seismic strong input motions to the recently spreading large-scale structures such as super high-rise buildings must be affected by deeper underground structure than in the past. This circumstance urges us to elucidate S wave velocities down to at least a few kilometers. In this paper a brief report on S wave velocity measurement of deep soil deposits is introduced, while considering its engineering seismological importance, by use of the deeply drilled earthquake observation well in Tokyo area.

I Research Associate of Architectural Engineering, Hokkaido University, Sapporo, Japan.

II Professor of Architectural Engineering, Hokkaido University, Sapporo, Japan.

III Lecturer of Architectural Engineering Hokkaido University, Sapporo Japan.

EXPERIMENT

(1) Test site and observation well

In Tokyo area wells effective for micro-earthquake observation have recently been constructed by the National Research Center for Disaster Prevention of Japan and in two of them the observations are already started (Fig.1). Details of one of the wells and of equipped instruments for routine geophysical observation are seen in Takahashi and Hamada (1). By temporary use of these wells and by help of research members of the above Research Center we could conduct deep S wave velocity measurement very recently. The wells are of 17.8 cm in diameter with steel casing pipe, cemented to the surrounding medium with water fulfilled. In the well the temperature increases gradually up to 80°C at the bottom, and the pressure is almost in hydrostatic condition.

(2) Experimental scheme and instruments

The experiment was planned essentially by means of a down-hole method, that is, the S (SV,SH) waves generated by explosion were recorded by a set of three-component seismometers in the well. A general scheme of the experiment is seen in Fig.2. For S wave generation two kinds of explosion sources were introduced. One is a simple detonation of small-size dynamite (100g-5kg) which produces more predominant SV waves than SH waves, although they are contaminated by P waves. The other is SH wave generator proposed and designed 10 years ago by Shima and Ohta (2). One set of three-component seismometer of which natural frequency is 4.5 Hz was fixedly packed in a specially made capsule having a clamping device to the borehole wall. This capsule, hung by a wire with signal lines inside, is clamped to the wall at the desired depth. Depth interval is scheduled as short (~100m) in shallower positions, but long (~500m) in deeper positions. A special attention was paid to covering a wide dynamic range by severing one signal to three stepwise gained amplifiers, although employed instruments are of conventional ones. A block diagram of total observation system is depicted in Fig.3.

EXPERIMENT AND RESULT

(1) Experiment at Iwatsuki

This was carried out in 6 days from Nov.8,1976. The observation well at Iwatsuki is as deep as 3500 m, and the boundary between soils and basemental rocks is at around 2800 m in depth. It is needless to say that the SH wave generator is much better for identification of S wave than the simple explosion source, but no researcher knew how deep the S wave signal reaches by use of the man made SH wave generator at that time. So, from the safety point of view SV wave detection by means of ordinary simple detection 10-20 m boreholes was mainly employed and the SH wave generator supplementarily. Measurements were conducted at 16 different depths, including the bottom of the well. Final paste-up and total travel time curves are shown in Fig.4. One may have a doubt about onset of SV waves in the paste-up, but these were obtained while comparing onset in the records by means of the SH wave generator at least at the depth of 1500 m, then extrapolatedly identified. A derived S wave velocities except near-surface of three layers and substratum are 0.44,0.76,1.3,1.6 and 2.5 km/sec from the top to the bottom. The velocity contrast at the soil-rock

boundary is, as expected, very remarkable.

The velocity profile is depicted in Fig.5 in comparison with geophysical data, which clearly satisfies mutual consistency.

(2) Experiment at Shimofusa

Shimofusa experimental site is located 28 km away from Iwatsuki in south-east direction. The experiment at Shimofusa was done in middle February, 1978. It took 8 days to measure S waves at 15 different depths to the bottom (2300 m). In this experiment the SH wave generator was, instead of the simple detonation of dynamite, mainly employed and was very useful. The experimental procedure was essentially the same to that at Iwatsuki. Final paste-up and travel time curves are shown in Fig.6. It is easily recognized that this time paste-up is clearer in identification of S onsets than that obtained at Iwatsuki. Therefore no question is introduced for determining the velocity structure. In Fig.7 the velocity profile essentially composed of four soil layers and substratum is compared with the other known data. Again these are mutually consistent. The largest S wave velocity contrast is between soil deposit and basemental rock. For the upper four layers another interpretation is also reasonable that the S wave velocity increases gradually with increasing depth.

DISCUSSION

(1) Comparison

The S wave velocities between two experimental sites correspond each other in the following manner, excluded the near-surface layers, that is,

Iwatsuki		Shimofusa
0.82 km/sec	0.76 km/sec
1.3 km/sec	1.2 km/sec
1.6 km/sec	?
2.5 km/sec	2.6 km/sec.

Except one point that at Shimofusa there appears no layer with the velocity of 1.6 km/sec, two sites are very similar in their velocity structure (Fig.8). This is clearly explained from the geological evidence that the lower Miocene soils are considerably thick at Iwatsuki but very scarce at Shimofusa. The basemental rock with 2.5-2.6 km/sec are mainly composed of pre-tertiary metamorphic rocks, and these spread widely in and around Tokyo area. This means that we may consider the pertinent substratum as so-called bedrock.

(2) Engineering seismological importance

Recent studies such as by Helmberger and Johnson (3) disclosed the importance of knowledge about the deep ground structure in seismic wave analysis aimed at mechanical solution of seismic source. Research on seismic input motion to current large-scale structures urges to elucidate effects of deep soils upon long-period seismic waves. Fig.9 shows the amplification of S wave with unit amplitude to the top of the bedrocks at the both experimental sites. This simplified assumption and calculation

suggests that deep soil deposit is markedly influential upon wave modification in the period range of 1-10 sec.

CONCLUSION

Deep shear wave velocity loggings were successfully conducted at two sites in Tokyo area, by an elaborated down-hole method under the specified condition that the very deep geophysical observation wells have been constructed. Fortunately other deep wells are planned at a few seismic stations in Tokyo area, where it is expected that more detailed underground structures will be clarified in very near future. In order to perform this, however, some development on SH wave generator should precede, since the 2-3 km in depth is the upper limit of clean onset of the S wave signal. By continuing this series experiments, deep underground structures in Tokyo area will be disclosed. This is nothing but to evaluate deep soils effect upon long period seismic input motions.

Finally the writers express their sincere thanks to many researchers who kindly help us at the experiments. They are Drs. H.Takahashi, F.Yamamizu and S.Kurihara et al. Thanks are also to Director of National Research Center for Disaster Prevention. Without their guidance and assistance no success was expected.

REFERENCES

- (1) Takahashi, H. and K.Hamada, 1975, Deep-Bore-hole Observation of the Earth's Crust Activities around Tokyo — Introduction of the Iwatsuki Observatory —, Pure and Appl. Geophys., 113, 311-320.
- (2) Shima, E. and Y.Ohta, 1968, Experimental Study on Generation and Propagation of S Waves: I. Designing SH-Wave Generator and Its Field Tests, Bull. Earthq. Inst., 45, 19-31.
- (3) HelMBERGER, D.V. and L.R.Johnson, 1977, Source Parameters of Moderate Size Earthquake and the Importance of Receiver Crustal Structure in Interpreting Observations of Local Earthquakes, Bull. Seism. Soc. Amer., 67, 301-313.

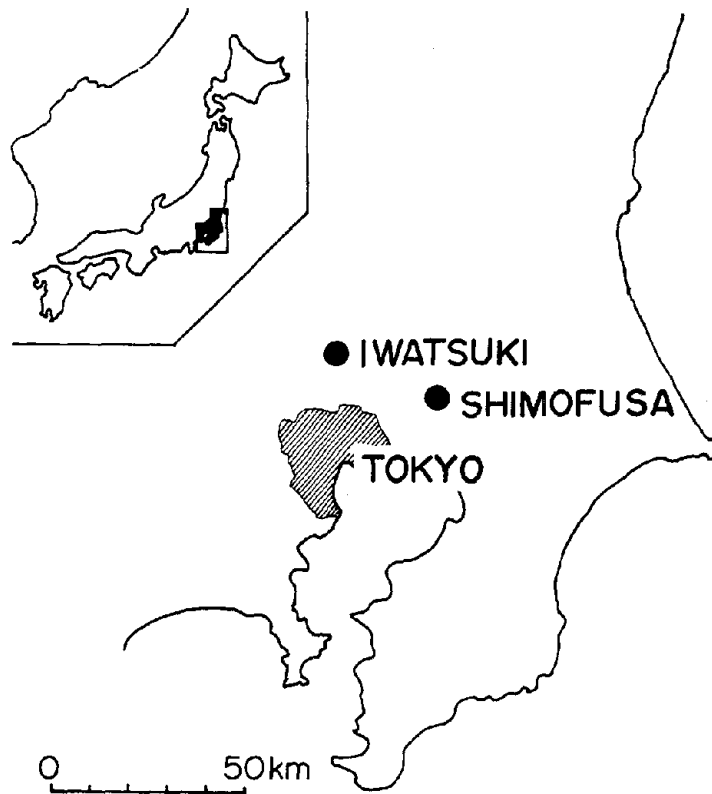


Fig.1 Map of Tokyo area and locations of the experimental sites.

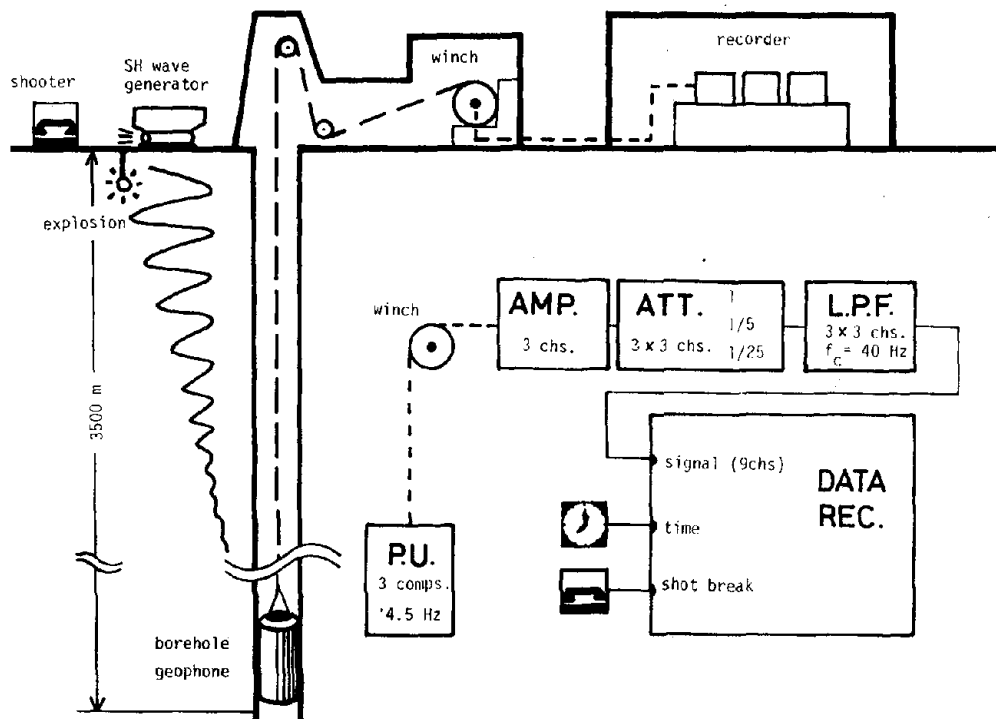


Fig.2 Schematic representation of the experiment for S wave measurement.

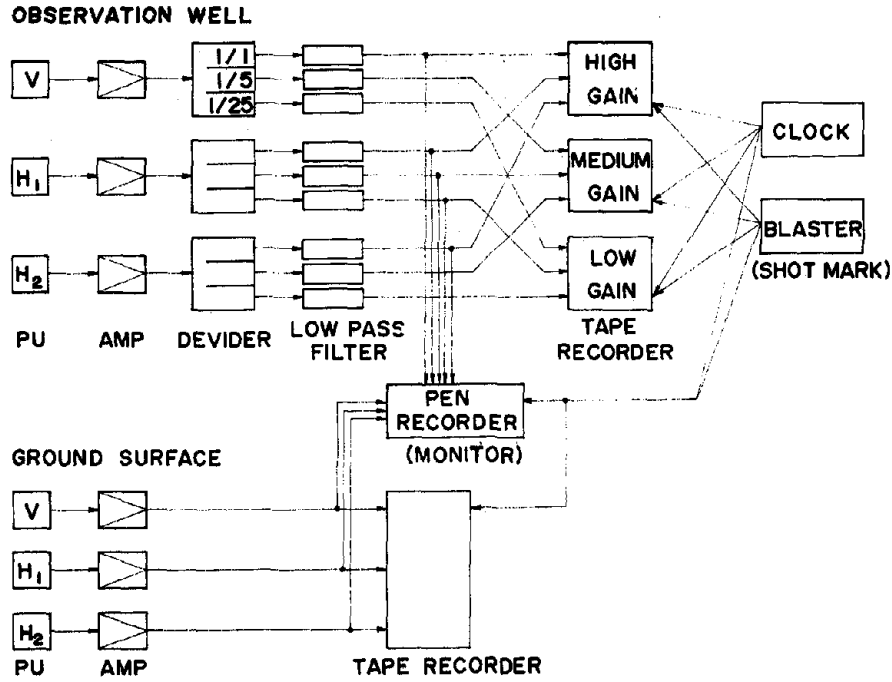


Fig.3 Block diagram of the observation system.

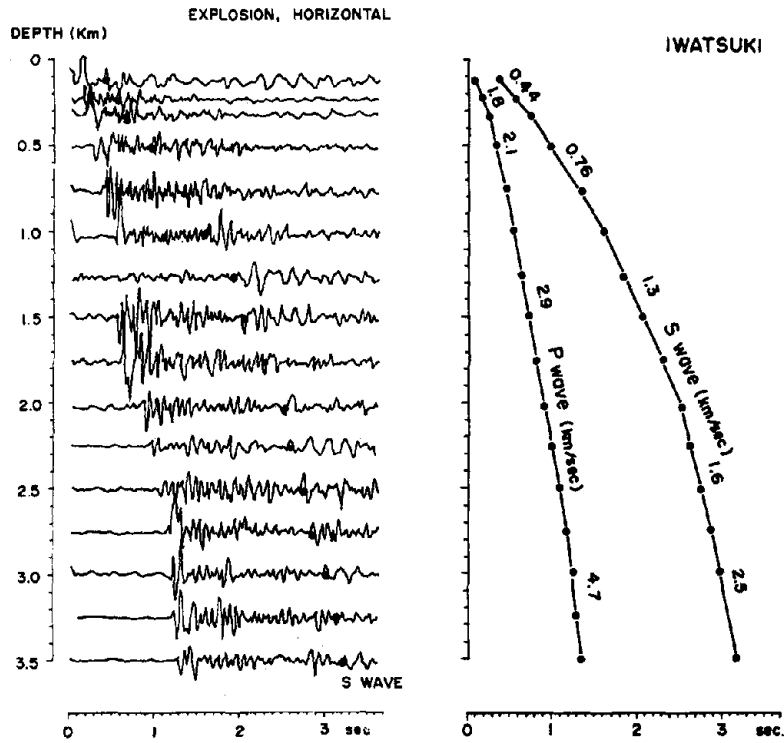


Fig.4 Paste-up of horizontal component records by explosions and travel time—depth curves at Iwatsuki.

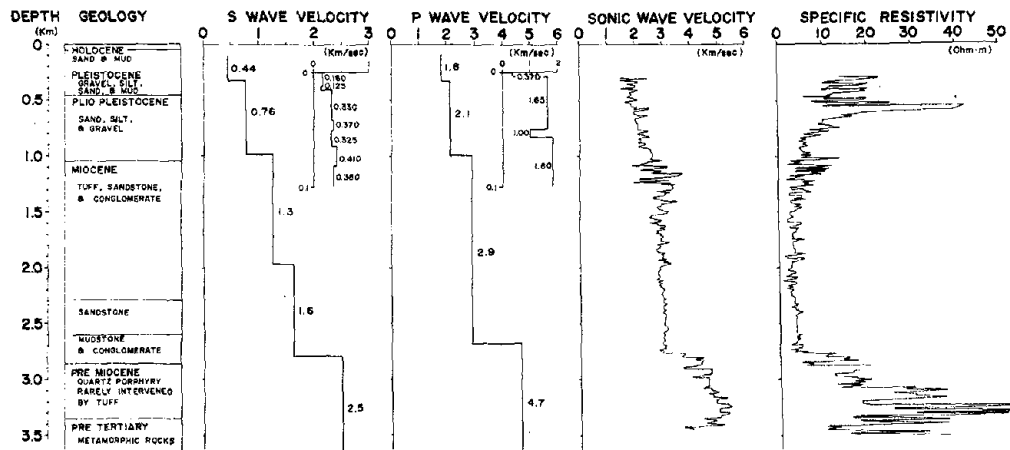


Fig.5 Velocity profile of S and P waves compared with geology, sonic wave velocity, and electric resistivity at Iwatsuki.

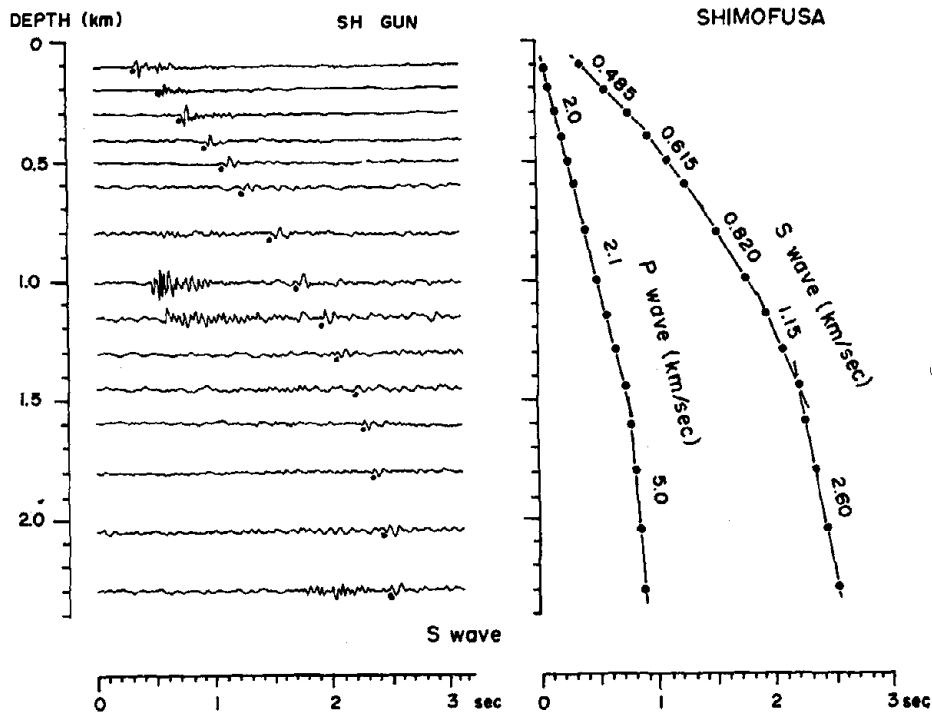


Fig.6 Paste-up of SH wave trains obtained by SH wave generator and travel time —depth curves at Shimofusa.

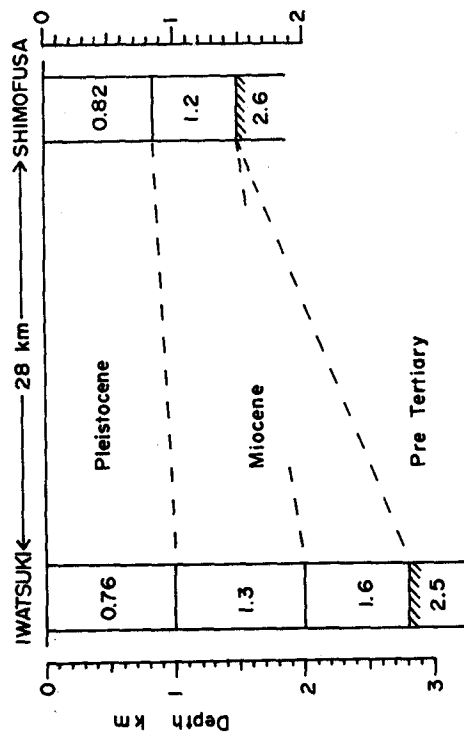


Fig.8 S wave velocity structures at two sites.

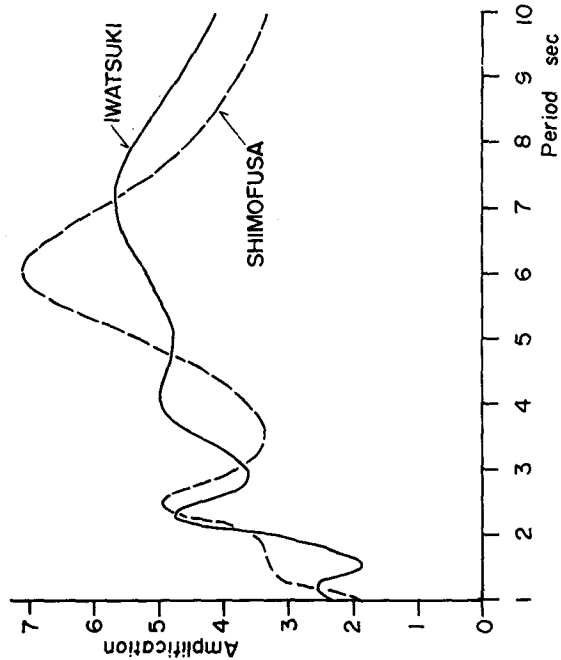


Fig.9 Response of the deep soil structure to normal incident S wave.

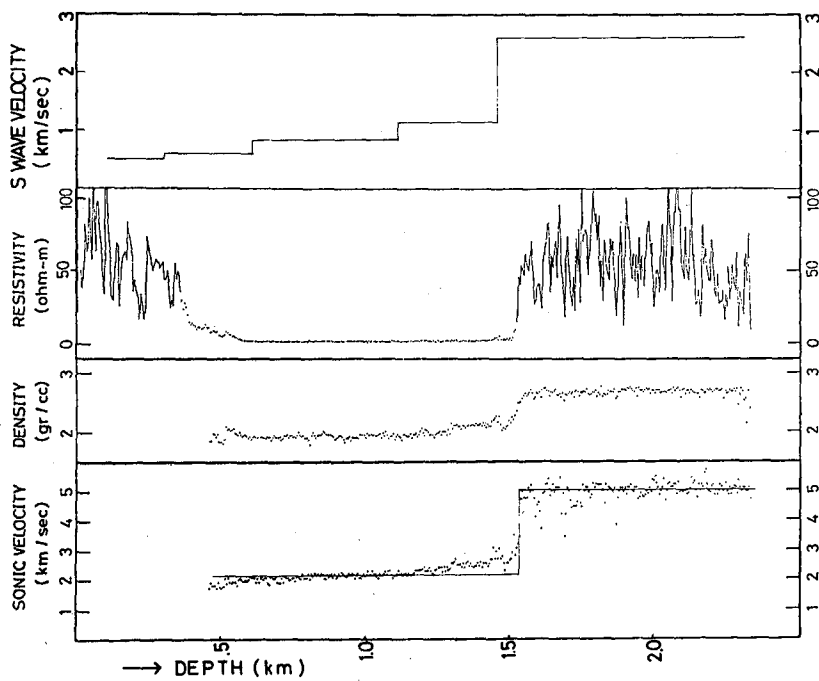


Fig.7 Velocity profile of S wave compared with sonic wave velocity, density and electric resistivity at Shimofusa.

PEAK HORIZONTAL AND VERTICAL ACCELERATIONS,
VELOCITIES, AND DISPLACEMENTS ON DEEP SOIL SITES DURING
MODERATELY STRONG EARTHQUAKES

By

K. Sadigh^I, M. S. Power^{II} and R. R. Youngs^{III}

ABSTRACT

This paper examines the relationships for horizontal and vertical peak ground motion parameters for moderately strong earthquakes in the Western United States using recordings obtained on deep soil sites. Attenuation relationships for peak ground motion parameters were derived by linear regression analyses using data from recordings obtained during earthquakes in the magnitude (M_L) range 6.3-6.5.

The vertical peak acceleration was found to attenuate at a faster rate than the horizontal peak acceleration. Horizontal and vertical velocities were found to attenuate at about the same rate; similarly, the rate of attenuation was about the same for horizontal and vertical displacements. For both horizontal and vertical components, the ratios of peak velocity to peak acceleration, v/a , were found to increase with distance, while the ratios of ad/v^2 were found to decrease slowly with distance.

INTRODUCTION

The subject of attenuation of earthquake ground motions has received considerable attention in past years, and a large number of attenuation relationships have been developed. The available relationships have incorporated, in varying degrees, the influence of distance, magnitude, and local site conditions on ground motion amplitudes. Most relationships have addressed the attenuation of peak acceleration, but some have also addressed the attenuation of peak velocities and displacements and response spectral values. By far greater attention has been given to horizontal components than to vertical components of ground motions.

The present study has examined the relationships for horizontal and vertical peak ground motion parameters (acceleration, a , velocity, v , and displacement, d) on deep soil sites for moderately strong earthquakes in the Western United States. In addition, the frequently-used ratios of the ground motion parameters (ie v/a , ad/v^2) have also been examined.

I Associate, Woodward-Clyde Consultants, San Francisco, CA.
II Associate, Woodward-Clyde Consultants, San Francisco, CA.
III Senior Staff Engineer, Woodward-Clyde Consultants,
San Francisco, CA.

DATA BASE

The data set used in deriving attenuation relationships consists of two horizontal components and one vertical component from each of 34 strong motion records. The records were obtained during 11 earthquakes in the magnitude (M_L) range 6.3 - 6.5 at 19 recording stations with site conditions classified as deep soil sites. The list of records used in the analyses is contained in Table 1. The recordings were obtained at source distances varying from about 10km to 200km, and the data are fairly uniformly distributed within this distance range. All the records are from shallow-focus earthquakes (focal depths less than 20km).

For this study, deep soil sites were defined as having more than 200 feet of soil above rock. Information on subsurface conditions was obtained from References (3, 5, 10 and 11).

The definition of distance used in the study is the closest inclined distance from the recording station to a horizontal line on the fault rupture surface that passes through the approximate center of energy release. In general, sufficient information was available on the depth, lateral extent, and geometry of faulting to estimate this distance. However, for records at some stations, particularly the northern California stations at Eureka and Ferndale, this distance is undefined. In these cases, hypocentral distance was used.

To the extent possible with available data, recordings from a variety of earthquakes (total number of 11) were represented in the data set. Still, almost one-half of the records used were obtained during the 1971 San Fernando Earthquake ($M_L = 6.4$).

All data on peak accelerations, velocities and displacements were obtained from the California Institute of Technology (C.I.T.) processed records (1 and 2). Peak accelerations were obtained from C.I.T. Volume I (1) and peak velocities and displacements from C.I.T. Volume II (2).

DATA ANALYSIS PROCEDURES

Attenuation relationships were derived through least-squares regression analyses. The following form of regression equation was used:

$$y = \alpha (D+C)^\beta \epsilon$$

where y is a , v , or d ; D is the source-to-site distance in km; α and β are regression coefficients, and ϵ is a random error term.

The parameter C is essentially a normalizing parameter for distance.

The studies by Sadigh et al (9) and Idriss and Power (4) indicated that for magnitude $M_L \approx 6.5$, a value of C equal to 20 is appropriate. This value of C was used in the present analyses.

The regression analyses provided estimates of the regression coefficients α and β as well as estimates (s^2) of the variance (σ^2) about

the regression (where s is the estimate of the standard error of prediction in $\ln y$). The attenuation relationship for median values is:

$$\hat{y} = \alpha (D+20)^\beta \quad (\text{median})$$

from which the mean and the 84th-percentile (corresponding to the median plus one standard deviation) relationships were obtained as:

$$\bar{y} = \hat{y} e^{s^2/2} = \alpha e^{s^2/2} (D+20)^\beta = \bar{\alpha} (D+20)^\beta \quad (\text{mean})$$

$$y = \hat{y} e^s \quad (84\text{th-percentile})$$

RESULTS AND DISCUSSION

Regression coefficients and standard deviations obtained from the analyses are tabulated below.

<u>Parameter</u>	<u>$\bar{\alpha}$</u>	<u>β</u>	<u>s</u>
$a_{\text{horiz}}(g's)$	76.5	-1.6	0.45
$v_{\text{horiz}}(\text{cm/sec})$	3140	-1.3	0.41
$d_{\text{horiz}}(\text{cm})$	810	-1.1	0.50
$a_{\text{vert}}(g's)$	232	-2.0	0.35
$v_{\text{vert}}(\text{cm/sec})$	2340	-1.4	0.47
$d_{\text{vert}}(\text{cm})$	265	-1.0	0.53

The mean and 84th-percentile attenuation curves derived from the regression results, along with the data points, are presented in Figures 1 through 6. Figures 1, 2, and 3 show the results for horizontal peak acceleration, peak velocity, and peak displacement, respectively, whereas Figures 4, 5, and 6 show the corresponding results for vertical motions.

Using the mean results from the regression analyses, the ratios of vertical to horizontal peak accelerations, velocities, and displacements can be expressed by:

$$\frac{a_{\text{vert}}}{a_{\text{horiz}}} = 3.0 (D+20)^{-0.4}$$

$$\frac{v_{\text{vert}}}{v_{\text{horiz}}} = 0.75 (D+20)^{-0.1}$$

$$\frac{d_{\text{vert}}}{d_{\text{horiz}}} = 0.33 (D+20)^{0.1}$$

These results indicate that vertical accelerations attenuate more rapidly than horizontal accelerations; however, vertical velocities attenuate at about the same rate as horizontal velocities and similarly for displacements. These trends can also be seen by examining the ratios of mean vertical to horizontal ground motions at selected distances, as summarized below:

Ratio	Source Distance (km)			
	10	30	50	100
$a_{\text{vert}}/a_{\text{horiz}}$	0.77	0.63	0.55	0.44
$v_{\text{vert}}/v_{\text{horiz}}$	0.53	0.51	0.49	0.46
$d_{\text{vert}}/d_{\text{horiz}}$	0.46	0.49	0.50	0.53

The preceding tabulation indicates that, on the average, the ratio of vertical to horizontal peak acceleration decreases from about three-fourths at close distances to about one-half at moderate to far distances, whereas the ratios of vertical to horizontal peak velocity or displacement are about equal to one-half over a large distance range.

It has been observed that vertical peak accelerations are often associated with higher frequency motions than horizontal peak accelerations. Since higher frequency motions attenuate faster than lower frequency motions, the faster attenuation observed for vertical accelerations as compared to horizontal accelerations appears reasonable.

The ratios v/a and ad/v^2 were also examined. Using the mean results of the regression analyses, the ratios can be expressed by:

$$\begin{array}{ll} \underline{v/a \text{ (cm/sec/g)}} & \\ 41 (D+20)^{0.3} & \text{(horizontal)} \\ 10 (D+20)^{0.6} & \text{(vertical)} \\ \\ \underline{ad/v^2} & \\ 6.2 (D+20)^{-0.1} & \text{(horizontal)} \\ 11 (D+20)^{-0.2} & \text{(vertical)} \end{array}$$

These results indicate that v/a increases with distance whereas ad/v^2 decreases slowly with distance. Similar trends for v/a were reported by Idriss and Power (4) for stiff soil sites, by McGuire (7) for rock and soil sites, and by McGuire (6) for combined site conditions. The trend for ad/v^2 to decrease with distance is consistent with the expected variation according to Newmark and Rosenblueth (8) and with results reported by Idriss and Power (4). However, McGuire (6 and 7) found that the ratio ad/v^2 increased slowly with distance.

Using the preceding expressions, typical ratios of v/a and ad/v^2 are:

	Source Distance (km)			
	10	30	50	100
v/a (cm/sec/g)				
horizontal	114	133	147	172
vertical	77	105	128	177
ad/v^2				
horizontal	4.4	4.2	4.1	3.8
vertical	5.6	5.0	4.7	4.2

These results indicate that at close distances, v/a is larger and ad/v^2 is smaller for horizontal than for vertical components; however at far distances, the ratios for horizontal and vertical components approach each other.

SUMMARY AND CONCLUSIONS

This paper has examined the relationships for peak horizontal and vertical accelerations, velocities, and displacements on deep soil sites during moderately strong earthquakes ($M_L = 6.3$ to 6.5 for the data set used). Linear regression analyses were made to develop attenuation relationships for horizontal and vertical components.

It was found that vertical peak accelerations attenuate at a faster rate than horizontal peak accelerations. Consequently, the ratio of a_{vert}/a_{horiz} decreased from about three-fourths at close distances (about 10km) to about one-half at moderate to far distances (about 50 to 100km). On the other hand, horizontal and vertical velocities and displacements were found to attenuate at about the same rate, and the ratios of v_{vert}/v_{horiz} and d_{vert}/d_{horiz} were equal to about one-half.

For both horizontal and vertical components, it was found that the ratios of peak velocity to peak acceleration, v/a , increased with distance, whereas the ratios of ad/v^2 decreased slowly with distance.

REFERENCES

1. California Institute of Technology (1971-1975) "Strong Motion Earthquake Accelerograms, Digitized and Plotted Data, Vol. I - Uncorrected Accelerograms", Pasadena, California.
2. California Institute of Technology (1971-1975) "Strong Motion Earthquake Accelerograms, Digitized and Plotted Data, Vol. II - Corrected Accelerograms and Integrated Ground Velocity and Displacement Curves", Pasadena, California.
3. Grant, W. Paul, Arango, I., and Clayton, D. N. (1978) "Geotechnical Data at Selected Strong Motion Accelerograph Station Sites", Proceedings, Second International Conference on Microzonation for

Safer Construction, Research and Application, San Francisco, California, November 26 - December 1.

4. Idriss, I. M., and Power, M. S. (1978) "Peak Horizontal Accelerations, Velocities and Displacements on Rock and Stiff Soil Sites for Moderately Strong Earthquakes", Submitted for possible publication in the Bulletin of the Seismological Society of America.
5. Maley, R. P., and Cloud, W. K. (1973) "Strong-Motion Accelerograph Records: in San Fernando, California, Earthquake of February 9, 1971", National Oceanic and Atmospheric Administration, Washington, D.C., Vol. 3.
6. McGuire, R. K. (1974) "Seismic Structural Response Risk Analysis, Incorporating Peak Response Regressions on Earthquake Magnitude and Distance", R74-51, Structures Publication 99, School of Engineering, Massachusetts Institute of Technology, Cambridge.
7. McGuire, R. K. (1978) "Seismic Ground Motion Parameter Relations", Journal of the Geotechnical Engineering Division, ASCE, Vol. 104, No. GT4, Proc. Paper 13771, April, pp. 481-490.
8. Newmark, N. M. and Rosenblueth, E. (1971) "Fundamentals of Earthquake Engineering", Prentice-Hall, Inc., Englewood Cliff, New Jersey.
9. Sadigh, K., Idriss, I. M. and Patwardhan, A. S. (1978) "Effect of Site Conditions on Attenuation of Ground Motions for Shallow Earthquakes", paper presented at the 1978 Annual Meeting of the Seismological Society of America, Sparks, Nevada, April.
10. Trifunac, M. D., and Brady, A. G. (1975) "On the Correlation of Seismic Intensity Scales with the Peaks of Recorded Strong Ground Motion", Bulletin of the Seismological Society of America, Vol. 65, No. 1.
11. U. S. Geological Survey (1977) "Western Hemisphere Strong Motion Accelerograph Station List, 1976", Open File Report No. 77-374.

Table 1
LIST OF RECORDS USED IN ANALYSIS

<u>Earthquake (Date)</u>	<u>Magnitude M_L</u>	<u>Recording Station</u>	<u>Source Distance (km)</u>
Long Beach (33-3-10)	6.3	Long Beach Public Util. Bldg.	9
Long Beach (33-3-10)	6.3	CMD Building, Vernon, CA	25
Lower Calif. (34-12-30)	6.5	El Centro, IVID	63
Imperial Valley (40-5-18)	6.4	El Centro, IVID	11
Northwest Calif. (41-2-9)	6.4	Ferndale City Hall	97
Northern Calif. (41-10-3)	6.4	Ferndale City Hall	50
Borrego Valley (42-10-21)	6.5	El Centro, IVID	49
Lower Calif. (54-11-12)	6.3	El Centro, IVID	151
Eureka (54-12-21)	6.5	Eureka Federal Building	26
Eureka (54-12-21)	6.5	Ferndale City Hall	48
Gulf of Calif. (66-8-7)	6.3	El Centro, IVID	149
Borrego Mt. (68-4-8)	6.4	El Centro, IVID	46
Borrego Mt. (68-4-8)	6.4	Orange Co., Eng. Bldg., Santa Ana	164
Borrego Mt. (68-4-8)	6.4	Terminal Is., SCE Plant, Long Beach	195
Borrego Mt. (68-4-8)	6.4	CIT Millikan Lib. Pasadena	203
Borrego Mt. (68-4-8)	6.4	CIT Athenaeum, Pasadena	203

Earthquake (Date)	Table 1 (continued)		Source Distance (km)
	Magnitude M_L	Recording Station	
Borrego Mt. (68-4-8)	6.4	CMD Building Vernon, CA	202
Borrego Mt. (68-4-8)	6.4	Hollywood Storage P.E. Lot	218
San Fernando (71-2-9)	6.4	8244 Orion Blvd. (Holiday Inn)	19
San Fernando (71-2-9)	6.4	Hollywood Storage P.E. Lot	34
San Fernando (71-2-9)	6.4	CMD Building, Vernon, CA	44
San Fernando (71-2-9)	6.4	Orange Co. Eng. Bldg., Santa Ana	80
San Fernando (71-2-9)	6.4	CIT Athenaeum, Pasadena	32
San Fernando (71-2-9)	6.4	CIT Millikan Lib. Pasadena	32
San Fernando (71-2-9)	6.4	900 S. Fremont Ave. Alhambra	36
San Fernando (71-2-9)	6.4	15107 Vanowen St.	22
San Fernando (71-2-9)	6.4	1150 S. Hill St. Occidental Life	38
San Fernando (71-2-9)	6.4	1 City Blvd., Orange	76
San Fernando (71-2-9)	6.4	Long Beach State College	70
San Fernando (71-2-9)	6.4	Long Beach Public Utilities Bldg.	69
San Fernando (71-2-9)	6.4	Terminal Is. SCE Plant, Long Beach	69
San Fernando (71-2-9)	6.4	San Bernadino Hall of Records	97
San Fernando (71-2-9)	6.4	Port Hueneme Naval Lab.	73
San Fernando (71-2-9)	6.4	3440 Univ. Ave., L.A.	41

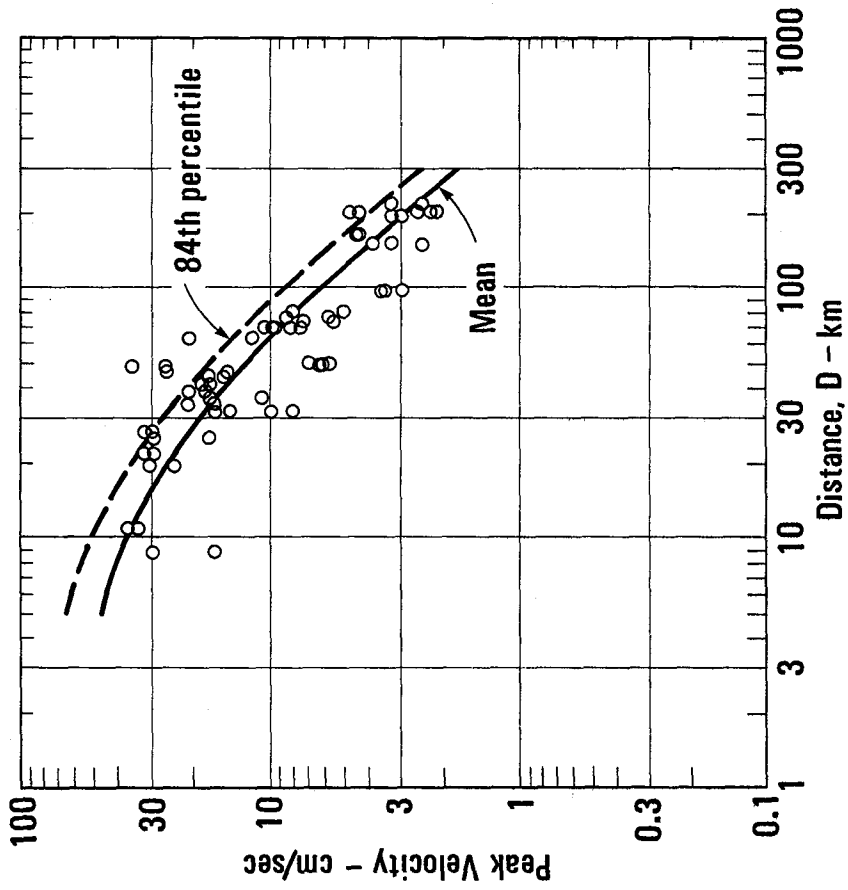


Fig. 2. PEAK HORIZONTAL VELOCITIES ON DEEP SOIL SITES

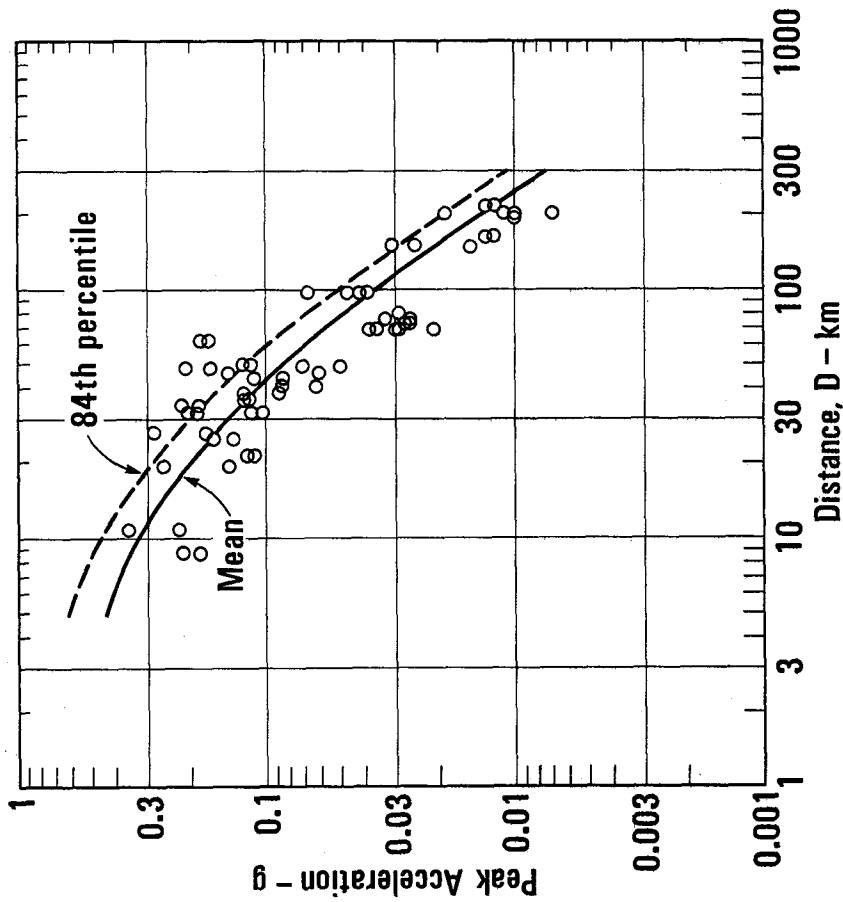


Fig. 1. PEAK HORIZONTAL ACCELERATIONS ON DEEP SOIL SITES

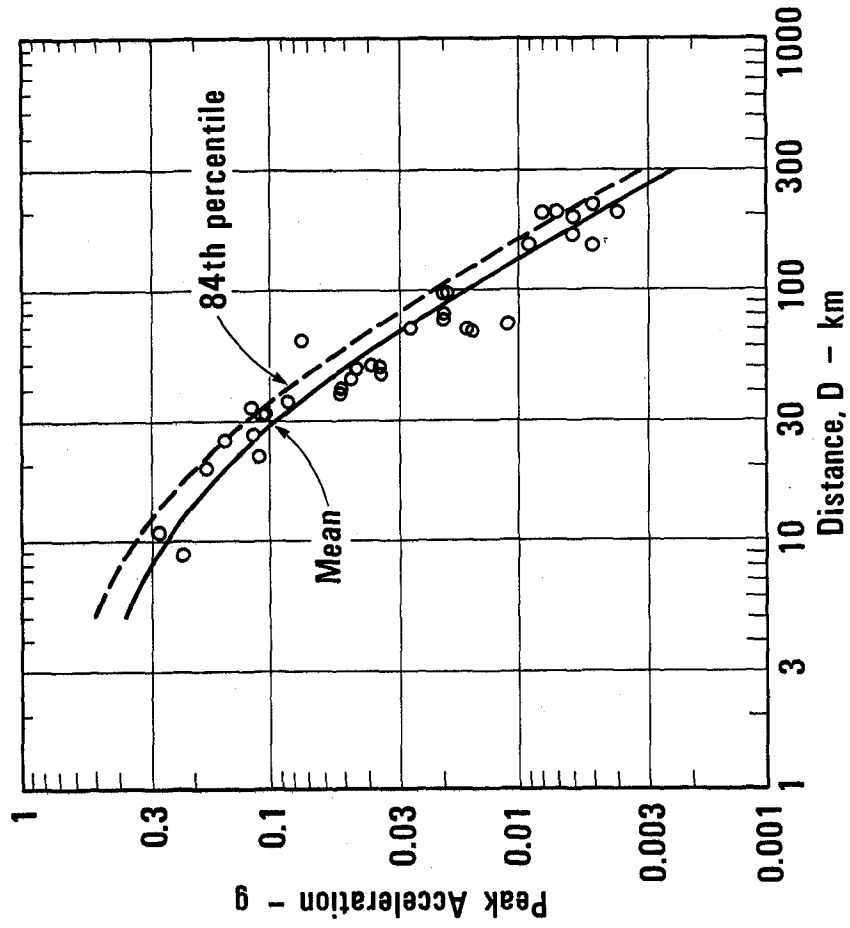


Fig. 4. PEAK VERTICAL ACCELERATIONS ON DEEP SOIL SITES

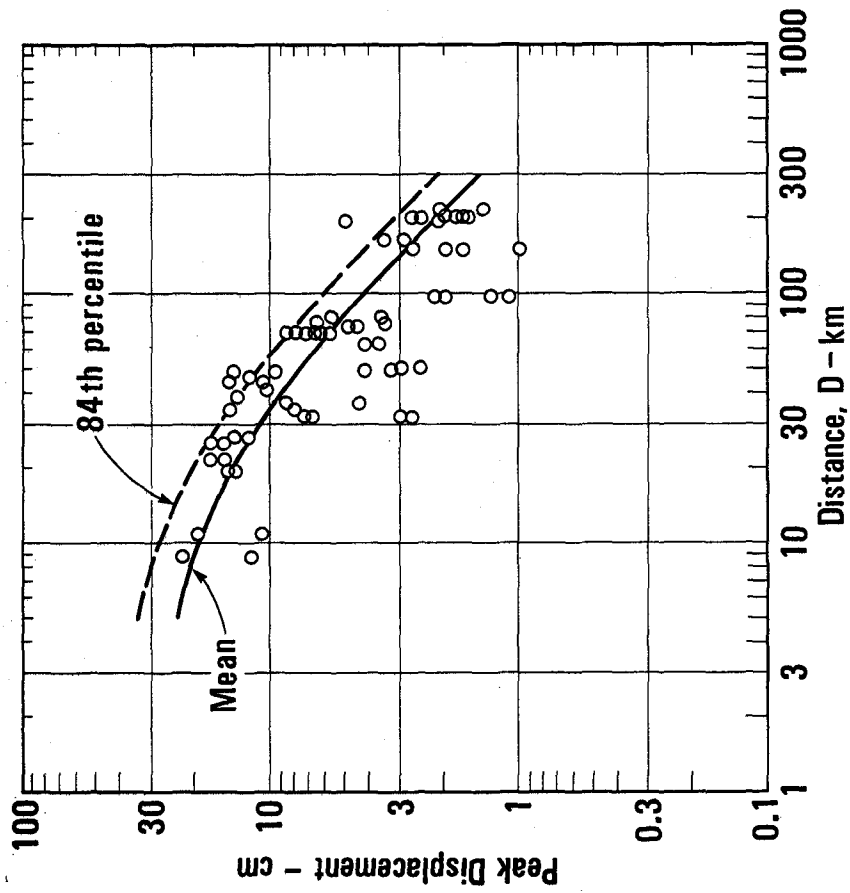


Fig. 3. PEAK HORIZONTAL DISPLACEMENTS ON DEEP SOIL SITES

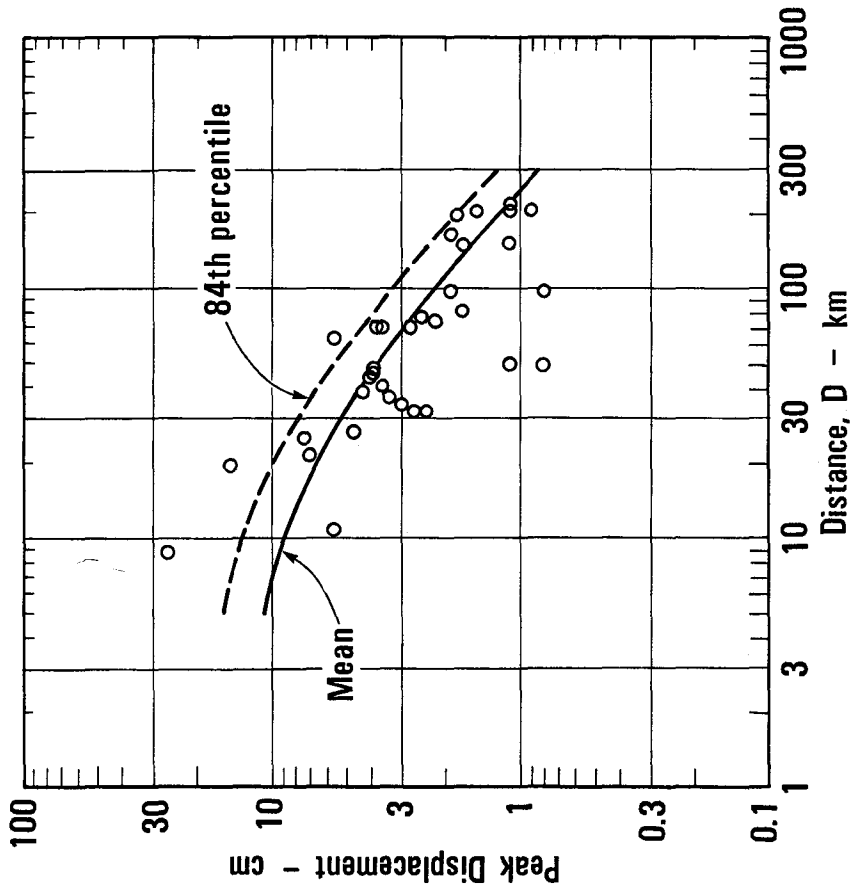


Fig. 6. PEAK VERTICAL DISPLACEMENTS ON DEEP SOIL SITES

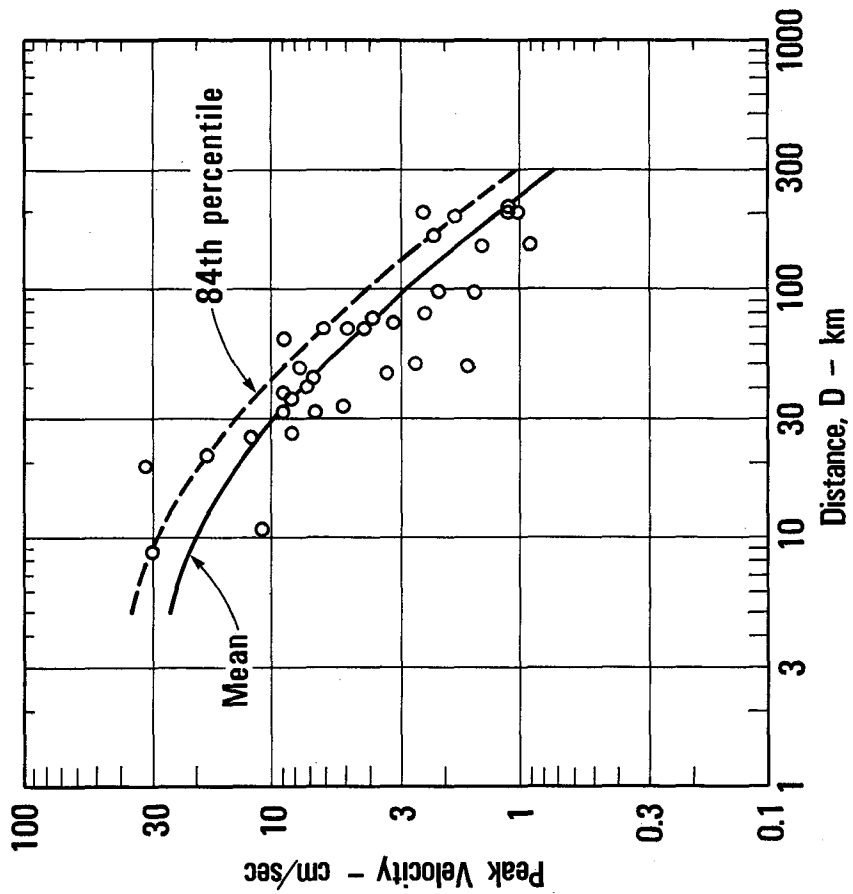


Fig. 5. PEAK VERTICAL VELOCITIES ON DEEP SOIL SITES

INTENTIONALLY BLANK

THEORY OF CONNECTIVITY: APPLICATIONS TO SCATTERING OF
SEISMIC WAVES. I. SH WAVE MOTION

by

F. J. Sabina^I, I. Herrera^{II} and R. England^{III}

ABSTRACT

The purpose of this paper is to present a method, based on the Theory of Connectivity recently developed, to solve numerically the problem of scattering of seismic waves by bounded obstacles of arbitrary shape in an infinite domain, such as a canyon in a half-space. This method reduces the dimension of the problem by one but avoids the introduction of singular integral equations. The results obtained are compared with some known exact solutions for SH wave motion, producing very good agreement. Results for an irregular shaped obstacle are also given. It is observed that, in some cases of a trench with vertical walls, local amplification factors can significantly exceed 100%.

INTRODUCTION

In earthquake engineering and strong-motion seismology, the surface motion at a given site due to incoming seismic waves is of interest. For rough topography this problem may be approached as one of scattering and diffraction of elastic waves by departures from flatness. Owing to its mathematical complexity, it has not been completely solved. There are a few known exact solutions (26, 28). Also some approximate solutions have been obtained by regular (9, 16) and singular perturbations (18, 19). In these the wavelength is taken to be large compared with a characteristic linear dimension of the topography, which is not the case in the present study.

Thus numerical methods are sought for intermediate values of the wavelength. Finite difference (3, 4) and finite element methods (24) have been used with some success. However, when applied to unbounded regions, they use a bounded domain involving "artificial" boundaries that contaminate the solution. The effect may be reduced by considering a larger domain, but this may produce computer storage difficulties. On the other hand, the problem of eliminating the errors introduced by artificial boundaries has only been partially solved (23).

Alternatively, boundary integral equations have been employed for this problem (27). The integral equation has a singularity which must be handled with care. As other boundary methods, this procedure reduces the dimension of the space, but the solution is non-existent or non-unique at certain frequencies (8). In another representation (21), this difficulty is avoided but the equation is still singular.

I Investigador Titular in Applied Mathematics, Instituto de Investigaciones en Matemáticas Aplicadas y en Sistemas, Universidad Nacional Autónoma de México, México, D. F.

II Professor of Applied Mathematics, Instituto de Investigaciones en Matemáticas Aplicadas y en Sistemas, and Instituto de Ingeniería, Universidad Nacional Autónoma de México, México, D. F.

III Investigador Titular in Numerical Analysis, Instituto de Investigaciones en Matemáticas Aplicadas y en Sistemas, Universidad Nacional Autónoma de México, México, D. F.

Other methods have been used: an acoustic approximation valid for saturated soils (22); the discrete wave-number representation of Aki, Larner and Bouchon (1, 5, 6, 7); a collocation method (20). This last one produces an over-determined system of equations which is solved in terms of a generalized matrix inverse, but it also suffers from a lack of uniqueness at certain frequencies.

In this paper the solution of the problem of scattering of a plane harmonic SH wave incident upon a bounded reentrant rough topography in an otherwise flat, traction-free surface, is sought. In the method of solution, the scattered field is represented as a linear combination of known solutions of the wave equation. The coefficients are chosen to minimize the mean-square error in the boundary condition. The development of this approach has been guided by a theory of connectivity recently developed (10, 11), which allows a systematic formulation of boundary methods (12) applicable to many other problems and which leads naturally to the complete system of functions used here for the half-space (13). However, the corresponding system of functions for problems formulated in the whole space has been used extensively in the null-field method of acoustics and electromagnetism (2). Minimization of the mean-square error on the boundary is a standard technique (15), whose implications have not been fully realized until recently. In (17), it is shown that when the mean-square error is minimized on the boundary, the resulting representation converges uniformly to the solution of the problem provided a complete set of functions is chosen, as is the case in the present work.

The procedure here presented reduces the dimension by one without introducing singular integral equations. The theory of connectivity (10, 11, 13) also simplifies the treatment of the problem of scattering by bounded inhomogeneities such as an alluvial valley, as will be shown in another paper.

STATEMENT OF THE PROBLEM

Consider a two-dimensional half-space, $y > 0$ (as in Fig. 1), consisting of

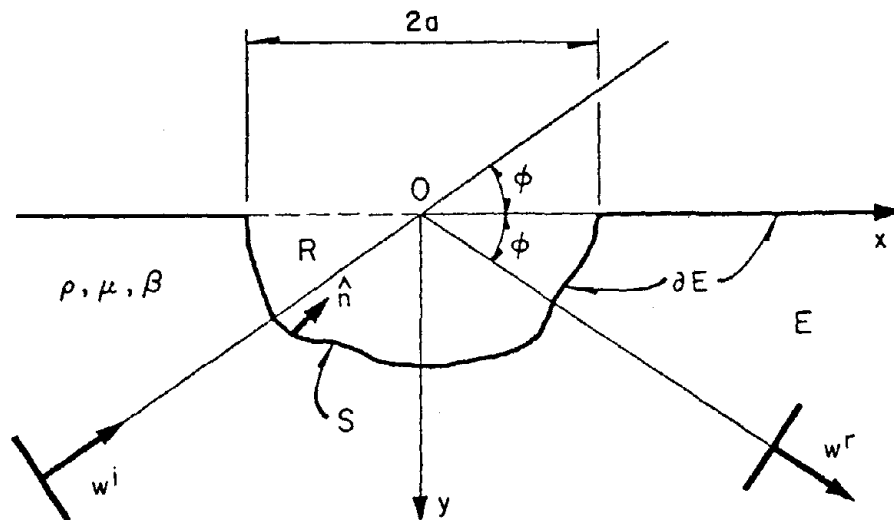


Figure 1. Illustrative topography.

two parts: an unbounded region E enclosing a bounded region R which contains

the origin of coordinates 0. Let the boundary of E be ∂E and the common boundary between R and E be S. The surface S is assumed smooth in the sense of having continuously turning normal vector \hat{n} . The unbounded region E is filled with a linear elastic, homogeneous, isotropic medium of density ρ and rigidity μ ; shear wave velocity is $\beta = (\rho/\mu)^{1/2}$. On the other hand, the bounded region R, having a characteristic horizontal linear dimension $2a$, is empty. The surface ∂E is traction-free.

A state of antiplane shear deformation and harmonic motions in time is considered, so that the only non-zero component of the displacement is $w = w(x,y)\exp(i\omega t)$ in the z (out-of-plane) direction where ω is the circular frequency. Consider a plane harmonic SH wave w^i of unit amplitude incident upon R at an angle ϕ measured with respect to the x -axis (Fig. 1)

$$w^i = \exp[ik(-x \cos \phi + y \sin \phi)] \quad [1]$$

with $k = \omega/\beta$. For convenience the factor $\exp(i\omega t)$ is omitted here and henceforth.

In the absence of the scattering region R, i.e. if the surface is flat, a reflected plane harmonic SH wave

$$w^r = \exp[-ik(x \cos \phi + y \sin \phi)] \quad [2]$$

arises, so that a total field $w^0 = w^i + w^r$ is produced in $y > 0$.

In the presence of R, the scattered wave w produced by R is sought, such that the total field w^t may be written as

$$w^t = w^0 + w \quad \text{in E} . \quad [3]$$

Thus the scattered field satisfies the following boundary value problem

$$\nabla^2 w + k^2 w = 0 \quad \text{in E} , \quad \frac{\partial w}{\partial n} = - \frac{\partial w^0}{\partial n} \quad \text{on } \partial E , \quad [4]$$

and w satisfies Sommerfeld's outward radiation condition at infinity, where $\nabla^2 \equiv \partial^2/\partial x^2 + \partial^2/\partial y^2$ is the Laplacian operator in two dimensions and $\partial/\partial n$ is the derivative in the direction of the outward unit normal \hat{n} to ∂E . It may be observed that the right-hand side of Eq. [4b] is, in general, non-zero only on S, i.e. the common boundary between R and E.

Once w is found, the total field w^t can be determined. In strong-motion seismology it is of interest to find the surface field i.e. w^t on ∂E , and in particular, on S and close to it. A method for doing this is described here.

METHOD OF SOLUTION

Consider the complete system of cylindrical wave functions derived in a previous paper (13):

$$v_p = H_p^{(1)}(kr) \cos p\theta , \quad p = 0, 1, 2, \dots \quad [5]$$

where $H_p^{(1)}(z)$ is Hankel's function of the first kind of order p and (r, θ) are the polar coordinates of the point (x, y) . Note that each v_p is a solution of Eq. [4a], fulfills $\partial v_p / \partial n = 0$ on $y = 0$, and satisfies a Sommerfeld outgoing radiation condition.

Let the N -th approximation to w be

$$w_N(r, \theta) = \sum_{p=0}^N a_p^N v_p(r, \theta) , \quad [6]$$

where the superindex N on the complex coefficients a_p^N has been introduced, to make explicit their dependence on the order of the approximation. In the work here reported, these coefficients were determined by minimizing the mean-square error on the boundary given as

$$\int_S \left| \frac{\partial w^0}{\partial n} + \frac{\partial w^N}{\partial n} \right|^2 ds . \quad [7]$$

By a straightforward derivation, this procedure yields an $(N+1) \times (N+1)$ system of linear algebraic equations

$$B \underline{a} = \underline{c} , \quad [8]$$

where the elements of the matrix B and the vector \underline{c} are

$$b_{pq} = \int_S \frac{\partial \bar{v}_p}{\partial n} \frac{\partial v_q}{\partial n} ds , \quad c_p = - \int_S \frac{\partial \bar{v}_p}{\partial n} \frac{\partial w^0}{\partial n} ds . \quad [9]$$

The bar indicates a complex conjugate. The matrix $B = [b_{pq}]$ is Hermitian and positive definite; a numerically advantageous fact.

Since it is known that the set of functions $\{\partial v_p / \partial n\}$ is complete with respect to all functions that are square-integrable on S , $\partial w_N / \partial n$ converges uniformly in S to $\partial w / \partial n$. A proof in a very similar case is given in (17). Furthermore, $w_N(r, \theta)$ converges uniformly in E to the solution w of Eqs. [4].

Hence, for given N , the system of Eq. [8] is solved for the coefficients a_p^N , and finally Eq. [6] will produce the scattered field at any desired point in E , or, in particular on ∂E .

It is worthwhile observing that when S is a semicircle of radius a , the functions $H_p^{(1)}(kr)$ and their derivatives are constant on S , and the set of basis functions $\{v_p\}$ or $\{\partial v_p / \partial n\}$ is orthogonal on S in the sense that the matrix B is diagonal. The coefficients a_p^N are then independent of N , and Eq. [6] represents simply $N+1$ terms of the trigonometric Fourier series for w at any fixed value of r .

Since the displacement w is a complex function, it is necessary to calculate, as functions of the normalized abscissa x/a , its modulus and its phase

$$|w| = [(\text{Re } w)^2 + (\text{Im } w)^2]^{1/2} , \quad \text{ph}(w) = \tan^{-1}(\text{Im } w / \text{Re } w) . \quad [10]$$

The latter is arbitrarily divided by a normalizing factor 2π , mainly to facilitate comparison with other known solutions. In addition, the appropriate value of \tan^{-1} is chosen to make $\text{ph}(w)$ a continuous function, and a constant is subtracted to make its value zero at $x/a = 0$.

To deal with incident waves of different frequencies for fixed topography, a normalized frequency (or wave number) is introduced $\eta = \omega a / \pi \beta = ka / \pi$.

NUMERICAL CONSIDERATIONS

While evaluation of Eq. [7] would provide a criterion for the accuracy achieved, this has not so far been done. The simpler process of repeating the method for different values of N has been used: it is concluded that

sufficient accuracy has been obtained when two solutions differ on S by less than the required error bound.

In addition to the value of N , it is necessary to fix some integration rule for the evaluation of Eqs. [9]. In view of the factor $\cos p\theta$ in v_p , there are integrands in Eq. [9a] with up to N complete oscillations on S . Numerical experiments have given very poor results when the integration rule used fewer than $2N$ points, confirming a result from (29), reported in (17). Further, by varying the distribution of points, unsatisfactory results have been obtained with fewer than two integration points in each cycle of the factor $\cos^2(N\theta)$ in b_{NN} . This suggests the use of θ as the most suitable parameter in terms of which to write the equation of the curve S . A compound trapezoidal rule, with equal intervals in θ , clearly showed convergence to the correct values of a_p^N as the number of points increased above $2N$. However, to obtain values of a_p^N with 1% accuracy, as many as $10N$ points were needed, using the trapezoidal rule with equal intervals in θ . Nevertheless, the same precision is attainable with fewer points using integration rules of higher order, provided the curve S , $r = r(\theta)$, is sufficiently smooth. In particular, with a compound 9 point Lobatto rule - coefficients from (25) - approximately $3N$ points were sufficient. A further increase in order did not appear productive, presumably because with increasing irregularity of the distribution of integration points, more than $3N$ points are required to maintain two in each cycle for $\cos^2(N\theta)$.

Having evaluated Eqs. [9], it remains to solve Eq. [8]. Since the matrix B is Hermitian and positive definite, an LU factorization without row interchanges should be possible, all the pivots being positive if rounding errors do not accumulate seriously. Further, it is possible to choose a Cholesky type factorization, $U = L^*$, the asterisk indicating the transposed complex conjugate, or to factorize B in the form LDL^* , where L is lower triangular with a unit diagonal, and D is real diagonal. This last form has in fact been used.

Probably the most costly part of the computation is the calculation of the Hankel functions $H_p^{(1)}(kr)$. These have been evaluated using Bessel function routines from the IBM Scientific Subroutine Package (14), slightly modified so as to provide values simultaneously for $p = 0, 1, \dots, N$.

It should be noted that the matrix B does not depend upon the angle of incidence ϕ . Thus a considerable economy of computation is achieved if several angles of incidence are analysed simultaneously for a given geometry and wave number k .

RESULTS

In order to assess the method, a computer program using it has been applied to two cases with known exact solutions: semicylindrical (26) and semielliptical (28) canyons.

The solution for a semicylindrical canyon is given as a Fourier series with coefficients involving Bessel functions (26). The series was reevaluated numerically in the interval $|x/a| < 3$ for $\eta = 0.25$ (0.25) 2.0 and angles of incidence $\phi = 0^\circ$ (30) 90° . Using the same number of terms for both methods (i.e. $N = 19, 26, 33, 36, 38, 41, 43, 45$ respectively), the modulus and phase of the displacement coincided in all the figures printed - a difference of less than 10^{-6} . Essentially the same precision could be

achieved with fewer terms.

For semielliptical canyons, the solution can be derived as a series involving Mathieu functions and the results are given in (28) as graphs of displacement amplitude and phase against normalized distance x/a from -3 to 3, with four angles of incidence 0° , 30° , 60° , 90° . Using the method of this article, semielliptical canyons of aspect ratio $b = 0.7$ have been analysed. ($b =$ ratio of minor axis to major axis. For each value of b , there is both a shallow and a deep canyon). In the shallow case, using $N = 22, 32, 36, 40$ for $\eta = 0.5, 1.0, 1.5, 2.0$ respectively, the differences with (28) were in general less than $0.05 \approx 2.5\%$ at $|x/a| = 0, 1, 2, 3$, which is as good as the precision with which it is possible to read the graphs in (28). For $\eta = 1.5, 2.0$ no results were available for $|x/a| = 3$. For $\eta = 2.0$, the differences were rather higher, rising as high as 0.25 at $|x/a| = 2, \phi = 90^\circ$. Similar results were obtained for the deep case. Using the same values of N for $\eta/b = 0.5, 1.0, 1.5, 2.0$, differences were in general less than 0.05, at $|x/a| = 0, 1, 2, 3$. For $\eta/b = 2.0$ no results were available for $|x/a| = 3$, but the differences rose as high as 0.31 at $|x/a| = 2, \phi = 0^\circ$.

However, by repeating the same cases with smaller values of N , successful convergence towards the solution was clearly observed. Estimated errors for the shallow canyon were less than 0.005 at $|x/a| = 0, 1$, and 0.0005 at $|x/a| = 2, 3$ (where results were available). Results for the deep canyon were even better. The discrepancies with (28) for the larger values of η might be due to the slow convergence of that series solution for $|x/a| \geq 2$ and those values of η . The authors report that more terms of the series are needed when η and $|x/a|$ increase, and the results given here suggest that they did not take sufficiently many in the cases indicated.

It may be concluded that the method presented here is very good for semielliptical canyons of aspect ratio $b > 0.7$ and at least for frequencies $\eta \leq 1.5$ ($\eta/b \leq 1.5$ in deep cases) and probably also for somewhat larger values of η . By way of example, graphs of canyon shape, displacement amplitude and normalized displacement phase against normalized distance x/a , for $b = 0.7$ and $\phi = 0^\circ, 30^\circ, 60^\circ, 90^\circ$ are given in Figs. 2 and 3 for shallow and deep semielliptical canyons respectively.

The validity of the method having been thus demonstrated, it has been applied to a trench with vertical walls $x = \pm a$ and curved floor with equation $r = a[\cos^2\theta + (d^2\cos^2\theta - \sin^2\theta)^2]^{-1/2}$, $|\tan\theta| > d$. In Figs. 4, 5 the form of this trench is shown for $d = \tan 30^\circ$, together with graphs of amplitude and phase of the surface motion w obtained for $\eta = 0.5, 1.0$ ($N=25$ and 36) respectively. Qualitatively similar results to those for semicylindrical and semielliptical canyons were observed. But it is of interest to note that, for waves propagating towards the right-hand side, the amplitude of the scattered wave near the left-hand wall can considerably exceed that of w^0 , the sum of the incident and reflected plane waves. Finally, in this example no limitation on the topography slope is imposed as in methods involving the Rayleigh hypothesis (1, 5, 6, 7). Lack of accuracy of that method for steep slopes was reported in (4, p. 277).

ACKNOWLEDGEMENTS

We wish to thank C. Ruiz de Velasco who wrote the program used to produce the graphs and F.J. Sánchez Sesma for providing his program for the

exact solution for the semi-cylindrical canyon. Also we thank F.J. Sánchez Sesma and E. Rosenblueth for a preprint of their paper.

BIBLIOGRAPHY

1. Aki, K. & Larner, K.L. 1970 Surface Motion of a Layered Medium Having an Irregular Interface Due to Incident Plane SH Waves, J. Geophys. Res. 75, 933-954.
2. Bates, R.H.T. 1975 Analytic Constraints on Electromagnetic Field Computations, IEEE Trans. Microwave Theory Tech. MTT - 23, 605-623.
3. Boore, D.M. 1972 Finite Difference Methods for Seismic Wave Propagation in Heterogeneous Materials, in Methods in Computational Physics, 11, 1-37.
4. Boore, D.M. 1972 A Note on the Effect of Simple Topography on Seismic SH Waves, Bull. Seism. Soc. Am. 62, 275-284.
5. Bouchon, M. 1973 Effect of Topography on Surface Motion, Bull. Seism. Soc. Am. 63, 615-632.
6. Bouchon, M. & Aki, K. 1977 Discrete Wave-Number Representation of Seismic-Source Wave Fields, Bull. Seism. Soc. Am. 67, 259-277.
7. Bouchon, M. & Aki, K. 1977 Near-Field of a Seismic Source in a Layered Medium with Irregular Interfaces, Geophys. J. Roy. astr. Soc. 50, 669-684.
8. Burton, A.J. & Miller, G.F. 1971 The Application of Integral Equation Methods to the Numerical Solution of Some Exterior Boundary-Value Problems, Proc. Roy. Soc. Lond. A. 323, 201-210.
9. Gilbert, F. & Knopoff, L. 1960 Seismic Scattering from Topographic Irregularities, J. Geophys. Res. 65, 3437-3444.
10. Herrera, I. 1977 General Variational Principles Applicable to the Hybrid Element Method, Proc. Natl. Acad. Sci. USA 74, 2595-2597.
11. Herrera, I. 1977 Theory of Connectivity for Formally Symmetric Operators, Proc. Natl. Acad. Sci. USA 74, 4722-4725.
12. Herrera, I. 1978 Theory of Connectivity: A Systematic Formulation of Boundary Element Methods, First International Seminar on Boundary Element Methods, Southampton, England, July 5-7, 1978.
13. Herrera, I. & Sabina, F.J. 1978 Connectivity as an Alternative to Boundary Integral Equations. Construction of bases, Proc. Natl. Acad. Sci. USA 75, 2059-2063.
14. IBM 1970 System/360 Scientific Subroutine Package, Version III. 454 pp.
15. Kantorovich, L.V. & Krylov, V.I. 1964 Approximate Methods of Higher Analysis, N.Y.: Interscience.

16. McIvor, I. 1969 Two-Dimensional Scattering of a Plane Compressional Wave by Surface Imperfections, Bull. Seism. Soc. Am. 59, 1349-1364.
17. Millar, R.F. 1973 The Rayleigh Hypothesis and a Related Least-Squares Solution to Scattering Problems for Periodic Surfaces and Other Scatterers, Radio Science 8, 785-796.
18. Sabina, F.J. & Willis, J.R. 1975 Scattering of SH Waves by a Rough Half-Space of Arbitrary Slope, Geophys. J. Roy. astr. Soc. 42, 685-703.
19. Sabina, F.J. & Willis, J.R. 1977 Scattering of Rayleigh Waves by a Ridge, J. Geophys. 43, 401-419.
20. Sánchez Sesma, F.J. & Rosenblueth, E. 1978 Ground Motion at Canyons of Arbitrary Shape Under Incident SH Waves, Int. J. Earthquake Engng. Struct. Dyn. Submitted.
21. Sills, L.B. 1978 Scattering of Horizontally Polarized Shear Waves by Surface Irregularities, To be published.
22. Singh, S.K. & Sabina, F.J. 1977 Ground-Motion Amplification by Topographic Depressions for Incident P Wave Under Acoustic Approximation, Bull. Seism. Soc. Am. 67, 345-352.
23. Smith, W.D. 1974 A Nonreflecting Plane Boundary for Wave Propagation Problems, J. Comp. Phys. 15, 492-503.
24. Smith, W.D. 1975 The Application of Finite Element Analysis to Body Wave Propagation Problems, Geophys. J. Roy. astr. Soc. 42, 747-768.
25. Stroud, A.H. & Secrest, D. 1966 Gaussian Quadrature Formulas, N.Y.: Prentice-Hall.
26. Trifunac, M.D. 1973 Scattering of Plane SH Waves by a Semi-Cylindrical Canyon, Int. J. Earthquake Engng. Struct. Dyn. 1, 267-281.
27. Wong, H.L. & Jennings, P.C. 1975 Effects of Canyon Topography on Strong Ground Motion, Bull. Seism. Soc. Am. 65, 1239-1257.
28. Wong, H.L. & Trifunac, M.D. 1974 Scattering of Plane SH Waves by a Semi-Elliptical Canyon, Int. J. Earthquake Engng. Struct. Dyn. 3, 157-169.
29. Yasuura, K. & Ikuno, H. 1971 On the Modified Rayleigh Hypothesis and the Mode-Matching Method, International Symposium on Antennas and Propagation, Sendai, Japan, pp. 173-174, Institute of Electronics and Communication Engineers of Japan, Tokyo, Japan.

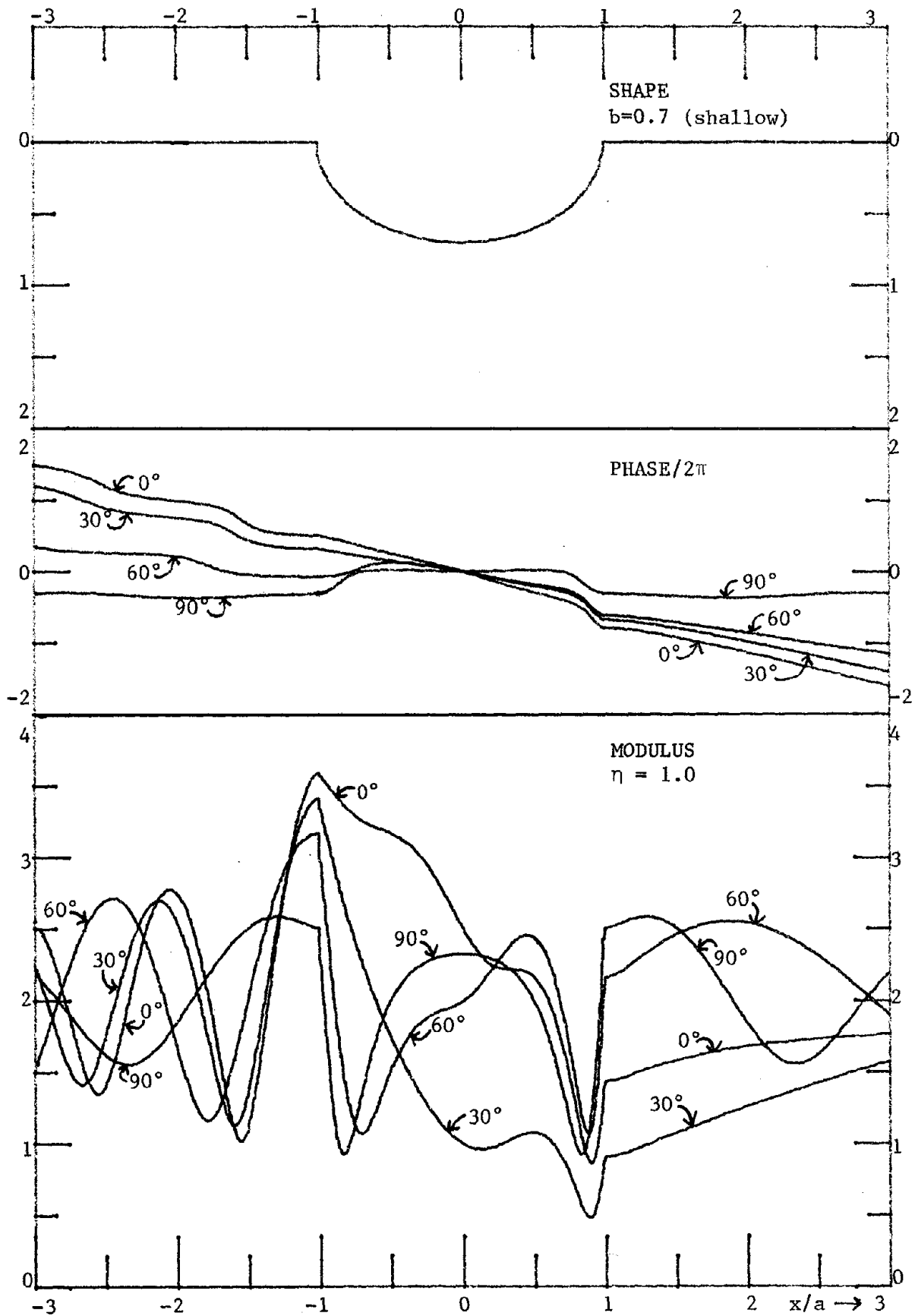


Figure 2. Surface displacement amplitudes and phases for incident SH waves and normalized frequency $\eta=1.0$. Shallow semiellipse of aspect ratio $b=0.7$.

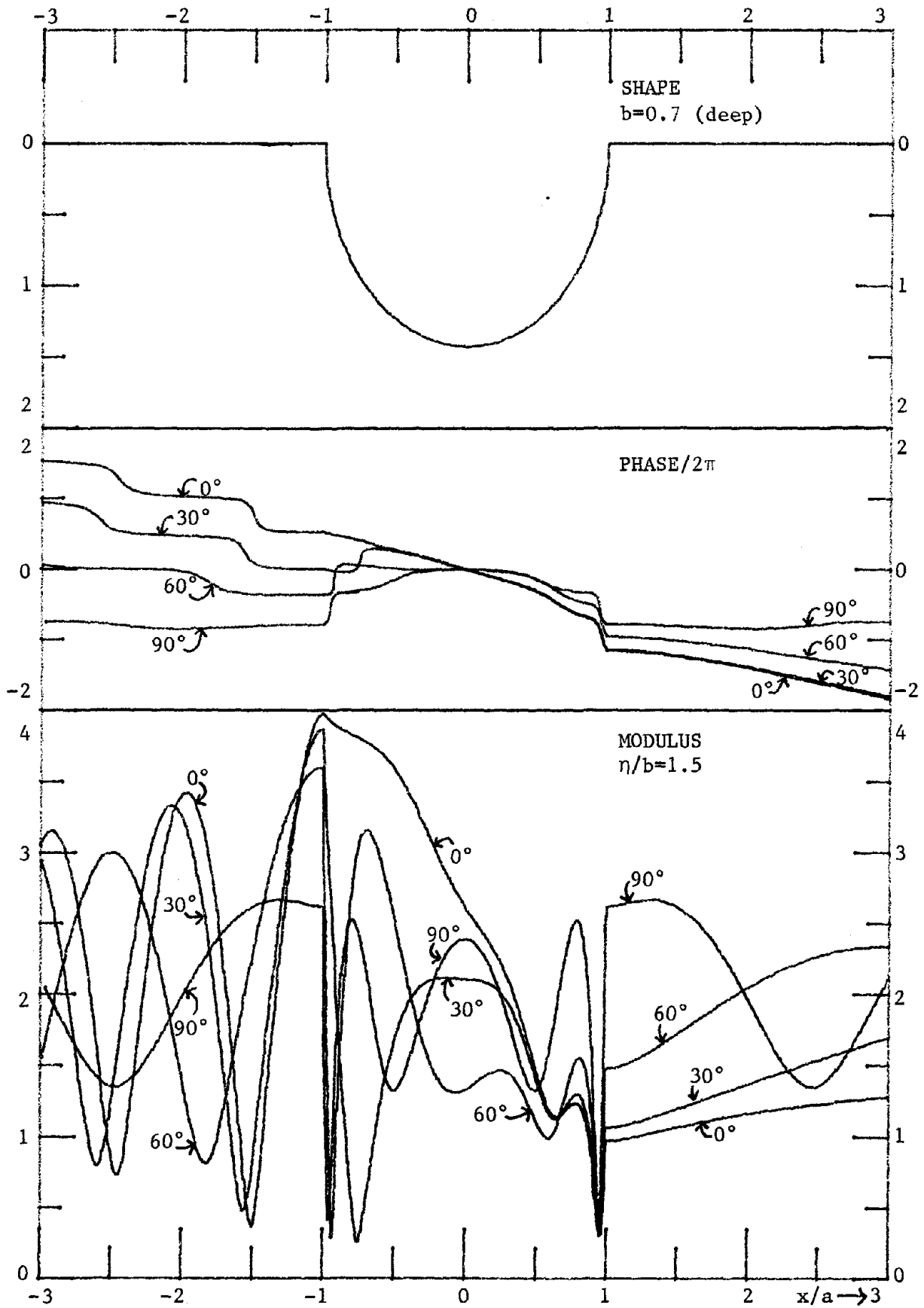


Figure 3. Surface displacement amplitudes and phases for incident SH waves and normalized frequency $\eta/b=1.5$. Deep semiellipse of aspect ratio $b=0.7$.

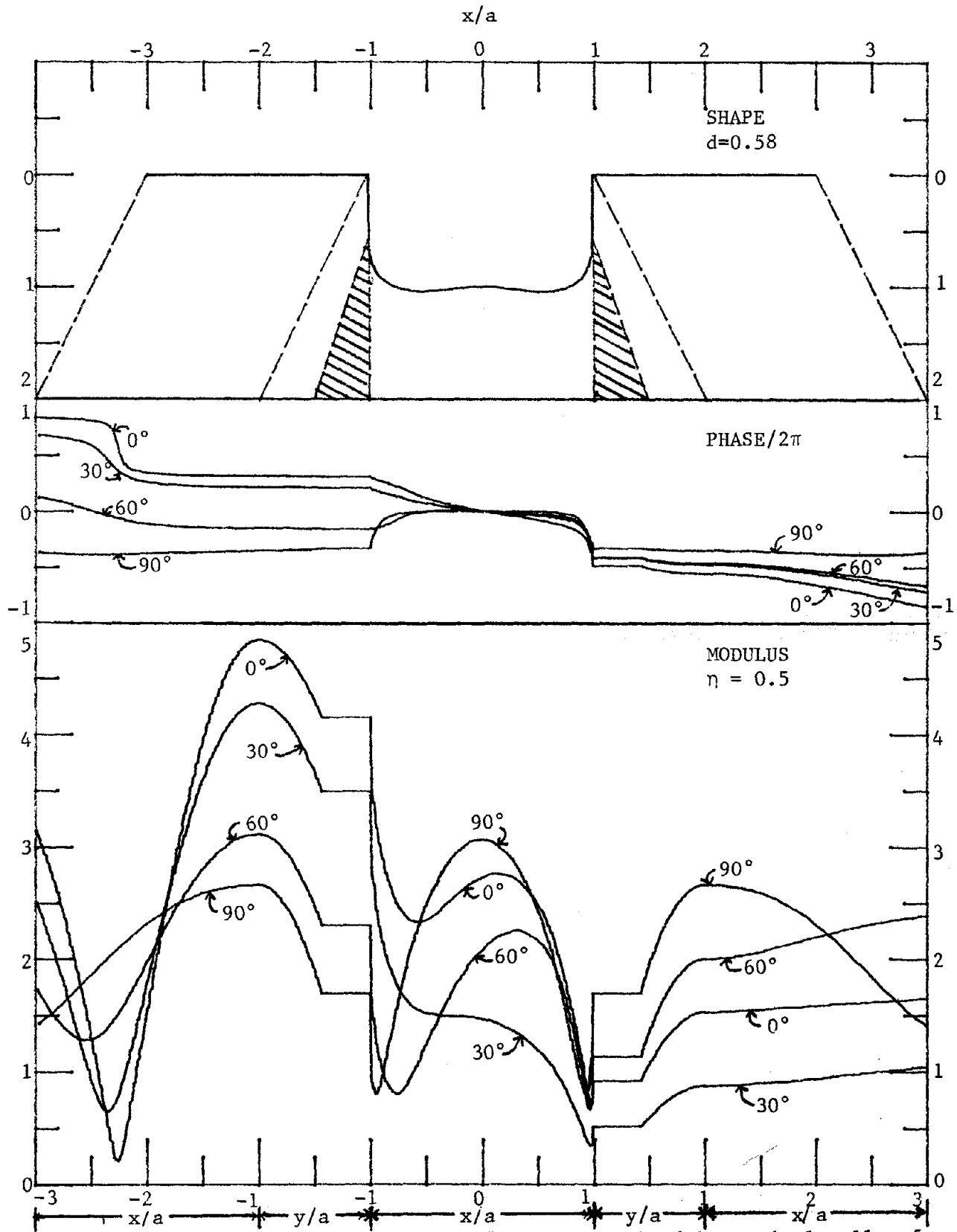


Figure 4. As Fig. 3 but for $\eta=0.5$ and a trench with vertical walls of depth $d=0.58$. The lower horizontal scale includes two intervals $[-1, -1]$, $[1, 1]$ which represent distances y/a (along the vertical wall); the flat part corresponds to the wall-floor intersection point only.

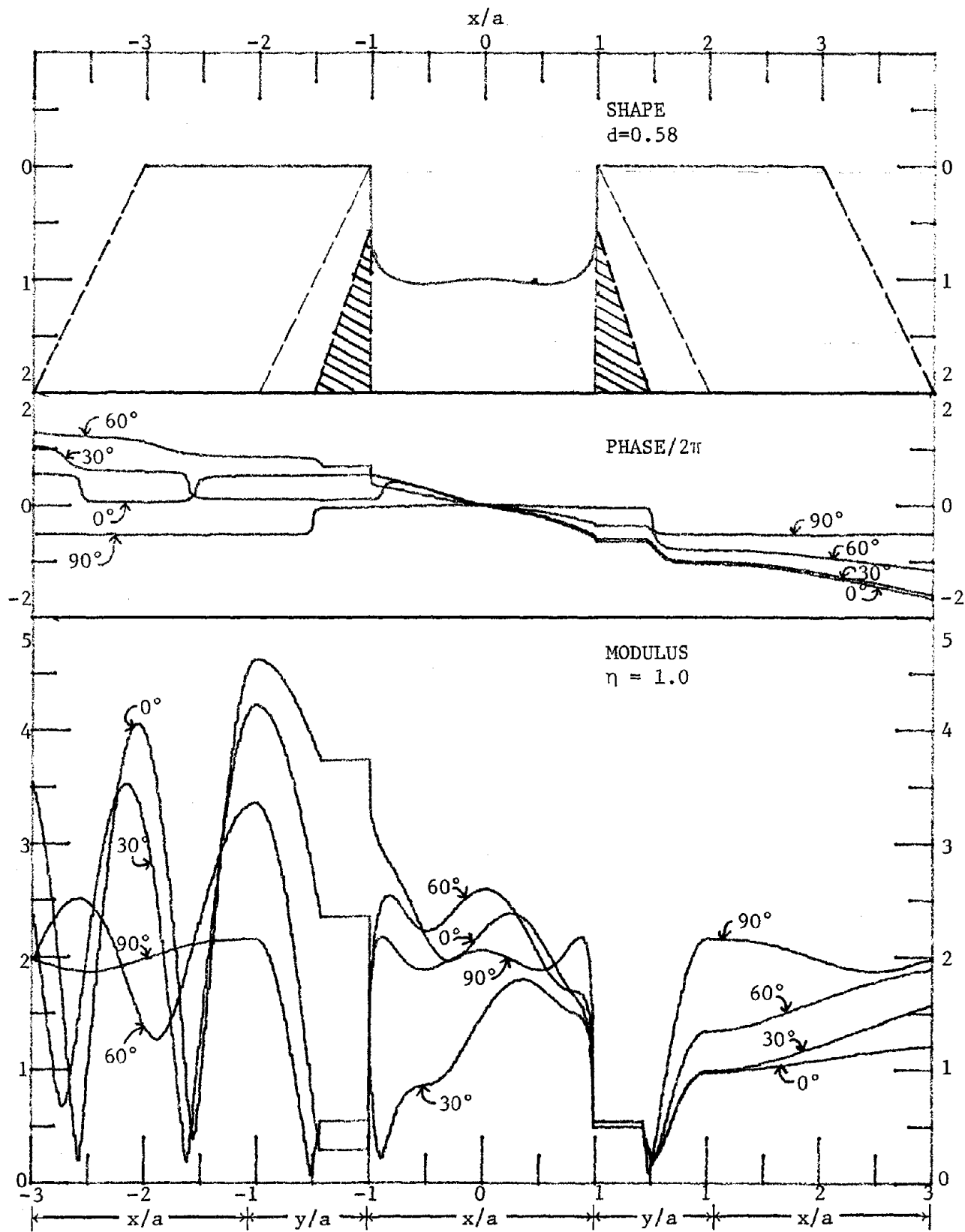


Figure 5. As Fig. 4 but for $\eta=1.0$.

ON ESTIMATION OF STRONG EARTHQUAKE MOTIONS WITH
REGARD TO FAULT RUPTURE

Saburoh MIDORIKAWA^I by
and Hiroyoshi KOBAYASHI^{II}

ABSTRACT

A method for the estimation of the near-field ground motions with regard to the shape and dimension of fault and the direction of rupture has been presented. Authors assumed that the earthquake ground motions in short period range of from 0.1 to 5 second can be regarded as the superposition of the impulses from the small elements of the fault plane. They determined the characteristics of the impulses according to earthquake magnitude, distance from the origin, fault dimension, rupture mode etc. from the empirical relations, and calculated the response spectra of the incident waves from the seismic bedrock by the superposition of these impulses. The results obtained by this calculation showed good agreements with the observed seismic intensities, peak accelerations and spectra of the near-field ground motions in cases of the Kanto Earthquake of 1923 and so on.

INTRODUCTION

One of the main objects in earthquake engineering is to estimate the spectral amplitude of the near-field ground motions. Many empirical formulae of the maximum amplitudes of the ground motions (1),(2) and a few of the spectral amplitudes (3),(4) have been proposed already. However, it is difficult to apply these empirical formulae to the near-field problem, because the used data were limited.

Few seismograms, but many distributions of the seismic intensities in near-field have been observed. From these distributions, it has been pointed out that the intensity of the ground motions reflect the nature of fault rupture strongly.(5) In seismology, the techniques of computing the near-field ground displacements by the dislocation theory have been developed. Though the short-period motions, which are important for engineering purposes, cannot be treated by this theory (6), it is inevitably necessary to introduce the conception of this theory into estimating the near-field ground motions. As the ground motion is regarded as the total sum of the contributions from finite moving sources, the envelope of the ground motion in short period range will be represented as the superposition of the impulses from the finite elements of the fault plane. Authors tried to determine the characteristics of the impulse from the empirical relations, and calculated the envelope of the ground motions.

1. EMPIRICAL FORMULA OF RESPONSE SPECTRA OF INCIDENT WAVES FROM SEISMIC BEDROCK

The spectra of the ground motions observed on the ground surface can be regarded as the product of the spectrum of the incident wave from the

^I Graduate Student, Tokyo Institute of Technology

^{II} Professor of Earthquake Engineering, Tokyo Institute of Technology,
Dr. of Eng.

seismic bedrock by the amplification factor of the ground.(1),(3) The amplification factor of the ground will be approximately equal to that due to the propagation of SH-waves after the many recent studies.(7),(8) Therefore the spectra of the incident waves from the seismic bedrock are to be examined for the estimation of those on the ground surface. Authors tried to correct the empirical formula of the velocity response spectra of the seismic bedrock motion proposed by Kobayashi et al.(3)

At first, the amplification factors of the ground proposed by Kobayashi et al.(3), which were obtained from the stationarity in the response spectra of the earthquake ground motions at the individual strong motion accelerograph site, were compared with those due to the propagation of SH-waves in the layered soil ground as shown in Fig.1. In calculation of the amplification factors due to the propagation of SH-waves, they adopted the upper boundary of the earth's crust, whose shear wave velocity is about 3 km/sec, as the seismic bedrock. On the peak period of the both results at five sites, that is Hachinohe, Kushiro Harbour, J.M.A. Station of Kushiro, Miyako and Hiroo, they got good agreement and it was affirmed that the former reflect the underground structure at the observed site. The average value of the ratios of the latter to the former has no particular periodicity as shown in Fig.2. So they defined the amplification factors of the ground as the product of those by Kobayashi et al. by the average value of ratios.

The velocity response spectra of the incident waves from the seismic bedrock were defined as the quotient of those on the ground surface, which were represented by the two dimensional velocity response spectra ($h=0.05$), by the amplification factor of the ground for the period range of from 0.1 sec. to 5 sec. Using 45 sets of strong motion accelerograms as shown in Table 1, the empirical formula of those in terms of earthquake magnitude and hypocentral distance as presented in equation 1 was calculated by the method of least square.

$$\log_{10} S_{vo}(T) = a(T) \cdot M - b(T) \cdot \log_{10} X - c(T) \quad \dots\dots\dots(1)$$

where $S_{vo}(T)$ is velocity response spectrum of the incident waves, M is earthquake magnitude (J.M.A. magnitude), X is hypocentral distance by km and $a(T)$, $b(T)$ and $c(T)$ are the coefficients which depend to period. Coefficients $a(T)$ and $b(T)$ were assumed the periodic functions on the basis of the results from the scaling model (9),(10) and the inelasticity of the propagation pass. The results of the coefficients $a(T)$, $b(T)$ and $c(T)$ were shown in Fig.3.

The velocity response spectra from the empirical formula were shown in Fig.4, which shows that in the period range of from 0.1 sec. to 0.2 sec. the velocity response spectra increase with period, and that in the period range of from 0.2 sec. to 5 sec. the spectra for the earthquake of magnitude is 6 or 7 are constant velocity and those of the smaller magnitude decrease with period and those of the larger magnitude, on the contrary, increase with period. The absolute values of the spectra are fairly small in comparison with those on the ground surface, and were compared with those from Ohta's semi-empirical formula of the spectral acceleration amplitude at seismic bedrock based on the earthquake fault model(9). The agreement between the spectral value of this empirical formula and Ohta's results is comparatively good. The response spectra of the empirical formula

mentioned above can be regarded as those of the incident waves from the seismic bedrock whose shear wave velocity is about 3 km/sec. However, this empirical formula cannot be applicable for the near-field problem directly, because the source of earthquake cannot be regarded as a point.

2. METHOD FOR ESTIMATION OF GROUND MOTIONS WITH REGARD TO FAULT RUPTURE

As mentioned above, it is clear that the intensity of the ground motion in near-field is dominated by the pattern of the fault rupture evaluating from the isoseismals near the source area.(5) Authors took a fault rupture into a consideration when they estimated the response spectra of the near-field ground motions.

They assumed the envelope of the time history of the power on the incident waves in short period range as following:

1) The envelope of the incident wave, $E(T)$, is represented as shown in Fig.5(a), and its duration, d , is the sum of d_{source} , which is the rupture duration, and d_x , which is the time interval between the fastest and the latest wave arrival at a seismometer site.(11)

2) The envelope of the incident wave is regarded as the superposition of the impulses from the finite elements of the fault plane, and the shape of the impulse is regarded as shown in Fig.5(b). The suffixes of d' are corresponding to those of d .

3) The response envelope of an oscillator, whose damping coefficient is relatively large, is similar to that of the input motion.

According to these assumptions, the fault plane was divided into n elements of the finite planes ΔS_i as shown in Fig.6. The characteristics of the impulse from the finite plane ΔS_i can be represented as

$$d'_{source} = \Delta L / V_R \quad \dots\dots\dots(2)$$

$$d'_x = C \times X_i \quad \dots\dots\dots(3)$$

$$I'_i = d / [n \times (2d'_{source} + d'_x)] \times I_0 \quad \dots\dots\dots(4)$$

Equation 4 was obtained from Equation 5, because the energy of the incident waves are to be independent to the divided number n .

$$\int E(t) dt = \sum \int E'_i(t) dt \quad \dots\dots\dots(5)$$

where L is length of ΔS_j , V_R is rupture velocity, X_j is distance from a observed point to the element ΔS_j , I'_j is intensity of the impulse, $E'(t)$ is envelope of the impulse and C is a constant which takes 0.15 after Trifunac and 0.3 after Esteva(11). In this study, authors adopted $C=0.24$.

From Equation 4, it is necessary to determine I_0 and d in order to get I'_i . I_0 is obtained by setting X , which is distance from a observed point to the center of the fault plane, in Equation 1. d_{source} can be given by;

$$d_{source} = L / V_R \quad (\text{in case of unilateral faulting})..(6)$$

$$0.5 L / V_R \quad (\text{in case of bilateral faulting})..(7)$$

As the average of Equations 6 and 7,

$$d_{\text{source}} = 0.75 L / V_R \quad \dots\dots\dots(8)$$

where L is fault length. The relations between L, V_R and M have been showed by R.J.Geller(10). These relations are represented as following:

$$L = 0.012 \times 10^{0.5M} \quad [\text{ km }] \quad \dots\dots\dots(9)$$

$$V_R = 0.7 \times 10^{0.08M} \quad [\text{ km/sec }] \quad \dots\dots\dots(10)$$

Using Equations 9 and 10, Equation 8 gives d_{source} in terms of earthquake magnitude.

$$d_{\text{source}} = 0.013 \times 10^{0.42M} \quad [\text{ sec }] \quad \dots\dots\dots(11)$$

d_x is given by

$$d_x = C \times X \quad \dots\dots\dots(12)$$

where a constant C is 0.24 as mentioned above. Finally they obtained Equation 13 as follows:

$$d = 0.013 \times 10^{0.42M} + 0.24X \quad [\text{ sec }] \quad \dots\dots\dots(13)$$

Equation 13 is a semi-empirical formula of the duration of the incident waves from seismic bedrock.

They determined the characteristics of the impulse using Equations 1, 2, 3, 4 and 13, and the relative arrival time of impulses according to the rupture mode and relative location of source area and the observed site. The response envelope was calculated and the velocity response spectrum was obtained from the maximum value of the envelope. The idealized examples of the calculated envelope were shown in Fig.7. The maximum value at station A, situated on the side of the direction of the rupture propagation, is stronger than that at station C, situated on the opposite side, and the duration at station A is shorter than that at station C. These trends are found in the observed strong motion accelerograms due to the Tokachi-oki Earthquake of 1968. The comparison of the envelopes of these power of accelerograms with those which were calculated on the basis of the fault parameters proposed by Fukao(12), which is indicated in Fig.12, was shown in Fig.8. From the results of these comparison, it was affirmed that the effects of the rupture propagation can be considered by this method.

3. ATTENUATION CURVE OF INTENSITY OF SEISMIC WAVES AT SEISMIC BEDROCK

Authors calculated the attenuation curves of the intensity of seismic waves at seismic bedrock, as the incident waves for layered soil structure of ground, by the method mentioned above. The velocity response spectra can be obtained by this calculation directly. So, it is desired to transform the response spectra into the peak value of acceleration or particle velocity. Authors tried comparison between the response spectra and peak values of acceleration or particle velocity of ground motion on the actual 75 accelerograms, and they got the relationships between the spectral intensity and the peak value of acceleration or particle velocity as shown in Equations 14 and 15:

$$A_{\max} = 1.2 \times \text{M.S.I.} \quad \dots\dots\dots(14)$$

$$V_{\max} = 0.3 \times \text{S.I.} \quad \dots\dots\dots(15)$$

where A_{\max} and V_{\max} are peak values of acceleration and particle velocity respectively, S.I. is G.Housner's spectrum intensity for $h=0.05$, and M.S.I. is modified spectrum intensity represented in Equation 16.

$$\text{M.S.I.} = \int_{0.1}^{0.5} S_a(T) dt \quad \dots\dots\dots(16)$$

where $S_a(T)$ is acceleration response spectrum ($h=0.05$).

Figs.9 and 10 showed the attenuation curves of peak accelerations and particle velocities of the seismic waves at seismic bedrock, which are evaluated as the incident waves for the ground structures. In this case, dip angle of the fault plane is 90° and rupture propagates unilaterally. The fine lines showed the fluctuation due to the change of the relative position of observed site against the fault rupture. Upper part of the figure showed the attenuation curve against the ordinary epicentral distance, which is given by the seismometric observation, and the fluctuation is very large. Middle part of the figure showed the curve against the shortest distance from fault plane, that is similar to H.B.Seed(2), and result is better than former. In case of lower one, taking the non-dimensional distance which is the quotient of the distance from the specified point, that is located $0.1L$ inside from the rupture terminus, by the fault length, the fluctuation becomes very small and the attenuation curves of accelerations seem to be independent of earthquake magnitude. The upper limit of the peak acceleration of the seismic waves at seismic bedrock is about 350 gals. On the contrary, upper limit of the peak value of velocity increases with earthquake magnitude and will not exceed 30 kins.

For checking of these results, the distribution of the peak values of acceleration of seismic waves at seismic bedrock were compared with seismic intensities measured by Japan Meteorological Agency. JMA intensity V corresponds to VII of MM intensity scale roughly. In case of the Izu-ohshima Earthquake of 1978, using the Shimazaki's model(13), they showed the results of calculation on the peak acceleration of seismic waves at seismic bedrock by broken line and isoseismal map by JMA scale, in Fig.11. This broken line should be compared with the upper boundary of intensity V. In Fig.12, using the Fukao's model(12), whose dip angle is small, they showed the results of the case of the Tokachi-oki Earthquake of 1968. In Fig.13, showed also the results of the Kanto Earthquake of 1923 by the Ando's model(14). Under the consideration of ground amplification for the seismic waves, these results showed good agreements for the relationship between calculated ground motion and observed one. For the assist of consideration, they showed geological map of disastered area of the Kanto Earthquake in Fig.14.

4. ESTIMATED RESPONSE SPECTRA OF NEAR-FIELD GROUND SURFACE MOTIONS

The response spectra on the ground surface can be calculated as the products of the response spectrum of the seismic waves at the seismic bedrock and the amplification factor of SH-waves due to propagation by multiple-reflection in the layered soil. Assuming the amplification factor as 3.5 at the rock site(8), authors calculated the attenuation curves of the peak value of accelration for the rock site. Fig.15 shows the comparison of these attenuation curves and observed relationships at rock sites(2). As the

evaluation of earthquake magnitude, they adopted JMA magnitude in the calculation of the empirical formula. So they regarded earthquake magnitude $M=5.3$ for the San Francisco Earthquake, $M=6.0$ for the Parkfield Eq., $M=6.4$ for the San Fernando Eq., and $M=7.2$ for the Kern County Earthquake respectively with reference to M_L and M_S of individual earthquake(16). In cases of the Parkfield and the San Fernando earthquake, they got good agreements between the calculated and observed data.

At the sites whose underground soil structures were known, they estimated the response spectra of ground surface motions of near-field. In Fig.16, they showed the estimated velocity response spectra at Hongo, Tokyo by the Kanto Earthquake of 1923. Observed response spectra of this site have been presented by Nasu et al.(17) and Yamahara(18). In this figure authors compared these results changing the earthquake magnitude. In Fig. 17, authors showed also the estimated response spectra of ground surface at Cholame and Temblor, California due to the Parkfield Earthquake. The underground structures of individual sites were modeled as shown in Fig.18(19),(20). The fault parameters proposed by J.Anderson(21) were adopted. These results mean that the response spectra of ground surface in the near-field can be estimated with comparatively good accuracy by this method.

CONCLUSION

As the conclusion of this study, authors pointed out following results:

- 1) The empirical formula of the response spectra of the seismic waves at the seismic bedrock, which is considered as the incident waves for the layered soil structures of subsurface ground, in terms of earthquake magnitude and hypocentral distance was proposed. As the seismic bedrock, stiff rock layer, whose shear wave velocity is about 3 km/sec, should be considered. This empirical formula can be used for the earthquakes of that the magnitude is less than 7.0 or 7.5 directly. For huge earthquakes, effect of the near-field motions should be considered.

- 2) Authors proposed a method for the estimation of the response spectra of the near-field ground motions by means of the superposition of the impulses from the small elements of the fault plane. Upper limit of the peak value of acceleration of seismic waves at seismic bedrock is specified, in spite of earthquake magnitude.

- 3) The results obtained by this method showed good agreements with the observed seismic intensities, peak accelerations and response spectra of the ground surface earthquake motions in near-field. Consequently, it was affirmed that this method is available for the estimation of the ground motions, including the near-field.

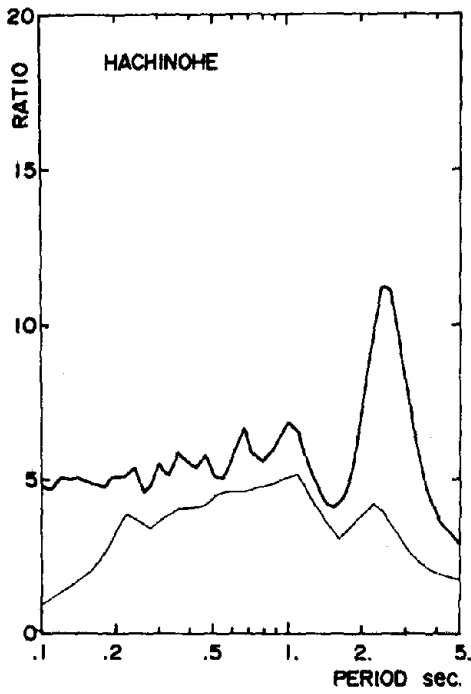
BIBLIOGRAPHY

- 1) Kanai,K;"An Empirical Formula for the Spectrum of Strong Earthquake Motions", Bull. of Earthquake Research Inst., Vol.39,1961
- 2) Schnable,P.B. and H.B.Seed;"Acceleration in Rock for Earthquake in the Western United States", Report, UC Berkeley, No.EERC 72-2, 1972
- 3) Kobayashi,H. and S.Nagahashi;"Response Spectra on Seismic Bedrock during Earthquake", Proc. of 6-WCEE, New Delhi, 1977

- 4) Trifunac, M.D.; "Preliminary Empirical Model for Scaling Fourier Amplitude Spectra of Strong Ground Acceleration in Terms of Earthquake Magnitude, Source-to-Station Distance, and Recording Site Conditions", Bull. of Seism. Soc. America, Vol.66, 1976
- 5) Kubotera, A. and T. Mitsunami; "Anisotropy of Isoseismals near the Epicenter", Zisin, Vol.29, 1976 (in Japanese)
- 6) Kanamori, H.; "Long-Period Ground Motion in the Epicentral Area of Major Earthquake", Tectonophysics, Vol.21, 1974
- 7) Kanai, K et al.; "Comparative Studies of Earthquake Motions on the Ground and Underground", Bull. of Earthquake Res. Inst., Vol.37, 1959
- 8) Lastrico, R.M. et al.; "Effects of Site and Propagation Path on Recorded Strong Earthquake Motions", Bull. of Seism. Soc. America, Vol.62, 1972
- 9) Ohta, Y. and H. Kagami; "Ultimate Values of Period and Amplitude on Seismic Input Motions in Relation to a Large Scale Structure", Trans. of Architectural Inst. Japan, No.249, 1976 (in Japanese)
- 10) Geller, R.J.; "Scaling Relations for Earthquake Source Parameters and Magnitude", Bull. of Seism. Soc. America, Vol.66, 1976
- 11) Trifunac, M.D. and A.G. Brady; "A Study on the Duration of Strong Earthquake Ground Motion", Bull. of Seism. Soc. America, Vol.65, 1975
- 12) Fukao, Y. and M. Furumoto; "Foreshocks and Multiple Shocks of Large Earthquake", Physics of Earth Planet. Inter., Vol.10, 1975
- 13) Shimazaki, K. and P. Sommerville; "Fault Parameters of the Izu-Ohshima Earthquake", Proc. of Seism. Soc. Japan, May 1978 (in Japanese)
- 14) Ando, M.; "A Fault-Origin Model of the Great Kanto Earthquake of 1923 as Deduced from Geodetic Data", Bull. of Earthquake Res. Inst., Vol.49, 1971
- 15) Kakimi, H. et al.; "Neotectonic Map, Tokyo", Geological Survey of Japan, 1973
- 16) Kanamori, H. and P.C. Jennings; "Determination of Local Magnitude, M_L , from Strong-Motion Accelerograms", Bull. of Seism. Soc. America, Vol.68, 1978
- 17) Nasu, N. and T. Morioka; "Revisional Investigation of the Ground Motion of Past Major Earthquake", Proc. of 6-WCEE, New Delhi, 1977
- 18) Yamahara, H. et al.; "Earthquake Response Analysis and Data Processing by the Fourier Transform", Proc. of 5-WCEE, Rome, 1973
- 19) Eaton, J.P. et al.; "Aftershocks of the 1966 Parkfield-Cholame, California, Earthquake: A detailed study", Bull. of Seism. Soc. America, Vol.60, 1970
- 20) Seed, H.B. et al.; "Site-Dependent Spectra for Earthquake-Resistant Design", Report, UC Berkeley, No.EERC 74-12, 1974
- 21) Anderson, J.; "A Dislocation Model for the Parkfield Earthquake", Bull. of Seism. Soc. America, Vol.64, 1974

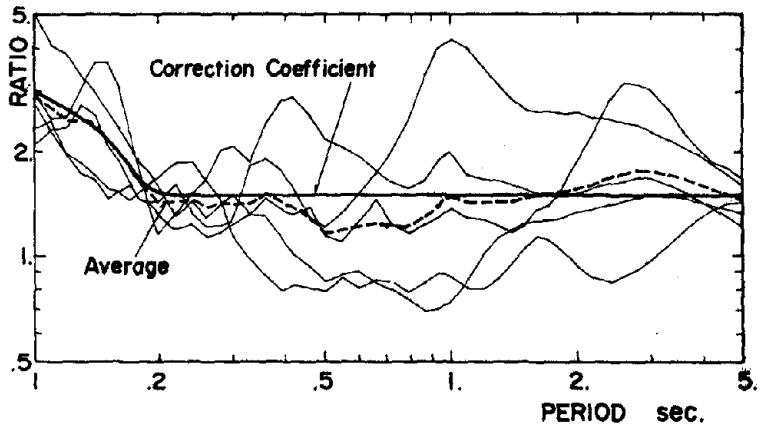
Table 1

SMAC Station			Kushiro JMA	Kushiro H	Hiroo	Muroran	Aomori	Hachinohe	Miyako	Tohkai	Hososhima
Date	M		Distance x km								
Nov. 15	1961	6.9	120								
Feb. 21	1962	6.2	110								
April 23	1962	7.0	120								
July 18	1962	5.9	100								
Feb. 5	1964	6.0								80	
June 23	1964	6.9	190								
Nov. 14	1964	5.1								50	
Sep. 18	1965	6.7								90	
Oct. 26	1965	6.8	200	200	290						
Sep. 19	1967	6.2			220						
Nov. 4	1967	6.5	60								
Nov. 19	1967	6.0								70	
April 1	1968	7.5									80
May 16	1968	7.5				230	220		210		
June 12	1968	7.2					280	220	130		
June 13	1968	5.7							130		
Aug. 6	1968	6.6									130
Aug. 7	1968	5.8		90							
Sep. 21	1968	6.8			100	170	230	210			
Oct. 8	1968	6.2			100						
April 21	1969	6.5									60
June 21	1969	5.6						90			
Jan. 21	1970	6.7		140	50	180					
April 1	1970	5.7							80		
July 26	1970A	6.7									60
July 26	1970B	6.1									60
Aug. 2	1971	7.0		220		260		210			
March 20	1972	6.3					130		150		
May 11	1972	5.8		90							
June 22	1972	5.4									80
June 17	1973	7.4		160							



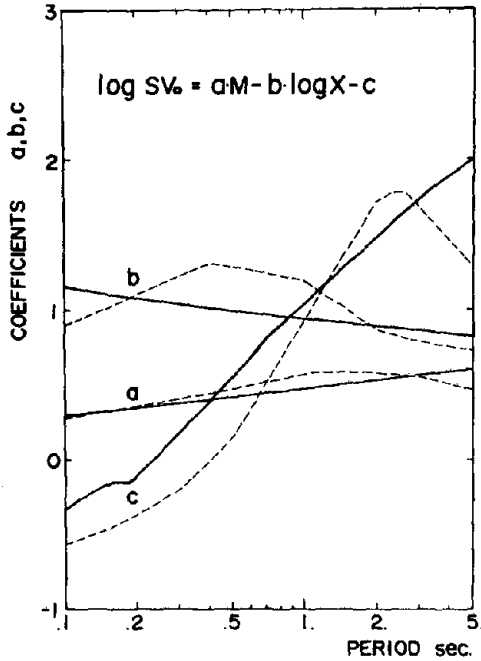
RATIO OF AMPLIFICATION OF SH-WAVES
(FINE LINE: KOBAYASHI & NAGAHASHI'S
AMPLIFICATION FACTOR)

Fig. 1



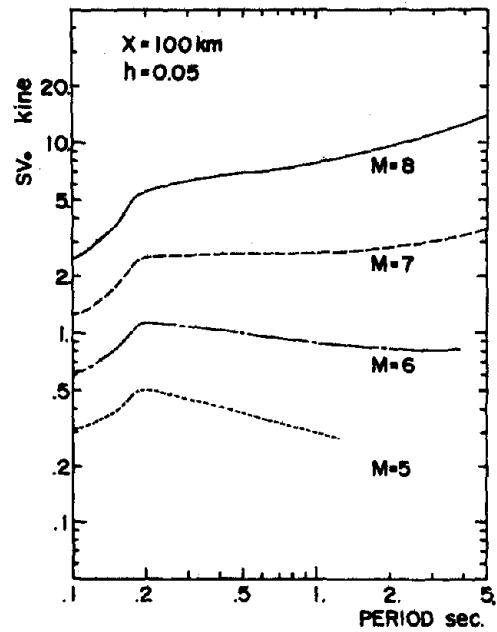
RATIO OF SPECTRAL RESPONSE DEU TO SH-WAVES
TO KOBAYASHI & NAGAHASHI'S AMPLIFICATION FACTOR

Fig. 2



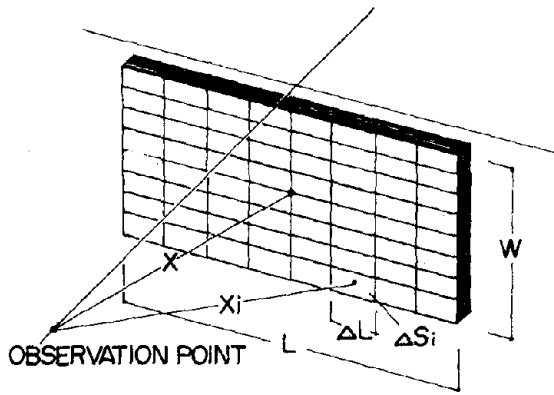
VARIATION OF THREE COEFFICIENTS IN THE
EXPERIMENTAL FORMULA OF VELOCITY
RESPONSE SPECTRA ON SEISMIC BEDROCK
(BROKEN LINE: AFTER KOBAYASHI & NAGAHASHI)

Fig. 3



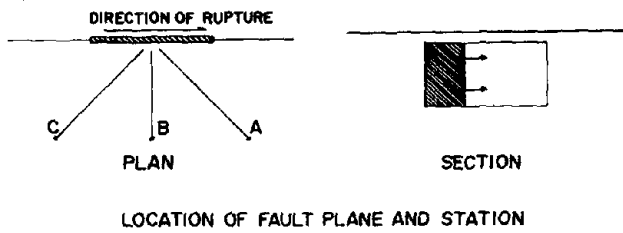
VELOCITY RESPONSE SPECTRA
ON SEISMIC BEDROCK

Fig. 4

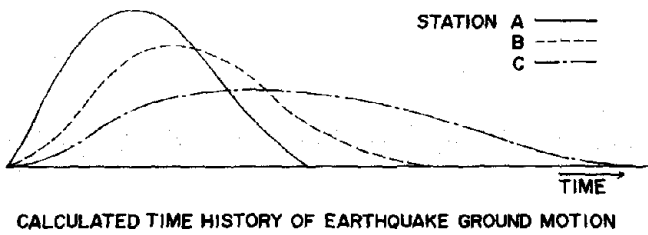


FAULT PLANE S

Fig. 6

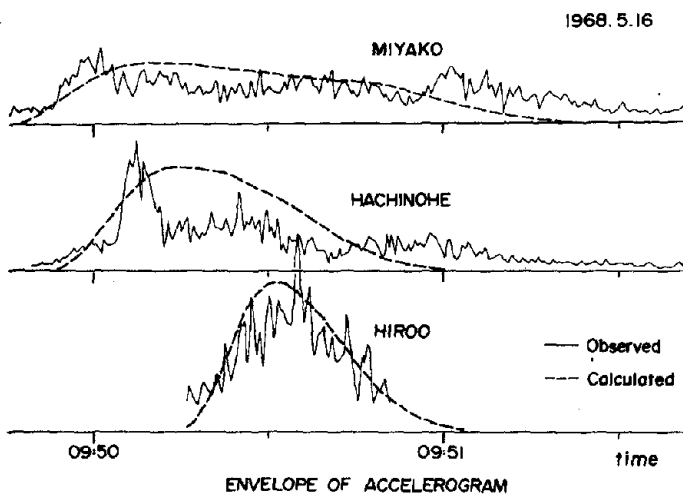


LOCATION OF FAULT PLANE AND STATION



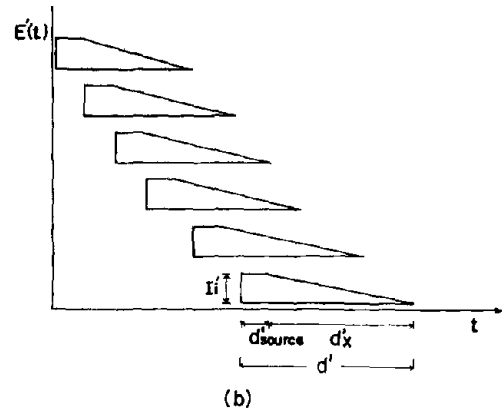
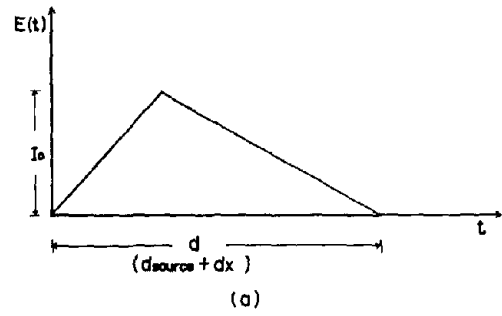
CALCULATED TIME HISTORY OF EARTHQUAKE GROUND MOTION

Fig. 7



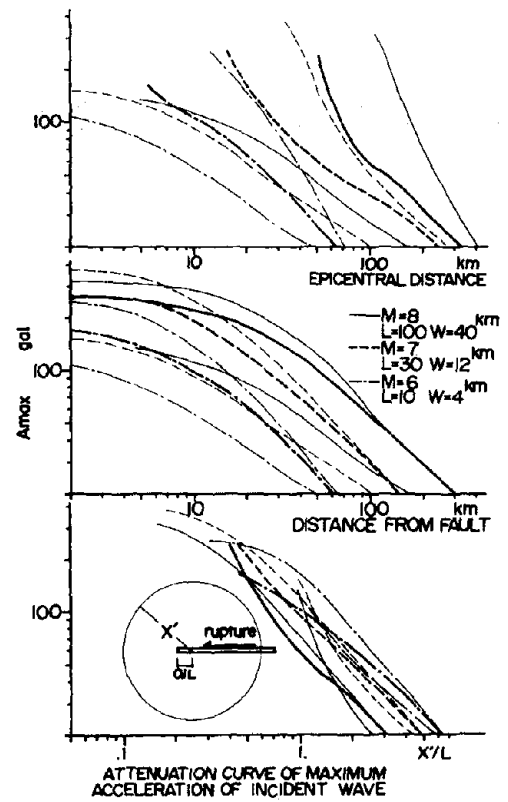
ENVELOPE OF ACCELEROGRAM

Fig. 8



ENVELOPE OF INCIDENT WAVE

Fig. 5



ATTENUATION CURVE OF MAXIMUM ACCELERATION OF INCIDENT WAVE

Fig. 9

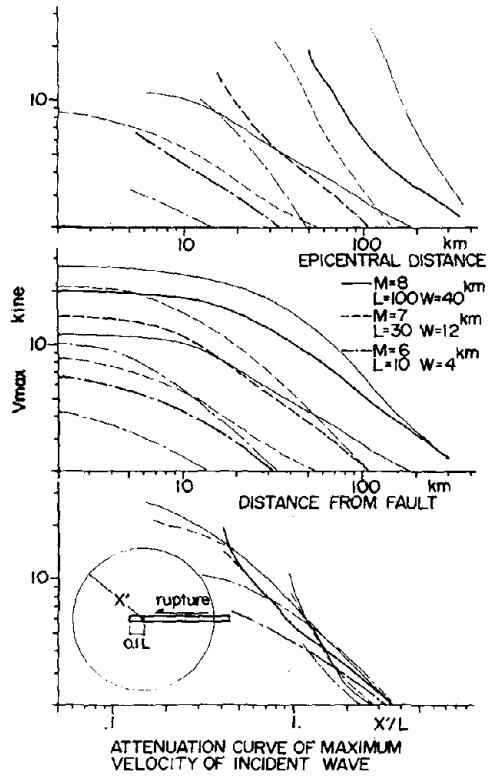


Fig. 10

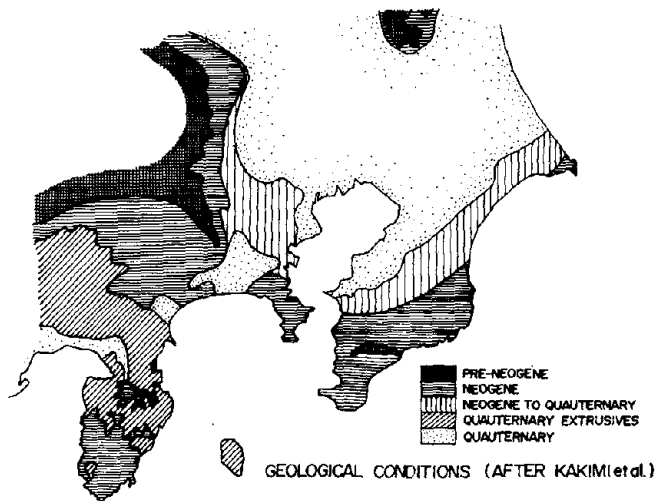
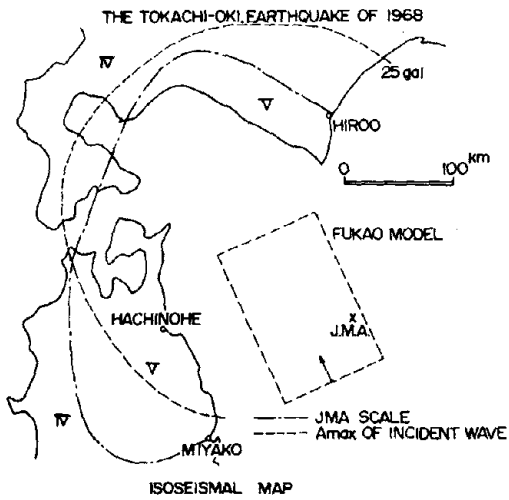
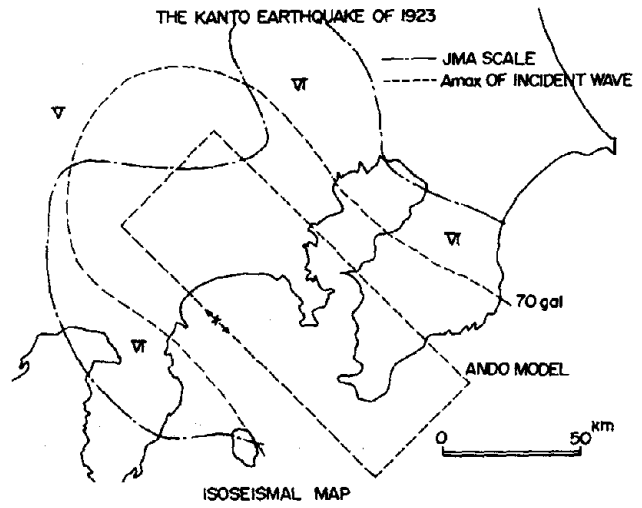
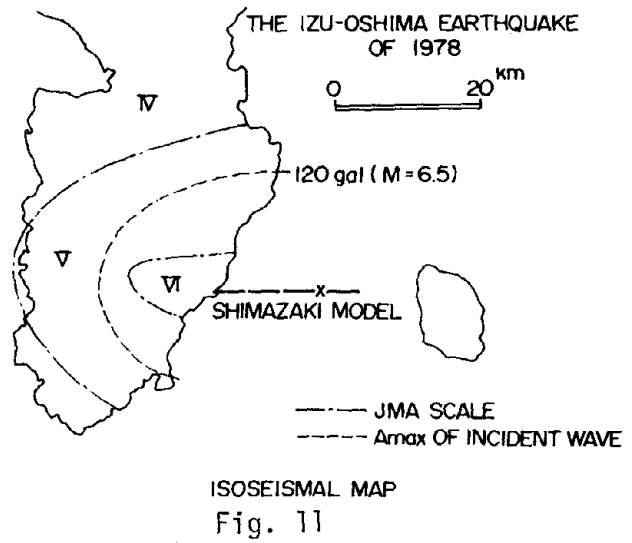


Fig. 14

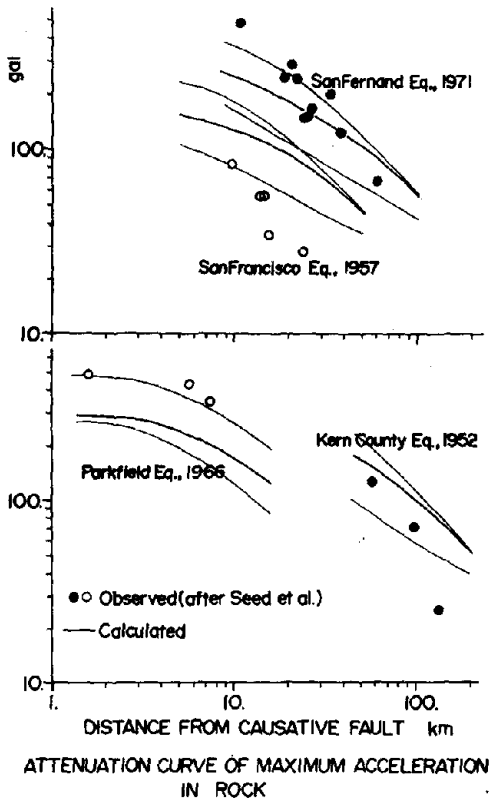


Fig. 15

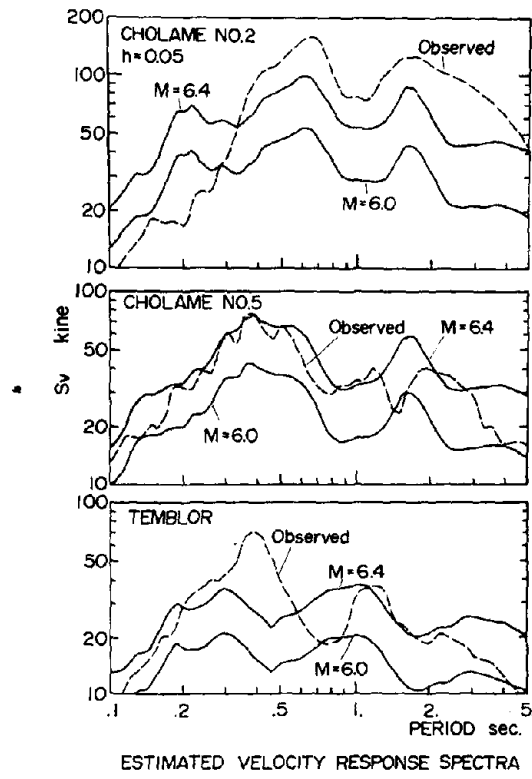


Fig. 17

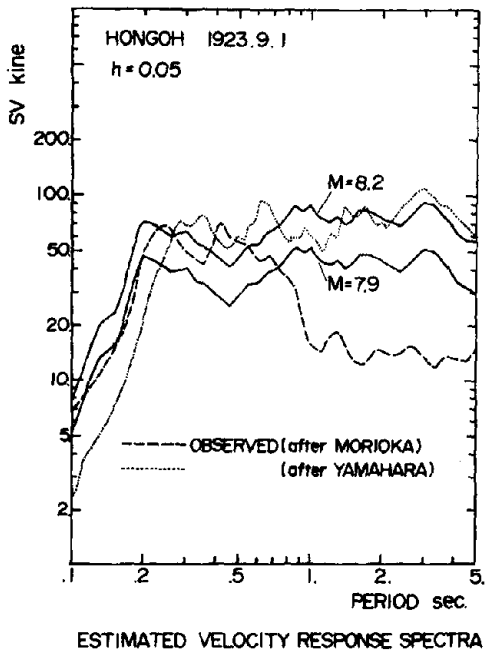
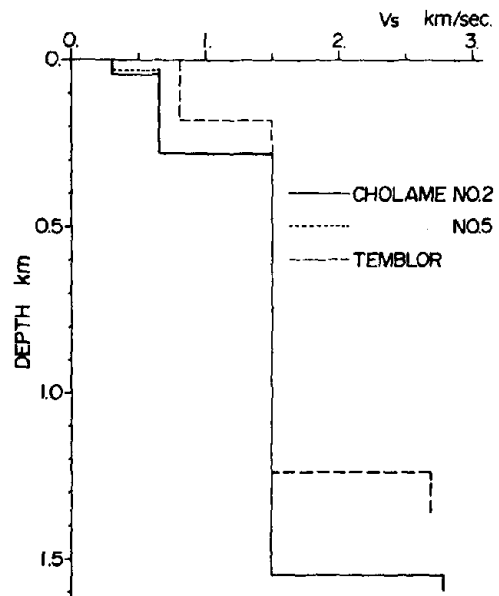


Fig. 16



S - PROFILE

Fig. 18

**SOIL DYNAMICS,
SOIL- STRUCTURE INTERACTION
AND GROUND EFFECTS SESSION**

INTENTIONALLY BLANK

CONSTANT VOLUME CYCLIC SIMPLE SHEAR TESTING

by

W.D. Liam Finn^I, M.ASCE, Y.P. Vaid^{II} and S.K. Bhatia^{III}

ABSTRACT

Compliance in systems for conducting undrained cyclic shear tests on saturated sands is equivalent to partial drainage and, therefore, can have a very significant effect on the measured liquefaction potential. A new "constant volume" cyclic simple shear test has been developed in which compliance is limited to very low values. This paper describes both the new test system and an improved method of sample preparation. Data from the new equipment are compared with cyclic simple shear data from conventional equipment to show directly the effect of system compliance. Lateral as well as vertical stresses are measured during cyclic loading.

INTRODUCTION

Laboratory methods currently in use for determining liquefaction potential of cohesionless soils are mainly cyclic triaxial tests and cyclic simple shear tests (5, 10, 12). Other, but less frequently used, techniques are cyclic torsional shear tests (7, 8) and shake table tests on large size samples (1, 3, 4). In evaluating the results of cyclic loading tests on saturated sands carried out under undrained conditions, it is assumed that no volume changes occur during the test. However, there is appreciable compliance in each of these test systems which allows significant volume expansion to occur in the supposedly constant volume saturated sample. This volume change, having the same effect as partial drainage would have, decreases the tendency for the porewater pressure to rise during cyclic loading. Therefore, undrained tests tend to overestimate the resistance to liquefaction. A theoretical analysis of the errors in liquefaction data caused by system compliance has been presented by Martin, Finn and Seed (9). These errors are always on the unsafe side and may range up to 100%.

Errors, due to system compliance, are common to all undrained liquefaction testing. The magnitude of the compliance is primarily a function of the type of test equipment and the grain size of the sand. In the various kinds of triaxial and shake table tests, compliance arises primarily as a consequence of membrane penetration effects and in simple shear tests with rigid container walls it is due to the membrane expanding into the corners of the sample cavity as the porewater pressure increases.

An alternative procedure for determining the undrained behaviour of sand without the complications of compliance is to conduct constant volume tests on dry sands. In these tests, the changes in confining

^I and Professor, Faculty of Applied Science, University of British Columbia, Vancouver.

^{II} Assistant Professor of Civil Engineering and Engineering Mechanics, McMaster University, Hamilton, Ontario.

^{III} Graduate Student, Dept. of Civil Engineering, University of British Columbia, Vancouver.

Preceding page blank

pressures to maintain constant volume are equivalent to the changes in porewater pressure in the corresponding undrained test. Constant volume triaxial testing of sand as an equivalent method of obtaining its behaviour under undrained loading was first suggested by Taylor (14). In such a test, there is no excess porewater pressure and the condition of constant volume is maintained by continuously varying the confining pressure in order to counteract the tendency to volume change when the sample is loaded axially. These changes in confining pressure are equivalent to changes in porewater pressure in the corresponding saturated undrained specimen. Application of the constant volume test to simple shear conditions was proposed by Pickering (11) in a technical note and he presented some preliminary results on the constant volume liquefaction of saturated Ottawa sand.

We present, herein, a description of a new cyclic simple shear test in which the compliance is negligible and hence the volume of the test sample may be considered constant for all practical purposes. In the proposed test a constant volume condition is achieved by locking the vertical loading head after the required vertical confining pressure has been applied. When cycles of shear stress or shear strain are now imposed, the tendency of the sand to compact during shaking causes a progressive reduction in vertical effective pressure on the loading head. This reduction in effective pressure is equivalent to the increase in porewater pressure in the corresponding undrained test. A preliminary description of this test has been given previously by Finn and Vaid (6).

DESCRIPTION OF TEST APPARATUS

The University of British Columbia (UBC) simple shear apparatus, described by Finn et al (5) has been modified to permit cyclic shear testing at constant sample volume. The modified apparatus is shown in Fig. 1. The two components of linear horizontal strain are identically zero in this simple shear apparatus. Thus, a constant volume condition is achieved by clamping the loading head to prevent vertical strain. A horizontal reaction plate is clamped to four vertical posts which are threaded into the body of the simple shear apparatus. A stiff vertical load transducer is attached to the sample loading head and carries on its upper side a heavy loading bolt which passes through a central hole in the reaction plate. The desired vertical pressure on the sample is applied by tightening the loading bolt nut on the underside of the reaction plate. Simultaneously, the loading head is clamped in position by tightening the loading bolt nut on the top side of the reaction plate. Two small stiff pressure transducers (350 kPa capacity and full scale deflection of 0.0015 cm) are permanently mounted on one of the moveable lateral boundaries in order to monitor the lateral stresses during cyclic loading.

Maximum gross volume change introduced at the onset of liquefaction in this so called constant volume test is very small and arises as a result of the recovery of elastic deformation in the vertical loading components when the load on the clamped loading head is reduced to zero. The use of a thick reaction plate, heavy vertical posts and loading bolt, and a very stiff load transducer reduces the vertical movement of the clamped head to a negligible amount. For liquefaction tests with initial

$\sigma'_{v0} = 2 \text{ kg/cm}^2$ (196 kPa) this movement amounted to a maximum of 5×10^{-4} cm which was only 5% of the movement of the floating head due to system compliance in liquefaction tests on saturated undrained samples in the same equipment and is equivalent to a total vertical strain of the order of 0.02%. Thus, a more accurate evaluation of liquefaction potential can be made using the new test.

EXPERIMENTAL PROCEDURE

An experimental procedure for preparing saturated sand samples within the simple shear apparatus has been described by Finn, Pickering and Bransby (5). Evolution in testing methods has since led to an improved procedure which gives samples of more uniform density and, therefore, yields more consistent and reproducible results. In the earlier procedure, densification of the sample to the desired relative density was carried out prior to siphoning off excess sand to achieve the final desired height and seating of the ribbed loading plate. A looser layer of sand tends to form at the top due partly to the siphoning action and partly to digging of the ribbed loading plate into the sand surface. Such a looser layer in an otherwise dense sample would lower the overall liquefaction resistance of the sand sample. In the improved procedure, the sand is not densified until after the top ribbed plate has been seated on the sand surface and the membrane has been sealed to the top loading cap.

A constant volume test can be performed on either dry or saturated sands. Dry sand is deposited within the membrane in the apparatus through a funnel tip permitting a free fall. The funnel is traversed across the plan area of the sample so that the sand surface remains sensibly level. Pouring is continued until an excess of sand over that required for the sample has been deposited. Excess sand over the final elevation is then siphoned off using a small vacuum. Saturated samples are prepared to the desired height by deposition under water in the manner described in (5). The top ribbed plate is now placed on the sand surface, the membrane closed over it, and sealed to the loading head. The desired final density for either kind of test is then obtained by vertical vibrations while the sample is kept under a seating pressure of approximately 0.1 kg/cm^2 . The top ribbed plate thus follows the settlement of the sand surface and assumes a proper seating, while the entire sample gets uniformly densified without development of looser zones under the top plate. The vertical pressure is then increased to the required value of the overburden pressure.

The cyclic shear load may be applied using either square, ramp or sine wave forms. The data presented herein were obtained using the square waveform with periods of zero load described previously by Finn et al (5) for undrained simple shear liquefaction tests. All tests were run at a loading frequency of 2 Hz. During the test, vertical pressure, cyclic shear strain and cyclic shear stress were monitored with electronic transducers and continuous records were obtained with a light beam chart recorder.

CONSTANT VOLUME CYCLIC SIMPLE SHEAR TESTS

All tests were performed on Ottawa sand, ASTM designation C.109. This is a natural silica sand consisting of rounded particles with grain

sizes between 0.15 and 0.59 mm and $D_{50} = 0.40$ mm. The maximum and minimum void ratios are 0.82 and 0.50, respectively.

A typical record of a constant volume simple shear cyclic loading test on medium dense dry sand is shown in Fig. 2. A similar record using a saturated undrained sample is shown in Fig. 11 in Ref. 5. The similarity between the two records may readily be noted, particularly in the rise of porewater pressure during the undrained liquefaction test and the decrease of vertical normal effective pressure during the constant volume liquefaction test. In the undrained test, the normal effective stress may eventually reduce to zero as the porewater pressure increases with cycles of loading, resulting in liquefaction. In the constant volume test, the porewater pressure remains constant (usually zero) and the normal effective stress may decrease to zero. The simultaneous reductions in horizontal and vertical effective stresses during cyclic loading are shown in Fig. 3 for a typical test.

Dry vs. saturated samples:-

In terms of effective stresses, the mechanical behaviour of cohesionless soils is not affected by whether the soil is saturated or dry (15). Fig. 4 shows data from constant volume liquefaction tests of both dry and saturated samples. Identical values of initial confining stresses, σ'_{v0} , and cyclic shear stress amplitude, τ , were used in all tests and only the relative density was varied. It can be seen in Fig. 4 that there is excellent agreement between results obtained from dry and fully saturated samples. This result is quite important because it is much easier and less time consuming to work with dry sands than with saturated sands. In view of these results, the tests described subsequently were carried out using dry samples.

Cyclic stress amplitude vs. cycles to liquefaction:-

A summary plot of the results of cyclic loading tests on samples normally consolidated under an initial confining stress, $\sigma'_{v0} = 2 \text{ kg/cm}^2$ (196 kPa) is shown in Fig. 5. Each contour in Fig. 5 was obtained by running a series of tests on samples with different relative densities but using a constant cyclic stress amplitude. The data shows very little scatter which is not generally the case with results from saturated undrained liquefaction tests.

From the results in Fig. 5, it is possible to obtain the relationship between cyclic stress ratio, τ/σ'_{v0} , vs. cycles to liquefaction for various relative densities of the sand. These relationships are plotted in Fig. 6 for four different relative densities of sand.

The relationships between cyclic stress ratio and cycles to liquefaction for overconsolidated sand are shown in Fig. 7 for $D_r = 50\%$. These results were obtained by running a series of tests similar to the normally consolidated series but now using samples with a fixed value of overconsolidation ratio (OCR). The rate of development of porewater pressure (decrease in vertical effective stress in constant volume tests) in overconsolidated samples with essentially the same relative density and under a constant τ/σ'_{v0} ratio is shown in Fig. 8. It may be seen in Fig. 8 that

higher resistance to liquefaction with increasing OCR is associated with a slower rate of porewater pressure generation during cyclic loading of the overconsolidated samples.

EFFECT OF SYSTEM COMPLIANCE

A series of conventional liquefaction tests was carried out on saturated undrained samples using the new procedure for sample formation. Constant values of initial confining stress and cyclic shear stress ($\tau/\sigma'_{v0} = 0.13$) were used and only the sample density was varied. The results from this series of tests are shown in Fig. 9. Corresponding results obtained by constant volume liquefaction tests (taken from Fig. 5) are also shown for comparison. It is clear from Fig. 9 that for identical methods of sample preparation the resistance to liquefaction measured in conventional cyclic simple shear tests on undrained saturated samples is consistently larger than that measured in the constant volume tests. Since the test samples were prepared in an identical manner, the increased resistance to liquefaction in undrained tests is directly attributable to the system compliance in the undrained test. The apparent volume change at the onset of liquefaction in undrained tests amounted to a movement of the loading head which was 20 times as large as the corresponding movement in the constant volume tests. Thus, the use of undrained test data may result in an overestimation of the liquefaction resistance of sand.

It may be seen, from Fig. 9, that with $\tau/\sigma'_{v0} = 0.13$ Ottawa sand at a relative density $D_r = 51\%$ will liquefy in 10 cycles in an undrained cyclic loading test. The data in Fig. 6 show that the same sand at the same relative density will liquefy in 10 cycles with $\tau/\sigma'_{v0} = 0.107$. Therefore, the undrained test, because of system compliance, overestimates the resistance to liquefaction by about 25% for the case under consideration. For any given apparatus and hence a given amount of system compliance, the degree of overestimation of the resistance to liquefaction will depend on the type of sand, the relative density and the number of cycles to liquefaction under consideration.

EFFECT OF IMPROVED SAMPLE PREPARATION TECHNIQUE

Liquefaction resistance vs. relative density:-

The influence of relative density D_r , on cyclic stress ratio τ/σ'_{v0} , to cause liquefaction in 10 and 30 cycles is illustrated in Fig. 10. There is a gradual increase in cyclic stress ratio to cause liquefaction with increase in relative density up to $D_r \approx 60\%$. However, for D_r in excess of about 60%, the stress ratio required to cause initial liquefaction or a shear strain $\gamma = \pm 5\%$ increased at a much faster rate. The rate of increase is much more rapid than has been recently reported by D'Alba et al (1) who found that τ/σ'_{v0} increases linearly with relative density up to $D_r \approx 80\%$. De Alba's data (1) has been corrected for compliance due to membrane penetration and so should be comparable to the results from the compliance free constant volume test.

The dramatic increase in resistance to liquefaction at higher densities is further illustrated by the results of tests on dense sand samples

with D_r in the range of 73% to 83%. In these dense samples, the vertical effective stress reduced to a small terminal value but never reached a state of initial liquefaction. Shear strains began to develop with cycles of loading only after the vertical stress had been substantially reduced. A summary of some of the test results is presented in Table 1 and it shows

TABLE I - Results of Constant Volume Cyclic Loading
Tests on Dense Ottawa Sand

D_r %	τ/σ'_{vo}	Cycles to develop specified percent shear strain		
		± 1	± 2	± 5
72.8	0.266	10	20	40
76.9	0.192	86	106	160
80.6	0.340	14	48	150
83.4	0.394	13	56	Could not achieve 5%

that large τ/σ'_{vo} ratios and/or very large numbers of cycles are required to generate 5% strain for relative densities over 70%. The results presented in Fig. 10 and Table 1 are in agreement with the field records of liquefaction (Fig. 11) analysed by Castro (2). From Fig. 11, it seems there is no evidence of reported liquefaction for sites with modified penetration (N) values greater than 40 which corresponds to $D_r \approx 70\%$ based on the Gibbs and Holtz correlation between N values and relative density.

The observed substantial increase in resistance to liquefaction of dense Ottawa sand in the present investigations is believed to be a consequence of the improved sample preparation technique. The improved technique aims at eliminating the possibility of the development of a looser layer at the top of an otherwise dense sample. The common practice of bringing the sand sample to the final grade and density before placing the loading head tends to develop a looser layer at the top. This is avoided in the improved sample preparation technique by vibrating the sand to the desired density after placing the loading cap and applying a small seating stress.

Liquefaction resistance vs. overconsolidation ratio:-

The results presented in Fig. 7 show a considerable increase in resistance to liquefaction with increase in the overconsolidation ratio, OCR. For the sand tested, the stress ratio required to cause liquefaction in 20 cycles at an OCR = 4 was almost double that for a normally consolidated sample. Results similar to that in Fig. 7 have also been reported by Seed and Peacock (13) for Monterey sand. Both Ottawa and Monterey

sands are medium uniform sands. However, the increase in resistance to liquefaction with similar increase in OCR is much smaller for Monterey than for Ottawa sand. It is believed that the improved sample preparation technique has been responsible for the greatly increased resistance to liquefaction of overconsolidated Ottawa sand, measured in the constant volume cyclic simple shear test.

CONCLUSION

A cyclic simple shear test has been developed for measuring the liquefaction potential of saturated sands which uses dry sand samples. The volume changes that occur during the test are so small that for all practical purposes the test may be considered a constant volume test. The test is based on the concept that the pressure reduction against a fixed loading head during cyclic loading is equivalent to the increase in pore-water pressure that would occur in the corresponding undrained test. Compliance in the constant volume test system is less than 1/20 that of the corresponding undrained test system and, consequently, the constant volume test gives more realistic estimates of liquefaction potential.

A new procedure for sample preparation has been developed in conjunction with the constant volume test. In this new procedure all activities associated with sample formation, instrumentation and loading are completed before the sample is vibrated to the final desired density. This procedure prevents the formation of a looser layer on top of an otherwise dense sample due to placement of loading head, sealing membranes and other manipulations of the sample after densification but prior to testing. Samples formed by the new procedure show very high resistance to initial liquefaction or straining at relative densities greater than 70% in comparison with samples formed to final density prior to placement of loading head and sealing of membrane. Overconsolidated samples formed by the new procedure also show a much higher resistance to liquefaction than similar samples formed by the more conventional procedure.

The constant volume test is very quick and easy to carry out and has none of the difficulties associated with undrained cyclic tests. There is an extraordinarily high degree of reproducibility and consistency in the test results.

ACKNOWLEDGEMENTS

The financial assistance under grant No. 1498 of the National Research Council of Canada is gratefully acknowledged.

REFERENCES

1. Alba, P. De, Chan, C.K. and Seed, H.B., "Determination of Soil Liquefaction Characteristics by Large-Scale Laboratory Tests," Report No. EERC 75-14, College of Engineering, University of California, Berkeley, May 1975.

2. Castro, G., "Liquefaction and Cyclic Mobility of Saturated Sands," *Journal of the Geotechnical Engineering Division, ASCE*, Vol. 101, No. GT6, Proc. Paper 11388, June 1975, pp. 551-569.
3. Finn W.D.L., Emery, J.J. and Gupta, Y.P., 1970, "A Shake Table Study of the Liquefaction of Saturated Sands During Earthquakes," *Proc. 3rd European Symp. Earthquake Eng.*, pp. 253-62.
4. Finn, W.D.L., Emery, J.J. and Gupta, Y.P., 1971, "Liquefaction of Large Samples of Saturated Sand on a Shake Table," *Proc. 1st Canadian Conf. Earthquake Eng.*, pp. 97-110.
5. Finn, W.D.L., Pickering, D.J. and Bransby, P.L., 1971, "Sand Liquefaction in Triaxial and Simple Shear Tests," *J. Soil Mech. and Found. Div., ASCE*, Vol. 97, SM4, pp. 639-59.
6. Finn, W.D.L. and Vaid, Y.P., "Liquefaction Potential from Drained Constant Volume Cyclic Simple Shear Tests," *Proceedings, Sixth World Conference on Earthquake Engineering, New Delhi, India, Jan. 1977, Session 6*, pp. 7-12.
7. Ishihara, K. and Li, S.I., 1972, "Liquefaction of Saturated Sand in Triaxial Torsion Shear Tests," *Soils and Foundations*, Vol. 12, No. 3, pp. 19-39.
8. Ishibashi, I. and Sherif, M.A., 1974, "Soil Liquefaction by Torsional Simple Shear Device," *J. Geotech. Eng. Div., ASCE*, Vol. 100, GT8, pp. 871-86.
9. Martin, G.R., Finn, W.D.L. and Seed, H.B., "Effects of System Compliance on Liquefaction Tests," *Journal of the Geotechnical Engineering Division, ASCE*, Vol. 104, No. GT4, Proc. Paper 13667, April 1978, pp. 463-479.
10. Peacock, W.H. and Seed, H.B., 1968, "Sand Liquefaction Under Cyclic Loading Simple Shear Conditions," *J. Soil Mech. and Found. Div., ASCE*, Vol. 94, SM3, pp. 689-708.
11. Pickering, D.J., 1973, "Drained Liquefaction Testing in Simple Shear," *J. Soil Mech. and Found. Div., ASCE*, Vol. 99, SML2, pp. 1179-84.
12. Seed, H.B. and Lee, K.L., 1966, "Liquefaction of Saturated Sands During Cyclic Loading," *J. Soil Mech. and Found. Div., ASCE*, Vol. 92, SM6, pp. 105-34.
13. Seed, H.B. and Peacock, W.H., 1971, "Test Procedures for Measuring Soil Liquefaction Characteristics," *J. Soil Mech. and Found. Div., ASCE*, Vol. 97, SM8, pp. 1099-1119.
14. Taylor, D.W., 1948, "Fundamentals of Soil Mechanics," John Wiley and Sons, New York.

15. Terzaghi, K. and Peck, R.B., 1967, "Soil Mechanics in Engineering Practice," John Wiley and Sons, New York, 2nd Ed.
16. Wong, R.T., Seed, H.B. and Chan, C.K., "Cyclic Loading Liquefaction of Gravelly Soils," J. Geotech. Eng. Div., ASCE, June 1975.

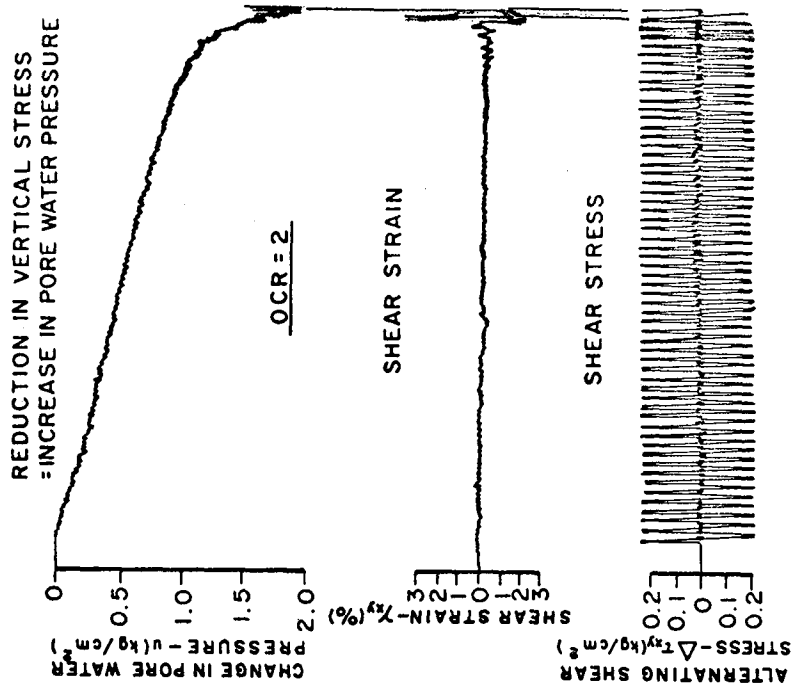


Fig.2: Data from a constant volume simple shear test on medium dense Ottawa sand.

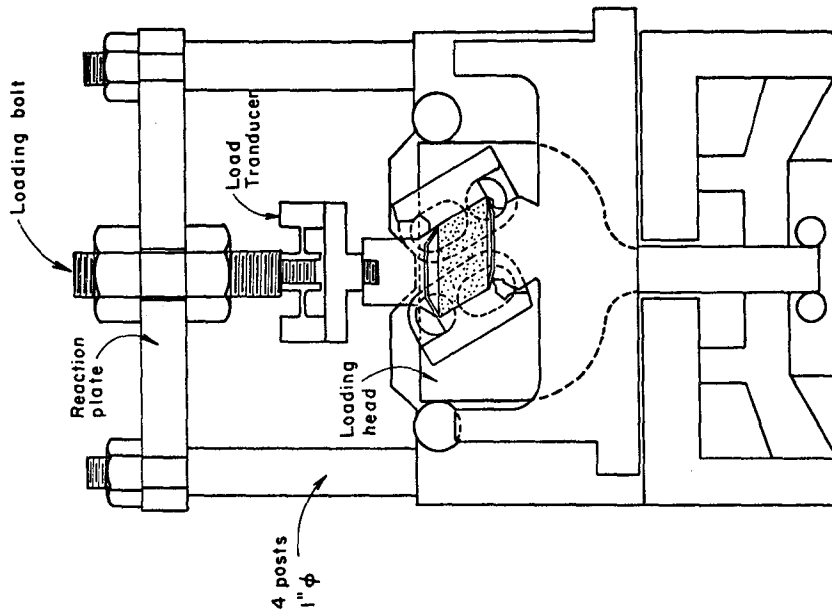


Fig.1: Constant volume simple shear apparatus.

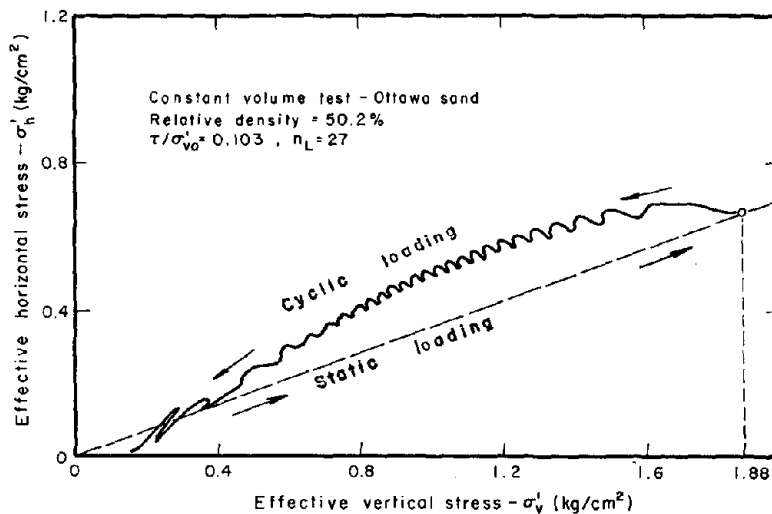


Fig.3: Variation of horizontal and vertical stresses during cyclic loading.

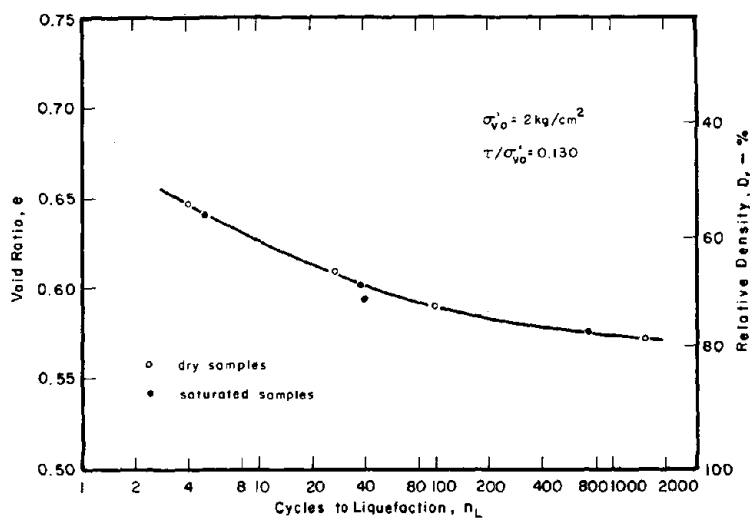


Fig.4: Comparison of liquefaction resistance of normally consolidated dry and saturated Ottawa sand in constant volume simple shear.

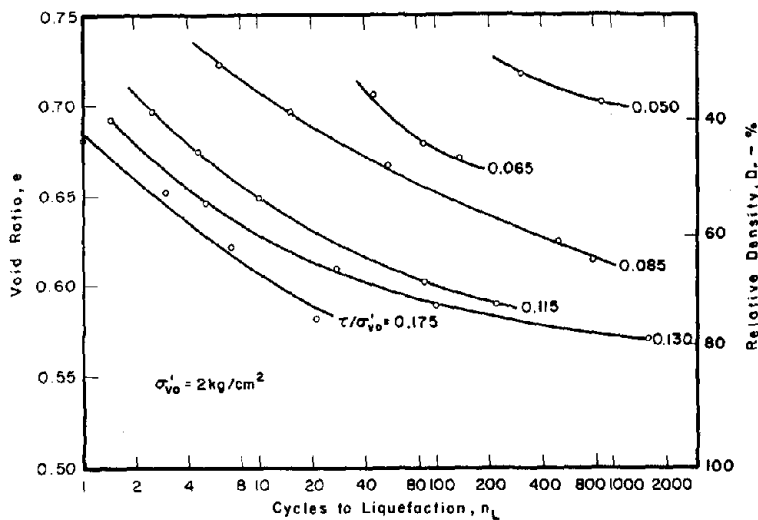


Fig.5: Resistance to liquefaction of normally consolidated dry Ottawa sand in constant volume simple shear.

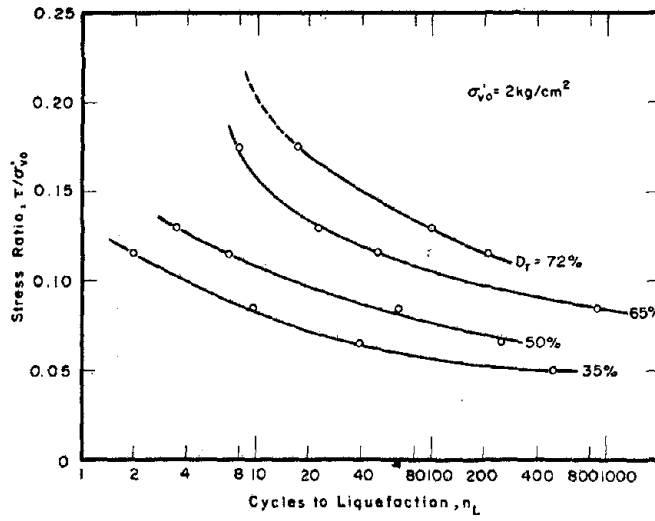


Fig.6: Resistance to liquefaction of normally consolidated Ottawa sand at various relative densities in constant volume simple shear.

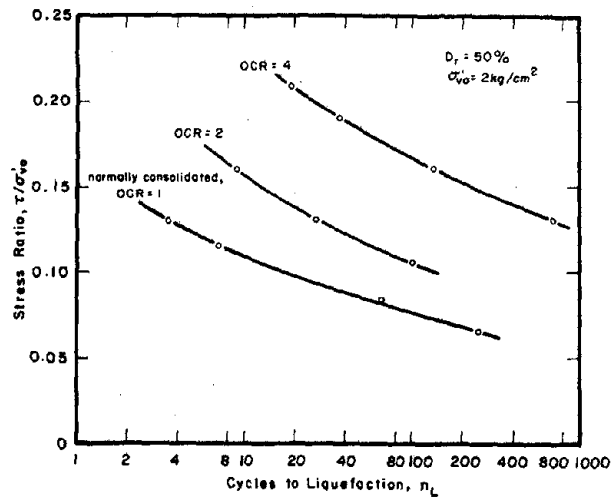


Fig.7: Effect of overconsolidation on liquefaction resistance of Ottawa sand in constant volume simple shear.

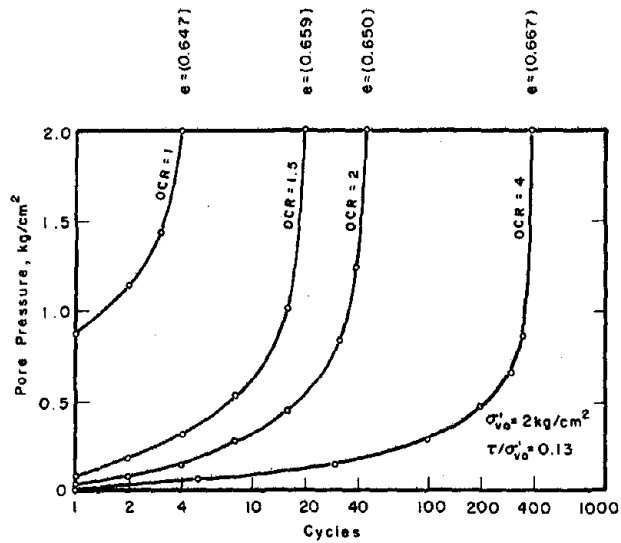


Fig.8: Effect of over-consolidation on pore pressure development in CVSS liquefaction.

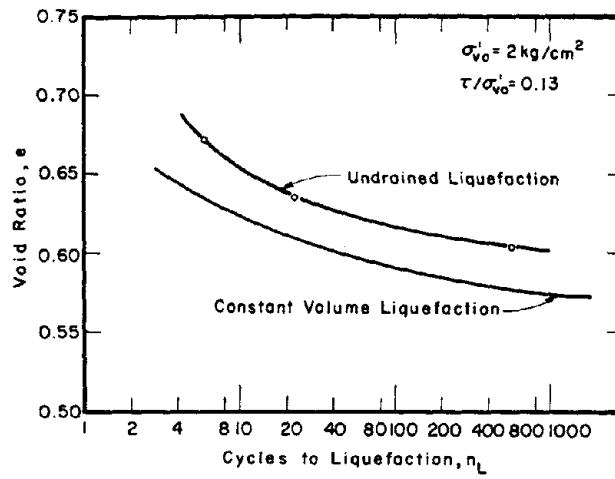


Fig.9: Liquefaction resistance of Ottawa sand in constant volume and undrained simple shear.

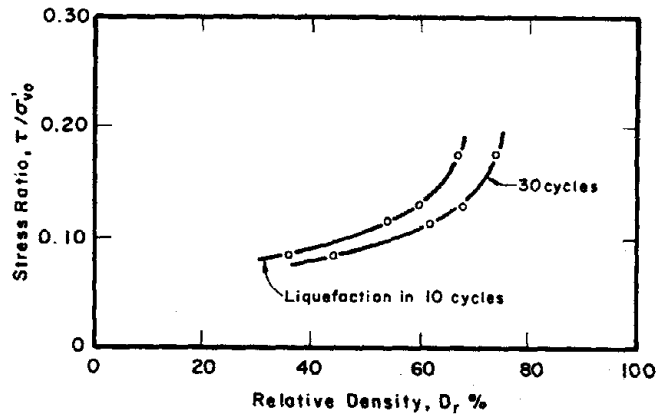


Fig.10: Relationship between relative density and cyclic shear stress for liquefaction in 10 and 30 cycles.

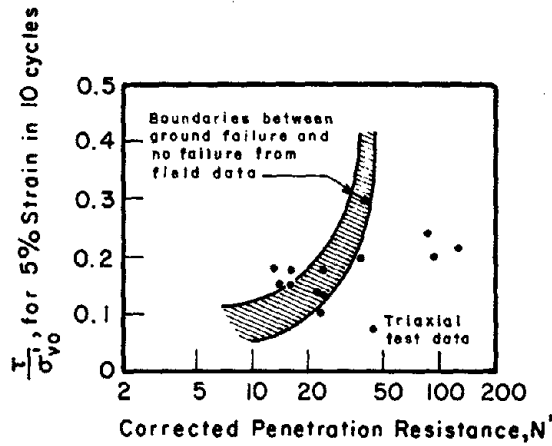


Fig.11: Comparison of Laboratories and Field Data (after Castro, 1975).

852

INTENTIONALLY BLANK

TWO-DIMENSIONAL PORE PRESSURE CHANGES IN SAND
DEPOSITS DURING EARTHQUAKES

by

Yoshiaki Yoshimi^I and Kohji Tokimatsu^{II}

ABSTRACT

An analytical method applicable to two- and three-dimensional problems is presented for evaluating generation and dissipation of pore water pressures in sand deposits during earthquakes, by extending Biot's consolidation equation. Shaking table tests were conducted on a horizontal layer of saturated sand supporting a structure, and the test results were compared with the computed values based on the mechanical properties of the sand which were determined at appropriate stress levels in the model tests. The computed pore water pressure time histories in the sand were in good agreement with the observed ones considering the fact that the pore water pressures were sensitive to a small variation in the table acceleration. It was indicated that redistribution of pore water pressures due to seepage should be taken into account for evaluating the bearing capacity of saturated sand subjected to cyclic loading.

INTRODUCTION

Previous studies on the generation and dissipation of pore water pressures in sand deposits during earthquakes (Ref. 8, for example) were based on the assumption that the total stresses in the soil remained constant, although such an assumption was justified in one-dimensional problems only. In two- and three-dimensional problems, however, the stress distribution in the soil may change because of uneven changes in the shear moduli of the soil as a result of generation of excess pore water pressures. The authors became aware of the need for solving the problem when they studied the behavior of buildings on saturated sand during earthquakes (11). The need also exists when we attempt to establish rational criteria for soil stabilization as a means to prevent damage due to liquefaction, in terms of area and depth of soil to be stabilized as well as requirements for density and permeability of the stabilized soil.

The object of this paper is to propose a method for assessing the pore water pressure changes in saturated sands involving two- or three-dimensional configurations or seepage paths. Shaking table tests on model ground supporting a structure are conducted to verify the analytical procedure. In order to bypass similitude requirements, the physical and mechanical properties of the sand in the model ground are evaluated at the actual stress level in the model which are quite low.

I Professor, Tokyo Institute of Technology, Tokyo, Japan.

II Graduate Student, Tokyo Institute of Technology, Tokyo, Japan.

Preceding page blank

METHOD OF ANALYSIS

Governing Equations

The governing equations developed by Sandhu and Wilson (7) which was based on Biot's theory of consolidation (1) are extended to account for the effects of cyclic shear stress, i.e., generation of excess pore water pressure and change in stresses in the ground. Accordingly, assumptions concerning the characteristics of sand subjected to cyclic shear are made in addition to assuming small deformations, linear stress-strain relationship, full saturation, incompressible water, and the validity of Darcy's law.

The equation of equilibrium of forces which permits an increase in the pore water pressure during earthquake can be expressed as follows:

$$\bar{\sigma}_{ki,k} + g'_{ki,k} + \delta_{ik}\pi_{,k} - \delta_{ik}g_{,k} + \rho F_i = 0 \quad (1)$$

in which $\bar{\sigma}$ = effective stress tensor, π = pore water pressure, F = body force vector, ρ = unit weight of soil, δ_{ik} = the Kronecker delta (equals 0 for $i \neq k$ and equals 1 for $i = k$), g = excess pore water pressure generated by cyclic shear stress, g' = change in the effective stress due to cyclic shear stress (estimated for the final state of equilibrium after the excess pore water pressure, g , has dissipated). Subscripts after a comma denote differentiation in that direction, and repeated indices denote summation (7).

The relationship between the strain, e , and displacement, u , for small deformations can be expressed as

$$e_{ij} = \frac{1}{2}(u_{i,j} + u_{j,i}) \quad (2)$$

Assuming that the change in the effective stress due to cyclic shear stress causes no change in the void ratio, the stress-strain relationship of the sand skeleton can be expressed as

$$\bar{\sigma}_{ij} = C_{ijkl}e_{kl} - g'_{ij} \quad (3)$$

in which C = elastic modulus tensor.

Assuming similarly that the excess pore water pressure due to cyclic shear stress causes no change in the void ratio, Darcy's law and the equation of continuity are expressed by Eqs. (4) and (5), respectively.

$$q_i = k_{ij}(\pi_{,j} - g_{,j}) \quad (4)$$

$$q_{i,i} = \dot{e}_{ii} = -\dot{u}_{i,i} \quad (5)$$

in which q = discharge velocity vector, k = permeability coefficient tensor, and a superposed dot denotes differentiation with respect to time.

Substituting Eq. (4) in Eq. (5) and integrating in time domain, one obtains Eq. (6) by virtue of $u_{i,i}(t=0) = 0$.

$$u_{i,i} + h\{k_{ij}(\pi_{,j} - g_{,j})\}_{,i} = 0 \quad (6)$$

in which $h = 1$ and the symbol $*$ denotes convolution product, such that

$$A*B = \int_0^t A(x, t)B(x, t - \tau) d\tau$$

Boundary Conditions

If surface force T is prescribed on boundary surface S_1

$$n_j \{\bar{\sigma}_{ij} + g_{ij} + (\pi - g) \delta_{ij}\} = T_i \quad \text{on } S_1 \quad (7)$$

in which n_j = directional cosine of a normal to the boundary surface. If rate of flow of pore water Q is prescribed on boundary surface S_2

$$n_j q_j = Q \quad \text{on } S_2 \quad (8)$$

If displacement \bar{u}_i and pore water pressure $\bar{\pi}$ are given on surfaces S_3 and S_4 , respectively

$$u_i = \bar{u}_i \quad \text{on } S_3 \quad (9)$$

$$\pi = \bar{\pi} \quad \text{on } S_4 \quad (10)$$

Variational Principle

Eq. (11) defines the functional $\Omega(t)$ that describes the deformation, and the generation and dissipation of excess pore water pressure during earthquake.

$$\begin{aligned} \Omega(t) = & \int_V [C_{ijkl} e_{kl} * e_{ij} + 2(\pi - g) * u_{i,i} - h * q_i * (\pi_{,j} - g_{,j}) - 2\rho F_i * u_i] dV \\ & + 2 \int_{S_2} h * Q * \pi dS - 2 \int_{S_1} T_i * u_i dS \end{aligned} \quad (11)$$

in which V = volume and S = surface area. The first variation of the functional $\delta\Omega(t)$ shows that Eq. (11) is equivalent to Eqs. (1) to (6) under the boundary conditions of Eqs. (7) to (10).

$$\begin{aligned} \delta\Omega(t) = & \int_V \{ 2[C_{ijkl} e_{kl} + \delta_{ij}(\pi - g)_{,j} + \rho F_i] * \delta u_i \\ & + 2[-\epsilon_{ii} + h * \{k_{ij}(\pi_{,j} - g_{,j})_{,i}\}] * \delta\pi \} dV \\ & + 2 \int_{S_1} [\{-T_i + n_j(C_{ijkl} e_{kl} + (\pi - g) \delta_{ij})\} * \delta u_i] dS_1 \\ & + 2 \int_{S_2} [\{h * (Q - n_j q_j)\} * \delta\pi] dS_2 = 0 \end{aligned}$$

Application of Finite-Element Method

The displacement and pore water pressure within an element can be expressed as follows:

$$\begin{aligned} \{u\} &= [N_u] \{q_n\} \\ \pi &= [N_\pi] \{P_n\} \end{aligned} \quad (12)$$

in which $[N_u]$ and $[N_\pi]$ are shape functions, and from which e , $\bar{\sigma}$, e_{ij} , etc. can be defined as follows:

$$\begin{aligned}
\{e\} &= [B]\{q_n\} & \{q\} &= [k]([G]\{P_n\} - [G]\{g_n\}) \\
\{\bar{\sigma}\} &= [C][B]\{q_n\} + \{g_n'\} & \{T\} &= [N_u]\{T_n\} \\
e_{ii} &= [D]\{q_n\} & \{Q\} &= [N_\pi]\{Q_n\}
\end{aligned} \tag{13}$$

in which $[B]$, $[D]$, $[G]$, etc. can be determined by differentiating Eq. (12).

Substituting Eq. (13) in Eq. (11), and equating the first variation of the functional to zero, and rearranging terms

$$\begin{aligned}
[L]\{u(t)\} + [R]\{\pi(t)\} - [R]\{g(t)\} &= \{M_2\} + \{P_1\} \\
[R]^T\{u(t)\} - h*[W]\{\pi(t)\} &= -h*\{M_3\} - h*\{P_2\}
\end{aligned} \tag{14}$$

$$\begin{aligned}
\text{in which } [L] &= \int [B]^T [C] [B] dV & \{M_2\} &= \int [N_u]^T \{\rho F\} dV \\
[W] &= \int [G]^T [k] [G] dV & \{M_3\} &= \int [G]^T [k] [G] \{g(t)\} dV \\
[R] &= \int [D]^T [N_\pi] dV & \{P_1\} &= \int [N_u]^T [N_u] \{T\} dS \\
& & \{P_2\} &= \int [N_\pi]^T [N_\pi] \{Q\} dS
\end{aligned} \tag{15}$$

Linearly interpolating Eq. (14) in time domain, and letting $Q = 0$

$$\begin{aligned}
[L]\{u(t + \Delta t)\} + [R]\{\pi(t + \Delta t)\} &= [L]\{u(t)\} + [R]\{\pi(t)\} + [R]\{\Delta g\} + \{\Delta P_1\} \\
[R]^T\{u(t + \Delta t)\} - \frac{\Delta t}{2}[W]\{\pi(t + \Delta t)\} &= [R]^T\{u(t)\} + \frac{\Delta t}{2}[W]\{\pi(t)\} + \frac{\Delta t}{2}[W]\{\Delta g\}
\end{aligned} \tag{16}$$

The incremental displacement for accounting for nonlinear properties of soil takes the following form:

$$\{\Delta u\} = \{u(t + \Delta t)\} - \{u(t)\} \tag{17}$$

From Eqs. (16) and (17)

$$\begin{aligned}
[L]\{\Delta u(t + \Delta t)\} + [R]\{\pi(t + \Delta t)\} &= [R]\{\pi(t)\} + [R]\{\Delta g\} + \{\Delta P_1\} \\
[R]^T\{\Delta u(t + \Delta t)\} - \frac{\Delta t}{2}[W]\{\pi(t + \Delta t)\} &= \frac{\Delta t}{2}[W]\{\pi(t)\} + \frac{\Delta t}{2}[W]\{\Delta g\}
\end{aligned} \tag{18}$$

which is the governing equation for predicting changes in pore water pressure in saturated soil during earthquakes. Eq. (18) can be solved by substituting the pore water pressure increment for the time increment Δt . The pore water pressure increment can be determined by combining the initial shear stress and the dynamic shear stress which in turn is determined by dynamic response analysis of the ground. When the process of pore water pressure generation ceases after earthquake ground motion has stopped, Eq. (18) is reduced to an equation for a consolidation process in which material nonlinearity is taken into account. In the present study, rectangular elements are employed, in which a quadratic interpolation is used for the displacement and a linear interpolation for the pore water pressure.

MECHANICAL PROPERTIES OF MODEL GROUND

The mechanical properties of the sand comprising the model ground were determined experimentally under the prevailing confining stresses that were quite small because of the small size of the model. By using these soil properties in the numerical analysis, it was possible to directly verify

the analytical method without relying on similitude relationships.

Shear Moduli and Damping Ratios

The shear moduli, damping ratios, and settlement characteristics of the sand were evaluated with the simple shear apparatus as shown in Fig. 1. The apparatus is similar to that used by De Alba et al (2), and the shaking table was actuated by an electric exciter which could produce clean, sinusoidal acceleration time histories. The inertia mass was a steel plate. By virtue of the friction-free shaking table and displacement measuring instruments (LVDT), it was possible to determine the shear moduli under small confining stresses and in small shear strains, as shown in Fig. 2. It can be seen in Fig. 2 that the shear moduli begin to decrease at smaller shear strains than the previously published data for higher confining stresses. We must, therefore, pay careful attention to the strain dependent behavior of sand even at small strains when we conduct small scale model tests.

The shear moduli of the sand following its liquefaction were determined on the basis of the one-dimensional volume change characteristics as shown in Fig. 3.

Liquefaction Model

Martin et al (3) and Oh-oka (5, 6) proposed methods to estimate generation of excess pore water pressure on the basis of volume change of dry sand subjected to cyclic shear. In the present study, the method by Oh-oka (6) is extended to predict the liquefaction resistance of sand on the basis of density and initial shear stress on the horizontal plane, as follows:

$$e_v = K \left(\frac{\bar{\sigma}_v}{\bar{\sigma}_{v1}} \right)^{\frac{1}{2}} \left(\frac{\tau_{eq}}{\bar{\sigma}_v} \right)^m N_{eq}^n \quad (19)$$

in which e_v = volumetric strain, $\bar{\sigma}_v$ = vertical effective stress, $\bar{\sigma}_{v1}$ = reference effective stress ($= 1 \text{ kg/cm}^2$), τ_{eq} = equivalent shear stress amplitude (Eq. 20), N_{eq} = equivalent number of cycles, n = empirical parameter, and K, m = functions of the relative density, D_r (Fig. 4). Although n varied somewhat with shear stress ratio, a constant value of 0.4 was used.

$$\tau_{eq} = \frac{\tau_d + a(\tau_i + \tau_d)}{1 + a} \quad (20)$$

in which τ_d = shear stress amplitude on the horizontal plane, τ_i = initial shear stress on the horizontal plane, and a = empirical parameter ($= 0.25$).

The above method together with the coefficients of volume change of sand shown in Fig. 3 were used to compute the response of saturated sand to cyclic shear, and the results are compared with a ring torsion apparatus (10) as shown in Figs. 5 to 8. The pore pressure ratios for the lower curves in Fig. 8 do not reach 1.0 because N_L in this case is defined as the number of cycles required to cause a sudden increase in shear strain. In the computation, the compliance ratio, C_R , similar to that defined by Martin et al (4) was assigned values between 0.25 and 0.50.

It can be seen that the influence of the relative density (Figs. 5

and 6) and of the initial shear stress on the horizontal plane (Figs. 7 and 8) are successfully represented by the analytical model. It should be pointed out, however, that the measured values in Figs. 5 to 8 were obtained under an initial effective vertical stress of about 1 kg/cm^2 . When the compressibility characteristics of the sand under low confining stresses were used, the computed values of liquefaction resistance were slightly lower than those shown in Figs. 5 and 7, although the difference is expected to diminish if the effects of sample preparation methods are taken into account.

SHAKING TABLE TESTS

As shown in Fig. 9, the model ground consisted of saturated sand placed in a box 140 cm long, about 20 cm wide, and 40 cm deep. The side walls of the box were transparent plastic plates 18 mm thick in which eight transducers were mounted for pore pressure measurements. The box was placed on a horizontal shaking table actuated with an electric exciter. See Ref. 11 for detailed description of the test procedure.

A clean sand from Toyoura (specific gravity of solids = 2.65, 10-percent size = 0.16 mm, uniformity coefficient = 1.35, the maximum and minimum void ratios = 0.983 and 0.640, respectively) was pluviated through aqueous solution of glycerin to a thickness of 20 cm and at a relative density of 40 percent. The coefficient of permeability of the sand saturated with the glycerin solution was about 0.005 cm/sec at 26°C . The purpose of using the glycerin solution was to facilitate observation of the pore pressure dissipation phase.

The width and the average contact pressure of the model structure were 20 cm and 20 g/cm^2 , respectively. Sinusoidal vibration at a frequency of about 3.5 Hz was applied to the shaking table, with the table acceleration and the duration of vibration varied for different tests. The pore water pressure, and the acceleration and displacements of the inertia mass were recorded simultaneously on oscillographs.

PORE PRESSURE CHANGES IN SAND SUPPORTING A STRUCTURE

Typical results of the shaking table tests in which the duration of vibration was 2 sec are shown on the left side of Figs. 10 to 12. The open symbols with dotted lines correspond to the shallow zone, the solid symbols with full lines indicate the deep zone, and the time scale during vibration (0 to 2 sec) is different from that afterwards.

The model shown in Fig. 9 subjected to the vibration tests was analyzed as a plane strain problem by solving Eq. (18). The ground (either side of the line of symmetry) was divided into 48 rectangular elements with 173 nodal points for the finite element analysis. The results of the analysis are plotted on the right side of Figs. 10 to 12.

No part of the sand was liquefied in Fig. 10, although the pore water pressure did increase considerably. The upper part of the sand away from the structure (encircled Nos. 5 and 7) was liquefied in Fig. 11, whereas the liquefied zone extended to the lower part of the sand away from the structure in Fig. 12 (encircled Nos. 5 to 8). Note a distinct difference in the pore water pressure dissipation time histories between the non-liquefied and liquefied zones, i.e., the pore water pressure in the non-

liquefied zone began to decrease immediately after the table motion had stopped, whereas in the liquefied zone the peak pore water pressure was sustained for some time before it began to decrease. As one might expect, the curves for Nos. 7 and 8 which are farthest from the structure are similar to those for level ground without a structure (12).

The accelerations for Figs. 10 to 12 are in a narrow, critical range in which the pore water pressures are sensitive to a small change in the acceleration. Considering the sensitivity of the pore water pressures and the complexity of the problem, the authors believe that the observed and computed values are in satisfactory agreement. It is expected, therefore, that the proposed method of analysis will be applicable to problems in the field, provided that the physical and mechanical properties of the soil are properly evaluated. Attempts are being made to apply the method to field problems.

Figs. 10 to 12 confirm the previous observation (11) that the sand below the center of the structure (Nos. 1 and 2) is less likely to liquefy than the sand away from the structure. That has been attributed to the confining effect by the weight of the structure. The beneficial effect of the confining stress, however, seems somewhat offset by redistribution of pore pressures due to seepage from the surrounding area. The increase in pore water pressures due to the seepage effect can be demonstrated by comparing the curves in Fig. 10 with the inset in the right side of the figure, which shows the number of cycles required to cause liquefaction if no seepage is permitted (under undrained conditions). The number of cycles less than 7 ($= 3.5 \text{ Hz} \times 2 \text{ sec}$) indicates that liquefaction would occur under undrained conditions. The inset figure shows a clear line of demarkation below the edge of the structure, in that the sand directly below the structure would not liquefy forever while the sand outside would liquefy quite easily.

On the other hand, the result of considerable redistribution of pore pressures is evident in the curves in Fig. 10 for which seepage is accounted for, in such a way that the pore water pressures directly below the structure are higher but those outside the structure are lower than the values which would be predicted by assuming no seepage. In this respect, the assumption of no seepage may not necessarily result in a conservative estimate of the bearing capacity of saturated sand during earthquakes.

CONCLUSIONS

On the basis of the analytical and experimental studies presented in this paper, it may be concluded that the proposed procedure is applicable to predicting pore water pressure changes in saturated sand during earthquakes for two- and three-dimensional problems in which generation and dissipation of excess pore water pressures may occur simultaneously. Unlike previous methods in which the vertical total stress is assumed constant, the present method can deal with changes in stress distribution caused by local softening of soil due to uneven pore water pressure development.

The excess pore water pressures in saturated sand supporting a structure indicate that redistribution of pore water pressures due to seepage should be taken into account in evaluating the bearing capacity of the sand during earthquakes.

ACKNOWLEDGMENTS

The authors gratefully acknowledge the valuable assistance provided by Messrs. S. Ishiwaki, Y. Ishii, and M. Yamagata, Graduate Students of the Tokyo Institute of Technology.

REFERENCES

1. Biot, M.A. (1941), "General Theory of Three Dimensional Consolidation," *Journal of Applied Physics*, Vol. 12, pp. 155 - 164.
2. De Alba, P., Seed, H.B., and Chan, C.K. (1976), "Sand Liquefaction in Large-Scale Simple Shear Tests," *Journal of the Geotechnical Engineering Division, ASCE*, Vol. 102, No. GT 9, pp. 909 - 927.
3. Martin, G.R., Finn, W.D.L., and Seed, H.B. (1975), "Fundamentals of Liquefaction under Cyclic Loading," *Journal of the Geotechnical Engineering Division, ASCE*, Vol. 101, No. GT 5, pp. 423 - 438.
4. Martin, G.R., Finn, W.D.L., and Seed, H.B. (1978), "Effects of System Compliance on Liquefaction Tests," *Journal of the Geotechnical Engineering Division, ASCE*, Vol. 104, No. GT 4, pp. 463 - 479.
5. Oh-oka, H. (1974), "Condition to Induce Liquefaction of Saturated Sand," *Doctoral Dissertation, Tokyo Institute of Technology*, 383 pp. (in Japanese).
6. Oh-oka, H. (1976), "Drained and Undrained Stress-Strain Behavior of Sands Subjected to Cyclic Shear Stress under Nearly Plane Strain Condition," *Soils and Foundations*, Vol. 16, No. 3, pp. 19 - 31.
7. Sandhu, R.S. and Wilson, E.L. (1969), "Finite Element Analysis of Seepage in Elastic Media," *Journal of the Engineering Mechanics Division, ASCE*, Vol. 95, No. EM 3, pp. 641 - 652.
8. Seed, H.B., Martin, P.P. and Lysmer, J. (1976), "Pore-Water Pressure Changes during Soil Liquefaction," *Journal of the Geotechnical Engineering Division, ASCE*, Vol. 102, No. GT 4, pp. 323 - 346.
9. Yoshimi, Y., Kuwabara, F., and Tokimatsu, K. (1975), "One-Dimensional Volume Change Characteristics of Sands under Very Low Confining Stresses," *Soils and Foundations*, Vol. 15, No. 3, pp. 51 - 60.
10. Yoshimi, Y. and Oh-oka, H. (1975), "Influence of Degree of Shear Stress Reversal on the Liquefaction Potential of Saturated Sand," *Soils and Foundations*, Vol. 15, No. 3, pp. 27 - 40.
11. Yoshimi, Y. and Tokimatsu, K. (1977), "Settlement of Buildings on Saturated Sand During Earthquakes," *Soils and Foundations*, Vol. 17, No. 1, pp. 23 - 38.
12. Yoshimi, Y. (1977), "Liquefaction and Cyclic Deformation of Soils Under Undrained Conditions," *State-of-the-Art Report, Proceedings of the 9th International Conference on Soil Mechanics and Foundation Engineering, Tokyo*, Vol. 2, pp. 613-623; originally from Tokimatsu, K.

and Yoshimi, Y. (1977), "Pore Water Pressure Changes in Sandy Ground During Earthquakes," Proceedings of the 12th Annual Meeting of the Japanese Society of Soil Mechanics and Foundation Engineering, pp. 949-952 (in Japanese).

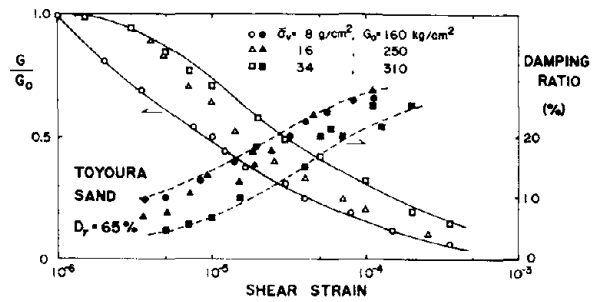
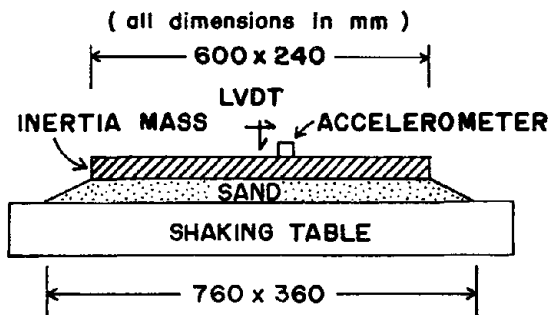


Fig. 1 Simple shear shaking table test apparatus for determining mechanical properties of sand

Fig. 2 Shear moduli and damping ratios of sand under low confining stresses

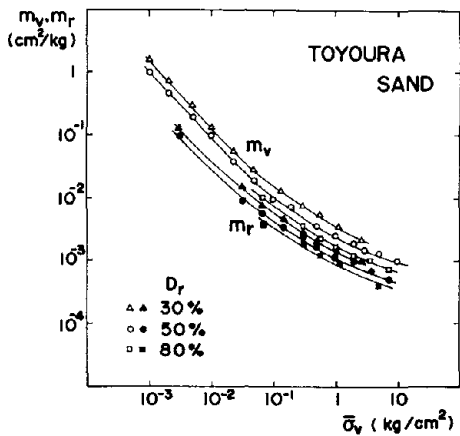


Fig. 3 Coefficient of volume change during post-liquefaction compression, m_v , and during rebound, m_r (9)

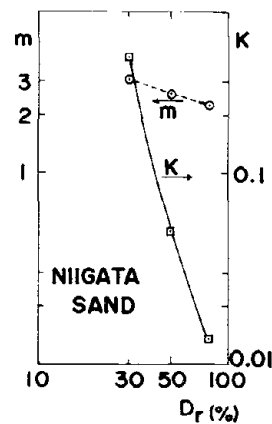


Fig. 4 Empirical parameters K and m for Eq. (19)

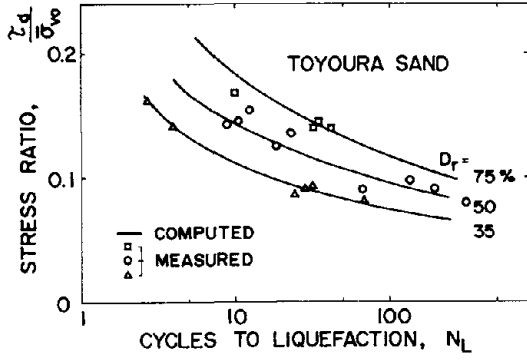


Fig. 5 Influence of relative density on liquefaction resistance of sand

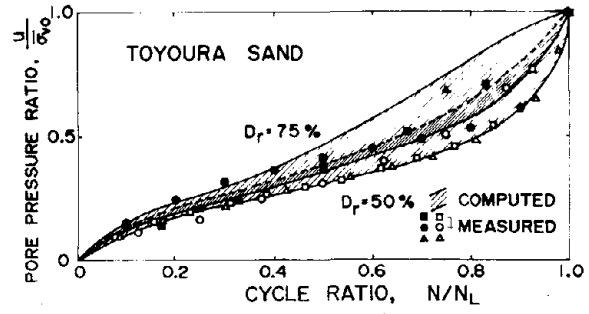


Fig. 6 Influence of relative density on normalized pore pressure generation

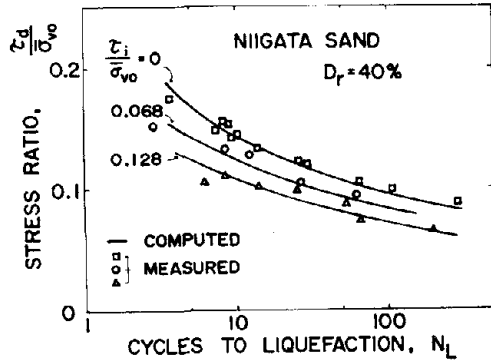


Fig. 7 Influence of initial shear stress on liquefaction resistance of sand

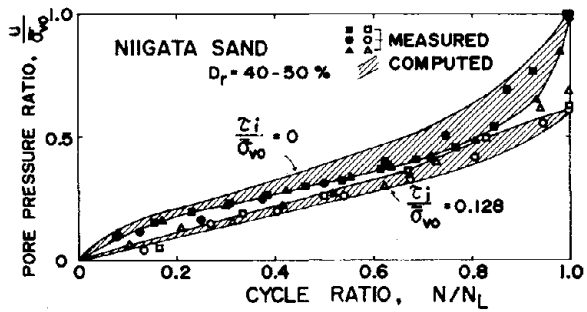


Fig. 8 Influence of initial shear stress on normalized pore pressure generation

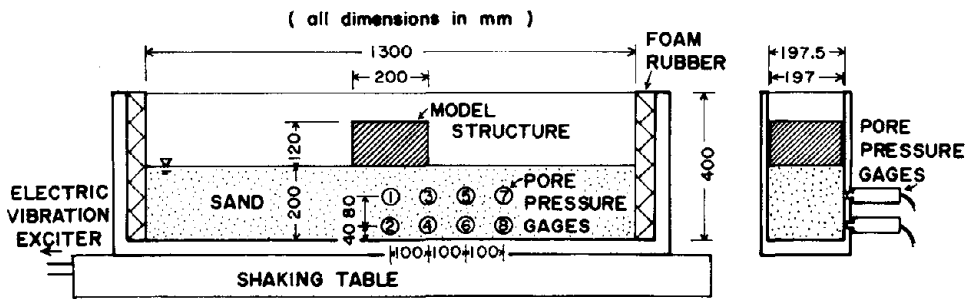


Fig. 9 Model ground and structure

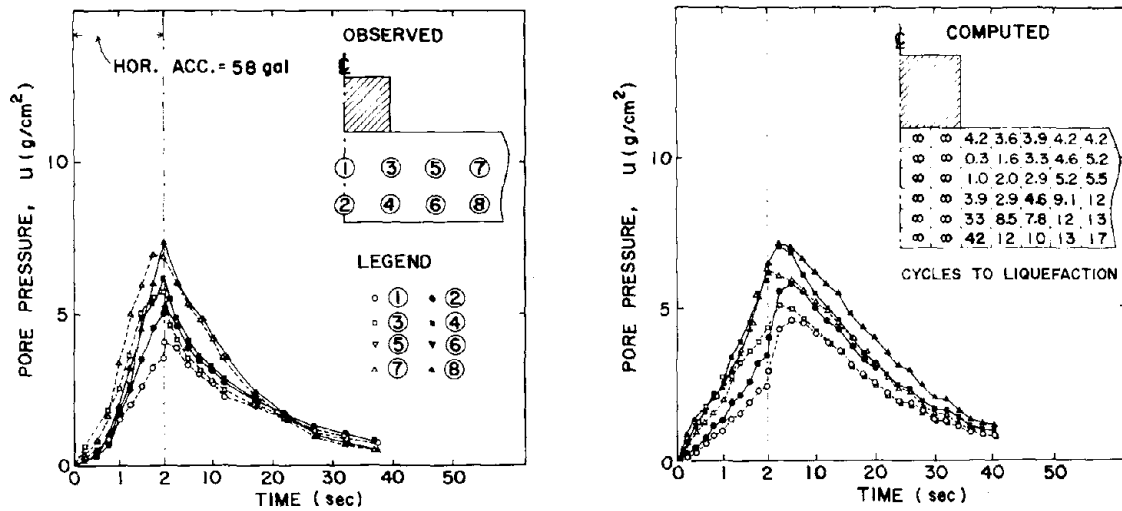


Fig. 10 Pore water pressures during and after vibration: No liquefaction (Inset on the right concerns undrained condition)

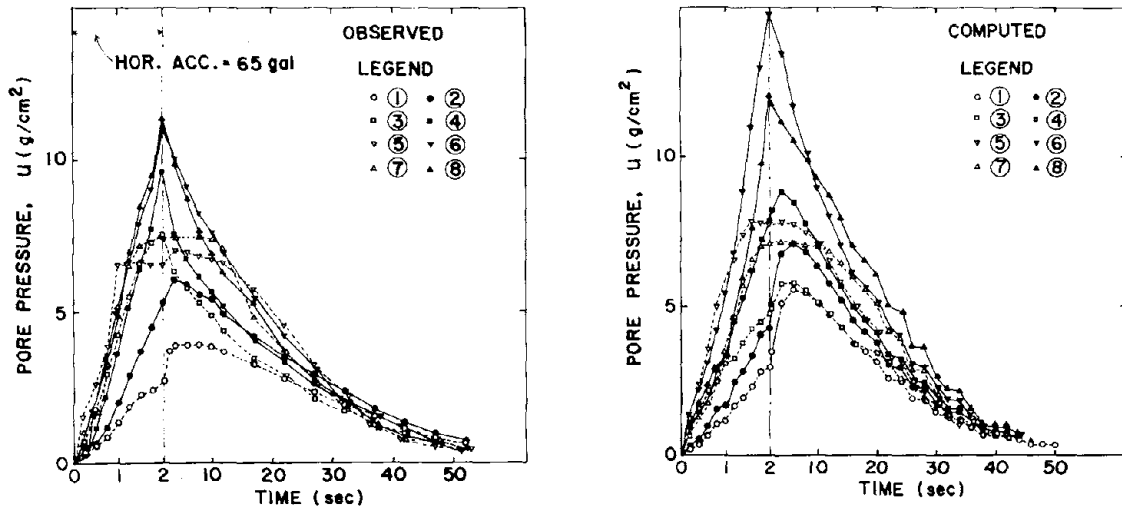


Fig. 11 Pore water pressures during and after vibration: Liquefaction at Nos. 5 and 7

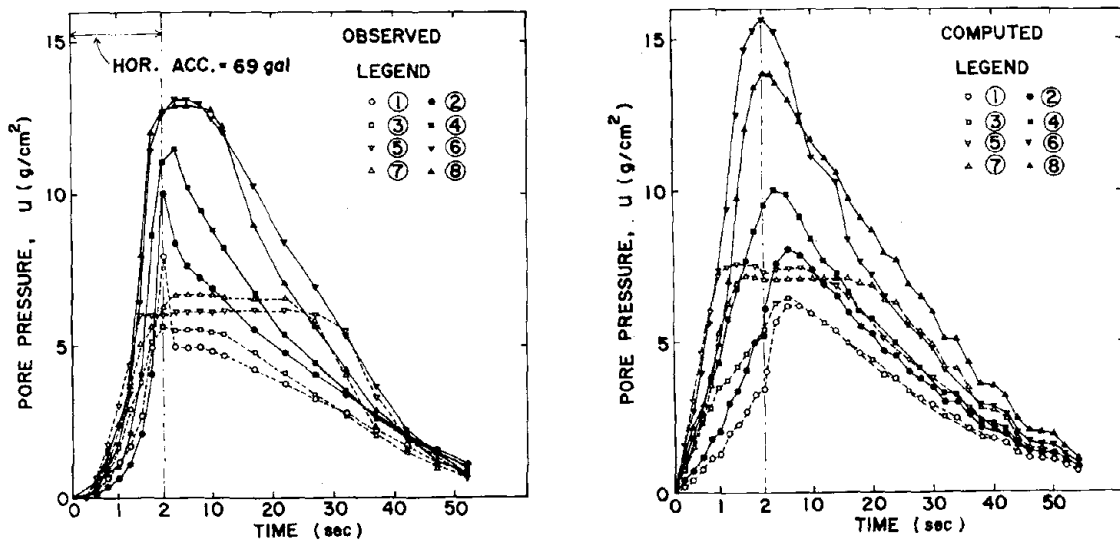


Fig. 12 Pore water pressures during and after vibration: Liquefaction at Nos. 5 to 8

864

INTENTIONALLY BLANK

VERIFICATION OF LIQUEFACTION POTENTIAL BY FIELD BLAST TESTS

A. S. Arya^I, P. Nandakumaran^{II}, V. K. Puri^{III} and S. Mukerjee^{IV}

ABSTRACT

Use of the data obtained from shake table on a cohesionless soil for evaluation of liquefaction potential of a deposit showed that the simplified procedure of Seed and Idriss (1970) gives highly conservative results. It was therefore felt desirable to verify the conclusions by blast tests at the site analysed. A method was evolved to compute the anticipated pore pressure rise due to the design earthquake. During the equivalent motions generated in the field, the rise in pore pressure were measured and compared with computed ones. It was observed that even the shake table test data were on the conservative side.

INTRODUCTION

Currently available procedures for evaluating the liquefaction potential of saturated deposits of cohesionless soils make use of soil strength data obtained in the laboratory. Serious doubts have, however, been raised on the amount of conservatism in the simplified procedure of Seed and Idriss (1970) which is based on the triaxial test data on soils of various grain sizes. The case histories analysed in support of the procedure also raised some questions as to the influence of the continually changing stiffness of the soil deposit due to pore pressure rise, on the ground motion parameters used in the design and also the non-availability of reliable soil parameters except in a very few cases. Test on large size sample on a horizontal shake table carried out to obtain data for use with the liquefaction analysis at a site, indicated that the amount of conservatism in the simplified procedure could be as high as 200 to 250 per cent. Therefore, it was felt necessary to verify the computation of liquefaction potential using some field tests.

The laboratory tests on a soil using a horizontal shake table and use of the data for working out the liquefaction potential based on the simplified procedure have been described. Since the analysis did not indicate liquefaction of the site during the expected earthquake, the validity of the analysis had to be ascertained in terms of the pore pressure rise that might be caused by the earthquake. A suitable technique had, therefore, to be developed for computation of the pore pressure rise at different elevations. The planning of the field tests had to be done so as to generate ground motions which would be equivalent of the expected earthquake motion and to measure the pore pressure rise at convenient depths for which analytical results were already available. In this investigation, however, the ground motions could not be reproduced as such and, only the equivalence vis-a-vis the capability to cause liquefaction was considered. For this purpose blasting of explosives in a bore hole penetrating below the water table was successfully used. The

-
- | | | | |
|------|-----------------------------------|---|---------------------------------|
| I) | Professor and Head |) | School of Research and Training |
| II) | Reader in Soil Dynamics |) | in Earthquake Engineering, |
| III) | Senior Scientist in Soil Dynamics |) | University of Roorkee, |
| IV) | Lecturer in Soil Dynamics |) | ROORKEE - 247672 (U.P.), INDIA |

Preceding page blank

rise in pore pressure was monitored by suitably designed piezometers implanted in the ground below the water table at various distances from the blast point. The studies described herein include the laboratory studies, computation of pore pressures, and the field studies. The site selected for this investigation consisted of moderately dense deposit of a uniform sand with little or no fines. The water table was at a depth of 10 m below the ground surface. The site in question was one of moderate seismic risk and the accelerogram selected for the site on the basis of a seismotectonic study had a peak ground acceleration of 0.3g and peak ground velocity of 30cm/sec.

LABORATORY INVESTIGATIONS

In the laboratory investigations a shake table was used to determine the liquefaction characteristic of the soil from the site. The test set-up consisted of a horizontal shake table capable of being excited sinusoidally up to a maximum acceleration of 2.0g. A bin 1.05m x 0.59m x 0.43m was mounted on the shake table for containing the soil sample. The depth of the soil sample was kept as 0.30 m. The rigid sides of the bin, containing the sample, do vitiate to some extent the deformation pattern near the ends, hence the required observations were confined to central portion of the bin. Sand samples from depths of 10.0 m and below from the site were used for the tests. The soil was deposited in the bin under submerged conditions and compacted to the desired initial relative density by vibration. Three standpipe piezometers placed at three elevations and a diaphragm type pore pressure pick up were used to measure the increase in pore pressures.

Results of tests carried out at an initial relative density of 30% are shown in Figure 1. Here the liquefaction potential, defined as the ratio of hydraulic gradient developed in 10 cycles of table motion to the critical hydraulic gradient, is plotted against the corresponding applied acceleration amplitudes. When liquefaction potential is unity, complete liquefaction is considered to have occurred.

Interpretation of Laboratory Test Results

From Figure 1, it is observed that the minimum horizontal acceleration (a) at which complete liquefaction takes place is 0.075g. The stress ratio between the shear stress and the effective normal stress causing liquefaction in a shake table sample will be given by the expression

$$\frac{a}{g} \cdot \frac{\gamma_{sat}}{\gamma_{sub}} \quad (1)$$

For the sample used at 30% relative density and liquefying at .075g, this ratio works out as $0.075 \times 2/1 = 0.1500$.

Seed and Idriss (1970) have reported the stress ratio causing liquefaction as obtained from triaxial tests as a function of mean grain size. These stress ratios are for a relative density of 50%. Hence to get a comparison between the shake table test data and the data given by Seed and Idriss the stress ratio obtained above is to be divided by $C_r \times 30/50$, where 'Cr' is a correction to be applied to the triaxial test data to obtain a more realistic stress ratio, the stress ratio that should have

been observed in triaxial tests as causing liquefaction in the shake table sample at a relative density of 50%, works out to be $0.15/(0.6 \times 0.53) = 0.472$. The corresponding value from the average curve reported by Seed and Idriss (1970) is 0.215. Therefore, in this particular case the actual stress ratio causing liquefaction would be $0.472/0.215$, i.e., 2.2 times the values reported by Seed and Idriss.

It was observed from computations made with test data from a limited number of tests with higher initial relative densities, that the higher the initial relative density the larger was the modification factor. In other words, data reported here leads to the evaluation of the smallest stress ratio causing liquefaction from shake table tests performed.

Analysis of the liquefaction potential for the soil data from bore hole was then carried out as proposed by Seed and Idriss (1970). The stress ratio causing liquefaction obtained by their method was then modified by multiplying by the factor evolved above. Figure 2 shows a plot of (a) the ratio between shear stress induced by the design earthquake and the effective overburden pressure that will cause liquefaction as a function of depth. This plot rules out the possibility of complete liquefaction occurring at the bore hole location but partial loss of strength is clearly a possibility.

COMPUTATION OF PORE PRESSURE

Let us define liquefaction potential as equal to the ratio between the two stress ratios plotted in Figure 2. That is,

$$\text{liquefaction potential} = \frac{\text{Stress ratio induced by the design earthquake}}{\text{Stress ratio that will cause liquefaction at the same depth}} \quad (2)$$

Assuming the relation between liquefaction potential and ground acceleration level as linear (as seen in Figure 1) till the value of liquefaction potential becomes unity, it is possible to evaluate the pore pressures which could develop at any depth during the design earthquake. Considering a depth of 10.67 meters at the given bore hole location, the loss of confining pressure will be seen to be 42.5%. It can therefore be concluded that the maximum pore pressure which could be induced by the design earthquake is 7.99 metres of water head.

FIELD INVESTIGATIONS

The field investigations comprised a series of five blast tests conducted at predetermined locations in the field so as to give fairly representative data for the entire site. The tests were aimed at verifying in the field, the validity of conclusions arrived at on the basis of shake table data and analytical studies regarding the liquefaction potential of the deposit. Ground vibrations were generated by blasting a charge of 10 Kg of special gelatin 60% in a blast hole about 16 m deep. Observations were made of the rise in pore pressure or rise in free water surface in five cased observation holes located at varying distances (3m to 20m) from the blast holes. The pore pressure rise was measured at a depth of 1 m below the water table using deep bore hole piezometers in

some of the observation holes and stand pipe piezometers in others. A section of the deep bore hole piezometer is shown in Figure 3. The sensing part here consists of a diaphragm type pressure cell with electric wire resistance strain gauges. The stand pipe piezometer consisted of a galvanized iron pipe painted to make it water sensitive. The output of the strain gauge type piezometers was suitably amplified through universal amplifiers and recorded directly on inkwriting oscillographs. In addition to the observation of rise in pore water pressures, the time history of horizontal ground accelerations was also recorded at different distances from the blast holes using accelerometers embedded to a depth of 30 cm below ground level. The output of accelerometers was similarly recorded using amplifier-recorder system. The data on peak horizontal ground acceleration vs. distance and pore pressure rise vs. distance have been plotted in Figures 4 and 5 respectively.

Interpretation of Field Test Data

As mentioned earlier, the object of field blast tests was to obtain the rise in pore pressures in field corresponding to the design earthquake for comparison with the results from laboratory tests. As seen from Figure 4, the horizontal ground accelerations associated with underground blasts show a fast attenuation with distance and the nature of recorded accelerogram is quite different from that of the earthquake and usually consists of a single peak which decays with time. However, a single pulse of large acceleration may produce rise in pore water pressures which may be produced by several cycles of small equivalent acceleration pulses. What is significant from point of view of liquefaction is the end product, namely the loss in effective confinement due to rise in pore pressures. Hence the concept of equivalent number of uniform stress cycles (Lee and Chan, 1972) was utilized for comparing the results of different type of tests, namely the shake table tests and the field blast tests in the present case. Following this procedure the design accelerogram for the site was seen to have an equivalent number $N_{eq} = 7.5$ of uniform acceleration cycles of intensity 0.225 g. Similarly the accelerograms of the blast tests obtained at various distances from the blast hole were converted into equivalent number of uniform stress cycles of 0.225 g. The variation of N_{eq} vs. distance for the blast tests is shown in Figure 6. It is observed from this figure that the blast accelerogram has the same N_{eq} as the design earthquake at a distance of 7m from the blast hole. The pore pressure developed at a distance of 7 m from the blast hole and at a depth of 10 m below ground level is observed to be 3 m of water head. This is equivalent to a loss of 20% in effective normal stress at this depth.

DISCUSSION

It may be observed in the present case that both the field and laboratory test data indicate loss in confinement leading to partial liquefaction. Shake table studies coupled with analysis for liquefaction indicated a loss of effective confinement of the order of 42.5% whereas the field blast test data indicated a loss in effective confinement of the order of 20% for the same design earthquake. This is the case when stress ratio causing liquefaction had been suitably multiplied by a factor in the light of shake table test results. A few additional tests conducted on samples with higher initial relative density than 30% for which the factor of 2.2 was worked out, indicated that the modification factor

of stress ratio causing liquefaction increases with increase in initial relative density. Therefore, predicted rise in pore pressures in this case is indeed on the conservative side and may be expected to compare favorably with field blast test data if larger values of the modification factors were used. The approach due to Seed and Idriss (1970), therefore, appears to yield highly conservative estimates of liquefaction potential. In the present case it indicates almost complete liquefaction in certain zones whereas only partial loss in strength is indicated by shake table as well as field test data.

CONCLUSION

The procedure for evaluation of liquefaction potential as given by Seed and Idriss appears to give highly conservative results. If this stress ratio causing liquefaction is modified to suit the results obtained by large sample shake table tests, as done in this study, fairly realistic values of liquefaction potential are obtained as verified by field blast tests.

REFERENCES

1. Seed, H.G., and Idriss, I.M. (1970) "A Simplified Procedure for Evaluating Soil Liquefaction Potential," Report No. EERC 70 - 9, University of California, Berkeley.
2. Lee, K.L., and Chan, K. (1972) "Number of Equivalent Significant Cycles in Strong Motion Earthquake," Proceedings of the International Conference on Microzonation for Safer Construction, Research and Application, Vol. II, U.S.A.

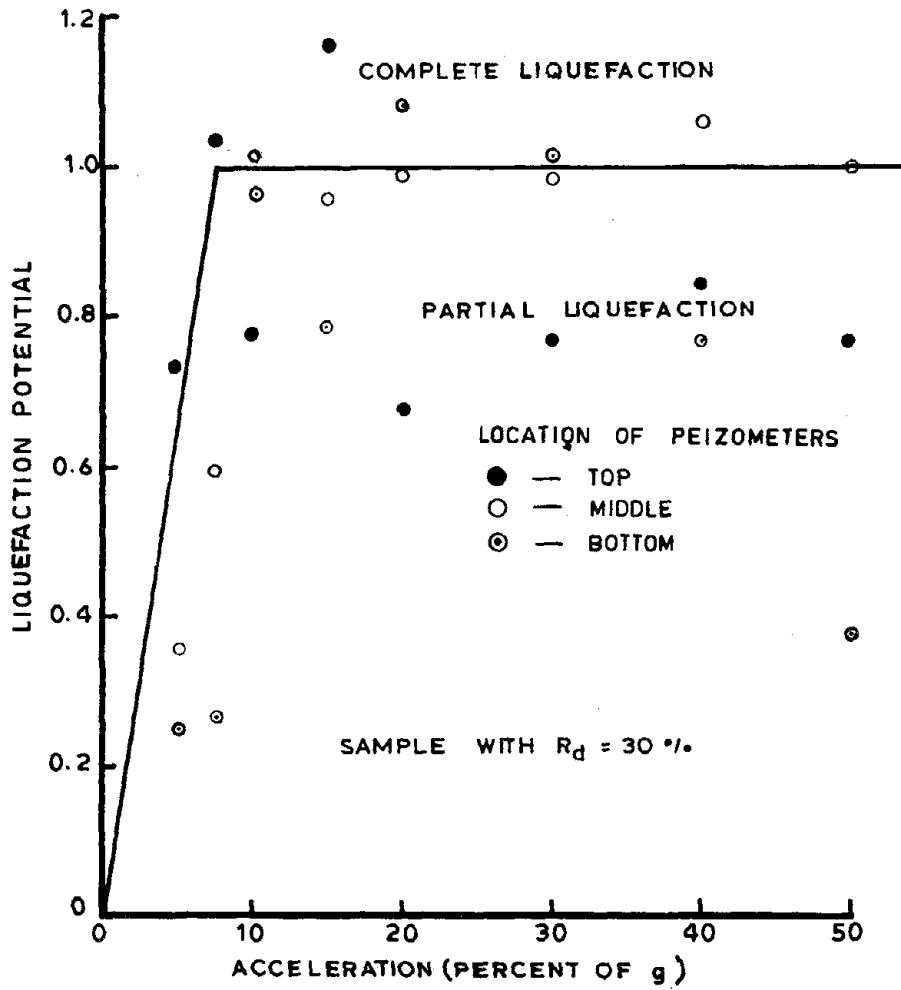


FIG.1_ LIQUEFACTION POTENTIAL VS ACCELERATION

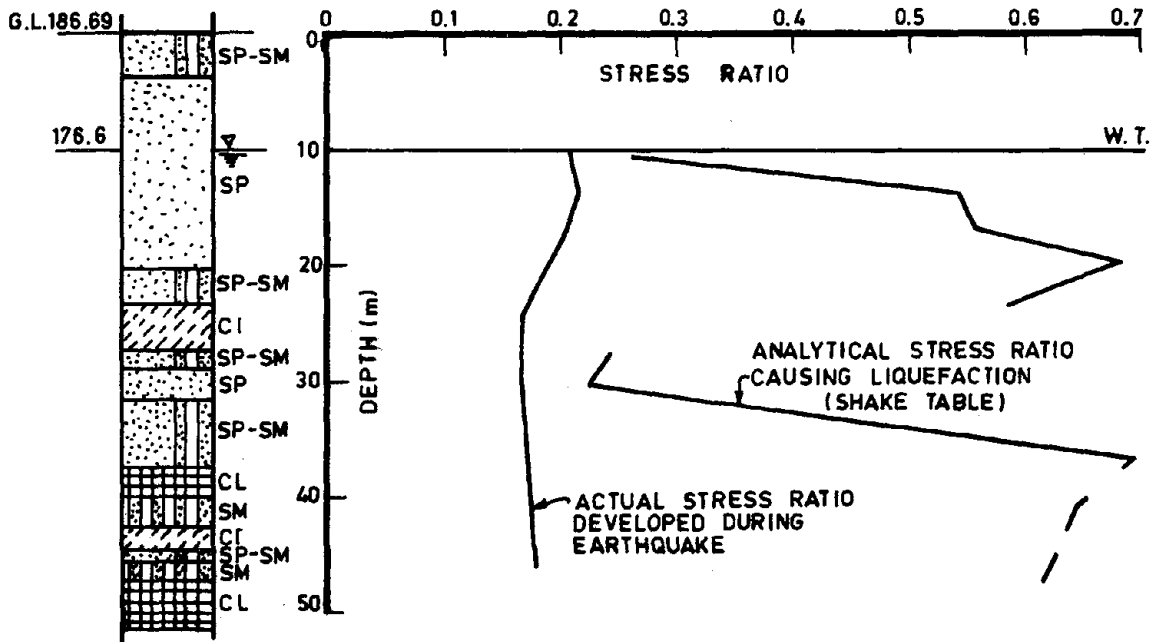


FIG.2_ RESULTS OF ANALYTICAL STUDIES AT BORE HOLE

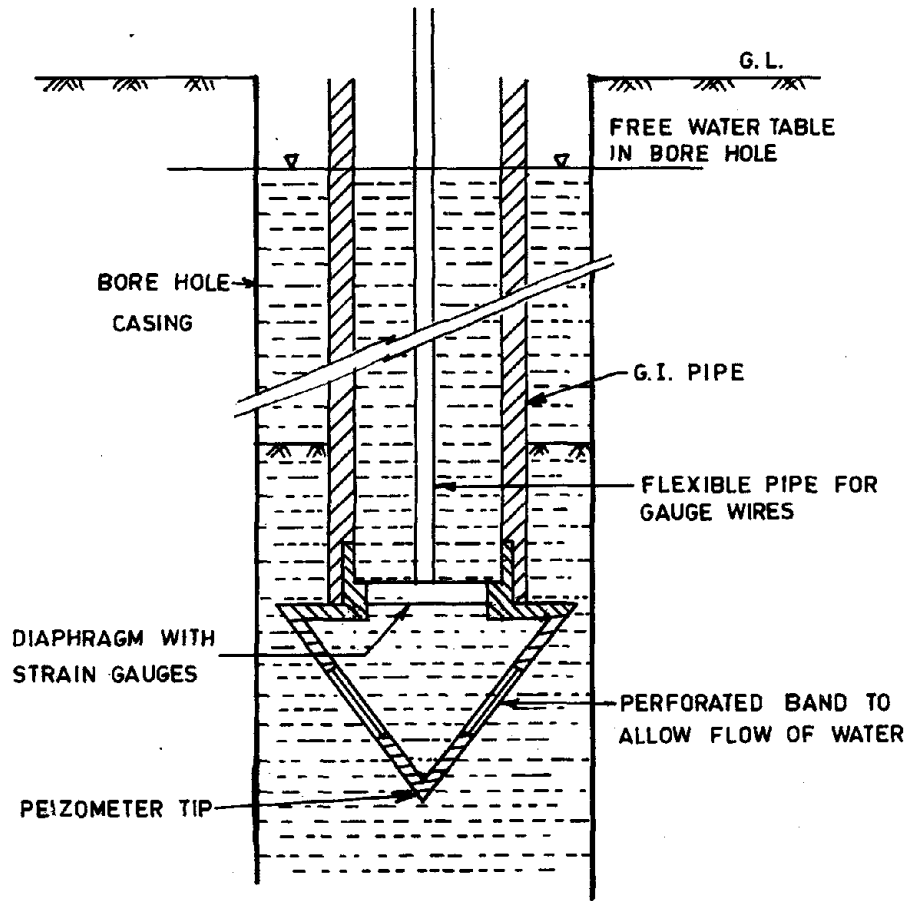


FIG.3_SCHEMATIC DIAGRAM OF DEEP BORE HOLE PEIZOMETER

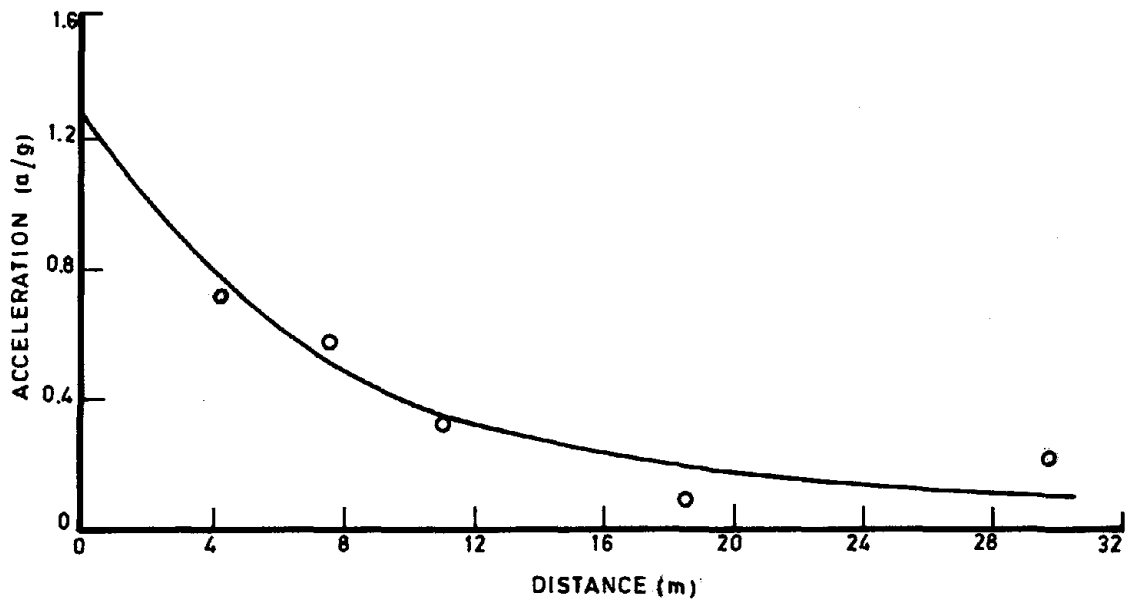


FIG.4_PEAK GROUND ACCELERATION (HORIZONTAL COMPONENT) VS DISTANCE

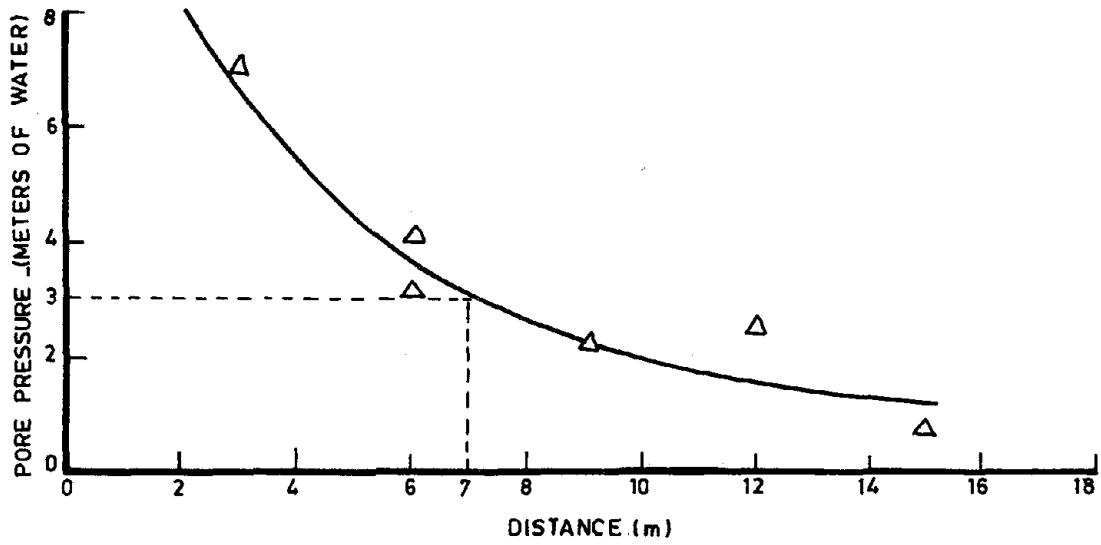


FIG.5_DYNAMIC PORE PRESSURE DEVELOPED VS DISTANCE

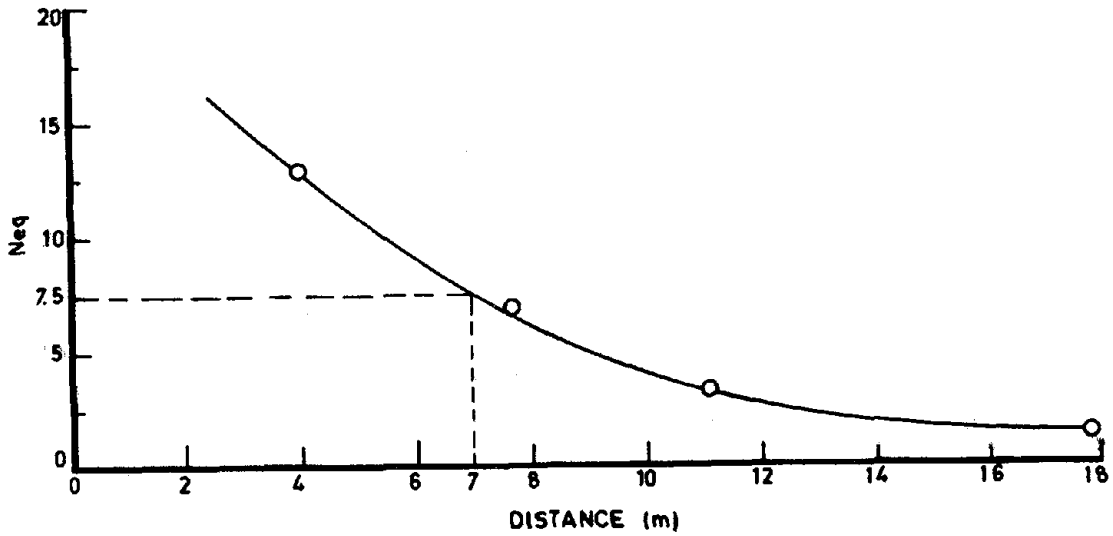


FIG.6_EQUIVALENT STRESS CYCLES OF 0.225g VS DISTANCE

USE OF PENETRATION DATA
FOR EVALUATION OF LIQUEFACTION POTENTIAL

by

Houshang Dezfulian, Ph.D.^I and Sheldon Ray Prager, M.S.^{II}

ABSTRACT

This paper presents results of a method using field data to evaluate the earthquake induced liquefaction potential of granular soils. Data was obtained from Standard Penetration Test results and static cone penetrometer soundings. Results from field and laboratory testing programs were used to identify the occurrence of granular layers and determine the characteristics of each layer. An analysis was made of relative density and the correlation between N values from the borings and q_c from the penetrometer soundings, enabling the penetrometer data to be converted to corrected N-values.

The liquefaction potential was evaluated by determining the resisting soil stress ratio from behavior of other granular sites during earthquakes and dividing by the induced stress ratio from the design earthquake. A correlation between soil characteristics (determined by the Standard Penetration Test) and liquefaction potential (using induced earthquake accelerations and observed site behavior) has been established by Professor Seed and is used in this paper. A comparison is also made between the factors of safety using the field data approach and the approach using induced stresses from acceleration time histories and strengths from laboratory cyclic triaxial testing.

INTRODUCTION

Analyses have been performed to determine the liquefaction potential of saturated granular soils underlying critical facilities for a nuclear power plant in southwest Iran. The analyses consisted of calculating factors of safety against liquefaction by two methods:

Method I: Observation of performance of sand deposits during previous earthquakes using field penetration data (6, 7, 9, 10), and

Method II: Comparison of induced stress conditions from earthquakes and stress conditions causing liquefaction in the laboratory based on cyclic strength curves (5, 8).

Method I uses field penetration data to evaluate the in-situ soil characteristics and compares this data to that from sites where earthquakes have occurred and soils have or have not been known to liquefy by field observation. Data for the evaluation was obtained from both test borings in which the Standard Penetration Test (SPT) was performed and from static cone penetrometer tests

I Director, Tehran Berkeley Consulting Engineers, Tehran, Iran

II Senior Engineer, Fugro, Inc., Long Beach, California

(CPT) in which the point resistance, q_c , was converted to an equivalent SPT value. Evaluation of the liquefaction potential by Method I involves the following steps:

1. Development of the soil profile from field and laboratory data,
2. Determination of the representative relative densities of the granular soil deposits to establish blowcount correction factors,
3. Determination of induced stresses from the design earthquake and corresponding values of cyclic stress ratio,
4. Determination of soil liquefaction resistance from the correlation between stress ratio required to cause liquefaction and the penetration resistance of the sands from field data, and
5. Determination of factor of safety against liquefaction.

Method II consists of calculating factors of safety against liquefaction by comparing the induced shear stresses for various input acceleration-time histories to the cyclic strengths of the granular soils as determined from laboratory tests on undisturbed samples.

This paper presents the approach and results for Method I and compares the results to those from Method II.

SUBSURFACE SOIL PROFILE

The site is located in a flat desert region. The ground surface was assumed to be raised about two meters due to future site development.

A general soil profile was developed from the results of the borings and cone penetrometer soundings and is shown in Fig. 1. The soils of primary interest were sands, and sandy silts. The design water depth below existing grade was assumed to be at a depth of about 1.5 to 2 meters.

Soils in the upper 15 meters consist predominantly of firm to stiff clays with soft to firm sandy silt at about 7 to 8 meters below the existing ground surface, and a medium dense silty sand at about 12 to 13.5 meters below the existing ground surface.

Below 15 meters, soils consist of stiff to very stiff clay with dense sand layers containing varying amounts of silt, encountered at depths of about 16, 27, 38, 44, and 58 meters. Additional sands were stratified throughout the clay matrix at other depths but no other continuous granular layers were discerned.

Fig. 2 shows a typical log of a CPT sounding. The data was obtained with a truck-mounted mechanical cone having a capacity of 10 tons. Penetration was normally limited by refusal at a depth of between 35 to 45 meters.

DESIGN ACCELERATIONS

The vibratory ground motion at the site was considered to be controlled by the following two earthquakes:

1. A local earthquake with magnitude 6 to 6-1/4 occurring below the site and having a focal depth of about 10 to 15 km.
2. A distant earthquake of magnitude 7 to 7-1/2 occurring at a distance of about 50 km from the site and having a focal depth of about 30 km.

Factors of safety against liquefaction were computed for maximum horizontal ground accelerations ranging from 0.25g to 0.35g.

APPROACH

The field analysis is based on an empirical relationship (9) where induced seismic stress ratios have been calculated for sites where earthquakes were known to have occurred and are underlain by sand deposits. Corrected blowcount values (N_1) derived using the Standard Penetration Test (SPT), ASTM D-1586, were compared by Seed, et al (9), to the induced stress ratios from the actual earthquakes, and a conservative boundary between observed cases of liquefaction and non-liquefaction was established. The results of this work are shown on Fig. 3 which can be used for any value of maximum ground acceleration. The curve on Fig. 3 is a lower bound for all sites known to have liquefied and includes data for earthquake magnitudes up to 7.5. A slightly modified version of this figure has been shown elsewhere (10). The basic assumption is that this figure is based on past soil behavior and can be used to predict future soil behavior.

Seed's correlation is based on data obtained for silty sands or sands and therefore the sandy silt at 7 m does not apply directly. For this study, information from the 7 m layer has been included in the basic data reduction but is not included in the safety factor determination.

In the analysis, the N-value (SPT) data is corrected to an equivalent overburden pressure of 1 tsf (about 1 kg/cm²). The correction factor is based on the work by Marcuson and Bieganouski of the U.S. Waterways Experiment Station (2). This correction factor is established for two relative density ranges:

- o Relative density between 40 and 60%, and
- o Relative density between 60 and 80%

The relative density for the granular materials was evaluated using both the SPT and CPT test results reported by Gibbs and Holtz (1) and Schmertmann (4). The Schmertmann correlation was for the Fugro electric cone penetrometer and was converted to the mechanical cone used in this investigation. Histograms for the distribution of relative density are presented on Fig. 4 and indicate the predominant relative density to be above 60%. The lower relative density values were found primarily in the two granular layers above a depth of 16 meters.

EVALUATION OF LIQUEFACTION POTENTIAL

The determination of corrected N-values for the liquefaction analysis for relative densities between 60 and 80% can be approximated as follows (6):

$$N_1 = N\sigma_o' (0.46)$$

where N_1 = N-value corrected to an effective overburden pressure of 1 tsf (about 1 kg/cm²),

N = SPT blowcount, and

σ_o' = effective overburden pressure in tsf.

Correlations between SPT and CPT results based on soil type have been proposed (3). For granular soil the value of q_c/N is normally between 3 and 6, with the higher value more applicable for coarser soils. CPT point resistance results obtained in this study were converted to an equivalent N-value by means of a comparison between SPT results from borings and q_c results from penetrometer tests located about 3 meters apart. Six adjacent sets of data were used for this comparison.

The value of q_c/N for the site granular materials is shown versus depth on Fig. 5 and ranged from 3.5 to 6. The average value is $q_c/N = 4.6$ and compares well with the published correlations (3). A value of $q_c/N = 4.5$ was used in the analysis. For the granular soil layers the average value of point resistance for each meter of depth was used. Both SPT blowcounts and equivalent CPT blowcounts ($q_c/N = 4.5$) were used to determine the corrected blowcount (N_1).

The average induced stress ratio (τ_{avg}/σ_o') arising from design earthquake shaking was computed using the following relationship (9):

$$\tau_{avg}/\sigma_o' = 0.65 \times a_{max}/g \times (\sigma_o/\sigma_o') \times r_d$$

where: τ_{avg}/σ_o' = average induced horizontal stress ratio,

a_{max} = maximum acceleration at the ground surface,

g = acceleration of gravity,

σ_o = total overburden pressure at depth considered,

σ_o' = effective overburden pressure at depth considered,

r_d = stress reduction factor varying from one at the ground surface, to 0.9 at a depth of 9.1 meters, 0.75 at a depth of 15.2 meters and 0.5 at a depth of 30 meters.

The induced stress ratio was calculated for the design ground surface accelerations. These stress ratios were converted to N_1 values required to resist liquefaction by using the curve on Fig. 3. A plot of the lower bound for sites where liquefaction has occurred is shown on Fig. 6 as a function of N_1 and depth. Data from individual corrected SPT results and the average q_c value

from 50 CPT soundings in the granular zones is plotted on Fig. 6. Histograms showing the percentage of points in each zone for different depth intervals are shown on Fig. 7. The CPT plots are based on 50 soundings in which q_c was averaged for each meter of the sandy zones shown in Fig. 1 up to a depth of 32 meters. The zone above 15 meters shows 1/3 of the data points in the liquefaction zone and 2/3 of the data points in the non-liquefaction zone. For the CPT data most of the liquefiable points came from the 7 meter sandy silt layer.

FACTORS OF SAFETY

Factors of safety against liquefaction were computed for the various granular layers by using the correlation shown in Fig. 3. The first potentially liquefiable zone at 7 meters was identified as a sandy silt. This zone was not included in the factor of safety calculation because Fig. 3 was developed from sand data. For each granular soil layer the average corrected N-value was determined from the SPT and CPT data. The factor of safety against liquefaction was then determined by dividing the stress ratio necessary to cause liquefaction (from Fig. 3) by the average induced cyclic stress ratio from the design earthquake.

The cyclic stress ratio required to cause liquefaction is based on an overburden pressure of 1 tsf (about 1 kg/cm²). A small correction to the cyclic stress ratio for other overburden pressures was applied by using laboratory cyclic triaxial test results. For the distant earthquake, a relationship between the stress ratio causing initial liquefaction (approximated by 5% axial strain) at 15 cycles and confining pressure was developed and is shown on Fig. 8. A similar figure was developed for the local earthquake.

Factors of safety were determined for the granular soil at a depth of 12, 16, and 27 meters and are shown on Tables 1 and 2. For the SPT calculation using the results shown on Fig. 6, average N_1 values from 10-15 meters were used for the 12 meter layer, average N_1 values from 15-20 meters were used for the 16 meter layer, and average N_1 values from 25-30 meters were used for the 27 meter layer. SPT and CPT data were generally unavailable below 32 meters. Table 1 shows good correlation between the factors of safety from the SPT and CPT data.

ANALYTICAL METHOD

The liquefaction potential for the granular soil deposits underlying the nuclear power plant was also analyzed by performing a one dimensional shear beam analysis for the determination of induced stress from representative earthquake records and comparing the induced stresses to the soil strengths under cyclic loading (Method II). The cyclic stresses induced in the ground were computed by deconvolution of a known ground surface motion by use of the computer program SHAKE (5). The evaluation of the laboratory cyclic strength of the on-site granular materials was performed by using the cyclic triaxial test (8). Factors of safety from the analysis are presented on Tables 2 and 3.

CONCLUSIONS

1. Liquefaction analyses can be performed using granular soil characteristics determined from field penetration data using SPT results from test borings or q_c results from cone penetrometer soundings.
2. Using site correlations of q_c/N , CPT results can be converted to a corrected blowcount (N_1).
3. Factors of safety can be obtained from the field data by dividing the soil strength by the induced shear stress. The soil strength is determined from the correlation between stress ratio causing liquefaction in the field and penetration resistance of sand. Induced stress is calculated from the equation presented herein.
4. Factors of safety from the SPT and CPT analyses were in good agreement.
5. Factors of safety from Methods I and II differed. The primary reason has been attributed to sample disturbance effects affecting the laboratory cyclic strength.

ACKNOWLEDGMENTS

The studies presented herein were conducted for the Atomic Energy Organization of Iran as part of the Site Safety Analysis Studies for a nuclear power plant. Permission to use the data for this paper by Dr. A. A. Nowroozi, Head of the Nuclear Regulatory Directorate and Director of the Environment Protection Division, is gratefully acknowledged.

Dr. N. D. Marachi and Dr. E. S. Nobari (Tehran Berkeley Consulting Engineers) and Dr. G. Martin and Mr. C. Espana (Fugro, Inc.) participated in the performance of the studies. Professor H. B. Seed (University of California at Berkeley) served as a special consultant for the studies and was most helpful in directing the studies.

REFERENCES

1. Gibbs, H. J., and Holtz, W. G., 1957, "Research on determining density of sands by spoon penetration testing," Proc.Int. Conf. Soil Mech. Found. Eng., 4th, London.
2. Marcuson, W. F., and Bieganousky, W. A., 1977, "Laboratory Standard Penetration Tests on fine sands," Journal of the Geotechnical Engineering Division, ASCE, Vol. 103, No. GT6, June.
3. Sanglerat, G., 1972, "The penetrometer and soil exploration," Elsevier Publishing Co., Amsterdam, The Netherlands.
4. Schmertmann, J. H., 1976, "Updated q_c -D correlation report," Contract report to WES, DA CW 39-76-M-6646, October.
5. Schnabel, P. B., Lysmer, J., and Seed, H. B., "SHAKE - A computer program for earthquake response analyses of horizontally layered sites," Report No. EERC 72-12, University of California, Berkeley.
6. Seed, H. B., 1976, "Preliminary report on evaluation of liquefaction potential of sand deposit at site of San Joaquin NPS based on observations of performance in previous earthquakes," unpublished report.
7. Seed, H. B., Arango, I., and Chan, C. K., 1975, "Evaluation of soil liquefaction potential during earthquakes," Report No. EERC 75-28, University of California, Berkeley.
8. Seed, H. B., and Lee, K. L., 1966, "Liquefaction of saturated sands during cyclic loading," Journal of the Soil Mechanics and Foundations Division, ASCE, Vol. 92, No. SM 6.
9. Seed, H. B., Mori, K., and Chan, C. K., 1975, "Influence of seismic history on liquefaction characteristics of sands," Report No. EERC 75-25, University of California, Berkeley.
10. Seed, H. B., Mori, K., and Chan, C. K., 1977, "Influence of seismic history on liquefaction of sands," Journal of the Geotechnical Engineering Division, ASCE, Vol. 103, No. GT4, April.

TABLE 1

FACTOR OF SAFETY CALCULATION BASED ON METHOD I

FOR $a_{\max} = 0.30g$ FROM THE DISTANT EARTHQUAKE

Depth to Sand Layer (m)	Induced $\tau_{\text{avg}}/\sigma'_o$	σ'_o (kg/cm ²)	Average N_1		Soil Strength (τ/σ'_o) for $\sigma'_o = 1 \text{ kg/cm}^2$		Confining Pressure Correction Factor	Factor of Safety	
			SPT Data	CPT Data	SPT Data	CPT Data		SPT Data	CPT Data
12	.25	1.4	20	28	.22	.32	0.98	0.9	1.3
16	.21	1.9	35	40	.48	>.50	0.96	2.2	>2.4
27	.18	2.9	35	32	.48	.40	0.91	2.4	2.0

TABLE 2

COMPARISON OF FACTORS OF SAFETY

FOR LAYER 12-13.5M

Cohesionless Layer	Peak Acceleration Method	Factor of Safety Against Liquefaction					
		Distant Earthquake			Local Earthquake		
		$a_{\max} = 0.25g$	$a_{\max} = 0.30g$	$a_{\max} = 0.35g$	$a_{\max} = 0.25g$	$a_{\max} = 0.30g$	$a_{\max} = 0.35g$
12-13.5m	I	1.40	1.15	1.00	1.73	1.44	1.24
	II	1.48	1.24	1.06	2.05	1.71	1.47
	Average of Methods I & II	1.44	1.20	1.03	1.89	1.58	1.36

TABLE 3

COMPARISON OF FACTORS OF SAFETY FROM METHODS I AND II

FOR $a_{\max} = 0.30g$ FOR THE DISTANT EARTHQUAKE

Depth to Sand Layer (m)	F.S. from SPT Data	F.S. from CPT Data	Avg F.S. of Method I	F.S. from Method II
12	0.9	1.3	1.15	1.4
16	2.2	>2.4	>2.4	1.5
27	2.4	2.0	2.2	1.6

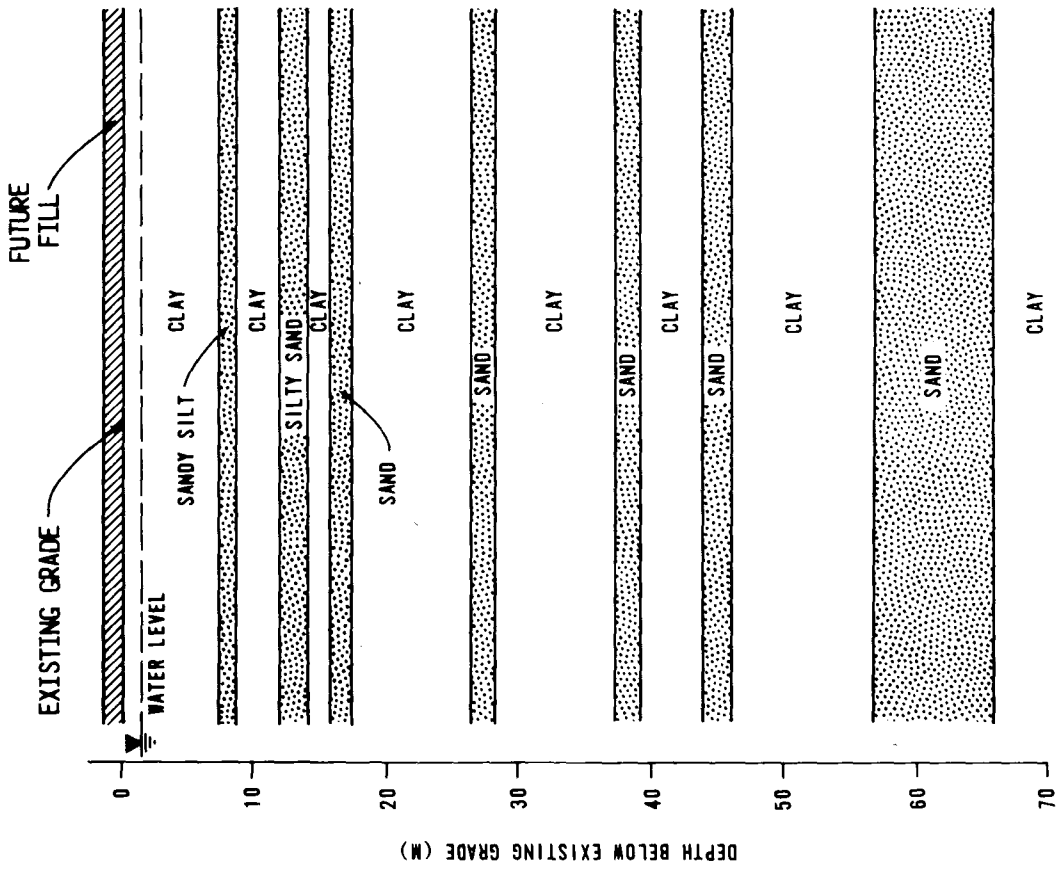
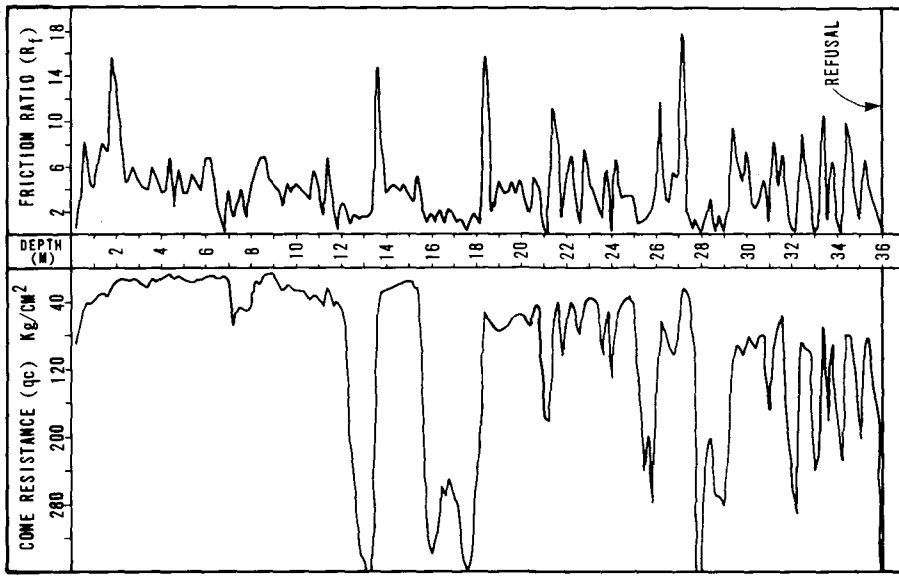


FIGURE 1 TYPICAL SOIL PROFILE



EXPLANATION

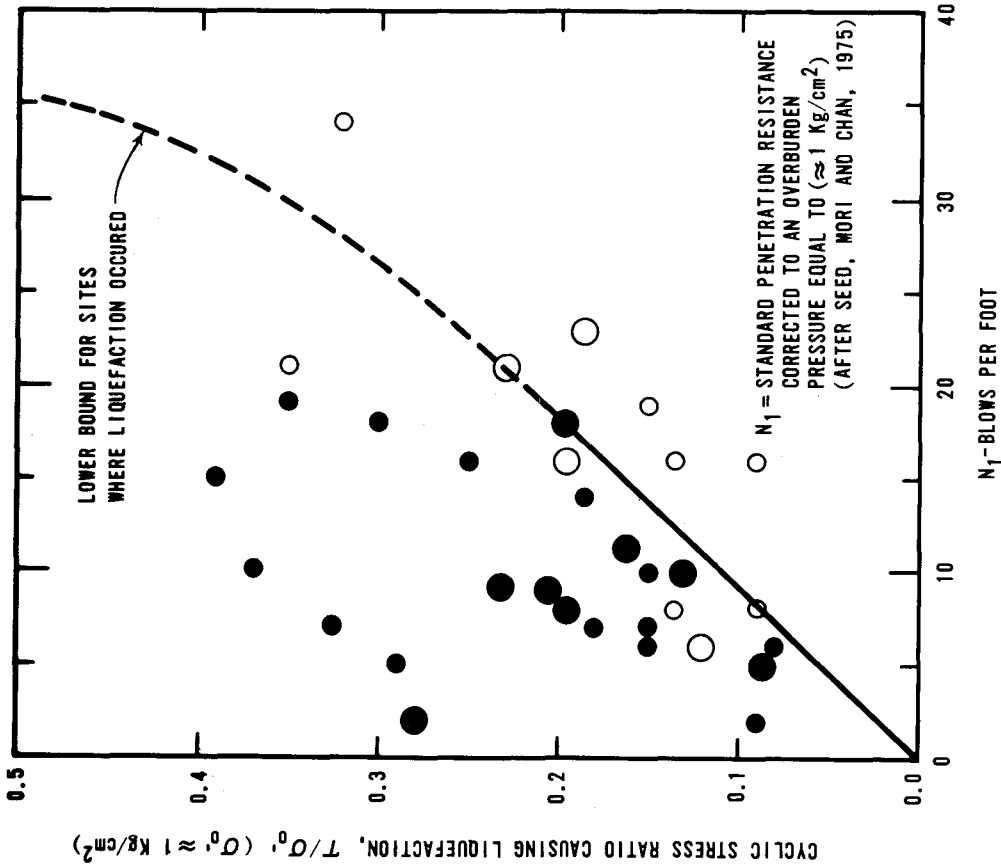
P_1 = LOAD ON CONE POINT A_c = CONE BASE AREA

P_2 = TOTAL FORCE = LOAD ON CONE + LOAD ON FRICTION SLEEVE R_f = FRICTION RATIO (f_s/q_c) X 100

A_s = SURFACE AREA OF SLEEVE q_c = CONE RESISTANCE (P_1/A_c)

f_s = FRICTION RESISTANCE ON SLEEVE ($\frac{P_2 - P_1}{A_s}$)

FIGURE 2 TYPICAL STATIC CONE PENETROMETER SOUNDING



- Liquefaction; stress ratio based on estimated acceleration data
- Liquefaction; stress ratio based on good acceleration data
- No liquefaction; stress ratio based on estimated acceleration data
- No liquefaction; stress ratio based on good acceleration data

FIGURE 3 CORRELATION BETWEEN STRESS RATIO CAUSING LIQUEFACTION IN THE FIELD AND PENETRATION RESISTANCE OF SAND.

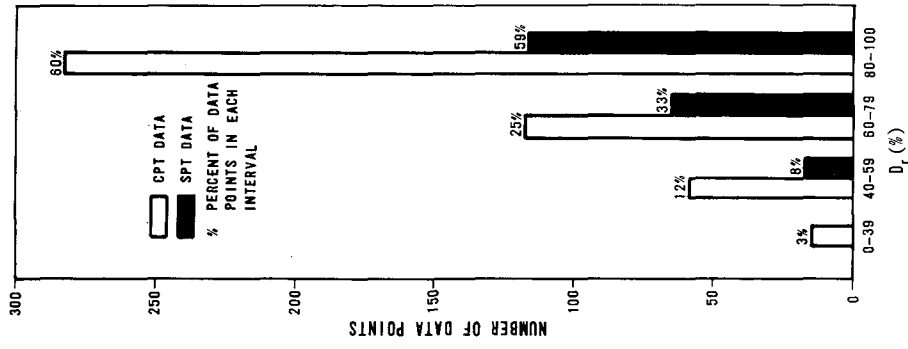


FIGURE 4 RELATIVE DENSITY DISTRIBUTION

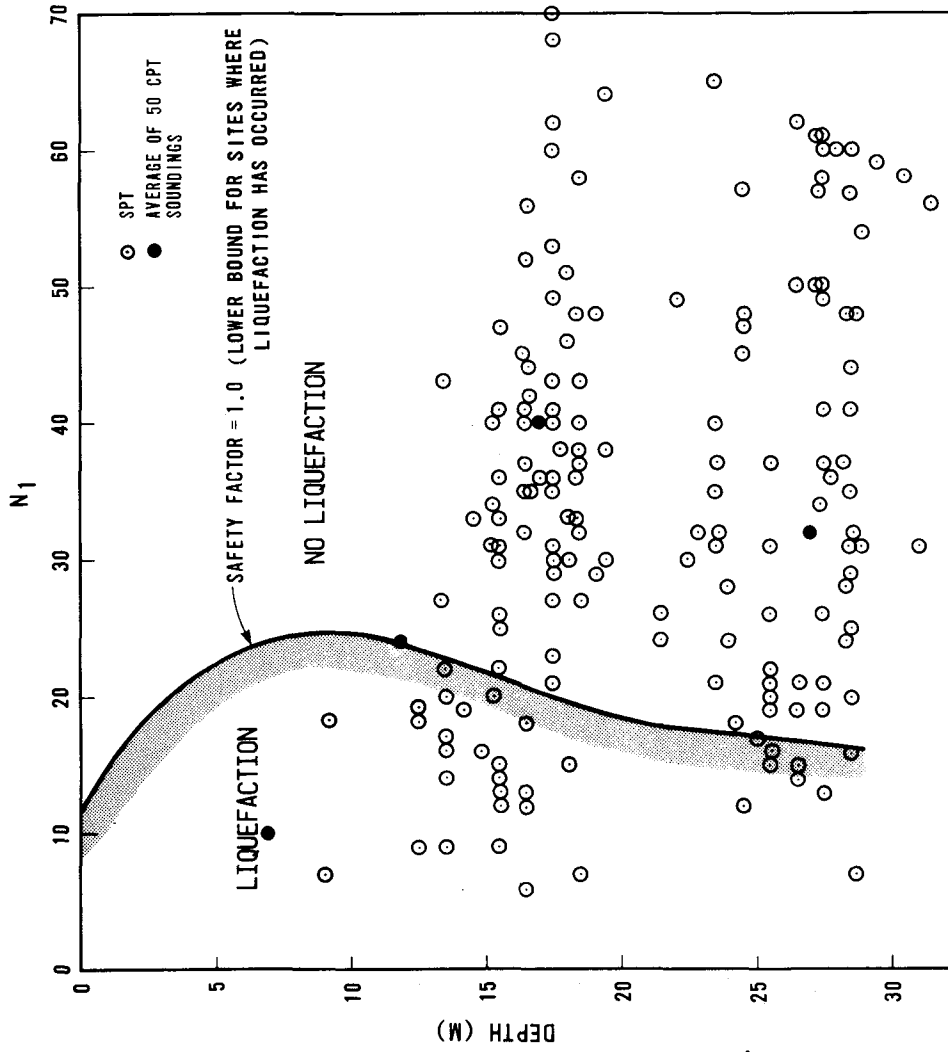


FIGURE 6 RELATIONSHIP BETWEEN N_1 AND DEPTH USING SPT AND CPT DATA

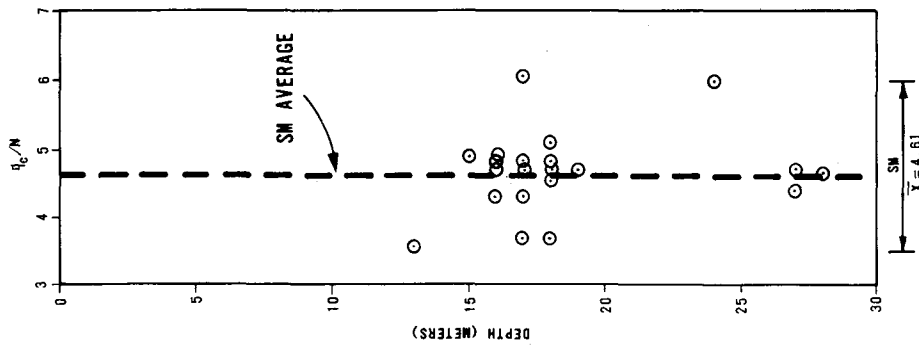
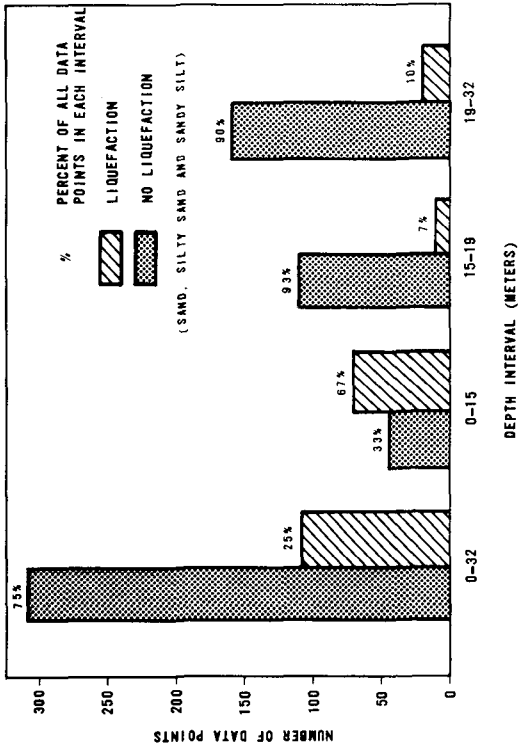
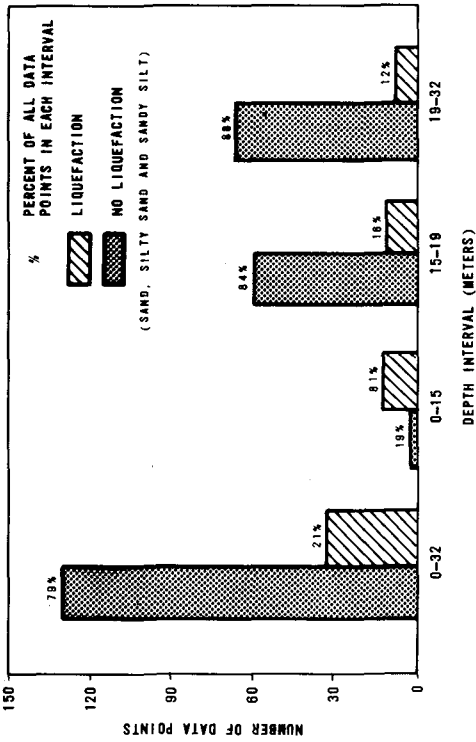


FIGURE 5 RELATIONSHIP BETWEEN q_c/N AND DEPTH



(a) SPT DATA



(b) CPT DATA

FIGURE 7 LIQUEFACTION ANALYSIS BASED ON SEED 1975, 1977.

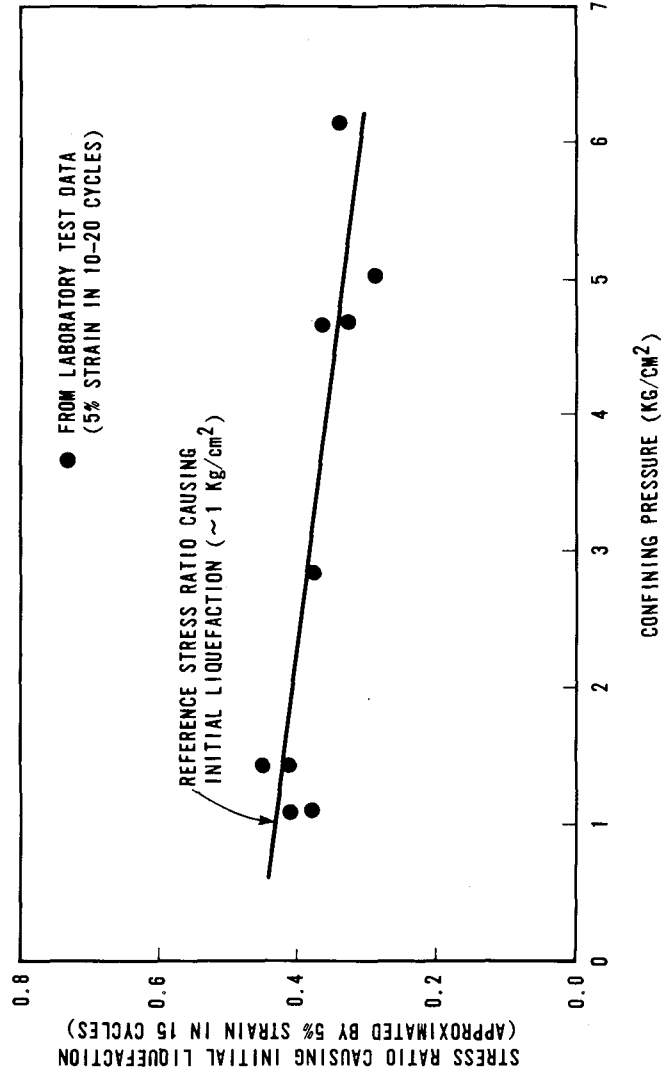


FIGURE 8 EFFECT OF CONFINING PRESSURE ON STRESS RATIOS CAUSING 5% STRAIN IN 15 CYCLES

A PRACTICAL METHOD FOR ASSESSING SOIL LIQUEFACTION POTENTIAL

BASED ON CASE STUDIES AT VARIOUS SITES IN JAPAN

by

Toshio Iwasaki^I, Fumio Tatsuoka^{II},
 Ken-ichi Tokida^{III} and Susumu Yasuda^{IV}

ABSTRACT

A simplified method for assessing soil liquefaction potential of sandy deposits is proposed. In this method, an ability of a soil deposit to resist the occurrence of liquefaction is represented by a liquefaction resistance factor $F_L = R/L$ in which R denotes undrained cyclic strength and L denotes earthquake-induced stress in grounds. Here proposed is a method to estimate R from standard penetration N -values, effective overburden pressure σ_v and mean diameter D_{50} . And L can be estimated from the estimated maximum horizontal acceleration at ground surfaces $(\alpha_s)_{max}$, a reduction factor to account for deformation of ground γ_d , soil density and water table, according to the concepts developed by previous investigators (20). This simplified method was applied to various sites where liquefaction took place in the past and where appropriate geotechnical information is available. From the comprehensive studies it is found that this simplified method is quite adequate for assessing liquefaction potential against earthquake disturbances.

INTRODUCTION

The methods to evaluate liquefaction potential of level grounds have been studied from several different points of view. Among them, basal are the methods based on observations of the performance of sand deposits in previous earthquakes (empirical methods) and those based on evaluation of stress conditions in the field and laboratory determinations of the stress conditions causing cyclic liquefaction of soils (analytical methods) (19). Firstly in this study, a simplified analytical method was developed following the previous methods (10, 19). Then, this method was applied to the previous liquefaction experiences in Japan.

OUTLINE OF THE ANALYTICAL METHOD

An element in surface soil deposits is subjected to cyclic shear stress histories. Dynamic loads to soil elements caused by earthquake motions can be defined as

-
- I Chief, Ground Vibration Section, Earthquake Disaster Prevention Division, Public Work Research Institute, Ministry of Construction, Chiba, Japan
 - II Associate Professor, Institute of Industrial Science, University of Tokyo, Tokyo
 - III Research Engineer, Ground Vibration Section, PWRI
 - IV Research Engineer, Engineering Center, Kisojiban Consultants Co., Ltd., Tokyo

$$L = (\tau/\sigma'_v)_{max} \quad (1)$$

in which τ means the maximum amplitude of shear stress in single amplitude and σ'_v is the effective overburden pressure at the static condition. Corresponding to L , the resistances of soil elements to dynamic loads can be defined as R . The method to evaluate R will be described later. Then, the ability to resist the occurrence of liquefaction of the soil elements can be expressed by

$$F_L = R/L \quad (2)$$

F_L is the liquefaction resistance factor. From the special distribution of the value of F_L in the ground concerned, the liquefaction potential can be evaluated. In this method, the effects of seepage of excessive pore pressure caused by cyclic earthquake-induced shear stress are not directly accounted for.

EVALUATION OF RESISTANCE R

To establish a simplified method for evaluating in situ undrained cyclic strength from blow counts by the standard penetration test (N-values), σ'_v and gradings of soil, a comprehensive series of geotechnical surveys and undrained cyclic triaxial tests on undisturbed specimens have been performed (21). The followings were found from that investigation.

- (1) It is rather difficult to estimate in situ relative density $D_r = (e_{max} - e)/(e_{max} - e_{min}) \times 100(\%)$ from N-values and σ'_v for a wide range of grain size (Fig. 1). (Figs. 1 through 3 were reproduced here from Tatsuoka et al (21).) In situ void ratios which are necessary to obtain D_r were evaluated by several methods of sand sampling. Dr^* in Fig. 1 means estimated relative density by

$$Dr^* = 21 \sqrt{\frac{N}{\sigma'_v + 0.7}} \quad (3)$$

in which σ'_v is in kg/cm^2 (5). As seen from Fig. 1, the scatter in the values of the difference $Dr - Dr^*$ is so large that it is apparent that Equation (3) is not adequate to estimate Dr . At present, any equation much better than Equation (3) has not been found.

- (2) There is not a unique relationship between undrained cyclic strength of undisturbed specimen R_1 and measured in situ relative density (Fig. 2). In this figure, R_1 is defined as

$$R_1 = (\sigma_{dp}/2\sigma'_c) \quad (4)$$

which is the stress ratio $(\sigma_{dp}/2\sigma'_c)$ at the number of loading cycles $N_C=20$ where the amplitude of axial strain in double-amplitude (DA) becomes 5 or 6 percent. In general, to obtain a value of R_1 , three to six specimens obtained from one liner were tested. Of course, the definition of strength as a function of the number of loading cycles and amplitude of axial strain should depend on the purpose of the study. Effects of changes in N_C and in amplitude of axial strain will be considered in future studies. It was found that the difference of R_1 between for DA=5%, and for 6% is quite small (3% at most). And in all of the tests referred, the Skempton's B-values were larger than 0.96.

The detailed procedures of sampling, transportation, sample preparation, triaxial tests or so were described in the previous papers (15, 21).

- (3) There is a high correlation between mean diameter D_{50} and DR_1^* which is defined as

$$DR_1^* = R_1 - 0.0042 D_r^* \quad (5)$$

in which R_1 is measured dynamic strength of undisturbed specimens by Equation (4) and D_r^* is measured value by Equation (3) (Fig. 3). It can be seen from Fig. 3 that for a wide range of D_{50} , there is a high correlation between DR_1^* and D_{50} . The average line drawn in Fig. 3 appears to be a reasonable representation of the relationship between DR_1^* and D_{50} . This average line can be represented by

$$\begin{aligned} DR_1^* &= -0.225 \log_{10} (D_{50}/0.35) \text{ for } 0.04 \leq D_{50} \leq 0.6 \text{ mm} \\ \text{and} \\ DR_1^* &= -0.05 \text{ for } 0.6 \leq D_{50} \leq 1.5 \text{ mm} \end{aligned} \quad (6)$$

From Equations (5) and (6)

$$\begin{aligned} R_1 &= 0.0042 D_r^* - 0.225 \log_{10} \left(\frac{D_{50}}{0.35} \right) \text{ for } 0.04 \leq D_{50} \leq 0.6 \text{ mm} \quad 7(a) \\ \text{and} \\ R_1 &= 0.0042 D_r^* - 0.05 \text{ for } 0.6 \leq D_{50} \leq 1.5 \text{ mm} \quad 7(b) \end{aligned}$$

In the later analyses, Equation 7(a) will be applied for $0.02 \leq D_{50} < 0.6$ mm and Equation 7(b) will be applied for $0.6 \leq D_{50} \leq 2.0$ mm. In situ dynamic strength R can be evaluated from R_1 which is defined by Equation (4) after several corrections (15) as

$$R = C_1 \cdot C_2 \cdot C_3 \cdot C_4 \cdot C_5 \cdot R_1 \quad (8)$$

C_1 is the correction factor for the difference of in situ confining pressures from those in triaxial tests and has been proposed as $(1 + 2 K_0)/3$ (7). C_2 is that for the difference between in situ "random" loading forms during earthquake motions and the sinusoidal loading form in triaxial tests and have been proposed as $1/0.55 \sim 1/0.7$, with the average being 1.62 (8). C_3 is that for the effect of soil disturbances in the process of sampling and handling. C_4 is that for the effects of densification in the process of sampling and handling. As samples tested in this study are relatively loose, it is likely that some increases in strength due to densification occurred. Because densification of samples is caused by disturbances during sampling and handling, those effects may cancel. Thus, the value of the product $C_3 \times C_4$ was taken to be unity in this study. C_5 is the correction factor for the multi-direction shaking which may be anticipated in actual in situ loading conditions. According to Seed (19), this factor is equal to 0.9. Using the values of C_1 through C_5 described above, Equation (8) becomes

$$R = 2/3 \times 1.62 \times 1.0 \times 0.9 \times R_1 = R_1 \quad (9)$$

for $K_0 = 0.5$. This value of K_0 can be considered adequate for reclaimed lands and alluvial deposits which will be analysed later.

EVALUATION OF DYNAMIC LOAD L

The dynamic load L defined by Equation (1) can be estimated from the following equation (20);

$$L = \alpha_{s_{max}}/g \cdot \sigma_v / \sigma_v' \cdot r_d \quad (10)$$

in which $\alpha_{s_{max}}$ means the estimated maximum acceleration on the ground surface in gals and g is the acceleration of gravity (980 gals), σ_v is the total overburden pressure, σ_v' is the effective overburden pressure and r_d means the reduction factor for dynamic shear stress accounting for the elastic performance of the ground. In the case studies, the values of $\alpha_{s_{max}}/g$ were estimated by the several methods as described in the footnote of Table 2. Figs. 4 and 5 show the typical results of earthquake response analyses using several earthquake records for an alluvial deposit, and a soft alluvial deposit, respectively. These analyses were performed by the computer program "SHAKE" (18). It can be seen in those figures that the value of r_d is, in general, smaller for the input earthquake motion with smaller predominant period T_e and for the subsoils with larger natural frequency T_g . It can be also expected that T_e is correlated with the magnitude of earthquake M, the epicentral distance Δ , or so. As a simple correlation among r_d , T_e (or M, Δ), T_g or so is not established yet, it was considered reasonable to estimate r_d for the simplified method from the average relationship as

$$r_d = 1 - 0.015Z \quad (Z: \text{depth in meter}) \quad (11)$$

CASE STUDIES

Fig. 6 shows the liquefaction experiences in Niigata city during the Niigata Earthquake of 1964 which was made on the basis of several other investigations (3, 4). The liquefaction potentials of several sites in Niigata city will be firstly analysed by the method proposed in this paper. The maximum acceleration of the recorded earthquake motion at the ground surface in Niigata city was around 170 gals and it was found from response analyses of sand deposits that $r_d = 1 - 0.015Z$ is reasonable for the sandy deposits in Niigata city. When only the name of soil type were available, the value of density and D_{50} were estimated following Table 1. The values of F_L were calculated by the methods described above for the soil layers whose mean diameter range from 0.02 to 2.0 mm. It was postulated that the soil layers whose D_{50} are less than 0.02 mm or larger than 2.0 mm do not liquefy. Except one case for the Fukui Earthquake, soil layers with D_{50} larger than 2.0 mm are not included in the surface deposits above the depth of 20 m. Figs. 7 and 8 show the variation of F_L with depth for the sites where liquefaction phenomena were not observed. It can be seen in these figures that the values of F_L are larger than 1.0. Figs. 9 and 10 show the variation of F_L with depth for the sites where severe liquefaction phenomena were observed. It can be seen in those figures that F_L is, in general, less than 1.0 for the liquefied zones. The ranges of liquefied zones were estimated from the damage to the pile of the bridge (in the case of Fig.9) or from the comparison of the grading of the spouted sand with those of the soil deposits (in the case of Fig.10). Fig.11 summarizes the results of the analyses for the sites in Niigata city in the $F_L - Z$ relationship. The ranges of liquefied zones were estimated from several observations as described above. It can be seen in Fig. 11 that the most data points with the values of F_L less than 1.0 are those of liquefied zones and that the most data points with the values of F_L larger than 1.0 are those of non-liquefied zones. This tendency is especially noted for a depth shallower than 10 m. From these facts, it can be concluded that, while some

modifications may be necessary, the simplified method proposed herein can be used for evaluating approximate liquefaction potential.

It is obvious that the damage to foundations due to soil liquefaction is considerably affected by the severity of liquefaction phenomena at each zone and the depth and the width of liquefied zones. For this purpose, the damage to foundation structures was compared with the distribution of the estimated values of F_L in the case of the Niigata Earthquake of 1964. It was found that the severe damage to foundation structures were found only when the value of F_L is considerably less than 1.0, say 0.6, and the zone where F_L is considerably less than 1.0 is not thin, say thicker than 5 m. To express the degree of severity of liquefaction phenomena, liquefaction potential index P_L or P_L^* was defined as

$$P_L = \int_0^{20} F_i \cdot w(z) dz \quad (12 a), \quad P_L^* = \int_0^{20} F_i \cdot w^*(z) dz \quad (12 b)$$

in which $F = 1 - F_L$ for $F_L \leq 1.0$ and $F = 0$ for $F_L > 1.0$ as illustrated in Fig. 12 (a) and $w(z) = 10 - 0.5Z$ (Z in meter) and $W^*(z) = 5$ as illustrated in Fig. 12 (b) and Fig. 12 (c), respectively. For the case of $F_L = 0.0$ for the entire range from $Z = 0$ to 20 m, both P_L and P_L^* become 100. And for the case of $F_L \geq 1.0$ for the entire range from $z = 0$ to 20 m, both P_L and P_L^* become 0.0. In other cases where F_L varies between 0 to 1.0 in some zones, P_L and P_L^* have values ranging from 0 to 100. The difference between P_L and P_L^* is due to the difference in the weight function, $W(z)$ and $W^*(z)$. $W(z)$ is based on the idea that shallower deposits can be more susceptible to liquefaction due to the seepage of pore water from deeper portions than deeper deposits for an equal value of F_L . The values of P_L and P_L^* were calculated for the sites where liquefaction or no liquefaction were experienced during earthquakes and good soil data were also available. (Table 2).

Fig. 13 shows the relationship of calculated values between P_L and P_L^* . It can be seen from this figure that P_L^* is less than P_L with P_L/P_L^* for the most data ranging from 1 to 1.6. Fig. 14 and 15 show the relationships among ground condition, liquefaction experience and P_L for two sections in Niigata city, A-A' and B-B', whose places are shown in Fig. 6. It can be seen from these figures that the higher values of P_L correspond well to the experiences of liquefaction. Fig. 16 shows the accumulative percentages of P_L for liquefaction sites and non-liquefaction sites and the distributions of P_L for both kinds of sites. The data in Fig. 16 show that all the values of P_L for non-liquefaction sites are less than 20 and P_L of their seventy percentage are less than 5. On the other hand, it can be seen that the value of P_L for eighty percentage of liquefaction sites are larger than 5 and that for their fifty percentage are larger than 15. Therefore, it is likely that severe liquefaction will not be expected at the sites with P_L less than 5 and moderate or severe liquefaction will be expected at the sites with P_L larger than 15 or 20. When the liquefaction potential index P_L or P_L^* is used in the procedures of earthquake resistant design of structures, their definition should depend on the kind of structure or the purpose of the design. Further studies on the form of weight function ($W(z)$ or $W^*(z)$) will be necessary.

CONCLUSIONS

A simplified procedure for assessing soil liquefaction potential has been proposed. In this method, liquefaction potential for a layer at a certain depth is expressed by the liquefaction resistance factor F_L and that for a soil deposit from the surface to the depth of 20 m is expressed by the liquefaction potential index P_L or P_L^* which can be obtained by integrating F_L with

a weight function $W(z)$ or $W^*(z)$. The values of F_L and P_L or P_L^* were calculated for the sites of liquefaction and non-liquefaction during previous earthquakes. It was found that the value of P_L or P_L^* are quite different between the sites of liquefaction and those of non-liquefaction.

ACKNOWLEDGEMENTS

The authors express their cordial appreciation to S. Watanabe, Earthquake Disaster Prevention Section, Shizuoka Prefecture and H. Sato, Kisojiban Consultants, Co., Ltd. for their helpful cooperations.

BIBLIOGRAPHY

- (1) BRI (1965). "Report on Damage to Buildings during the Niigata Earthquake," The Building Research Institute, Ministry of Construction, No. 42, 1965 (in Japanese).
- (2) BRI (1969). "Investigation on Liquefaction of Saturated Sand and Some Problems on Soil-Structure-Interaction," The Building Research Institute, Ministry of Construction, No. 55 (in Japanese)
- (3) Geological Survey Institute (1965). "Damage and Ground Condition during the Niigata Earthquake" (in Japanese).
- (4) Geological Survey Institute (1966). "Survey on Damage by the Niigata Earthquake and Ground Condition," (in Japanese).
- (5) Gibbs, H.J. and Holtz, W.G. (1957). "Research on Determining the Density of Sand by Spoon Penetration Test," Proc. 4th International Conference on Soil Mechanics and Foundation Engineering, London, Vol.1, pp. 35-39.
- (6) Hatanaka, M. (1977). "Fundamental Studies on Undisturbed Sampling of Saturated Sands by Freezing" A thesis for the Degree of Doctor of Eng., Tokyo Institute of Technology.
- (7) Ishihara, K. and Li, S. (1972). "Liquefaction of Saturated Sand in Triaxial Torsion Shear Test," Soils and Foundations, Japanese Society of Soil Mechanics and Foundation Engineering, Vol.12, No.2, June, pp. 19-39.
- (8) Ishihara, K. and Yasuda, S. (1975). "Sand Liquefaction in Hollow Cylinder Torsion under Irregular Excitation" Soils and Foundations, Japanese Society of Soil Mechanics and Foundation Engineering, Vol.15, No.1, March, pp. 29-45.
- (9) Ishihara, K. (1976), "Report of Liquefaction Tests of at the Site of Shinanogawa Water Gate," Report to the Hokuriku Regional Construction Bureau, the Ministry of Construction (in Japanese).
- (10) Ishihara, K. (1977). "Simple Method of Analysis for Liquefaction of Sand Deposits during Earthquakes," Soils and Foundations, Vol.17, No.3, pp. 1-18.
- (11) Ishizawa, M., Nakagawa, S. and Kurohara, I. (1977). "Liquefaction Test of Undisturbed Samples Containing Fine Content," Proc. the 12th Annual Meeting of JSSMFE, pp. 397-400 (in Japanese).
- (12) Japanese Society of Soil Mechanics and Foundation Engineering (1976). "Report on Earthquake Damage of Subground Streets and Structures," March (in Japanese).
- (13) Japanese Society of Civil Engineers. "The Report on the Damage during the Niigata Earthquake of 1964" (in Japanese).
- (14) Kishida, H. (1970). "Characteristics of Liquefaction of Level Sandy Ground during the Tokachi-Oki Earthquake," Soils and Foundations, Vol.X, June, No.2.
- (15) McGuire, R.K., Tatsuoka, F., Iwasaki, T. and Tokida, K. (1978). "Probabilistic Procedures for Assessing Soil Liquefaction Potential," Journal of Research, Public Works Research Institute, Vol.19, March, 1978.

- (16) Ohashi, M., Iwasaki, T., Wakabayashi, S. and Tokida, K. (1977). "Statistical Analysis of Strong-Motion Acceleration Records," 9th Joint Meeting, U.S.-Japan Panel on Wind and Seismic Effects, U.J.N.R., May.
- (17) Ohsaki, Y. (1970). "Effects of Sand Compaction on Liquefaction during the Tokachi-Oki Earthquake," Soils and Foundations, Vol. X, June, No.2.
- (18) Schnabel, P.B. and Lysmer, J. (1972). "SHAKE-A Computer Program for Earthquake Response Analysis of Horizontally Layered Sites," Report No. EERC 72-12, Earthquake Engineering Research Center, University of California, Berkeley.
- (19) Seed, H.B. (1976). "Evaluation of Soil Liquefaction Effects on Level Ground during Earthquakes," State-of-the-Art Report, Preprint of ASCE Annual Convention and Exposition on Liquefaction Problems in Geotechnical Engineering, Philadelphia.
- (20) Seed, H.B. and Idriss, I.M. (1971). "A Simplified Procedure for Evaluating Soil Liquefaction Potential," Journal of the Soil Mechanics and Foundations Division, ASCE, Vol.97, No. SM9, Sept., pp. 249-274.
- (21) Tatsuoka, F., Iwasaki, T., Tokida, K., Yasuda, S., Hirose, M., Imai, T. and Kon-no, M. (1978). "A Method for Estimating Undrained Cyclic Strength of Sandy Soils Using Standard Penetration Resistances," Soils and Foundations, Vol.18 (in press).
- (22) Yoshimi, Y., Hatanaka, M. and Oh-oka, H. (1977). "A Simple Method for Undisturbed Sand Sampling by Freezing," Proc. of Specialty Session 2, ICSMFE, Tokyo, pp. 23-28.

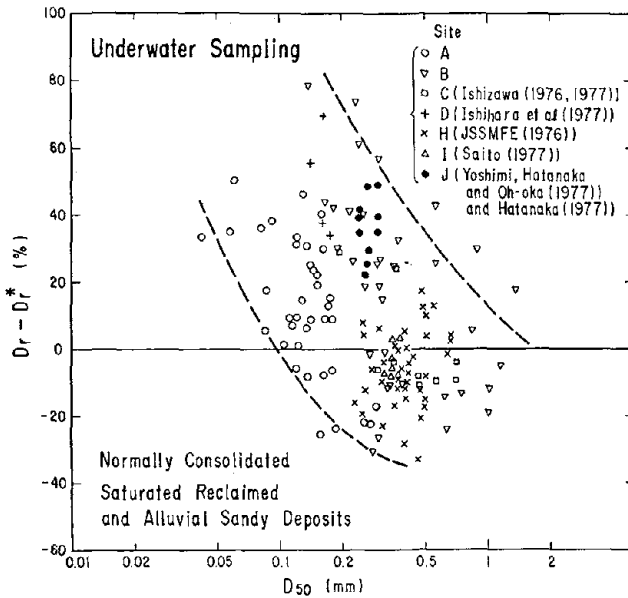
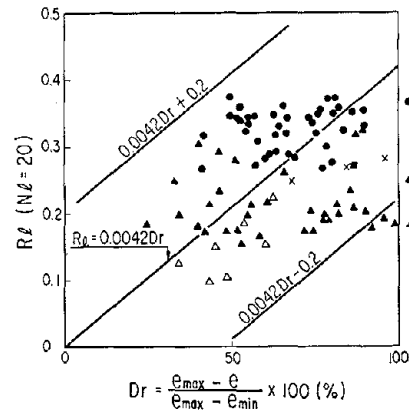


Fig. 1 $D_r - D_r^*$ and D_{50} Relation (21)



LEGEND

Site	e	DA (%)	σ'_v (kg/cm ²)
•	e_f	6	$\sigma'_v = 0.2 \sim 1.15$
▲	e_f	5	$\sigma'_v = 0.45 \sim 1.75$
△	e_0	5	1.5 (Ishihara (1976, 1977))
×	e_0	5	0.5 (Ishizawa et al (1977))
■	e_0	6	$\sigma'_v = 0.8 \sim 1.14$

Fig. 2 R_d and D_r Relation (21)

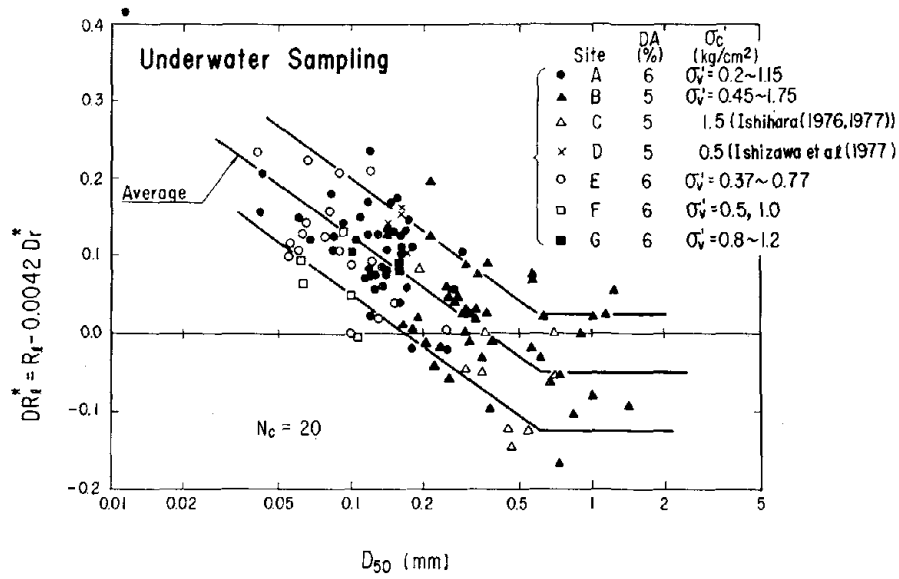


Fig. 3 DR_1^* and D_{50} Relation (21)

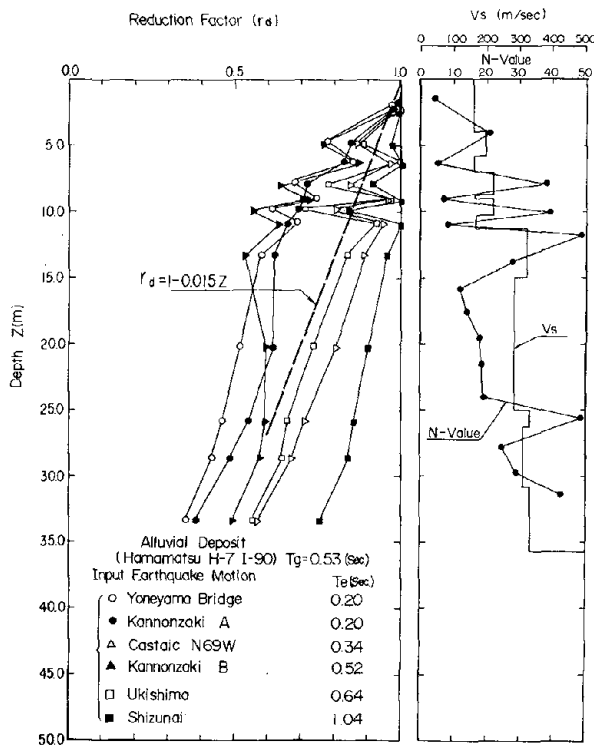
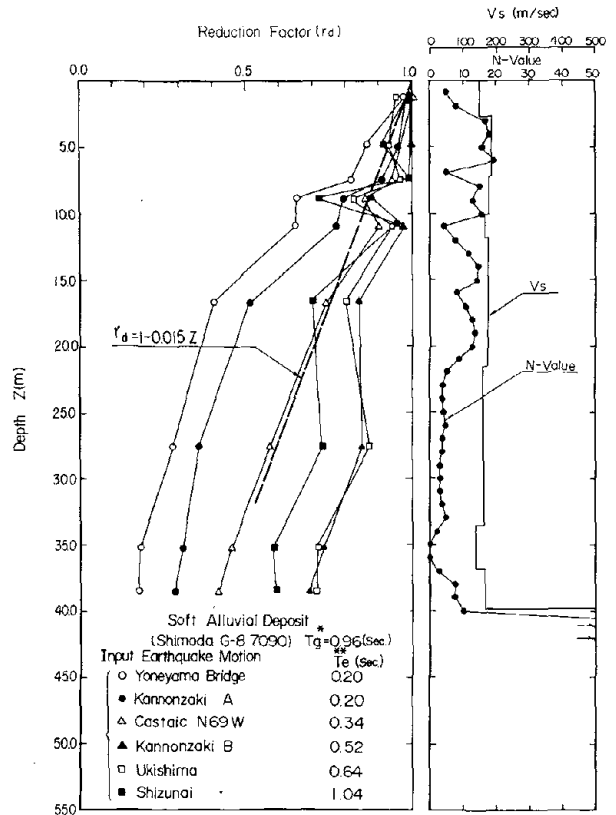


Fig. 4 Computed Reduction Factor for an Alluvial Deposit



* First Natural Period of Surface Deposit above Bed Rock
 ** Predominant Period of Earthquake Motion at the Surface of Bed Rock

Fig. 5 Computed Reduction Factor for a Soft Alluvial Deposit

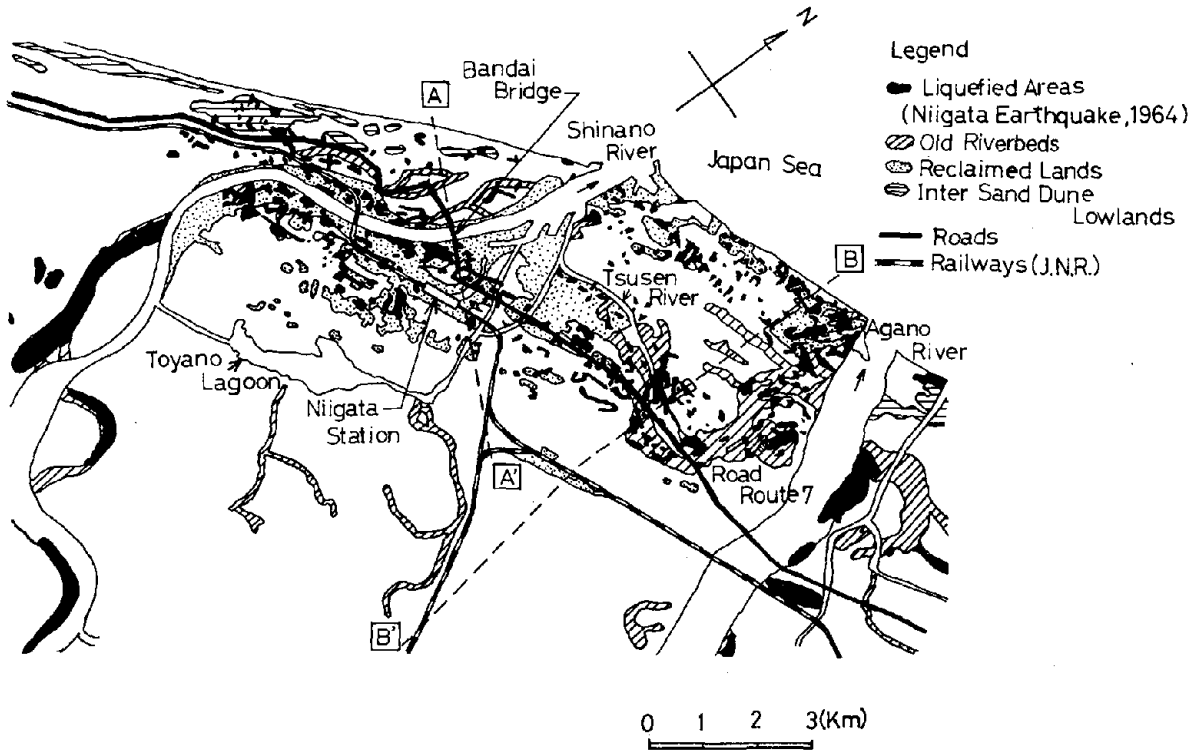


Fig. 6 Liquefied Zones in Niigata city during the Niigata Earthquake of 1964 (3, 4)

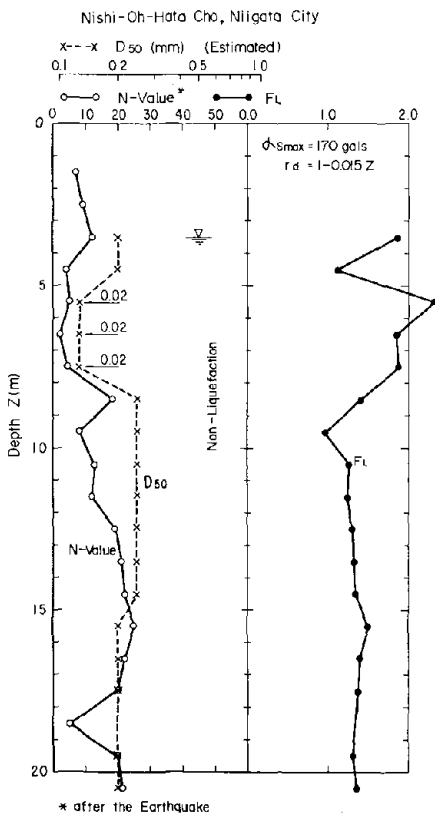


Fig. 7 F_L at a Non-Liquefied Site

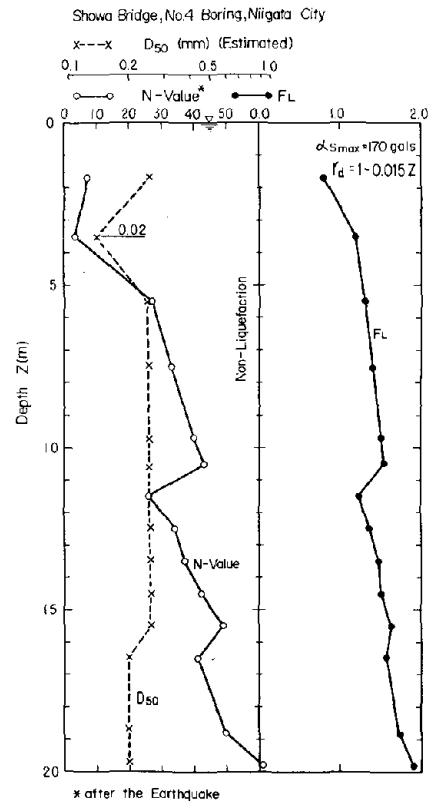


Fig. 8 F_L at a Non-Liquefied Site (13)

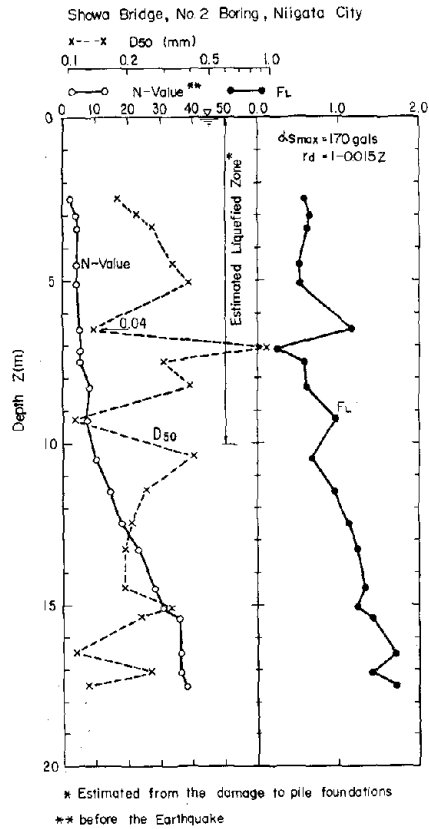


Fig. 9 F_L at a Liquefied Site (13)

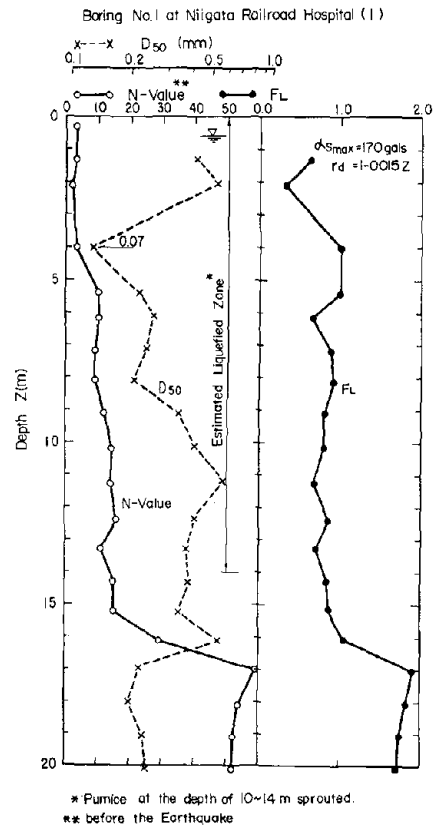


Fig. 10 F_L at a Liquefied Site (1)

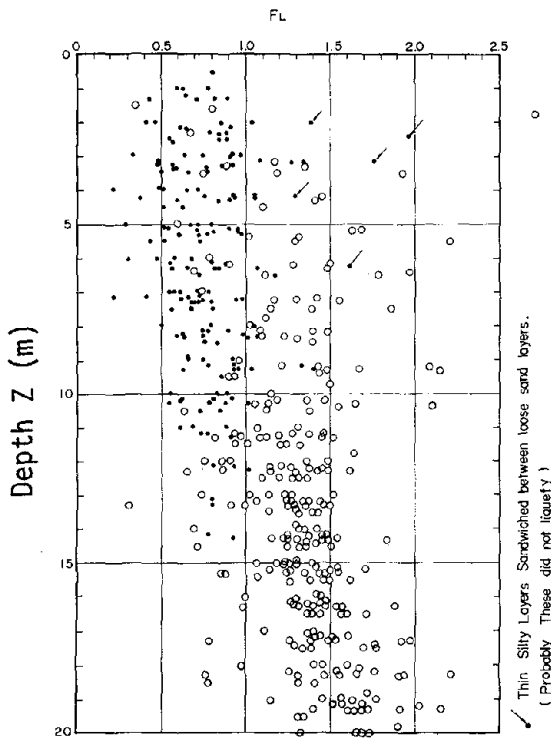


Fig. 11 F_L at Several Sites in Niigata city during the Niigata Earthquake

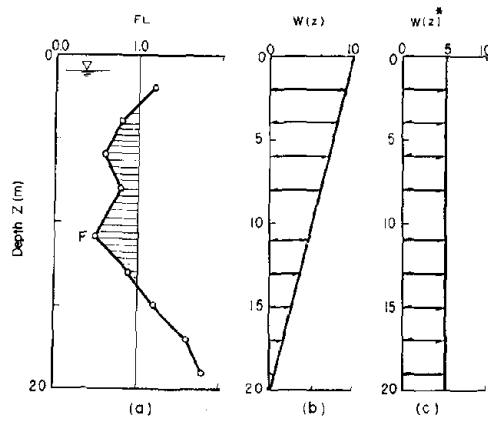


Fig. 12 Integration of F_L

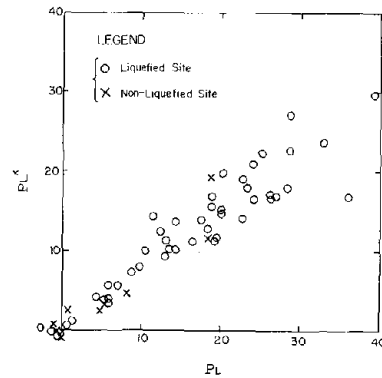


Fig. 13 P_L^* and P_L Relation

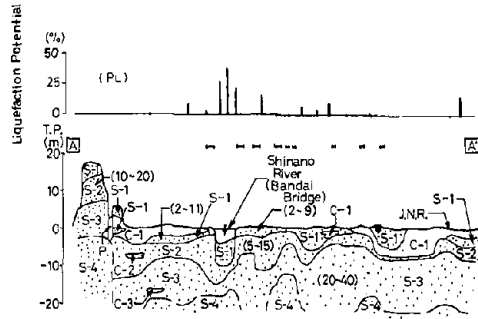
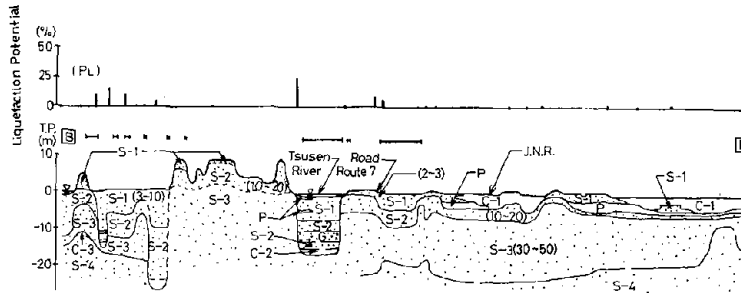


Fig. 14
Soil Profile, Liquefaction Experience and F_L at the Section A-A' in Niigata city (See Fig.6)



Legend
 L Liquefied Areas
 S Sand
 C Clay
 P Peat
 G Gravel
 () N Value

Fig. 15 Soil Profile, Liquefaction Experience and F_L at the Section B-B' in Niigata city (See Fig. 6)

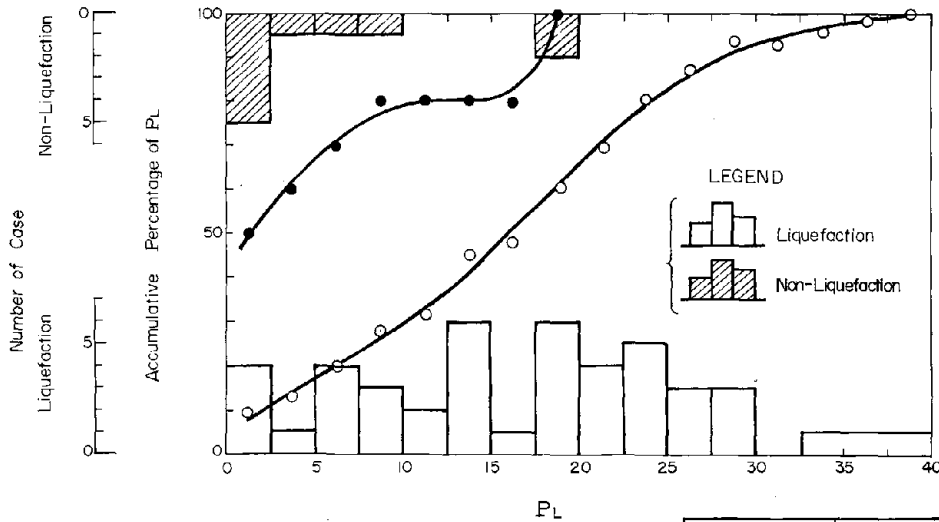


Fig. 16 Relation between Number of Case and P_L and Relation between Accumulative Percentage of P_L and P_L for Sites of Liquefaction and those of Non-Liquefaction

Table 1. γ_t and D_{50}
 (This table was used only when these values were not reported)

Soil Type	γ_t (t/m^3)	D_{50} (mm)
Surface Soil	1.7	0.02
Gravel	2.1	0.6
Sand	1.9	0.25
Coarse Sand	1.9	0.3
Medium Sand	1.9	0.25
Fine Sand	1.9	0.2
Silt	1.7	0.02
Silty Sand	1.9	0.1
Sandy Silt	1.7	0.04

Table 2 Cases of Liquefaction and Non-Liquefaction Investigated in This Study

Site		Earthquake	Soil Data	Depth of Water Table	D ₅₀	Major Soil Type	σ _{smax} (gals)	P _L	P _L *	Field Behavior	Ref.	
Jindo-ji		Niigata, 1964, M=7.5	A	2.3	E	Fine Sand	170 ^①	0.0	0.0	X	(13)	
Kogane Cho			A	5.2	E	Medium Sand		0.0	0.0	X		
Shinano River Railroad Bridge			1	A	2.0	M	Fine to Med. Sand		9.0	5.7		0
			2	A	2.5	M	"		24.9	16.4		0
Higashi-Kosen Bridge			Br. 1	A	0.5	E,M	Fine to Coarse Sand		5.8	5.6		0(6)
			Br. 2	B	2.5	M	"		1.3	1.0		0(8)
			Br. 4	B	2.5	M	"		0.6	0.4		0(5)
			Br. 5	B	2.5	M	"		0.0	0.0		X
Bandai Bridge			Br. 6	A	0.0	M	Medium Sand		20.2	19.8		0(9)
Yachiyo Bridge			Br. 1	B	0.0	E,M	Fine to Med. Sand		18.3	12.7		0(11)
			Br. 5	B	0.0	E,M	"		39.5	29.8		0(11)
			Br. 7	B	0.0	E,M	"		26.2	17.2		0(11)
Shin-Matuhama Bridge			Br. 1	A	1.2	M	Med. to Coarse Sand		18.6	11.7		X
			Br. 2	A	0.0	M	"		24.0	20.8		0(11)
Taihei Bridge			Br. 1	A	1.56	M	Coarse Sand		32.9	23.5		0(11)
			Br. 2	A	0.0	M	"		19.6	11.7		0(5)
Niigata city Ōmi				A	0.0	M	Fine Sand		8.2	4.6		X
Showa Bridge			Br. 1	A	0.0	E	Coarse Sand		28.2	17.8		0(10,25)
			Br. 2	A	0.0	M	Med. to Coarse Sand		16.5	11.2		0(10,25)
			Br. 3	A	0.0	M	"		14.3	10.2		0(10,25)
			Br. 4	A	0.0	E	Medium Sand		4.6	2.5		X
			Br. 2	B	0.0	E	Med. to Coarse Sand		22.7	14.1		0(10,25)
			Br. 3	B	0.0	E	"		23.2	17.9		0(10,25)
Nishi Oh-Hata Cho				A	3.5	E	Fine to Med. Sand		0.4	1.3		X
Niigata Airport				U	0.8	E	Med. to Coarse Sand		13.1	11.2		0(10)
Sekiya				A	0.6	M	Coarse Sand		28.6	22.5		0
Niigata Railroad Hospital			Br. 1	B	1.4	M	Fine Sand		20.1	14.7		0(10-14)
		Br. 2	B	1.3	M	Fine to Med. Sand		5.8	4.0	0(10-14)		
		Br. 1	A	0.63	M	Fine Sand		13.5	10.3	0(10-14)		
		Br. 2	A	1.18	M	Fine Sand		10.5	10.0	0(10-14)		
Kawagishi Cho		Br. 1	A	1.25	M	Coarse Sand		18.9	15.8	0		
		Br. 2	A	1.25	M	Coarse Sand		20.1	15.1	0		
		Br. 3	A	1.25	M	Coarse Sand		18.9	16.7	0		
		Br. 4	A	1.25	M	Coarse Sand		14.5	12.3	0		
Kawagishi Cho		BC2f-2	B	1.2	E	Medium Sand		5.1	3.9	0		
		BC2f-3	B	1.2	E	Medium Sand		9.7	8.0	0		
		BC104	A	1.2	E	Medium Sand		14.2	13.6	0		
		BC14	A	1.35	E	Fine to Med. Sand		4.4	4.2	0		
Gatanda Bridge		Br. 1	A	0.10	M	Fine to Silty Sand		5.3	3.3	X		
		Br. 2	A	4.3	M	Fine Sand to Silt		0.0	0.0	X		
Nanae Beach, Hokkaido		Br. 1	A	0.95	M	Fine Sand	200 ^②	0.0	0.0	0		
		Br. 2	A	0.95	M	Fine Sand		0.0	0.0	0		
		Br. 3	A	1.1	M	Fine Sand		5.8	3.6	0		
Hachinohe			A	0.57	E	Fine Sand	235 ^③	26.7	16.8	0		
Gifu			A	0.9	M	Med. Sand	255 ^④	36.1	16.8	0		
Unuma Kagami-gahara		Gifu Pref.	A	0.75	M	Gravelly Sand	210 ^⑤	13.0	9.4	0		
Ogaseike			A	2.10	M	Gravelly Sand	210 ^④	8.8	7.2	0		
Mangaku, Ohgaki			A	1.20	M	Sand to Grav. Sand	270 ^④	28.7	27.3	0		
Meikodori		Nagoya City	A	0.6	M	Med. Sand	200 ^⑤	19.5	11.5	0		
Kohmei			A	0.9	M	Coarse Sand		26.3	16.6	0		
Inaei			A	0.23	M	Silty to Fine Sand		17.7	13.9	0		
Tokayo 45			A	4.2	M	Med. to Coarse Sand	325 ^⑤	22.7	29.0	0		
Maruoka No.1		Fukui Pref.	A	1.8	M	Silt to Med. Sand	295 ^⑥	18.7	19.2	X		
Maruoka No.2			A	1.8	M	Med. Sand to Gravel	315 ^⑥	24.9	22.5	0		
Takaya 2-168,			A	4.2	M	Sandy Silt to Med. Sand	325 ^⑥	11.4	14.4	0		

(NOTE) * B: Soil Data before Earthquake, A: Soil Data after Earthquake, U: Unknown
 ** E: Estimated by Using Table 1, M: Measured
 *** X: Non-Liquefaction, O: Liquefaction
 The Numbers in () are estimated depths of liquefaction in meter.

① Recorded Value at Kawagishi cho.
 ② Estimated from Recorded Values at Other Sites.
 ③ Recorded Value at Hachinohe.
 ④ Estimated by the Empirical Equation for Alluvial Deposits (16):
 $\sigma_{smax} \text{ (gals)} = 32.1 \times (0.0254M)^{-0.757}$
 in which M is the Richter's magnitude and Δ is the epicentral distance in km.
 ⑤ Estimated from Damage to Structures.

LIQUEFACTION SUSCEPTIBILITY MAP
OF DOWNTOWN TOKYO

by

Kenji Ishihara^I and Kaihei Ogawa^{II}

ABSTRACT

To provide a basis for the estimate of seismic risk resulting from liquefaction of the ground during future earthquakes, over one thousand boring records obtained within the downtown area of Tokyo were examined and classified into three groups according to the extent of liquefaction as to whether there is a possibility, a slight possibility or no possibility. The classification was made on the basis of three rules of identification with regard to soil type, stratification and N-value in the standard penetration test. The result of the study showed that liquefaction-induced ground failure could occur at about one third of the sites investigated.

INTRODUCTION

Liquefaction-induced ground failures such as flow slides or ground settlements have been a major cause of damage to buildings and other civil engineering facilities during past large earthquakes. In recognition of the potential hazard posed by liquefaction, the Tokyo metropolitan office undertook a comprehensive investigation of the likelihood of liquefaction occurring during future large earthquakes within the Koto-Sumida ward area of Tokyo. In this downtown area, elevation of the ground is near or below the sea water level with subsurface soils consisting of soft and weak fluvial or deltaic deposit. This area is also the most densely populated district in Tokyo Metropolis. Consequently, these unfavorable conditions existing in this area have been potential factors easily leading to widespread occurrence of liquefaction and consequent catastrophic disaster. The present investigation commenced with an examination of the damage feature incurred in this area during three large past earthquakes. Assessment of the seismic intensity in these past tremblers was made through literature survey in order to determine a value of maximum ground acceleration that is expected to occur in future earthquakes. On the basis of this information together with a number of soil profile data, evaluation of liquefaction potential was made for over one thousand sites in the downtown area of Tokyo. The details of the study and its result will be described in the following pages.

SEISMIC INTENSITY OF THE PAST LARGE EARTHQUAKES AND RECORDS OF LIQUEFACTION

During the last century, the area of Tokyo has been subjected to three major destructive earthquakes which had inflicted considerable loss of life and damage to property. For each of these earthquakes there exist today several documents describing the damage found in soil deposits such as ground fissures, spouting of sand and mud water. The following is the

I Professor of Civil Engineering, University of Tokyo, Bunkyo-ku,
Tokyo, Japan

II Bureau of General Affairs, Tokyo Metropolitan Office, Chiyoda-ku,
Tokyo, Japan

summary of the information obtained from these documents.

1. Edo-Ansei earthquake of 1855

A violent tremor shook the downtown area of Tokyo at about 10 o'clock in the evening of November 11, 1855. The magnitude of the earthquake is estimated as $M=6.9$, and its epicenter is inferred to have lain almost immediately underneath the Sumida ward area (Fig.1). There was a concentration of inhabitants and private dwellings in the region of very strong shaking, and the resulting damage was considerable. A total of as many as 7000 people was reported killed and about 4700 people wounded.

An attempt was made recently by Sayama (1972) to map out the distribution of the earthquake intensity based on the damage extent and severity of the shaking reported in old documents in each locality over the area inflicted. The result of this study is presented in Fig.1 where the intensity of the shaking is indicated in terms of the modified Mercalli scale. In order to make a rough estimate of the maximum horizontal accelerations from the knowledge of the Mercalli scale as above, the relationship as indicated in Table 1 may be useful.

Table 1 Relationship between Mercalli scale and probable range of maximum ground accelerations (Okamoto, 1973)

Modified Mercalliscale	V	VI	VII	VIII	IX	X	XI	XII
Max.horizontal acceleration (gal)	10	20	45	95	200	greater than 430		

Because the eastern half shown in Fig.1 was the area where the population was very sparse, there exists few documents that can be used to assess how strong the shaking was. Within the area of Sumida and Koto wards bounded by the two rivers flowing into the Tokyo bay, it appears likely that the shaking was strongest in the northwest quarter with the intensity of X to XI and weakest in the southeast quarter where the intensity was in the order of IX in the modified Mercalli scale. While the shaking intensity varied locally from one place to another as above, it may be assumed that the two ward area being considered might have been shaken by the motion having a maximum horizontal acceleration exceeding 200 gal as inferred from the relationship indicated in Table 1. The document survey by Sayama (1972) has also disclosed the locations as shown in Fig.2 where the soil deposits were most severely damaged in the form of surface fissures or ground settlements. It would be of interest to note that the locations of the surface rupturing as indicated in Fig.2 coincide approximately with the places where the shaking intensity was strongest in Fig.1.

2. Tokyo earthquake of 1894

An earthquake with an estimated magnitude in the order of 6.5 shook

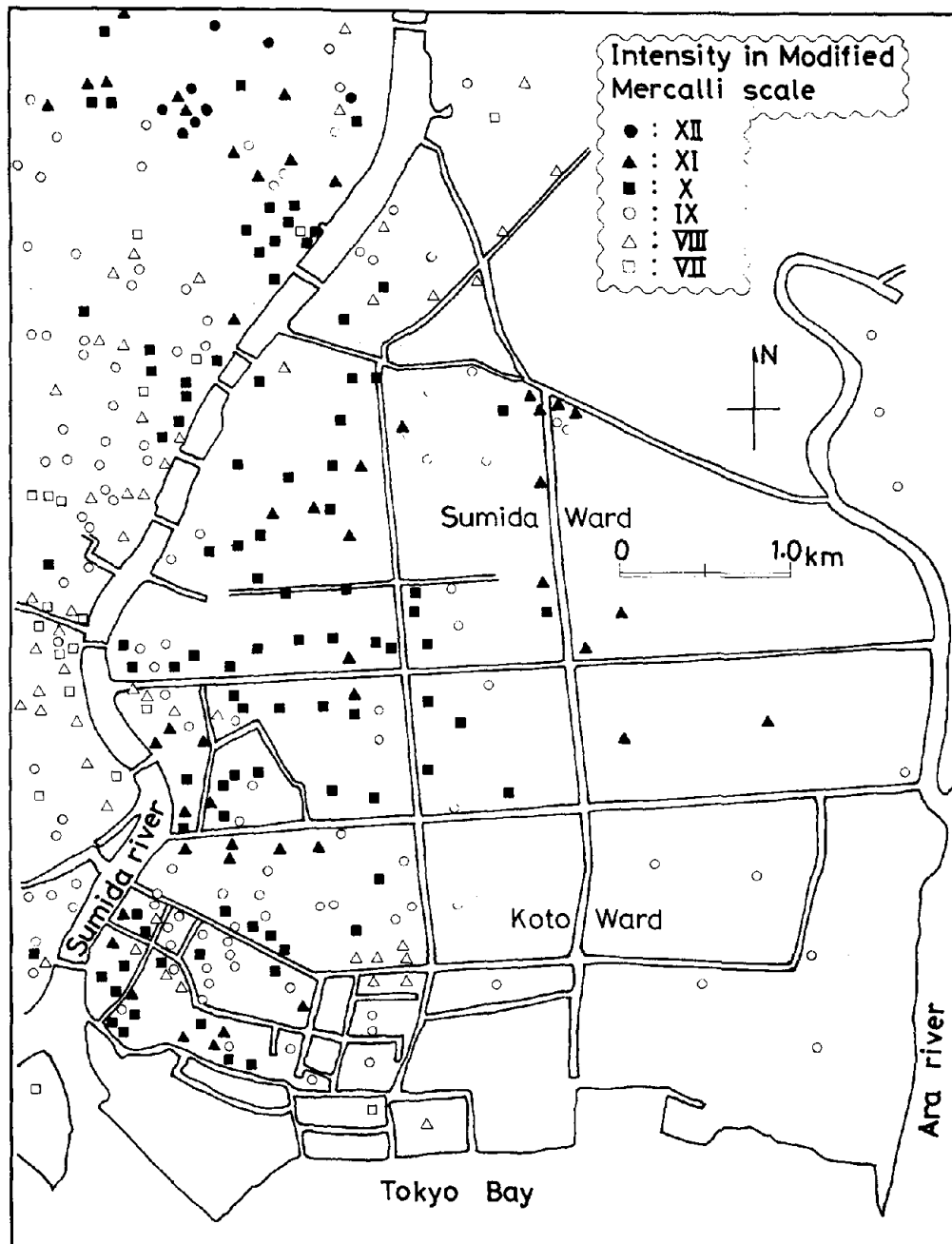


Fig.1 Distribution of shaking intensity in the downtown area of Tokyo in the Edo-Ansei earthquake of 1855.

the western part of Tokyo, at 2:04 p.m. on June 20, 1894, killing 24 people and destroying many brick structures and chimneys.

An assessment of the damage distribution showed the epicenter of the quake to have lain approximately on the north-south line going through the western part of the downtown Tokyo. The seismic intensity distribution map prepared by Hagiwara (1974) is presented in terms of the 12 step intensity scale similar to the modified Mercalli scale in Fig.3. From this figure it can be seen that the maximum shaking intensity on the order of 8 concentrated in the downtown Tokyo. With reference to Table 1, it may be assumed

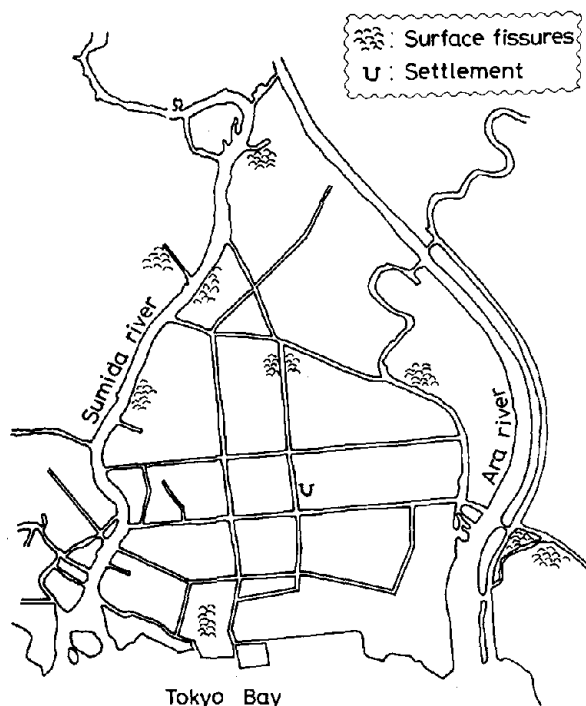


Fig.2 Locations of the ground failure in the downtown area of Tokyo in the Edo-Ansei earthquake of 1855

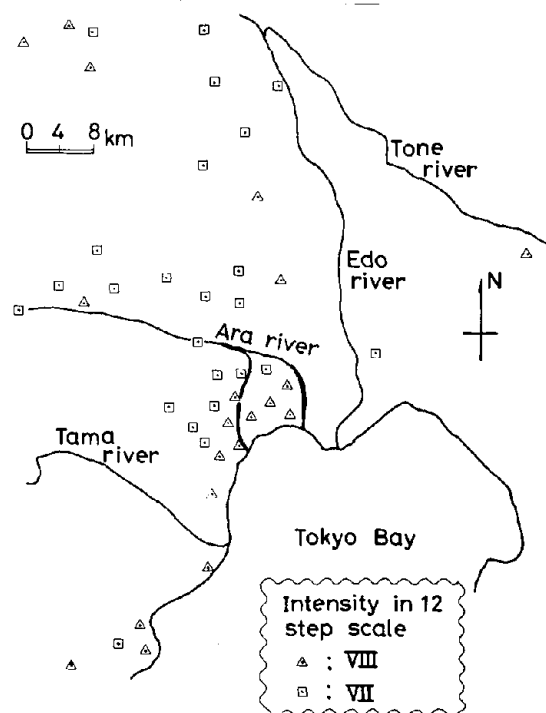


Fig.3 Distribution of shaking intensity in Tokyo area in the Tokyo earthquake of 1894 (Hagiwara, 1974)

that the maximum accelerations probably ranged from about 100 to 200 gal or even more. Signs of liquefaction in the ground were observed in many places in the form of surface fissuring, spouting mud and sand water. In one place called Fukagawa located on the west bank of the Sumida river near the Tokyo bay, a big spring developed from a fissure and continued to eject water for as long as one and half hours. The places where spouts of sand or mud water were reportedly observed are plotted in the map of Fig.4.

3. Great Kanto earthquake of 1923

The great Kanto earthquake of September 1, 1923 (Magnitude 7.9) was the most disasterous earthquake in Japanese history. The tremors reportedly lasted for longer than one minute. About 14 thousand people were reportedly killed or missing, mostly victims of fires which broke out after the quake. The damage to buildings and other civil engineering facilities spread throughout the Kanto plain. Destruction was particularly severe in the downtown area of Tokyo, although the epicenter had been located about 80 km southwest of the city.

The distribution of the seismic shaking over the metropolitan area of Tokyo was established, as shown in Fig.5, by Imamura (1937) on the basis of damage investigation and observation of aftershocks. He classified the region hit by the earthquake into four areas where the ground had experienced different levels of shaking with an average acceleration of 0.1, 0.15, 0.20 and 0.25g. It may be seen in Fig.5 that the triangular shaped area enclosed by the two rivers had undergone the heaviest shaking with a ground acceleration between 0.15g and 0.25g. In the southern part near the coastal

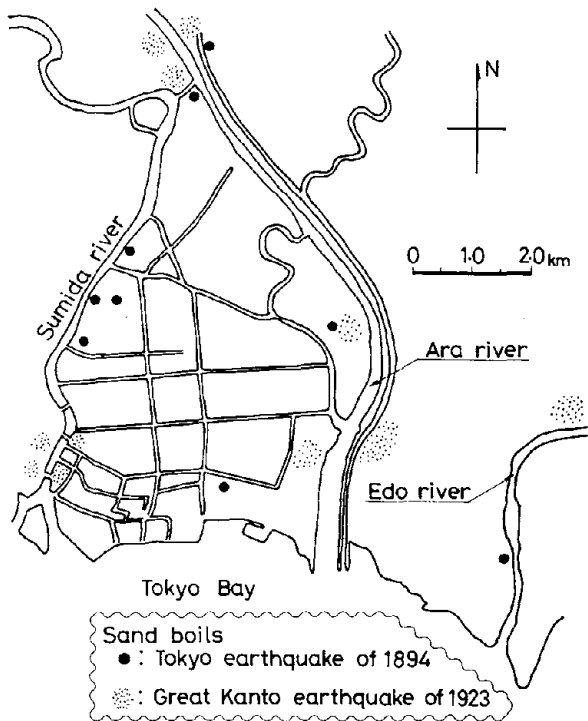


Fig.4 Locations where sand boils were observed in the Tokyo earthquake of 1894 and the great Kanto earthquake of 1923 (Kuribayashi and Tatsuoka, 1975)

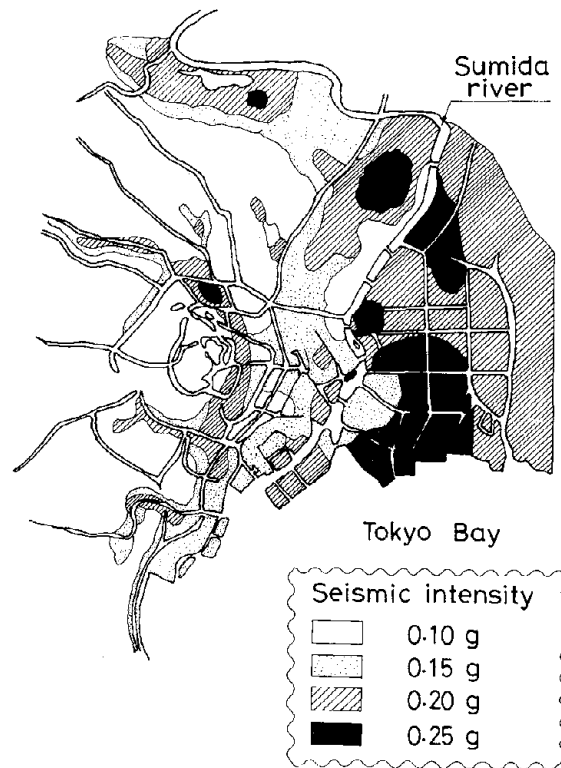


Fig.5 Seismic intensity in the downtown area of Tokyo, Kanto earthquake of 1923 (Imamura, 1937)

line, the shaking was estimated to have been particularly severe with an estimated ground acceleration in the order of 0.25g.

A similar seismic microzoning was also worked out by Kitazawa (1950) for the 1923 Kanto earthquake. An effort was first made to find some correlations between seismic intensity, damage extent of wooden structures and penetration resistance of soil deposits for limited damaged areas where any relevant data were available. Then, for other wider areas where only the data of the penetration resistance were available, the ground accelerations were estimated by using the relationship derived above. This region was then divided into four areas according to the seismic intensity level of 0.1, 0.2, 0.3 or 0.4g. The result of microzoning carried out by the above procedure is presented in Fig.6 where it may be seen that the low-lying delta area east of the Sumida river had been subjected to the heaviest shaking amounting to a seismic coefficient as strong as 0.4g.

More recently, an attempt was made by Kagami and Kobayashi (1971) to estimate the ground accelerations at the time of the 1923 earthquake at various places in downtown Tokyo by using the one-dimensional wave propagation theory. The N-S component of the acceleration record having a predominant period of 0.4 sec. obtained in the Taft earthquake of 1952 was modified to have a peak acceleration of 90 gal at the bedrock. As a result of the computation employing this modified wave form, it was suggested that the computed accelerations on the ground surface were approximately equal to the motions estimated on the basis of an empirical formula proposed by Kanai (1966). The seismic zoning map established as presented in Fig.7 showed that the maximum horizontal accelerations might have been in the

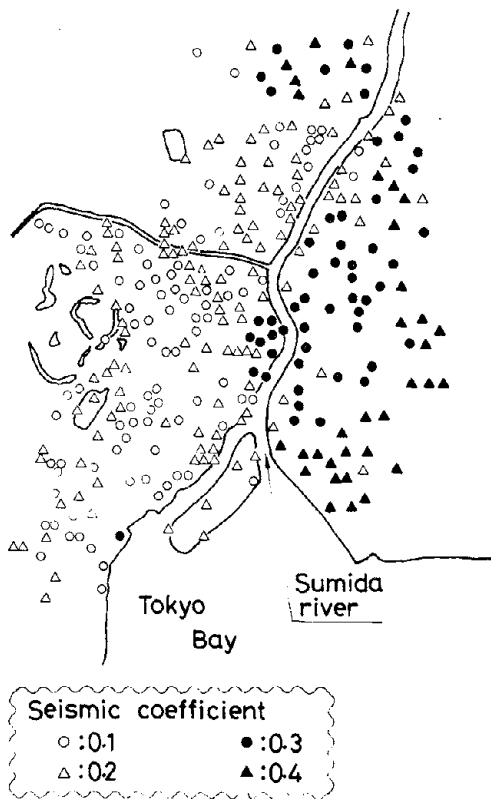


Fig.6 Seismic Coefficient in the downtown area of Tokyo, Kanto earthquake of 1923 (Kitazawa, 1950)

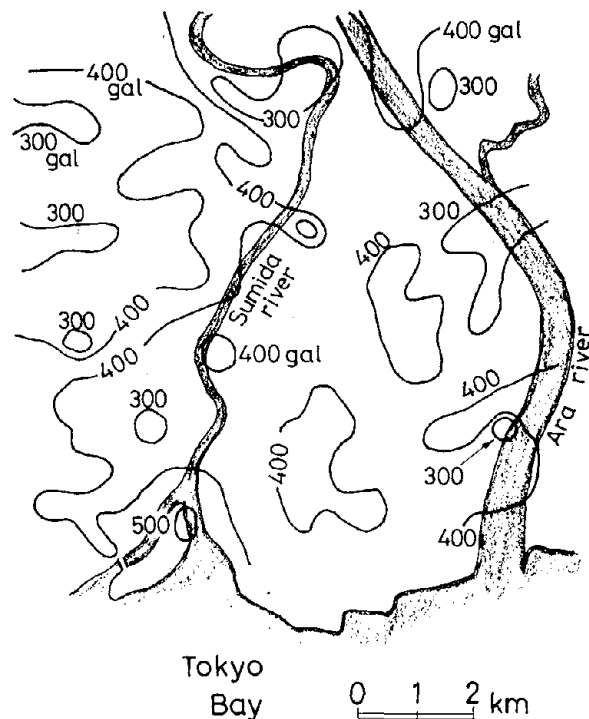


Fig.7 Distribution of shaking intensity in the downtown area of Tokyo in the Kanto earthquake of 1923 (Kagami-Kobayashi, 1971)

order of 400 gal. However, at two small sections along the Sumida river, somewhat greater acceleration in the order of 500 gal was assumed to have occurred.

Following the 1923 Kanto earthquake, damage surveys reported evidence of liquefaction at many places in the form of surface cracking and sand volcanoes accompanied by spouting of water and sand over the ground surface. The places where sand boils were observed were picked up from old documents and plotted in Fig.4. It is noted that the liquefaction occurred in the areas where the ground accelerations were greater than approximately 150gal, for whichever seismic intensity map was considered.

SELECTION OF SEISMIC INTENSITY FOR MAKING LIQUEFACTION SUSCEPTIBILITY MAP

In order to assess the likelihood of liquefaction in given soil deposits in Tokyo for earthquakes as strong as the three as described here, it is necessary to set an appropriate maximum horizontal acceleration which is likely to be encountered in the future. The value of this acceleration need not necessarily be a probable maximum in view of the circumstances in design practice but should be reasonably a good estimate considering the accuracy in the predicted consequences. To determine this acceleration, the range of the maximum horizontal accelerations that might have been experienced within the two ward area of downtown Tokyo during the past big earthquakes was inferred from the seismic intensity distribution maps shown in Figs.1, 3, 5, 6 and 7. The ranges of accelerations based on the estimated seismic intensity by various investigators are summarized in Fig.8. For the Kanto earthquake of 1923, it is noted that the estimation by Imamura

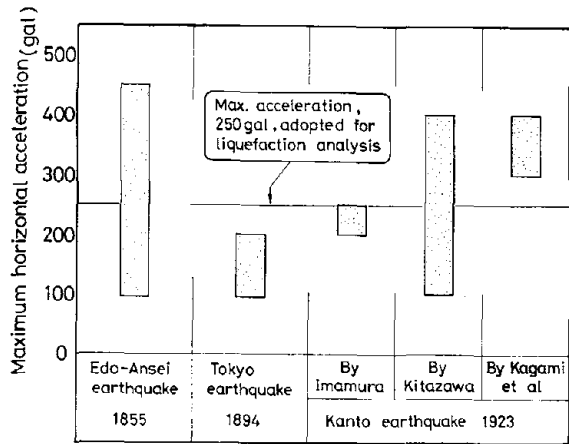


Fig.8 Probable ranges of maximum accelerations within the Koto and Sumida ward area in the three big past earthquakes

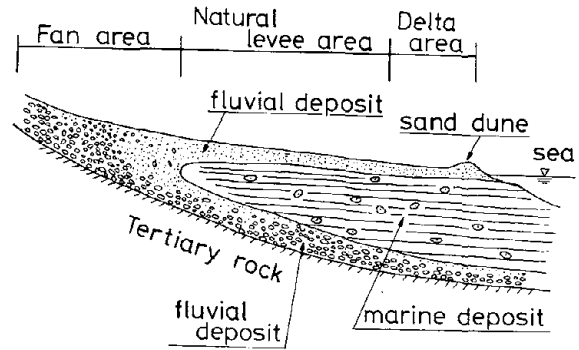


Fig.9 Illustration for formation of alluvial deposit

gives the lowest acceleration, while Kagami and Kobayashi assigned the highest acceleration. Notwithstanding the scatters involved in this kind of estimation, it may be reasonable to assume that the maximum acceleration at the time of the 1923 earthquake might be on the order of 0.25g on the average throughout the region being considered. Fig.8 also shows that the acceleration of 0.25g might as well be the average for the downtown area at the time of the 1855 Edo-Ansei earthquake, although somewhat lower acceleration was suggested for the 1894 Tokyo earthquake. From the above consideration, it was decided to adopt the maximum acceleration of 0.25g as being the standard acceleration representing the magnitude of the future earthquake as well as the past earthquakes that had jolted the downtown area of Tokyo. In the following liquefaction analysis, the value of 0.25g will be used as the input acceleration on the ground surface.

GEOLOGICAL SETTINGS AND TYPICAL SOIL PROFILE

The downtown area of Tokyo being considered in this investigation is basically composed of what is known as fluvial deposit or deltaic deposit. In modern subsurface geology, the formation of these deposits is illustrated as follows. Approximately 20 thousand years ago when the average temperature on earth was lowest, it was estimated that the sea level was about 100m lower than the present level, as much of the sea water existed in the form of ice. In this diluvial era, the ground surface in the downtown area of Tokyo is thought to have been sloped steeper than it is at present era as illustrated in Fig.9, as this area used to be located farther away from the sea coast. Consequently, cobbles, gravels or coarse sands were transported and deposited by the flow of rivers during flooding. In the subsequent era, the earth is thought to have been gradually warmed up as it came into the alluvial era, and correspondingly the sea level rose and the coastal line advanced inland. The soft marine deposit was then formed under sea water as illustrated in Fig.9. This marine deposit consisted mostly of soft silt or clay with dark grey color and characteristically contained remains of shellfish. In the downtown area of Tokyo, this marine deposit has a thickness of 10 to 50 meters. Approximately six thousand years ago, the temperature of the earth rose to its peak and, accordingly, the sea water

was raised to its highest level estimated as being approximately 5m above the present sea level. Since then the temperature on earth has been decreasing slowly and hence the sea level has been gradually lowered. During this era where the coastal line was regressing, the ground surface was nearly flat and fine grained soils were transported and deposited by the flow of rivers, forming a fluvial deposit known as natural levee deposit or deltaic deposit near the sea coast, as illustrated in Fig.9. In the downtown area of Tokyo, this deposit consists mainly of fine to coarse sands and has a thickness of about 3 to 15 meters. In some places, this sand layer does not exist, but wherever it does, it becomes the critical deposit for which the possibility of liquefaction occurring need be checked. A typical soil profile in this area obtained by boring is shown in Fig.10 for the site indicated in the map of Fig.16. The soil profile at the boring site A is the place where liquefaction is known to have occurred at the time of the 1923 Kanto earthquake as can be seen in the damage map in Fig.4. The clay-rich sediment below the depth of 8m is the very soft marine deposit as exemplified by a low blow count value of 1 to 3. The layer at the shallower depths between 2 and 8m consisting essentially of sands represents the fluvial or deltaic deposit formed more recently by the flow of rivers. In the soil profile shown in Fig.10, the ground surface is covered by what is generally termed surface soil. This name designates the soil which had not preserved any trace of inherent layered structures which had been formed during deposition. In many cases, the surface soil consists of various materials such as gravel, sand, silt, clay, crushed stones and bricks.

PROCEDURES FOR CLASSIFYING POTENTIALLY LIQUEFABLE SOIL DEPOSIT

In order to work out zoning of potentially liquefable area, it would be necessary to have as many information as possible at hand with regard to soil profile and its constituting soil characteristics within the area in question. Raw information on subsoil conditions that is made available most readily today is a number of boring records obtained on various occasions by public organizations and private enterprises. A review of over one thousand of these boring data has shown that the most reliable information commonly available were : (1) soil type; (2) layering of deposits; and, (3) N-value in standard penetration resistance. Then, it was considered appropriate to identify the liquefaction potential at a given site on the basis of these data. The background concept and procedures for making the identification are described below.

(1) Identification based on soil type

The first step towards identifying liquefable deposits would be to distinguish soil types that are potentially prone to liquefaction. It is well-known that sandy soils are potentially liquefable while silty or clayey soils are not. To be more specific, studies were made by Ishihara, Sodekawa and Tanaka (1978) for clarifying the possibility of liquefaction occurring in silty sand or sandy silt in terms of the fines contained in cohesionless soils. However, information on the grain size characteristics was not always available to permit the classification of the thousands of actual soils on this basis. For this reason, identification of potentially liquefable or nonliquefable soils was made only on the basis of the soil names recorded on individual boring log. The designation of soil type used for the identification is shown on Table 2.

(2) Identification based on layering of deposits

As mentioned in the foregoing section, the sand deposit for which

Table 2 Soil type classification of liquefiable and non-liquefiable soils according to the names of the soils written on the boring logs

	Soil type
Liquefiable soils	Sand , Fine sand , Medium sand , Silty sand , Sand with clay partings Sand containing fractured shells, Sand containing rotted plants , Sand with gravel partings
Non liquefiable soils	Surface soil , Surface fill , Clay Silt , Loam , Rotted soil , Gravel

liquefaction susceptibility is to be examined in the downtown area of Tokyo is either the fluvial-deltaic deposit or reclaimed deposit which lies a few meters from the ground surface. This sand deposit is generally covered by what is called surface soil consisting of dumped materials or artificial fills that are unlikely to develop liquefaction. As explained previously, the sand is generally underlaid by soft clay or silt layers as thick as 10 to 50 meters which are also considered potentially immune to liquefaction. Therefore, the general subsurface stratification in the area of downtown Tokyo can be characterized as a liquefiable sand layer sandwiched between non-liquefiable cohesive soil deposits. Should the surface soil be thick enough, the underlying sand deposit will not produce uplift pressure needed to break off the overlying surface soil and exert damaging effect on the ground surface. In this case, there will be no surface manifestation and consequently little damaging effect occurs, even if the sand deposit does liquefy. Therefore, when a criterion is to be established from the viewpoint of damaging effect rather than from the inducement of liquefaction itself, it would be necessary to specify the thickness of the overlying surface soil. If the thickness of the sand deposit itself is small, it will not produce pore water pressure high enough to bring about the damaging effect on the ground surface. Thus, it would also be necessary to take into account the thickness of the sand layer itself to establish the liquefaction criterion in the above vein. In order to set up the criterion for liquefaction with accompanying damaging effect, soil profile data for those sites where surface manifestation of liquefaction existed during the past earthquakes were compiled from previous study (Kishida, 1969). The thickness of the sand layer, H_2 , known from these compiled data, are plotted in Fig.11 versus the thickness of the overlying surface layer, H_1 . It may be seen in this figure that the damaging effect on the ground surface is brought about when the thickness of the surface soil layer is smaller than 3.0m. Therefore, the soil deposit having a surface soil thicker than 3.0m will be identified as a deposit where liquefaction may not occur in the following analysis. It may also be seen in Fig.11 that there was no case reported where surface evidence of liquefaction was observed in the deposit having a sand layer thinner than about 3.0m. This fact does not, however, preclude the possibility of liquefaction manifestation occurring in the soil profiles where both the surface soil and sand layer are less than 3.0m in

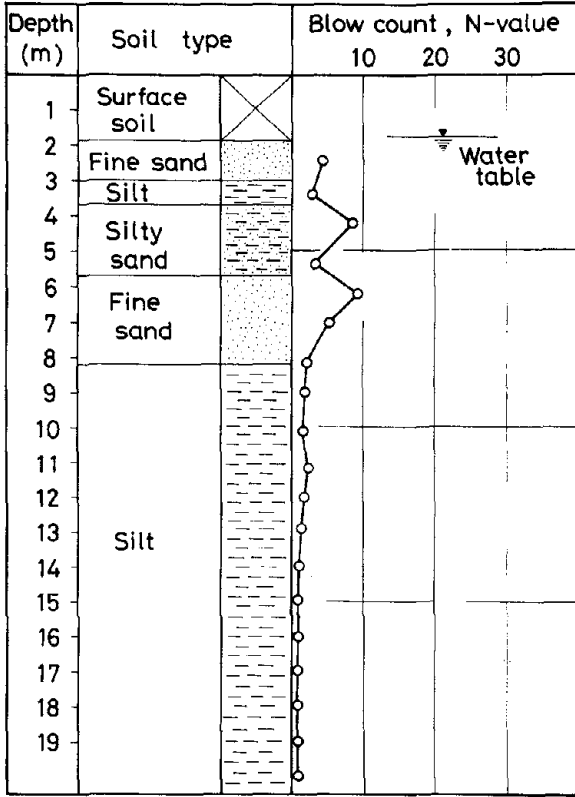


Fig.10 Soil profile at the boring site A

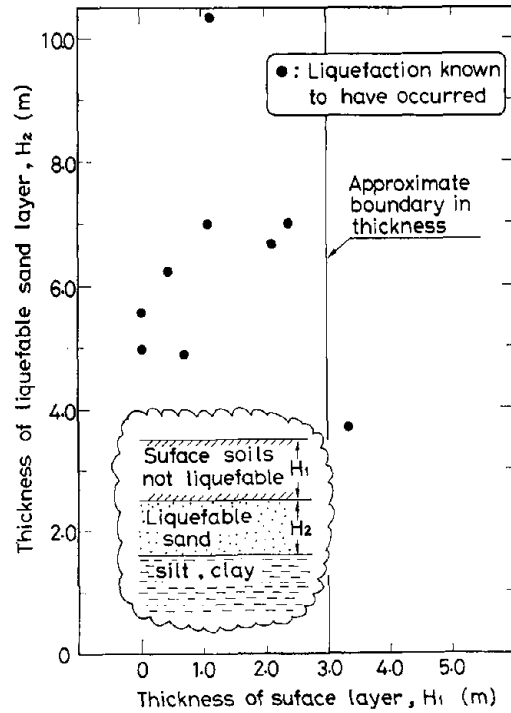


Fig.11 Effect of surface layer in causing surface manifestation of liquefaction

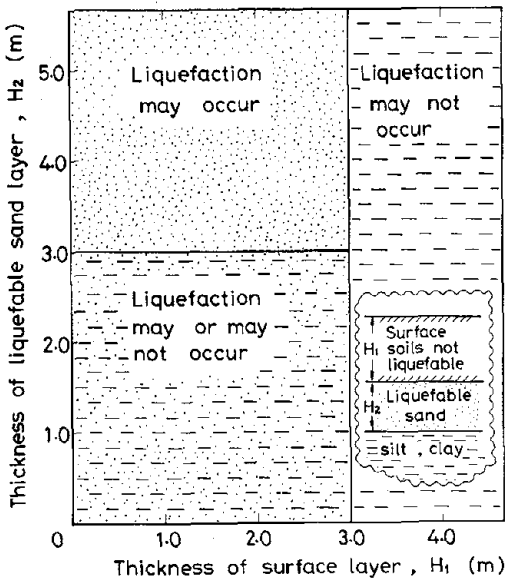


Fig.12 Criterion for considering the effect of thickness of liquefiable sands

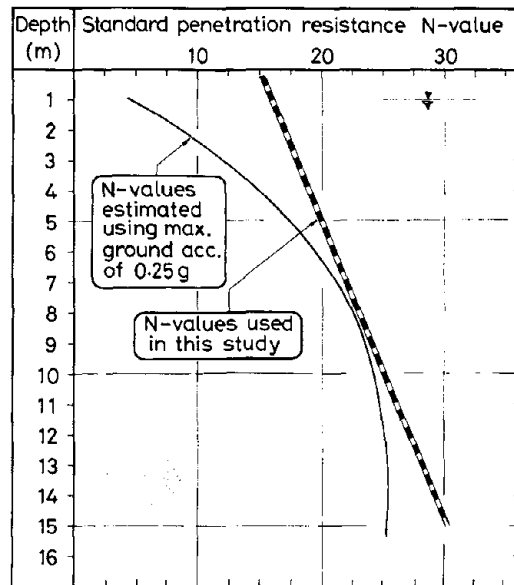


Fig.13 Threshold N-values computed for the max. ground acceleration of 0.25g

thickness. In this case, therefore, the soil deposit will be categorized as a deposit where liquefaction may or may not occur. In all except for the above two cases, the soil deposit will be identified as a deposit where liquefaction may occur. The criterion for identification as above is summarized in Fig.12.

(3) Identification based on the density of sand

When a sand layer is identified as potentially possessing the damaging effect in view of an unfavorably layered profile as explained above, what needs to be examined next is the density of the sand layer. At present, a simplest way of evaluating the effect of insitu density of sand would be to make use of available N-value from the standard penetration test. For practical purposes, it would be convenient to set up some threshold N-value below which liquefaction may occur and above which liquefaction may not occur. This critical N-value may be determined through procedure suggested by Ishihara (1977), when the maximum horizontal acceleration is specified on the ground surface. In the present investigation, the maximum acceleration will be set at 0.25g on the basis of the conclusion derived in the preceding section. Furthermore, experience in the field has shown that the ground water table is located approximately 1.0m below the ground surface and also that the earth pressure coefficient at rest is equal to 0.5. Assuming further that the wave form of the acceleration time history is of the shock type (Ishihara, 1977), one can compute the cyclic stress ratios to which soil elements at various depths in a deposit will be subjected during a future earthquake. If this cyclic stress ratio is equated to the cyclic strength of the sand which is correlated in turn with the N-value, it becomes possible to determine the threshold N-value.

Several empirical relationships have been suggested by various investigators to correlate the N-value and the cyclic strength. However, recent laboratory test results on many undisturbed sand specimens have indicated that this relationship may be best represented by the formula,

$$\frac{\sigma_{dl}}{2\sigma_0'} = 0.0882 \frac{N}{\sigma_v' + 0.7} \quad \text{-----} \quad (1)$$

where, σ_{dl} is the amplitude of cyclic axial stress in the triaxial test to cause initial liquefaction under 20 cycles; σ_0' is the confining pressure; and, σ_v' denotes the effective overburden pressure in kgf/cm^2 at a depth in question. The threshold N-value computed as above using the relation (1) is plotted versus depth in Fig.13. For processing a vast majority of data on the standard penetration resistance, a curved line as shown in Fig.13 was not convenient for carrying out a routine analysis of liquefaction. Therefore, the computed threshold N-value was replaced by a straight line as indicated in Fig.13, and this straight line distribution was used throughout the present investigation. For comparison purposes, the straight line is replotted in Fig.14, together with similar curves proposed by other investigators. Note that the other curves have lower threshold N-values because these are all based on the experience gained from the Niigata earthquake of 1964, Japan, where the recorded maximum surface acceleration was 0.162g, a value smaller than 0.25g being considered in this study.

At all sites where liquefaction potential was investigated, the soil susceptibility was examined down to a depth of 15m.

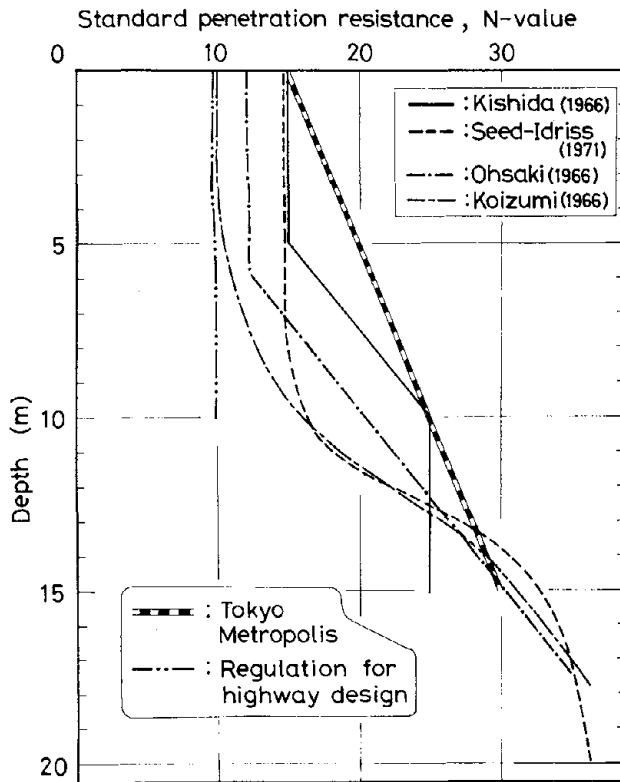


Fig.14 Threshold N-value for liquefaction analysis

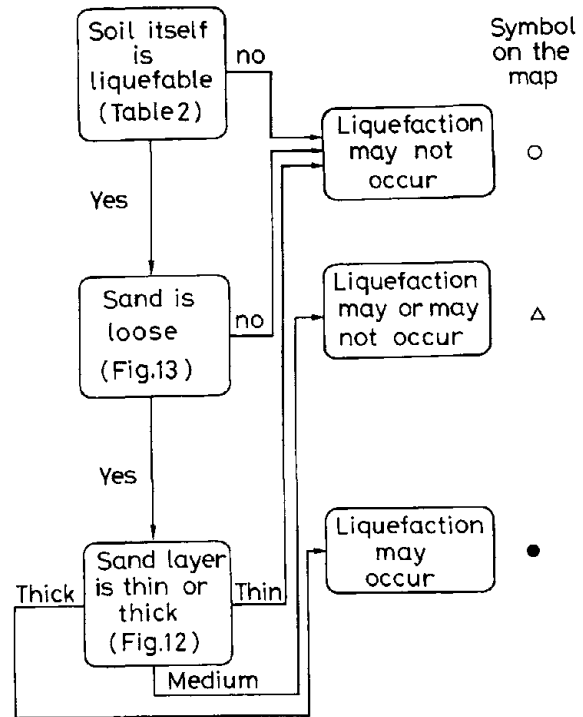


Fig.15 Procedures for predicting the likelihood of liquefaction

PROCEDURES FOR MAKING LIQUEFACTION SUSCEPTIBILITY MAP AND ITS RESULT

On the basis of the three criteria as postulated above for identifying liquefaction potential of soils, each soil profile within the downtown area of Tokyo was classified into one of the three groups of domains where: (1) Liquefaction may occur; (2) Liquefaction may or may not occur; and, (3) Liquefaction may not occur. Each data on soil profile was processed by following the steps indicated in the flow chart of Fig.15. As many as 1370 soil profile data were used for the present study. The results of the identification work are mapped out in Fig.16. Within the Koto and Sumida ward area, 33 percent of the sites investigated were identified as the deposits where liquefaction may occur, and 25 percent where liquefaction may or may not occur, and the remaining 42% as where liquefaction may not occur. In Fig.16 the coastal lines at the time of the 1855 Edo-Ansei earthquake and the 1923 Kanto earthquake are indicated. The land south of these coastal lines was reclaimed by depositing artificial fills after the last large tremblers and, since then has not yet experienced any large earthquake. Consequently this area was considered more prone to liquefaction than was the northern area which had experienced liquefaction up to the present time.

CONCLUSIONS

Literature survey has shown that it would be appropriate to conduct analysis of liquefaction susceptibility by assuming that the maximum ground acceleration would be 0.25g. On the basis of this level of shaking

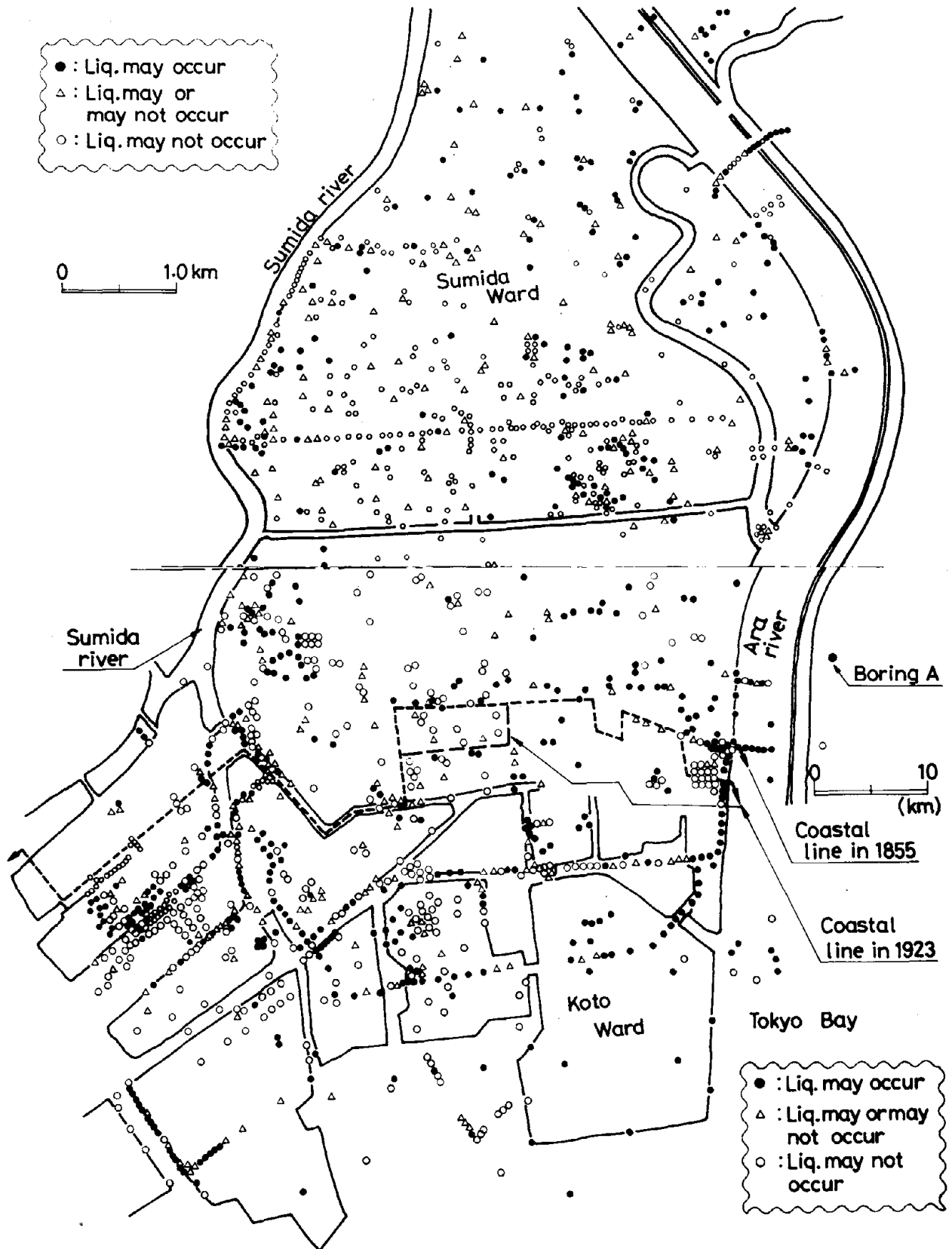


Fig.16 Likelihood of liquefaction occurrence in downtown area of Tokyo

intensity, likelihood of liquefaction was examined for 1370 sites in the downtown area of Tokyo. The result of the analyses showed that for the 33 percent of the total sites investigated liquefaction was expected to occur; and for 42 percent of the total sites liquefaction may not occur.

ACKNOWLEDGEMENTS

In carrying out this investigation, Civil Engineering Research Institute of Tokyo Metropolis offered the soil profile data. Professor M.Fukuoka gave valuable advices and encouragement. Messrs. Y. Yoshida, K. Sugo and M. Seki, research staffs in the Soil Mechanics Laboratory of the University of Tokyo were engaged in this program. Dr. K. Mori kindly reviewed the draft of this paper. The efforts of these persons are sincerely acknowledged.

REFERENCES.

- Hagiwara, T. (1974), "Distribution of Seismic Intensities of the Tokyo Earthquake in 1894, the Edo (Old Tokyo) Earthquake in 1855 and the Kanto Earthquake in 1703, as Estimated from Ancient Manuscripts", Report on the Earthquake near Tokyo, Vol.3, Tokyo Metropolitan Office, pp.323-327
- Imamura, A. (1937), Theoretical and Applied Seismology, p.187, Maruzen And Co.
- Ishihara, K. (1977), "Simple Method of Analysis for Liquefaction of Sand Deposits during Earthquakes", Soils and Foundations, Vol.17, No.3, pp.1-17
- Ishihara, K., Sodekawa, M. and Tanaka, Y. (1978), "Effects of Overconsolidation on Liquefaction Characteristics of Sands Containing Fines", submitted to ASTM Symposium on Dynamic Soil and Rock Testing in The Field and Laboratory for Seismic Studies, Denver.
- Kanai, K. (1966), "Empirical Formulae for the Ground Motion Characteristics during Earthquakes", Proc.Japan Earthquake Engineering Symposium, pp.1-4 (in Japanese)
- Kishida, H. (1966), "Damage to Reinforced Concrete Buildings in Niigata City with Special Reference to Foundation Engineering", Soil and Foundation, Vol.6, No.1, pp.71-88
- Kishida, H. (1969), "Characteristics of Liquefied Sands during Mino-Owari, Tohankai and Fukui Earthquakes", Soils and Foundations, Vol.9, No.1, pp.75-92
- Kitazawa, G. (1950), "Seismic Distribution in the downtown area of Tokyo", Earthquake, Vol.3, No.1, pp.32-35 (in Japanese)
- Koizumi, Y. (1966), "Change in Density of Sand Subsoil Caused by the Niigata Earthquake", Soil and Foundation, Vol.6, No.2, pp.38-44
- Kuribayashi, E. and Tatsuoka, F. (1975), "Brief Review of Liquefaction during Earthquakes in Japan", Soils and Foundations, Vol.15, No.4, pp.81-92
- Kagami, H. and Kobayashi, T. (1971), "Distribution of the Ground Surface Accelerations in the Eastern Tokyo in the Kanto Earthquake", Journal of the Japan Architectural Society, No.184, pp.41-48, (in Japanese)
- Ohsaki, Y. (1966), "Niigata Earthquakes, 1964 Building Damage and Soil Condition", Soil and Foundation, Vol.6, No.2, pp.14-37
- Okamoto S. (1973), Introduction to Earthquake Engineering, University of Tokyo Press, p.33
- Sayama, M. and Tokyo Metropolitan Government (1972), Collected Damage documentation of Ansei-Edo Earthquake (in Japanese)
- Seed, H.B. and Idriss, I.M. (1971), "Simplified Procedure for Evaluating Soil Liquefaction Potential", Proc. of ASCE, SM9, pp.1249-1273

THREE-DIMENSIONAL NONLINEAR ANALYSIS OF SOIL-STRUCTURE INTERACTION
IN A NUCLEAR POWER PLANT CONTAINMENT STRUCTURE

by

J. Isenberg^I and D. K. Vaughan^{II}

ABSTRACT

The soil island approach to soil-structure interaction is applied to the SIMQUAKE 1 series of explosive field tests designed to simulate earthquake ground motion effects on model nuclear containment structures. These tests indicate strong nonlinear response of the model structures. The three-dimensional, nonlinear finite element computer program TRANAL is used to simulate the response of a 1/12 scale model containment structure in SIMQUAKE 1a. Results are compared with measured data.^{III}

INTRODUCTION AND SUMMARY

The soil island approach (1) to analysis of structure-medium interaction was adapted to simulate model power plant containment structures subjected to explosively generated ground shaking. Field tests which are referred to as Events SIMQUAKE 1A and 1B (2), sponsored by the Electric Power Research Institute, provide an ensemble of input ground motion and structural response records which are currently being used to evaluate procedures for modeling site characteristics and structure-medium interaction. A three-dimensional, nonlinear finite element computer program (TRANAL) (3) was used to represent the response of a one-twelfth scale, cylindrical containment structure and that of a portion of the surrounding backfill and undisturbed soil, called the soil island.

One of the main findings of the field tests is that the natural frequency of the rocking mode, measured during the era after the strong shaking has subsided, depends strongly on the amplitude of the shaking. Encouraging agreement between nonlinear analysis performed with TRANAL and the measurements has been obtained (4). The computer resources required for such analyses are of order one and a half hours on CDC 7600 for 1.5 seconds of response of the 1/12 scale model (18 seconds for full scale).

SOIL ISLAND APPROACH

The soil island approach is a method of applying ground motion to a structure. In its most general form, it involves a two-step procedure for which free field motions are computed by any method that is consistent with the site characteristics and governing equations of motion; this includes vertically traveling SH waves or more complete descriptions underlying surface wave effects. The first step is to designate a fictitious boundary in the free field which surrounds the location of the structure; free field motions on this boundary are stored for future use. In the second step, this volume of soil and the structure, referred to as the soil island, are analyzed in detail using the stored free field ground motions as boundary con-

I Associate Partner, Weidlinger Associates, Menlo Park, California.

II Senior Research Engineer, Weidlinger Associates, Menlo Park, California.

III This work was sponsored by the Electric Power Research Institute, Nuclear Power Division, as part of their program in soil-structure interaction.

ditions. As is illustrated in Fig. 1, this reduces the structure-medium interaction model to manageable size.

The boundaries of the soil island are chosen far enough from the location of the structure that, when it is included, it causes only a slight perturbation at the boundaries. The efficiency and accuracy of the soil island approach depends on choosing an island which is small enough to be manageable and large enough that boundary effects are negligible. Previous studies (1,5) suggest that distances of soil cover equal to 2 to 3 characteristic dimensions are adequate. New studies were conducted by the present authors to guide selection of island size. Two different site profiles, each with a different horizontal ground motion input at bedrock level, were postulated. Case 1 uses the N69°W component of the 1951 Taft earthquake record as uniform bedrock motion input to a homogeneous site at a depth of 300 feet. Case 2 uses a layered site with the input bedrock motion, being a combination of the Taft record plus the N69°W component of the 1971 Castaic record. Free field motions for all depths from the surface to bedrock level were first calculated using a shear beam analysis. These motions were then used as input to the soil island analyses. For each case, three different sizes of island with embedded structure were analyzed in plane geometry. The dimensions of the soil islands are shown in Fig. 2. The complete set of six calculations was analyzed for 10 seconds of strong ground shaking. The main results are presented in the form of peak spectral rocking velocity as a function of distance from the structure to the side boundary. The rocking velocity is the angular velocity of the structure multiplied by the radius of the structure. As shown in Fig. 3, the rocking response in each of the two cases converges to a constant value for island sizes between medium and large. This is consistent with previous findings that island size on the order of 2 to 3 times the diameter of the structure appear to give satisfactory results.

TRANAL

TRANAL (TRANsient Nonlinear anALysis) is a computer program which was developed by Weidlinger Associates, under sponsorship of the Defense Nuclear Agency, for problems in soil and structural dynamics. The code uses a finite element discretization in space. The single finite element type is an eight node, isoparametric hexahedron. The equations of motion are integrated using an explicit, second order central difference operator. A subcycling scheme has been incorporated in TRANAL which approximately optimizes time step in each of several zones. The only restrictions on material models which TRANAL can accept are those which should be used to screen all models, namely that they are stable, unique and lead to solutions which depend continuously on the boundary conditions. The cap model (6) which is currently incorporated in TRANAL is of this type. The efficiency of TRANAL is measured in terms of computer time to process an element-time step, which is about 0.4×10^{-3} seconds on CDC 7600. For a typical three-dimensional, nonlinear problem involving simulation of a power plant containment structure subjected to 15 to 20 seconds of strong ground shaking, the computer time required is of order 1½ to 2 hours. The code is operational on CDC 6600 and CDC 7600 equipment. The capacity of the code is approximately 50,000 equations on CDC 7600.

ANALYTIC MODEL

Simulation of Event SIMQUAKE 1A requires representing the properties of the site, the geometry of the partially embedded 1/12 scale containment

structure and the ground motion input to the soil island. Details of the SIMQUAKE 1A test layout and the 1/12 scale containment structure are shown in Figs. 4 and 5. The properties of the soil are represented by the cap model, an elastic, strain-hardening version of the classical incremental theory of plasticity. This model represents such important characteristics as compaction, shear hysteresis and failure (6).

The cap model consists of a yield surface, a moveable cap and a plastic strain rate vector. An early version of the model, which consists of a fixed yield surface as illustrated in Fig. 7, is used in the calculations reported below. The model has recently been amended to include nonlinear hardening yield surfaces and a state limit or failure surface in shear to improve modeling of hysteresis in cyclic shear. Subject to theoretical restrictions (6,7,8), the yield surface, the shape of the cap and its hardening rule and the bulk and shear moduli must be selected using laboratory and field data for a specific site as a guide. This was done for the test site. Uniaxial stress/strain curves for the two soil layers used in the SIMQUAKE 1A analysis are shown in Fig. 8.

The properties of the backfill which surrounds the lower one-fourth of the structure and the properties of the interface between the soil and structure have a significant influence on the dynamic response of the model. As an interim step, the backfill in the model is assumed to be softer than the physical backfill; this is a continuum approximation to the discontinuous processes of debonding and rebonding between the sides of the structure and adjacent backfill due to rocking. A debonding-rebonding criterion based on a critical value of tensile pressure (average direct stress) is used on the bottom of the structure. These approximations are currently being refined to represent the "beating back" phenomenon which has been observed in Event SIMQUAKE and elsewhere (9).

The finite element soil island model, including layered site, backfill and structure, is shown in Fig. 6. There are three elements in the vertical direction between the surface and the bottom of the structure. There are six elements across a diameter of the structure and, in all, 30 elements define the interface between the floor (of the half structure) and underlying soil. The resulting finite element model has about 5,000 elements with over 17,000 degrees of freedom.

The input to the analysis is derived from horizontal and vertical velocity-time histories (from velocity gages or integrated accelerometer records) at nine points as shown in Fig. 4. The points lie on the centerline of the test bed and on the boundaries of a rectangle whose length is 100 feet, whose depth is 62.5 feet and which encloses the structure. Typical boundary velocity-time histories for SIMQUAKE 1A are shown in Figs. 9 and 10. A preliminary plane strain finite element calculation without structure was performed in which the measured velocities and interpolated records at intermediate points were applied to the boundaries. An imaginary soil island was defined within this model having a length of 70 feet and a depth of 35 feet. Motions along this boundary were used as input to the three-dimensional calculation of the soil island with structure.

The cost of analyzing the three-dimensional, nonlinear soil island model with embedded structure for 1.5 seconds of response (18 seconds for full scale structure) is 5,700 CP seconds on CDC 7600. At rates pre-

vailing on government computers, this costs about \$400; at rates prevailing at commercial computer centers, the cost is about \$4,000.

RESULTS OF SIMQUAKE 1A ANALYSIS

To illustrate the application of the cap model, the soil island approach and TRANAL, selected results of posttest simulation of Event SIMQUAKE 1A and comparison with field data are presented below. The measured and calculated horizontal velocity-time histories at the top of the 1/12 scale structure are compared in Fig. 11. Qualitative agreement is satisfactory with regard to the period of the first three peaks (outward, inward, outward). Recent improvements in the site model have eliminated the discrepancy between times of peak response.

Measured and calculated horizontal interface stresses on front and rear faces of the structure are shown in Figs. 13 and 14. On the side near the source there is initial compression; on the side away from the source there is initial tension (measurement) or zero stress (calculation). This behavior is associated with initial counterclockwise rocking (top of structure rocks toward source). This initial phase is followed by a reversal in the sense of the stresses; the side near the source becomes compressed. This is associated with clockwise rocking (top of structure rocks away from source).

The rocking velocity-time history is computed by subtracting the horizontal velocity-time histories at the top and bottom of the structure. Fig. 12 compares the result of doing this with both calculated and measured velocities. There is qualitative agreement in the sense of the initial rocking (top rocks toward source) and in the sense of the first clockwise peak at $t \approx .35$ sec to $t \approx .4$ sec. The second major counterclockwise peak at $t \approx .6$ sec (measured) to $t \approx .7$ sec (calculated) is also correctly simulated, as is the frequency of the rocking mode.

SUMMARY AND CONCLUSIONS

This paper describes briefly the application of the cap model, the soil island approach and the TRANAL three-dimensional nonlinear finite element code to analysis of the response of a 1/12 scale nuclear power plant containment structure subjected to simulated earthquake ground shaking. Encouraging qualitative agreement between measured and calculated structural response, especially with respect to rocking and the interface stresses generated by rocking, were obtained. The computer cost for the three-dimensional nonlinear analyses of the 1/12 scale structure for 1.5 sec (18 sec for full scale) was \$400 on U. S. government computer facilities and would be about \$4,000 at commercial rates on a CDC 7600. Similar calculations are being performed for a subsequent test, SIMQUAKE 2.

REFERENCES

1. I. Nelson, and J. Isenberg. "Soil-Structure Approach to Structure/Media Interaction," 2nd Int. Conf. on Numerical Methods in Geomechanics, Virginia Polytechnic Institute and State University, June 1976.
2. C. Chan et al. "Experimental and Analytical Investigation in Non-linear Dynamic Soil-Structure Interaction," 4th Int. SMIRT Conf., San Francisco, Aug. 1977.
3. J. L. Baylor, M. P. Bienick, and J. P. Wright. "TRANAL: A 3-D Finite Element Code for Transient Nonlinear Analysis," DNA 3501F, Weidlinger Associates, June 30, 1974.
4. J. Isenberg, D. K. Vaughan, and I. Sandler. "Nonlinear Soil-Structure Interaction for Nuclear Power Plants Subjected to Earthquake Excitation," Research Project RP 810-2 by Weidlinger Associates for Electric Power Research Institute, June 1978.
5. I. M. Idriss, and K. Sadigh. "Seismic SSI of Nuclear Power Plant Structures," Journal of the Geotechnical Engineering Division, Proc., ASCE, Vol. 102, No. GT7, July 1976.
6. I. Sandler. "The Cap Model for Static and Dynamic Problems," 17th U.S. Symposium on Rock Mechanics, Snowbird, Utah, Aug. 1975.
7. F. L. DiMaggio, and I. Sandler. "Material Models for Soils," Journal of Engineering Mechanics, Proc., ASCE, June 1971, pp. 935-950.
8. I. Sandler, F. L. DiMaggio, and G. Y. Baladi. "Generalized Cap Model for Geological Materials," Journal of the Geotechnical Engineering Division, Proc., ASCE, Vol. 102, No. GT7, July 1976.
9. G. E. Howard, P. Ibanez, and C. B. Smith. "Seismic Design of Nuclear Power Plants--An Assessment," Research Project 273 1087-2A by Applied Nucleonics Company for Electric Power Research Institute, June 1975.

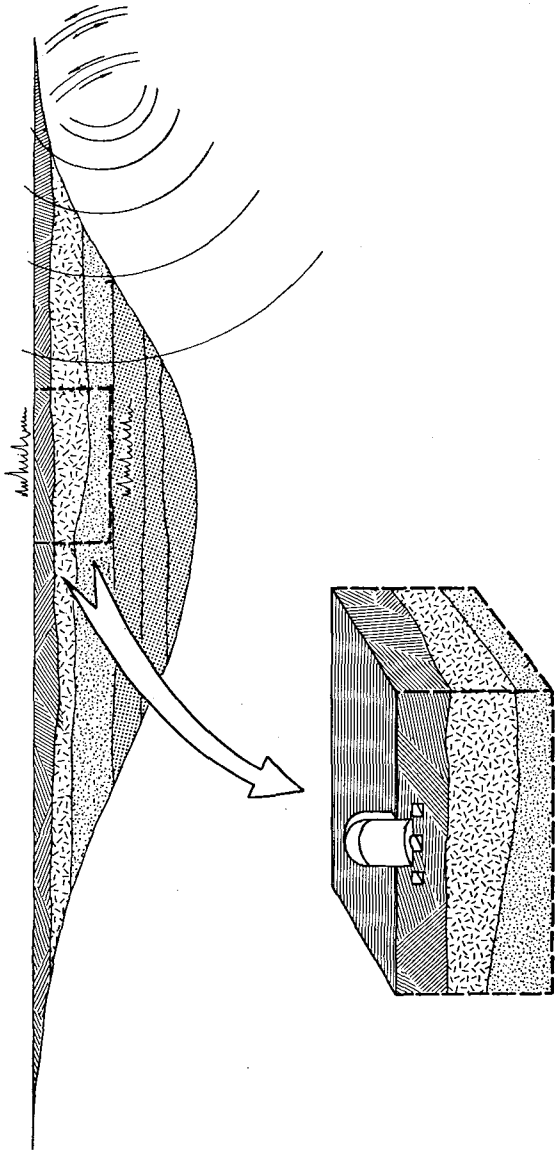


Figure 1. Soil Island Approach Applied to Power Plant Subjected to Seismic Ground Shaking.

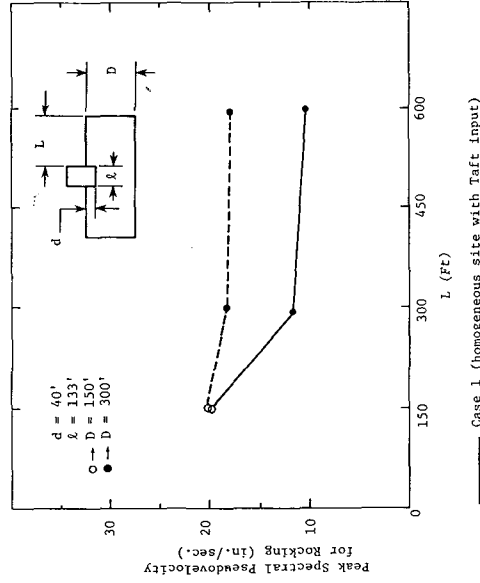


Figure 3. Peak Spectral Rocking Velocity of Reactor for 2 Cases and Various Sizes of Soil Island.

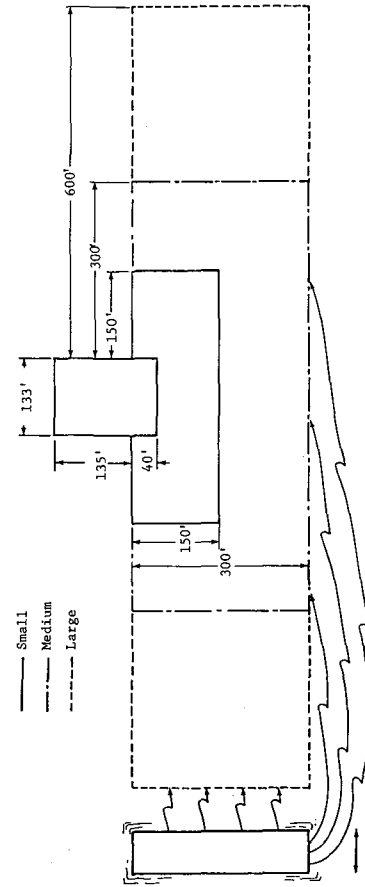


Figure 2. Different Soil Island Sizes Used to Study Boundary Proximity Effects on Reactor Subjected to Seismic Ground Shaking.

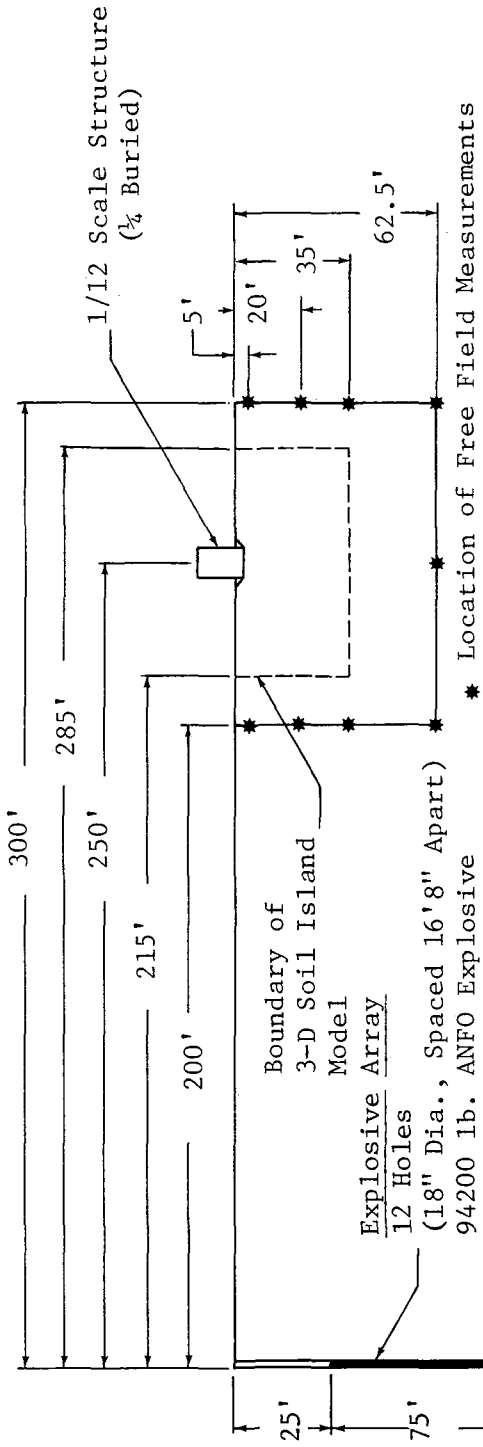


Figure 4. Elevation View of SIMQUAKE 1A Including 1/12 Scale Containment Structure.

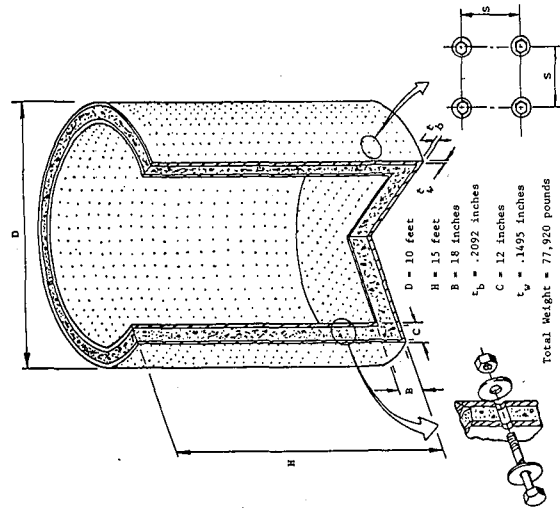


Figure 5. 1/12 Scale Nuclear Containment Structure Used in SIMQUAKE 1.

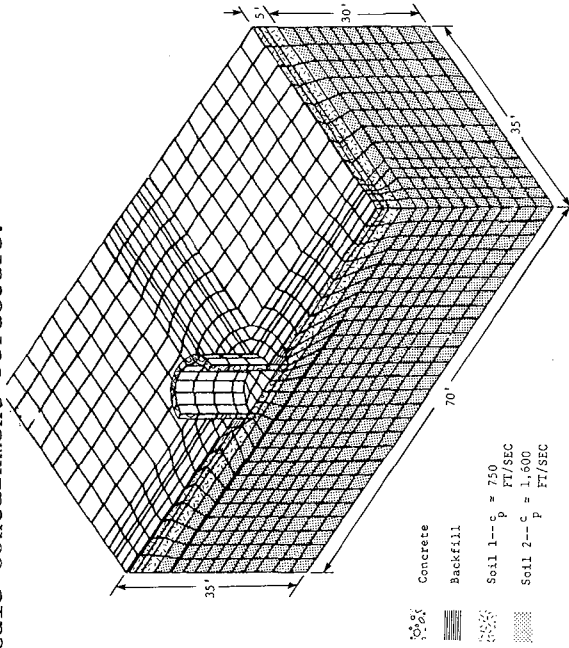
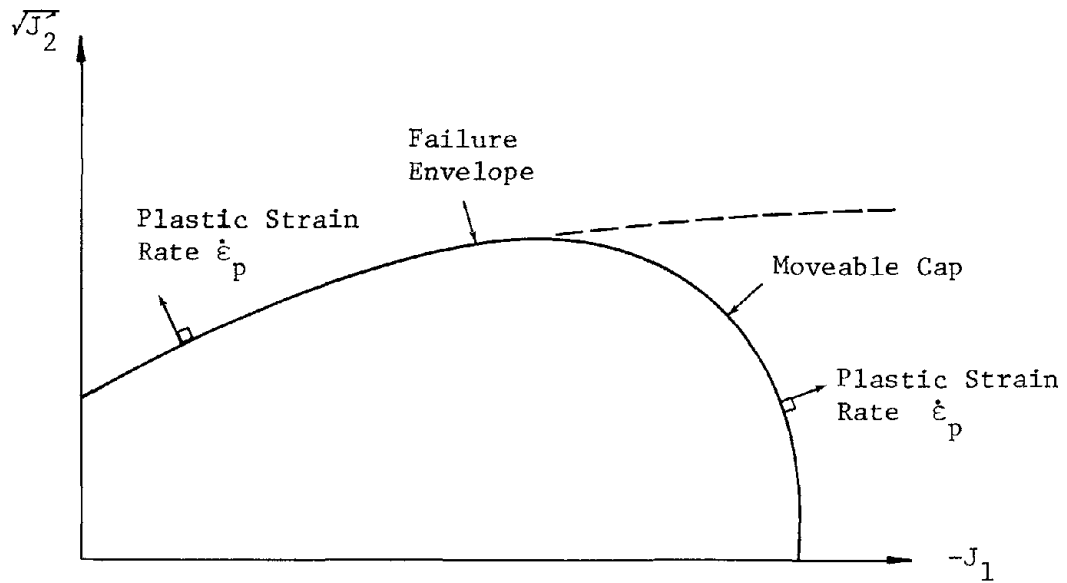


Figure 6. 3-Dimensional TRANAL Soil Island Model Used for SIMQUAKE 1A Calculation.



Failure Envelope: Fixed in Stress Space
 Cap: Movement of Cap is Related to the Plastic Volumetric Compaction of the Soil

Figure 7. Typical Cap Model Yield Surfaces for Compressive Stresses.

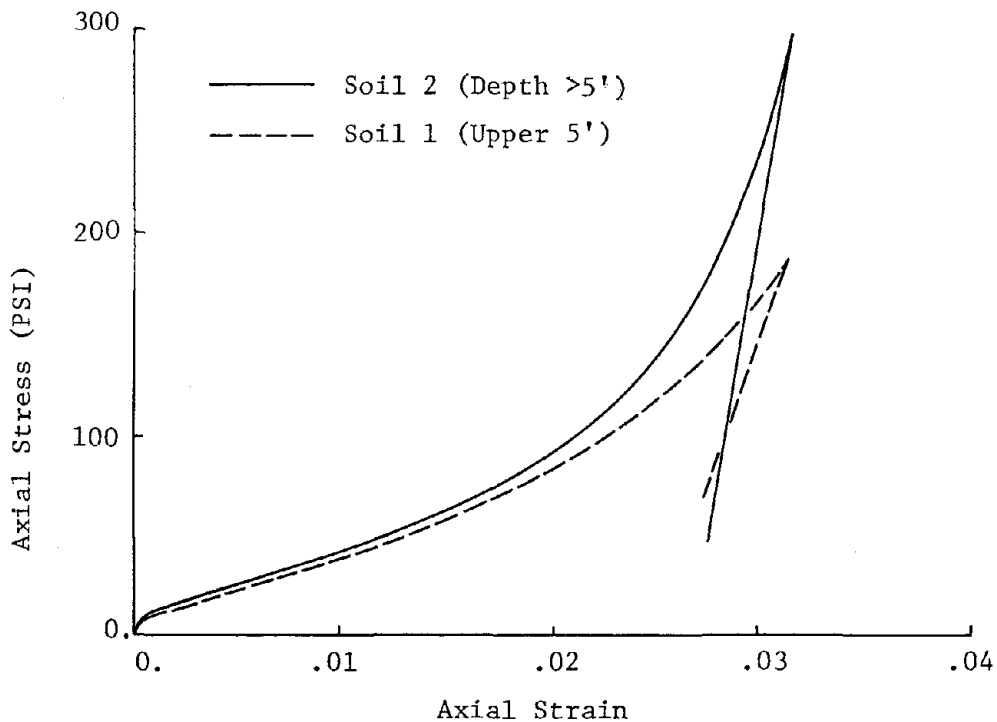


Figure 8. Uniaxial Stress Strain Curves for Soil Models Used in SIMQUAKE 1A Analysis.

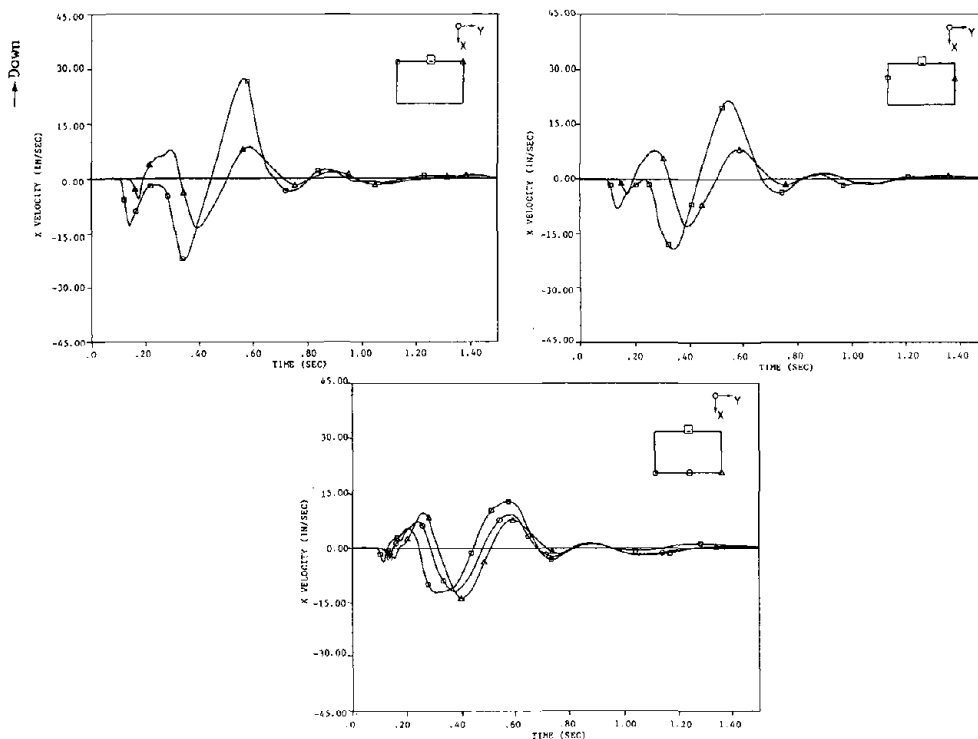


Figure 9. Typical Vertical Velocity-Time Histories Used as Input to Post-Test Analysis of SIMQUAKE 1A Obtained from Ground Motion Records.

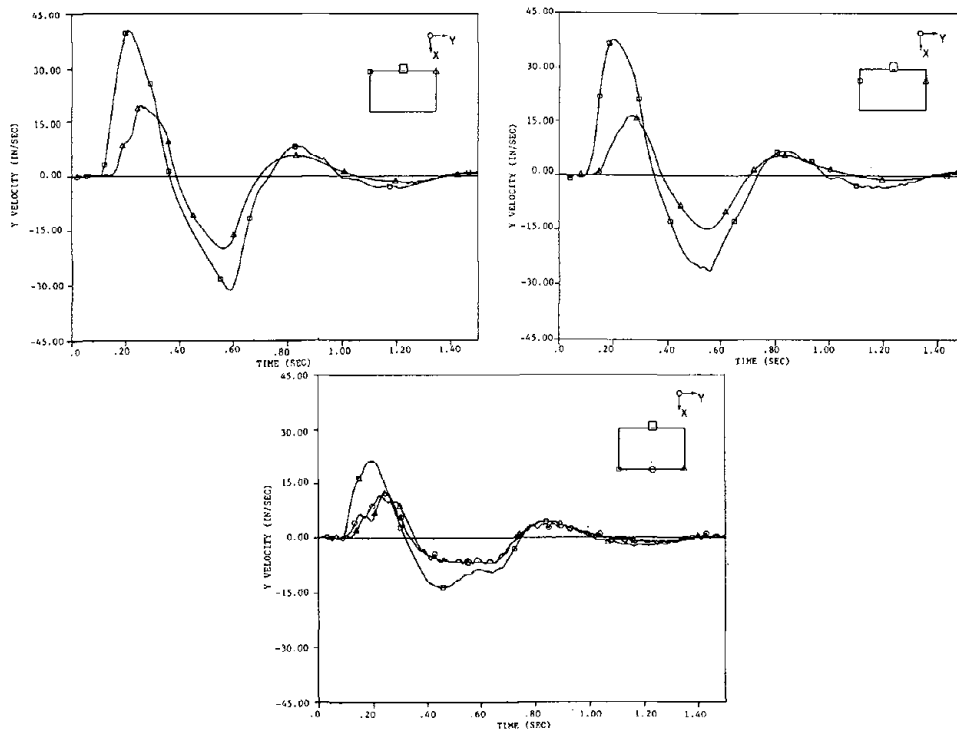


Figure 10. Typical Horizontal Velocity-Time Histories Used as Input to Post-Test Analysis of SIMQUAKE 1A Obtained from Ground Motion Records.

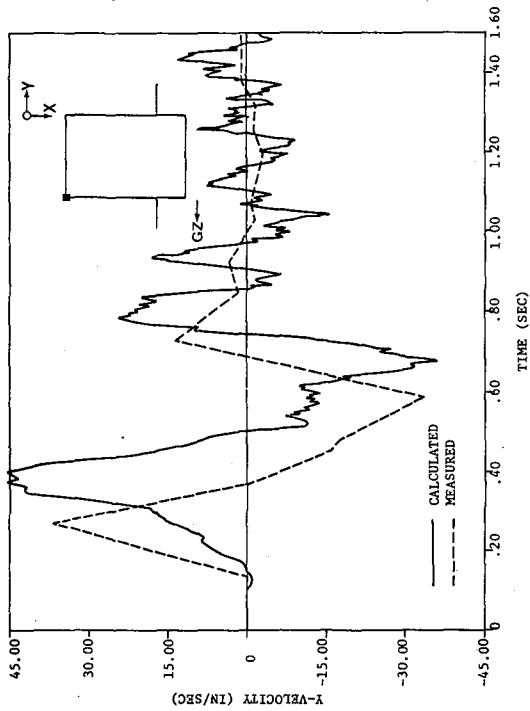


Figure 11. Horizontal Velocity at Top of 1/12 Scale Structure for SIMQUAKE 1A.

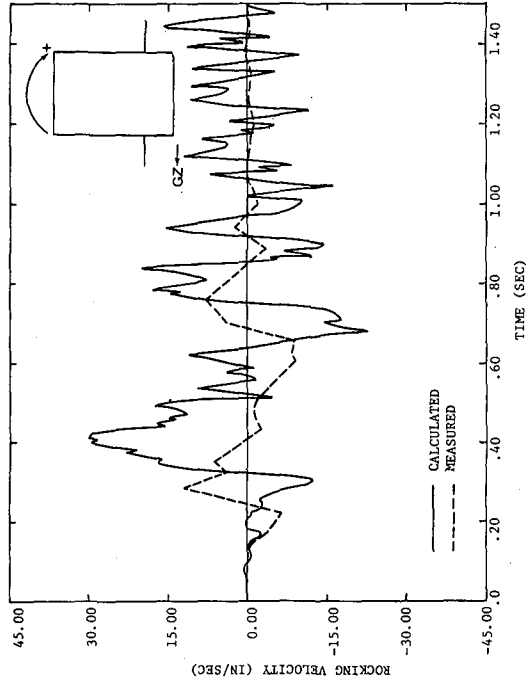


Figure 12. Rocking Velocity of 1/12 Scale Structure for SIMQUAKE 1A.

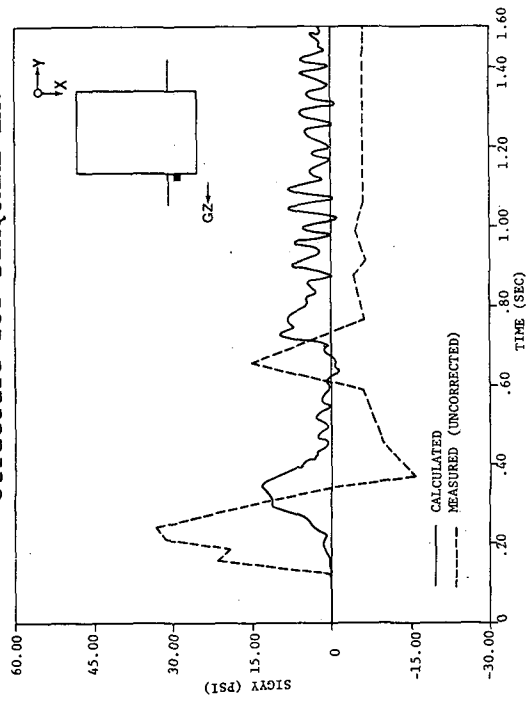


Figure 13. Upstream Horizontal Interface Stresses for 1/12 Scale Structure in SIMQUAKE 1A.

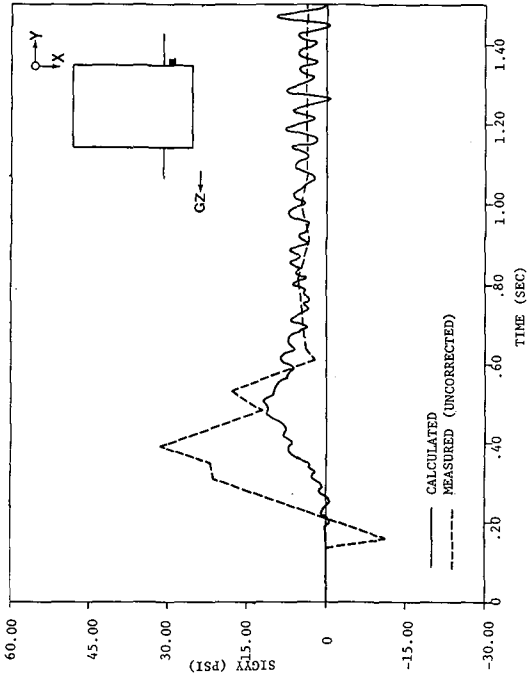


Figure 14. Downstream Horizontal Interface Stresses for 1/12 Scale Structure in SIMQUAKE 1A.

BOUNDARY METHODS IN SOIL-STRUCTURE INTERACTION

by

E. Alarcón, J. Domínguez, A. Martín, F. Paris §

ABSTRACT

A general theory that describes the B.I.E.M. Approximation in steady-state elastodynamics, is developed. Constant and linear elements in plane problems are presented and also some results which are compared with previous one. Finally the capabilities of the method are presented.

1. SOIL-STRUCTURE INTERACTION

A problem which has traditionally fascinated soil dynamic researchers has been the foundation design of vibrating machinery. Several methods based either in the WINKLER idea (BARKAN(1962), SAVINOV(1955), etc.) or in the assumption of a elastic homogeneous, isotropic halfspace (REISSNER(1936), QUINLAN (1953), SUNG(1953) has been developed.

Using that experience soil authors have the usefulness of those results to earthquake engineering problems.

The starting point was a paper published by REISSNER in 1936, in which, trying to establish a theoretical basis for the DEGEBO (Deutschen Forschungsgesellschaft für Bodenmechanik) experimental research, used the LAMB'S(1904) problem solution (halfspace under harmonic load fig. 1(a)) to obtain the soil response to a oscillating load applied through a rigid circular plate.

The solution method was the integration to LAMB results in the circular area, which means a uniform contact pressure (fig. 1(b)).

REISSNER results were very different of experimental ones mainly because a sign error (SHEKTER 1948) in the algebra and also because the uniform distribution doesn't produce the equality of displacements required by the plate rigidity.

In the "Fifty-Six Annual Meeting of the American Society for Testing Materials (July 1953)", P.M.QUINLAN and T.Y.SUNG presented two papers in which they repeated the analysis for the (fig. 1(c)) cases. The first is a static rigid plate distribution, the second a uniform one and the third a parabolic one more similar to a flexible plate case.

As can be seen all results were obtained through a simplification of the initial boundary problem.

For the rigid disk it is a mixed problem in which the displacement shape is known in the part under it and the tractions are nil in the remainder of the half-space boundary.

§ E.T.S. Ingenieros Industriales
Universidad Politécnica de Madrid
MADRID . SPAIN

REISSNER and SUNG solved a different problem when they assumed a prescribed traction distribution under the plate. This leads, as was said, to a series of displacements incompatible with the hypothesis of rigid plate and, consequently, the results must be used with great care.

In several reports, specially in the 1971 & 1973 ones, VELETOS and coworkers presented an interesting new approach and also useful numerical results. For instance, the case of rocking and horizontal displacement was treated (VELETOS & WEI (1971)) with the following hypothesis:

- a) during the horizontal imposed displacements there are no normal stress in the halfspace boundary, in spite of the existence of vertical displacements.
- b) in the rocking case there are no tangential stress in the surface of the halfspace, in spite of the existence of horizontal displacements.

These hypothesis allow the computation of the horizontal case independently of the rocking one, but on the other hand, they produce non-rigid displacements of the plate. Nevertheless through the use of a weighted reciprocity relation, this approach produced very accurate results.

The viscoelastic case (MEEK & VELETOS (1973)) was also studied after a polynomial representation of previous elastic results.

By the way it is worth noting that more promising appears to be the method presented by DASGUPTA & SACKMANN (1977) using a correspondence principle for discretized set of values.

The importance of the embedment of the footing was also recognized very early (RICHART 1960) and a large amount of work has been done by NOVAK and coworkers (1972, 1973, 1974, ... etc.). The fundamental idea is to admit that the soil round the footing is built by a series of elemental layers which react independently of the halfspace over which they are resting. The agreement with experimental results is, of course, not very good.

After these pioneering works a considerable amount of work has been done in recent years to determine the dynamic stiffness of foundations of various shapes (GAZETAS & ROESSET, 1976, WONG & LUCO, 1976, ELSABEE & MORRAY, 1977, KAUSEL, ROESSET & CHRISTIAN, 1976, ...)

An interesting comparison between two and three-dimensional solutions including the influence of embedment has been recently published (JAKUB, 1977)

All these results are currently applied to the cases in which the base of the structure behaves as a single rigid footing (base slab in nuclear reactor buildings, high-rise buildings on mat foundation, etc.). In order to permit analysis of other structures where this idealization is unreasonable CHOPRA & coworkers (1969, 1974, 1975, 1976, etc.) have obtained results using a different approach.

The halfspace is treated as a substructure and the dynamic (frequency-dependent) stiffness matrix is of order equal to the number of connection degrees of freedom on the structure-foundation interface.

In this way the i_j term of the matrix is defined as the force in the i mode when in the j one is applied a harmonic unit displacement $e^{i\omega t}$, with all other d.o.f. being kept fixed (fig. 3).

In the case of the pure plane horizontally homogeneous halfspace one needs the results only for two boundary problems: the vertical displacement and the

horizontal one. An appropriate translation will provide the results for all the degrees of freedom. The displacement between the activated node and the neighbouring ones is assumed according to the isoparametric representation to be used in the subsequent F.E. analysis of the above-ground structure.

Instead of solving this mixed problem directly CHOPRA et al. prescribe zero displacements also outside the structure-foundation interface, and after a standard condensation, they get the correct dynamic foundation stiffness matrix.

2 BOUNDARY INTEGRAL EQUATION METHOD.

The first idea of B.I.E.M. was presented as early as 1963 by JASWON in a paper on potential problems. RIZZO (1967) successfully extended the method to more complicated problems, and CRUSE and coworkers (1969, 1972, 1973, etc.) have shown the possibilities of the method.

The B.I.E.M. is based upon the existence of two items: a fundamental solution of the field equation and a reciprocity theorem, which in elasticity is the BETTI'S theorem:

$$\int_{\partial D} \underline{T}^v \cdot \underline{u}^* ds + \int_D \underline{X} \cdot \underline{u}^* dv = \int_{\partial D} \underline{T}^v \cdot \underline{v} ds + \int_D \underline{X}^* \cdot \underline{u} dv \quad \dots (1)$$

where

\underline{T}^v is the vector traction in a boundary ∂D with normal \underline{v}

\underline{X} the body force in the volume D

\underline{u} the displacement vector and a * means the corresponding variables in the fundamental solution. If this is expressed in the form

$$\underline{u}_k^* = U_{ki} \cdot e_i \quad \underline{t}_k^{v*} = T_{ki} \cdot e_i \quad \dots (2)$$

where e_j are directions of actuation of unitary loads. (KELVIN solution) and in the absence of volume forces (1) is transformed in

$$u_i(p) + \int_{\partial D} T_{ki}(p, q) u_k(q) ds = \int_{\partial D} U_{ki}(p, q) T_k^v(q) ds \quad \dots (3)$$

which is known as SOMIGLIANA'S identity. p is the point of actuation of the load and q the point in the boundary along which is carried the integration.

The following step is to write eq 3 when $p \rightarrow P$, P being a point of the boundary. After some algebra the results can be written in the form

$$\underline{c} \cdot \underline{u}(P) + \int_{\partial D} \underline{T} \cdot \underline{u} ds = \int_{\partial D} \underline{u} \cdot \underline{T}^v ds \quad \dots (4)$$

where \underline{c} is a diagonal matrix in the case of a smooth boundary.

In the case of a harmonic oscillation CRUSE & RIZZO (1968) presented the fundamental solutions as

$$U_{ij} = \frac{1}{\alpha \pi \rho c_i^2} \left[\psi \delta_{ij} - \chi r_{ii} r_{ij} \right]$$

$$T_{ij} = \frac{1}{\alpha \pi} \left[\left(\frac{d\psi}{dr} - \frac{1}{r} \chi \right) (\delta_{ij} \frac{\partial r}{\partial v} + r_{ij} v_i) - \frac{2}{r} \chi (v_j r_{ii} - 2 r_{ii} r_{ij} \frac{\partial r}{\partial v}) - \right. \\ \left. - 2 \frac{d\chi}{dr} r_{ii} r_{ij} \frac{\partial r}{\partial v} + \left(\frac{c_j^2}{c_i^2} - 2 \right) \left(\frac{d\psi}{dr} - \frac{d\chi}{dr} - \frac{\alpha}{2r} \chi \right) r_{ii} v_j \right] \quad \dots (5)$$

and for two dimensions

$$\begin{aligned} \Psi &= k_0 \left(\frac{kr}{c_2} \right) + \frac{c_2}{kr} \left[K_1 \left(\frac{kr}{c_2} \right) - \frac{c_2}{c_1} K_1 \left(\frac{kr}{c_1} \right) \right] \\ \chi &= K_2 \left(\frac{kr}{c_2} \right) - \frac{c_2^2}{c_1^2} K_2 \left(\frac{kr}{c_1} \right) \end{aligned} \quad \dots (6)$$

in which

$$c_1^2 = \frac{\lambda + 2\mu}{\rho} \quad \lambda, \mu : \text{Lame' constants}$$

$$c_2^2 = \frac{\mu}{\rho}$$

$$k = i \omega$$

$$K_i(P, Q) = k_0 \left[\frac{k}{c} r(P, Q) \right]$$

$r(P, Q)$ = distance between P, Q points.

and k_0 is the modified Bessel function of the 2nd kind of zero order.

The method presented by CRUSE (1968) used a constant element to discretize the boundary, and, in it, the traction and the displacement are assumed constants.

The equations to be solved are then

$$\sum t_i \int_{\Delta s} U_{ji} ds = \sum u_i \int_{\Delta s} T_{ji} ds + \frac{1}{2} u_j \quad \dots (7)$$

which can be written as

$$\underline{B} \times \underline{\sigma} = \underline{A} \cdot \underline{u}.$$

In general, there are data and unknowns in $\underline{\sigma}$ and \underline{u} . After a reordering system (8) can be put in the classical form

$$\underline{K} \cdot \underline{x} = \underline{F}$$

where the data are collected in \underline{F} and \underline{x} is the vector of unknowns.

The efficiency of the approach is showed with some examples.

In fig. 4 we present the results obtained with a constant element program when the rocking case ($\phi = 5^\circ$) is studied. The results were compared with those resulting of the application of JAKUB formulas. Taking:

$$c_1 = 2; \quad c_2 = 1; \quad \omega = 1/2; \quad \rho = 1; \quad B = 1$$

and following JAKUB'S notation

$$\left. \begin{aligned} k_\phi &\approx \frac{1.62}{1-\nu} G B^2 = 2.43 \\ k_2 &= 1 - 0.2 \alpha_0 = 0.9 \end{aligned} \right\} k_\phi k_2 = 2.187$$

for the relation between the moment applied and the angle.

The corresponding moment in the first case (40 elements)

$$0.45 \times 0.938 = 0.4221$$

$$0.17 \times 0.813 = 0.1382$$

$$0.12 \times 0.688 = 0.0825$$

$$0.084 \times 0.563 = 0.0472$$

$$0.059 \times 0.438 = 0.0258$$

$$0.039 \times 0.313 = 0.0122$$

$$0.022 \times 0.188 = 0.0041$$

$$0.0075 \times 0.063 = 0.0004$$

$$0.7325 \times 0.125 \times 2 = 0.1832$$

and dividing by 5°

$$K \phi k_2 = \frac{0.1832}{0.0872} = 2.1009$$

In order to analyse the importance of discretization a coarser one (10 elements). The results are

$$\begin{aligned} 0.4614 \times 0.938 &= 0.4327 \\ 0.2249 \times 0.813 &= 0.1828 \\ 2 \times 0.0477 \times 0.625 &= 0.0596 \\ 4 \times 0.0262 \times 0.25 &= 0.0262 \\ \hline &0.7013 \end{aligned}$$

The error is $0.0312/0.7325 \approx 0.042$ very good for the sparse discretization used.

In fig. 5 we have presented also some displacements out of the plate.

As can be seen the method is very accurate and produce several useful results. For instance, the displacements outside the plate and inside the halfspace can be used to study the reciprocal influence with neighbouring structures.

It is important to notice that the mixed boundary problem has been handled directly, without any additional hypothesis and also that the embedded foundation with a general geometry can be analysed in the same fashion.

As an exemple an embedded strip foundation with a deep half of the plate size and the same material and discretization that the previous exemple was run in 5% rocking. The results under the plate are in a half of the plate are

X/B	Traction X		Traction Z	
	Real part	Imag. part	Real part	Imag. part
0.938	0.1043	-0.1046E - 01	-0.2786E+0.0	0.4539E-01
0.813	0.5783-0.1	-0.1064E-01	-0.127E+0.0	-0.2339E-01
0.688	0.5140E-01	-0.1038E-01	-0.9159E-01	-0.1719E-0 1
0.563	0.4775E-01	-0.1035E-01	-0.6597E-01	-0.1263E-01
0.438	0.4586E-01	-0.1033E-01	-0.4744E-01	-0.9215E-02
0.313	0.4485E-01	-0.1031E-01	-0.3193E-01	-0.6286E-02
0.188	0.4430E-01	-0.1029E-01	-0.1861E-01	-0.3705E-02
0.063	0.4408E-01	-0.1029E-01	-0.6093E-02	-0.1205E-02

The problem of the elastic foundation can be also analyzed. Nevertheless a constant element evolution of displacements is a bad representation in order to a subsequent conection with a F.E. mesh in the structure of interest.

A linear variation can be hauled in the following way:

$$\underline{u} = \begin{Bmatrix} u \\ v \end{Bmatrix} = \begin{bmatrix} N_1 & N_2 & 0 & 0 \\ 0 & 0 & N_1 & N_2 \end{bmatrix} \begin{Bmatrix} u_1 \\ u_2 \\ v_1 \\ v_2 \end{Bmatrix} ; \quad T^D = \begin{Bmatrix} \bar{x} \\ \bar{y} \end{Bmatrix} = \begin{bmatrix} N_1 & N_2 & 0 & 0 \\ 0 & 0 & N_1 & N_2 \end{bmatrix} \begin{Bmatrix} x_1 \\ x_2 \\ y_1 \\ y_2 \end{Bmatrix}$$

$$ds = \frac{L}{2} d\xi ; \quad N_1 = -\frac{1}{2}(\xi-1) ; \quad N_2 = \frac{1}{2}(\xi+1) ; \quad -1 \leq \xi \leq 1.$$

In every one can write two equations

$$\begin{bmatrix} c_{11} & c_{12} \\ c_{21} & c_{22} \end{bmatrix} \begin{Bmatrix} u_i \\ v_i \end{Bmatrix} + \sum_{j=1}^N \begin{bmatrix} A_{11}(i,j) & A_{12}(i,j) & A_{13}(i,j) & A_{14}(i,j) \\ A_{21}(i,j) & A_{22}(i,j) & A_{23}(i,j) & A_{24}(i,j) \end{bmatrix} \begin{Bmatrix} u_j \\ u_{2j} \\ v_j \\ v_{2j} \end{Bmatrix} =$$

$$= \sum_{j=1}^N \begin{bmatrix} B_{11}(c_{ij}) & B_{12}(c_{ij}) & B_{13}(c_{ij}) & B_{14}(c_{ij}) \\ B_{21}(c_{ij}) & B_{22}(c_{ij}) & B_{23}(c_{ij}) & B_{24}(c_{ij}) \end{bmatrix} \begin{Bmatrix} x_{1j} \\ x_{2j} \\ y_{1j} \\ y_{2j} \end{Bmatrix}$$

The only difficulty now is the treatment in sharp corners with displacement conditions (for example in the low corner nodes of a embedded foundation). The analysis of this case can be seen elsewhere (ALARCON, MARTIN & PARIS 1978).

In this way higher order elements can also be used but, for the soil representation the errors introduced with the elastic model make illusory every precision.

3. CONCLUSION

The B.†.E.M. appears as a powerful tool in the analysis of soil-structure dynamic interaction problems.

With this method it is very easy the treatment of elastic seminfinite media and the embedment partial or total (i.e. a lined tunnel (6.a) of the structure is not a problem. Also every shape of the interface between soil and structure is also easily handled. (6.b)

The original mixed boundary problem is solved but there is no problem if one wants to relax the condition of perfect bonding in the interface and employ the so-called "rigid-smooth" and "rigid-pressureless" conditions along the foundation boundary in order to model more closely the real situation. (6.c).

The presence of an arbitrary rigid boundary (6.d) can be solved without problems, and also the layered (6.e) case with the appropriate fundamental solution.

In the general case (6.f) a subdivision between different regions and the establishment of the compatibility and equilibrium in the interfaces allows one to write a banded system of equations (see for instance, LACHAT & WATSON, 1977).

Finally the response to incident waves can be obtained without problems and for every angle of incidence (6.g).

ACKNOWLEDGMENTS

The authors, should like to acknowledge the valuable suggestions made by prof. J.M.ROESSET and his guidance during the stay of one of them (J.D.) at M.I.T.

- 1.- ANESTI VELETOS, and YAU T.WEI, "Lateral and rocking vibration of footing" Journal of the Soil Mechanics and foundations division. 1971
- 2.- MOSME JAKUB. "Dynamic stiffness of foundations" M.I.T. Publication No. R77-36. 1977
- 3.- CHOPRA, CHAKRABARTI, DASGUPTA, "Dynamic stiffness Matrices for viscoelastic half-plane foundations", Journal of the engineering mechanics division. 1976
- 4.- CRUSE and RIZZO. "A direct formulation and numerical solution of the General Transient Elastodynamic Problem". Journal of Mathematical analysis and applications. 1968.
- 5.- LACHAT and WATSON. "Progress in the use of boundary integral equations". Computer methods in applied mechanics and engineering. 1977.

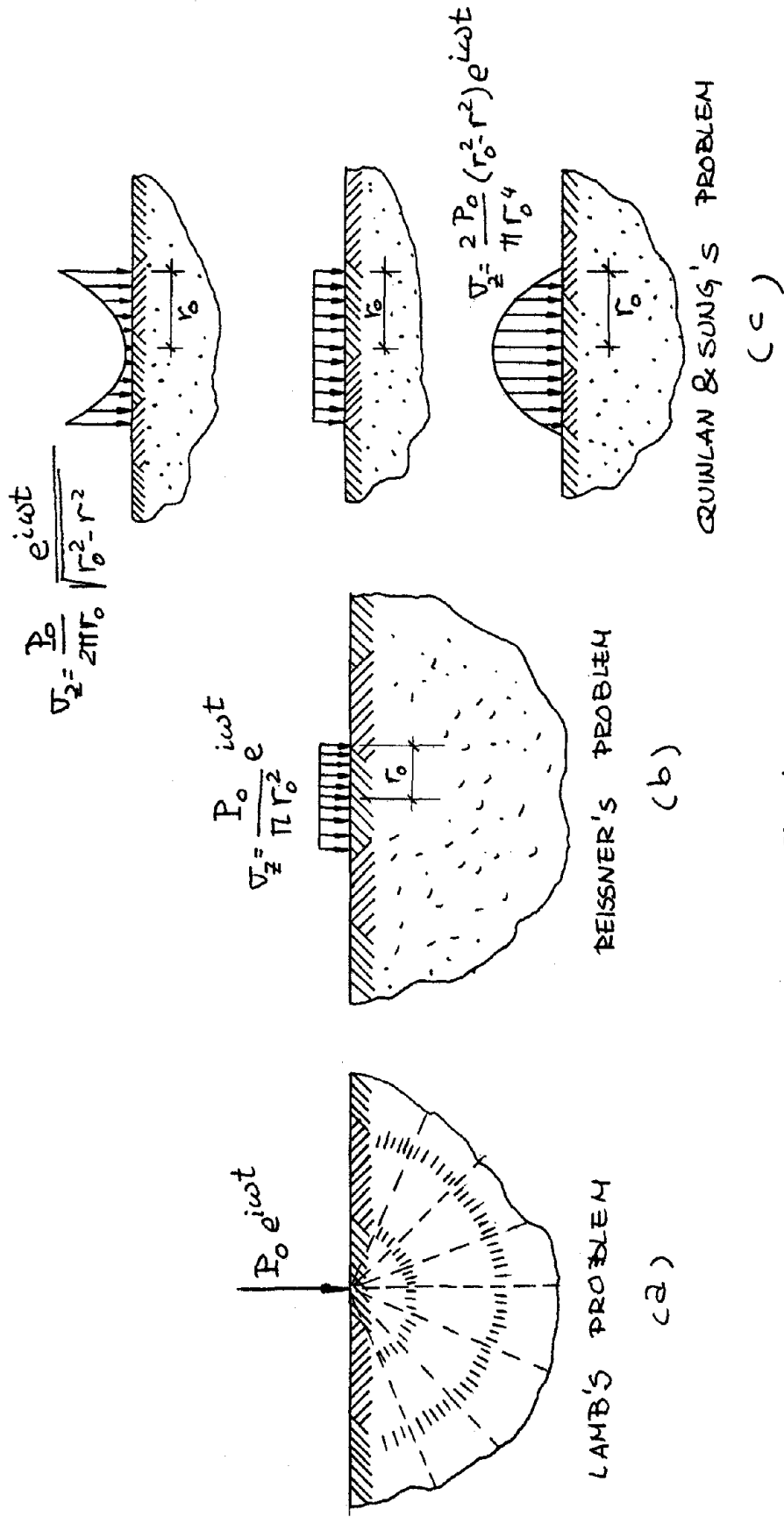
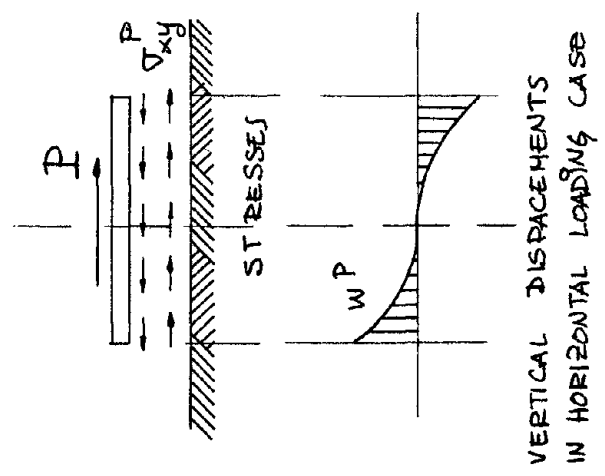
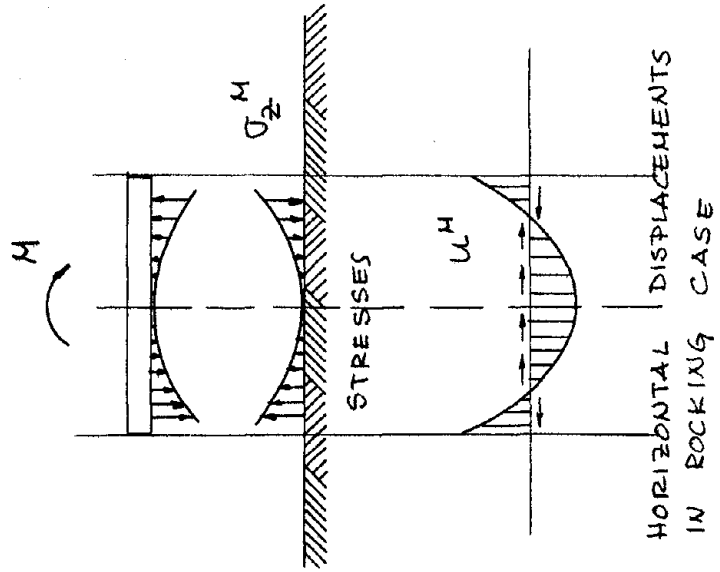
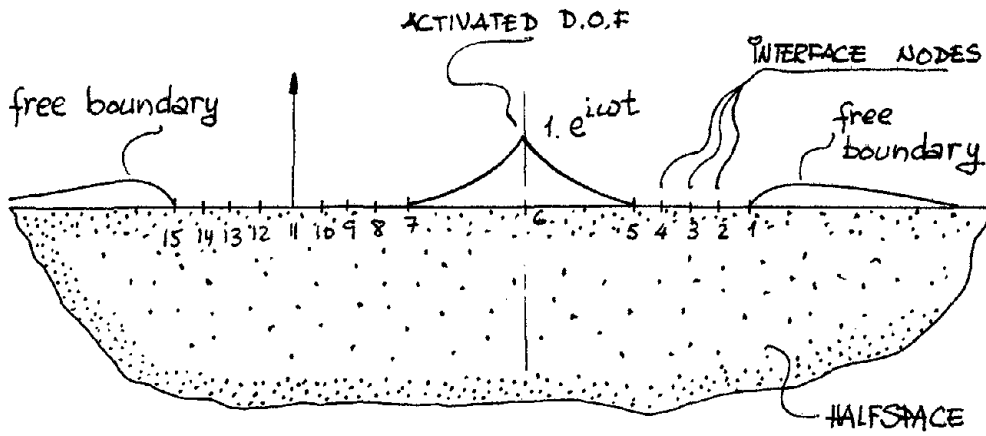


Fig. 1



VELETOS & WEI HYPOTHESIS

Fig. 2



BASIC PROBLEM IN THE FLEXIBLE FOOTING CASE.

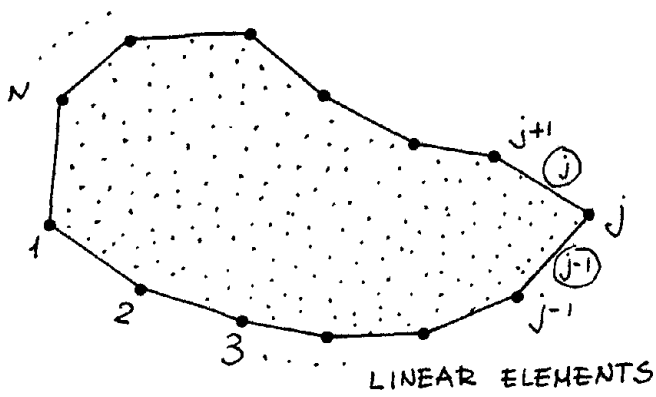
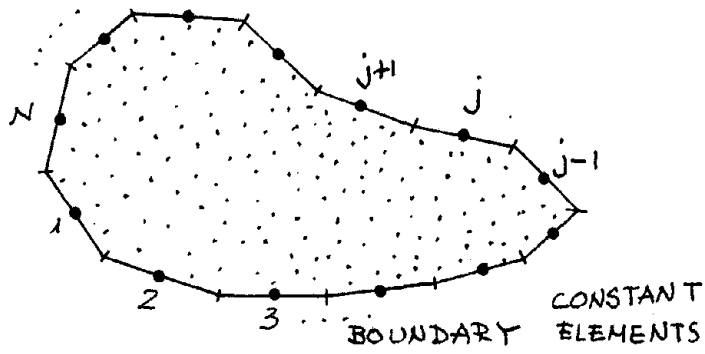
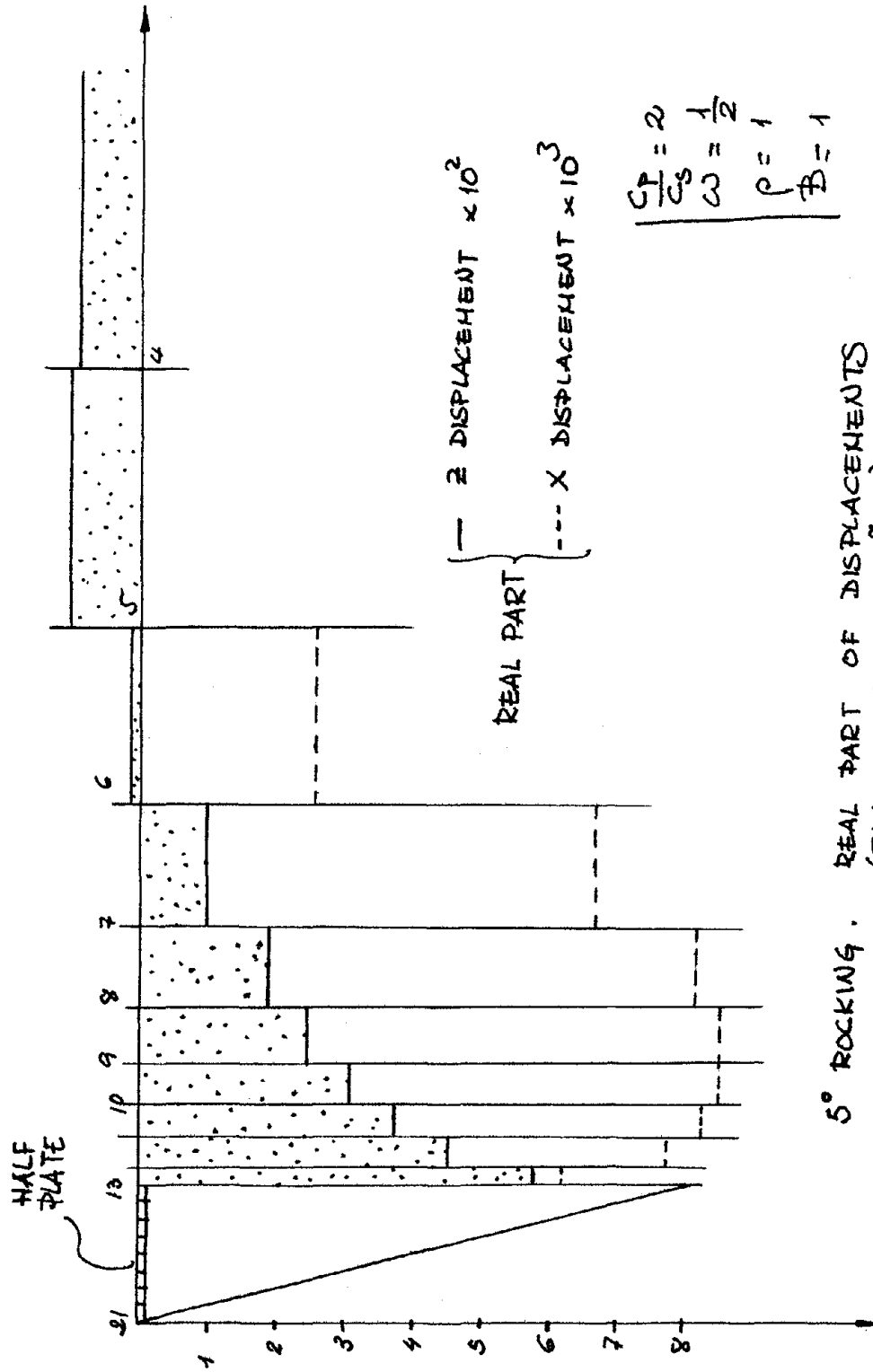


Fig. 3



5° ROCKING. REAL PART OF DISPLACEMENTS (FINER DISCRETIZATION)

Fig. 4

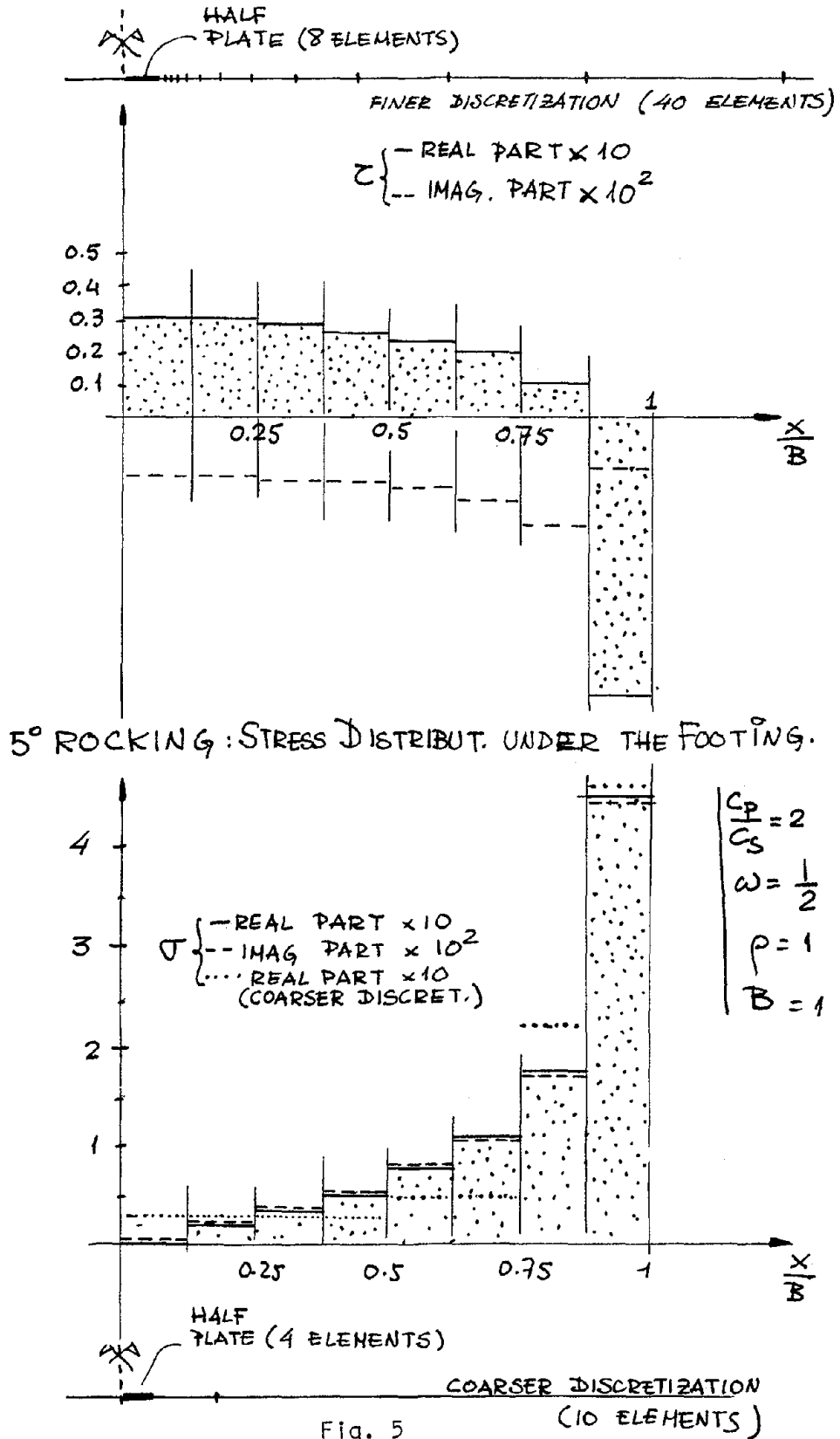


Fig. 5

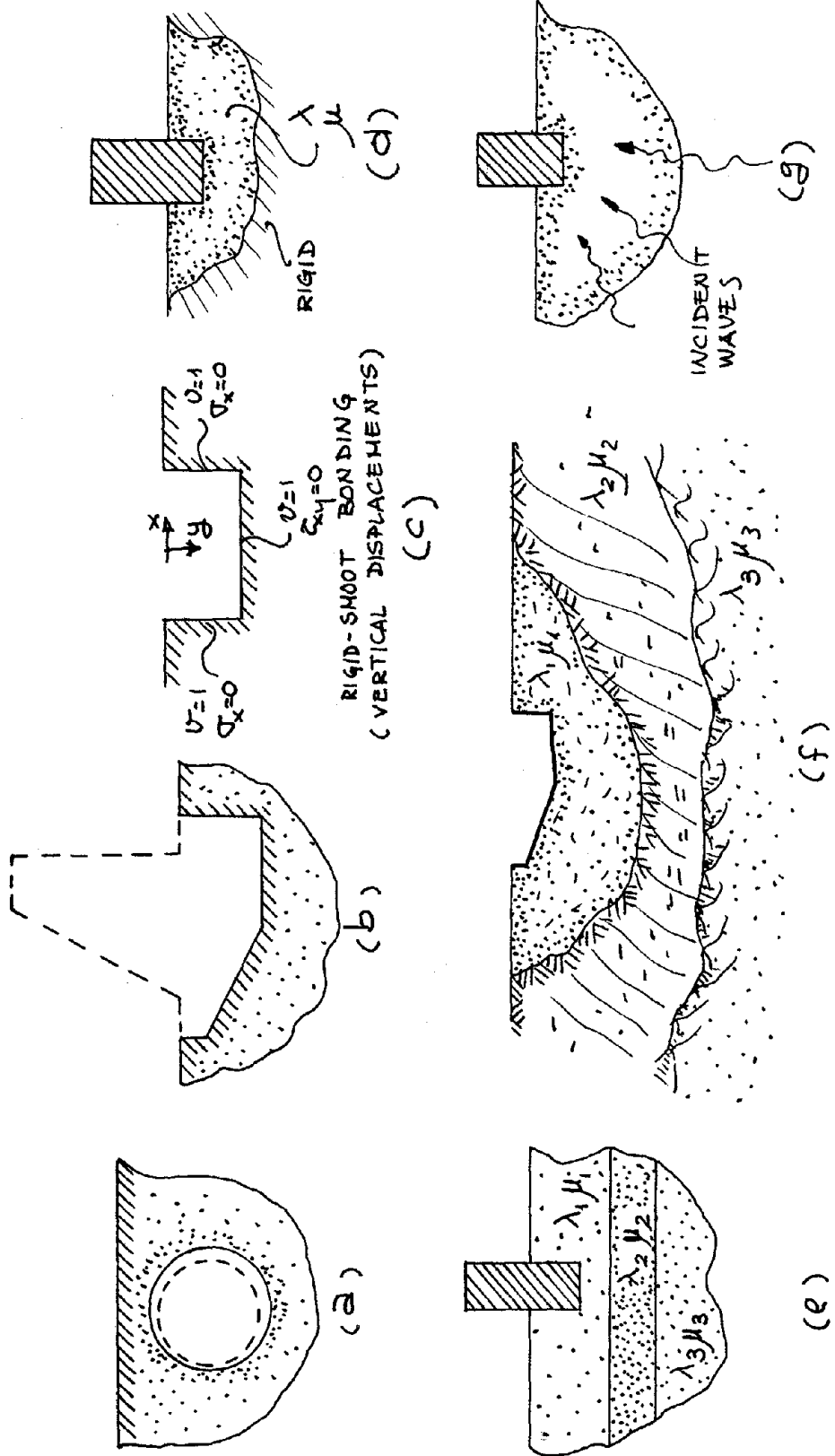


Fig. 6

SEISMIC SHEAR STRAIN INDUCED IN SOIL DEPOSITS

by

Yoshihiro SUGIMURA^I

Abstract

A method of estimating the seismic ground strain by using elastic wave propagation technique for strong motion data and some computed results from this technique are presented in this paper. One hundred and fourteen components in total of strong motion data recorded at 15 sites in California, of which soil condition is known, are used as analytical examples to determine the seismic shear strains in the ground. According to these results, the conclusions so far achieved can be expressed as the following two categories. (1) There exists a set of directions, the predominant and the lowest components perpendicular to each other, and the parallel and normal directions to the causative fault line correspond to such a coordinate system. (2) There exists some correlation between the maximum velocity response at the ground surface and the maximum shear strain in the soil deposits such as the form of $\gamma_{\max} = 0.00262V_{\max}$.

INTRODUCTION

It is generally known that local soil conditions at sites subjected to seismic shaking considerably affect damage to structures at the site. Hence, many analytical studies and laboratory tests have been performed to determine the dynamic characteristics of various types of soil deposits. It is important to consider "strain dependence" of soils, i.e., nonlinearity of shear modulus and damping ratio with shear strain which has been clarified mainly by laboratory tests [1, 2, 3, 4, 5, 6, 7]. A clue to the relationship between earthquake ground shaking and damage to structures may be found, therefore, if strains induced in the ground during earthquakes are evaluated and then compared with the results of laboratory tests. However, except for some geophysical and geotechnical surveys such as triangulation which are mostly in a static sense, no suitable instruments equivalent to strong motion accelerographs for ground acceleration have been developed to measure local seismic strain waves.

This paper presents some computed results of the shear strains induced in soil deposits during earthquakes by using elastic wave propagation technique for strong motion data. Some researchers including the writer already got the results of some examples by the similar method [8, 9, 10], but all of those are limited to only a few cases. It seems to be a worthwhile subject to investigate such data as many as possible and statistically, on which the purpose of this paper is concentrated.

SHEAR STRAIN IN SOIL DEPOSITS BY ELASTIC WAVE PROPAGATION THEORY

Let consider the multiple horizontal soil deposits and \dot{f}_i and \dot{g}_i as the upward and downward shear velocity waves, respectively, which propagate in

^I Head of Geotechnical Engineering Division, Structural Engineering Department, Building Research Institute, Ministry of Construction, Japan

each soil layer. The velocity response in each layer, then, can be expressed by the following equation.

$$\dot{u}_i(t, z_i) = \dot{f}_i(t - \frac{z_i}{V_i}) + \dot{g}_i(t + \frac{z_i}{V_i}) \quad (1)$$

in which,

- i = layer number from the ground surface
- t = time (sec)
- z_i = depth from each upper boundary with negative sign (m)
- V_i = shear wave velocity in each layer (m/sec)

At the ground surface ($z_1=0$), the upward and downward velocity waves become equally halves of the recorded velocity wave $\dot{u}_1(t,0)$, from the boundary condition, i.e., the shear stress is equal to zero, then,

$$\dot{f}_1(t,0) = \dot{g}_1(t,0) = \frac{1}{2} \dot{u}_1(t,0) \quad (2)$$

Therefore, the shear strain wave in the top layer can be expressed as following equation.

$$\gamma_1(t, z_1) = \frac{1}{V_1} [-\dot{f}_1(t - \frac{z_1}{V_1}) + \dot{g}_1(t + \frac{z_1}{V_1})] \quad (3)$$

From the second layer, each shear strain wave can be expressed in the same way as above by the equation,

$$\gamma_i(t, z_i) = \frac{1}{V_i} [-\dot{f}_i(t - \frac{z_i}{V_i}) + \dot{g}_i(t + \frac{z_i}{V_i})] \quad (4)$$

The first and second terms in the parenthesis of the right hand side of Eq. (4) are determined by using the upward and downward velocity waves at the each upper boundary as shown below, which satisfy the continuity condition related to displacements and shear stresses.

$$\dot{f}_i(t,0) = \frac{1}{2} [(1+\alpha_{i-1})\dot{f}_{i-1}(t - \frac{H_{i-1}}{V_{i-1}}) + (1-\alpha_{i-1})\dot{g}_{i-1}(t + \frac{H_{i-1}}{V_{i-1}})] \quad (5)$$

$$\dot{g}_i(t,0) = \frac{1}{2} [(1-\alpha_{i-1})\dot{f}_{i-1}(t - \frac{H_{i-1}}{V_{i-1}}) + (1+\alpha_{i-1})\dot{g}_{i-1}(t + \frac{H_{i-1}}{V_{i-1}})] \quad (6)$$

in which, H_i is the thickness of each layer (m) and α_i is the impedance ratio of wave propagation defined by the following equation.

$$\alpha_i = \frac{\rho_i V_i}{\rho_{i+1} V_{i+1}} \quad (7)$$

in which, ρ_i is the mass density of each layer.

There appears here one of the difficulties to use the elastic wave propagation theory. Parameters such as shear moduli of soils would not be constant during a destructive ground shaking, since soils are not elastic in general. If one changes, the other would also change because of the interdependence between elastic moduli and the amplitude of velocity, so that actual strains in soil deposits may not be determined, in a strict sense, directly and definitely from seismic records. But in spite of this difficulty, the application of the simple method mentioned above for estimation of strains appears to be, at present, the best available first approximation for engineering use.

EARTHQUAKE DATA AND GEOTECHNICAL DATA FROM THE SITES OF THE STATIONS

Twenty four earthquakes with some aftershocks and foreshocks are used as the analytical examples in this paper as listed in Table-1. And Table-2 shows the fifteen stations which are also selected for analytical purpose. It will result in fifty seven strong motion records in combination of the earthquakes and the stations as shown in these tables. All of these records were processed at the Earthquake Engineering Research Laboratory, California Institute of Technology and finally, the results were published as corrected accelerograms and integrated ground velocity and displacement curves [11]. Each number in parentheses in Table-1 and Table-2 is corresponding to the arrangement number of CIT. One hundred and fourteen horizontal components in total of these velocity curves are used as the original waves recorded at the ground surface of each station.

Geotechnical data from the sites of the stations were given by C. M. Duke and D. J. Leeds, 1962 [12]; W. R. Hansen et al., 1973 [13]; and the U. S. Department of the Interior, Geological Survey, 1976 [14]. Subsurface conditions of these sites from Duke and Leeds are shown in Table-3, and are used as basic in subsequent sections.

LOCATIONAL RELATION OF STATION, EPICENTER AND FAULT LINE

Locational relation of stations, epicenters and fault lines in southern California is shown in Fig. 1. Since earthquakes occur at random locations, the direction of each component of a seismograph at a station does not ordinarily coincide with the direction to the focus. Therefore, initially original records should be decomposed into the available coordinate system under consideration. The combination of longitudinal and tranverse direction to the epicenter, or normal and parallel direction to the causative fault line can be a typical example of such a coordinate system. The effect of the depth of the focus is neglected in this paper because each case shown in Table-1 is a comparatively shallow earthquake.

In addition to the nonlinearity of soil modulus during ground shaking, it will be necessary to examine what kind of wave is contained within the recorded data. This judgement was made hereon mainly by drawing the particle orbits of the recorded waves compared with various conditions such as the direction of causative fault break, the distance and the locational relation between each station and the fault line or the epicenter. And it was clarified through this process that the large shaking component is induced along the direction of the causative fault line rather than any other directions, especially for the cases shown as follows:

Earthquake	Causative Fault	Station
Imperial Valley 1940	Imperial Fault	El Centro
Kern County 1952	White Wolf Fault	Taft
Long Beach 1933	Newport-Inglewood Fault	Long Beach
Parkfield 1966	San Andreas Fault	San Luis Obispo

It will be reasonable at least for these examples, to assume the data decomposed into the corresponding directions as the shear waves and to apply Eq. (3) and Eq. (4) to them. An analytical example is shown in the next section for the case of Imperial Valley earthquake in 1940 recorded at El Centro site.

EXAMPLE OF IMPERIAL VALLEY EARTHQUAKE IN 1940 RECORDED AT EL CENTRO SITE

The Imperial Valley earthquake in 1940 has the following two distinctive features. (1) The causative fault line is nearly straight and its movement is horizontally right-lateral. (2) The observation station is located at the very short right angle distance (about 6 Km) from the causative fault line as shown in Fig. 1.

Figure 2 shows the horizontal particle orbits in every 5 sec. of velocity response recorded at El Centro site. The up-down component is neglected in this figure, because it is quite small compared with horizontal movements. The original components of seismograph are shown by the signs NS ($S00^{\circ}E$) and EW ($S90^{\circ}W$), respectively. The signs LO and TR indicate the components of longitudinal ($S53.4^{\circ}E$) and transverse direction ($S36.6^{\circ}W$) to the epicenter, and the signs NO and PA indicate the components of normal ($N53^{\circ}E$) and parallel direction ($S37^{\circ}E$) to the causative fault line. Figure 3 shows the velocity waves decomposed into the corresponding directions as well as the original ones. It is clarified from these figures that the largest ground motion would occur in the direction parallel to the causative fault line, especially in the initial 5 or 10 seconds. This fact suggests the possibility of the existence of the principal axes of seismic ground motion, the major of which agrees with the parallel direction to the causative fault line.

Time histories of the seismic shear strains at every one tenth depth of the top layer are shown in Fig. 4 and Fig. 5 for the cases NO and PA, respectively. These figures lead to the followings: (1) The shear strains always become zero at the ground surface as might be suspected from the relation of Eq. (3). (2) The maximum values of shear strain are 0.151 (%) for the case NO and 0.129 (%) for the case PA, both of which occur at the vicinity of the lower boundary of the top layer by the effect of impedance ratio between the top and the second soil layers. It can be estimated that the soils in the top layer at this site got into the nonlinear state to a certain extent because the shear strain grows up more than 0.1 (%), around which the reduction of shear moduli of soils is pointed out to be conspicuous from many laboratory soil tests.

RELATION BETWEEN THE MAXIMUM VELOCITY AND THE MAXIMUM SHEAR STRAIN

In the same way as above, shear strains in soil deposits were computed for the each site condition of the station shown in Table-3 by using the corresponding strong motion data. Those results are shown in Fig. 6a to Fig. 6c as the relation between the maximum velocity at the ground surface and the maximum shear strain in the soil deposits. The results shown here include, however, the cases in which original recorded data are simply applied to Eq. (3) and Eq. (4), because it doesn't always follow that the condition such as the direction of the causative fault line and the locational relation between the station and the epicenter is clear.

Although it is necessary to treat these results as the first approximation of seismic shear strains induced in the ground, these figures suggest the fact that there exists the correlation between the maximum velocity amplitude at the ground surface and the maximum shear strain induced in soil deposits. The first order linear function by the least square approximation is given for each case as follows.

For the case of 25 earthquakes recorded at El Centro site (No. 117),

$$\gamma_{\max} = 0.00378V_{\max}, \quad \sigma = 0.00105 \quad (8)$$

For the case of 3 earthquakes recorded at Taft site (No. 1095),

$$\gamma_{\max} = 0.00320V_{\max}, \quad \sigma = 0.00130 \quad (9)$$

For the case of 57 earthquakes recorded at all of the stations,

$$\gamma_{\max} = 0.00262V_{\max}, \quad \sigma = 0.00115 \quad (10)$$

in which,

γ_{\max} = the maximum shear strain induced in soil deposits (%)

V_{\max} = the maximum velocity at the ground surface (kine)

σ = standard deviation (%)

The coefficients of above equations are slightly changed to each other, i.e., it appears the effect of soil condition of each site — the softer soil condition is, the greater coefficient grows. Furthermore, it seems to be possible the classification of the relation between earthquake intensity and the ground behavior. And for instance, if the soil behavior can be classified from the dynamic laboratory soil tests into three different ranges, such as elastic, medium and plastic states, around the boundaries of the maximum shear strains 3×10^{-2} (%) and 1×10^{-1} (%), the values 10 and 30 kine in average will be corresponding to the boundaries of the ground shaking, respectively.

CONCLUSIONS

The conclusions achieved in this paper can be divided into the following two categories.

(1) The maximum value of the ground motion at a site changes corresponding to the difference of direction under consideration. There exists a set of directions, the predominant and the lowest components perpendicular to each other, which form the principal axes when considered as the coordinate system for the strong motion data. The parallel and normal directions to the causative fault line correspond to such a coordinate system.

(2) There exists some correlation between the maximum velocity amplitude at the ground surface and the maximum shear strain in the soil deposits. The coefficients of linear equation approximated by the least square method are 0.00378 and 0.00320 for the cases of El Centro site and Taft site, respectively. And for the case of all stations, that becomes 0.00262. Though the coefficient changes slightly by the effect of soil condition at sites, the classification is possible, on the whole, for the relation between soil behavior and intensity of ground shaking. And for instance, if the soil behavior is classified into three different ranges, i.e., elastic, medium and plastic states, around the boundaries of the maximum shear strains such as the values of 3×10^{-2} (%) and 1×10^{-1} (%), the values about 10 and 30 kine will be corresponding to the boundaries of the ground shaking, respectively.

REFERENCES

1. Y. Ohsaki, "The Effects of Local Soil Conditions upon Earthquake Damage," Soil Dynamics, Proc. of Specialty Session 2, 7th ICSMFE, Mexico, 1969.
2. H. B. Seed, "The Influence of Local Soil Conditions on Earthquake Damage," Soil Dynamics, Proc. of Specialty Session 2, 7th ICSMFE, Mexico, 1969.
3. B. O. Hardin and V. P. Drnevich, "Shear Modulus and Damping in Soils, I - Measurement and Parameter Effects," Technical Report UKY 26-70-CE2, University of Kentucky, 1970.
4. B. O. Hardin and V. P. Drnevich, "Shear Modulus and Damping in Soils, II - Design Equations and Curves," Technical Report UKY 27-70-CE3, University of Kentucky, 1970.
5. F. E. Richart, Jr., J. R. Hall, Jr. and R. D. Woods, "Vibrations of Soils and Foundations," Prentice-Hall, 1970.
6. H. B. Seed and I. M. Idriss, "Soil Moduli and Damping Factors for Dynamic Response Analyses," EERC 70-10, University of California, Berkeley, 1970.
7. Y. Yoshimi, F. E. Richart, Jr., S. Prakash, D. D. Barkan and V. A. Ilyichev, "Soil Dynamics and Its Application to Foundation Engineering," State-of-the-Art Reports, Main Session 4, 9th ICSMFE, Tokyo, 1977.
8. K. Toki, "Strain Level of the Ground Estimated from Strong Motion Records (in Japanese)," Proc. of 2nd Symposium of Seismic Ground Motion, The Architectural Institute of Japan, 1973.
9. M. Kohyama, "On Stress and Strain in the Ground during Earthquakes (in Japanese)," Proc. of 9th Research Meeting of Japanese Society of Soil Mechanics and Foundation Engineering, 1974.
10. Y. Sugimura, "Seismic Strain Induced in the Ground during Earthquakes," UCB/EERC - 77/14, University of California, Berkeley, 1977.
11. California Institute of Technology, Earthquake Engineering Research Laboratory, "Strong Motion Earthquake Accelerograms, Digitized and Plotted Data," Volume II - Corrected Accelerograms and Integrated Ground Velocity and Displacement Curves, Part A, EERL 71-50, California Institute of Technology, Pasadena, 1971 and so on.
12. C. M. Duke and D. J. Leeds, "Site Characteristics of Southern California Strong-Motion Earthquake Stations," Report No. 62-55, Department of Engineering, University of California, Los Angeles, 1962.
13. W. R. Hansen, R. B. Weiss, I. M. Idriss and L. S. Cluff, "Geotechnical Data Compilations for Selected Strong-Motion Seismograph Sites in California," prepared for National Oceanic and Atmospheric Administration, Woodward-Lundgren & Associates, Consulting Engineers and Geologists, Oakland, 1973.
14. United States Department of the Interior Geological Survey, "Strong-Motion Accelerograph Station List-1975," Open File Report No. 76-79, 1976.

Table- 1 List of Earthquakes

	Date & Time(PST)	Location	Lat. N	Long. W	Int.	Mag.	Station No. & CIT No.
1	Mar 10 1933 1754	Long Beach	33 35	117 59	IX	6.3	131(V315) 136(V314) 288(B021)
2	Oct 2 1933 0110	Southern California	33 47	118 08	VI	5.4	133(B023)
3	Dec 30 1934 0552	Lower California	32 12	115 30	IX	6.5	117(B024)
4	Apr 12 1938 0825	Imperial Valley	32 54	115 35	-	3.0	117(T274)
5	Jun 5 1938 1842	Imperial Valley	32 54	115 13	-	5.0	117(T275)
6	Jun 6 1938 0437	Imperial Valley	32 15	115 10	-	4.0	117(T276)
7	May 18 1940 2037	Imperial Valley and Aftershocks	32 44	115 27	X	7.1	117(A001, T277-T285)
8	Jun 30 1941 2351	Santa Barbara	34 22	119 35	VIII	5.9	283(U299)
9	Nov 14 1941 0042	Torrance-Gardena	33 47	118 15	VII	5.4	131(V316)
10	Oct 21 1942 0822	Borrego Valley	32 58	116 00	VII	6.5	117(T286)
11	Jan 23 1951 2317	Imperial Valley	32 59	115 44	VII	5.6	117(T287)
12	Jul 21 1952 0453	Kern County	35 00	119 02	XI	7.7	133(A006) 283(A005) 475(A003) 1095(A004)
13	Nov 21 1952 2346	Southern California	35 50	119 01	XI	7.7	1083(V319)
14	Jun 13 1953 2017	Imperial Valley	32 43	115 43	VII	5.5	117(T288)
15	Jan 12 1954 1534	Wheeler Ridge	35 00	119 01	VIII	5.9	1095(B031)
16	Nov 12 1954 0427	Lower California	31 30	116 00	V	6.3	117(T289)
17	Dec 16 1955 2207	Imperial County and Foreshocks	33 00	115 30	-	5.4	117(T290-T292)
18	Feb 9 1956 0633	Baja California and Aftershock	31 45	115 55	VI	6.8	117(A011, A012)
19	Mar 18 1957 1056	Southern California	34 07 06	119 13 12	VI	4.7	272(V329)
20	Jun 27 1966 2026	Parkfield	35 54	120 54	VII	5.6	1083(B038) 1095(U311)
21	Aug 7 1966 0936	Gulf of California	31 48	114 30	VI	6.3	117(T293)
22	Apr 8 1968 1830	Borrego Mountain	33 11 24	116 07 42	VII	6.4	113(Y370) 117(A019) 130(Y372) 133(Y380)
23	Sep 12 1970 0630	Lytle Creek	34 16 12	117 32 24	VII	5.4	136(Y378) 288(Y379) 310(Y377)
24	Feb 9 1971 0600	San Fernando	34 24 00	118 23 42	XI	6.4	113(W339)
							113(F101) 131(O204) 133(D057, D058)
							266(G106) 272(P222) 288(F086)
							475(G107, G108) 2002(O213)

Table- 2 List of Stations

Station	Lat. N	Long. W	Earthquake No. & CIT No.
1	34 03 34	117 18 45	22(Y370) 23(W339) 24(F101)
2	32 47 43	115 32 55	3(B024) 4(T274) 5(T275) 6(T276) 7(A001,T277-T285) 10(T286) 11(T287) 14(T288) 16(T289) 17(T290-T292)
3	33 45 53	118 13 30	18(A011,A012) 21(T293) 22(A019)
4	33 46 11	118 11 35	22(Y372)
5	34 05 00	118 20 00	1(V315) 9(V316) 24(O204)
6	34 03 00	118 15 00	2(B023) 12(A006) 22(Y380) 24(D057,D058)
7	34 08 55	118 10 15	1(V314) 22(Y378)
8	34 09 00	119 12 00	24(G106)
9	34 25 28	119 42 05	19(V329) 24(P222)
10	34 00 00	118 12 00	12(A005) 8(U299)
11	34 03 00	118 15 00	1(B021) 22(Y379) 24(F086)
12	34 08 20	118 07 17	22(Y377)
13	35 17 00	120 40 00	12(A003) 24(G107,G108)
14	35 09 00	119 27 00	20(B038) 13(V319)
15	36 01 00	114 44 00	12(A004) 15(B031) 20(U311)
			24(O213)

Station	130			131			133			136			283		
	z	Y	Vs	z	Y	Vs	z	Y	Vs	z	Y	Vs	z	Y	Vs
1	30.5	2.05	159.2	1.5	1.52	146.1	3.0	1.71	127.2	4.6	1.76	136.0	9.1	1.92	224.8
2	335.5	2.23	857.0	76.2	2.08	180.2	21.3	2.08	214.4	61.0	1.92	329.1	122.0	2.05	437.3
3	1250.4	2.23	1104.0	228.7	2.19	249.8	152.5	2.08	365.7	228.7	2.16	731.6	609.9	2.19	1073.2
4	2317.8	2.35	1235.1	1524.9	2.19	819.5	701.4	2.19	804.8	686.2	2.19	951.2	1524.9	2.37	1194.0
5	3385.2	2.35	2195.8	2592.3	2.37	1126.9	2531.3	2.32	1317.2	2211.1	2.37	1244.0	2439.8	2.32	1492.8
6	-	2.76	3049.7	-	2.72	2883.2	-	2.72	2883.2	-	2.66	2829.9	-	2.66	2976.2
288				310			272			475			1095		
1	12.2	1.76	120.8	9.1	1.92	224.8	1.5	1.52	123.2	3.0	1.76	133.9	12.2	2.24	163.2
2	30.5	1.84	756.3	122.0	2.05	374.8	14.9	1.76	358.0	45.7	1.92	355.3	61.0	2.31	731.6
3	579.5	2.19	1155.9	609.9	2.19	1073.2	30.5	1.92	750.5	106.7	2.00	808.2	213.5	2.31	951.2
4	1585.9	2.19	1598.1	1524.9	2.37	1194.0	1219.9	2.24	1125.0	411.7	2.10	1074.7	1219.9	2.37	1170.8
5	2592.3	2.37	2287.3	2439.8	2.32	1492.8	-	2.44	1803.9	-	2.76	3348.3	-	2.72	2883.2
6	-	2.66	3049.7	-	2.66	2976.2	-	2.66	2976.2	-	2.66	2976.2	-	2.66	2976.2
1083				2002			266								
1	1.5	1.81	312.3	122.0	2.60	490.7	18.3	2.76	985.7						
2	6.4	2.16	526.7	183.0	2.64	841.4	-	2.76	3348.3						
3	24.4	2.40	792.6	-	2.90	1317.2									
4	-	2.80	2424.2												

z: depth (m)
 Y: unit weight (t/m³)
 Vs: shear wave velocity (m/sec)

Table- 3 Soil Condition at Each Station Site After Duke & Leeds(1962)

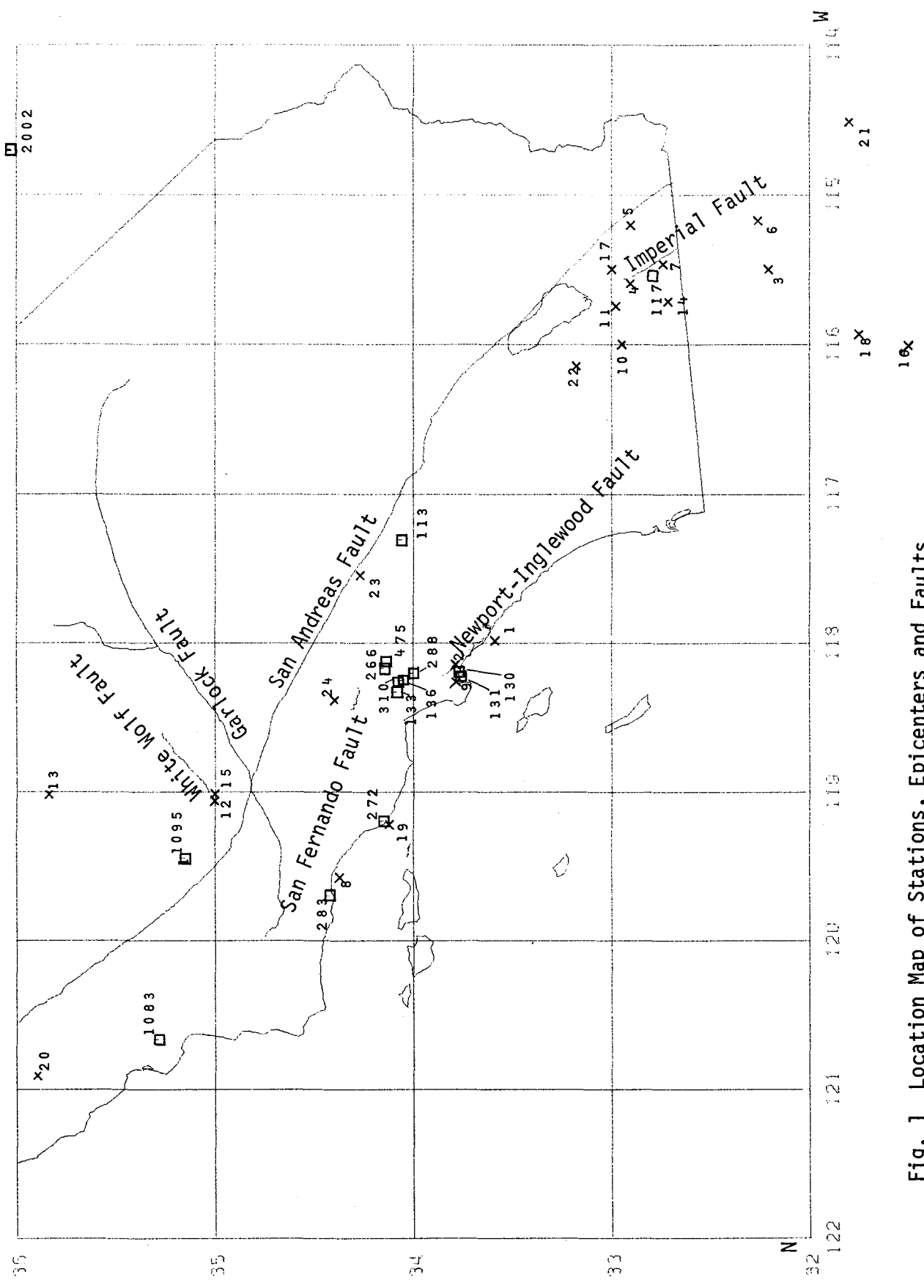


Fig. 1 Location Map of Stations, Epicenters and Faults

IIA001
 IMPERIAL VALLEY EARTHQUAKE MAY 18, 1940
 EL CENTRO SITE IMPERIAL VALLEY IRRIGATION DISTRICT
 RADIUS= 50.0 KINE

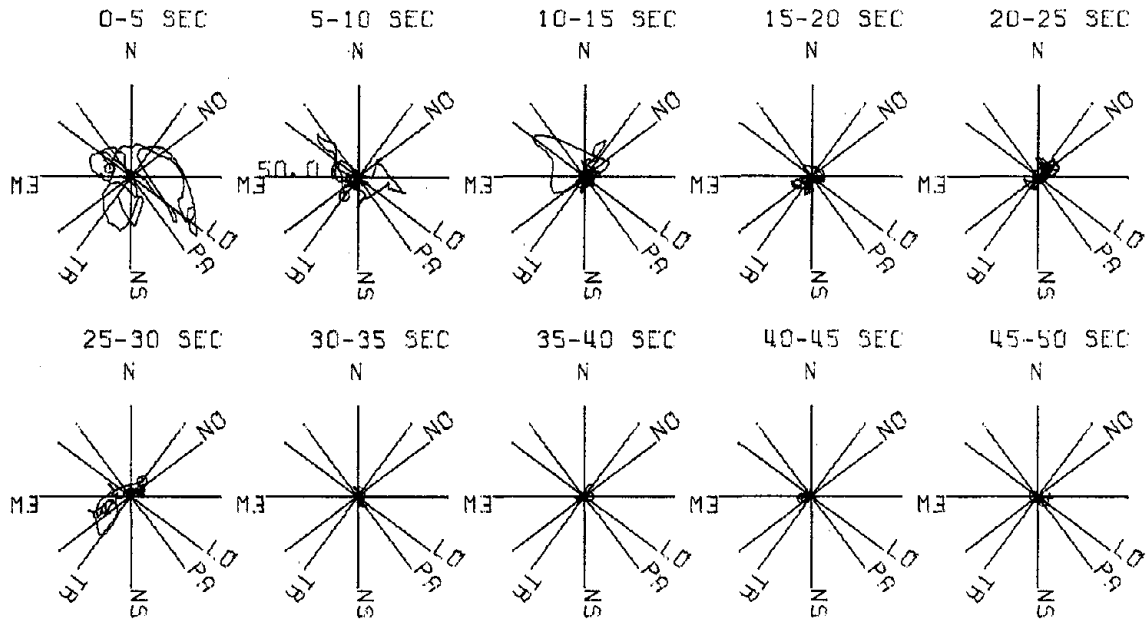


Fig. 2 Particle Orbits of Velocity Response at El Centro Site (Imperial Valley Earthquake 1940)

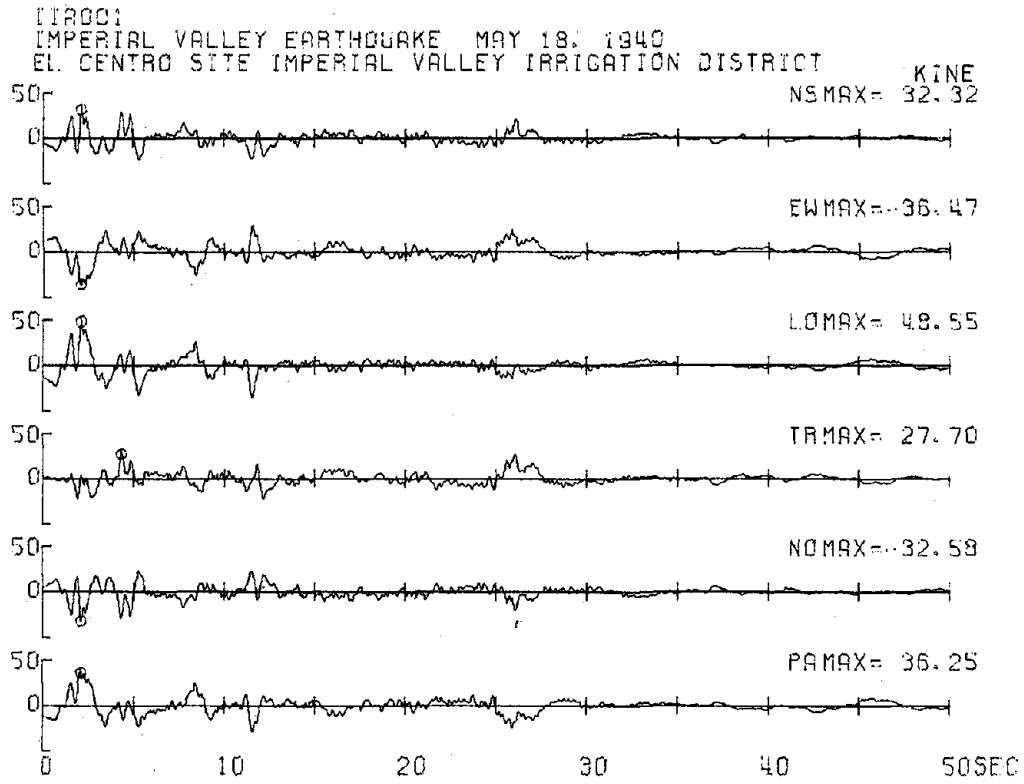


Fig. 3 Velocity Wave in Each Direction at El Centro Site (Imperial Valley Earthquake 1940)

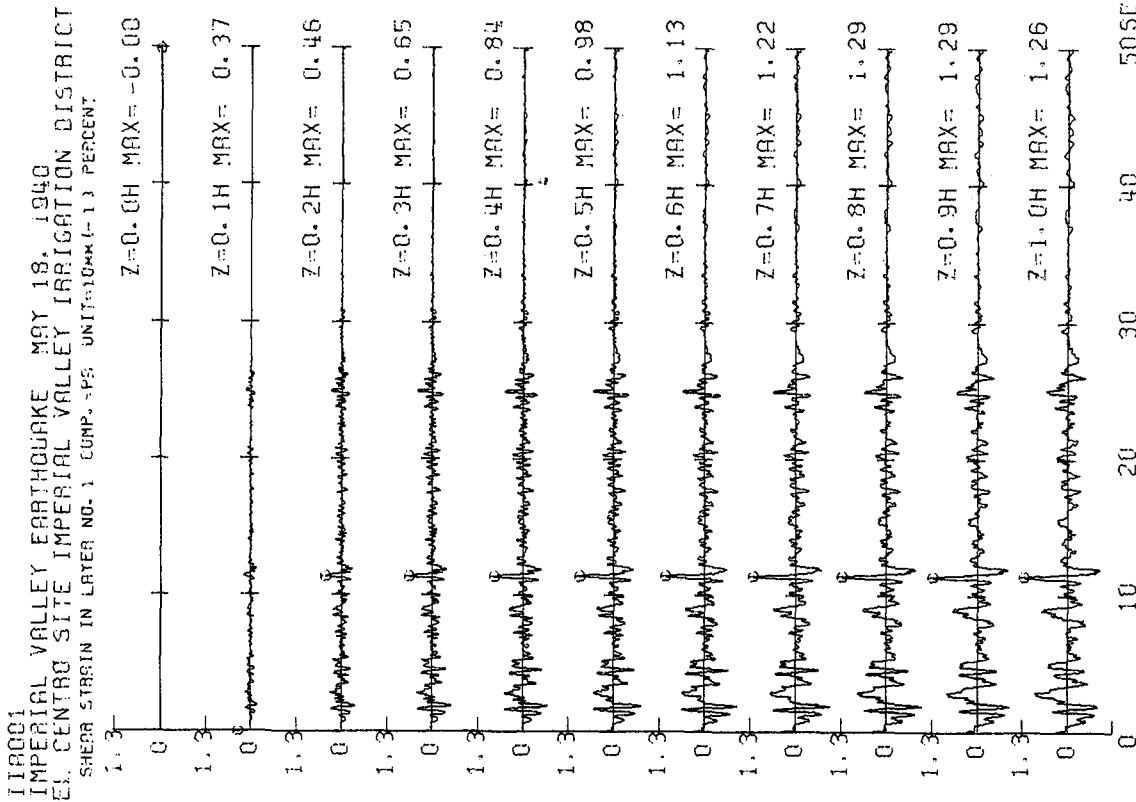


Fig. 5 Seismic Shear Strain PA Component in Top Layer at El Centro Site (Imperial Valley Earthquake 1940)

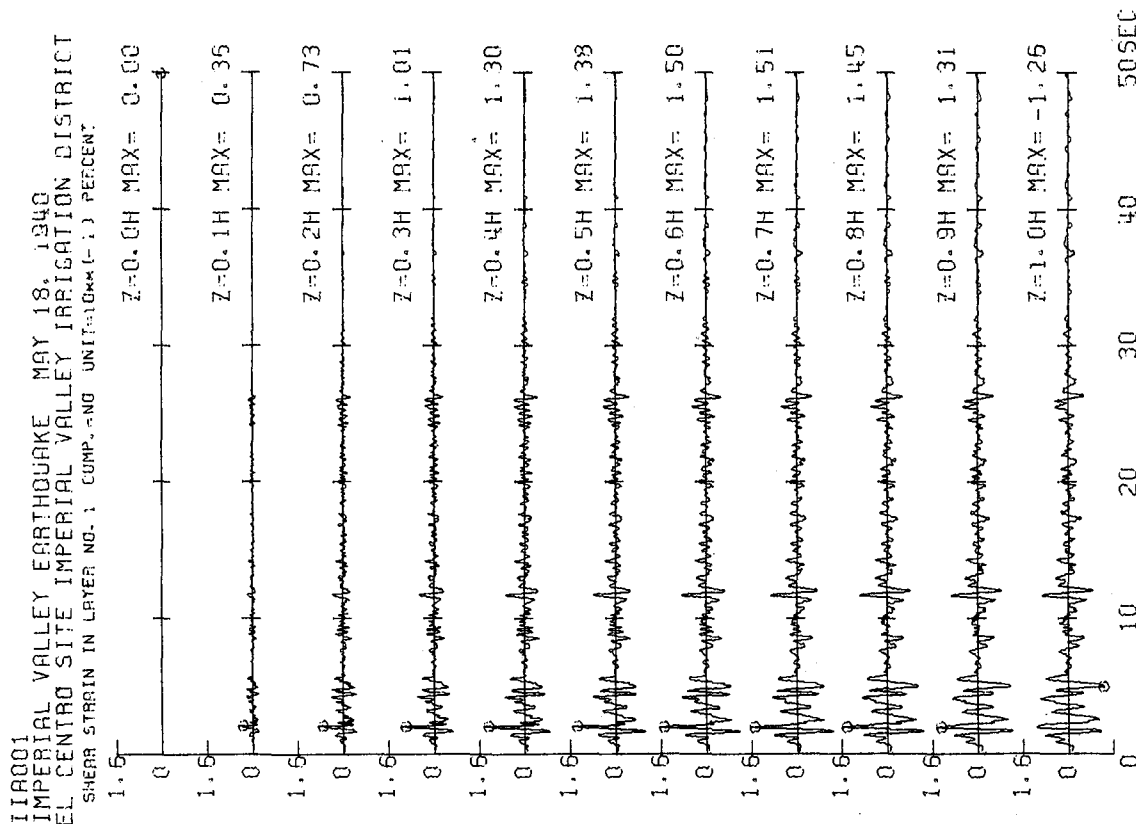


Fig. 4 Seismic Shear Strain NO Component in Top Layer at El Centro Site (Imperial Valley Earthquake 1940)

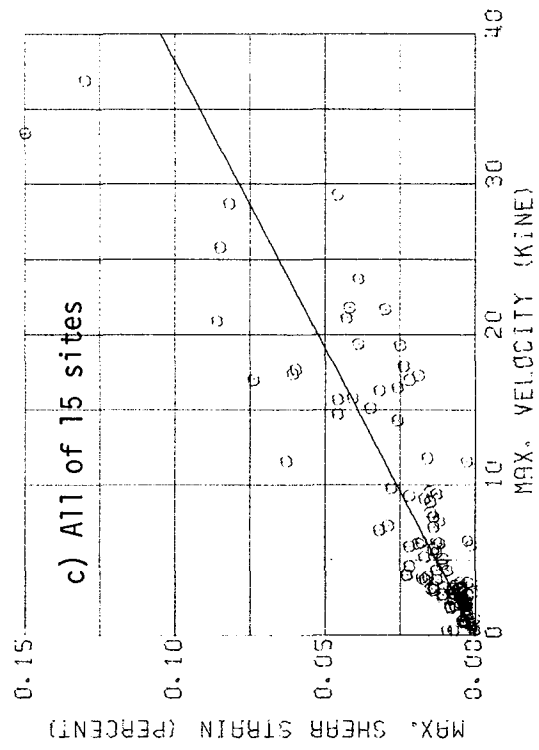
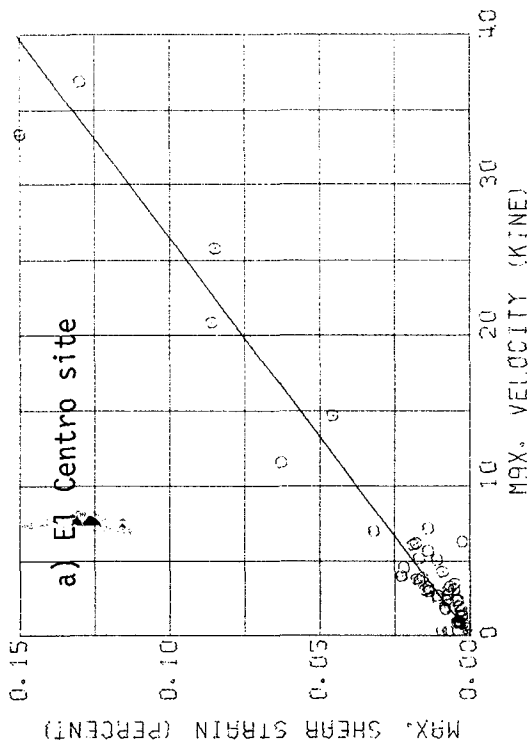
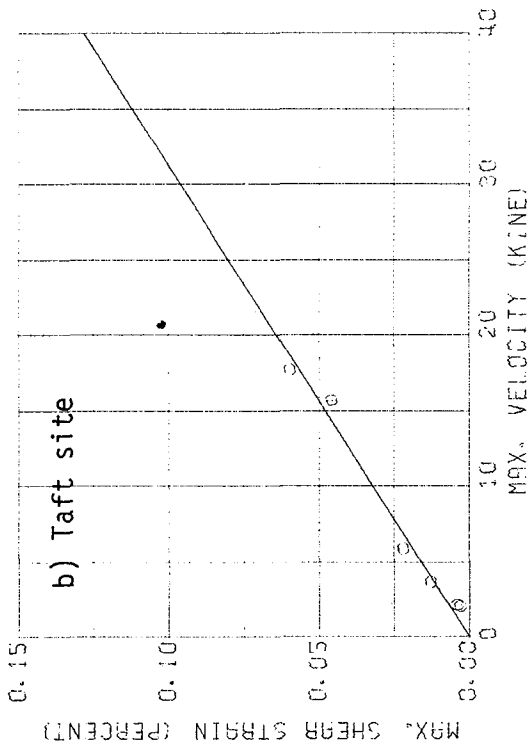


Fig. 6 Relation between The Maximum Shear Strain and The Maximum Velocity Response

POST CYCLIC LOADING BEHAVIOR OF SOFT CLAYS

by

R.D. Singh^I, W.S. Gardner^{II} and R. Dobry^{III}

ABSTRACT

The load-deformation behavior of soft silty clay has been investigated with specific reference to the change in undrained static shear strength and stress-strain behavior induced by prior undrained cyclic loading. Both controlled-strain triaxial compression and direct simple shear tests were employed in the laboratory testing program as well as procedures to mitigate the effects of sample disturbance. Static loading to failure was conducted after cyclic loading subsequent to a pore water pressure equalization period. Experimental results suggest that the effect of cyclic loading is to induce a partial remolding of soil structure which is represented by the amount of excess pore pressure existing after cyclic loading. Both stress-strain and shear strength characteristics were found to be affected by cyclic loading, the effect on the stress-strain relationship being the more significant.

In general, the observed post-cyclic loading behavior was found to be consistent with the findings of Castro and Christian (1976), Gardner (1977) and Koutsoftas (1978). The concept of describing the behavior of cyclically loaded overconsolidated clays suggested by Gardner and Koutsoftas is developed into a formal model and its validity is assessed. The model is an extension of the Normalized Soil Parameter (NSP) characterization method proposed by Ladd and Foott (1974). It is proposed that the model be used to predict post-cyclic stress-strain behavior as well as undrained strength after either steady state or transient cyclic loading.

INTRODUCTION

As an outgrowth of worldwide economic development, an increasing number of major structures are being constructed in both marine and terrestrial environments which are subject to significant seismic disturbances and/or storm waves. The stability of soft clay deposits often found in the marine environment is an important consideration in the design of these structures. Of particular interest to the designer is the change in soil properties such as strength and stiffness. It has been demonstrated that the effect of undrained cyclic loading on soft clays is to cause a stiffness degradation (Idriss, et al. 1978), excess

-
- I Senior Project Engineer, Woodward-Clyde Consultants, Plymouth Meeting, Pennsylvania
- II Principal Engineer, Woodward-Clyde Consultants, Plymouth Meeting, Pennsylvania
- III Associate Professor of Civil Engineering, Rensselaer Polytechnic Institute, Troy, New York.
-

pore pressure and a decrease in the pre-cyclic undrained shear strength (Thiers and Seed, 1969).

The excessive deformation and loss of strength which may be realized after cyclic loading of soft clays can significantly increase the risk of failure of slopes and structures upon subsequent environmental loading. The potential for such failures was recognized by Seed and Chan (1966). A survey of research work in this area has been presented by Lee and Focht (1976). The strength reduction due to cyclic loading has been studied by Thiers and Seed (1969); and more recently by Castro and Christian (1976), Gardner (1977) and Koutsoftas (1978).

Specific objectives of this study are to further explore the utility of applying the NSP technique of soil property characterization to post-cyclic soil behavior; to investigate the effects of stress history on residual pore water pressure; and to assess the effect of the cyclic loading technique on the post-cyclic load-deformation behavior of soft silty clays. A post-cyclic loading soil behavior model is described which incorporates stress history, residual pore water pressure and pre-cyclic undrained strength parameters. These parameters are normalized with respect to both the pre-cyclic and post-cyclic effective consolidation pressures.

EXPERIMENTAL PROGRAM AND RESULTS

The soft clay tested is a geologically recent (Holocene) cohesive marine sediment. The dominant clay mineral of the clay is illite (about 50 percent); salinity is 29 to 31 ppm and the sensitivity usually ranges between 4 and 8. The overconsolidation ratio (OCR) of the clays was assessed to be 1.5 with remarkably little variations. Representative physical and index properties of the clay tested are:

Natural water content (%)	= 37 to 48
Total unit weight (t/m^3)	= 1.78 to 1.90
Specific Gravity	= 2.76 to 2.79
Liquid Limit (%)	= 33 to 40
Plastic Limit (%)	= 18 to 20

Three inch O.D. samples recovered by gravity sampling in water depths of about 300 feet were consolidated prior to testing under pressure at least 1.5 times greater than the estimated maximum past consolidation pressure to mitigate the effects of sampling disturbance. Subsequently, the test samples were unloaded to produce specimens of known OCR. Selected samples were then subjected to 10 or 100 load cycles at various constant strain amplitude. Both triaxial compression and constant volume direct simple shear cyclic loading modes were utilized. After cyclic loading the cell pressure was maintained without drainage to allow an over-night equalization of pore pressure. Failure was induced by monotonic (static) loading without drainage at a rate of 3 percent per hour (triaxial) or 6 percent per hour (simple shear). For comparative purposes, companion specimens were tested to failure without imposition of cyclic loading.

PRE-CYCLIC BEHAVIOR

Three typical normalized stress paths representing pre-cyclic

consolidated-undrained triaxial tests are presented in Figure 1. In each of these tests, the sample was first isotropically consolidated to the maximum consolidation pressure ($\bar{\sigma}_{cm}$) and then was unloaded to the consolidation pressure ($\bar{\sigma}_c$). The three stress paths, normalized with respect to $\bar{\sigma}_{cm}$ are for OCR's of 1, 2 and 4, corresponding to the curve abscissa points 1.0, 0.50 and 0.25. After unloading, each sample was monotonically loaded in undrained condition to failure. Figure 2(a) presents the three corresponding normalized stress strain curves for these tests. The shapes of the normalized stress paths and stress strain curves are shown to be consistent with the reported normalized stress-strain behavior of clays not subject to significant structural alterations under elevated consolidated stress (Ladd, 1964).

POST CYCLIC BEHAVIOR

Subsequent to cyclic loading and after stabilization of excess pore pressures, static triaxial tests were performed on three companion samples. For each of these tests, the pore pressure was measured at the beginning and during the tests. All cyclically loaded samples had initial OCR's of 1 or 4 prior to cyclic loading.

The stress paths of the post-cyclic samples have been superimposed on Figure 1 for comparison with the stress paths of the pre-cyclic tests. For the post-cyclic tests, the starting point of the stress path corresponds to effective post-cyclic consolidation pressure normalized with respect to the maximum past consolidation pressure expressed as the quantity ($\bar{\sigma}_c - \Delta u / \bar{\sigma}_{cm}$). From Figure 1 it is evident that the post-cyclic paths are shifted by the amount of the excess pore pressure but that the shape of the curves is very similar. This observation clearly suggests that the shape of the stress path is a function of the initial pre-shear stress state.

Figure 3, demonstrates that the influence of residual excess pore pressure on the shape of the stress-strain curves is to cause an S shape effect at small axial strains as well as a reduction in the maximum deviator stress. However, the shape effect induced by cyclic triaxial tests appears to be significant only when $\bar{\sigma}_{cm} / (\bar{\sigma}_c - \Delta u)$ (defined as OCR_{max}) becomes more than 10.

THE OCR_{max} PARAMETER

Recognizing that the residual pore pressures induced by cyclic loading change the effective stress state which controls undrained load-deformation behavior, a new parameter termed OCR_{max} is defined to describe the normalized stress state at the end of cyclic loading and prior to monotonic static loading. The parameter is defined by Equation [1].

$$OCR_{max} = \frac{\bar{\sigma}_{cm}}{\bar{\sigma}_c - \Delta u} \quad [1]$$

OCR_{max} represents the maximum overconsolidation ratio where $\bar{\sigma}_{cm}$, $\bar{\sigma}_c$ and Δu are as defined previously. It is proposed that the OCR_{max} parameter for post-cyclic loading behavior is analogous to the conventional OCR term as applied to pre-cyclic static load behavior. It follows that

the NSP technique described by Ladd and Foott (1974) is applicable to the post-cyclic soil behavior of soft clays as suggested by Gardner (1977).

MODEL FOR POST CYCLIC LOADING BEHAVIOR

A proposed NSP model for post-cyclic loading behavior incorporates the following soil behavior characteristics.

1. Clays which are not highly structured are assumed to have a unique normalized stress-strain behavior under pre-cyclic static loading which is dependent only on stress history.
2. The pore pressure increase and stiffness degradation imposed by cyclic loading is reflected as a decrease in the effective confining pressure, expressed as $(\bar{\sigma} - \Delta u)$ and an associated increase of the OCR_{max} parameter, and
3. OCR_{max} controls the normalized undrained stress-strain, strength and pore pressure behavior, under post-cyclic monotonic (static) loading.

Consistent with these characteristics it is hypothesized that stress paths and stress-strain relationships can be predicted from pre-cyclic tests on soft clays where OCR is equated to $(OCR)_{max}$. Similarly, the model is applicable to the prediction of the loss in undrained shear strength subsequent to cyclic loading.

CONSEQUENCES AND VALIDITY OF PROPOSED MODEL

Some consequences and the validity of the proposed model as well as its conformance with relevant published data are considered as follows.

STRESS-STRAIN CHARACTERISTICS

As demonstrated by Figures 2(b) the post-cyclic normalized CIU stress-strain curves of the marine clays tested are a unique function of OCR_{max} . It is also evident that Figure 2(b) can be almost precisely simulated from Figure 2(a) by equating OCR_{max} to OCR as predicted by the post-cyclic soil behavior model. The same conclusions can be reached from the results of additional investigations of the relationship between OCR_{max} and stress-strain behavior as are summarized in Figures 4 through 7.

Figure 4 presents a variation of the pre-cyclic secant modulus (E_s) for a range of deviator stress levels (q) where both E_s and q have been normalized by the undrained shear strength (s_u). Figure 6 presents similar curves for UU tests performed after cyclic loading and demonstrates a consistent pattern of E_s/s_u variation as OCR_{max} increases. The E_s/s_u values defined by static tests for OCR 's of 1, 2 and 4 have been superimposed on Figure 5 and represent predictions of post-cyclic E_s/s_u at OCR_{max} values of 1, 2 and 4. The excellent correlation of the predictions with the trend of the post-cyclic test measurements is evident.

In Figure 6, a residual modulus ratio (E_r) is defined as the

ratio of E/s_u at a given OCR_{max} to E/s_u at an OCR of 1.0 and is plotted versus OCR_{max} for a stress-strength ratio (q/s_u) of one half. This figure clearly demonstrates the degradation of the secant modulus as OCR_{max} increases. For comparison, data from undrained pre-cyclic (static) CIU tests conducted by the Norwegian Geotechnical Institute on Drammen Clay (Andersen, 1975) are also included. Again, the post-cyclic soil behavior model is shown to produce a remarkably good prediction of undrained post-cyclic deformability from the static test results.

PORE WATER PRESSURE

Another post-cyclic soil parameter of interest is the pore pressure parameter at failure (A_f). For pre-cyclic loading, the A_f factor has been uniquely expressed for a given clay as a function of OCR (Bishop & Henkel, 1962). A similar relationship is shown for the post-cyclic triaxial compression tests if A_f is expressed as function of OCR_{max} . Typical pre-cyclic test results for Weald clay ($PI = 20\%$) together with the post-cyclic tests are shown on Figure 7. The agreement is again remarkable. It demonstrates that OCR_{max} is the governing parameter for the pore pressure development after cyclic loading in that A_f can be predicted for post-cyclic loading from pre-cyclic test results by equating OCR to OCR_{max} .

SHEAR STRENGTH

As described by Ladd (1977), the pre-cyclic undrained normalized strength ($s_u/\bar{\sigma}_c$) of a given clay has a unique relationship with OCR expressed as Equation [2].

$$\frac{s_u}{\bar{\sigma}_c} = K(OCR)^n \quad [2]$$

In Equation [2], K is the normalized undrained strength of the clay for its normally consolidated state and has been shown to vary with the plasticity index of the soil. The parameter n is a function of the failure mode induced by the type of shear test. Following the post-cyclic soil behavior model, it should be possible to predict the post-cyclic $s_u/\bar{\sigma}_c$ by replacing OCR in Equation [2] by OCR_{max} and $\bar{\sigma}_c$ by $\bar{\sigma}_c - \Delta u$. Figure 8 demonstrates the locus of Equation [2] for both pre- and post-cyclic direct simple shear tests using data from this study and for Drammen clay as reported by Andersen (1975). The post-cyclic shear strength predicted by Equation [2] is almost exact even considering the expected variation in soil properties from sample to sample. It is significant to note that the parameters K and n are identical for both the pre-cyclic and post-cyclic tests. A similar plot using triaxial compression test data from the same sources is shown in Figure 9. For these tests, the conformance is not as exact; the post-cyclic slope parameter (n) being steeper than derived from the static test results.

Applying the post-cyclic soil behavior model to Equation [2], it is also possible to predict the loss of strength induced by post-cyclic excess pore water pressures. The strength reduction (R) can be readily

shown to be given by the following expression:

$$R = 1 - \left(\frac{\text{OCR}_{\text{max}}}{\text{OCR}} \right)^{1-n} \quad [3]$$

In Equation [3], R represents the ratio of the difference of the undrained shear strength after cyclic loading to the initial undrained shear strength. This relationship suggests that the post-cyclic reduction in strength is independent of K and is dependent only on n and the $\text{OCR}_{\text{max}}/\text{OCR}$ ratio.

The locus of Equation [3] is shown in Figure 10 for both the triaxial and simple shear tests. The strength reduction curves for the marine clays tested indicate that the cyclic simple shear test causes a significantly greater strength loss than is imposed by the cyclic triaxial compression test mode used by most previous investigators. It is also relevant to note that the direct simple shear test more correctly simulates shear stresses induced by horizontally propagating seismic shear waves.

CONCLUSIONS

The data evaluated as part of this study indicates that the proposed post-cyclic soil behavior model generally predicts with a good degree of confidence the stress-strain characteristics and undrained strength of soft clays which have been subjected to cyclic loading. Additional investigations, not reported herein, also suggest (Gardner, 1977) that the model is applicable to overconsolidated clays and provides a comprehensive characterization of the post-cyclic behavior of clays.

Limitations of the model currently identified include the inability to predict the stress-strain curve at low strain levels for specimens with large OCR_{max} values, i.e., where the single amplitude cyclic strain for the applied cycles exceeds about 1 percent in the triaxial testing mode- a condition representative of the most extreme environmental loading conditions. Further it remains to be confirmed that the initial S shape configuration of these curves represents fundamental soil behavior and not test induced behavior. Another significant limitation is inherent in the NSP characterization employed in the model. By this inclusion, the model is not applicable to highly sensitive cemented or other highly structured soils subject to significant structure changes under elevated consolidation pressures.

ACKNOWLEDGEMENTS

The development of the model outlined in this paper is part of ongoing research on the nonlinear behavior of clays under cyclic loading and was supported by a research grant from the Professional Development Program of Woodward-Clyde Consultants (WCC). This support is gratefully acknowledged. The writers specially thank I.M. Idriss for his encouragement and advice during this research effort. Sincere thanks are due to R.S. Ladd for the conduction of the testing program and to Y. Moriwaki for his contributions to this study. Several WCC engineers also contributed to the present experimental program; they include J. Kim, E. Ng and M. Perlow. The assistance provided by these colleagues is gratefully acknowledged.

REFERENCES

- Andersen, K.H. (1975), "Research Project, Repeated Loading on Clay; Summary and Interpretation of Test Results" Report 74037-9, Norwegian Geotechnical Institute, Oslo, Norway.
- Bishop, A.W. and Henkel, D.J. (1962), "The Measurement of Soil Properties in the Triaxial Test", Edward Arnold Ltd., London, England, 2nd Edition.
- Castro, G. and Christian, J.T. (1976), "Shear Strength of Soils and Cyclic Loading", Journal of the Geotechnical Engineering Division, ASCE, Vol. 102, No. GT 9, September.
- Gardner, W.S. (1977), "Soil Property Characterization in Geotechnical Engineering Practice", Third Woodward Lecture. Geotechnical/Environmental Bulletin, Vol X, No. 2, Woodward-Clyde Consultants, San Francisco.
- Idriss, I.M., Dobry, R. and Singh, R.D. (1978), "Nonlinear Behavior of Soft Clays During Cyclic Loading", paper submitted to ASCE for possible publication in the Journal of Geotechnical Engineering, March.
- Koutsoftas, D.C. (1978), "Effect of Cyclic Loads on Undrained Strength of Two Marine Clays", Journal of the Geotechnical Engineering Division, ASCE, Vol. 104, No. GT5, Proc. Paper 13751, pp. 609-620.
- Ladd, C.C. (1964), "Stress-Strain Behavior of Saturated Clay and Basic Strength Principles", Research Report 1264-17, Dept. of Civil Engineering, M.I.T., Cambridge, Massachusetts.
- Ladd, C.C. and Edgers, L. (1972), "Consolidated-Undrained Direct Simple Shear Tests on Saturated Clays", Research Report R72-8w, Department of Civil Engineering, Massachusetts Institute of Technology, Cambridge, Massachusetts.
- Ladd, C.C. and Foott, R. (1974), "New Design Procedures for Stability of Soft Clays", Journal of the Geotechnical Engineering Division, ASCE, Vol. 99, No. GT7, Proc. Paper 19664, pp. 763-786.
- Ladd, C.C. (1977), "Stress-Deformation and Strength Characteristics", State-Of-The-Art Report for Session No. 1, 9th International Conference on Soil Mechanics and Foundation Engineering, Tokyo.
- Lee, K.I. and Focht, J.A. (1976), "Strength of Clay Subjected to Cyclic Loading", Marine Geotechnology, Vol. 1, No. 3, pp. 165-186.
- Seed, H.B. and Chan, C.K. (1966), "Clay Strength Under Earthquake Loading Conditions", Journal of the Soil Mechanics and Foundations Division, ASCE, Vol. 92, No. SM2, Proc. Paper 4723, pp. 53-78.
- Thiers, G.R. and Seed, H.B. (1969), "Strength and Stress-Strain Characteristics of Clays Subjected to Seismic Loading Conditions", ASTM STP 450 American Society for Testing and Materials, Philadelphia, Pennsylvania.

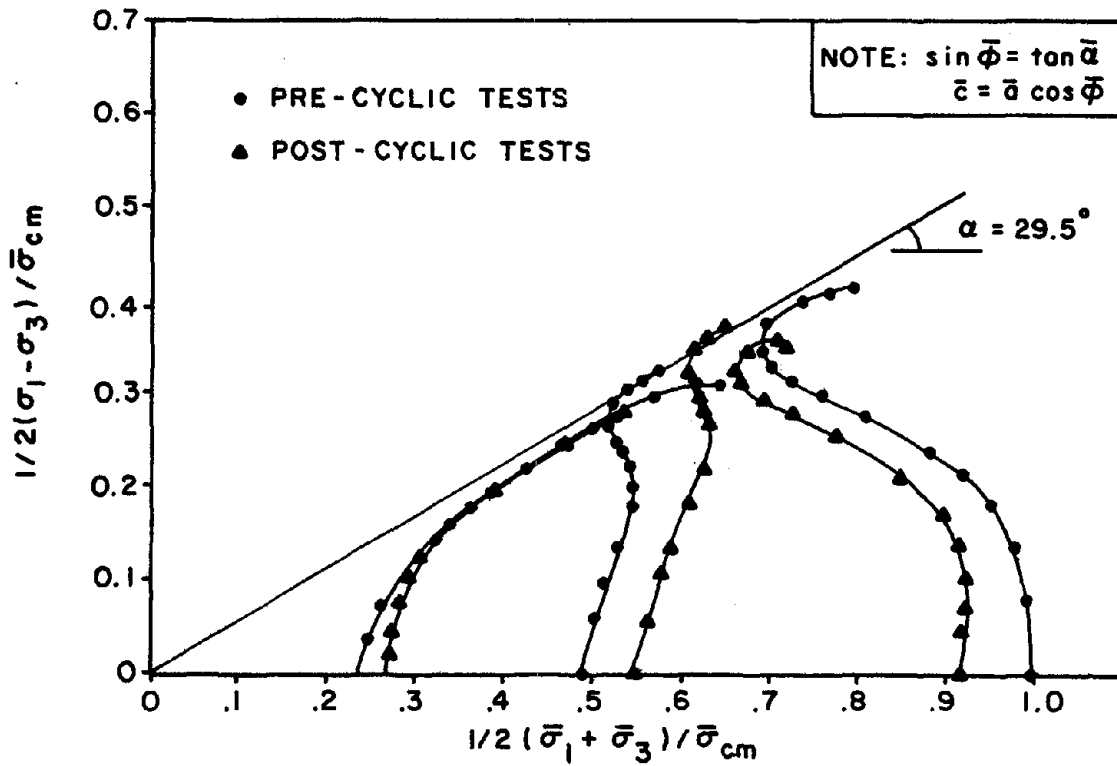


FIG.1 STRESS PATHS FOR MONOTONIC LOADING

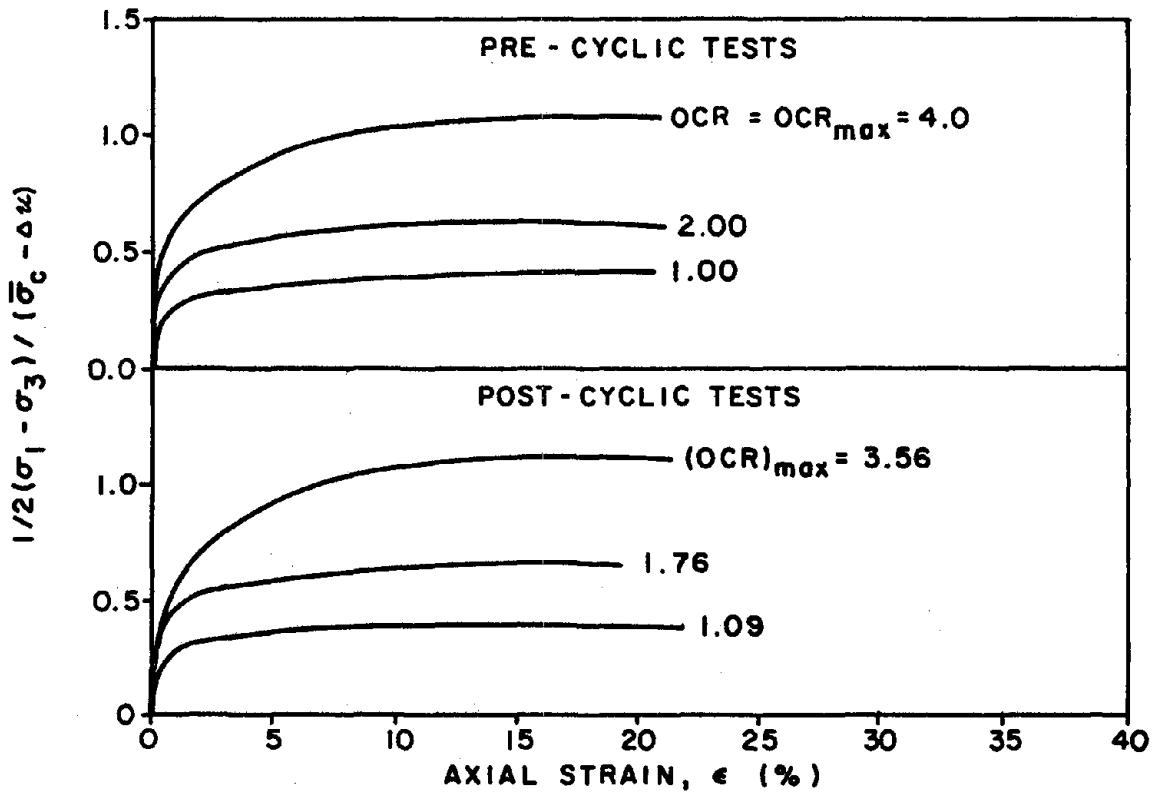


FIG.2 NORMALIZED STRESS-STRAIN CURVES

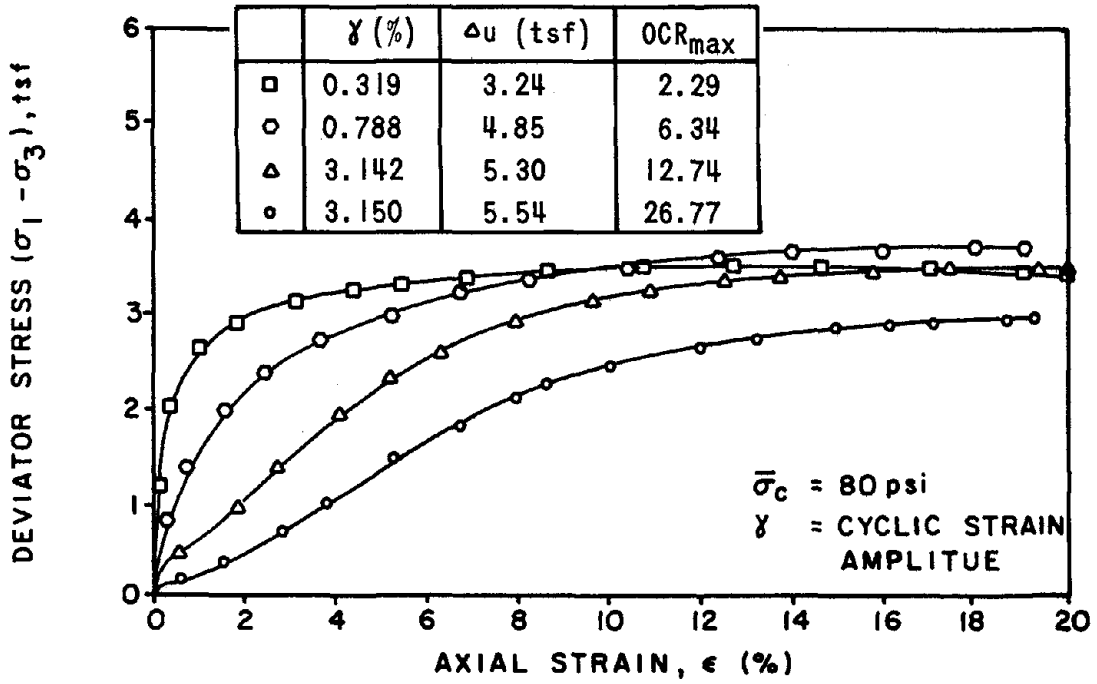


FIG.3 TYPICAL STRESS-STRAIN CURVES FOR NORMALLY CONSOLIDATED SPECIMENS SUBJECTED TO CYCLIC LOADING.

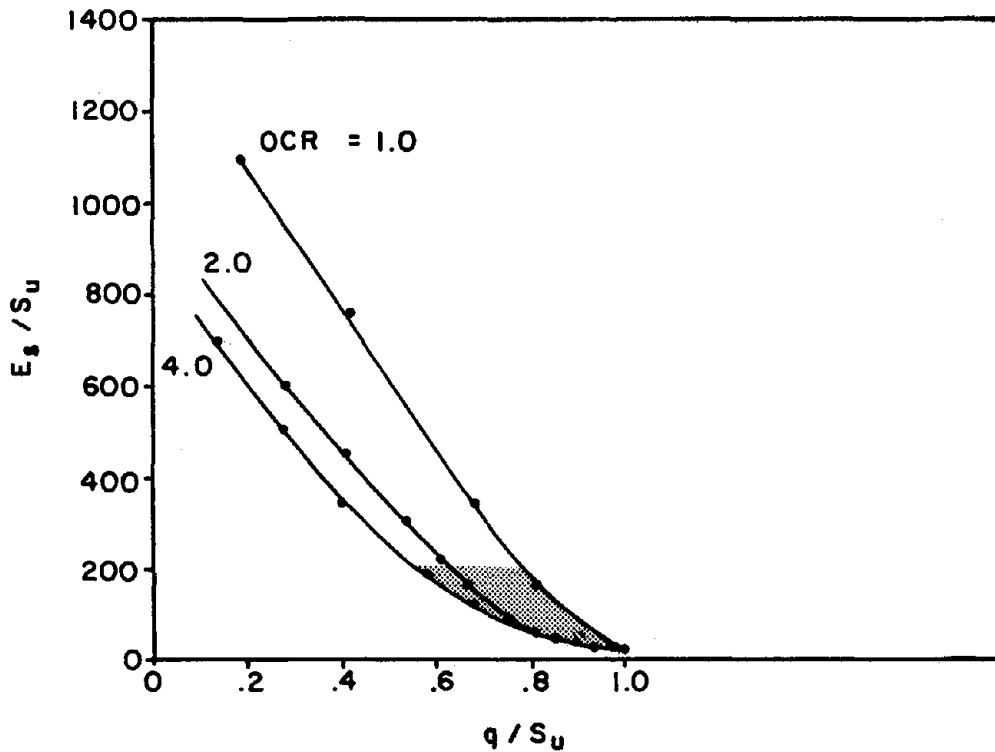


FIG.4 NORMALIZED MODULUS VS NORMALIZED DEVIATOR STRESS FROM PRE-CYCLIC CIU TESTS

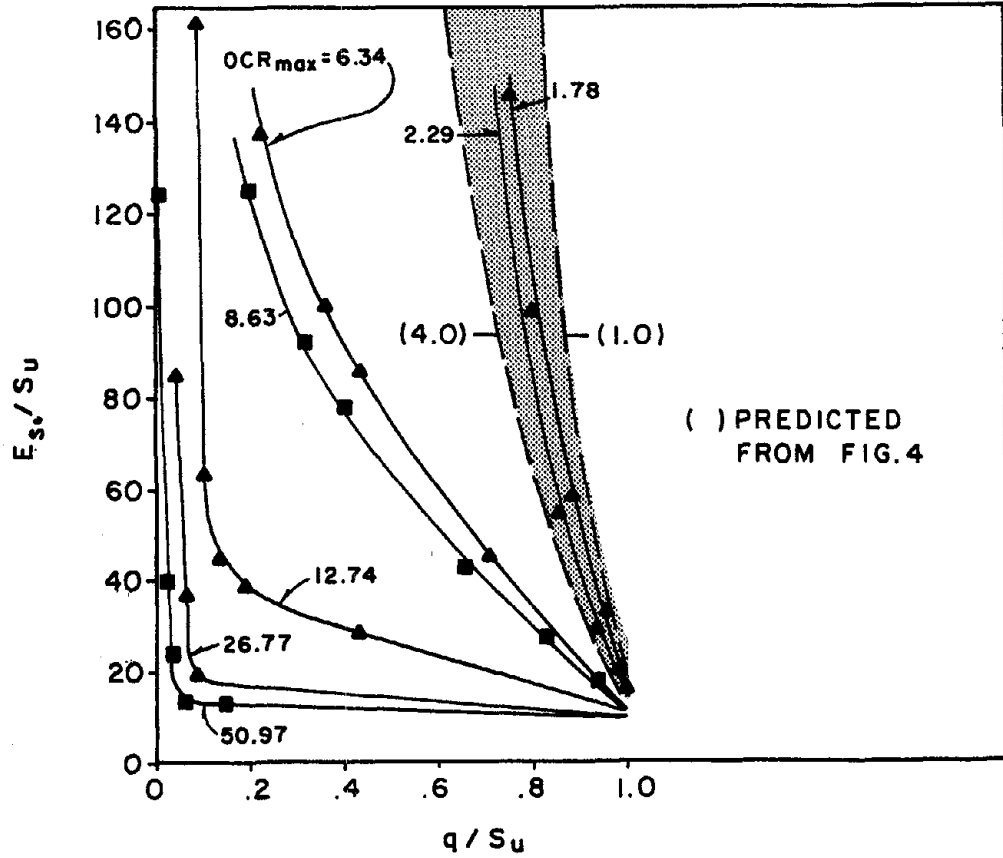


FIG.5 NORMALIZED MODULUS VS NORMALIZED DEVIATOR STRESS FROM POST-CYCLIC CIU TESTS

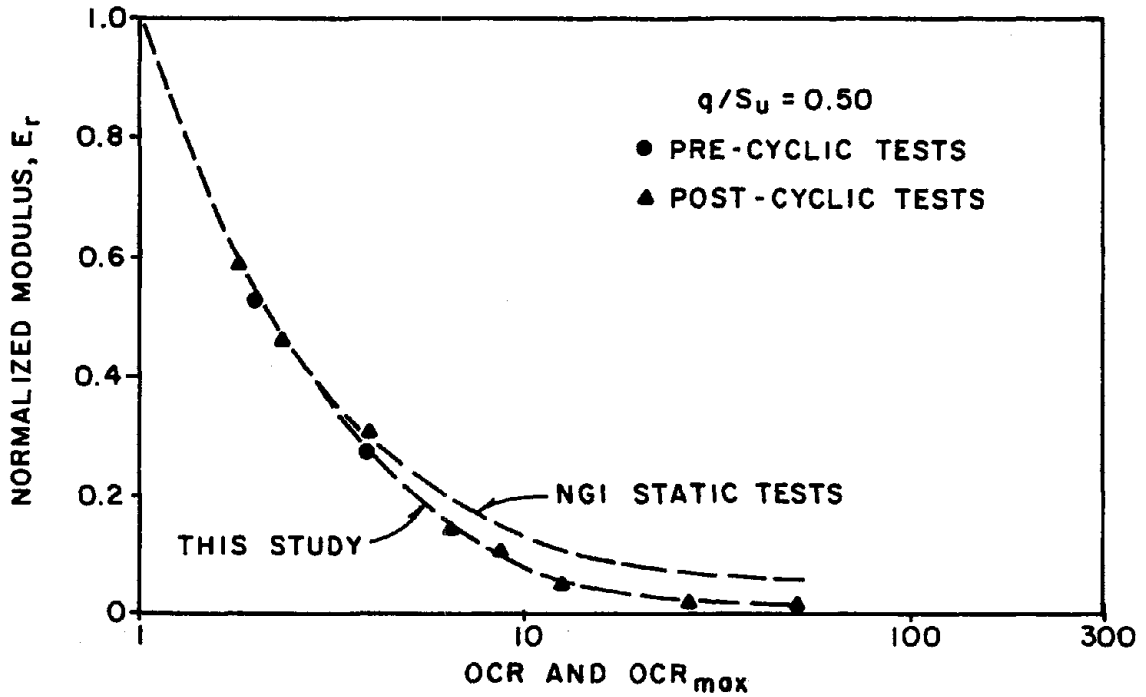


FIG.6 NORMALIZED MODULUS E_r VS OCR_{max}

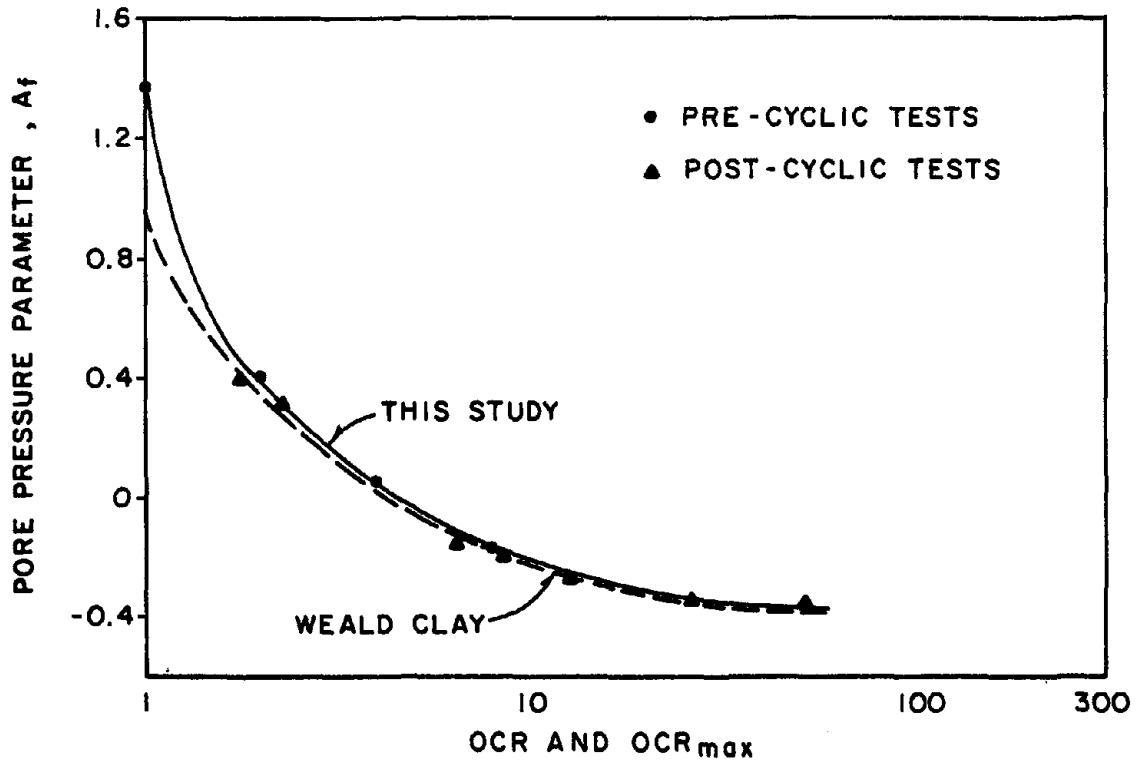


FIG.7 PORE PRESSURE PARAMETER VS OCR AND OCR_{max}

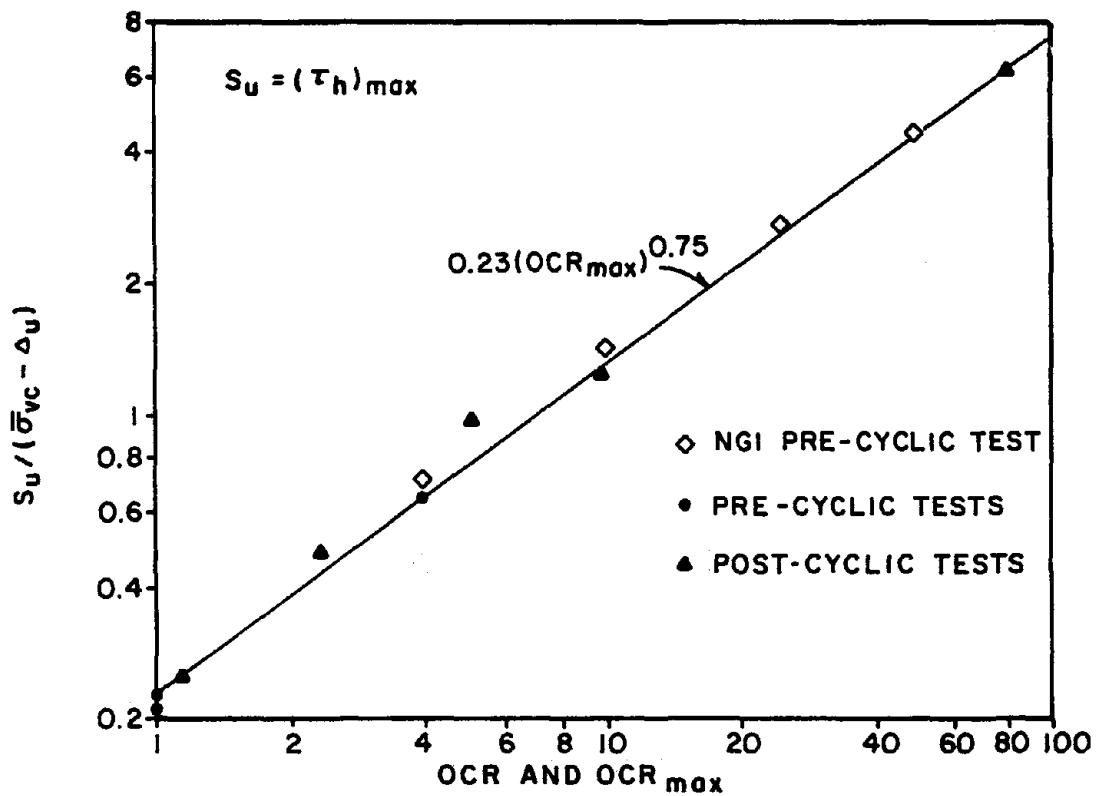


FIG.8 STRENGTH RATIO OBTAINED IN SIMPLE SHEAR TESTS VS OCR_{max}

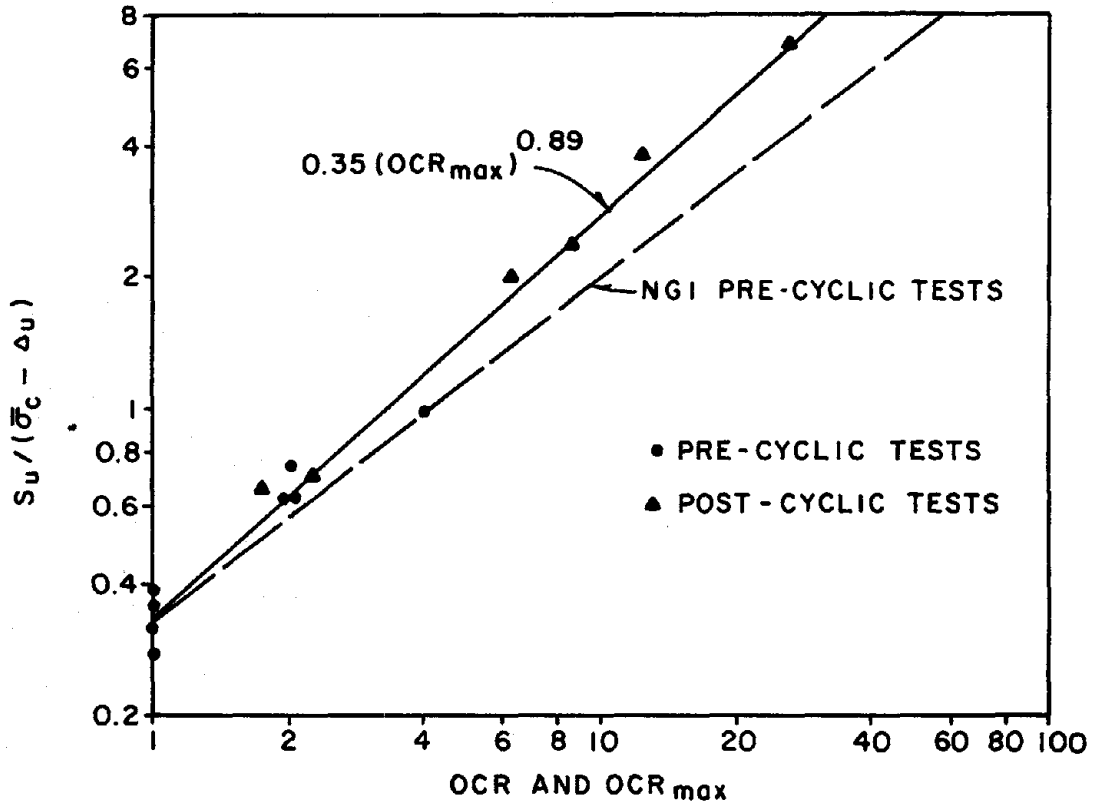


FIG.9 STRENGTH RATIO OBTAINED IN TRIAXIAL TESTS VS OCR_{max}

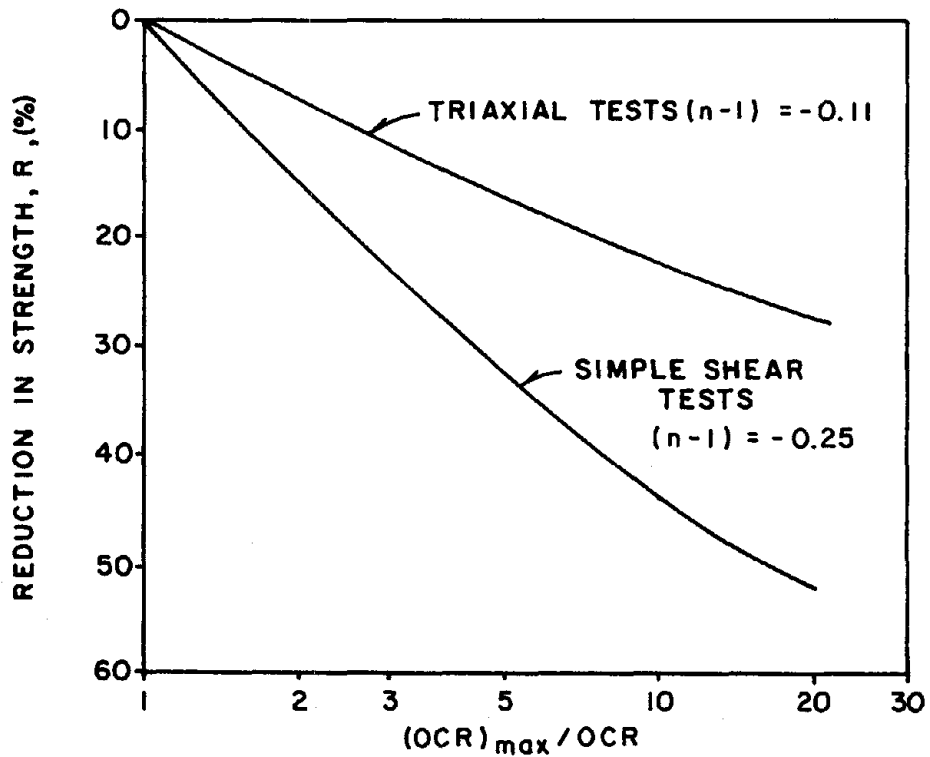


FIG.10 LOSS OF STRENGTH IN SIMPLE SHEAR AND TRIAXIAL TESTS DUE TO CYCLIC LOADING

A NEW APPROACH FOR THE ANALYSIS OF
LIQUEFACTION OF SAND IN CYCLIC SHEARING

by

S. Nemat-Nasser^I and A. Shokoh^{II}

ABSTRACT

When a sample of sand under fixed confining pressure is subjected to cyclic shearing, its grains are rearranged, and as a consequence the saturated undrained sample may liquefy. This work gives a fundamental systematic approach for the prediction of stress-strain relations in terms of the number of cycles and other relevant parameters: for stress-controlled test, the strain amplitude is expressed as a function of the number of cycles, the prescribed stress amplitude, and other parameters. The results are applied to predict some of the existing experimental results, obtaining good correlations.

1. INTRODUCTION

During an earthquake, saturated loose sand may liquefy, resulting in a temporary loss of its bearing capacity. Phenomena of this kind have been observed in the Alaskan earthquake of 1964, in the Niigata earthquake of 1964, and recently in the 1977 earthquake of San Juan, Argentina; see, Coulter and Migliaccio (1), and Lambe and Whitman (2). Because of this, considerable effort has been devoted to understanding and quantifying the mechanics of liquefaction in the recent past. Most of the work has been experimental, and except for recent studies by the authors (3,4), there exists no fundamental theoretical quantification of this important problem; for references, see Refs. (5)-(11).

In this paper we shall consider liquefaction of the saturated cohesionless loose sand in cyclic shearing, and within the framework of the thermodynamics of irreversible processes, see, for example, Nemat-Nasser (12,13), we shall develop a mathematical foundation for the prediction of the shear strain amplitude in terms of the prescribed shear stress amplitude and the number of cycles. We shall then apply our results to predict some of the existing experimental results. It is our hope that the basic approach presented here will provide a framework for future experimental and theoretical investigations.

2. STATEMENT OF PROBLEM

We consider a sample of cohesionless saturated sand of (arbitrary) unit volume under a prescribed confining pressure σ_c . We assume that the sample is subjected to cyclic shearing with shear stress amplitude $\hat{\tau}_0$, we denote the excess pore water pressure by \hat{p} , and introduce the following dimensionless quantities:

I Professor of Civil Engineering and Applied Mathematics, Northwestern University, Evanston, Illinois 60201.

II Postdoctoral Research Fellow, Department of Civil Engineering, Northwestern University, Evanston, Illinois 60201.

$$\tau_0 = \hat{\tau}_0 / \sigma_c, \quad p = \hat{p} / \sigma_c \quad (2.1)$$

Let the prescribed shear stress be given by

$$\tau = \tau_0 \phi(t), \quad -1 \leq \phi(t) \leq 1, \quad (2.2)$$

where $\phi(t)$ is a periodic function of time, and denote the corresponding shear strain by γ .

We shall assume that the sample is macroscopically homogeneous, and consider the isothermal case only; hence, in all our subsequent equations we shall suppress explicit reference to the temperature. Furthermore, we shall assume that the thermodynamic state of the sample is defined by only two state variables the shear stress τ which is controlled externally, and the excess pore water pressure p which, in this case, serves as the only internal variable that represents in a global average way the extent of irreversible microstructural rearrangements that take place during the course of cyclic shearing. (This is the simplest theory that one can consider.)

Let the Gibbs function be given by

$$\chi = \hat{\chi}(\tau, p), \quad (2.3)$$

and observe that, by definition,^{III} the shear strain is

$$\gamma = \partial \hat{\chi} / \partial \tau = \hat{\gamma}(\tau, p). \quad (2.4)$$

To complete the formulation, one must obtain the excess pore water pressure p as a function of the prescribed stress history. The general treatment of this problem will not be considered here. Instead, we shall focus attention on obtaining for a stress-controlled cyclic shearing the build-up of the excess pore water pressure, and hence the corresponding shear strain amplitude in terms of the shear stress amplitude, the number of cycles, and the other relevant initial conditions for the sample. To this end we shall first briefly review the results obtained by the authors in (3,4).

The basic idea in (3) is that a change in the void ratio of the drained sample from e to $e + de$ by cyclic shearing requires an expenditure of the energy dW which increases as the void ratio approaches its absolute minimum e_m . If the sample is undrained, then the tendency toward the reduction of the void ratio causes an increase in the excess pore water pressure, which in turn decreases the effective forces between adjacent grains, and therefore decreases the required energy dW . These physical observations can be expressed by

III We also note that the thermodynamic variable conjugate to p is defined by

$$\lambda = \partial \hat{\chi} / \partial p = \hat{\lambda}(\tau, p),$$

and that the second law of thermodynamics requires

$$\dot{p}\lambda \geq 0,$$

which is the dissipation inequality; here superposed dot denotes time derivative.

$$dW = -\tilde{v} \frac{de}{f(1+p)g(e-e_m)} \quad , \quad (2.5)$$

where the material functions f and g must be such that

$$f(1) = 1, \quad f' \geq 0, \quad g(0) = 0, \quad g' \geq 0; \quad (2.6)$$

here, prime denotes differentiation with respect to the corresponding argument. Since

$$de = -\frac{e\sigma_c}{\kappa_w} dp \quad ,$$

where κ_w is the bulk modulus of water, Eq. (2.5) becomes

$$dW = v \frac{edp}{f(1+p)g(e-e_m)} \quad , \quad (2.7)$$

where $v = \tilde{v}\sigma_c/\kappa_w$.

It is now observed that liquefaction initiation occurs when the excess pore water pressure equals the confining pressure, i.e. when $p = 1$. Usually the confining pressure σ_c is (for experimental data) of the order of 10 psi, and since the bulk modulus of water is about 300,000 psi, the volumetric strain and the corresponding work per unit volume per unit confining pressure (dimensionless work) are of the order of 10^{-5} to 10^{-4} , and hence can be ignored without introducing any measureable error. Therefore, the void ratio e in (2.7) can be replaced by its initial value e_0 .

With this substitution and upon integration, we obtain, from (2.7),

$$\Delta W = \frac{ve_0}{g(e_0 - e_m)} \int_0^p \frac{dp'}{f(1+p')} \quad . \quad (2.8)$$

In references (3,4) for the functions g and f the following approximations were used:

$$g(e - e_m) = (e - e_m)^n \quad , \quad n > 1 \quad , \quad (2.9)$$

and

$$f(p) = (1+p)^r \quad , \quad r > 1 \quad , \quad (2.10)$$

and good correlation with experimental results for both densification of dry sand and liquefaction of saturated undrained sand was obtained.

In Eq. (2.8) we must obtain an explicit expression for ΔW which is the work consumed in rearranging the particles. This work is a fraction of the total hysteretic loss for the sample; a typical hysteretic loop is shown by the dashed curves in Fig. 1. It has been shown in (3) that the corresponding energy ΔW_i in the i^{th} cycle of cyclic shearing for cohesionless sand may be approximated by (this is for a cyclic shearing with the hysteretic loop shown by the dashed curves in Fig. 1),

$$\Delta W_i = \hat{h}_i \tau_0^{\alpha_i+1} \quad , \quad (2.11)$$

where \hat{h}_i depends on the number of preceding cycles as well as other

relevant parameters, and α_i (on the basis of experimentally observed symmetry in the hysteretic loop, see Fig. 1) must be assigned an even value. Furthermore, it has been argued that when the dimensionless stress amplitude τ_0 is suitably large, then one may assume that \hat{h}_i , as well as α_i , is essentially independent of the number of preceding cycles, and hence, as a first order approximation, use the average quantities h and α for these parameters. In this manner, after N cycles of cyclic shearing (stress-controlled), one may write,

$$\Delta W = hN\tau_0^{\alpha+1}, \quad (2.12)$$

where α is an even constant, and h is a parameter which, in general, increases with increasing relative density D_r , and with increasing confining pressure σ_c . In (3) $\alpha = 4$ has been used to fit all the considered experimental results. In the present work we shall use the same value for α .

3. STRAIN-, STRESS-AMPLITUDE RELATION

We now consider the Gibbs function (2.3) and the corresponding expression for the shear strain γ defined in (2.4). We first observe that if the shear stress τ is changed to $-\tau$, the shear strain γ in expression (2.4) must change to $-\gamma$, and therefore the function $\hat{\gamma}(\tau, p)$ must be odd in the variable τ , i.e.

$$\hat{\gamma}(-\tau, p) = -\hat{\gamma}(\tau, p). \quad (3.1)$$

To proceed further, we shall introduce the following approximation of the Gibbs function (2.3),

$$\hat{\chi}(\tau, p) = \frac{\hat{\chi}_1(\tau)}{\hat{\chi}_2(p)}, \quad (3.2)$$

and hence, obtain

$$\begin{aligned} \hat{\gamma}(\tau, p) &= \frac{1}{\hat{\chi}_2(p)} d\hat{\chi}_1(\tau)/d\tau \\ &= \frac{\hat{\gamma}_1(\tau)}{\hat{\chi}_2(p)}. \end{aligned} \quad (3.3)$$

Let us now consider cyclic shearing at a prescribed (dimensionless) stress-amplitude τ_0 . To be definite, we define the beginning of the i^{th} cycle as the state at which the shear stress τ has just attained the value τ_0 in the preceding cycle, and is being decreased. When the shear stress is decreased to the value $-\tau_0$, we consider that half of the i^{th} cycle is completed, and hence the other half is completed as soon as the shear stress τ again attains the value τ_0 ; see Fig. 1. We denote the value of the shear strain at the completion of the i^{th} cycle by γ_M , and the corresponding value of the excess pore water pressure, by P_M , and we seek to obtain an explicit relation for γ_M in terms of the number of cycles N , the

shear stress amplitude τ_0 , and other parameters; for a fixed number of cycles, a typical γ_M , τ_0 -relation is shown by the solid curve POQ in Fig. 1. It should be noted however, that in the stress-controlled cyclic shearing of undrained saturated sand, the shear strain, in general, attains its maximum value somewhat after the shear stress has attained the value τ_0 , and has actually decreased slightly below this value. However, the difference between γ_M and the maximum strain attained immediately after the completion of the i^{th} cycle is probably very small; moreover, from the application point of view, γ_M , as defined above, provides an adequate measure of the shear strain build-up.

From Eq. (3.3) we therefore obtain,

$$\gamma_M = \frac{\hat{\gamma}_1(\tau_0)}{\hat{\chi}_2(p_M)} \quad , \quad (3.4)$$

where we must have (see Fig. 1)

$$\hat{\gamma}_1(-\tau_0) = -\hat{\gamma}_1(\tau_0) \quad , \quad \hat{\gamma}_1(0) = 0 \quad , \quad (3.5)$$

and since the strain amplitude must increase with increasing excess pore water pressure, we require that $\hat{\chi}_2$ be a decreasing function of p_M , i.e.

$$\hat{\chi}_2' < 0 \quad . \quad (3.6)$$

In particular, as p_M approaches 1, i.e. as the excess pore water pressure approaches the confining pressure σ_c , we expect that the positive function $\hat{\chi}_2(p_M)$ takes on small values.

Let us now consider power series expansions for the functions $\hat{\chi}_2(p_M)$ and $\hat{\gamma}_1(\tau_0)$, and write

$$\gamma_M = \frac{a_1\tau_0 + a_3\tau_0^3 + \dots}{1 + c_1p_M + c_2p_M^2 + \dots} \quad , \quad (3.7)$$

where the material parameters c_1, c_2, \dots , and a_1, a_3, \dots , are possibly functions of $e_0 - e_m$. Further, based on our previous requirements we take a_1, a_3, \dots , positive and c_1, c_2, \dots , negative such that $-\sum_{i=1}^{\infty} c_i < 1$. We point out that the formulation (3.7) is valid only for $N \leq N_\ell$, i.e., for $P < 1$ and for initial liquefaction, i.e., when $P = 1$ for the first time. This limitation on relation (3.7) is a result of the fact that we have separated the function $\hat{\chi}$ into two parts, one only a function of τ and the other only a function of p , as in (3.2). In order to estimate the response for $N > N_\ell$, in particular, to obtain the limiting value of γ_M , we have to work directly with $\hat{\chi}$.

As a special case of (3.7) consider

$$\gamma_M = \frac{a_1 \tau_0 + a_3 \tau_0^3 + \dots}{1 - c p_M}, \quad 0 < c < 1. \quad (3.8)$$

Note that as the excess pore water pressure p approaches 1, γ_M becomes very large, especially if c is assigned a value close to unity. The parameter c as well as the constants a_1, a_3, \dots , must be fixed by comparison with the experimental results. Note that for the general application the approximation (3.8) may not be adequate, in which case one must consider the more general representation (3.7). In the next section however, we shall use (3.8) and retaining only two terms in the series, compare our results with the experimental data reported in (14).

To apply (3.7) or (3.8) to a given experimental result for stress-controlled cyclic shearing of a sample of saturated undrained cohesionless sand, we first obtain from Eq. (2.8) in conjunction with, say, (2.9), (2.10) and (2.12), an explicit expression for the excess pore water pressure in terms of the prescribed shear stress amplitude τ_0 , the initial and the minimum void ratios e_0 and e_m , the number of cycles N , and other relevant parameters. With the excess pore water pressure p_M calculated in this manner, we now use (3.7) or (3.8) and employing only a finite number of terms for the series, we fix the corresponding constants by comparison with the required number of test points. To establish the validity of the basic approach, we then compare the results predicted by the final equation with other experimental results obtained for the same sand, but under different test conditions. In the sequel, the basic procedure will be illustrated in its simplest form.

4. COMPARISON WITH EXPERIMENTAL RESULTS

Substituting the approximate expressions (2.9), (2.10), and (2.12) into (2.8) and carrying out the indicated integration, we obtain

$$h N \tau_0^{\alpha+1} = \frac{\hat{v} e_0}{(e_0 - e_m)^n} [1 - (1 + p_M)^{1-r}], \quad n, r > 1, \quad (4.1)$$

where $\hat{v} = v/(r-1)$. This equation now yields,

$$p_M = \left\{ 1 - N \tau_0^{\alpha+1} (e_0 - e_m)^n / \hat{v} e_0 \right\}^{\frac{1}{1-r}} - 1, \quad (4.2)$$

where $\hat{v} = \hat{v}/h$.

Equation (4.2) gives the excess pore water pressure in terms of the number of cycles N , the dimensionless shear stress amplitude τ_0 , and the initial and the minimum values of the void ratio. In (3) the results of this equation have been compared with several sets of experimental data reported by DeAlba *et al.* (14). These experimental results have been obtained at the University of California at Berkeley with the aid of a large shaking table, and using rather large samples of saturated cohesionless Monterey number 0 sand with minimum void ratio $e_m = 0.564$, and maximum void ratio $e_M = 0.852$. The experiments were performed on samples with 54,

68, 82, and 90% relative densities, for confining pressure of about 8 psi, and for various fixed shear stress amplitudes. The excess pore water pressure and the shear strain amplitude have been reported in terms of the number of cycles for the above stated values of the initial relative density.

In (3) first theoretical results based on basic Eq. (2.5) for the densification of dry sand ($p = 0$) have been obtained and compared with the extensive experimental data reported by Youd (15, 16). In this manner it was found that for a first-order approximation, $n = 3.5$ fits nicely all the experimental results reported by Youd. Then liquefaction data of DeAlba *et al.* (14) and others (17, 18) were considered in connection with (4.2), and it was found that $r = 2.5$ with $\alpha = 4$ fits all reported experimental results. In the present work, therefore we shall use the same values for these parameters, i.e., we shall set $\alpha = 4$, $n = 3.5$, and $r = 2.5$.

The parameter \hat{v} in (4.2) is inversely proportional to parameter h which occurs in the expression for the work in Eq. (2.12). It is reasonable to expect that h should increase with increasing confining pressure σ_c and with increasing relative density D_r (or with decreasing $e_0 - e_m$); this is because under a larger confining pressure or when one starts with a denser sand, more work will be required to rearrange the sand grains in the course of cyclic shearing. Therefore, the parameter \hat{v} in (4.2) is expected to decrease with increasing confining pressure or with increasing relative density.

If we set in (4.2) $p_M = 1$, and denote by N_ℓ the corresponding number of cycles to liquefaction initiation, we obtain

$$N_\ell \tau_0^{\alpha+1} \frac{(e_0 - e_m)^n}{e_0} = \hat{v} (1 - 2^{1-r}) \equiv \eta . \quad (4.3)$$

In (3), experimental results reported by DeAlba *et al.* (14) for less than 70% relative densities, corresponded to $\eta = 0.87 \times 10^{-6}$, and those for 82% relative density corresponded to $\eta = 0.40 \times 10^{-6}$. Figures 2, 3, and 4, taken from Nemat-Nasser and Shokoh (3), show experimental results in relation to the theoretical predictions based on Eq. (4.2) and the values of the parameters stated above. We shall use these results in connection with the following approximate version of Eq. (3.8), in order to predict the strain amplitude build-up in terms of the number of cycles and other relevant parameters:

$$\gamma_M = (a_1 \tau_0 + a_3 \tau_0^3) / (1 - c p_M) . \quad (4.4)$$

A systematic approach to this problem would require the following steps and corresponding experimental data:

1. For the drained sample, $p_M = 0$, one would first consider

$$\gamma_M = a_1 \tau_0 + a_3 \tau_0^3, \quad p_M = 0 , \quad (4.5)$$

and seek to obtain the parameters a_1 and a_3 as functions of the confining pressure σ_c and the relative density D_r (or, more appropriately, $e_0 - e_m$),

i.e. one writes

$$a_i = a_i(\sigma_c, e_0 - e_m), \quad i = 1, 3 \quad (4.6)$$

Intuitively it is clear that for a given sand, both a_1 and a_3 must be positive and must decrease with increasing σ_c and with decreasing $e_0 - e_m$, because, for the same stress amplitude and the same number of cycles, the shear strain amplitude should be smaller under a larger confining pressure, or under the same confining pressure, but for an initially denser sand. Unfortunately, however, we do not have any systematic experimental data to establish the functional form of these parameters. In the sequel, therefore, we assume as a first order approximation that these parameters are constant.

2. Then one considers test results for liquefaction and with p_M given by Eq. (4.2), establishes the value of the parameter c , in Eq. (4.3), using a set of data points.

Finally, the results must be compared with other experimental points, in order to verify the validity of the basic approach.

We have used the experimental results for 54% relative density, in order to establish the following form for Eq. (4.3):

$$\gamma_M = (3/2 \times 10^{-4} \tau_0 + 10^{-1} \tau_c^3) / (1 - 4/5 p_M), \quad (4.7)$$

which is intended for small strain amplitudes. The corresponding results are compared with experimental points in Fig. 5, for 54 and 68, and in Fig. 6 for 82% relative densities, respectively. As is seen, the comparison for 54% and 82% relative densities is quite good, especially since primitive forms for the material functions have been used. For 68% relative density, however, the comparison is not good for small number of cycles. We feel, however, that in this range the experimental results are not compatible with those reported for 54 and 82% relative densities. As was pointed out above, for the same confining pressure and the same shear stress amplitude, one expects that, initially, say, after one or two cycles, the strain amplitude should be smaller for the denser sand than for the looser one. Some of the experimental points for 68% relative density violate this expectation. For example, experimental points for $\tau_0 = 0.135$ and $D_r = 54\%$, are reported to fall below the corresponding points for $\tau_0 = 0.134$ and $D_r = 68\%$, for the number of cycles from one to twelve. Notwithstanding this, the experimental results reported by DeAlba et al. (14) seem to be the most extensive ones that the present authors have been able to obtain so far. These results certainly confirm the validity of our basic theoretical approach. However, a systematic coordinated theoretical and experimental work is still required, in order to establish a reliable stress-strain relation for cyclic shearing of saturated drained or undrained sand.

ACKNOWLEDGMENT

This work was supported by the Atomic Energy Organization of Iran under a contract to Northwestern University, Evanston, Illinois, USA, and Pahlavi University, Shiraz, Iran.

REFERENCES

1. Coulter, H. W., and Migliaccio, R. R., (1966) "Effect of the Earthquake of March 27, 1964, at Valdez, Alaska," Geological Survey Professional Paper 542-C, Washington, D.C.: U.S. Department of the Interior.
2. Lambe, T. W., and Whitman, R. V., (1969) Soil Mechanics, John Wiley and Sons, Inc.
3. Nemat-Nasser, S., and Shokoh, A., (1977) "A Unified Approach to Densification and Liquefaction of Cohesionless Sand," Earthquake Research and Engineering Laboratory, Technical Report No. 77-10-3, Dept. of Civil Engineering, Northwestern University, Evanston, IL; submitted for publication.
4. Nemat-Nasser, S., and Shokoh, A., (1978) "Densification and Liquefaction of Sand in Cyclic Shearing," Proceedings of the Central American Conference on Earthquake Engrg., San Salvador, El Salvador, C.A., January 9-12, 1978; vol. 2, in press.
5. Faccioli, E., and Reséndiz, D., (1976) "Soil Dynamics: Behavior Including Liquefaction," Seismic Risk and Engineering Decisions, C. Lomnitz and E. Rosenblueth (eds.), Elsevier Scientific Pub. Co., Chapter 4, pp. 71-139.
6. Castro, G., and Poulos, S., (1977) "Factors Affecting Liquefaction and Cyclic Mobility," Journal of the Geotechnic Engineering Div., ASCE 103 #GT6, pp. 501-516.
7. Seed, H. B., and Idriss, I. M., (1967) "Analysis of Soil Liquefaction: Niigata Earthquake," Journal of the Soil Mechanics and Foundations Div., ASCE 93 #SM3, pp. 83-108.
8. Seed, H. B., and Idriss, I. M., (1969) "Influence of Soil Conditions on Ground Motions during Earthquakes," Journal of the Soil Mechanics and Foundations Div., ASCE 95 #SM1, pp. 99-137.
9. Seed, H. B., and Lee, K. L., (1966) "Liquefaction of Saturated Sands during Cyclic Loading," Journal of the Soil Mechanics and Foundations Div., ASCE 92 #SM6, pp. 105-134.
10. Seed, H. B., and Peacock, W. H., (1971) "Test Procedures for Measuring Soil Liquefaction Characteristics," Journal of the Soil Mechanics and Foundations Div., ASCE 97 #SM8, pp. 1099-1119.
11. Martin, G. R., Finn, W. D. L., and Seed, H. B., (1975) "Fundamentals of Liquefaction under Cyclic Loading," Journal of the Geotechnic Engineering Div., ASCE 101 #GT5, pp. 423-438.
12. Nemat-Nasser, S., (1975) "On Nonequilibrium Thermodynamics of Continua," Mechanics Today, Vol. 2, S. Nemat-Nasser (ed.), Pergamon Press, New York, Chapter II, pp. 94-158.

13. Nemat-Nasser, S., (1977) "On Nonequilibrium Thermodynamics of Continua: Addendum," Mechanics Today, Vol. 4, S. Nemat-Nasser (ed.), Pergamon Press, New York, Chapter VI, pp. 391-405.
14. DeAlba, P. S., Chan, C. K., and Seed, H. B., (1975) "Determination of Soil Liquefaction Characteristics by Large-Scale Laboratory Tests," NUREG-0027, NRC-6, Shannon and Wilson, Inc., and Agbabian Assoc., Seattle, Washington, Sept. 1976, prepared for the U.S. Nuclear Regulatory Commission under Contract Number AT(04-3)-954; manuscript completed May, 1975; see also EERC Report 75-14, Univ. Calif. Berkeley, CA.
15. Youd, T. L., (1970) "Densification and Shear of Sand during Vibration," Journal of the Soil Mechanics and Foundations Div., ASCE 96 #SM3, pp. 863-880.
16. Youd, T. L., (1972) "Compaction of Sands by Repeated Shear Straining," Journal of the Soil Mechanics and Foundations Div., ASCE 98 #SM7, pp. 709-725.
17. Yoshimi, Y., and Oh-Oka, H., (1975) "Influence of Degree of Shear Stress Reversal on the Liquefaction Potential of Saturated Sand," Soils and Foundations, 15 #3, pp. 27-40.
18. Peacock, W. H., and Seed, H. B., (1968) "Sand Liquefaction under Cyclic Loading Simple Shear Conditions," Journal of the Soil Mechanics and Foundations Div., ASCE 94 #SM3, pp. 689-708.
19. Hardin, B. D., and Drnevich, V. P., (1972) "Shear Modulus and Damping in Soils: Design Equations and Curves," Journal of the Soil Mechanics and Foundations Div., ASCE 98 #SM7, pp. 667-692.

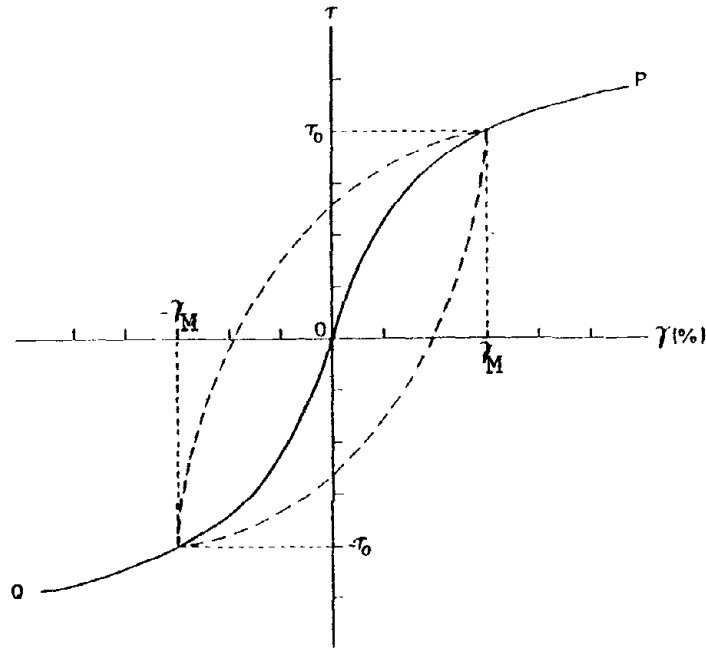


Fig. 1. A typical maximum shear stress - shear strain curve in cyclic shearing (from Hardin and Drnevich (19)).

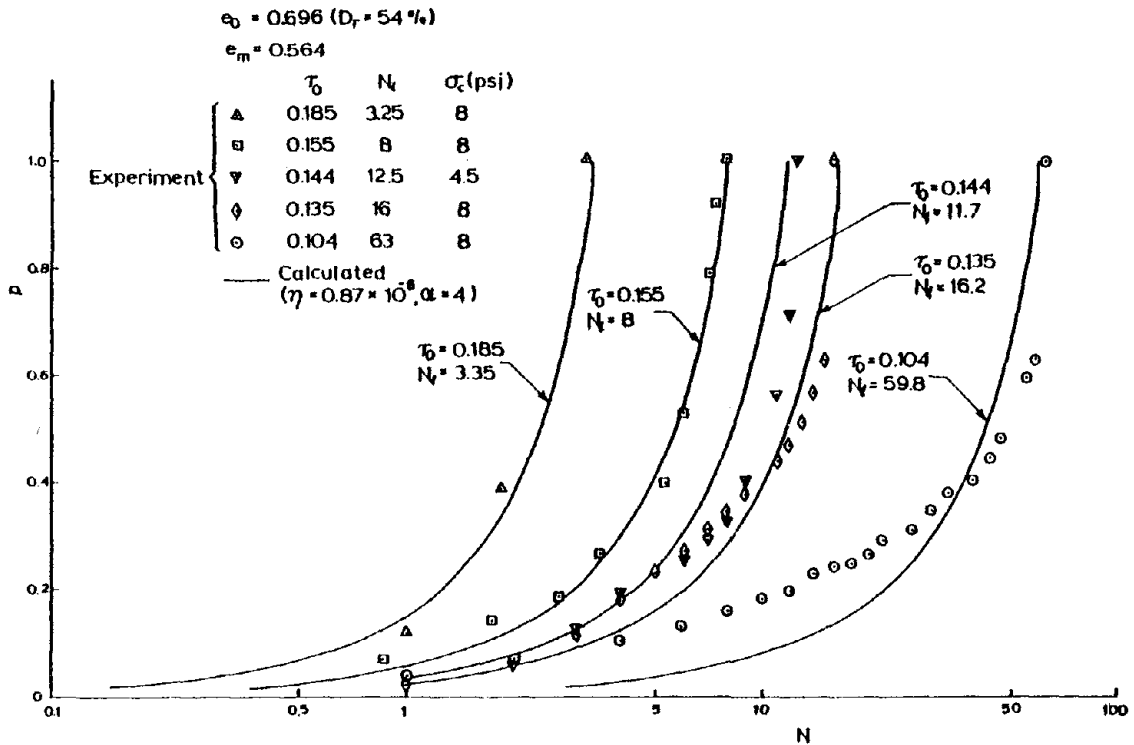


Fig. 2. Normalized excess pore water pressure p versus number of cycles in cyclic shearing of undrained saturated sand (data from DeAlba *et al.* (14)).

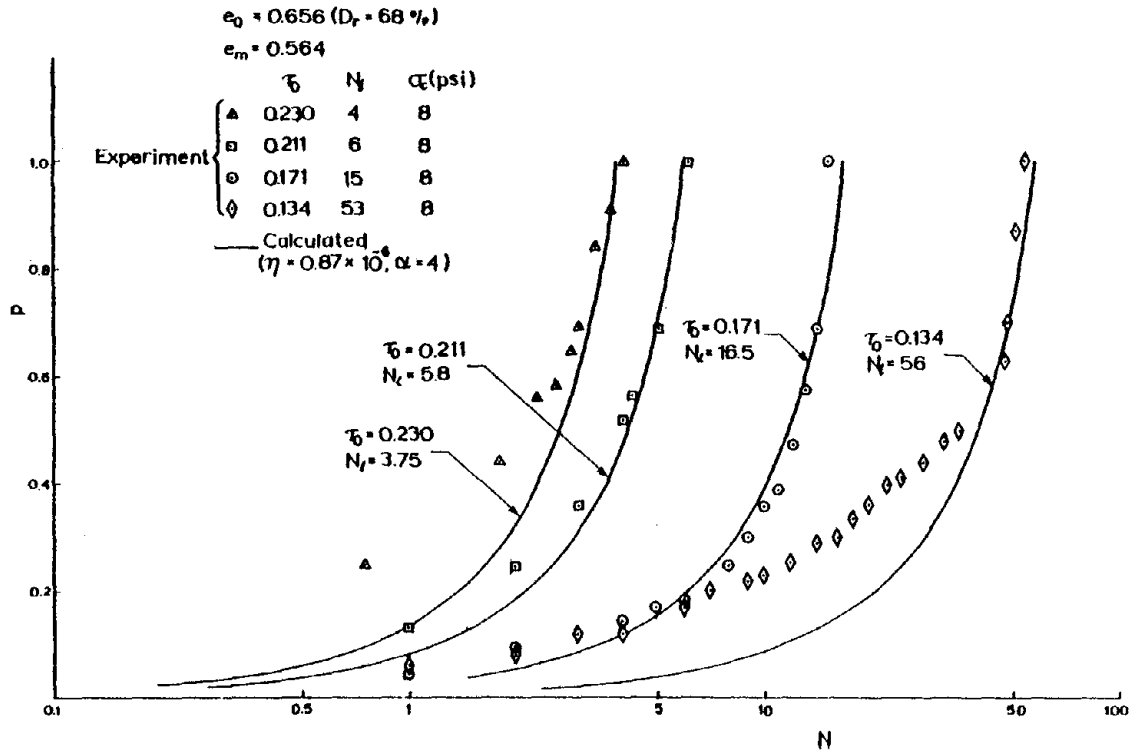


Fig. 3. Normalized excess pore water pressure p versus number of cycles in cyclic shearing of undrained saturated sand (data from DeAlba et al. (14)).

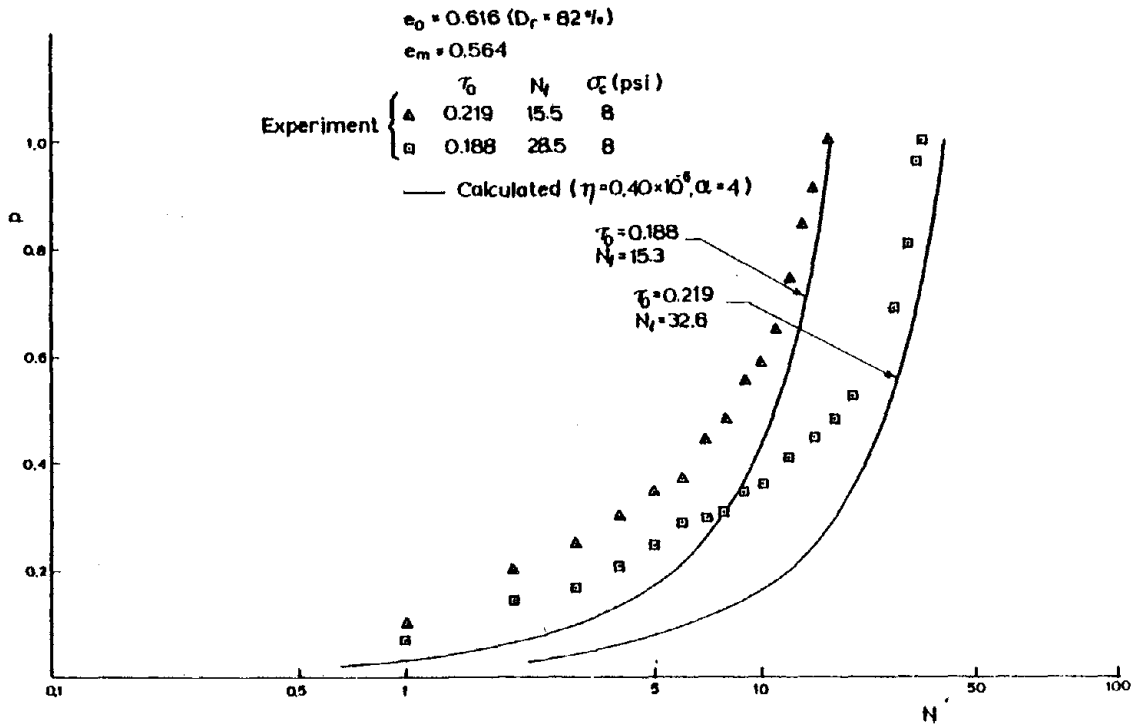


Fig. 4. Normalized excess pore water pressure p versus number of cycles in cyclic shearing of undrained saturated sand (data from DeAlba et al. (14)).

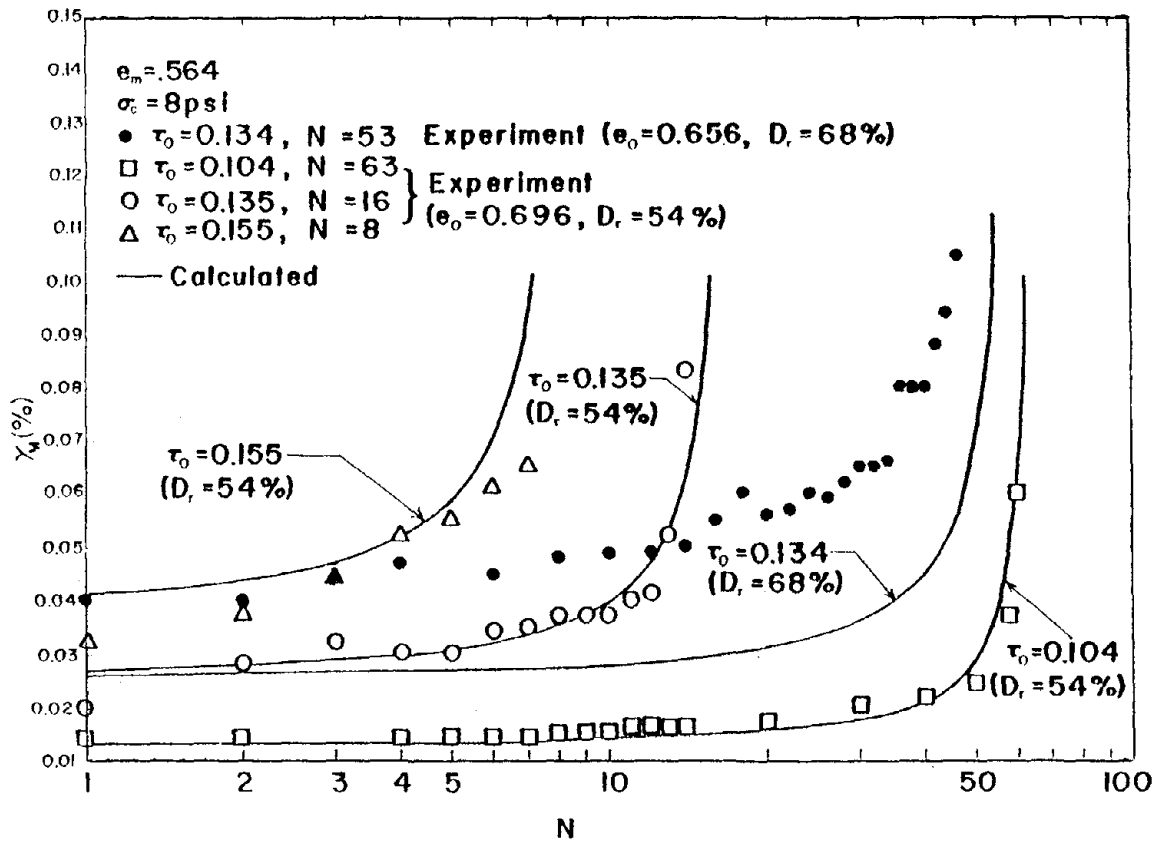


Fig. 5. Strain amplitude vs. number of cycles in cyclic shearing of undrained saturated sand (data from DeAlba *et al.* (14)).

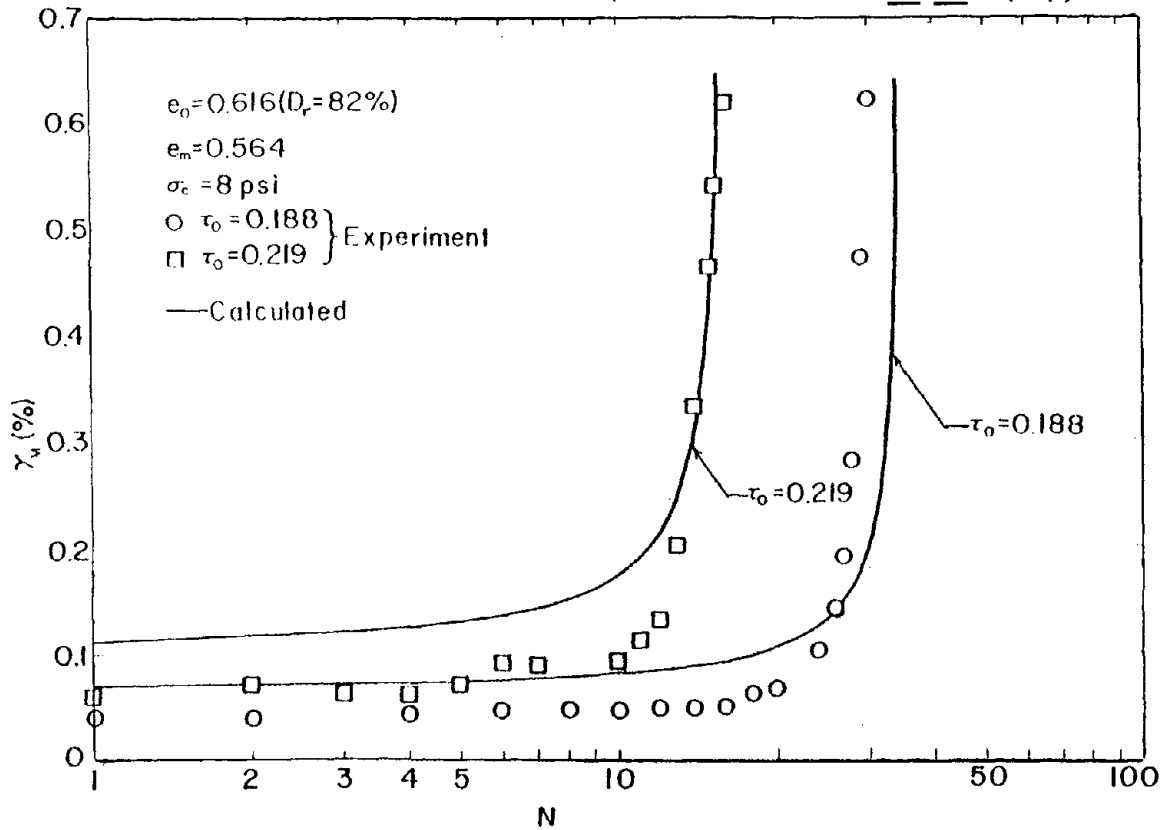


Fig. 6. Strain amplitude vs. number of cycles in cyclic shearing of undrained saturated sand (data from DeAlba *et al.* (14)).

970

INTENTIONALLY BLANK

A STUDY OF SHEAR DEFORMATION PROCESS OF SANDY SOILS
BY THE OBSERVATION OF ACOUSTIC EMISSION RESPONSE

by

K. Tanimoto,^I M. Nishi^{II} and T. Noda^{III}

ABSTRACT

Acoustic emission in triaxial soil samples is observed to make clear their shear processes to failure on the basis of the characteristics of acoustic emission. Acoustic emission is supposed to be generated from inter-particle friction during shear, and the patterns of acoustic emission or emission count may have some connections with the growth of shear strain or time to failure. Also, acoustic emission may be related with work dissipated in friction during shear. This paper is to seek these relationships from two series of tests, strain controlled and stress controlled, under various confined stresses and soil conditions. The followings are obtained from the study. The correlation between time to failure and emission rate, defined by the patterns of emission count, is linear on log-log scale as seen in a previous paper (1). The recent data on some different soils substantiate this linear correlation. Also, accumulated emission count monitored during a specified period of time is proportional to accumulated work done by external stresses during the same period, taken instead of work dissipated in friction.

INTRODUCTION

Most materials when subjected to certain stresses emit acoustic energy. This phenomenon is called acoustic emission or microseismic activity. The techniques of monitoring acoustic emission have been widely used in the studies of various materials, such as rocks (2, 3, 4), metals (5, 6), woods, plastics, etc., in connection with instability within such materials under certain stresses. However, only a limited number of research work in soil engineering (7, 8, 9) has so far been reported.

This paper succeeds the previous one on the characteristics of acoustic emission from soils during triaxial shear, and discusses shear deformation process in more detail on the basis of the pattern of acoustic emission monitored in triaxial tests conducted under various confined stresses and soil conditions.

TEST PROCEDURES

The acoustic emission monitoring system used in this research is as seen in Fig. 1. The triaxial compression test apparatus shown is for strain control tests, and is modified to allow stress control tests when necessary. A piezoelectric transducer, fixed in the base plate of the triaxial apparatus. Emissions monitored by the transducer is amplified and kept in a

I Professor of Civil Engineering, Kobe University, Kobe, Japan
 II Associate Professor of Civil Engineering, Kobe University, Kobe, Japan
 III Director of Soil Consultants Co. Ltd., Osaka, Japan

data recorder which can replay at a suitable speed for the analyses of the data.

Test soils are sands and mixed soils, and their grain-size distribution curves are given by Fig. 2. Two series of tests, strain controlled and stress controlled, are carried out under drained condition for unsaturated samples of 5 cm in diameter and 12 cm in height. Volume change of samples during shear is measured, in recent tests, by strain gages put on steel tapes in contact with the samples. Test conditions are summarized in Table 1.

Table 1. Test conditions

Type of test	Strain control	Stress control
Loading speed		0.02~1.22 kg/cm ² /min
Strain rate	0.016~3.36 %/min	
Confined stress (kg/cm ²)	0.5, 1.0, 1.5	0.5, 1.0, 1.5
Test soils	K-1 through K-5	K-1
Water content (%)	0~14	0~14
Dry density (g/cm ³)	1.51~1.83	1.53~1.75
Transducer	DC~40 kHz	
Pre-main amplifier	60 dB, 100 kHz - 3dB	
Data recorder	Max. 15 ips, 10 ² ~6 × 10 ⁴ Hz ± 3dB	
Digital rate meter	Discr. 0~5 v, Sample rate 1~60 sec.	

TYPE OF LOADING AND EMISSION COUNT DURING SHEAR

Acoustic emission observed during tests is a group of transient vibrations of various amplitudes and frequencies. Fig. 3 is an example of the power spectra of emissions monitored in the midst stage of shear process. From this and other similar data, it is noted that the dominant range of frequency is 0 to 13 kHz, though it may change with confined stress and the loading stage of axial stress.

Fig. 4 shows the variation of emission count per minute with strain growth obtained in a stress control test. As seen in this figure, emission count depends on the level of discrimination or the gain of amplification to be employed. However, it is also recognized that the pattern of variation is similar to one another. In the following, almost all of the data of emission count are given at the discrimination level of 1.0 volt at the input to the digital rate meter.

It is also noted in Fig. 4 that emission count per minute N_t increase slowly with increase in axial strain until the strain attains a certain magnitude, and promptly increase after exceeding that value, indicating that the overall process is made of two distinct processes. The rapid increase in emission count in the latter process may be related to the quick rate of strain immediately before failure.

A typical example of the plots of emission count on a stress-strain diagram in strain control test is given by Fig. 5. It is seen that the emission count increases with the strain growth during the first process and becomes nearly constant during the second process. It seems that steady state interparticle friction occurs during the latter process.

Fig. 6 is a result obtained in a special test under repetitive loading with gradually increasing peak loads. Of interest is that the emissions can be monitored only in the virgin state of loading and few emissions are observed in the range of pre-loading. Such phenomenon is called the Kaiser effect in the study of acoustic emission of metals, rocks, etc.

RELATIONSHIP BETWEEN ACOUSTIC EMISSION AND TIME TO FAILURE

In granular soils under shear, acoustic emission is supposed to be generated from interparticle friction at relatively low energy level in the beginning of shearing, and at relatively high energy level when failure is imminent. Therefore, it may be possible to predict time to failure by the characteristics of acoustic emission monitored halfway in the test.

The correlation of time to failure with an index, emission rate, was explored in the previous paper (1). Fig. 7 is the results supplemented by many tests recently done on various soils, where time to failure t_f is measured from the start of tests and emission rate, R , is defined by

$$R = \Delta N / N_1, \quad (1)$$

where ΔN : emission count observed in a small period of time (30 sec in the present) directly after the end of the first process, and
 N_1 : total emission count observed during the first process.

Fig. 7 shows that the correlation between t_f and R is linear, regardless of the confined stress, the rate of strain, water content and dry density of samples as far as the present tests are concerned. Of more importance is that this correlation is hardly affected by the sensitivity of monitoring apparatus and a discrimination level employed. The regression line for the correlation is approximately expressed by

$$\log_{10} t_f = -0.98 \log_{10} R + 2.36, \quad (2)$$

where t_f is measured in minute.

In the previous paper, similar correlation is given for stress control tests, as seen in Fig. 8. Emission rate in this case is defined in the corner of the figure. This correlation is also linear, regardless of the rate of loading and soil conditions. The regression line is given by

$$\log_{10} t_f = -0.88 \log_{10} R + 2.30, \quad (3)$$

and both the equations (2) and (3) are not much different from each other.

RELATIONSHIP BETWEEN ACOUSTIC EMISSION AND WORK DISSIPATED IN FRICTION

When a triaxial sample is placed under increments in axial and radial

strains $\delta \epsilon_1$ and $\delta \epsilon_3$, respectively, the work per unit volume, δE , done on the sample by axial and radial stresses, σ_1' and σ_3' , respectively, can be expressed by

$$\delta E = \sigma_1' \delta \epsilon_1 + 2 \sigma_3' \delta \epsilon_3 \quad (4)$$

If volumetric strain $\Delta V / V_0$ is expressed by ν , the increment in volumetric strain $\delta \nu$ is equal to $\delta \epsilon_1 + 2 \delta \epsilon_3$. Then eq. (4) is rewritten as

$$\begin{aligned} \delta E &= \sigma_1' \delta \epsilon_1 + \sigma_3' (\delta \nu - \delta \epsilon_1) \\ &= (\sigma_1' - \sigma_3') \delta \epsilon_1 + \sigma_3' \delta \nu \end{aligned} \quad (5)$$

The term δE is the sum of the increment in internal energy, δU , and the work dissipated in friction, δW . Therefore,

$$\delta W = (\sigma_1' - \sigma_3') \delta \epsilon_1 + \sigma_3' \delta \nu - \delta U \quad (6)$$

However, the internal energy is difficult to estimate during shear process and also may be negligibly small as compared with the work dissipated in friction. Therefore, total energy transmitted across the boundary of samples, δE , is employed in this stage to correlate with acoustic emission.

Fig. 9 illustrates some notations to be used for the correlation between acoustic emission and work done in the following. Accumulated acoustic emissions during the first and the second process in strain control tests are denoted by N_1 and N_2 , respectively, and the sum of N_1 and N_2 by N_T . Similarly, E_1 , E_2 and E_T are used as the notations of work done.

The relationship between E_i and N_i and that between E_T and N_T are shown in Fig. 10. It is noted from the figure that the accumulated emission count is roughly proportional to the accumulated work done during the same period. The data presented here may not be enough to discuss closely the relationship, and also there may be some errors in the measurement of volume change. Accordingly, the results should be supplemented by further tests under various soil and stress conditions.

CONCLUSIONS

A study of acoustic emission with concentration on sandy soils is done with triaxial compression test apparatus to make clear shear deformation process of such soils on the basis of the characteristics of acoustic emission.

From the test results described in the above, it may be temporarily concluded that:

Acoustic emission monitored in this research is internally generated sound during triaxial shear of soils. Emissions are a group of transient vibrations of various amplitudes and frequencies, and emission count depends on a discrimination level to be set up.

The growth of shear strain to failure is composed of two distinctly different processes, though of different forms for each of strain control tests and stress control tests, in view of the characteristics of acoustic

emission. The correlation between time to failure and emission rate is obtained in the previous paper, and the results of tests recently performed in a manner of strain control method on various soils substantiate the previous results.

Acoustic emission is supposed to be generated from interparticle friction and may be related to energy dissipated in friction during shear. Accumulated emission count monitored during a specified period of time is roughly proportional to accumulated work, during the same period, done by external stresses taken in this stage instead of work dissipated in friction.

From the tests of soils under repetitive loading with gradually increasing peak loads, it is confirmed that emissions can be observed only in the virgin state of loading and few emissions are observed in the range of pre-loading. Accordingly, it may be concluded that the phenomenon called the Kaiser effect can be seen in soils, too.

ACKNOWLEDGEMENTS

Some of the test data described in this paper were already published in the previous paper, which was contributed by Messrs. H. Noguchi, A. Tanaka and Y. Nakashiba. The recent experiments were cooperated by Messrs. Y. Kyogoku and T. Matsushita, and the preparation for the manuscript by Mr. J. Nakamura. The authors wish to thank them for their assistance.

BIBLIOGRAPHY

1. Tanimoto, K. and T. Noda (1977). A Study of Acoustic Emission from Sandy Soils, Proc. 9th Int. Conf. Soil Mech. Found. Engrg., Vol. 1, pp. 315-318.
2. Mogi, K. (1962). Study of Elastic Shocks Caused by the Fracture of Heterogeneous Materials and its Relations to Earthquake Phenomena, Bull. Earthq. Res. Inst., Univ. of Tokyo, Vol. 40, pp. 125-173.
3. Sholz, C. H. (1968). The Frequency-Magnitude Relation of Microfracturing in Rock and its Relation to Earthquake, Bull. Seism. Soc. of Ame., Vol. 58, No. 1, pp. 399-415.
4. Hardy, H. R. Jr. (1973). Microseismic Techniques-Basic and Applied Research, Rock Mech., Springer-Verlag, Suppl. 2, pp. 93-114.
5. Gerberich, W. W. and C. E. Hartbower (1967). Some Observations on Stress Wave Emission as a Measure of Crack Growth, Int. Jnl. of Fracture Mech., Vol. 3, pp. 185-192.
6. Tetelman, A. S. and R. Chow (1972). Acoustic Emission and Microcracking Processes, Acoustic Emission, Ame. Soc. Test. Mat., STP-505, pp. 30-40.
7. Hakuno, M. et al. (1969). Analysis of Noise Generated by Sand Particles when They Slide, Trans. Jap. Soc. Civ. Engrs., No. 164, pp. 51-58. (in Japanese)

8. Koerner, R. M. and A. E. Lord Jr. (1972). Acoustic Emission in Medium Plasticity Clayey Silt, Proc. Ame. Soc. Civ. Eng., Vol. 98, No. SM 1, pp. 161-165.
9. Koerner, R. M., A. E. Lord, Jr., W. M. McCabe and J. W. Curran, Acoustic Emission Behavior of Granular Soils, Proc. Ame. Soc. Civ. Eng., Vol. 102, No. GT7, pp. 761-773.

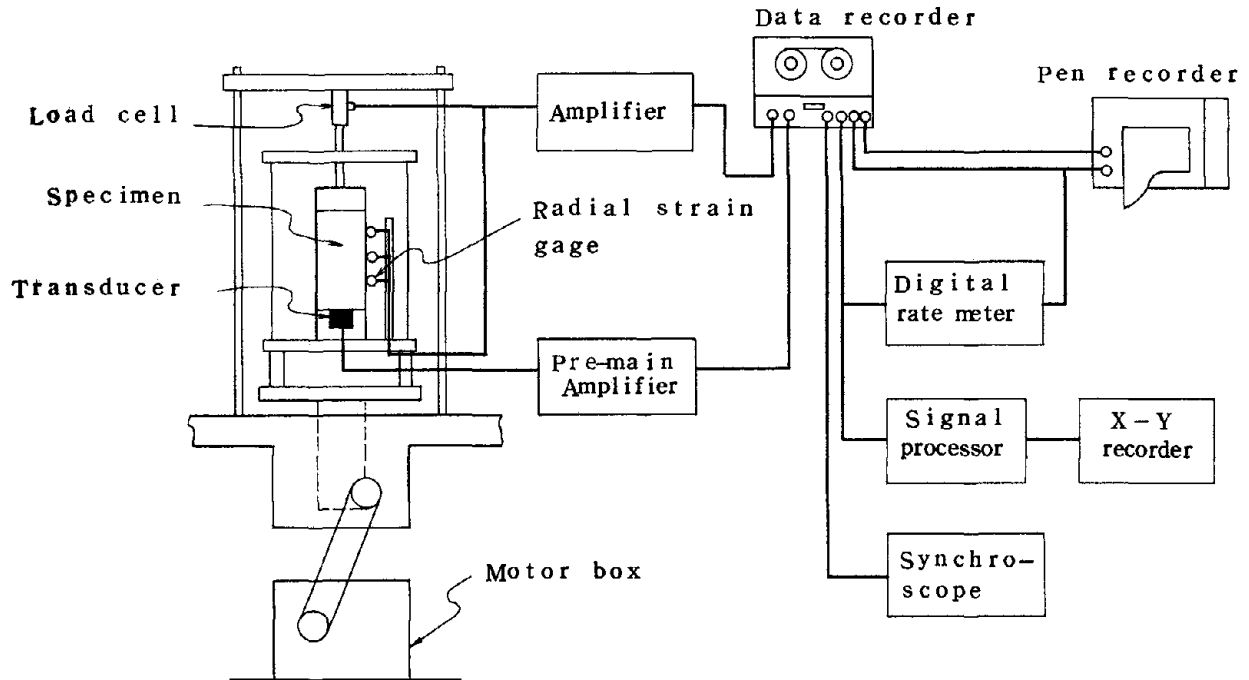


Fig. 1. Acoustic emission monitoring system for a triaxial sample.

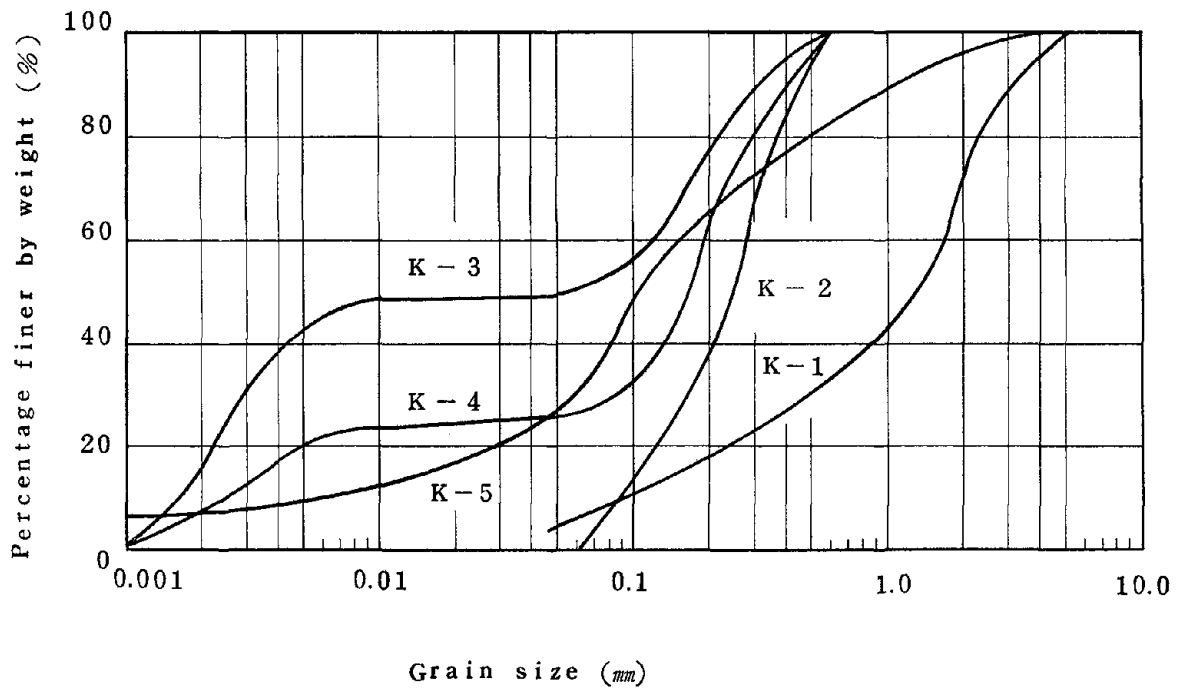


Fig. 2. Grain-size distribution curves of test soils.

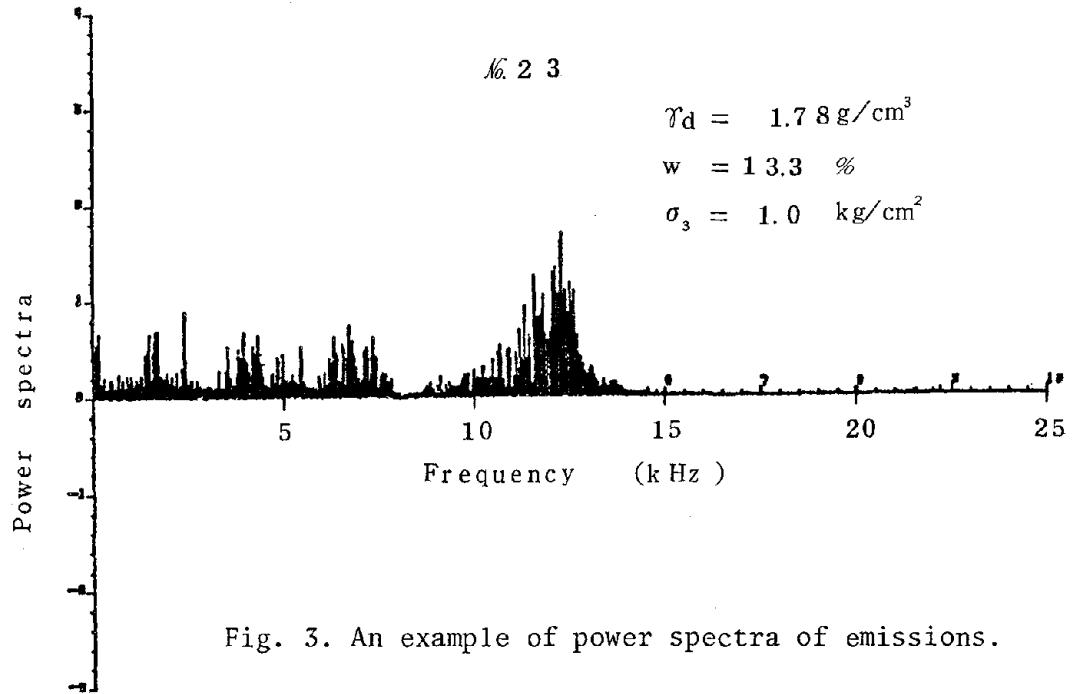


Fig. 3. An example of power spectra of emissions.

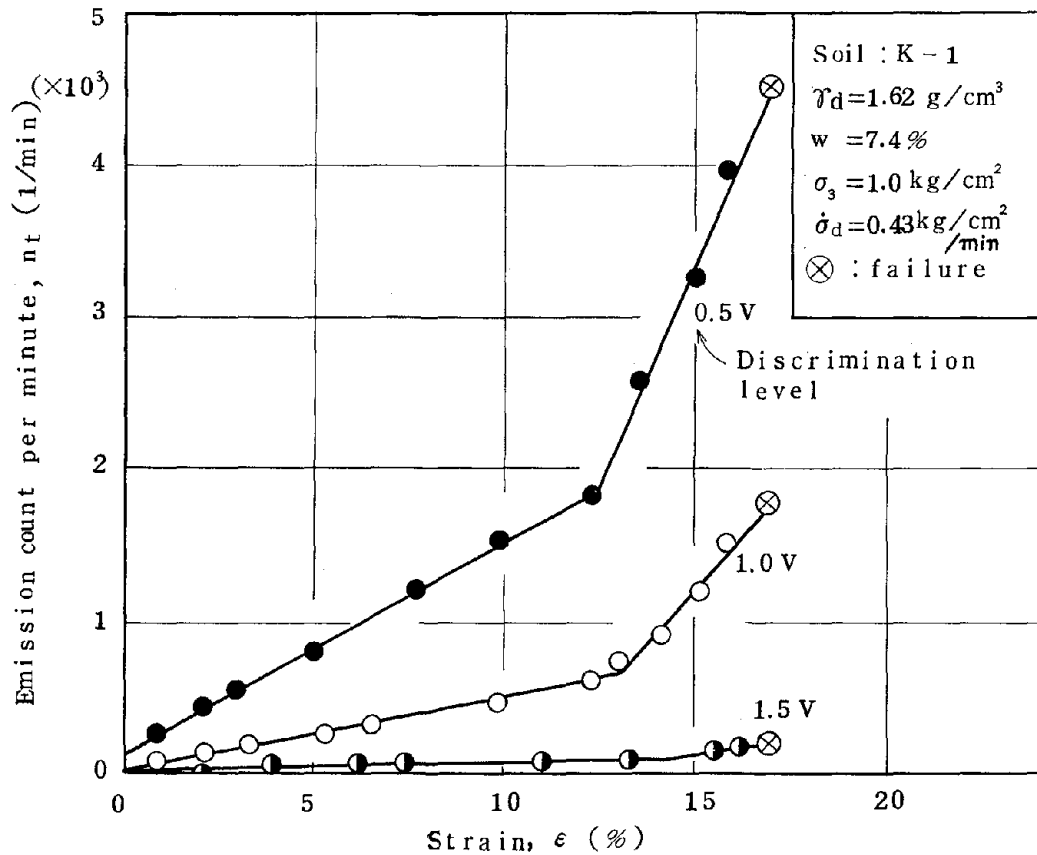


Fig. 4. Emission count and strain relationship for three levels of discrimination in a stress control test.

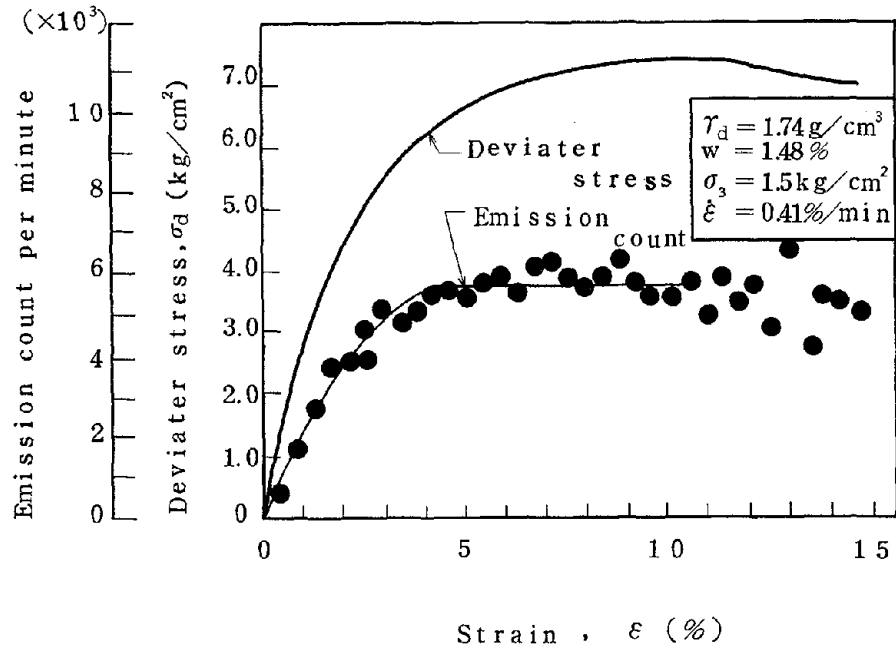


Fig. 5. Emission count per minute, deviator stress and axial strain relationship in a strain control test.

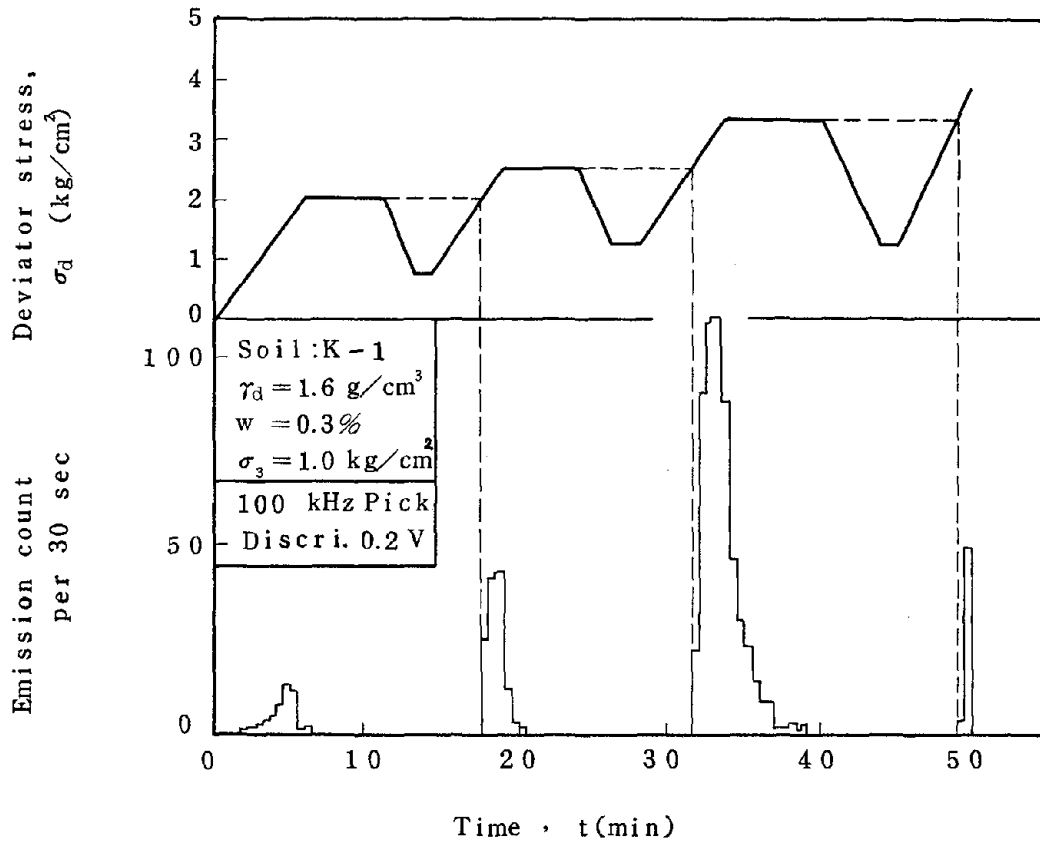


Fig. 6. Emission count in a repetitive loading test.

Test conditions:

strain rate 0.016~3.36 %/min
 confined stress 0.5, 1.0, 1.5 kg/cm²
 soils K-1~K-5
 water content 0~14 %
 dry density 1.51~1.83 g/cm³

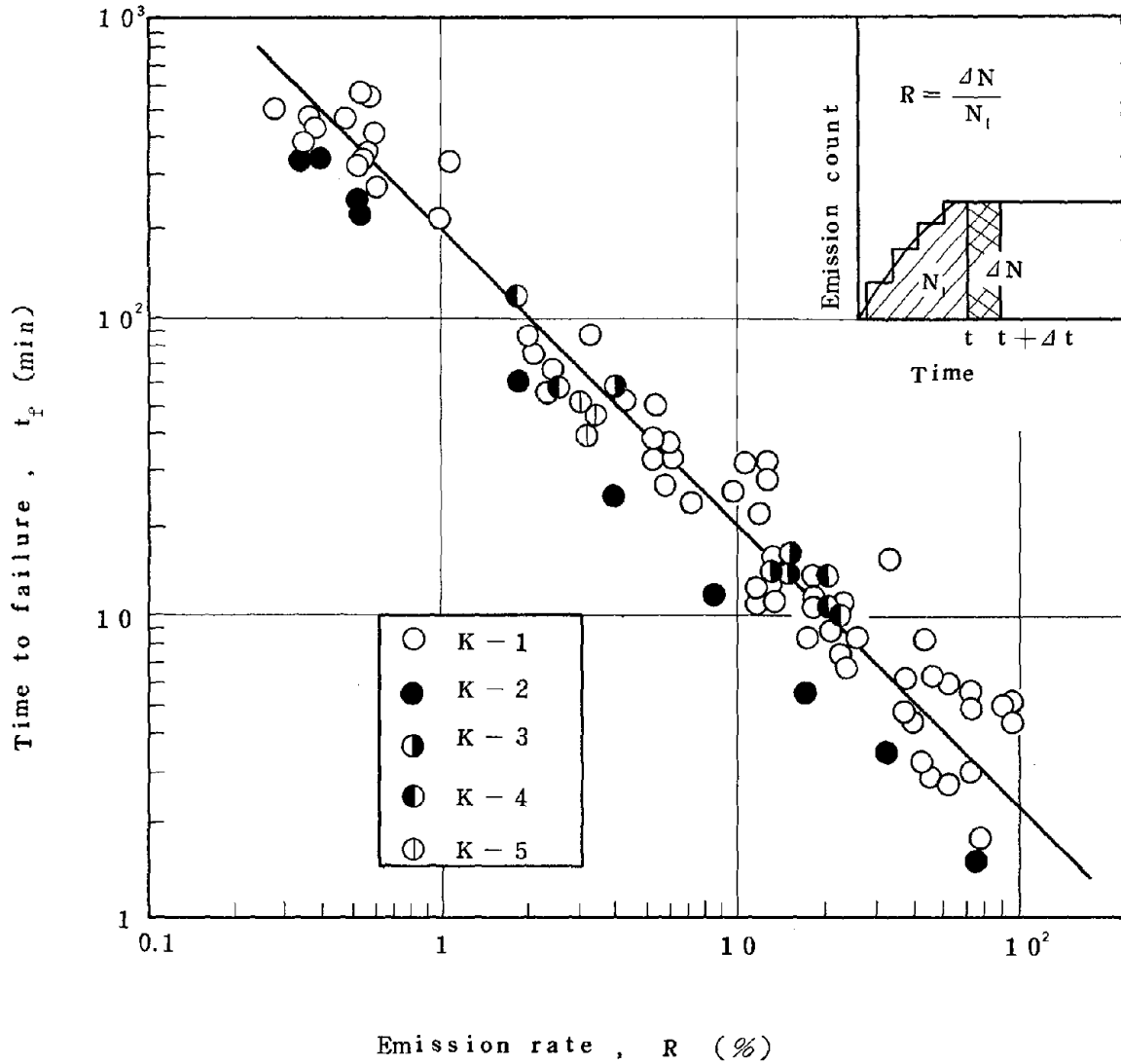


Fig. 7. Time to failure and emission rate relationship in strain control tests.

Test conditions:

loading speed	0.22~1.22 kg/cm ² /min
confined stress	0.5, 1.0, 1.5 kg/cm ²
soil	K-1
water content	0~14 %
dry density	1.53~1.75 g/cm ³

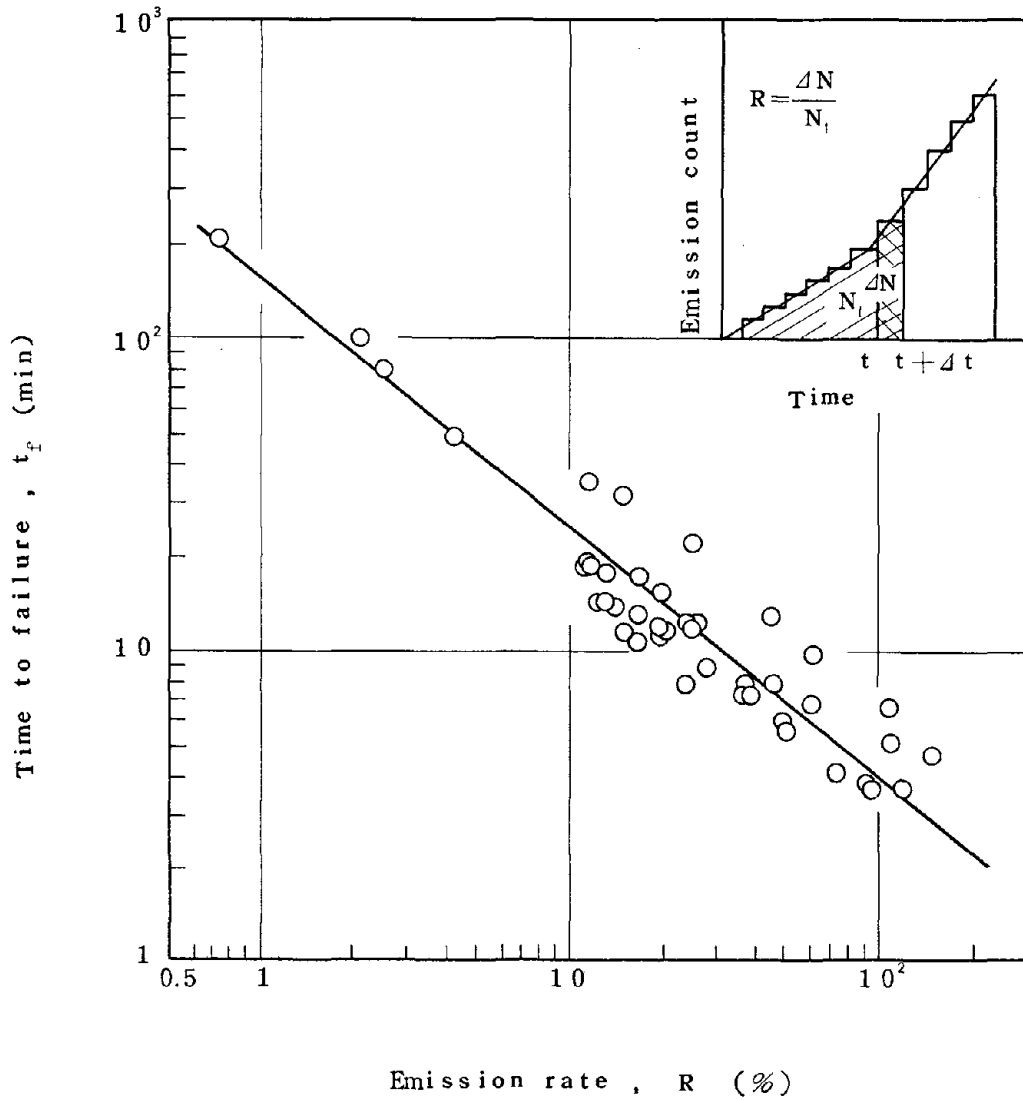


Fig. 8. Time to failure and emission rate relationship in stress control tests.

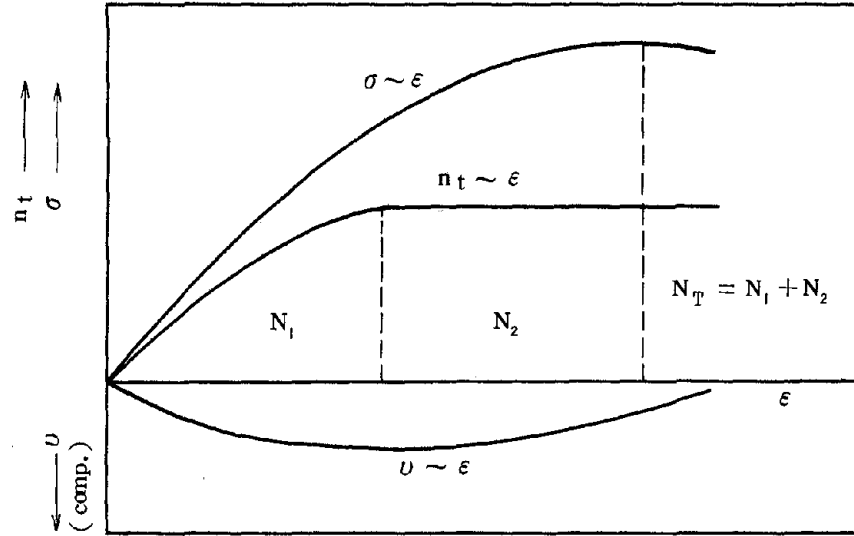


Fig. 9. Illustration of notations.

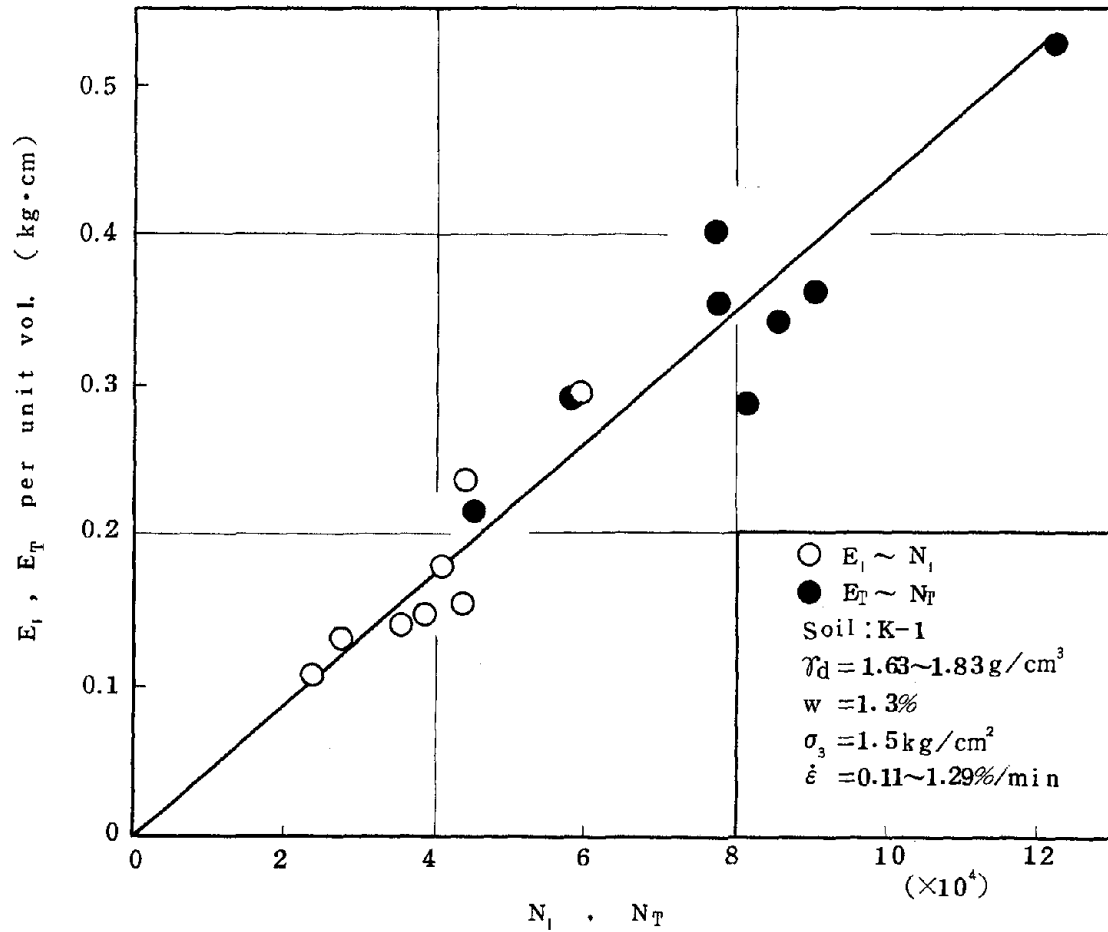


Fig. 10. $E_1 \sim N_1$ relationship and $E_T \sim N_T$ relationship.

GEOTECHNICAL DATA AT SELECTED STRONG

MOTION ACCELEROGRAPH STATION SITES

by

W. Paul Grant^I, I. Arango^{II}, and D.N. Clayton^{III}

ABSTRACT

In the period from 1975 to 1978 the subsurface conditions at over 70 accelerograph stations in the United States were investigated. The results of these studies are contained in a series of reports to the U.S. Regulatory Commission. The format of these data reports is summarized in this paper. Since many of the accelerograph stations that were studied are located in southern California the subsurface conditions at selected sites in the Los Angeles basin is discussed. For study purposes, all of the sites that were investigated were organized into three groups depending upon the depth to bedrock or "rock-like" material: a) rock at or within 30 feet of the ground surface, b) rock within 50 to 200 feet of the surface, c) rock at a depth greater than 300 feet. The significance of this grouping scheme is discussed and use of this system is illustrated in plots of peak ground motion for the two extreme data groups. The basic trends of the data plotted in this manner are briefly discussed.

INTRODUCTION

The influence of local soil conditions upon ground response recorded at accelerograph stations during earthquakes has been widely recognized and studied by various investigators (1-6). Unfortunately, there is little detailed information available on the subsurface conditions of many of these accelerograph stations, and previous investigators have had to base their studies on sketchy subsurface data or on general geologic maps. Without detailed site information, an accurate evaluation of the influence of local soil conditions upon ground response to earthquakes may not be possible.

To provide an increased understanding of the effect of local soil conditions on earthquake response, the joint venture of Shannon & Wilson, Inc. and Agbabian Associates (SW-AA) has undertaken a study of the subsurface soil conditions at over 70 accelerograph stations. This particular study is part of an overall research program into the evaluation of soil behavior under earthquake loading conditions. This research program is funded by the U.S. Nuclear Regulatory Commission in their desire to improve the earthquake design criteria for nuclear power plants.

^I Associate Engineer, Shannon & Wilson, Inc., Seattle, WA.
^{II} Senior Project Engineer, Woodward-Clyde Consultants, San Francisco, CA.
^{III} Senior Geologist, Shannon & Wilson, Inc., Seattle, WA.

SITE INVESTIGATIONS

The general locations of the stations which were investigated are shown in Fig. 1. The criteria for selecting the stations for study included the number of significant accelerograms recorded at the station, the use of the accelerogram by others in design, and the estimated potential of the station for recording future earthquakes. Of the stations that were studied, 67 sites (88%) are located in California. Approximately 80% of the California sites are located in the southern portion of the state and have recorded the San Fernando earthquake. Thus sites in southern California account for most of the stations that were investigated and have the heaviest contribution to the earthquake data set.

The site investigations fall under two main categories as listed in Table I: soil sites and rock sites. The soil site investigations are studies in which borings were advanced at the individual accelerograph stations or within the vicinity of several sites. The rock site investigations are studies of the subsurface conditions at accelerograph stations which are regarded by others (1,3,5 & 6) as being founded on rock. Differing from the soil site studies, borings were generally not advanced at the rock site stations. Instead, the subsurface conditions at these locations were evaluated from foundation reports and logs of borings made by others in the area and from a surface geological reconnaissance performed at each site. Generalized data on the site conditions at all of the stations investigated to date has been compiled and presented in a Summary Report (15).

The reports listed in Table I generally follow the same format of data presentation. The main text of the report presents information on the station housing structure, Geology of the area, and local site conditions. Following the main text are three appendices which contain information on the earthquakes which have been recorded at the site, details on the field explorations and the results of the laboratory testing program.

Data on the subsurface conditions disclosed in the soil site investigations is generalized into the format illustrated in Fig. 2. The extreme left portion of the figure contains the field log of the boring advanced at the site. Immediately to the right are summary tables and plots of the static engineering properties of the soil. The dynamic properties of the soil, as determined by field geophysical tests and laboratory resonant column and cyclic triaxial tests, are presented in the right hand portion of the figure.

At eight of the soil sites, in situ impulse geophysical testing was conducted in addition to a conventional downhole geophysical survey. Whereas downhole geophysical testing is commonly used to measure shear wave velocities at low amplitudes of shear strain (10^{-4} %), the in situ impulse technique allows velocity measurements at both low and high levels of shear strain. This testing technique is basically a modified cross-hole method of geophysical exploration utilizing equipment and test procedures developed by the SW-AA joint venture for the U.S. Nuclear Regulatory Commission with details discussed elsewhere (16). Typical results from the testing technique are summarized in Fig. 2.

FINDINGS

Site Conditions in the Los Angeles Basin

Since the majority of sites which were investigated are located in southern California, an overview of the subsurface conditions of the Los Angeles basin sites is in order. The following summarizes our findings of site conditions in this area.

The locations of the sites investigated within the Los Angeles area are indicated in Fig. 3. The majority of sites are located on or near Wilshire Blvd. which runs in a westerly direction from the downtown area. Of the remaining sites, most are located north of the downtown area.

As indicated in Fig. 3, seven borings were advanced in our investigation of the Los Angeles sites. Accelerograph station locations which are not in the vicinity of one of our borings were investigated through means of a geologic reconnaissance and available soils and foundation reports for the building and surrounding area.

A generalized geologic cross-section of the Los Angeles basin, represented as line A-A' in Fig. 3, is presented in Fig. 4. This section indicates that the downtown area is situated in a region of uplifted sedimentary rocks of Miocene and Pliocene age. These beds dip to the southwest where a veneer of unconsolidated Quaternary sediments generally mantles the Pliocene and Miocene strata.

Based upon the results of the geophysical and laboratory testing programs conducted for the Los Angeles sites, it is concluded that the Miocene and Pliocene strata in the downtown area behave more like stiff clay than rock. That is, the shear wave velocities and shear strength values of these deposits are closer to those of a stiff soil rather than a competent sandstone or shale.

Summarized in Fig. 5 are the shear wave velocities which were measured in the Los Angeles area. All measurements were performed using downhole geophysical testing techniques. Based on this limited data the following may be concluded. First, there is a minor but consistent difference in the strength and consequently shear wave velocity of the Miocene and Pliocene strata, in that the sedimentary deposits of Miocene age are slightly stronger than those of Pliocene age. Secondly, the downhole shear wave velocities obtained within both strata are generally low for "rock" above a depth of about 200 feet. Below this, the measured values from both strata approach 2000 to 2500 fps. These higher values at depth are considered to be more typical of soft rocks. Consequently, the dynamic behavior of these materials may be more similar to that of stiff or hard clay and silts than to that of rock.

Site Classifications

The Summary Report (15) includes information on the subsurface conditions of all the stations that were investigated between 1975 and 1978. As an illustration of how this data may be used to study the effects of local soil conditions upon earthquake response, the Summary Report contains a classification system which allows interpretation of the data into three categories based on subsurface conditions at the sites. The common denominator in the classification system is the depth to rock or

"rock-like" material beneath the site. This system is similar to that used by Seed et al. (1) in which "rock-like" material is considered to have a shear wave velocity greater than about 2500 fps. The three groups of the classification system are as follows:

1. Rock sites - Where rock was encountered within about 30 feet of the ground surface.
2. Stiff soil sites - Where rock was overlain by less than about 200 feet of stiff clay, sand or gravel.
3. Deep soil sites - Where rock was overlain by at least 300 feet of soils.

Each of the 76 sites discussed in the data reports was reviewed in an attempt to place it within the classification system and the results are presented in Table II. This review was conducted jointly by Professor H. Bolton Seed of the University of California, Berkeley, and the first two authors. In instances where the site conditions were not clearly within one grouping, the site was assigned a dual classification such as stiff soil/rock, where the first classification would indicate the consensus of our opinion. In other cases where the data was insufficient to make a meaningful classification, the site classification was omitted.

Data Trends

Using the site classification system described above, plots of attenuation of peak ground acceleration, velocity and displacement were prepared and are presented in Figs. 6, 7 and 8, respectively. Most of the rock site data in these plots correspond to recordings of the San Fernando earthquake. All of the peak ground motions are plotted according to epicentral distance without consideration to the azimuth of the station location.

These figures indicate that the peak velocities and displacements at deep soil sites are greater than those of rock sites. Acceleration peaks of the deep soil sites may be greater or less than those of rock sites depending upon the epicentral distance of the recording station.

SUMMARY

The subsurface conditions at over 70 accelerograph stations have been investigated and presented in a series of data reports (7-14) and a summary report (15) to the U.S. Nuclear Regulatory Commission. The purpose of the study was to provide data on the stations which would serve as a basis for interpreting the effects of local soil conditions upon ground response to earthquakes. To facilitate interpretation of the data, a classification scheme was devised which would separate the sites into three categories based upon subsurface conditions. An example of the use of this system is demonstrated in the data plots of peak ground motions (Figs. 6, 7 & 8) for the two extreme site categories. Further research into earthquake ground motions utilizing this classification system may provide refinement to seismic design regarding the effects of local site conditions.

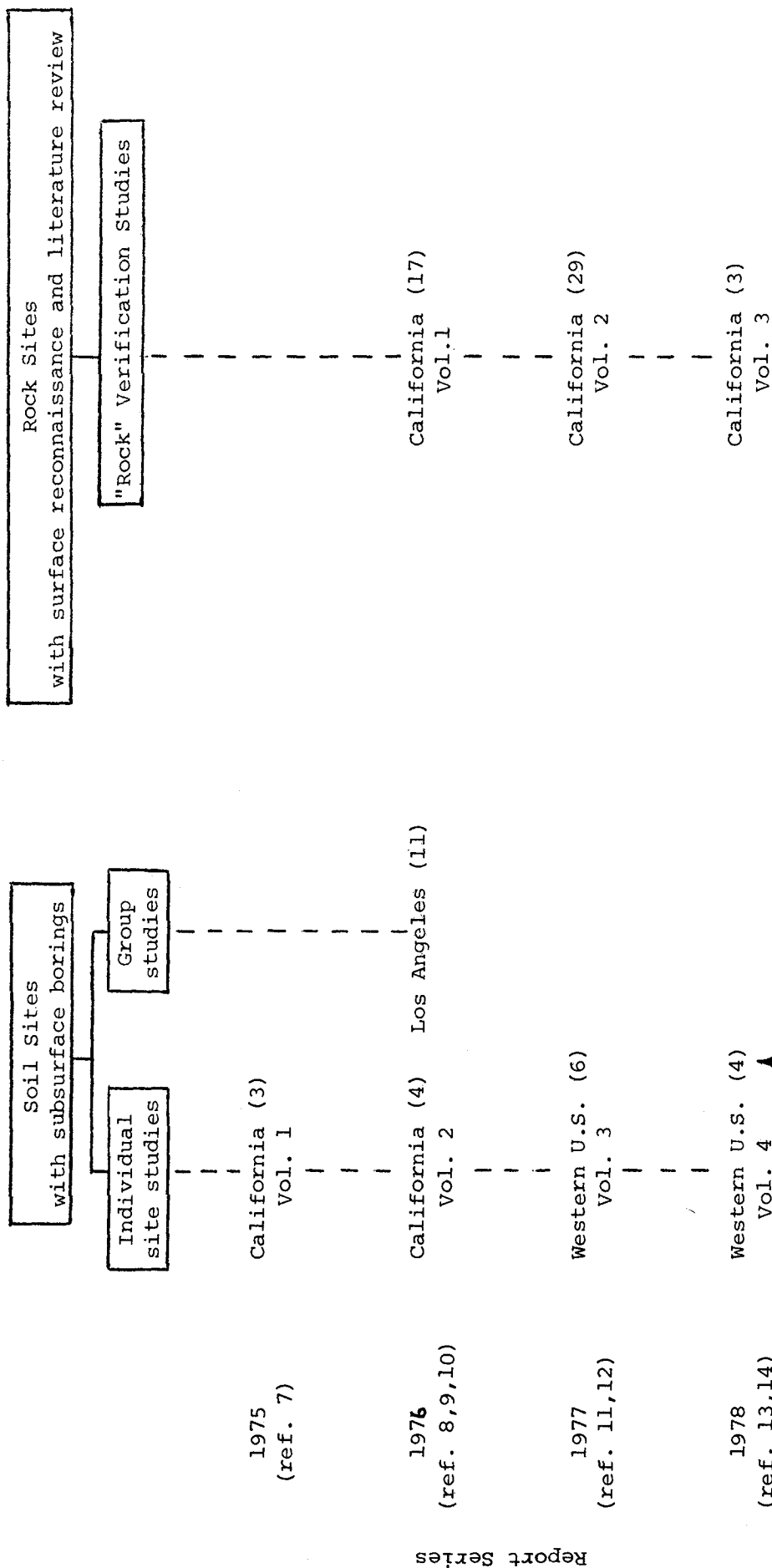
REFERENCES

1. Seed, H.B., R. Murarka, J. Lysmer and I.M. Idriss (1975)
"Relationships Between Maximum Acceleration, Maximum Velocity, Distance from Source and Local Soil Conditions for Moderately Strong Earthquakes," University of California, Berkeley, Earthquake Engineering Research Center, Report No. EERC 75-17.
2. Trifunac, M.D. (1976)
"Preliminary Analysis of the Peaks of Strong Earthquake Ground Motion - Dependence of Peaks on Earthquake Magnitude, Epicentral Distance, and Recording Site Conditions," Bulletin of the Seismological Society of America, Vol. 66, No. 1, p. 189-219.
3. Trifunac, M.D., and A.G. Brady (1975)
"On the Correlation of Seismic Intensity Scales with the Peaks of Recorded Strong Ground Motion," Bulletin of the Seismological Society of America, Vol. 65, No. 1, p. 139-162.
4. Trifunac, M.D., and A.G. Brady (1975)
"A Study on the Duration of Strong Earthquake Ground Motion," Bulletin of the Seismological Society of America, Vol. 65, No. 3, p. 581-626.
5. Seed, H.B., C. Ugas, and J. Lysmer (1974)
"Site-Dependent Spectra for Earthquake-Resistant Design," university of California, Berkeley, Earthquake Engineering Research Center, Report No. EERC 74-12.
6. Mohraz, B. (1976)
"A study of Earthquake Response Spectra for Different Geological conditions," Bulletin of the Seismological Society of America, Vol. 66, No. 3, p. 915-935.
7. Shannon & Wilson, Inc., and Agbabian Associates (SW-AA) (1975)
"Geotechnical and Strong Motion Earthquake Data from U.S. Accelerograph Stations, Vol. 1, Ferndale, Cholame, and El Centro, California," Report to the U.S. Nuclear Regulatory Commission, NUREG-0029, distributed by the National Technical Information Service, Springfield, Virginia, PB-257-234/5SL.
8. _____ (1976)
"Geotechnical and Strong Motion Earthquake Data from U.S. Accelerograph Stations, Vol. 2, Pasadena (CIT Millikan Library), Santa Barbara County Court House, Taft (Lincoln School Tunnel), and Hollister (Melendy Ranch Barn), California," Report to the U.S. Nuclear Regulatory Commission.
9. _____ (1976)
"Data from Selected Accelerograph Stations at Wilshire Boulevard, Century City, and Ventura Boulevard, Los Angeles, California," Report to the U.S. Nuclear Regulatory Commission, NUREG/CR-0074 NRC-6A.

10. _____ (1976)
"Verification of Subsurface Conditions at Selected "Rock" Accelerograph Stations in California, Vol. 1," Report to the U.S. Nuclear Regulatory Commission (unpublished).
11. _____ (1977)
"Geotechnical and Strong Motion Earthquake Data from U.S. Accelerograph Stations, Vol. 3, Gilroy, CA (Gavilan College - C6); Logan, UT (Utah State Univ.); Bozeman, MT (Montana State Univ.); Tacoma, WA (County-City Bldg.); Helena, MT (Federal Bldg. and Carroll College)," Report to the U.S. Nuclear Regulatory Commission (unpublished).
12. _____ (1977)
"Verification of Subsurface Conditions at Selected "Rock" Accelerograph Stations in California, Vol. 2," Report to the U.S. Nuclear Regulatory Commission (unpublished).
13. _____ (1978)
"Geotechnical and Strong Motion Earthquake Data from U.S. Accelerograph Stations, Vol. 4, Anchorage, AK (Alaska Methodist Univ.); Seattle, WA (Federal Office Building); Olympia, WA (Highway Test Lab.); and Portland, OR (State Office Bldg./Portland State Univ.)," Report to the U.S. Nuclear Regulatory Commission (unpublished).
14. _____ (1978)
"Verification of Subsurface Conditions at Selected "Rock" Accelerograph Stations in California, Vol. 3," Report to the U.S. Nuclear Regulatory Commission (unpublished).
15. _____ (1978)
"Geotechnical and Strong Motion Earthquake Data from U.S. Accelerograph Stations, Summary Report on the Stations Investigated During the Period 1975 - 1978," Report to the U.S. Nuclear Regulatory Commission (unpublished).
16. _____ (1974)
"In situ Impulse Test for Determination of Shear Modulus for Seismic Response Analyses, Progress Report" Report to the U.S. Nuclear Regulatory Commission, Distributed by the National Technical Information Service, Springfield, Virginia, TID-26813

TABLE I

SITE INVESTIGATIONS



Report Series

1975
(ref. 7)

1976
(ref. 8,9,10)

1977
(ref. 11,12)

1978
(ref. 13,14)

No. of stations included
in report

TABLE II
SITE CLASSIFICATION

<u>U.S.G.S.</u> <u>No.</u>	<u>Station Name</u>	<u>Category</u>	<u>Remarks</u>
<u>ALASKA</u>			
2702	Anchorage, AMU Gould Hall	SS	
<u>CALIFORNIA</u>			
108	Carbon Canyon Dam (Crest)	--	Omit - dam crest
110	Castaic, Old Ridge Route	SS	
111	Cedar Springs, Allen Ranch	R	
112	Cedar Springs, Pumphouse	SS/DS	
1013	Cholame-Shandon Sta. 2	DS/SS	
1438	Cholame-Shandon, Temblor	R	
114	Costa Mesa, 666 W. 19th	SS	
1027 (991)	Edmonston Pumping Plant	R	
117	El Centro, Terminal Substa.	DS	
1022	Eureka, Federal Bldg.	DS	
121	Fairmont Reservoir	R	
1023	Ferndale, City Hall	DS	
1096 (998)	Fort Tejon	SS	
1250	Gilroy, Gavilan Col. Geol. Bldg.	SS	
122	Glendale, 633 E. Broadway	SS	
282	Goleta, UCSB Fluid Mech. Lab.	SS	
125 (828)	Lake Hughes Sta. 1	--	Insufficient data
126	Lake Hughes Sta. 4	R	
127	Lake Hughes Sta. 9	R	
128	Lake Hughes Sta. 12	R	
184	Los Angeles, 1900 Ave. of Stars	SS	
187	Los Angeles, 1901 Ave. of Stars	SS	
425	Los Angeles, 1800 Century Park E.	SS	
440	Los Angeles, 1880 Century Park E.	SS	
145	Los Angeles, 222 Figueroa	SS	
148	Los Angeles, 234 Figueroa	SS	
157	Los Angeles, 445 Figueroa	SS	
172	Los Angeles, 800 W. First	SS	
154	Los Angeles, 420 S. Grand	SS	
141	Los Angeles, Griffith Obs.	R	
220	Los Angeles, 3838 Lankershim	SS/R	
431	Los Angeles, 616 S. Normandie	SS	
199	Los Angeles, 3407 W. Sixth	SS	
226	Los Angeles, 4867 Sunset	SS	
253	Los Angeles, 14724 Ventura	SS/DS	
466	Los Angeles, 15250 Ventura	SS/DS	
461	Los Angeles, 15910 Ventura	SS/DS	
137	Los Angeles, 111 N. Hope	SS	
449	Los Angeles, 2500 Wilshire	SS	
196	Los Angeles, 3345 Wilshire	SS	

TABLE II (Cont'd)

SITE CLASSIFICATION

<u>U.S.G.S. No.</u>	<u>Station Name</u>	<u>Category</u>	<u>Remarks</u>
<u>CALIFORNIA (cont'd)</u>			
202	Los Angeles, 3411 Wilshire	SS	
208	Los Angeles, 3470 Wilshire	SS	
211	Los Angeles, 3550 Wilshire	SS	
217	Los Angeles, 3710 Wilshire	SS	
223	Los Angeles, 4680 Wilshire	SS	
428	Los Angeles, 5900 Wilshire	SS	
443	Los Angeles, 6200 Wilshire	SS	
190	Los Angeles, 2011 Zonal	SS	
1211	Melendy, Ranch Barn (Hollister)	SS	
1049	Oakland, City Hall	--	Insufficient data
1052 (993)	Oso Pumping Plant, (Gorman)	SS	
279	Pacoima Dam	R	
411	Palos Verdes, 2516 Via Tejon	SS	
264	Pasadena, CIT Millikan Library	SS/DS	
266	Pasadena, CIT Old Seismic Lab.	R	
267	Pasadena, 4800 Oak Grove (JPL)	SS	
278	Puddingstone Reservoir	SS	
1083	San Luis Obispo, City Rec. Bldg.	R	
1065	San Francisco, Alexander Bldg.	SS	
1117	San Francisco, Golden Gate Park	R	
1080	San Francisco, State Bldg.	SS	
280	San Onofre, Nuclear Gen. Sta.	--	Insufficient Data
104	Santa Anita Dam	R	
283	Santa Barbara, Courthouse	DS	
284	Santa Felica Dam, Outlet Works	R	
1094	Taft, Lincoln School Tunnel	SS	
290	Wrightwood, 6074 Park Drive	--	Insufficient Data
<u>MONTANA</u>			
2205	Bozeman, MSU Engr. Bldg.	SS	
2202	Helena, Carroll College	R	
2229	Helena, Federal Bldg.	R	
<u>OREGON</u>			
2110	Portland, State Office Bldg.	SS	
2172	Portland, Cramer Hall	SS	
<u>UTAH</u>			
2203	Logan, USU Old Main Bldg.	SS	

TABLE II (Cont'd)

SITE CLASSIFICATION

<u>U.S.G.S. No.</u>	<u>Station Name</u>	<u>Category</u>	<u>Remarks</u>
<u>WASHINGTON</u>			
2101	Olympia, Hwy. Test Lab.	DS	
2102	Seattle, Federal Office Bldg.	SS	
2104	Tacoma, County-City Bldg.	--	Too difficult to classify

1. Categories

- R - Rock sites
- SS - Stiff soil sites
- DS - Deep soil sites

SS/DS }
 DS/SS } Dual classification where first designation
 SS/R } indicates preference

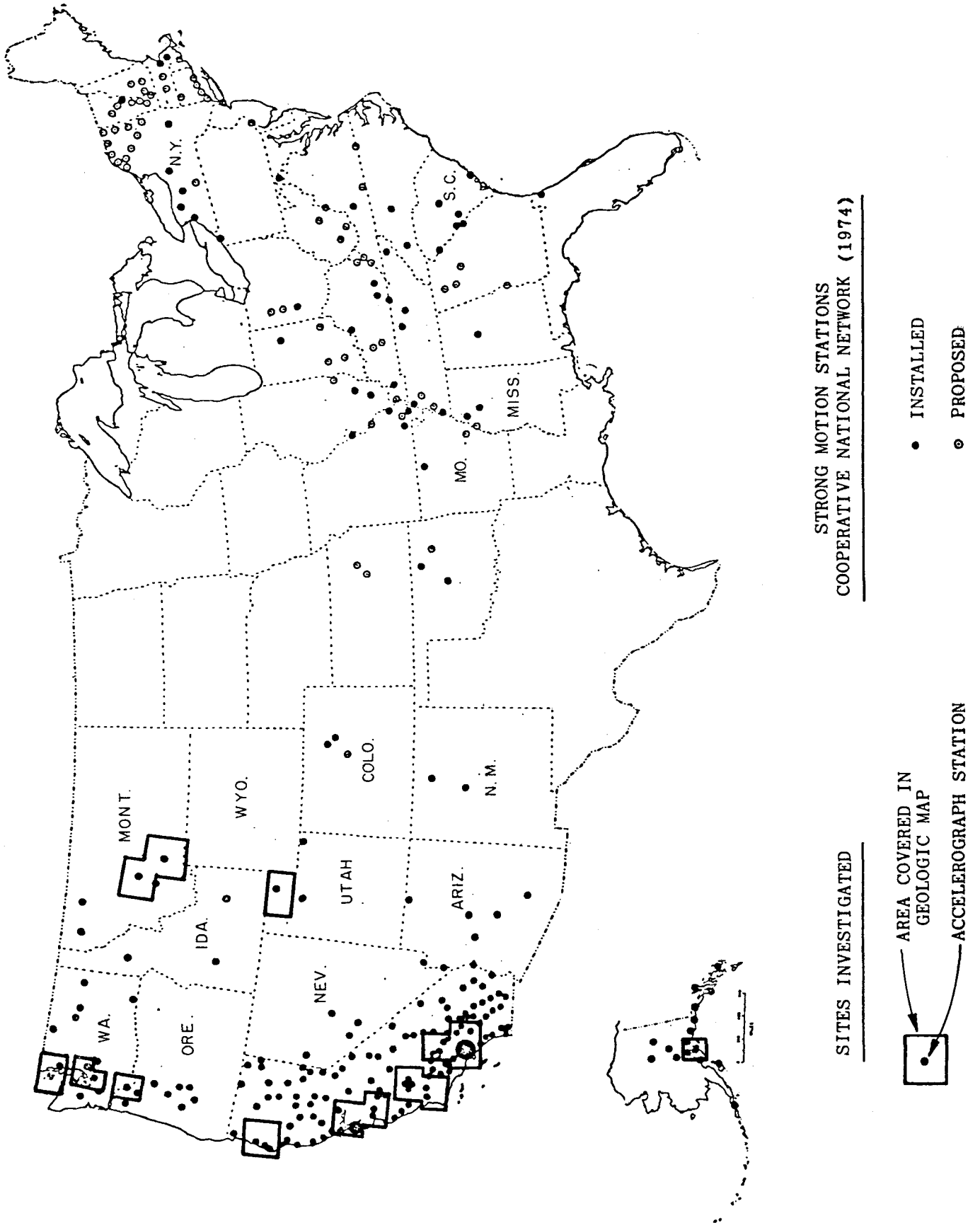
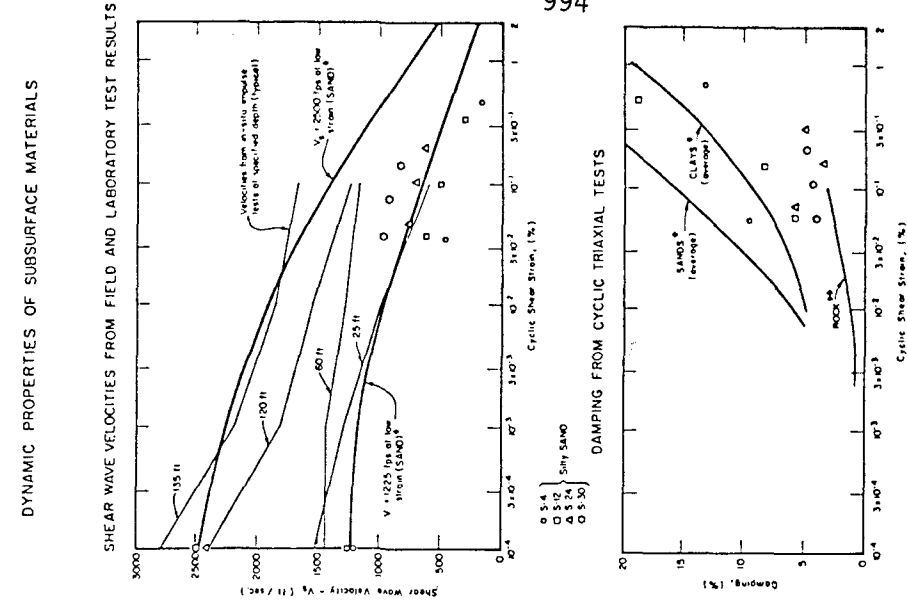
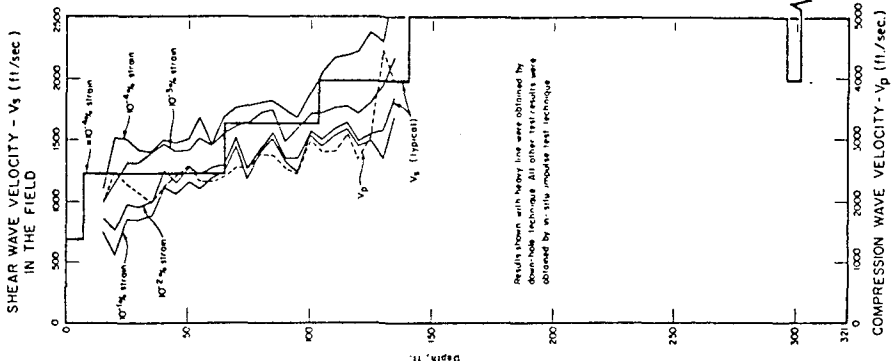


FIG. 1 - STRONG MOTION ACCELEROGRAPH STATIONS AND SITE LOCATIONS INVESTIGATED FROM 1975 THROUGH 1978.

DYNAMIC PROPERTIES OF SUBSURFACE MATERIALS

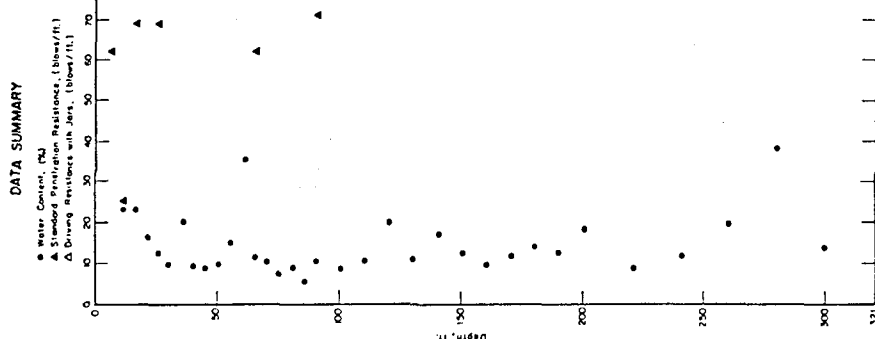


* From Sherman B. Wilson, Inc. and Astiphan-Jacobson Associates (1972)
 ** From Schmidt, Seed, and Lunner (1971).



7. V_s determined from laboratory testing as follows:
 $V_s = \sqrt{\frac{G}{\rho}}$, where ρ = mass density
 Modulus value uncorrected for possible sample disturbance

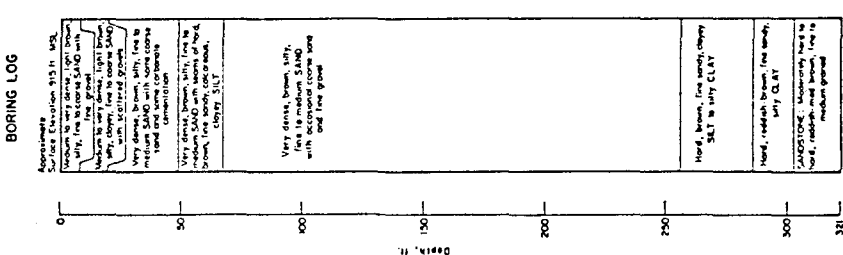
DATA SUMMARY



- 5. Other Tests:
 CF: Cyclic Triaxial Tests
 Mo. Grain Size Distribution
- 6. Standard Penetration Resistance (S.P.), based on 60 lb hammer falling 30 in., driving a 2 in. O.D. split spoon sampler.
 Driving Resistance with Jan. (blows/ft), driving 2 in. O.D. split spoon sampler.
 0.2 in. O.D. split spoon sampler.

Sampling	Indicated Depth, ft.	Dry Density, pcf	Other Tests
S1	14	110	CTMA
S2	109		
S3	24	93	CTMA
S4	31	80	CTMA
S5	150	114	CTMA
S6			
S7			
S8			
S9			
S10			
S11			
S12			
S13			
S14			
S15			
S16			
S17			
S18			
S19			
S20			
S21			
S22			
S23			
S24			
S25			
S26			
S27			
S28			
S29			
S30			
S31			
S32			
S33			
S34			
S35			
S36			

- 1. The stratification lines in the boring log represent the approximate boundaries between soil types, and the transition may be gradual.
- 2. Boring elevation obtained by hand leveling from U.S.G.S bench marks.
- 3. Laboratory tests performed on samples from indicated depth, as described in the Laboratory Testing Appendix.
- 4. Split spoon sample
- 5. Undisturbed sample
- 6. Sample not recovered



Notes
 1. The stratification lines in the boring log represent the approximate boundaries between soil types, and the transition may be gradual.
 2. Boring elevation obtained by hand leveling from U.S.G.S bench marks.
 3. Laboratory tests performed on samples from indicated depth, as described in the Laboratory Testing Appendix.
 4. Split spoon sample
 5. Undisturbed sample
 6. Sample not recovered

FIG. 2 - TYPICAL BORING LOG AND SUMMARY OF TEST RESULTS

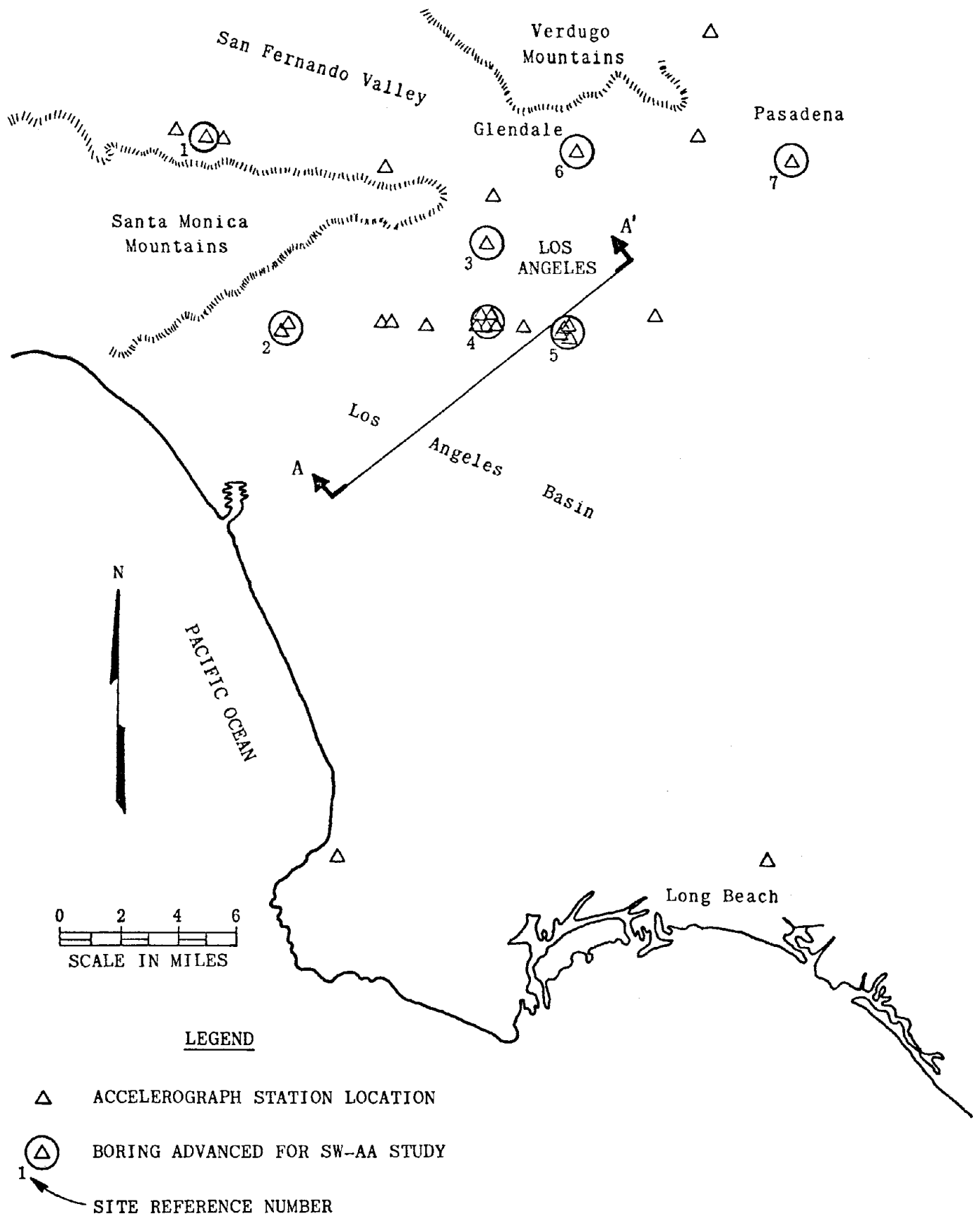
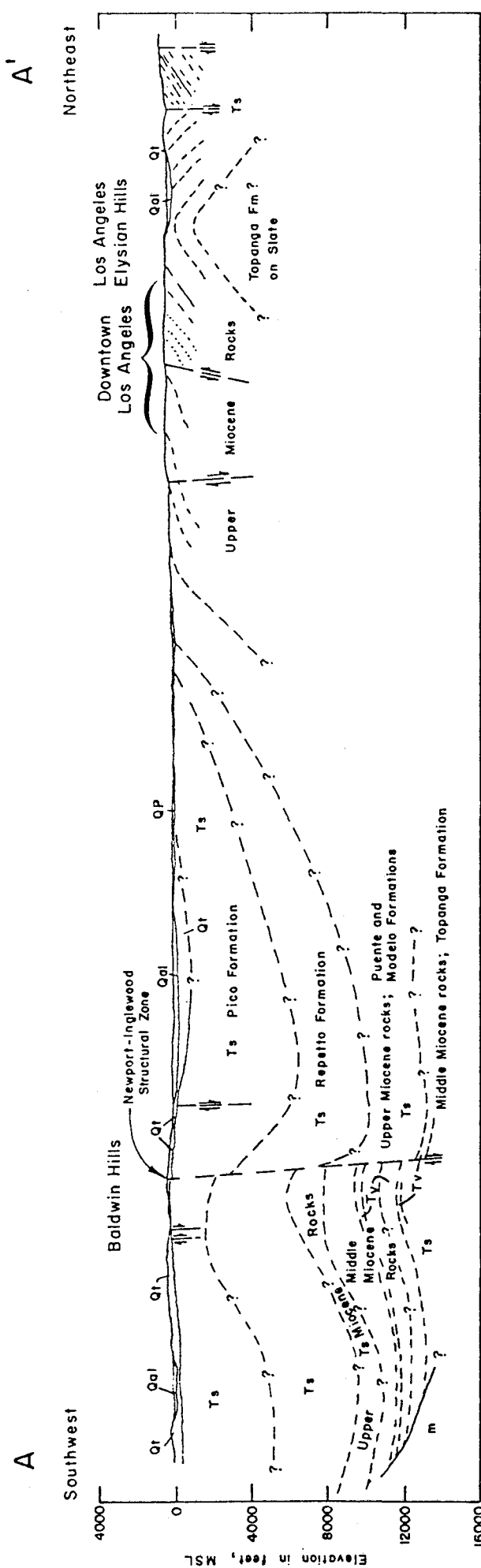


FIG. 3 - ACCELEROGRAPH STATIONS INVESTIGATED IN THE LOS ANGELES AREA



Cross-section modified after
Schoellhamer et al., 1954

EXPLANATION

Holocene Qal Alluvium

Quaternary Qt Marine and non-marine terrace deposits,

Plio-Pleistocene QP Non-marine sedimentary deposits

Pliocene-Miocene Ts Tertiary sedimentary rocks includes Pico and Repetto Formations, Puente and Modelo Formations, and the Topanga Formation

Tertiary Tv Volcanic rocks

Pre-Cretaceous m Basement rock complex; Catalina Schist west of the Newport-Inglewood fault, chiefly granitic rocks east of the fault

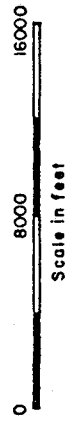
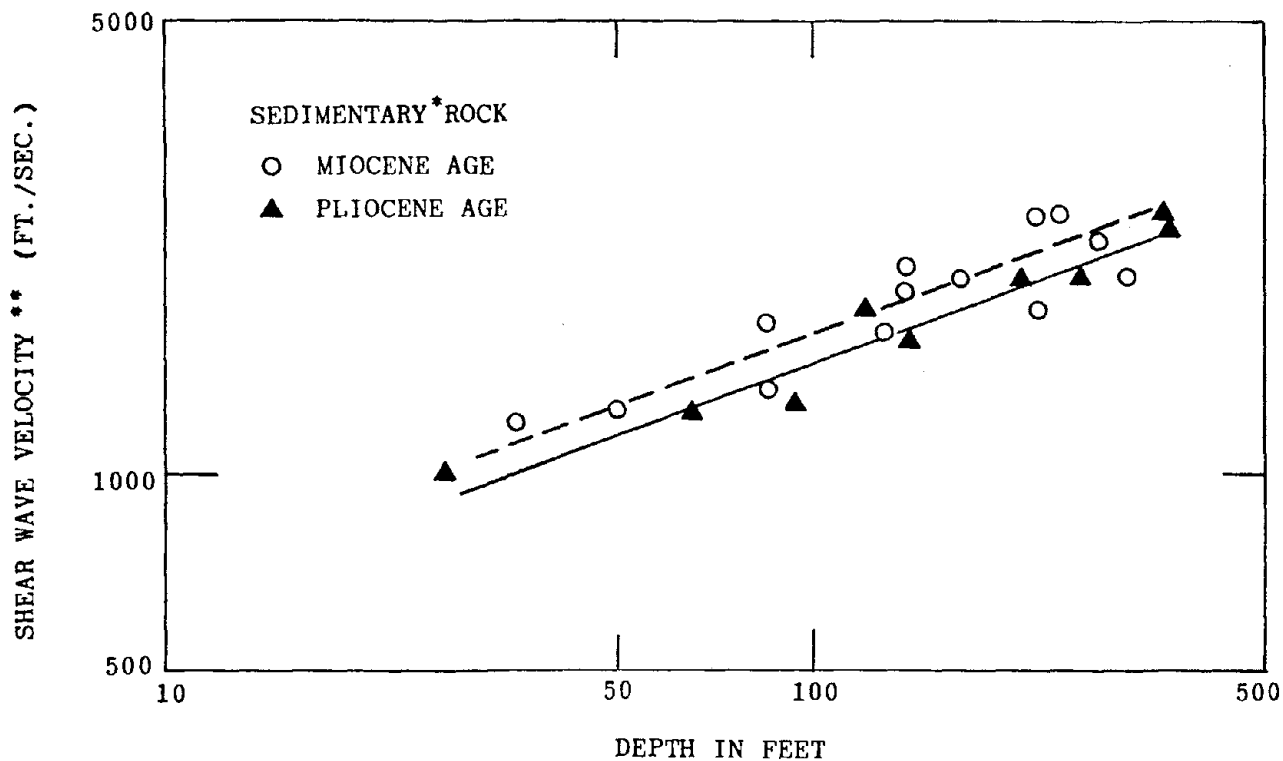


FIG. 4 - GEOLOGIC CROSS-SECTION A-A' OF LOS ANGELES BASIN



SITE* NO.	STATION LOCATION	USGS STATION	PREDOMINANT GEOLOGIC FM.
1	15250 Ventura Blvd., L.A.	466	○ Modelo
2	1880 Century Park East, L.A.	440	▲ Pico
3	4867 Sunset Blvd., L.A.	226	○ Puente
4	3345 Wilshire Blvd., L.A.	196	○ Puente
5	234 Figueroa, L.A.	148	▲ Fernando

* Site numbers correspond to the locations shown on Fig. 3. Sites 6 and 7 shown on Fig. 3 are on alluvium.

** Shear wave velocities from downhole geophysical measurements at each site.

FIG. 5 - PLOT OF SHEAR WAVE VELOCITY VERSUS DEPTH FOR SEDIMENTARY ROCK IN THE LOS ANGELES BASIN

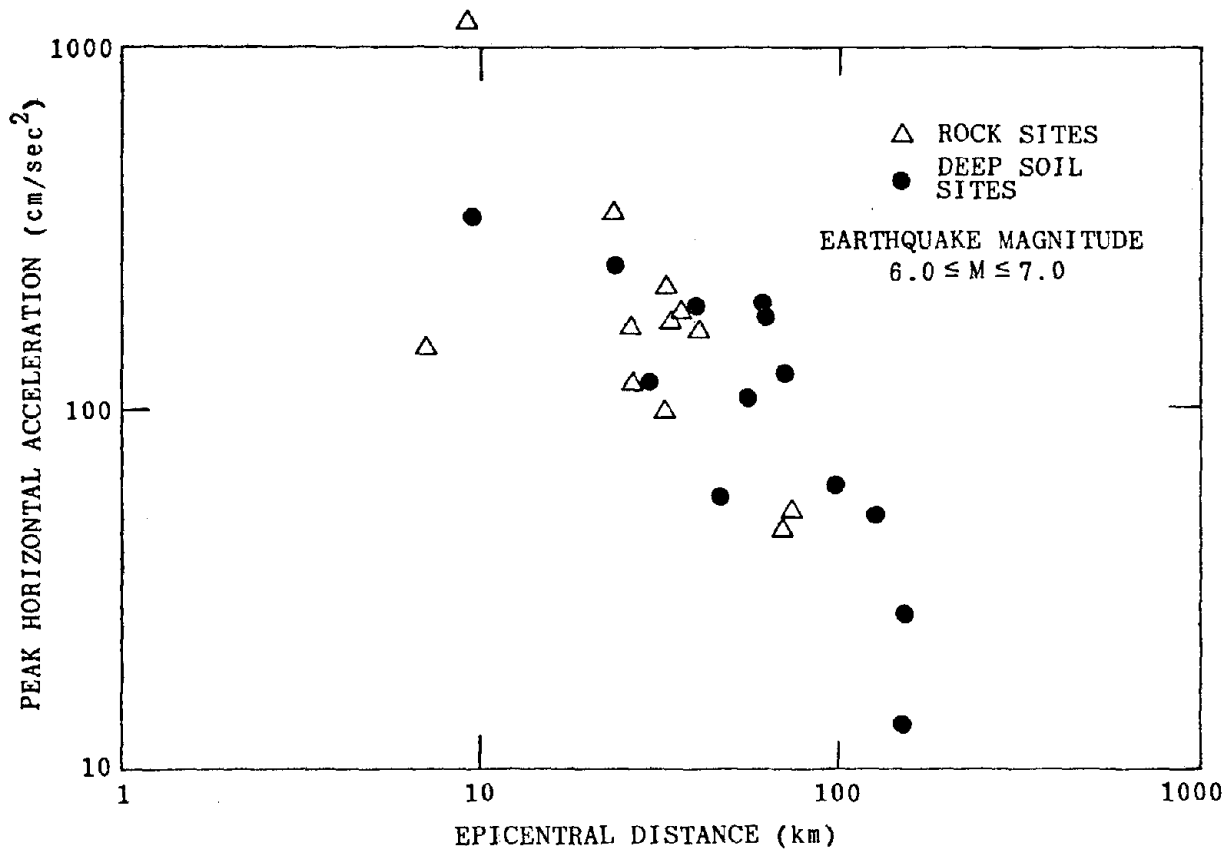


FIG. 6 - ATTENUATION OF PEAK HORIZONTAL ACCELERATION WITH DISTANCE

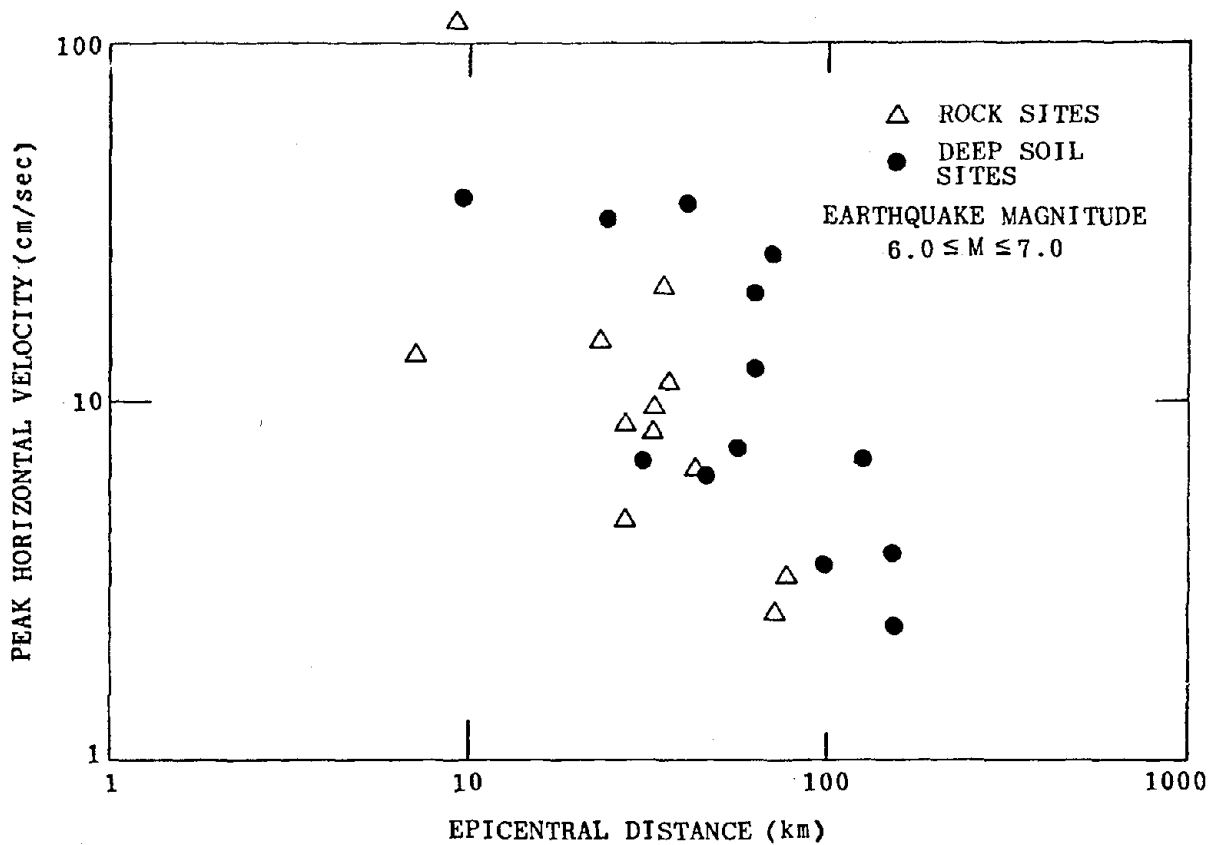


FIG. 7 - ATTENUATION OF PEAK HORIZONTAL VELOCITY WITH DISTANCE

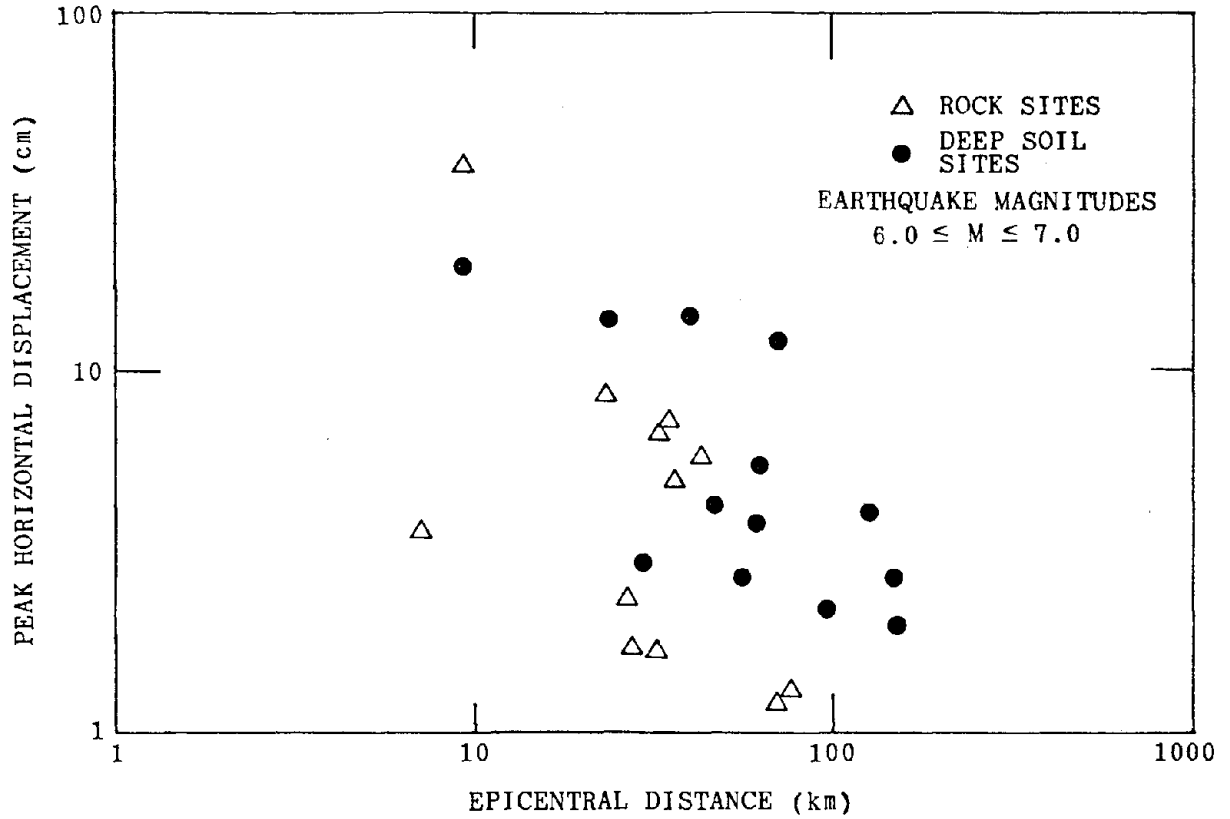


FIG.8 - ATTENUATION OF PEAK HORIZONTAL DISPLACEMENT WITH DISTANCE

1000

INTENTIONALLY BLANK

RECENT EARTHQUAKE RESISTANT DESIGN METHODS FOR
DIFFERENT TYPES OF FOUNDATIONS IN JAPAN

by

Yukitake Shioi^I, Toshio Furuya^{II}, Michio Okahara^{II},
and Yasuo Mitsuie^{II}

ABSTRACT

The current earthquake resistant designs of bridge foundations are mainly based on the so called seismic coefficient method and the modified seismic coefficient method. The larger the bridge foundations become in scale and the greater its importance, characteristics of seismic force such as frequency, time duration etc. as well as acceleration should better be considered in designing.

In order to get the present situation of earthquake resistant design methods taken in Japan for bridge foundations 31 examples of long span bridges are collected. The foundations are classified into four types. That is, a spread foundation, a pile foundation, a caisson foundation, and a multi-column foundation. For each type we surveyed on the design methods taken and methods of setting up models with respect to the interaction of the foundation and the surrounding soils.

1. RESULTS OF SURVEYS

We show the result of survey for each type of foundation as follows.

1.1 Type of foundation:

Spread foundation (large-scale)

Setting up of earthquake resistant design objectives:

Selection of earthquake calculation method:

- . Even in the case of a large-scale structure, modal analysis by a simple system with two degrees of freedom is possible because the earthquake behavior of the entire foundation can be examined by assuming it as a rigid foundation.
- . Calculations are made by response spectra, treating the maximum response alone.

Modeling for earthquake resistant design:

- . For the purpose of maintaining the continuity between superstructure and substructure, a part of the weight of superstructure

-
- I) Head of Foundation Engineering Section, Structure and Bridge Division
Public Works Research Institute, Ministry of Construction
- II) Research Engineer of Foundation Engineering Section, Structure and
Bridge Division, Public Works Research Institute, Ministry of Construction

is treated as a weight added to substructure and superstructure and substructure are separated.

- When substructure is under water, dynamic water pressure during earthquake is to be calculated in terms of virtual mass.

$$M_w = \frac{0.6\rho Ahw}{(a/hw)^{2/3}}$$

ρ : bulk density of water

A : sectional area

a : width in the direction of vibration

h_w : depth of water
($0.8 \leq a/h_w \leq 4.0$)

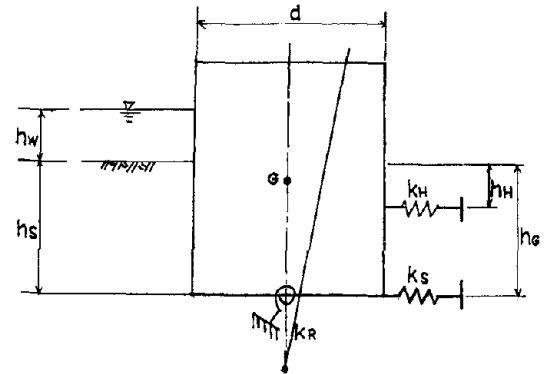
- The soil surrounding substructure is to be calculated in terms of virtual mass, assuming it to vibrate together with the structure during earthquake.

$$M_s = 1/2(\gamma_s/g)a^2 d$$

γ_s : weight of soil

g : acceleration of gravity

d : thickness of soil layer



(In the direction of length b)

- Earthquake force is to be calculated by the use of response acceleration spectrum (statistical value obtained from observations made in the vicinity).

Related constants:

- As for the dynamic spring constant of the subgrade, the lowest value of the modulus of deformation of the original position measured by the pressiometer is to be used. The spring constants in the horizontal, vertical, rotational and shearing directions are to be determined as instructed in the "Specification for Highway Bridge Substructure Design (Caisson)".

$$K_H = k_H'(b/D)^{3/4}, \quad k_H = \frac{1.2}{D}E_p, \quad b : \text{width } (b = \sqrt{A_H})$$

$$K_V = k_V'(a/D)^{3/4}, \quad k_V = \frac{1.0}{D}E_p, \quad a : \text{length } (a = \sqrt{A_V})$$

$$K_R = K_V \cdot I, \quad I : \text{moment of inertia of the bottom}$$

$$K_S = \lambda K_V, \quad \lambda = 1/3$$

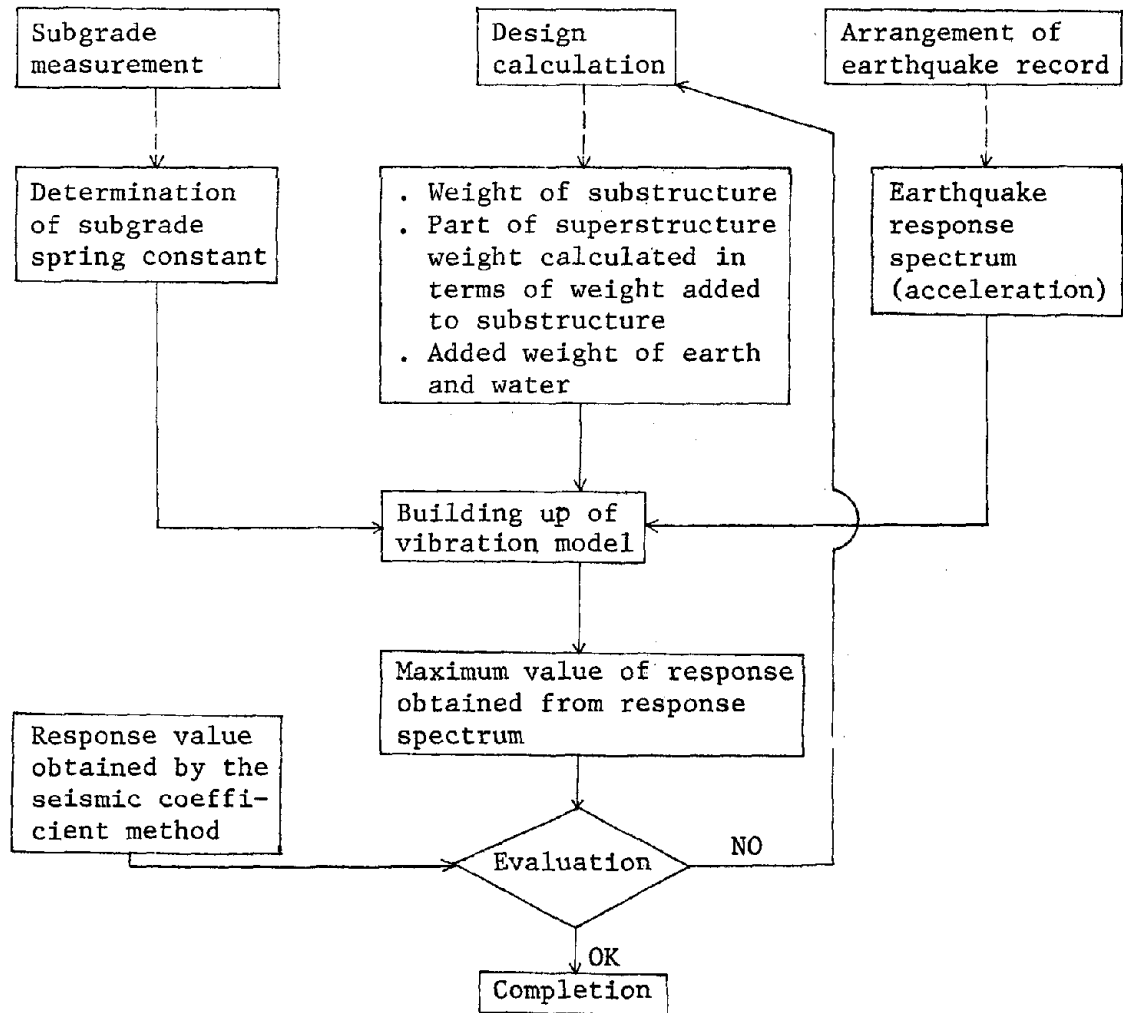
- Or Blot's equation $K_R = \frac{E_R}{(1-\nu^2)k} a^2 b$, $K_S = \frac{E_R}{2(1+\nu)bk}$
 E_R : Voigt's elastic module, ν : Poisson's ratio

Evaluation of earthquake resistant design calculation and precautions required:

- The values to be obtained by calculations are natural period, center of rotation, displacement of gravity center and angle of rotation of the model.
- The above values are used to evaluate the subgrade reaction,

distance of eccentricity, bearing power, sliding and tipping.

Flowchart of earthquake resistant design calculation:



1.2 Type of foundation:

Pile foundation (Multiple -layer shearing model)

Setting up of earthquake resistant design objectives:

- . When the soft soil stratum extends deep beneath the surface, the ground movement is estimated to be large.
- . Since the structural type and dimensions are fixed, it is necessary for the bearings to be of flexible structures to reduce the section force, and therefore.

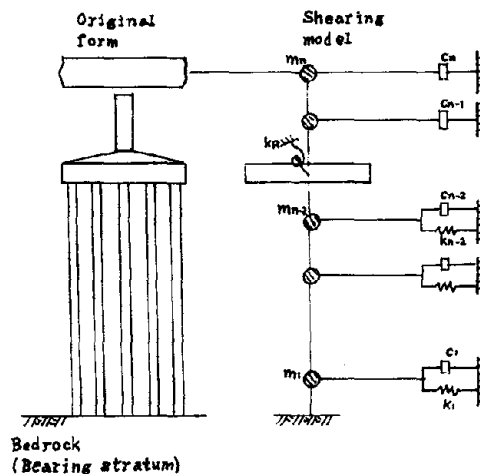
Selection of earthquake calculations method:

- . When the piles are likely to vibrate, coupled with the surrounding soil, the ground is to be replaced by a multiple-layer shearing model.

- . When there are no seismic wave records available for the same stratum of soil, the incident wave to the pile bearing stratum is to be estimated from the estimated acceleration of the seismic foundation, using the shearing wave theory.
- . Since the coefficient of subgrade reaction cannot be obtained, the dynamic reaction coefficient is to be obtained by modeling the subgrade by the finite element method.

Modeling for earthquake resistant design:

- . The ground is replaced by shearing models, stratum by stratum.
- . In the case of superstructure, only damping is to be considered, neglecting the reaction characteristic.
- . In the footings, the righting moment of rotation and rotational inertia are to be considered.



- . The incident wave to the bearing stratum is to be calculated by means of the following equation, using the laws of reflection and refraction.

$$U_k(t, z) = f_k\left(t - \frac{z}{V_k}\right) + g\left(t - \frac{H_k - z}{V_k}\right)$$

The stratum where the response $U_k(t, z)$ little changes is to be regarded as input bedrock (bearing stratum).

Related constants:

- . The spring constant of subgrade is to be estimated, using FEM in plane strain.

$$K = \frac{1}{x} = k - S^T K^{-1} S$$

- . As for the added mass, it is assumed that footing or piles have kinetic energy equal to that of the subgrade.

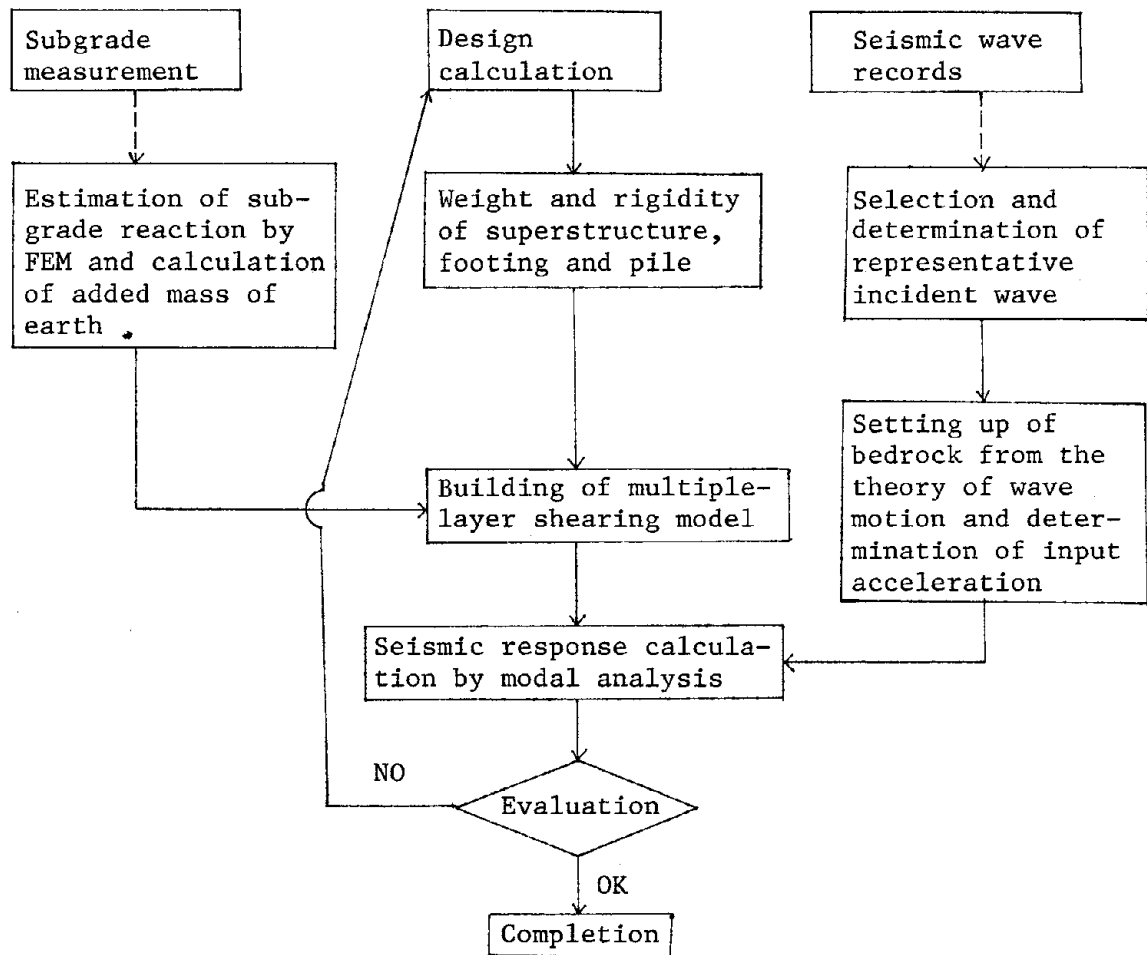
$$m_a = \frac{1}{x^2} X^T M X$$

Evaluation of earthquake resistant design calculation and precautions required:

- . In the case of soft ground, there is so great a difference in the acceleration of seismic waves between the bedrock and ground surface that it is necessary to make investigations on the ground responses.
- . The bending moment in a pile is greater in its lower part because the seismic waves are rapidly amplified.

Problems

- . If there is a limit to the application of the theory of shearing wave (multiple-stratum ground, great earthquake).
- . Consideration to the effects of the group of piles on the shearing model.
- . Consideration to the damping mechanism and nonlinearity.

Flowchart of earthquake resistant design calculation:1.3 Type of foundation:

Caisson foundation

Setting up of earthquake resistant design objectives:

- . In the case of soft ground, there are problems with the caisson behavior during earthquake.
- . Effects of the type of superstructure.

Selection of earthquake calculation method:

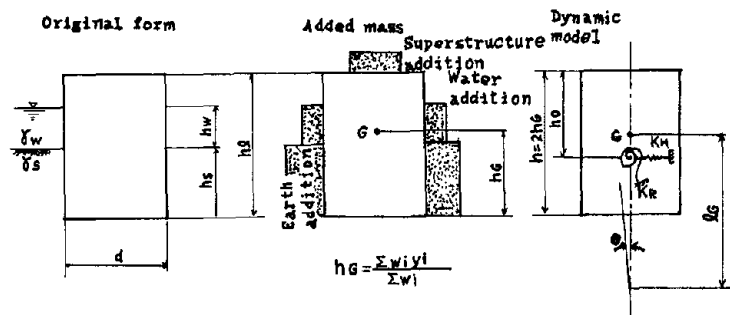
- . As for ground modeling, the model of spring-dashpot system is to be used from a practical viewpoint although there are the wave motion theory and finiti element method.
- . Response spectrum analysis by a model with two degrees of freedom, horizontal translation and rocking motion.

Modeling for earthquake resistant design:

- . Effects of superstructure and water are to be treated as added mass.

$$M_W = \frac{0.6\gamma_w A_w h_w}{(b/h_w)^{2/3}}, \quad M_S = \frac{1}{2}\gamma_s g b^2 d$$

- . When the side ground is very soft, it is to be treated as a plastic state if the horizontal reaction exceeds the allowable bearing capacity.
- . In the case of a large caisson, the response spectrum of earthquake records in the vicinity is to be used.
- . The maximum design acceleration shall be 180 to 250 gal.



Related constants:

- . It is necessary to examine the subgrade spring constant by a variety of Boussinesq's equation as given below and other methods. (Pauw, Tajimi, Richart)

$$K_V = \frac{E}{I_p (1-\nu^2) B_V^{3/4}}$$

E : Ground deformation modulus = $6E_0 \sim 5E_0$

E_0 : Pressiometer deformation modulus

B_V : Foundation conversion width = $\sqrt{A_V}$

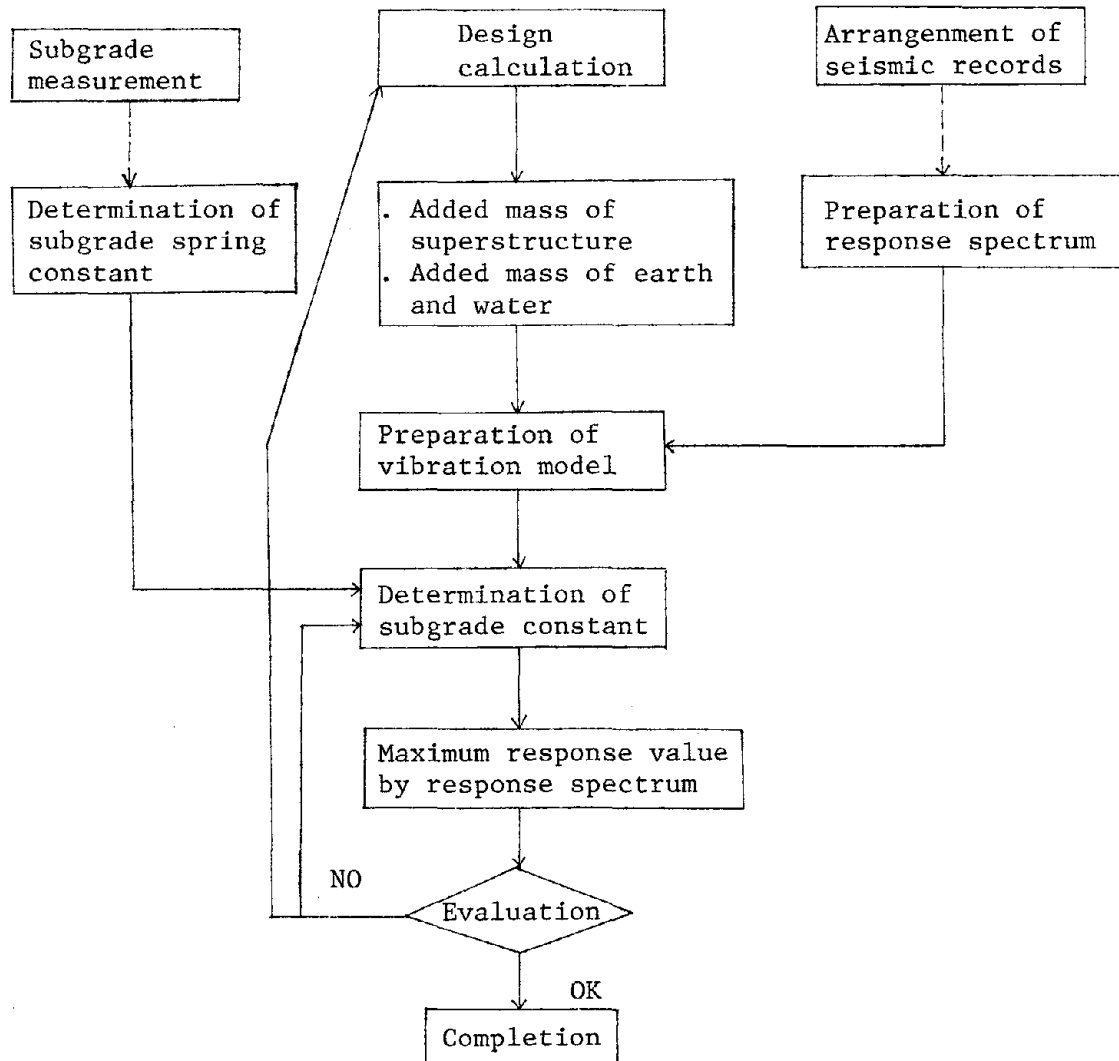
ν : Poisson's ratio

I_p : Shape factor

Evaluation of earthquake resistant design calculation and precautions

required:

- . There are some problems about the conversion of superstructure by added mass but in general there is not much difference from the results of analysis by the whole system model.
- . The response is governed by the evaluation of the subgrade spring constant. Particularly, the evaluation of the effects of caisson shape.
- . The values to be calculated are the natural period, the horizontal and rotational displacement of gravity center, and maximum acceleration response.
- . Since the substructure response is influenced by the structural type of superstructure, it is necessary to make response analysis at the basic design stage.

Flowchart of earthquake resistant design calculation:1.4 Type of foundation:

Multi-column foundation

Setting up of earthquake resistant design objectives:

- . Since this is a flexible structure, the elastic behaviors of the foundation and footings are to be investigated.
- . The coupled vibration with the superstructure must be considered.

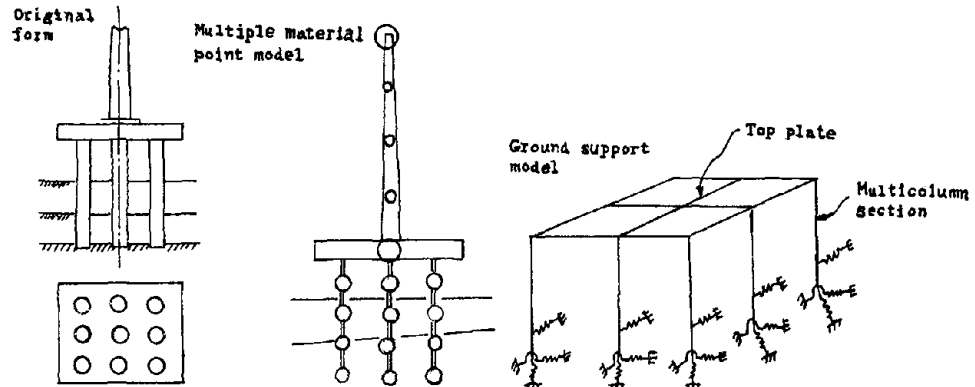
Selection of earthquake calculation method:

- . It is necessary to investigate the three-dimensional behavior for reasons of topographic inclination, arbitrariness of earthquake input direction, eccentricity of superstructure reaction and asymmetry of the foundation structure. Since it is impossible to estimate the condition in which the foundation and ground are bound together (the spring constant is not uniform), added mass of ground and damping constant, there is the necessity for analysis of three-dimensional vibration.

- . In order to make calculation in terms of a multiple system of material points, modal analysis is to be used.

Modeling for earthquake resistant design:

- . Considering the three-dimensional vibration, the deformations are to be taken as unknown quantities.
 Pier: Horizontal x and y displacements (2)
 Footing: Horizontal x and y displacements, torsional angle and rotational angle (10)
 Superstructure: Horizontal x and y displacements and torsion (4)

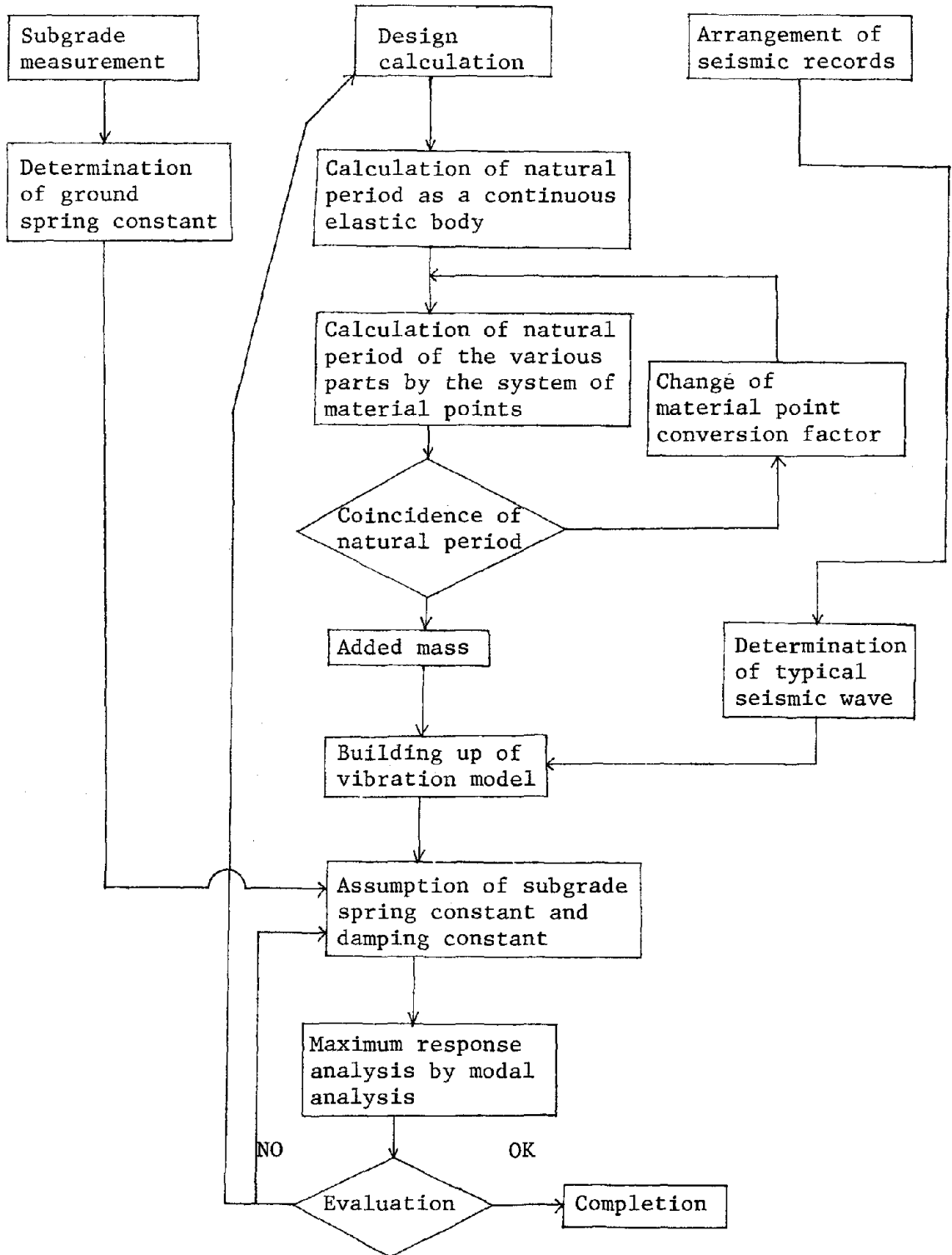


Related constants:

Evaluation of earthquake resistant design calculation and precautions required:

- . Comparison of static calculation and dynamic calculation results.
- . Comparison of calculated values with vibration experimental results.
- . It is necessary to check the responses by varying the subgrade reaction coefficient.
- . Since the foundation has so great influence on the superstructure, its coupling to the superstructure is also investigated.

Flowchart of earthquake resistant design calculation:



2. CONCLUSION

Earthquake resistant design methods, mainly the modeling techniques for the earthquake resistant design of bridge foundations, have been summarized. As seen from the examples, the objectives of earthquake resistant design mainly concerns the following two cases.

- i) The bridge is very long.
- ii) The ground is poor.

The details of these two items are

- i) a. The effects of the seismic responses of substructure on the superstructure due to the long span of the bridge.
- b. Dynamic characteristics of the substructure.
- ii) a. The ground behavior during earthquake is not well known.
- b. The behavior of the foundation structure itself during earthquake.

The current trend is obviously to evaluating the behaviors during earthquake whic are difficult to grasp by the seismic coefficient method due to the maximum acceleration, frequency and time of duration, which are the seismic force characteristics, and the response characteristics (natural period) of ground and structures, in order to design structures with a higher degree of safety. However, the behaviors during earthquake have not yet been fully clarified in the analysis of seismic responses.

Many studies involving actual observations and analysis of experimental results have been made about the way the subgrade spring constant, damping constant and added mass are to be treated and increased knowledge will be obtained in the near future. From a methodological standpoint, the earthquake resistant design calculation has now reached a state capable of making sufficient evaluations required in designing earthquake resistant structures.

1012

INTENTIONALLY BLANK

COMPARISON OF PENETRATION RESISTANCE VALUES
TO IN SITU SHEAR WAVE VELOCITIES

by

W. F. Marcuson, III,^I R. F. Ballard, Jr.,^{II} and S. S. Cooper^{III}

ABSTRACT

Standard Penetration Tests (SPT), Dutch cone penetration tests, and rotary cone penetration tests were conducted in adjacent borings in hydraulic fill material at Fort Peck Dam. Fort Peck Dam, located on the Missouri River in Montana, is the Corps of Engineers largest hydraulic fill earth dam. The dam was constructed during the late 1930's and is approximately 250 ft high (76 m) at its maximum section and 20,000 ft long (6100 m).

A geophysical investigation including crosshole, downhole, surface vibratory, and refraction seismic techniques was conducted to determine the in situ shear wave velocity profile with depth at the penetration test locations. Relationships between the various penetration resistances were developed and correlations between the penetration resistance and the in situ shear wave velocities are presented.

It was concluded that comparisons such as these can assist the engineer in estimating the shear modulus of the in situ material by indirect means. This, of course, is an extension of the present study which is limited to Fort Peck Dam. Future investigations will include the gathering and analysis of data at other test sites.

INTRODUCTION

In order to evaluate the liquefaction potential of a given site or deposit, the in situ shear modulus of each soil layer of interest must be determined. Current analytical procedures require that the shear modulus be specified as a function of shear strain. Modulus versus strain data are routinely evaluated in the laboratory; however, in situ shear moduli at very small strains (i.e. strains less than 10^{-7} percent) are best determined using field geophysical methods. Comparisons have been made of in situ shear moduli determined by geophysical methods and shear moduli determined in the laboratory for small strain amplitudes by resonant column test techniques (1). These comparisons indicate that the in situ modulus may be as much as twice the laboratory determined value (1). Generalized modulus versus strain curves for sands and clays at various densities, relative densities, and void ratios, have also been developed and are presented in the literature (2,3,4). For preliminary liquefaction

-
- I Research Civil Engineer, Earthquake Engineering and Vibrations Division, Geotechnical Laboratory, U. S. Army Engineer Waterways Experiment Station, CE, Vicksburg, MS.
- II Supv Research Geophysicist, Chief, Geodynamics Branch, Earthquake Engineering and Vibrations Division, Geotechnical Laboratory, U. S. Army Engineer Waterways Experiment Station, CE, Vicksburg, MS.
- III Geophysicist, Geodynamics Branch, Earthquake Engineering and Vibrations Division, Geotechnical Laboratory, U. S. Army Engineer Waterways Experiment Station, CE, Vicksburg, MS.

Preceding page blank

evaluations, it would be helpful if the in situ shear modulus at small strain levels could be estimated from data obtained by routine field testing.

The purpose of this paper is to present an observation that the shear wave velocity (shear modulus) of the materials at Fort Peck Dam can be estimated from SPT N values, or Dutch cone penetration resistance. A secondary purpose is to suggest that additional data be collected and that further evaluation of these correlations be conducted.

BACKGROUND AND SCOPE

In the mid 1970's, the Waterways Experiment Station (WES) conducted a dynamic analysis of Fort Peck Dam to evaluate the liquefaction potential of the embankment and alluvial foundation (5). Fort Peck Dam, located on the Missouri River in northeast Montana, was constructed during the period 1934-1940 using the hydraulic fill method. Figure 1 shows a typical cross section of the dam which is founded on 120-ft-thick (37 m) alluvial valley settlements underlain by shale. Maximum height of the dam is about

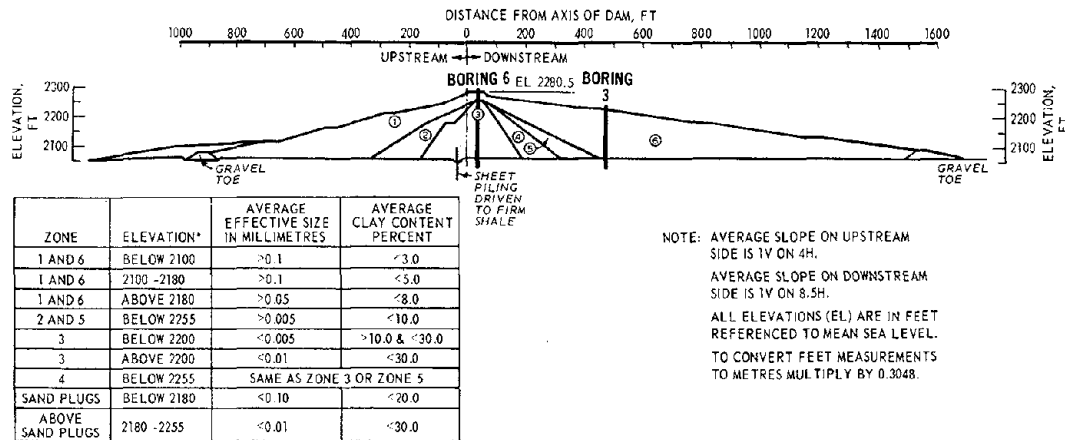


Figure 1. Typical cross section of Fort Peck Dam

250 ft (76 m). Also shown on Figure 1 is a table listing the average effective particle size and average clay content of the soil in the various zones of the dam. The data presented and discussed in this paper were obtained from locations at sta 42+00 and ranges 0+35 and 4+75 downstream (zones 3 and 6; see Figure 1). Zone 3 is the impervious core of the dam. Typically, this material is classified an SM and has an in situ dry density of approximately 103 pcf (1.65 g/cm^3). Zone 6 is the downstream shell of the dam, typically classified an SP with a maximum density of 108.5 pcf (1.74 g/cm^3), a minimum density of 90.3 pcf (1.45 g/cm^3), and an in situ dry density of 95 to 98 pcf (1.52 to 1.57 g/cm^3).

The field investigation and sampling program conducted at Fort Peck Dam included (a) nine Standard Penetration Test borings, (b) six borings in which continuous 3-in.-diam (7.6 cm) samples were obtained using a

Hvorslev fixed piston sampler, (c) four borings in which the SPT and 3-in.-diam (7.6 cm) samples obtained with the Hvorslev fixed piston sampler were alternately taken at 5-ft (1.5 m) intervals, (d) four rotary cone penetration borings, and (e) four Dutch cone penetration borings (5,6). As part of the field investigation, an in situ seismic investigation was also conducted (7). Because the use of the rotary cone is largely restricted to WES, the data obtained by this apparatus will not be discussed further. In summary, the following data were collected and used in this study:

- a. In situ shear wave velocity data,
- b. Standard Penetration Test N values, and
- c. Dutch cone penetration resistance values.

TEST PROCEDURES

Details of the test procedures are presented elsewhere (5, 6, 7); therefore, only summaries are presented herein. The Standard Penetration Tests were conducted in accordance with ASTM Standard D 1586-67 (8), and the U. S. Army Corps of Engineers Manual EM 1110-2-1907 (9).

Dutch cone penetrometer data are usually presented as cone and cone plus skin friction readings (kg/cm^2) versus depth in approximately half-foot (0.3 m) increments. In this study, values of point resistance, P, have been corrected by the formula (10,11,12)

$$P_{\text{corr}} (\text{kg}/\text{cm}^2) = 2P (\text{kg}/\text{cm}^2) + \frac{\text{rod wt (kg)}}{10 \text{ cm}^2} \quad (1)$$

The corrected Dutch cone data have been plotted two ways, i.e. versus depth and SPT N values.

Crosshole shear wave velocity tests were conducted using a set of three boreholes (one seismic source hole and two geophone holes) drilled and cased with plastic pipe to bedrock. The holes were located on a line parallel to the axis of the dam. A 20-ft (6 m) depth interval between tests was adopted, based on evaluations of the boring logs. The test locations were positioned so that at least one test would be conducted in each material type. Downhole tests were also conducted at 20-ft (6 m) intervals so that a corresponding vertical velocity assessment could be made.

PRESENTATION OF TEST RESULTS

In situ geophysical tests, SPT's, and Dutch cone penetration tests were conducted at four locations at Fort Peck Dam (5,6,7). The data presented herein will be limited to investigations conducted at sta 42+00 and ranges 0+35 and 4+75, downstream. Figure 2 presents boring log and SPT N values as a function of depth for boring No. 6, located at sta 42+00 and range 0+35 downstream (5). Results of Dutch cone point resistance measurements (6) performed in boring No. 6 DC, located at sta 41+80 and 0+41.5, downstream, are also shown on Figure 2. It should be noted that boring 6, located on the crest of the dam, encountered a

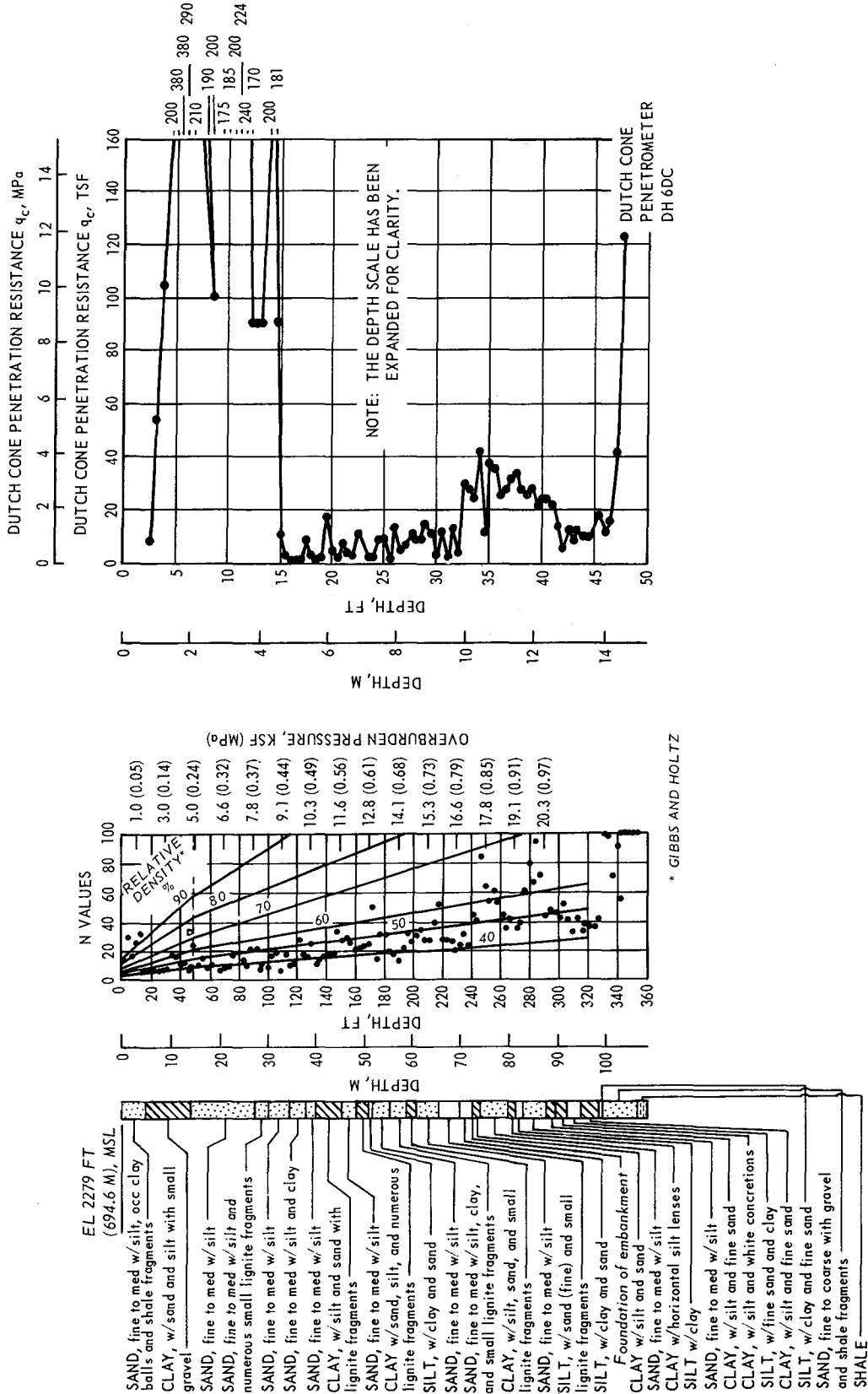


Figure 2. Boring log, Standard Penetration Test and Dutch cone data for sta 42+00 and range 0+35 downstream

15-ft-thick (4.5 m) rolled fill cap followed by hydraulic fill core material to a depth of 240 ft (73 m).

Figure 3 presents the boring log for boring No. 3, located at sta 42+00 and range 4+75 downstream (5). The SPT N values for boring No. 3 are plotted as a function of depth. Also shown on Figure 3, is a plot of Dutch cone point resistance versus depth for boring No. 3 DC, located at sta 42+00 and range 4+57.7 downstream (6). Boring 3 penetrated the hydraulic fill shell material from surface to a depth of 165 ft (50 m).

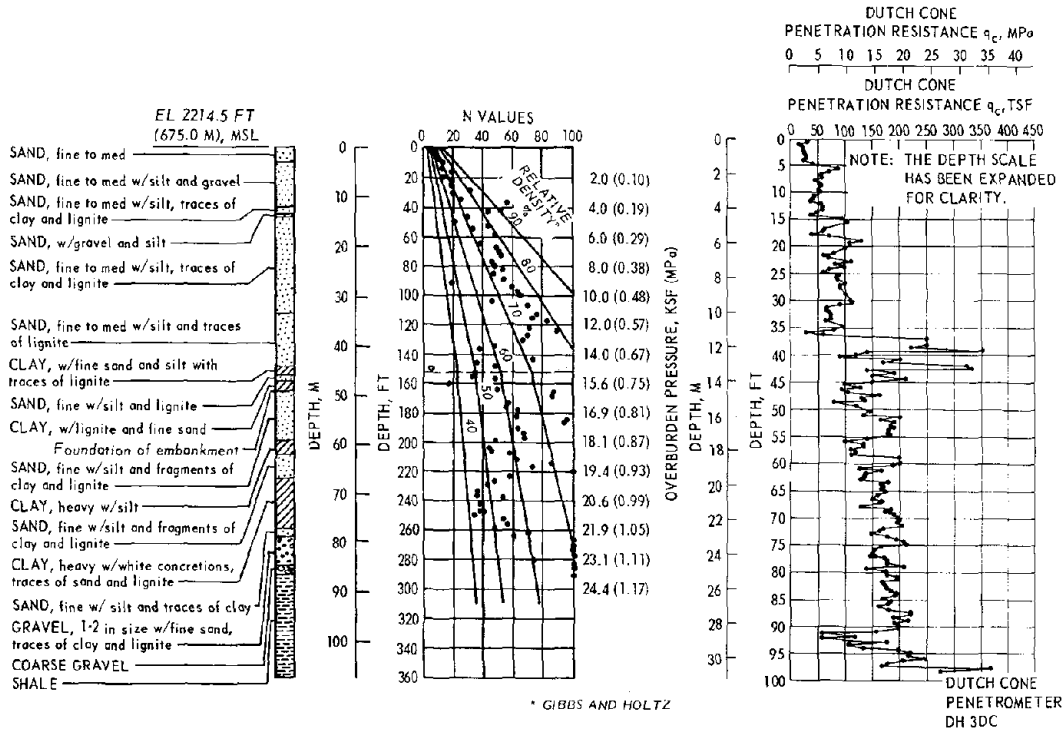


Figure 3. Boring log, Standard Penetration Test, and Dutch cone data for sta 42+00 and range 4+75 downstream

Below a depth of 165 ft (50 m), Boring 3 penetrated the alluvial foundation material. Note that at the time the field investigation was conducted, the groundwater table was at a depth of 150 ft (45 m).

Figure 4 presents the shear wave velocity, V_s as a function of depth for sta 42+00 and ranges 0+35 and 4+75 downstream (7). The data presented are for crosshole testing; however, the data identified by an asterick (*) are values obtained using the downhole testing technique.

DISCUSSION

Comparison of Standard Penetration (SPT) and Dutch Cone Resistance

Figure 5 presents plots of Dutch cone penetration resistance versus SPT resistance N for sta 42+00 and ranges 0+35 downstream (Figure 5a) and 4+75 downstream (Figure 5b). If n is defined as q_c divided by N, as suggested by Schmertmann (10), then a line which corresponds to an n of 3 or 4, fits the data reasonably well (See Figure 5b). This is in agreement with Schmertmann for fine to medium sands and silty sands. Data obtained

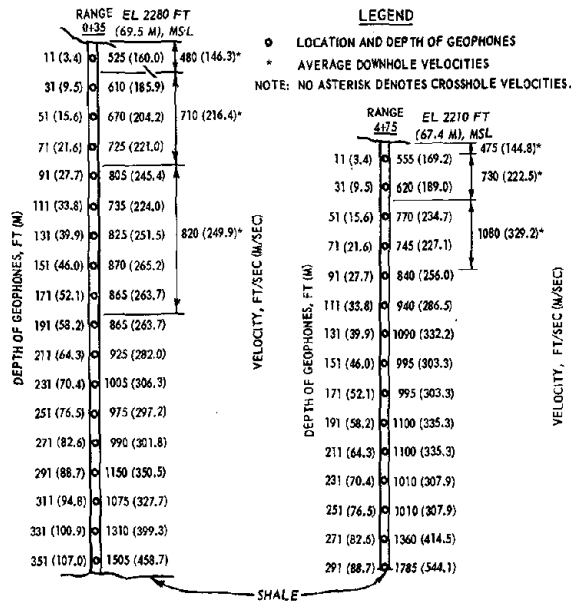


Figure 4. Shear wave velocities for sta 42+00

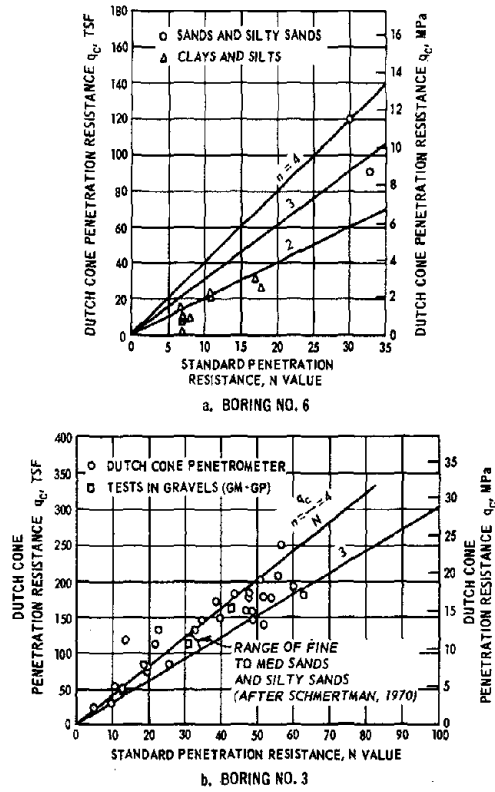


Figure 5. Comparison of Standard Penetration Test and Dutch cone data

at range 0+35 downstream are essentially representative of the hydraulic fill core material. The core material is considerably finer than the material at range 4+75 downstream, and $n = 2$ appears to be a better data fit for the finer material.

Figures 2 and 3 illustrate that the SPT and Dutch cone data obtained at this site exhibit similar trends with depth. However, in this case Dutch cone does appear to be more sensitive to soil stratigraphy.

Correlation between Shear Wave Velocity and Penetration Resistance

Shear wave velocity, V_s , SPT values, N , and Dutch cone point resistance, q_c , have been presented for a rolled filled, a hydraulic fill core material, and a hydraulic fill sand shell material. Shear wave velocity, V_s , and SPT N values have also been presented for the same materials. Penetration resistance may be related to shear wave velocity through an equation of the form

$$V_s = \alpha X \quad (2)$$

where α = empirically derived coefficient, and

X = SPT N value or the Dutch cone penetration resistance value, q_c , TSF.

The following tabulation presents the various values of α which have been developed from the Fort Peck Dam data.

<u>Material</u>	<u>α if X is equal to N</u>	<u>α if X is equal to q_c, TSF</u>
Rolled fill	28	4
Hydraulic fill core	46	33
Hydraulic fill sand	20	6
Alluvial foundation	7	No data

No Dutch cone penetration test data were obtained in the alluvial foundation underlying Fort Peck Dam.

SPT N Value

From the tabulation, it is seen that the coefficient, α varies from 15 to 46, depending on the material type, if the SPT N value is the known variable used to predict V_s . In the rolled fill material, α is equal to about 28. In the case of the hydraulic fill core material, the value α is equal to 46. This coefficient predicts the shear wave velocity within ± 20 percent most of the time. The exception is the layer at a depth of 211 ft (64 m) at range 0+35. At this depth, the shear wave velocity is approximately 925 fps (282 m/sec), and the average SPT N value

is about 35. Using a coefficient of 46 would predict a shear wave velocity of 1650 fps (503 m/sec) which is about 80 percent too high. Outside of this isolated value, coefficient 46 appears to be satisfactory for hydraulic fill core material.

Finally, using an α of 18 for the hydraulic fill sand, it was determined that all V_s values, save one, could be predicted for the borings and data shown on Figures 2-4. The single exception occurred at a depth of 311 ft (95 m) at range 0+35. In this case, V_s was predicted to be 720 fps (220 mps) compared to a measured value of 1075 fps (328 mps).

Dutch Cone Penetration Resistance

The tabulation also shows that the coefficient α varies from 4 to 33, depending on the type of soil, if cone penetration resistance, q_c is used to predict the shear wave velocity. The coefficient 4 predicts the shear wave velocity in the rolled fill material with ± 20 percent. The α value of 33 predicts the shear wave velocity in the hydraulic fill core material within ± 20 percent for the majority of cases. At a depth of 20 ft (6 m), at range 0+35 downstream, the core material has a shear wave velocity of about 600 fps (183 mps). The cone penetration resistance averages about 9 at this depth. Thus, an α of 33 would predict a shear wave velocity of about one-half the measured value. This is the only case where the coefficient 33 does not predict the shear wave velocity within ± 20 percent for the hydraulic fill core material.

An α value of 6 predicts the shear wave velocity in the hydraulic fill sand material reasonably well. These predicted values are within ± 25 percent of the measured value most of the time. Exceptions to this are: (a) the near surface material at range 4+75 exhibited a shear wave velocity of about 555 fps (170 mps) and an average penetration resistance value of 57, an α coefficient of 6 would predict a shear wave velocity of about 350 fps (107 mps) or approximately 60 percent of the measured value; and (b) observing Figure 4, the measured shear wave velocity is about 840 fps (256 mps) at a depth of 91 ft (28 m) and cone penetration resistance averages about 182 tons per sq ft. If the coefficient of 6 is used to predict shear wave velocity, a 1090 fps (332 mps) value will be predicted. This value is approximately 33 percent too high. Except for these two locations, the predicted shear wave velocities are within ± 25 percent of the measured values.

Theoretical Considerations

Assuming that the penetration resistance is a measure of shear strength and that the shear wave velocity is a function of shear modulus, there appears to be no theoretical reason why the penetration resistance should correlate with the shear wave velocity. The shear strength, τ , is a function of normal stress to the first power.

$$\tau = c + \bar{\sigma} \tan \phi \quad (3)$$

where c = cohesion

$\bar{\sigma}$ = effective normal stress, and

ϕ = angle of internal friction.

The shear modulus, G , is a function of the shear wave velocity, V_s , and mass density, ρ , i.e.

$$G = V_s^2 \rho \quad (4)$$

Shear modulus has also been empirically (2,3,4) proportioned to the square root of the mean effective principle stress, $\bar{\sigma}_m$, or empirically equated to $1000 K_2 \sqrt{\bar{\sigma}_m}$, where K_2 is an empirically developed coefficient which is a function of soil type, void ratio, etc. Therefore, V_s can be written as:

$$V_s = \sqrt{\frac{1000 K_2 \sqrt{\bar{\sigma}_m}}{\rho}} \quad (5)$$

As a consequence, one would not expect the shear modulus or shear wave velocity to correlate with penetration resistance since they appear to be functions of effective normal stress raised to different powers. However, the data presented in this paper indicate that site specific correlations can be developed which will allow the prediction of the shear wave velocity within ± 25 percent most of the time. This is probably adequate for preliminary feasibility studies and the like.

CONCLUSIONS

From the data presented herein, it is concluded that site specific correlations exist among the shear wave velocity of the materials if the SPT N values or the Dutch cone penetration resistance values are known. This has been done at Fort Peck Dam using the equation $V_s = \alpha X$ where X is equal to a penetration resistance. If the penetration resistance is the SPT N value, then the coefficient α ranges from 15 to 46 depending on material type. If the penetration resistance is the Dutch cone resistance, q_c , in TSF, then the coefficient α ranges from 4 to 33, again, depending on the material type. This equation generally predicts the shear wave velocity within ± 20 to 30 percent most of the time. While this accuracy is less than desired, it is probably adequate for initial investigations and feasibility studies.

RECOMMENDATIONS

It is recommended that additional data of the type presented herein be obtained and analyzed. Such action will lead to further evaluation and

refinement of the correlations which were developed at Fort Peck Dam using very limited data. The fruits of this undertaking will be a means of predicting shear wave velocity knowing penetration resistance values which are routinely obtained.

ACKNOWLEDGEMENT

The authors would like to thank the U. S. Army Engineer District, Omaha, for funding this work. Thanks are also due to their colleagues at WES who assisted in the review of this paper.

REFERENCES

1. Richart, F. E., Jr., Anderson, D. G., and Stokoe, K. H., II, "Predicting In Situ Strain Dependent Shear Modulus of Soils," Proceedings, Sixth World Conference on Earthquake Engineering, Vol IV, New Delhi, India, January 1977, pp 159-164.
2. Seed, H. B., and Idriss, I. M., "Soil Moduli and Damping Factors for Dynamic Response Analysis," Report No. EERC-70-10, Earthquake Engineering Research Center, College of Engineering, University of California, Berkeley, CA, 1970 (PV 197869).
3. Hardin, B. O., and Drnevich, V. P., "Shear Modulus and Damping in Soils: I - Measurement and Parameter Effects," Journal of the Soil Mechanics Foundations Division, ASCE, Vol 98, No. SM 6, June 1972, pp 630-624.
4. Hardin, B. O., and Drnevich, V. P., "Shear Modulus and Damping in Soils: II - Design Equations and Curves," Journal of Soil Mechanics and Foundations Division, ASCE, Vol 98, No. SM7, July 1972, pp 667-692.
5. Marcuson, W. F., III, and Krinitzsky, E. L., "Dynamic Analysis of Fort Peck Dam," Technical Report No. S-76-1, U. S. Army Engineer Waterways Experiment Station, CE, Vicksburg, MS, March 1976.
6. _____, "Report on Rotary and Dutch Cone Data," U. S. Army Engineer District, Omaha, Omaha, NB, November 1975.
7. Curro, J. R., Jr., Horn, J. E., and Ballard, R. F., Jr., "In Situ Seismic Investigation, Fort Peck Dam Montana," Miscellaneous Paper S-75-4, U. S. Army Engineer Waterways Experiment Station, CE, Vicksburg, MS, February 1975.
8. "Penetration Tests and Split-Barrel Sampling of Soils," ASTM D 1586-67, Part 19, American Society of Testing and Materials, Philadelphia, PA, 1976.
9. Office, Chief of Engineers, "Soil Sampling," Engineer Manual EM 1110-2-1907, Washington, DC, March 1972.
10. Schmertmann, J. A., "Predicting the $q_c - N$ Ratio," Final Report D-636, College of Engineering, University of Florida, Gainesville, FL, October 1976.
11. Sanglerat, G., The Penetrometer and Soil Exploration, Elsevier Publishing Company, Amsterdam, London, New York, 1972.
12. de Mello, V. F. B., "The Standard Penetration Tests," Proceedings, 4th Pan American Conference on Soil Mechanics and Foundation Engineering, San Juan, Puerto Rico, Vol 1, 1971, pp 1-86.

1024

INTENTIONALLY BLANK

SITE EFFECTS FROM FOURIER TRANSFORMS

by

C. Martin Duke^I and George C. Liang^{II}

ABSTRACT

The San Fernando, Kern County and Managua earthquakes yielded a substantial number of strong motion accelerograms. These records have been found to express the effects of local site conditions when the latter are available in terms of shear wave velocities and depths. Given these subsurface properties with sufficient detail and precision, the respective subsurface characteristics may be expressed in the frequency domain using Fourier transforms.

Multiple records are available from all three of the earthquakes cited. This makes possible the optimization of the subsurface mathematical models between bedrock and the ground surface. The product of the optimization is an instrumental subsurface model whose precision exceeds that of the initial models that were based only on exploration data.

INTRODUCTION

The characteristics of an earthquake accelerogram are influenced primarily by three factors: the source characteristics, the effect of the transmission path and the effect of local site geology. The earthquake motion that a structure may experience can be predicted by the appropriate incorporation of these three factors. Such a prediction provides a design base for the seismic safety of structures. However, at the present state of the art, this may only be done in principle, but not in practice. The lack of reliable understanding on the characteristic of the three effects limited such a task.

In order to be able to predict ground motion, it is of interest to examine the contributions of the source characteristics, the path effect and the site effect in the recorded strong motion accelerograms. The amount of recorded accelerograms from past earthquakes makes such a study plausible. These accelerograms contain the clue to the characteristics of source, path and site effects. It is conceivable that a combined analysis incorporating theory and experiment will provide the information sought.

The analysis may be done either in the time domain or the frequency domain. The latter was preferred for this study. This was because the spectral analysis could be directly related to wave propagation theory, and the frequency spectrum was more descriptive of the behavior of the accelerogram than the time history itself.

The use of Fourier transforms to convert accelerograms into the frequency domain provides a convenient use of linear system theory. The conversion of convolution integration in the time domain to a simple multiplication in the frequency domain makes linear system modeling an

^I Professor, School of Engineering and Applied Science, University of California, Los Angeles, California.

^{II} Post Graduate Research Engineer, School of Engineering and Applied Science, University of California, Los Angeles, California.

Preceding page blank

attractive method for analysis. A linear system model (1) was developed by Lastrico, Duke and Ohta (1972),

$$G = EWX = IX \quad (1)$$

where all factors are complex Fourier spectrum in the frequency domain, and

G is the free field ground motion

E is the source function

W is the crustal transfer function for the transmission path

X is the subsurface transfer function for the local site effect

I is the motion near the recording site, but before it is influenced by the local site geology.

Two linear system equations of identical form may be written in parallel, one for the propagation of body waves, and one for the propagation of surface waves. In this study, the surface wave effects will be assumed negligible.

BODY WAVE TRANSFER FUNCTIONS

Of primary concern in this report are the effects of site conditions on earthquake ground motion. Linear system theory will be applied to this section to establish methods for use in determining subsurface transfer functions, X, by means of the simplified model using body waves only, Fig. 1. Also of interest here will be the body wave crustal transfer functions, W, ratios of body wave subsurface transfer functions, and estimations of ground motions at a site in the absence of strong motion instrumental data.

The description for the body wave crustal and subsurface transfer functions are described in Lastrico, Duke and Ohta (1972) as the following. The crustal transfer function accounts for the geometrical attenuation and damping of the crustal transmission path by the following equation

$$W = \frac{1}{r} e^{-\alpha r}$$

with

$$\alpha = \frac{\omega}{2Qv}$$

(2)

where

r is the hypocentral distance along the crustal path

α is the damping factor

v is the mean shear wave velocity along the path

Q is the specific damping of shear waves

ω is the circular frequency.

The subsurface transfer function is modeled as vertically propagating shear waves. It is based on Haskell's formulation (1960), modified to include damping.

METHOD 1

A computational method will be introduced for use in determining the transfer functions and ground motions of concern.

Transfer functions computed using an appropriate theory, with field or structural measurements of essential material properties and geometrical quantities, are called "exploration transfer functions." They are based on mathematical models formed from exploration data measured in the field or on the structure. "Instrumental transfer functions,"* on the other hand, are computed using data from strong motion accelerograms.

In general, the method, which will be identified as Method 1 from here on, applies to a procedure in which one first constructs exploration transfer functions, subsequently incorporating instrumental data to obtain the instrumental transfer functions. Several illustrations of Method 1 will be presented.

The first illustration involves the 1952 Kern County earthquake (Lastrico, Duke and Ohta, 1972) in which strong motion accelerograms were recorded in the Los Angeles area at UCLA, Hollywood, Subway Terminal and Vernon due to a source near Wheeler Ridge. Fig. 2 shows these locations and the causative fault.

Fig. 1 shows the system model which was used in this case. The purpose is to improve the exploration transfer functions and the corresponding subsurface exploration models for the four Los Angeles sites, by adjusting them using some of the instrumental data.

We begin with the four subsurface models shown in Figs. 3 and 4. Computation using these models provides the dotted curves in Fig. 5. Bedrock is defined as the top of crystalline rock, which was found at from 8,000 to 20,000 feet of depth at different sites. See Fig. 3.

The basic equation is (1), which may be written four times, once for each of the recording sites, or

$$I_i = \frac{G_i}{X_i} \quad (3)$$

in which G_i is obtained from accelerograms and X_i is obtained from exploration data.

It is reasonable to assume that the incident motion from bedrock was the same beneath each site, because of the order of magnitude difference between the epicentral distance and the intersite distances, which justifies

* Sometimes called final transfer functions.

$$\bar{I} = \frac{1}{4} \sum_1^4 \frac{G_i}{X_i} = \frac{1}{4} \sum_1^4 I_i \quad (4)$$

in which \bar{I} is the mean bedrock Fourier spectrum under Los Angeles in the 1952 earthquake, and its standard deviation is σ_I . The subscript designates the several recording sites. The standard deviation of the bedrock motion computed using the exploration transfer functions appears in Fig. 6.

It is to be noticed that G is a known quantity at each site. Now these quantities can be used in the form

$$X_i = \frac{G_i}{\bar{I}} \quad (5)$$

to compute the approximate instrumental subsurface transfer functions at the four sites.

The graph obtained for σ_I in Fig. 6 shows that the standard deviation in I is approximately 32 percent averaged over all frequencies. This is a large figure, so it was determined to try adjusting the exploration subsurface models, within the uncertainties of their properties, to minimize the standard deviations in I . The adjustment was done at the lower frequencies by adjusting shear velocities, at the higher frequencies by adjusting damping, and in general over the upper 600 feet. The effect was substantial, amounting to a reduction of the average σ_I to 23 percent, as shown in Fig. 7. See Fig. 5 for the model changes involved.

The "final" results were obtained by dividing the measured surface spectra by the bedrock Fourier moduli after minimization of σ_I . The term "final" is used to signify what is considered the all around best X . Fig. 4 shows in the solid lines the resulting subsurface transfer functions. Except at Subway Terminal the spread between exploration X and final X is rather large.

It is of interest and perhaps of practical value to observe that the final transfer functions showed, generally, highest amplifications at Hollywood and UCLA, with a 100 percent spectral amplitude range at the latter.

A second illustration of Method 1 is that of the 1971 San Fernando earthquake (Duke and Hradilek, 1973). In this case there were available eleven sites at which detailed subsurface and crustal exploration models had been developed and at which strong motion accelerograms had been recorded during the main shock. Four of the 11 were in the Century City area and another four in the southern San Fernando Valley. Fig. 8 shows the locations of the recording sites, the main shock energy center, four aftershocks and the causative fault. It is seen that the estimated center of energy release is somewhat removed from the main shock epicenter; the former will be used for analysis.

The purpose of this study was to establish both the exploration and the instrumental transfer functions of the subsurface models at Century

City, and to compare them.

The system model used is essentially that of Fig. 1. The technique used is first to compute the eleven source functions by tracing the recorded accelerograms from the respective sites back to the source,

$$E_i = \frac{G_i}{W_i X_i} \quad (6)$$

which utilizes the recorded ground motion and the exploration transfer functions for W and X. Then a mean equivalent source function may be computed as

$$\bar{E} = \frac{1}{11} \sum_1^{11} \frac{G_i}{W_i X_i} = \frac{1}{11} \sum_1^{11} E_i$$

The use of Method 1 can be explained in terms of the following procedure. The exploration X functions were provided through application of the Haskell-Thomson formulation. This made use of exploration subsurface models consisting of viscoelastic horizontal layers extending down to the top of basement complex. The exploration W functions were computed using the common expression for damped spherical spreading (2). The resulting main shock equivalent source function appears in Fig. 9, with both the radial and the tangential components shown. Having established the eleven exploration models, the corresponding subsurface exploration transfer functions were computed.

Next the instrumental X spectra were computed for each recording site using

$$X_i = \frac{G_i}{\bar{E} W_i} \quad (7)$$

Note that the same W is used in both (6) and (7).

Figure 10 presents the average of the four Century City instrumental X spectra. Only the average of the instrumental spectra is shown because the four subsurface models were quite similar, and it seemed natural to represent the Century City subsurface amplification as a single spectrum. However, the corresponding four exploration models are somewhat different from one another in the top layers, which is evident in comparing the four pairs of transfer functions in the figure.

An optimization procedure was used to cause the exploration spectra to coincide as closely as feasible with the instrumental spectra. Nature set limits of adjustment in the optimization procedure, these being the limits of uncertainty of the properties and geometry of the exploration models. These limits resembled those used above with the 1952 earthquake data.

The solid lines are the instrumental X spectra, all four having been shown the same, as explained. The dotted lines on the figure are the exploration values, which in the form shown have previously gone through the

optimization process.

Another use of Method 1 is provided by

$$G_1 = G_2 \frac{W_1 X_1}{W_2 X_2} \quad (8)$$

This permits a synthesis of the ground motion at a place where it was not measured. Illustration of (8) is made for the 1972 Managua Earthquake (Johnson, 1976). In this illustration, subscripts 1 and 2 refer to Banco Central and ESSO, respectively. Fig. 11 shows the location of the recording stations and the mainshock energy center. For the mainshock of December 23, 1972, the only set of accelerograms recorded was at ESSO. By applying Method 1 as given in (8), the accelerograms for the two horizontal components at Banco Central were computed, Fig. 12.

DISCUSSION AND CONCLUSIONS

Prediction of ground motion time histories requires detailed analysis of past recorded strong motion accelerograms. Contributions of the earthquake source, the transmission path and the local site geology must all be examined in order that the safety of structures from future earthquakes may be provided. Linear system modeling is a method to achieve this objective. Its convenience in mathematical manipulations allows the source, the path and the site effects to be examined separately.

The studies presented here made use of a simplified linear system model in which only body wave effects were considered. Emphasis was placed on the effect of local site geology on the accelerograms. The simplicity of mathematical manipulations such as multiplication and division of Fourier spectra showed the attractiveness of such analysis.

In summary of the numerical studies presented, the subsurface transfer functions from both the Kern County and the San Fernando earthquakes are suitable for application in creating design earthquakes at and near the sites investigated. Also, a degree of confidence can be placed on the computed Managua ground motion.

REFERENCES

- Duke, C. Martin, and Peter J. Hradilek, "Spectral Analysis of Site Effects in the San Fernando Earthquake," Proceedings, 5WCEE, Vol. 1, pp. 680-690, Rome, 1974.
- Haskell, N. A., "Crustal Reflections of Plane SH Waves," J. Geophys. Res., Vol. 65, pp. 4147-4150, 1960.
- Johnson, J. A., Site and Source Effects on Ground Motion in Managua, Nicaragua, UCLA-ENG-7536, School of Engineering and Applied Science, UCLA, May, 1975.
- Lastrico, Roberto M., C. Martin Duke, and Yutaka Ohta, "Effects of Site and Propagation Path on Recorded Strong Earthquake Motions," Bull. Seis. Soc. Am., Vol. 62, No. 4, pp. 933-954, August 1972.

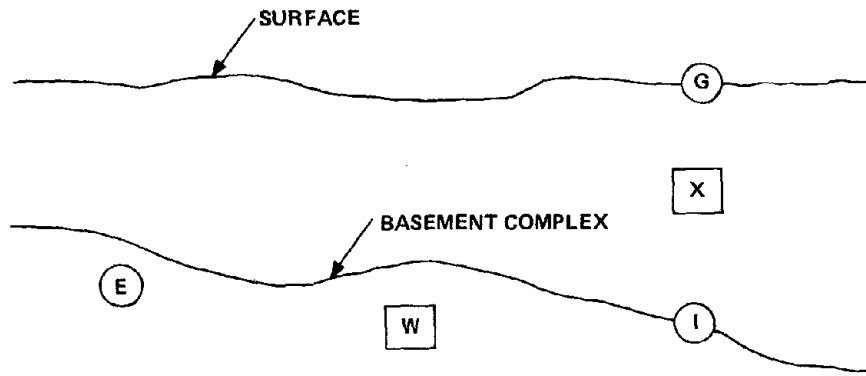


Figure 1. Simplified Model Based on Body Wave Transfer Functions.

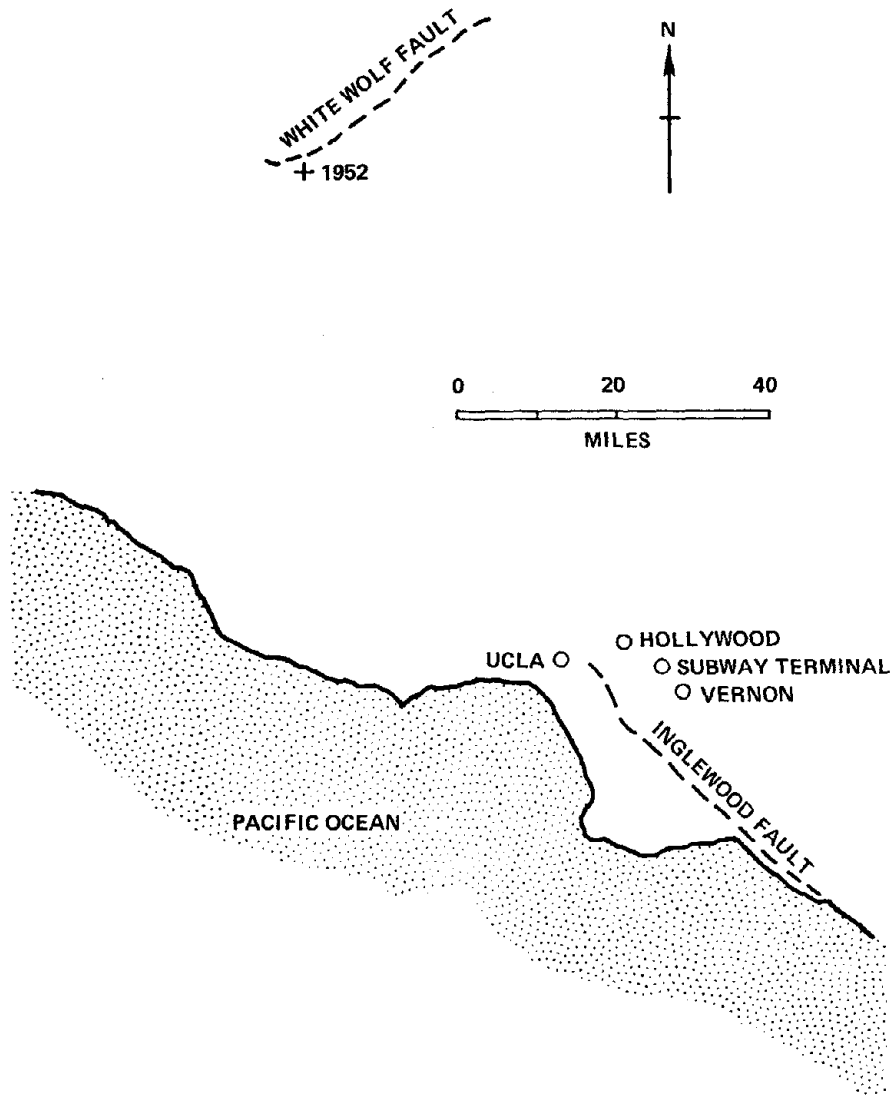


Figure 2. Vicinity Map for 1952 Earthquake.

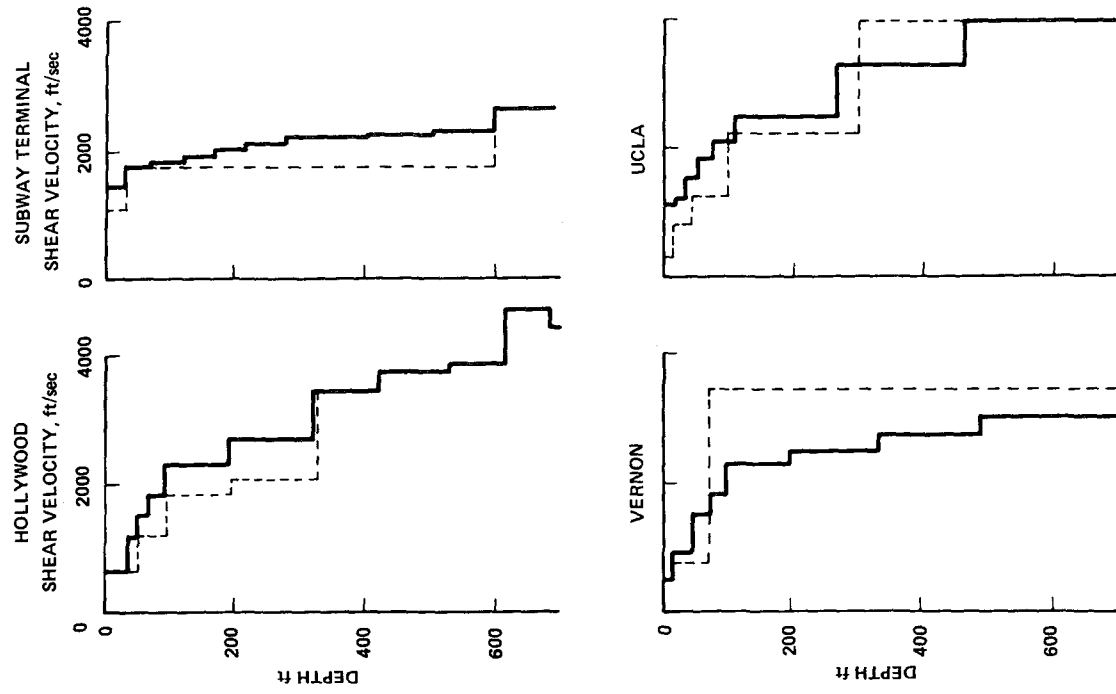


Figure 4. Near-Surface Velocities, Los Angeles Sites. Dotted Lines Show Exploration Values. Solid Lines Show Values Used in Final Computations.

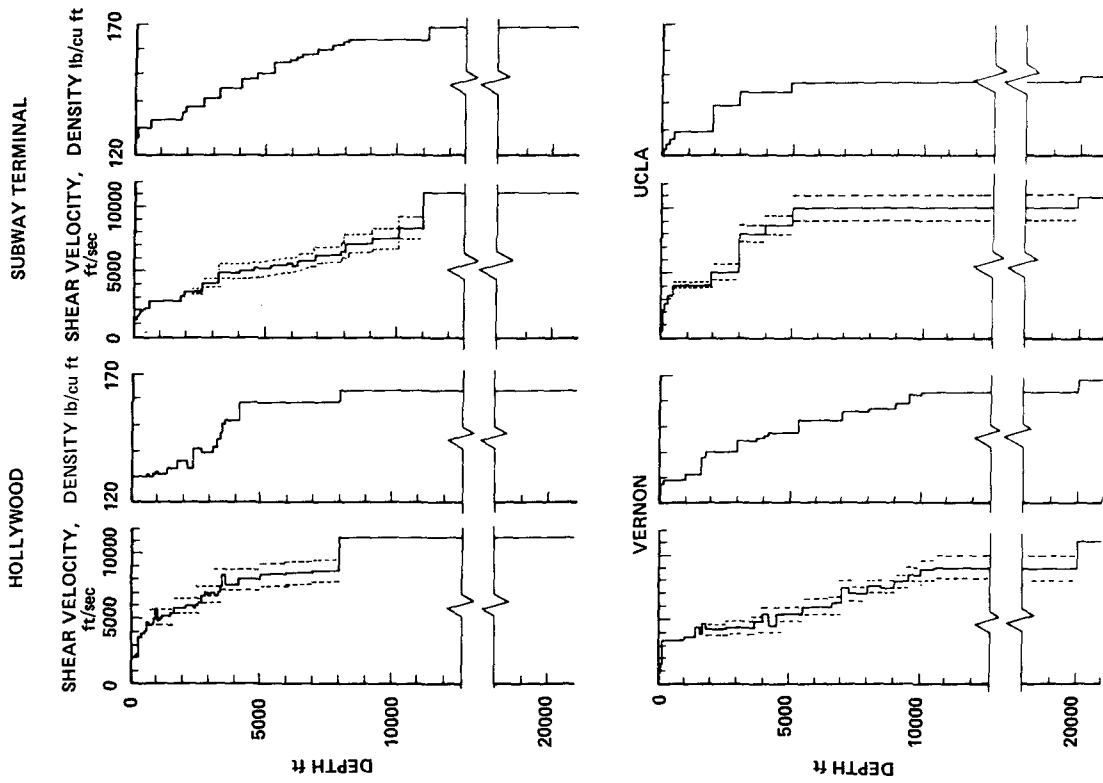


Figure 3. Complete Subsurface Models, Los Angeles Sites. Dotted Lines Show One Standard Deviation Relative to Solid Lines.

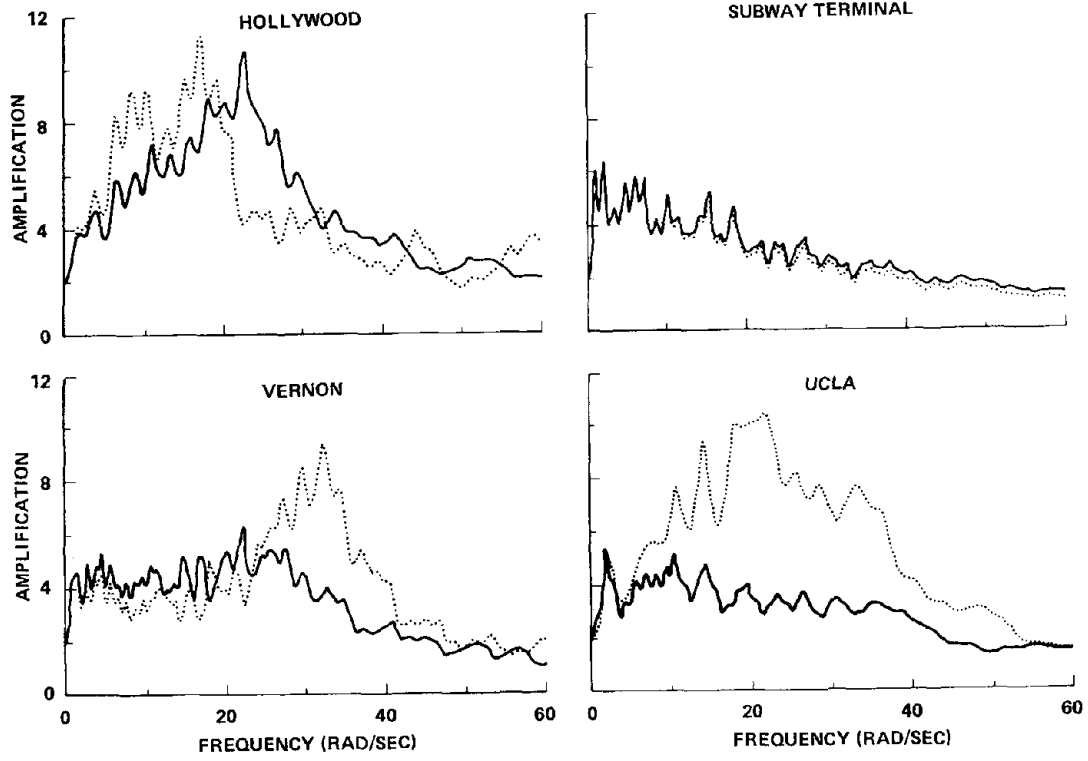


Figure 5. Subsurface Transfer Functions, Los Angeles Sites. Dotted Lines Based on Exploration Models. Solid Lines Based on Final Models.

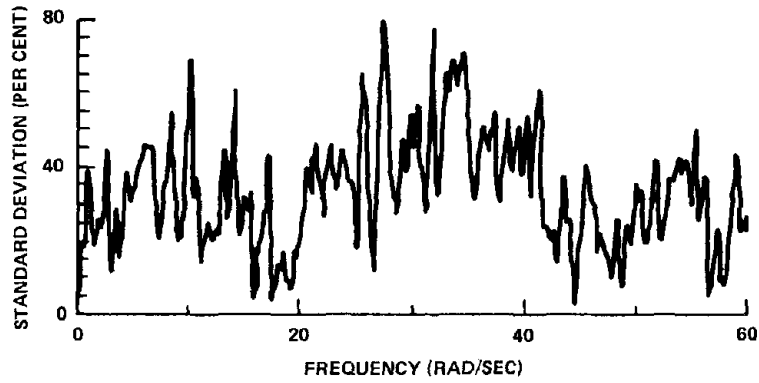


Figure 6. Standard Deviation of Bedrock Fourier Moduli, Los Angeles Sites. Based on Exploration Subsurface Models.

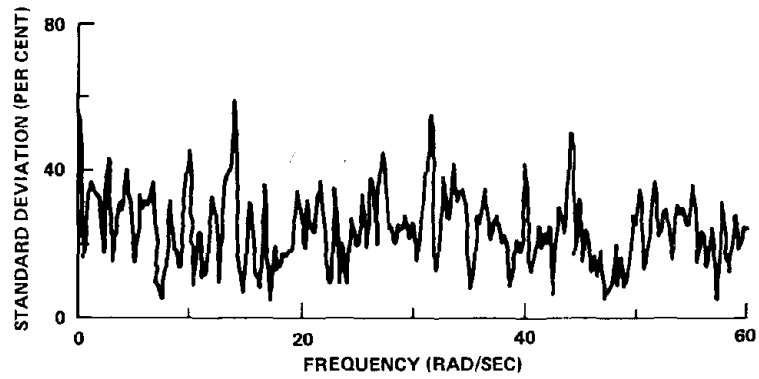


Figure 7. Standard Deviation of Bedrock Fourier Moduli, Los Angeles Sites. Based on Final Subsurface Models.

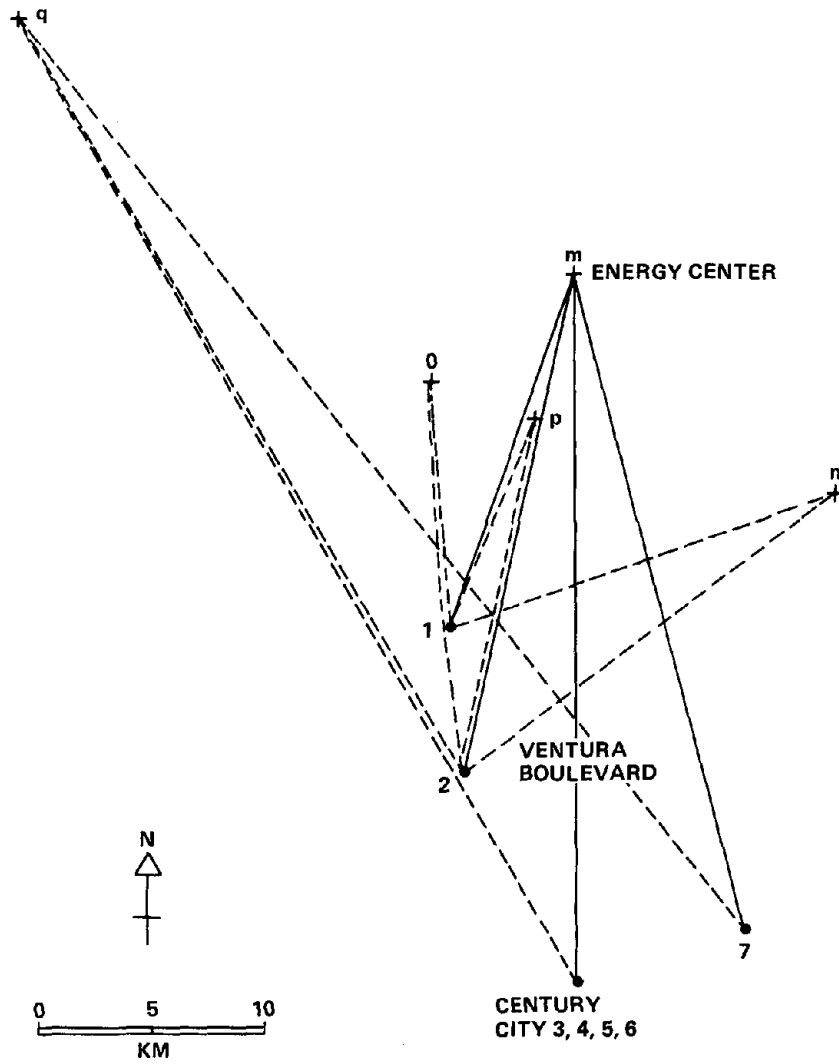


Figure 8. Vicinity Map for 1971 Earthquake.

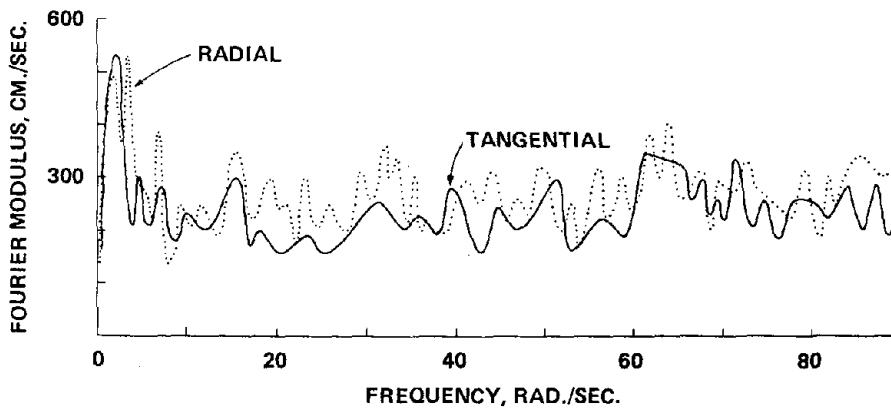


Figure 9. Main Shock Equivalent Source Function.

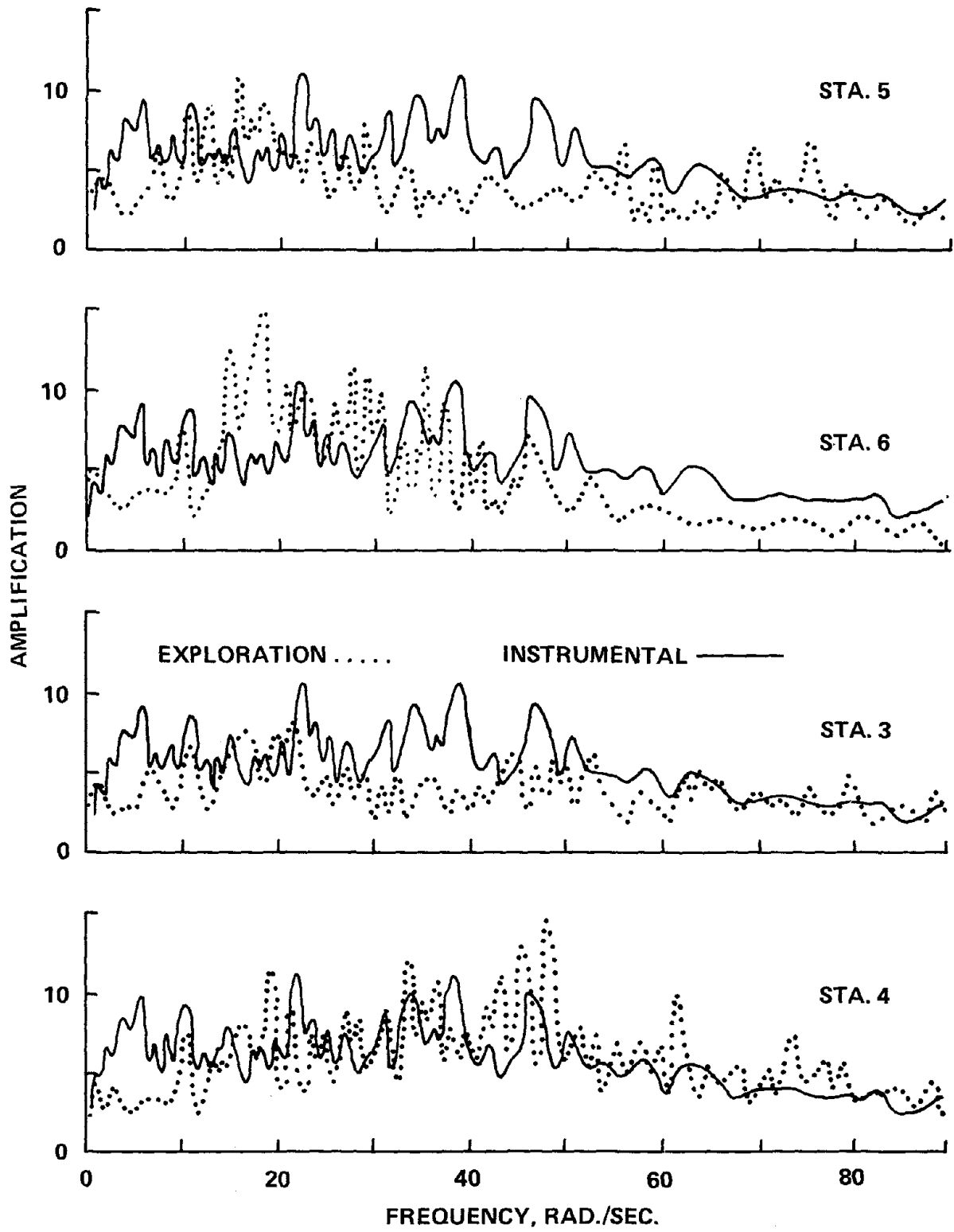


Figure 10. Century City Subsurface Transfer Functions.

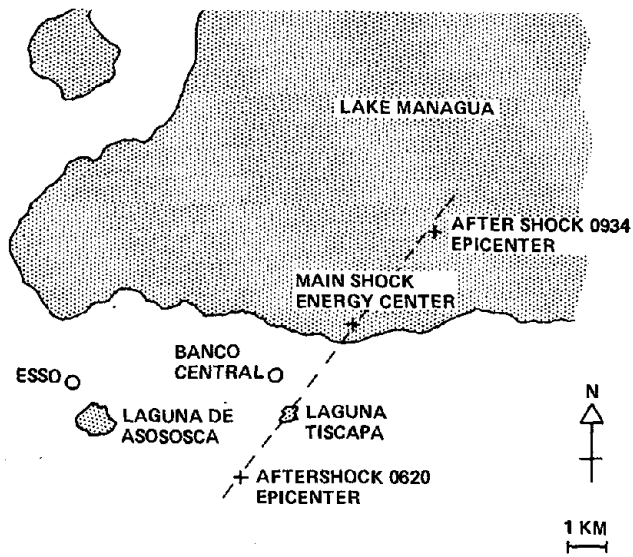


Figure 11. Vicinity Map for Managua Earthquake

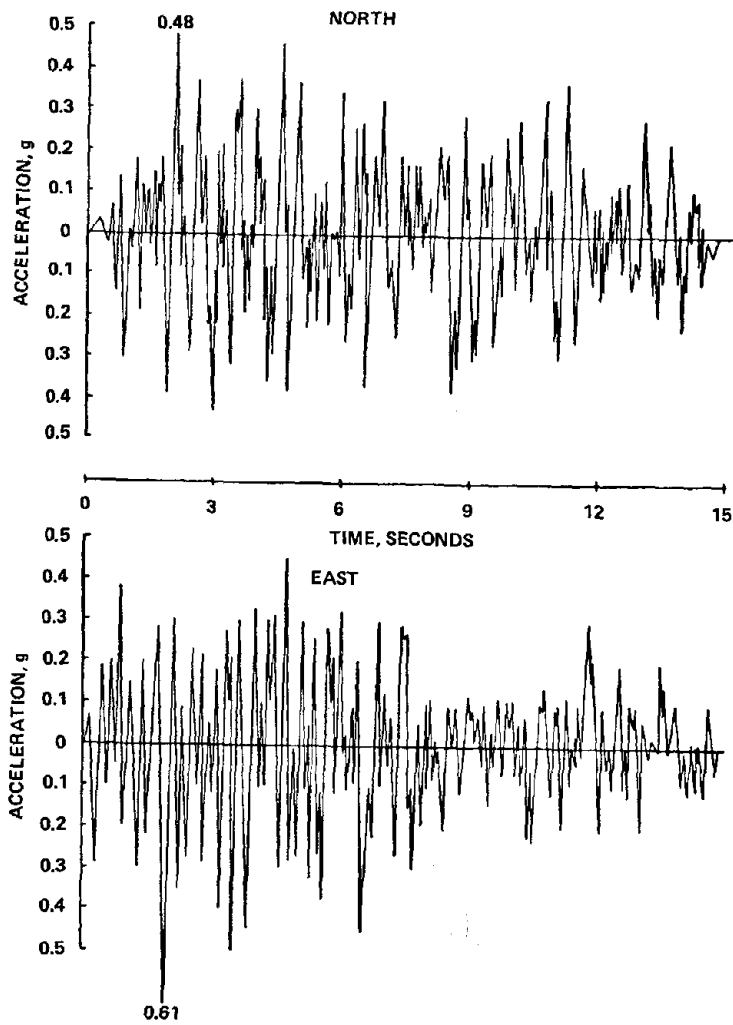


Figure 12. Time History of Managua Main Shock, Computed for Banco Central, Based on ESSO Record.

DYNAMIC CHARACTERISTICS OF AN EARTH DAM FROM TWO
RECORDED EARTHQUAKE MOTIONS

by

A. M. Abdel-Ghaffar^I and R. F. Scott^{II}

ABSTRACT

An investigation has been made of the effect of two earthquakes (with $M_L = 6.3$ and 4.7) on a modern rolled-fill earth dam. The purposes of the investigation are: (a) to study the nonlinear behavior of the dam, (b) to provide data on the in-plane dynamic shear moduli and damping factors for the materials of the dam during real earthquake conditions, and (c) to compare these properties with those indicated by laboratory investigations, and commonly used in dynamic analyses.

INTRODUCTION

Measurement of the soil properties which control the dynamic behavior of an earth dam is extremely difficult because samples taken for laboratory tests have necessarily been disturbed and may not reflect actual behavior of the soil in place. In addition, laboratory measurements on a small soil sample may not be representative of soil properties in the mass. In this study on an earth dam, a rational procedure is developed to estimate its dynamic soil properties, such as shear moduli and damping factors, from its measured response to real earthquakes; the procedure uses strong-motion records from the crest and the dam base. This permits study of nonlinear behavior by the variation of stiffness and damping properties with strain levels. The Santa Felicia earth dam, located in Southern California, was chosen for the analysis because it had been subjected to strong shaking during two earthquakes: the strong, 6.3 magnitude San Fernando earthquake of 1971 and a 1976 earthquake of magnitude 4.7, and was equipped with motion sensors that yielded data on how it responded to the shaking. In the past, either earth dams that experienced strong shaking were not instrumented, or else instrumented dams were not strongly shaken. Few earth dams, including Santa Felicia, are adequately instrumented for earthquake studies. Santa Felicia has the minimum equipment which still permits some useful analysis. The investigation is limited to the upstream-downstream response since existing analytical techniques for earth dams are restricted to horizontal shear deformation in that direction (2,4). The data obtained on the shear moduli and damping factors for the material of the dam are compared with those indicated previously by laboratory investigations.

I Research Fellow in Civil Engineering, California Institute of Technology, Pasadena, California.

II Professor of Civil Engineering, California Institute of Technology, Pasadena, California.

DESCRIPTION OF THE DAM

Santa Felicia Dam (Fig. 1) is a modern rolled-fill embankment. It is 273 ft high above its lowest foundation and 200 ft above the original stream bed; it is 450 ft long across the valley of the base and 1,275 ft long at the crest. The dam has a central impervious core and pervious shells upstream and downstream. The core and shell materials are basically alluvial, consisting of clay, sands, gravel and boulders. It was built in 1955. The dam was equipped in 1967 with two accelerographs which recorded the earthquakes of 1971 and 1976; one instrument was located at the central section of the crest and the other was placed at the right abutment on the downstream side.

PERFORMANCE OF THE DAM DURING THE TWO EARTHQUAKES

The dam was about 33.4 km west of the epicenter of the 1971 San Fernando earthquake ($M_L = 6.3$). Figures 2-a and b show the crest and base accelerograph records obtained along with the calculated velocities and displacements in the upstream-downstream direction. The first 3 to 3.5 seconds of the abutment record have been lost due to double exposure. The crest displacement (Fig. 2-a) is a combination of the structural motion of the crest with respect to the base superimposed upon the ground motion, representing the transient displacement of the bedrock at the site. The maximum long-period amplitude of the bedrock displacement appears to be about 8 cm. Superimposed on this, the amplitude of the dam's fundamental mode of displacement (with a period of about 0.7 seconds) seems to be on the order of 1.3 cm. It is apparent, therefore, that relatively small deformations and strains must have been generated in the structure during the earthquake. During the 1976 earthquake ($M_L = 4.7$), the dam was 14 km northeast of the epicenter. The observed responses of crest and abutment are shown in Figs. 2-c and d. The fundamental mode with an apparent period again of about 0.7 seconds is indicated best by the computed velocity plot of Fig. 2-c.

ANALYSES OF THE RECORDED MOTIONS

1 - Amplification Spectra

The amplification spectra were computed by dividing Fourier amplitudes of acceleration of the crest records (Figs. 3-a, c) by those of the base records (Figs. 3-b, d) for the two earthquakes. The spectra show the natural frequencies of the dam and enable an estimate of the relative contribution of different modes to be made. Figure 5 shows a predominant frequency of 1.45 Hz in the upstream-downstream direction.

2 - Relative Motion

Relative motions of the crest with respect to the base are shown in Fig. 4 for the two earthquakes. For the 1971 event, the time difference of the crest and base records was taken into consideration. Subtraction of the long-period ground motion did not result in even comparatively smooth curves for relative structural displacement, as

anticipated: instead, the relative displacement still included large fluctuations with longer period. This could be due to techniques of digitization. The relative velocity and displacement of Fig. 4 show a dominant period of 0.7 seconds superimposed on long-period motion.

BASIS OF THE ANALYSIS

Examination of the two observed earthquake records indicate that the dam responded primarily in its fundamental mode ($f = 1.45$ Hz) of vibration in the upstream-downstream direction, although there is some contribution of the higher modes apparent in the response. In this analysis, the fundamental mode response is treated as that of a single-degree-of-freedom (S.D.O.F.) hysteretic structure, as suggested for building structures by Iemura and Jennings (3). The equation of motion of a S.D.O.F. system excited by an earthquake can be written as

$$M\ddot{x} + F(x, \dot{x}) = -M\ddot{z} \quad \text{or} \quad F(x, \dot{x}) = -M(\ddot{x} + \ddot{z}) \quad , \quad (1)$$

in which $F(x, \dot{x})$ represents the nonlinear restoring force due to relative velocity \dot{x} and displacement x ; M is the mass and \ddot{z} is the ground acceleration (Fig. 6). The hysteretic response of the system can be obtained by plotting the relative displacement x against the absolute acceleration $(\ddot{x} + \ddot{z})$. Thus, a preliminary version of the hysteretic response of the dam can be obtained by plotting the relative displacement of the crest with respect to the base versus the absolute acceleration of the dam. Equivalent shear moduli and damping factors can be estimated from the slope and the area, respectively, of the hysteretic response.

DYNAMIC SHEAR MODULI AND DAMPING FACTORS OF THE DAM MATERIAL

Three types of digital band-pass filtering (designated by A, B and C in Fig. 6-b) of the crest and base records were used to eliminate contributions from higher modes to the response so that the hysteresis loops of only the fundamental mode response could be isolated. The response resulting from both filtering type A (Caltech standard strong-motion processing) and type B (4 seconds filtering, Fig. 7-a) showed marked fluctuations along the badly tangled trajectory of the supposedly first-mode hysteresis loops as shown in Fig. 8 for the first four seconds of the records. A narrow band-pass filtering (type C of Fig. 6) around the natural frequency (1.45 Hz) of the dam was applied in order to produce reasonable loops as shown in Fig. 9. A method, using some of the existing elastic shear-beam theories (Refs. 2 and 4), was developed to enable the shear stress and strain and consequently the shear modulus to be evaluated from each hysteresis loop [Abdel-Ghaffar and Scott (1)]. The shear strain and stress for the central region of the dam can be written as

$$\gamma_{11} = \bar{q}_{11}(y) h \left(\frac{\omega_{11}}{v_s} \right)^2 \cdot x_{\max} \quad , \quad (2)$$

$$\tau_{11} = \bar{\phi}_{11}(y) \rho h \cdot (\ddot{x} + \ddot{z})_{\max} \quad (3)$$

where $\bar{\phi}_{11}(y)$ is the modal participation factor for the first mode at depth y (from the crest), h is the dam depth, ω_{11} is the fundamental frequency ($= 2\pi \times 1.45$ rad/sec), v_s is the shear wave velocity of the dam material [850 ft/sec at 0.7 to 0.75h below the crest from field-measurements (1)], and ρ is the mass density of the dam materials ($= 4.02$ lb sec²/ft⁴ (slugs) based on average unit weight; x_{\max} and $(\ddot{x} + \ddot{z})_{\max}$ are the maximum relative displacement and absolute acceleration in each hysteresis loop, respectively. Thus, the equivalent shear or secant modulus G for each loop can be expressed by the slope of the line joining the extreme points of the loop as follows:

$$G = \frac{\tau_{11}}{\gamma_{11}} = \rho \left(\frac{v_s}{\omega_{11}} \right)^2 \cdot \frac{(\ddot{x} + \ddot{z})_{\max}}{(x)_{\max}} \quad (4)$$

The maximum shear strain occurs at an elevation of about 0.7 to 0.75 of the dam height where $\bar{\phi}_{11} = 0.47$. Since the various loops have different sizes, it is possible to obtain both modulus and damping as functions of strain in the dam. The relationship between the estimated shear modulus and the dynamic shear strain is illustrated by the results shown on the semi-log plots of Fig. 10-a for the first 20 seconds of the 1971 earthquake and the first 6 seconds of the 1976 earthquake. It is apparent that the modulus depends on the magnitude of the strain in the hysteresis loop. The relationship between the estimated equivalent viscous damping factor from the area of each hysteresis loop, and the corresponding shear strain amplitude is also shown in Fig. 11-a. While there is a considerable scatter in the data, most of the results fall within the dashed lines in Figs. 10-a and 11-a. These provide reasonable estimates of dynamic properties for the soil of the dam.

COMPARISON

To compare the results obtained in this investigation from the two earthquake observations, one has to know the confining pressure of the dam material at a depth of 0.75h (178 ft below the crest). The results obtained here for shear moduli are shown on Fig. 10-b along with the curves suggested by Seed and Idriss (5) for Southern California soils (dense sand and sandy gravel) at pressures equivalent to a depth of 175 ft. The sandy gravel curve in Fig. 10(b) comes from an in situ wave velocity measurement (square solid point in the figure) at a low strain, and the assumption (5) that the material would follow the behavior of the dense sand (lower curve) at intermediate and higher strains. At lower and medium strains, it seems that the results of the present investigation lie in a region halfway between the curves suggested for the gravelly soil and for sand. At higher strains the shear moduli obtained in this investigation for the dam material appear to decrease in a manner dissimilar to that suggested by Seed and Idriss.

Results of previous investigations (5) leading to suggested ranges of damping ratios for saturated clays and sands are presented along

with the results of this study in Fig. 11-b. It is apparent that damping ratios for the gravelly soils of the dam are somewhat different from those suggested for sands and clays.

Clearly, more data on these dynamic characteristics is required particularly for very low and very high strain levels in full-scale structures.

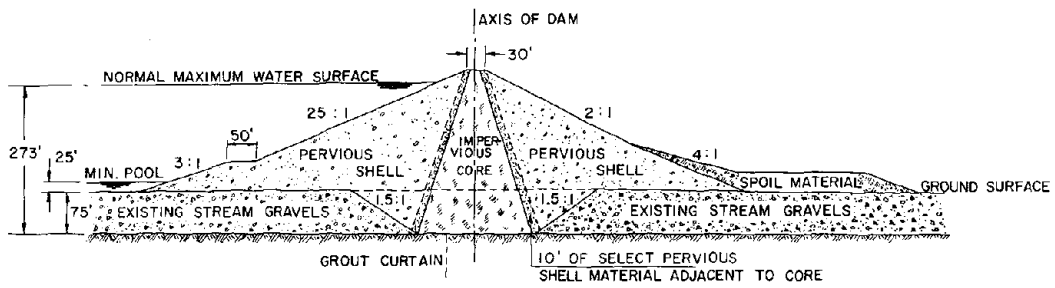
ACKNOWLEDGEMENT

This investigation was supported by the National Science Foundation and by the Earthquake Research Affiliates of the California Institute of Technology.

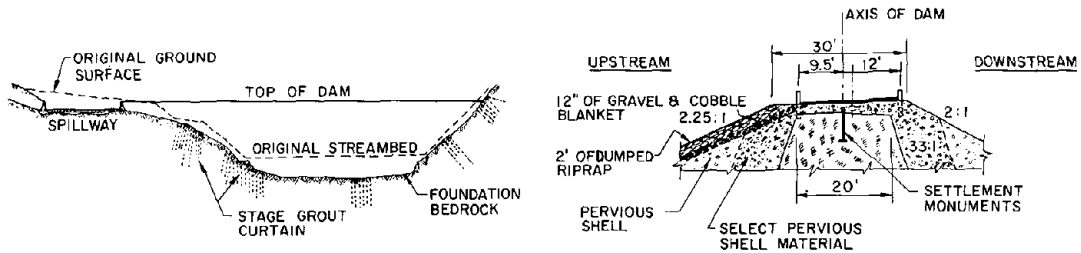
REFERENCES

1. Abdel-Ghaffar, A.M. and Scott, R.F., "An Investigation of the Dynamic Characteristics of an Earth Dam from the Analysis of Two Recorded Earthquake Motions", Earthquake Research Laboratory, EERL 77-04, California Institute of Technology, Sept. 1977.
2. Ambraseys, N.N., "On the Shear Response of a Two Dimensional Wedge Subjected to an Arbitrary Disturbance", Bulletin of the Seismological Society of America, Vol. 50, Jan. 1960, pp. 45-56.
3. Iemura, H. and Jennings, P., "Hysteretic Response of a Nine-Story Reinforced Concrete Building During the San Fernando Earthquake", Earthquake Engineering Research Laboratory, EERL 73-07, California Institute of Technology, Oct. 1973.
4. Martin, G.R., "The Response of Earth Dams to Earthquakes", Ph.D. Thesis, 1965, Civil Engineering Department, University of California, Berkeley.
5. Seed, H.B. and Idriss, I.M., "Soil Moduli and Damping Factors for Dynamic Response Analyses", Report No. EERC 70-10, College of Engineering, University of California, Berkeley, December 1970.

SANTA FELICIA DAM
SANTA PAULA, CALIFORNIA

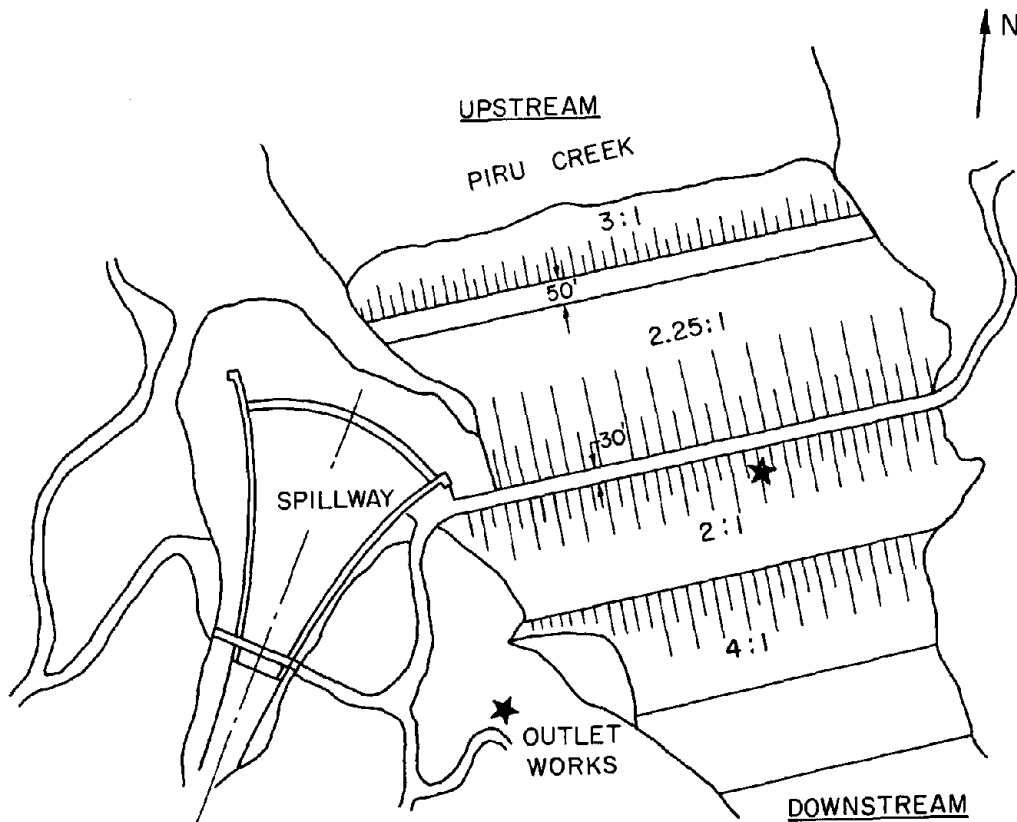


CROSS SECTION OF THE DAM

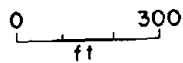


DEVELOPED PROFILE ON AXIS DAM LOOKING UPSTREAM

CREST DETAIL



★ Location of Accelerographs



PLAN VIEW

Fig. 1 Structural details of Santa Felicia Dam

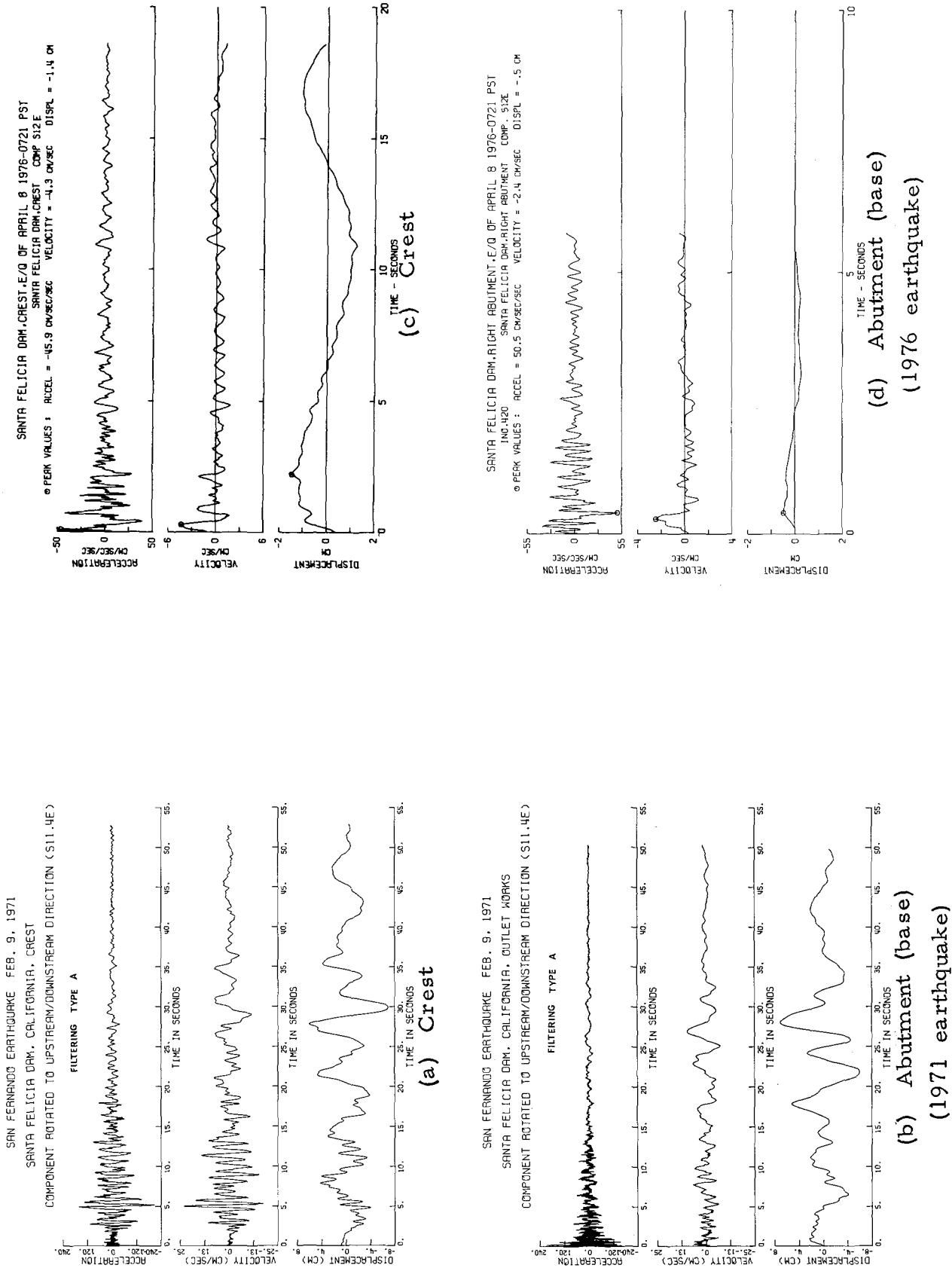


Fig. 2 Accelerograms and integrated velocity and displacement curves of the upstream/downstream component

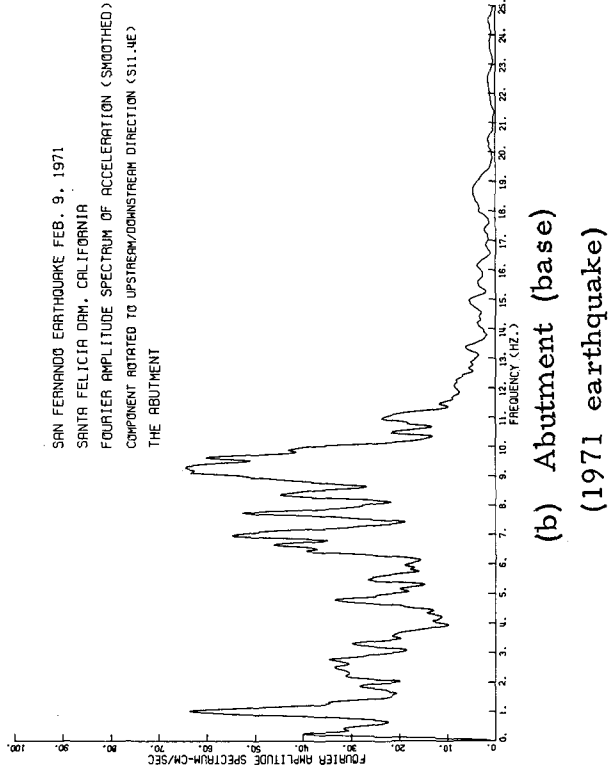
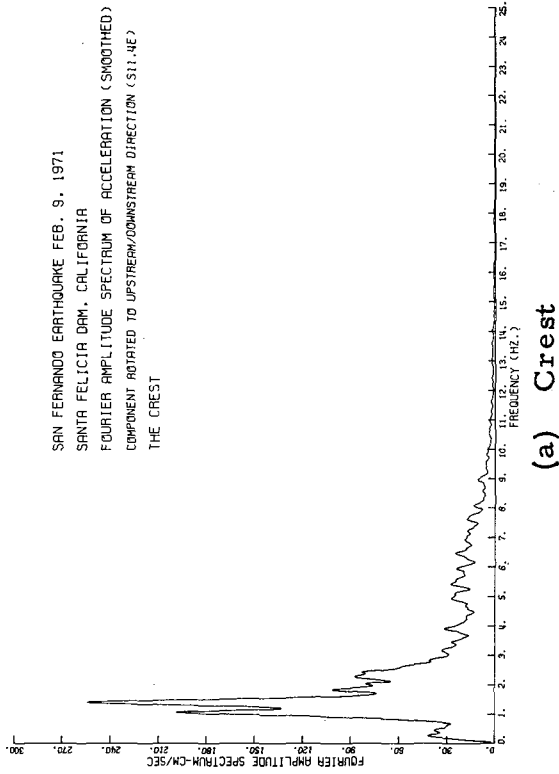
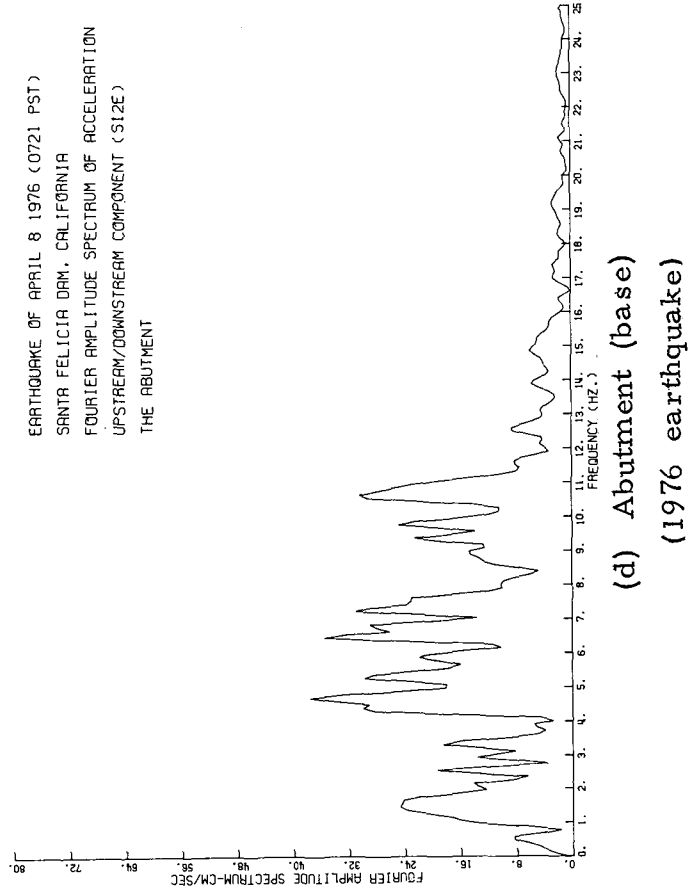
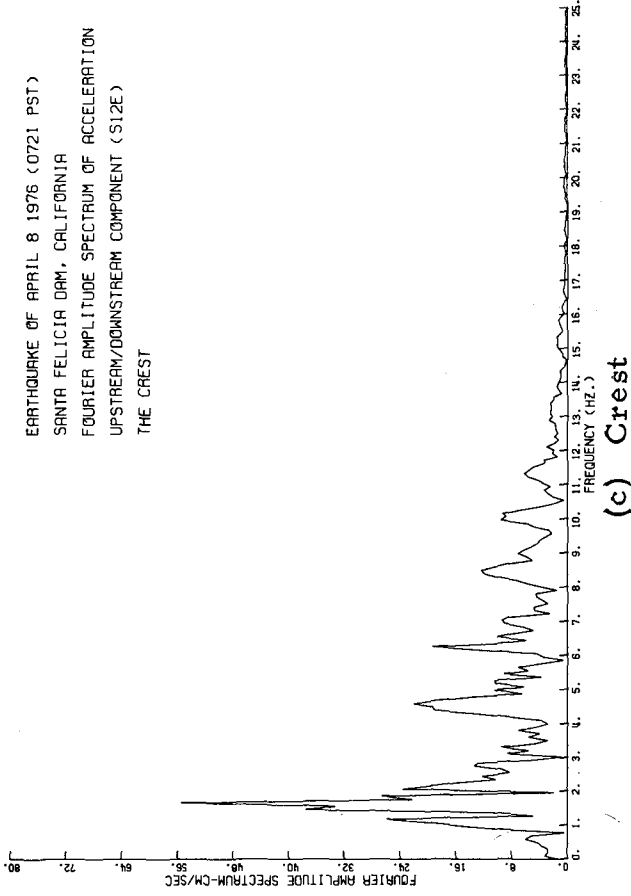
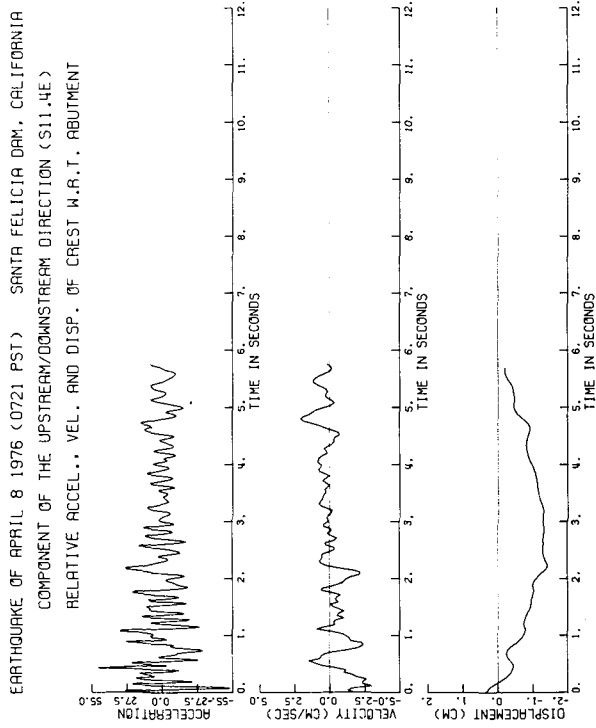
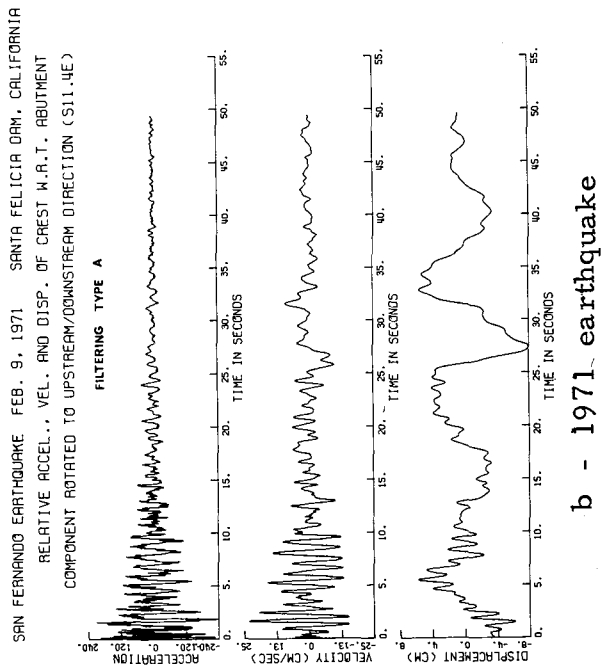


Fig. 3 Fourier amplitude spectra

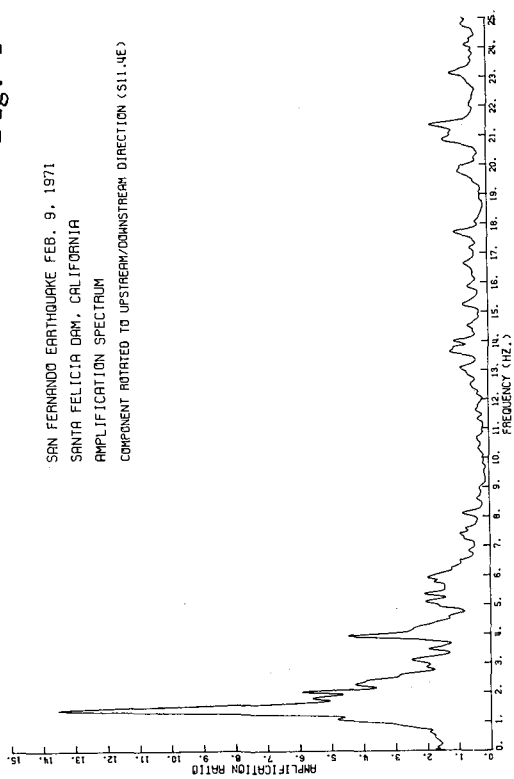


a - 1976 earthquake

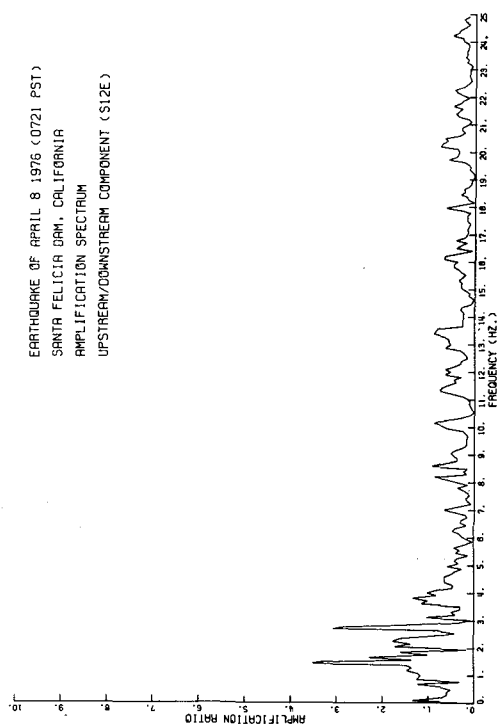
Fig. 4 Relative motion



b - 1971 earthquake



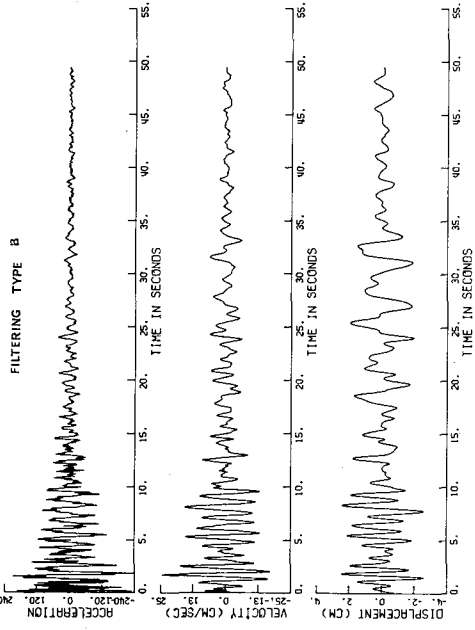
a - 1971 earthquake



b - 1976 earthquake

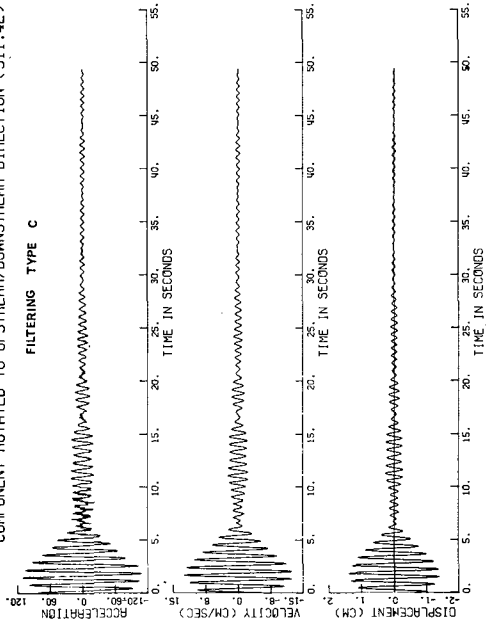
Fig. 5 Amplification spectra

SAN FERNANDO EARTHQUAKE FEB. 9, 1971 SANTA FELICIA DAM, CALIFORNIA.
RELATIVE ACCEL., VEL., AND DISP. OF CREST W.R.T. ABUTMENT
COMPONENT ROTATED TO UPSTREAM/DOWNSTREAM DIRECTION (S11.4E)



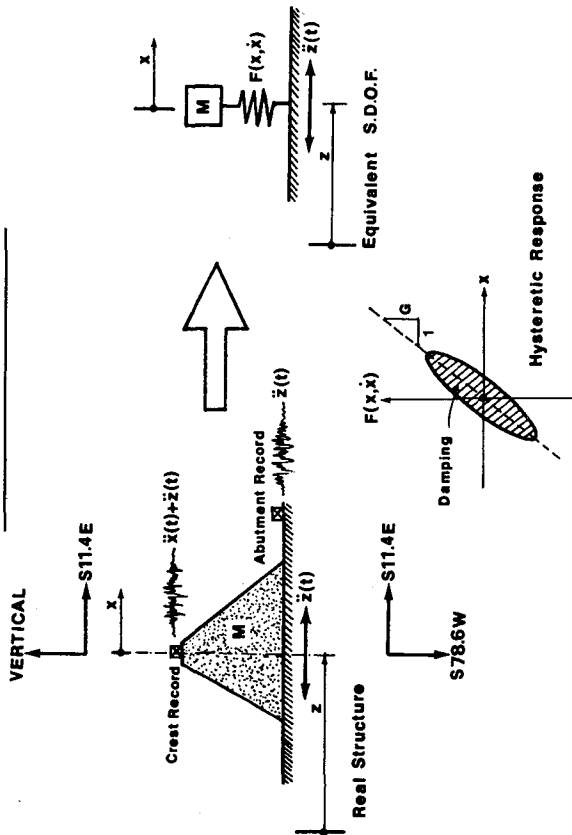
(a)

SAN FERNANDO EARTHQUAKE FEB. 9, 1971 SANTA FELICIA DAM, CALIFORNIA.
RELATIVE ACCEL., VEL., AND DISP. OF CREST W.R.T. ABUTMENT
COMPONENT ROTATED TO UPSTREAM/DOWNSTREAM DIRECTION (S11.4E)



(b)

(a) BASIC IDEA OF THE ANALYSIS



(b) DIFFERENT FILTERINGS

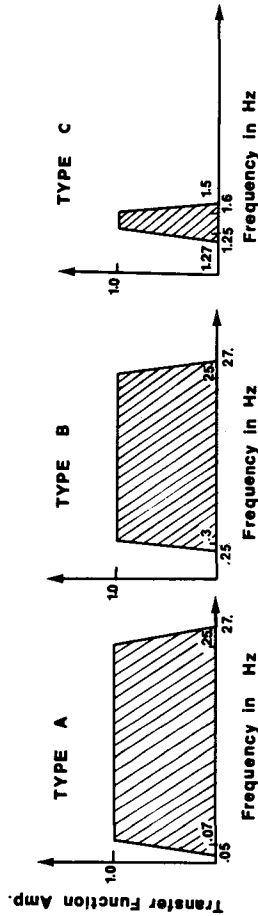
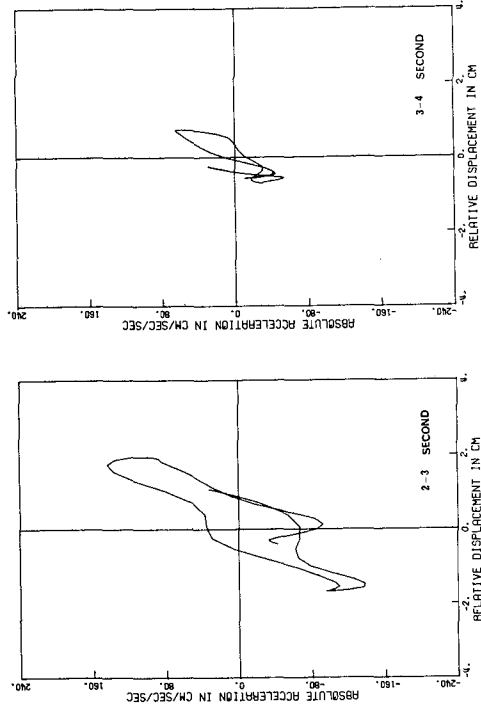
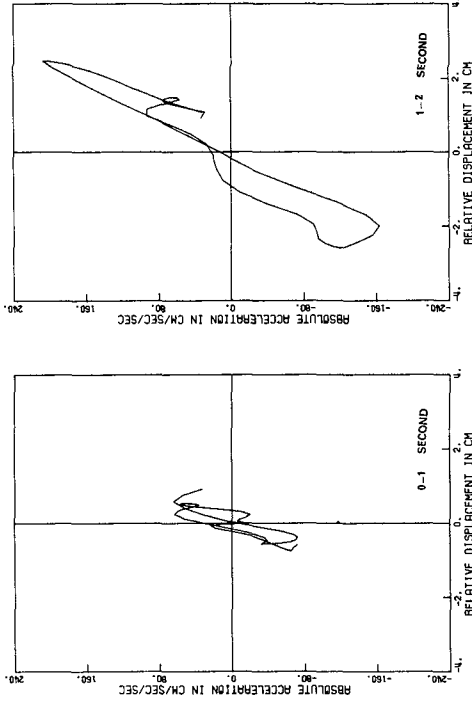


Fig. 6

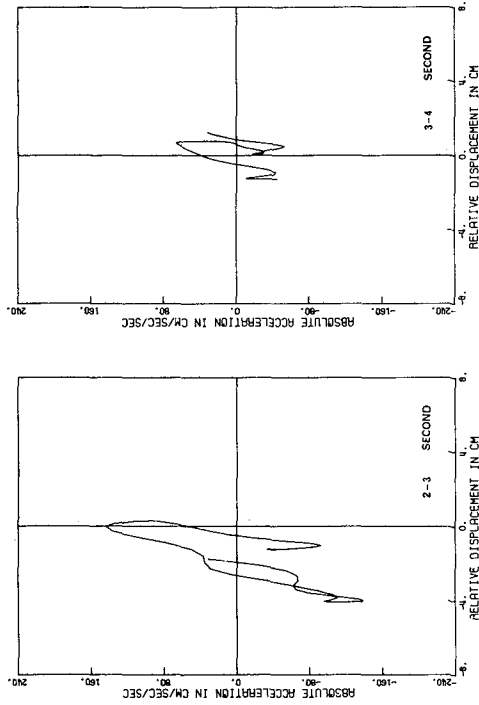
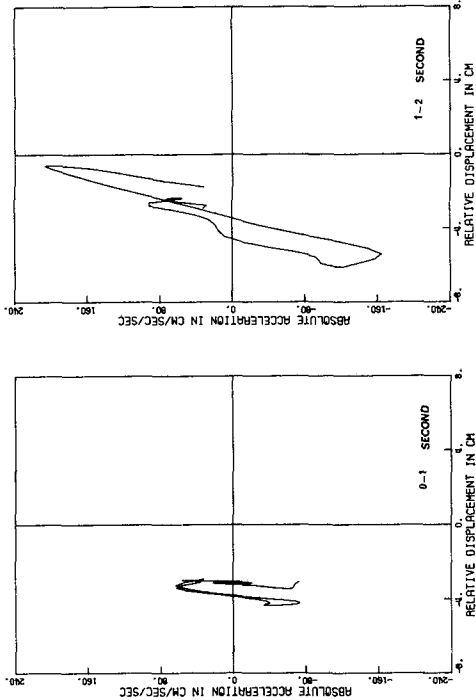
Fig. 7 Filtered motion for the 1971 earthquake

SAN FERNANDO EARTHQUAKE FEB. 9, 1971
SANTA FELICIA DAM, CALIFORNIA.
COMPONENT ROTATED TO UPSTREAM/DOWNSTREAM DIRECTION (S11.4E)
HYSTERETIC RESPONSE
FILTERING TYPE B



b - Filtering type B

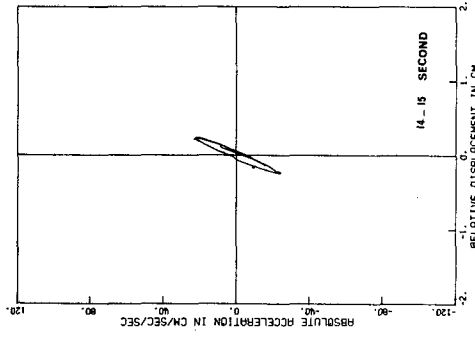
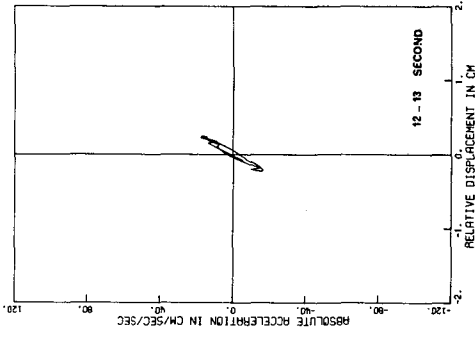
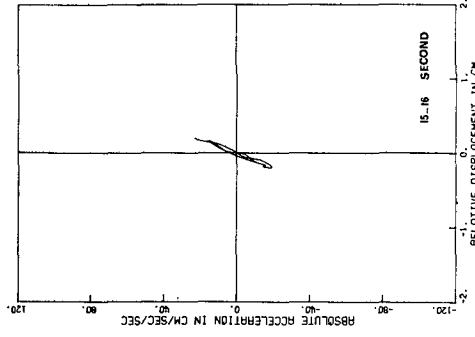
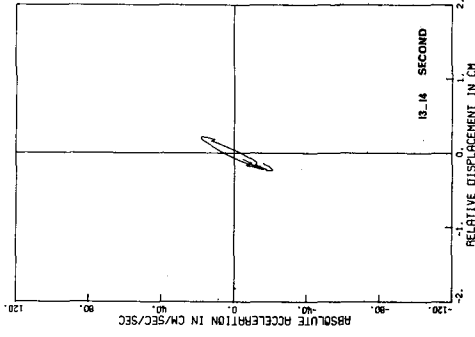
SAN FERNANDO EARTHQUAKE FEB. 9, 1971
SANTA FELICIA DAM, CALIFORNIA.
COMPONENT ROTATED TO UPSTREAM/DOWNSTREAM DIRECTION (S11.4E)
HYSTERETIC RESPONSE
FILTERING TYPE A



a - Filtering type A

Fig. 8 Hysteretic response (1971 earthquake)

SAN FERNANDO EARTHQUAKE FEB. 9, 1971
SANTA FELICIA DAM, CALIFORNIA,
COMPONENT ROTATED TO UPSTREAM/DOWNSTREAM DIRECTION (S11.4E)
FILTERING TYPE C
HYSTERETIC RESPONSE



SAN FERNANDO EARTHQUAKE FEB. 9, 1971
SANTA FELICIA DAM, CALIFORNIA,
COMPONENT ROTATED TO UPSTREAM/DOWNSTREAM DIRECTION (S11.4E)
FILTERING TYPE C
HYSTERETIC RESPONSE

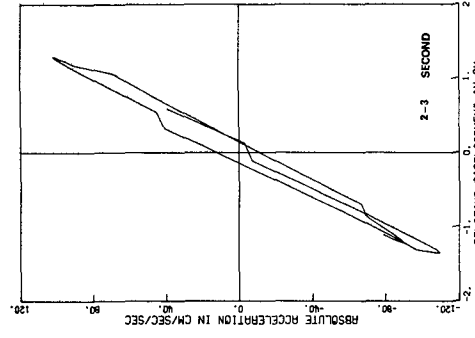
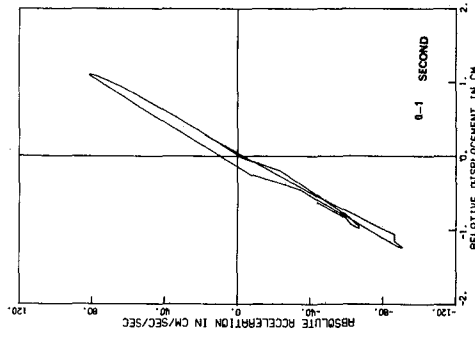
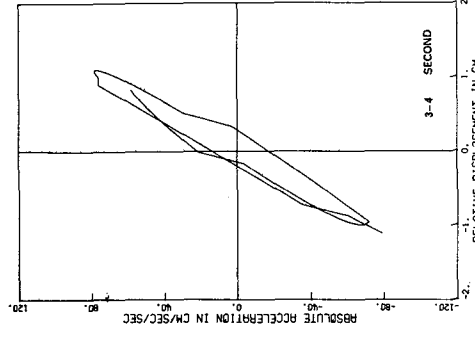
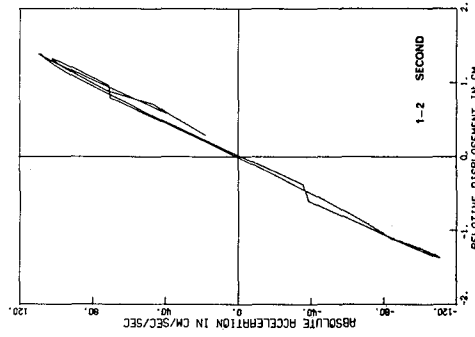
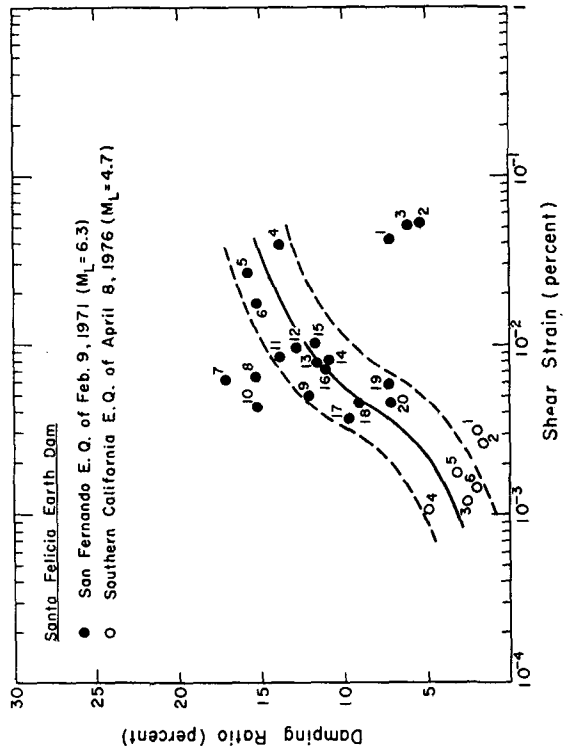


Fig. 9 Hysteretic response of the 1971 earthquake (Filtering type C)



(a)

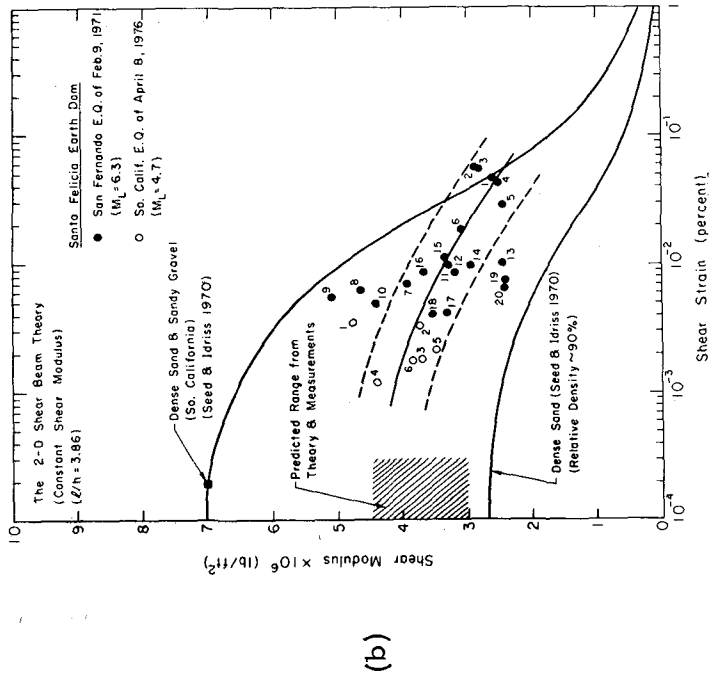
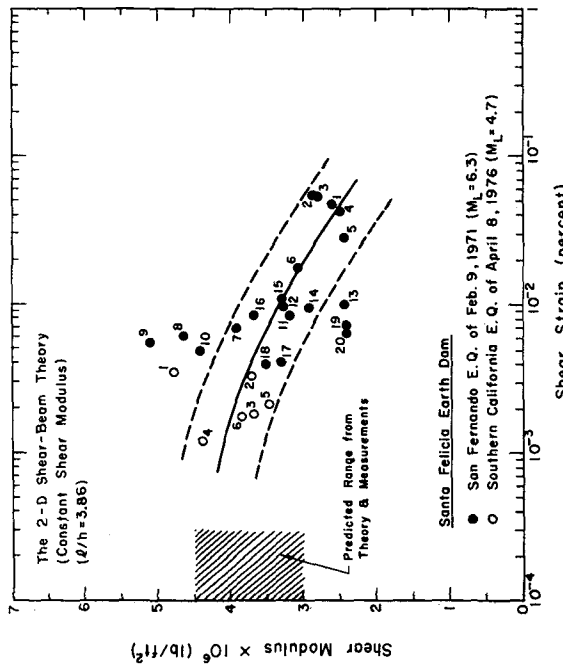
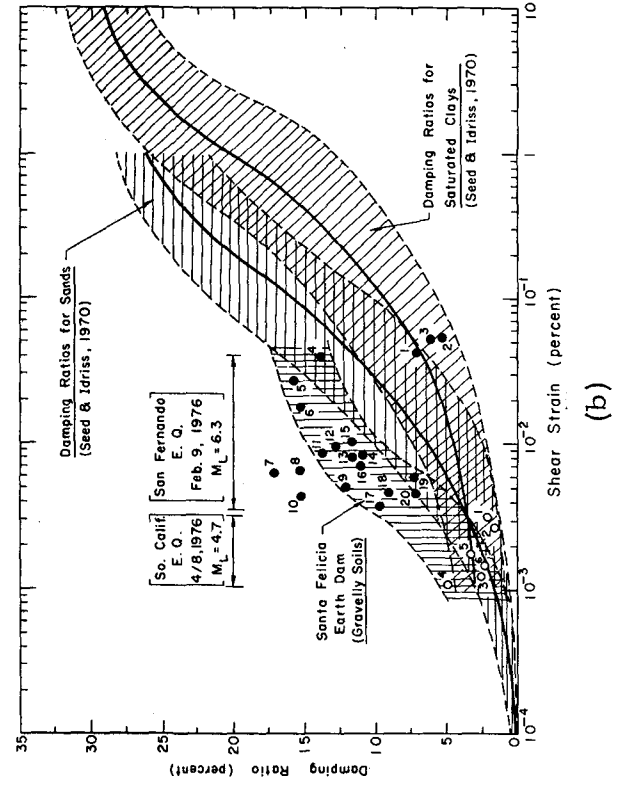


Fig. 10



(a)



(b)

Fig. 11

1050

INTENTIONALLY BLANK

A PRELIMINARY REPORT ON A STUDY OF THE SEISMIC RESPONSE OF
THREE SEDIMENT-FILLED VALLEYS IN THE GARM REGION OF THE USSR

by

B. Tucker¹, J. King², K. Aki¹, J. Brune², I. Nersesov³,
W. Prothero⁴, G. Shpilker³, G. Self⁵

ABSTRACT

In 1976 and 1977 experiments were conducted to determine the response to earthquake motion of three sediment-filled valleys in the Garm region of the USSR. Twelve intermediate-period seismometers were deployed in various profiles across the valleys, with another three-component set of seismometers on the country rock bordering and underlying each valley. Recording was direct-digital using four four-channel portable digital recorders. The experimental setting and equipment are briefly described, and some preliminary results on the valleys' responses to steeply incident P waves are presented.

INTRODUCTION

This preliminary report concerns a particular aspect of the problem of the effect of local geology upon seismic waves, namely the response to earthquake motion of sediments in valleys. This is of interest because of the concentration of populations in sediment-filled valleys, and because sediment response has been determined to have been a significant factor in the damage resulting from several destructive earthquakes, e.g. at Mexico City in May 1962 (1) and at Caracas in July, 1967 (2).

SETTING OF EXPERIMENT

During 1976 and 1977 we investigated the response of three sediment-filled valleys in the Garm region of the USSR (see Figure 1). The Institute of Physics of the Earth, Moscow, maintains a seismological expedition at Garm and operates a network of fourteen permanent stations, whose locations are indicated in Figure 1. The area is characterized by high and diffuse seismicity with mostly shallow events having variable focal mechanisms and frequency content. In addition, the Hindu Kush range, 200 km to the south, is a continual source of deep (100-250 km) earthquakes. Hypocentral locations for local earthquakes within and near the net are routinely catalogued by expedition scientists.

-
- I Department of Earth and Planetary Sciences, Massachusetts Institute of Technology, Cambridge, MA 02139
 - II University of California, San Diego, Scripps Institution of Oceanography, La Jolla, CA 92093
 - III Institute of Physics of the Earth, Academy of Sciences of the USSR, Moscow, USSR.
 - IV Department of Geological Sciences, University of California, Santa Barbara, Santa Barbara, CA 93106
 - V IBM Corporation, Menlo Park, CA

The locations of Chusal, Yasman and Runo valleys, chosen here for study, are also indicated in Figure 1. Chusal and Yasman Valleys lie in the granitic rock of the Alayskiy Range, while Runo Valley lies in the deformed metamorphic rock of the Peter-the-First Range. The valley geometry and velocity structure of Chusal are well-known from a seismic reflection study by Sedova (3); see Figure 2. Yasman and Runo are long, linear valleys trending east-west and northwest-southeast, respectively, and are 1.2 km and 0.7 km wide, respectively, where our profiles were located. There is a large difference between the seismic velocities of the country rock to the north of the Surkhob River and the rock to the south of the Surkhob River, resulting in a high sediment-basement seismic impedance contrast for Chusal and Yasman valleys and a low contrast for Runo Valley.

DESIGN OF EXPERIMENT

For the most intensive study we chose an area of Chusal Valley for which there is good control on subsurface velocity-depth structure from Sedova's (3) study. In 1976 we occupied twenty-one different sites (indicated by numbered circles in Figure 2) at different times with twelve matched, intermediate-period seismometers, in seven different profiles. The sites occupied and the configuration of the seismometers are indicated in Table I for the seven profiles, C1 through C7. At all times during the Chusal experiments a three-component station was operated in a tunnel into the crystalline rock on the east side of the valley. In 1977 we deployed single profiles of four three-component sites across the half-widths of Yasman and Runo Valleys (see Table II), reserving a fifth three-component site for the country rock bordering each valley. Finally, in 1977 we returned to Chusal and installed three-component stations in the tunnel site and across a narrower part of the valley (experiment C8 in Table I). At all sediment sites the seismometers were placed in holes approximately one-half meter deep, which were then covered with thermally insulating roofing material.

EQUIPMENT

Technical details of the recording system may be found in an earlier paper by Prothero (4). Briefly, the output of each seismometer is amplified by a remote preamplifier and transmitted via a shielded cable to one of four channels of the recorder. The recorder amplifies, filters, digitizes and multiplexes the input signals, mixes them with an internally generated time code, and writes them onto a Sony reel-to-reel tape recorder. The Sony tape data is then read and copied onto computer-compatible tape using a mini-computer system at the Garm base.

The Soviet model S-5-S seismometers were operated with a natural period of 4.0 seconds and damping of .46 of critical. They can be deployed either horizontally or vertically. The recorders sample at 128 samples/sec/channel with 12-bit resolution; they are triggered units, with about one second of pre-trigger memory. The system response, including the anti-aliasing filters in the recorders, peaks at 18 Hz and provides a usable bandpass of 0.1 to 64 Hz.

Relative calibration of the entire system was performed before and after the experiments described herein by recording earthquakes with the seismometers placed on the same pier. We conclude that the maximum deviation in response level between any two channels is less than 20% and that differences greater than this in the relative amplitudes of the seismograms and spectra presented below may be remarked with confidence.

SOME RESULTS

For this preliminary study we chose to look at the valleys' response to P waves from deep Hindu Kush events. The angle of incidence of these phases in a tunnel of crystalline rock at the Garm station (No. 3 in Figure 1) ranges between 60 and 70 degrees from the horizontal (5) and may be supposed to be not much different at Chusal and Yasman. The angle of incidence at the base of the sediments in Runo is probably even steeper due to the lower velocity in the Peter-the-First range. On the basis of seismograms alone, the valleys' response to these P waves appears to be more simple than for, say, local S waves, in that the changes in the character of the record as a function of position in the valley are more gradual and orderly. Vertical-component seismograms of four different Hindu Kush events recorded during the C5, C8, Yasman and Runo experiments are presented in Figures 3, 4, 5 and 6.

The profiles all show that there are very significant differences in the character of the ground motion between different sites within a given valley, and quite strong amplification at certain frequencies with respect to the rock sites. Note the short distances over which these changes occur; the spacing between the C8 valley sites is less than 60 meters. Note especially the highly amplified energy near 12 Hz in the Yasman hole No. 1 record (Figure 5), resulting in a monochromatic-looking seismogram. The horizontal-component seismograms (not shown here) exhibit similar frequency content and relative amplitudes, lending confidence to the observations.

Relative Fourier spectral amplitudes for the C5 event, tunnel and hole No. 11 records, are plotted at the top as in Fig. 7. The spectra are calculated for the first 8 seconds of the P wave. From such pairs of spectra we obtained spectral ratios by differencing the logarithms of the spectral ordinates. This gives a measure of the valley's response, at this point, with respect to the location of the hard-rock station. In this manner we calculated spectral ratios for sites at the edge and middle of each valley, with respect to the bordering rock-sites, for each of the four profiles. Smoothed versions of these spectral ratios are plotted in Figure 8. The letters "E" and "M" indicate edge and middle, respectively.

We regard several features of these spectral ratios as noteworthy: (1) the existence of peaks indicating relative amplification factors of more than 25; (2) the amplification of frequencies between 3 and 10 Hz at the middle sites of C5, C8 and Yasman; (3) the peak around 15 Hz at the Yasman edge site, corresponding to the amplification evident from the seismogram in Figure 5; (4) the deamplification of frequencies greater than 30 Hz at Yasman; and (5) the uniformity of response of the two Runo sites.

FINAL REMARKS

One cannot generalize on the basis of the analysis of one earthquake for each valley. There are many questions regarding the stability of the spectral ratios in Figure 8 with respect to earthquake parameters and analytical techniques that must be answered before the peaks and valleys of the plots can be interpreted in terms of local geologic structure. The valleys' response to local S waves is, of course, of paramount importance for engineering considerations, as is the problem of scaling these weak-motion responses to large amplitudes. To help solve the latter problem we are installing a network of strong-motion instruments, and reoccupying some of the same valley sites; future direct comparisons between weak and strong ground motion responses will hopefully be possible.

ACKNOWLEDGMENTS

We express our gratitude for the invaluable assistance of Yuri Kopnichev who acted as liaison between the American authors and their Soviet hosts, and to Zhora Viborniy who helped us with the field work. This research was supported under NSF/RANN Grant No. 76-23279ENV and by the Institute of Physics of the Earth, Moscow.

1. Zeevaert, L. (1964). "Strong Ground Motion Recorded During Earthquakes of May 11th and 19th 1962 in Mexico City," Bull. Seism. Soc. Am., 54 (1).
2. Algermissen, S.T. and D.M. Perkins, (1976). "A probabilistic estimate of maximum acceleration in rock in the contiguous United States. U.S. Geol. Surv.," Open-File Rept., 36 pp.
3. Sedova, E.N. (1962). "Correlation of Dynamic Properties of Weak Earthquake with Ground Conditions," Publications of the Institute of Physics of the Earth, Academy of Sciences of the USSR (Trudi IFZ AN SSSR), No. 25, p. 192.
4. Prothero, Wm. A. (1976). "A Portable Digital Seismic Recorder with Event Recording Capability," Bull. Seism. Soc. Am. 66 (3).
5. Khalturin, V.I. (1978). Personal communication.

Table I

Chusal Valley Experiments

<u>Name</u>	<u>Holes Occupied (see Figure 2)</u>	<u>Number of Seismometers in Each Hole</u>	<u>Orientation of Seismometers in Each Hole</u>
C1	2, 13, 7, 14, 11, 15	2	EW
C2	2, 13, 7, 14, 11, 15	2	NS
C3	1, 2, 3, 4, 5, 6, 7, 8, 9, 10, 11, 12	1	NS
C4	2, 4, 7, 8, 10, 12	2	EW and Z
C5	2, 5, 8, 11	3	EW, NS and Z
C6	16, 2, 17, 18	3	EW, NS and Z
C7	19, 11, 20, 21	3	EW, NS and Z
C8	22, 23, 24, 25	3	EW, NS and Z

Table 2

Yasman: Valley width = 1.2 km; East-West Profile

<u>Hole No.</u>	<u>Distance from (South) Side of Valley</u>
1	0 meters
2	122 meters
3	363 meters
4	616 meters

Master unit on hard rock approximately 500 m to the east.

Runo: Valley width = 0.7 km; Northwest-Southeast Profile

<u>Hole No.</u>	<u>Distance from (Northeast) Side of Valley</u>
1	0 meters
2	123 meters
3	244 meters
4	366 meters

Master unit on country rock approximately 100 m to the northeast.

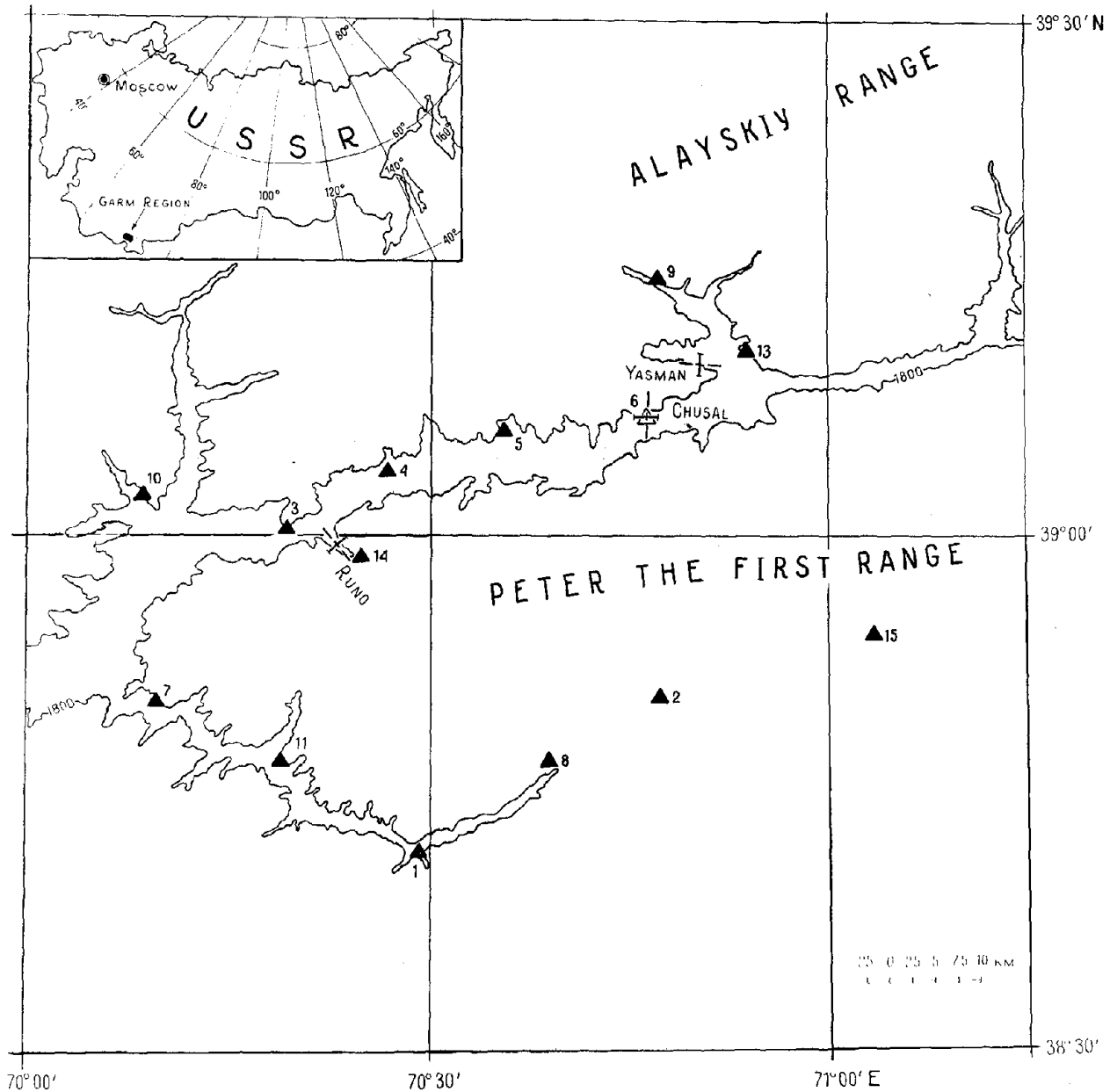


Figure 1. Map of the Garm region showing the locations of the permanent Soviet stations (triangles) and the valley profiles (crosses). The dashed lines of the crosses indicate the approximate axes of the valleys, and the orthogonal solid lines indicate the directions of the profiles. The 1800 meter contour outlines the valleys of the Surkhob River (trending NE) and the Obikingou River (trending SE). The Surkhob River marks the boundary, in this region, of the granitic rocks of the Southern Tien Shan complex to the north and the deformed metamorphosis of the Northern Pamir complex to the south. The Alayskiy and Peter-the-First ranges are part of the Tien Shan and Pamir complexes, respectively. The Garm Seismological Expedition is located next to Station No. 3.

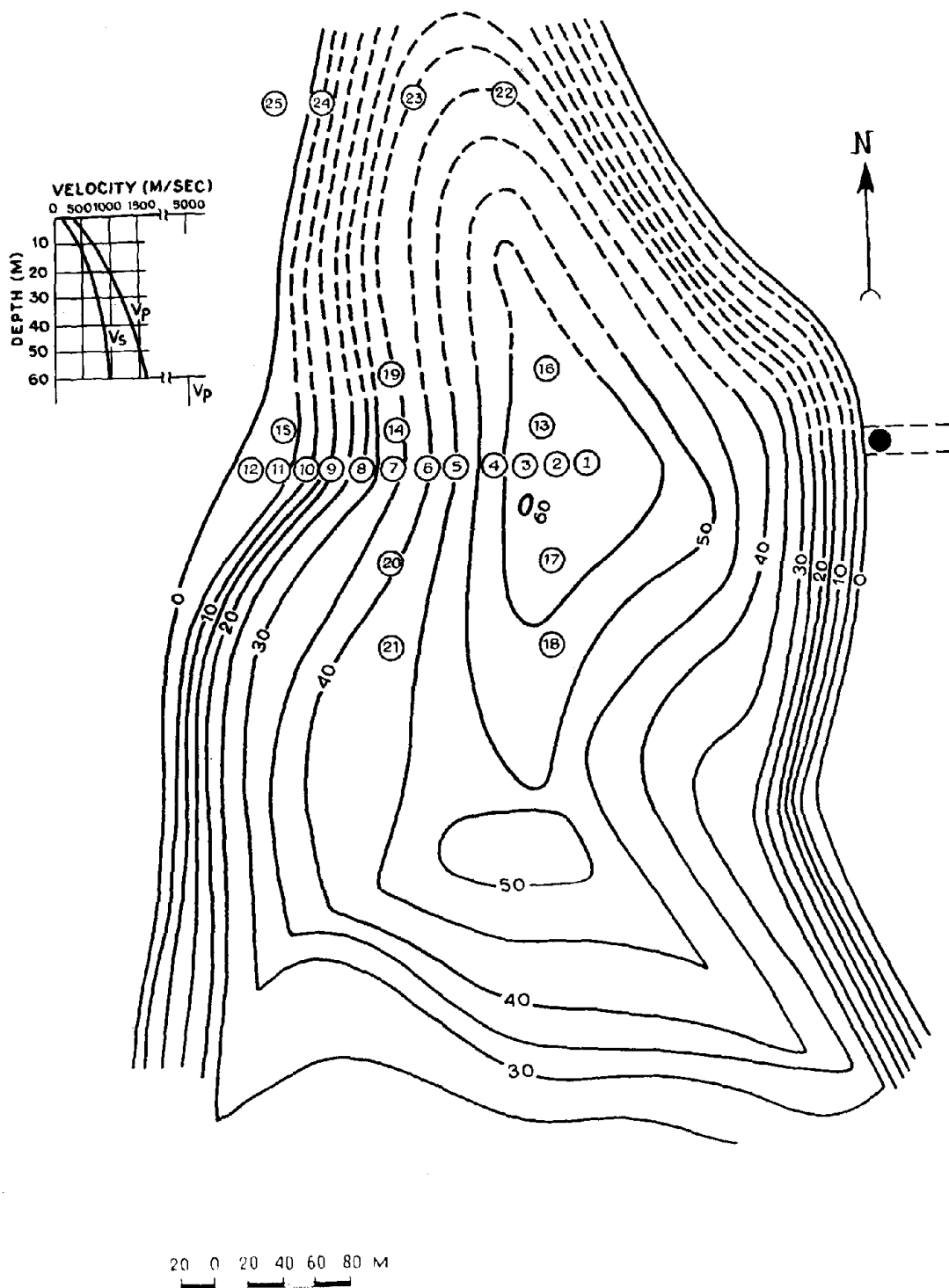


Figure 2. Depth to basement contour map of Chusal Valley, modified from Sedova (3).

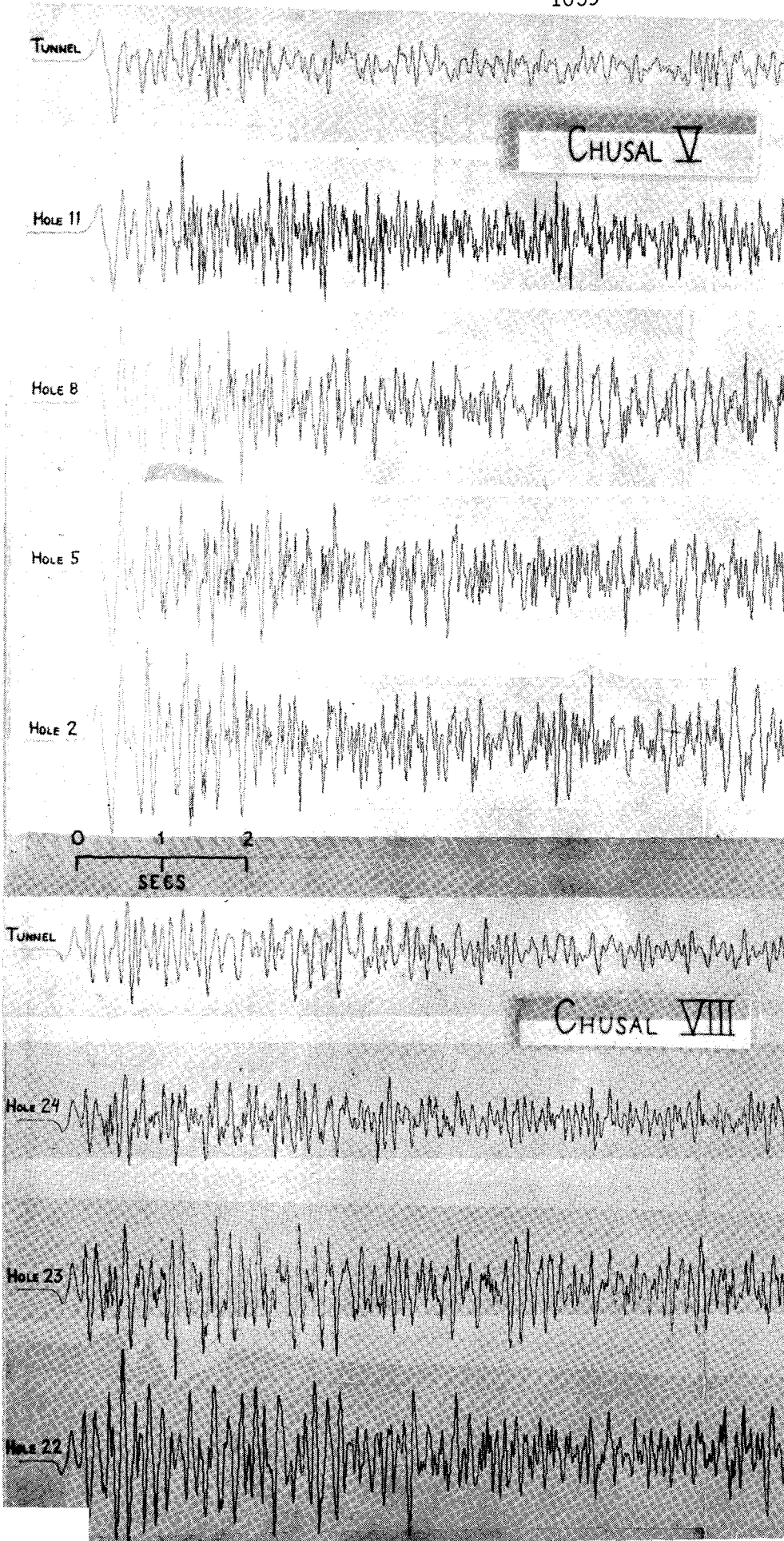


Figure 3. Vertical component seismograms for 17 November 1976, 10:55
CUT Hindu Kush event; C5 profile.

Figure 4. Vertical component seismograms for 21 November 1977, 19:44
CUT Hindu Kush event; C8 profile.

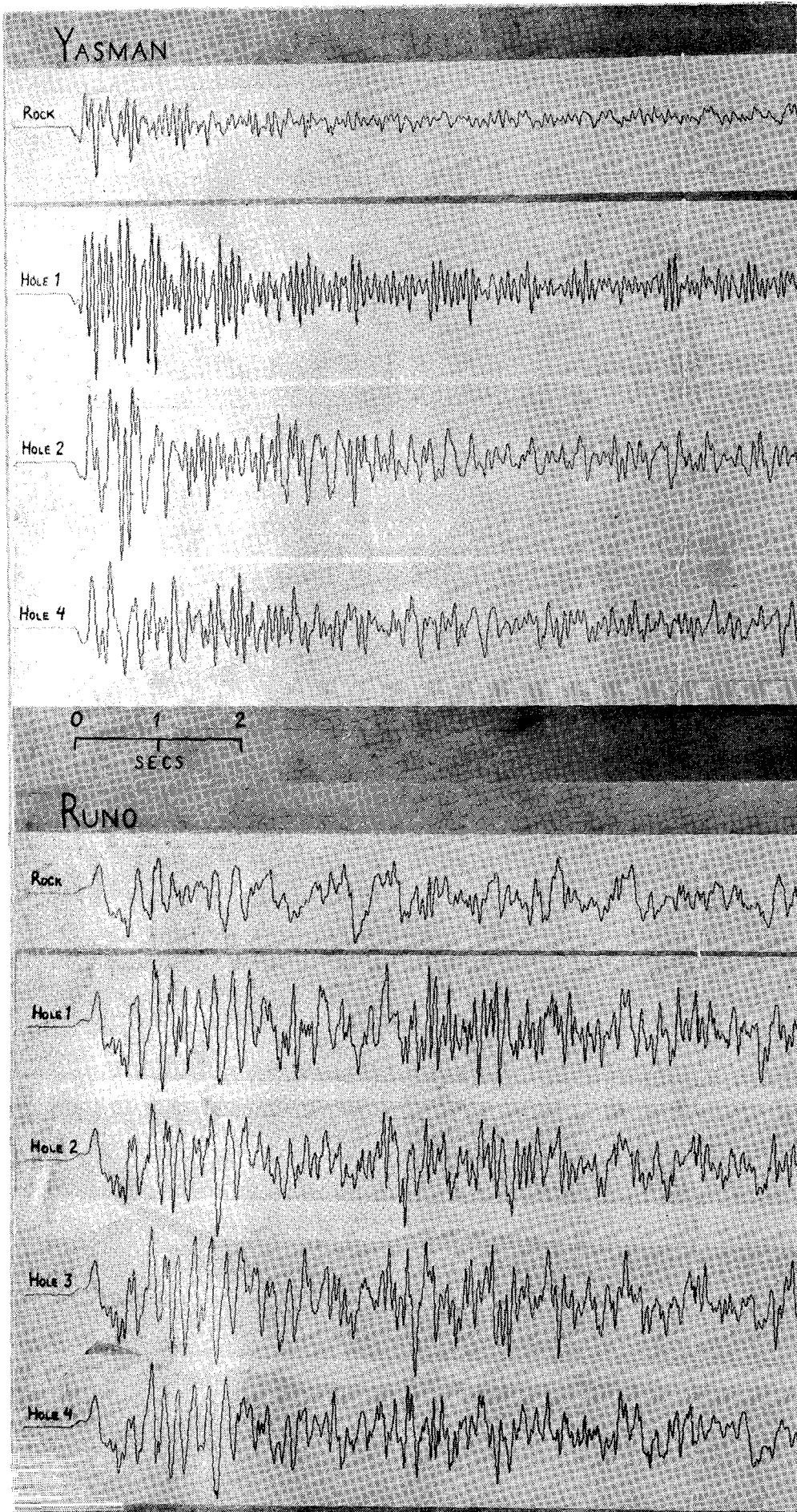


Figure 5. Vertical component seismograms for 25 September 1977, 15:08 CUT
Hindu Kush event; Yasman profile.

Figure 6. Vertical component seismograms for 4 October 1977, 20:16 CUT
Hindu Kush event; Runo profile.

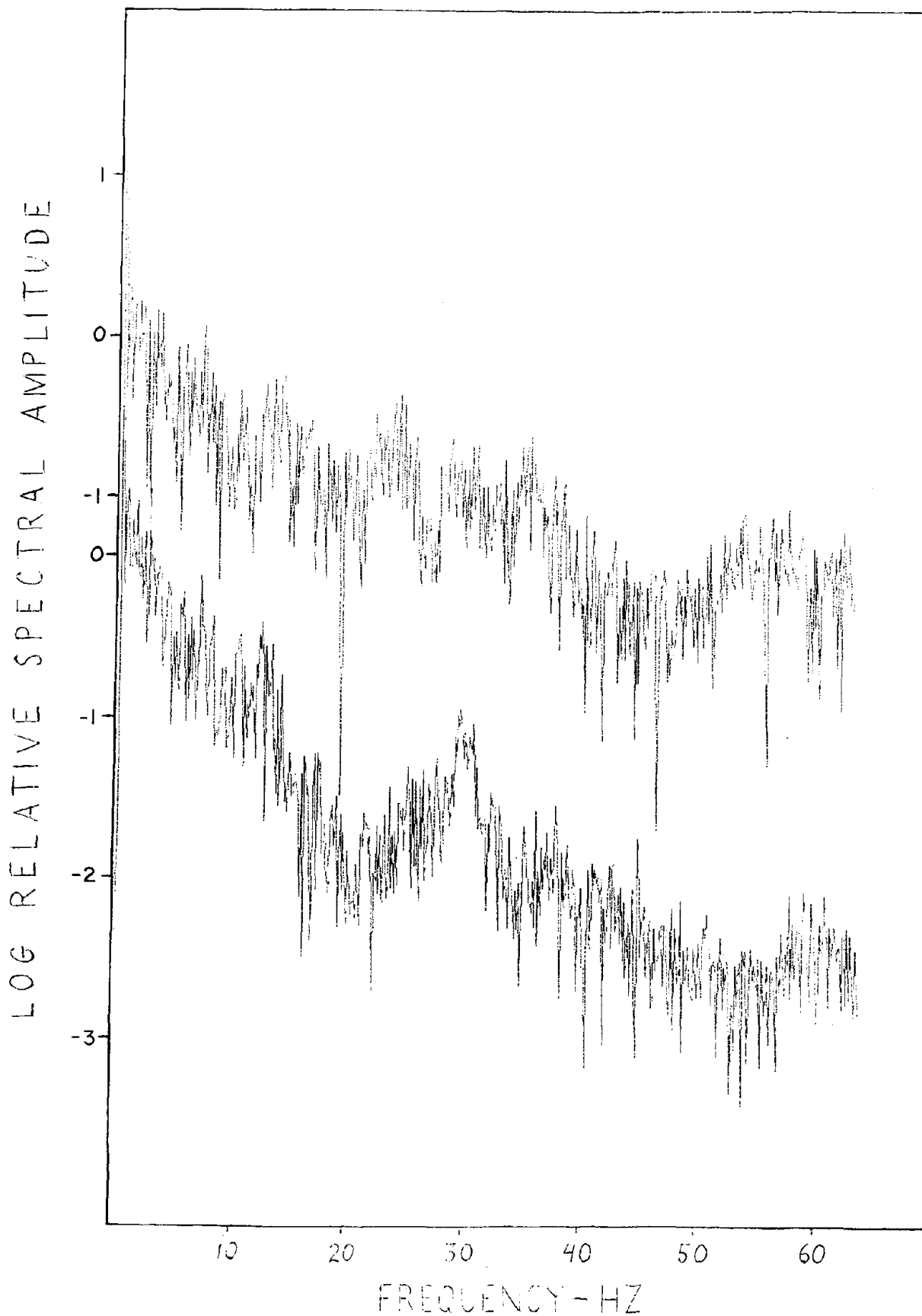


Figure 7. Relative Fourier amplitude spectra of Hindu Kush event P wave recorded at Chusal site No. 11 (top) and Chusal tunnel (bottom); vertical component.

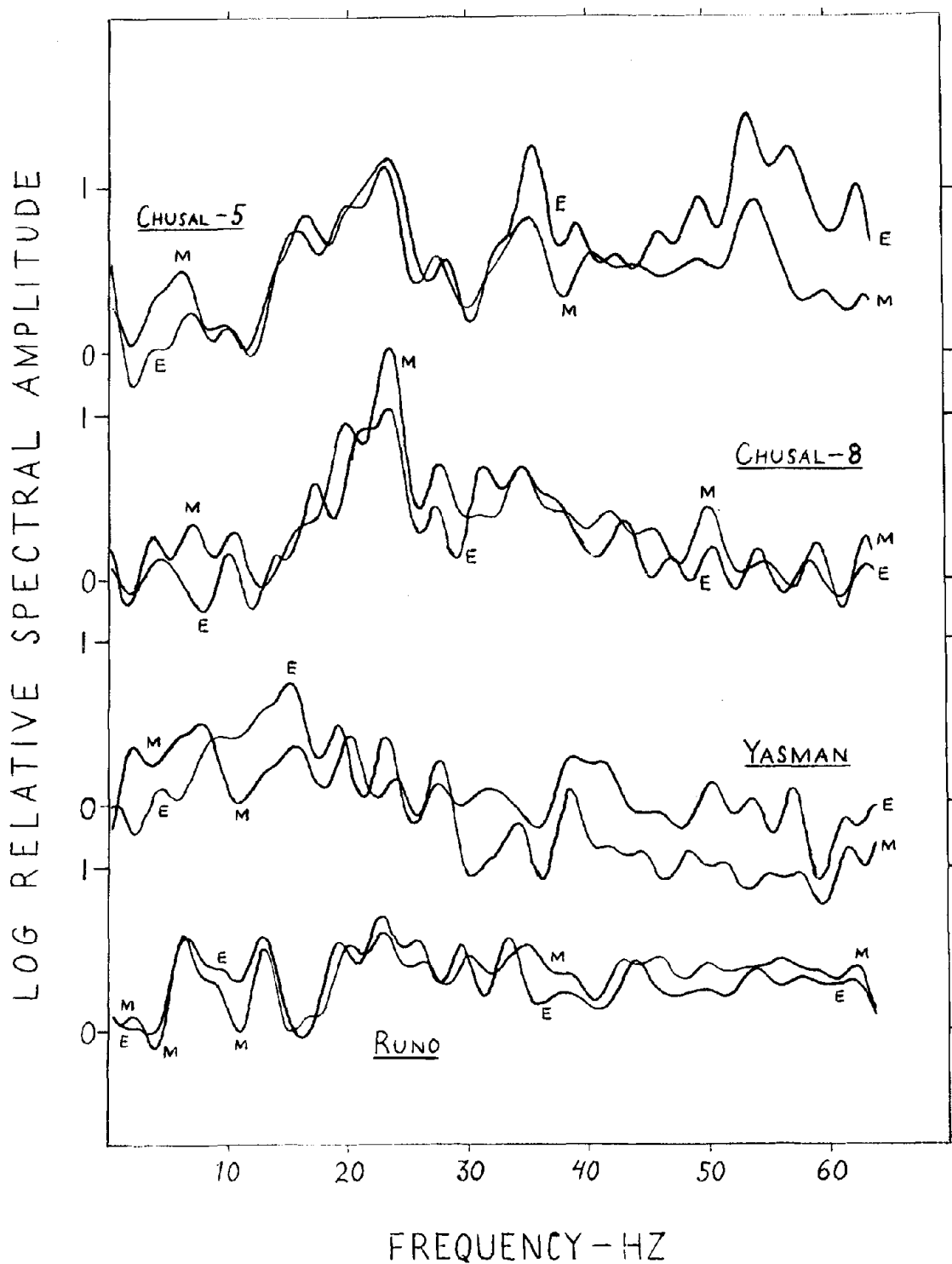


Figure 8. Smoothed spectral ratios between valley sites and rock sites. See text for details.

EMPIRICAL SYNTHESIS OF SEISMIC VELOCITY PROFILES
FROM GEOTECHNICAL DATA

by

Kenneth W. Campbell^I

ABSTRACT

A method has been developed by which a shear-wave velocity profile beneath a site may be synthesized from such readily available geotechnical information as geology maps, water well logs, soil boring logs, and water table depths. The method is based on empirical correlations among shear-wave velocity, depth and a Geotechnical Classification system developed from 109 in-situ measurements conducted throughout the Southern California area since 1971. Synthetic velocity profiles developed in this way may be used for microzonation purposes and for other applications where seismic velocity measurements are unfeasible.

INTRODUCTION

Microzoning for such site-related ground motion parameters as intensity, maximum acceleration, duration or site period requires a widespread knowledge of regional site characteristics if site effects are to be reliably and consistently included in the microzonation process. One of the more important dynamic properties of the site required in site response analyses or site period determinations is the shear-wave (S-wave) velocity profile beneath the site. Yet in-situ measurements are relatively expensive and time consuming to conduct and analyze. Thus, actual measurements are not feasible as the sole means of determining shear-wave velocities for most microzoning applications.

For such applications it is more convenient to estimate velocities from the more readily available geotechnical data as provided by geology maps, soil boring logs, and water well logs. This may be done statistically by correlating shear-wave velocity with the type of ground. In this way synthetic velocity profiles may be established from a geotechnical profile for the site. The correlations presented here are based on 109 seismic velocity measurements conducted throughout the Southern California area since the San Fernando earthquake of 1971.

VELOCITY AND GEOTECHNICAL DATA

Standard engineering-geophysical techniques (15) were used to measure seismic velocities at 109 sites in Southern California (2,3,4). Approximately two-thirds of these were investigated using the seismic refraction method. Spread lengths ranged from about 150 to 360 ft. The more accurate Down-Hole survey was used to investigate the majority of the remaining sites to depths generally between 50 and 135 ft. Cross-Hole surveys were used at a few sites.

Computed S-wave velocities represent the average velocities within

I. Engineer, J.H. Wiggins Company, Redondo Beach, California

layers of approximately constant velocity. At least two points within the layer were used to establish these velocities. Therefore, velocities were not generally computed for layers of less than about five feet in thickness. Exceptions to this were thin surface layers and anomolous velocity layers at depth where the geophone spacing was reduced.

Soil data and water table depths were taken from exploration borings at the site of the survey. In most cases this information was available for the boring in which the survey was conducted for Down-Hole measurements or very near the geophone spread in the case of Refraction surveys. If borings were not available, water well logs were used. The geology of the site was obtained from detailed geologic investigations when available, otherwise, published geology maps were used.

VELOCITY CORRELATIONS

It has been found that S-wave velocities may be grouped into relatively well defined geotechnical classification as given in Figure 1. The four major catagories are Soil, Sand and Gravel, Fill, and Rock. Subcatagories are based on such geotechnical data as soil type, gravel content, dry density, saturation, geologic age, rock type and hardness, degree of weathering, and depth. A complete description of each catagory is given in Table 1.

Correlations among shear-wave velocity, geotechnical data and depth have been developed by several investigators from both laboratory (6,10,13) and in-situ data (5,8). A preliminary attempt at correlating seismic velocity with geology for Southern California was made by the author (3) in conjunction with an investigation of site effects in the San Fernando earthquake of 1971. These correlations were subsequently updated (1) with additional data to include both soil type and depth. The correlations presented here have been further updated (2) with very accurate velocity and geotechnical data to bring the total data base to 109 sites.

Near-Surface Velocities. Geotechnical correlations of S-wave velocity for surface layers and near-surface deposits of Soft Clays, Sands and Gravels, and Soft Sedimentary Rock are presented in Tables 2-4. Results are given in terms of the number of samples used, the range of the velocities, the mean velocity (\bar{V}), the standard deviation (σ), and the coefficient of variation (VAR). The dimensionless coefficient of variation, defined as the ratio σ/\bar{V} , is a convenient means of expressing the statistical uncertainty in the data. These coefficients are relatively constant for all classifications, ranging from 0.06 to 0.16.

Shear-wave velocities for Soils and Fills generally increase with increasing firmness and age from about 455 ft/sec for Unconsolidated Soils to 935 ft/sec for Old Alluvium. Velocities for Sands and Gravels increase with increasing overburden and gravel content and range from 975 ft/sec for surface deposits of moderate gravel content to 1780 ft/sec for deposits at depth containing gravel and cobbles. Velocities for Rock are seen to increase with increasing age and hardness, varying from 1160 ft/sec for Soft Sedimentary Rock outcrops to 4040 ft/sec for Fractured Basement Complex.

Velocity Versus Depth. In a previous study (1), it was found that the

correlation of shear-wave velocity with depth for each of four classifications could be adequately described by the following:

$$V_s = Kd^n \quad (1)$$

where V is S-wave velocity, d is depth, and K and n are constants dependent upon the geotechnical classification.

For the current study the above expression has been slightly modified to account for the asymptotic behavior of shear-wave velocity at shallow depths. This new expression given by

$$V = K(d + c)^n \quad (2)$$

introduces a term ' c ' to represent the asymptotic behavior of V . Thus, as d approaches zero, shear-wave velocity approaches the finite value Kc^n .

To simplify the computation of the constants K , d and n for each of six geotechnical classifications for which sufficient data were available, Equation (2) was linearized by taking the natural logarithm of both sides, resulting in the expression

$$\ln V = \ln K + n \ln (d + c) \quad (3)$$

A summary of this regression analysis is given in Table 5, where shear-wave velocity has units of ft/sec and depth has units of feet. For this purpose, the depth was taken as the vertical distance from the ground surface to the top of the layer, not the middle of the layer as some investigators have used. For the surface layer, the depth was taken as one-third the thickness of the layer. From the statistical summary presented in Table 5, the average correlation coefficient is found to be 0.93 and the average standard deviation of $\ln V$ to be 0.14 (representing an uncertainty of 1.15 in V). These values suggest that Equation (3) may be used to adequately represent the relationship of V and depth.

The data for Unconsolidated Soils include Down-Hole seismic velocities determined for the accelerograph sites at El Centro in the Imperial Valley and at Cholame near Parkfield given in Reference 14. These velocities are observed to be somewhat lower than those generally obtained in the greater Los Angeles area for similar soils. Figure 2 displays the mean value curves for all six classifications. This plot emphasizes the significant differences among the shear-wave velocities obtained in these various types of ground.

SYNTHETIC VELOCITY PROFILES

The correlations among shear-wave velocity, depth and the type of ground developed in the previous sections can be used to estimate the low-strain shear-wave velocity profiles at a site of interest in the Southern California area from only a modest amount of soil and geological data. Such estimates are useful when in-situ velocity data are not available or would be uneconomical to measure. The technique for estimating such velocity profiles from geotechnical data is demonstrated for two sites for which velocity measurements are available for comparison.

The two sites, one located in the city of Los Angeles, and the other in the Long Beach Harbor, represent contrasting geotechnical characteristics; the former consisting of shallow alluvium over rock, and the latter consisting of deep hydraulic fill. Brief descriptions of the soil and geologic characteristics together with the measured velocity data for the two sites can be found in Table 6. The data were provided by LeRoy Crandall and Associates, consulting geotechnical engineers in Los Angeles, California.

The velocity boundaries determined from the seismic surveys, Table 6, represent clearly-identifiable physical changes in the geotechnical profiles of the two sites. A possible exception is the increase in shear-wave velocity at 10 feet in the Long Beach profile. No obvious indication for such a change could be observed in the boring logs or dry densities of the fill. However, since the fill below 10 feet is below sea level, there is a notable increase in total unit weight below this depth. The Japanese (9) have found from in-situ measurements that moist loose sand will have a higher shear-wave velocity than dry sand of the same dry density. This may be due to an increase in the shear strength of moist sand. For the purposes of developing the synthetic velocity profiles, the layer boundaries are taken to coincide with the velocity boundaries presented in Table 6.

The shear-wave velocities for the geotechnical profiles in Table 6 can be estimated from the correlations presented in the previous sections. A generalized procedure used to estimate the velocities for the two Los Angeles area sites is summarized as follows:

- The surface-layer velocity for the Long Beach site was taken from curve 1 of Figure 2 and Table 5 using a depth of 3.3 ft (one-third the thickness of the layer). The velocity for the compacted Fill at the Los Angeles site was taken from Table 2.
- The velocity for the Sand and Gravel occurring at depth at the Los Angeles site was taken from Table 3.
- The velocity for the Unconsolidated Soil layers at the Long Beach site occurring at depths of 10 and 60 ft. were taken from curve 1 of Figure 2 and Table 5.
- The velocity for the massive, dark grey Pliocene Siltstone at the Los Angeles site occurring at a depth of 35 ft. was taken from curve 4 of Figure 2 and Table 5.

The estimated and measured shear-wave velocity profiles determined by the above procedure are compared in Table 6 and in Figure 3. The mean estimated velocities are observed to deviate from the measured velocities by less than about 15%. This agreement is considered quite good.

The selection of potential velocity boundaries may, in general, be more difficult for profiles other than the two presented here. When obvious changes in geology or soil conditions are absent in the field data, other changes may have to be identified. For instance, abrupt changes in dry densities, blow counts, gravel content, soil type, or relative firmness may indicate changes in velocity. When more detailed data such as water content, void ratios, shear strengths, and consolidation data are available, they may also be used to identify velocity boundaries. If detailed

data are not available, arbitrary layer boundaries must be selected. For fairly uniform deposits, layer thicknesses increasing from about 5 ft. at the surface to 50-200 ft. below a 100 ft. depth may be used (11).

Laboratory data (6,13) have demonstrated the significant effect that shear-strain amplitude may have on the dynamic shear modulus and shear-wave velocity of soils. The shear-strain amplitudes expected to occur in soil deposits during strong earthquake shaking may extend into the non-linear range of dynamic stress-strain curves determined in the laboratory. Low-strain velocity profiles determined by the procedures described above should be modified for the effects of shear-strain amplitude in order to represent earthquake conditions. One method for doing this is simply to reduce the shear-wave velocities by a constant factor dependent upon the expected intensity of seismic shaking. A factor of 0.67 has been adopted in the building codes (7,12) for correcting low-strain characteristic site periods in seismic zones 3 and 4 for strong shaking effects. A more sophisticated technique which incorporates the effects of depth and ground acceleration is described in Reference 1.

CONCLUSIONS

Correlations among shear-wave velocity, depth, and the type of ground have been developed, using in-situ velocity and geotechnical data in the Southern California area. These correlations are considered good enough to justify their use in estimating shear-wave velocities to depths of about 100-150 ft. at a site where a generalized geotechnical classification can be assigned under one or more of the groups of a Geotechnical Classification system. Extrapolations to greater depths should be used with judgement, since only a limited amount of data are available.

A procedure for constructing synthetic velocity profiles for low-strain conditions was outlined and demonstrated for two sites in the greater Los Angeles area. The good agreement between the estimated and measured velocities was encouraging. The procedure requires only a moderate amount of geotechnical data in order that the layers can be identified and classified with respect to the various geotechnical groups. However, any additional laboratory or field data, such as moisture content, density, shear strength, blow counts, etc., can help considerably in identifying velocity boundaries and should be used when available.

It should be emphasized that the statistical correlations developed herein are based on a limited amount of data, thus, careful judgement should be exercised in the application of the results. It is hoped that the correlations can be strengthened in the future with the accumulation of more data.

REFERENCES

1. Campbell, K.W. and C.M. Duke (1976). "Correlations Among Seismic Velocity, Depth and Geology in the Los Angeles Area," School of Engineering and Applied Science, University of California, Los Angeles, UCLA-ENG-7662.
2. Campbell, K.W., M. Lew, C.M. Duke, and R. Chieruzzi (1978). "Geotechnical Correlations of In Situ Seismic Velocity in Southern California,"

School of Engineering and Applied Science, University of California
Los Angeles and LeRoy Crandall and Associates, Los Angeles.

3. Duke, C.M., J.A. Johnson, Y. Kharraz, K.W. Campbell, and N.A. Malpiede (1973). "Subsurface Site Conditions in the San Fernando Earthquake Area," The San Fernando, California, Earthquake of February 9, 1971, edited by L.M. Murphy, NOAA, U.S. Dept. of Commerce, Washington, D.C., Vol. II, Part B, pp. 785-799.
4. Eguchi, R.T., K.W. Campbell, C.M. Duke, A.W. Chow, and J. Paternina (1976). "Shear Velocities and Near-Surface Geologies at Accelerograph Sites that Recorded the San Fernando Earthquake," School of Engineering and Applied Science, University of California, Los Angeles, UCLA-ENG-7653.
5. Fumal, T.E., T.F. Gibbs, and R.D. Borcherdt (1978). "Correlations Between Shear-Wave Velocities and Physical Properties of Near-Surface Geologic materials in the Southern San Francisco Bay Region," (abstract), Earthq. Notes, 49: 4-5.
6. Hardin, B.O. and V.P. Drnevich (1972). Shear Modulus and Damping in Soils: Design Equations and Curves, J. Soil Mech. and Found. Div., ASCE, 98: 667-692.
7. ICBO (1976). Uniform Building Code, International Conference of Building Officials.
8. Ohta, Y. and N. Goto (1976). "Empirical Equation of Shear-Wave Velocity in Terms of Characteristic Indexes of Soil," Dept. of Architectural Engr., Hokkaido Univ., Japan.
9. Okamoto, S. (1973). Introductions to Earthquake Engineering, John Wiley and Sons, New York.
10. Richart, F.E., J.R. Hall and R.D. Woods (1970). Vibrations of Soils and Foundations, Prentice-Hall, Englewood Cliffs, New Jersey.
11. Schnabel, P.B., J. Lysmer, and H.B. Seed (1972). "SHAKE-A Computer Program for Earthquake Response Analysis of Horizontally Layered Sites," Earthq. Engr. Res. Center, Univ. of California, Berkeley, EERC 72-12.
12. SEAOC (1974). Recommended Lateral Force Requirements and Commentary, Structural Engineers Association of California.
13. Seed, H.B. and I.M. Idriss (1970). Soil Moduli and Damping Factors for Dynamic Response Analyses, Earthq. Engr. Res. Center, University of California, Berkeley, EERC 70-10.
14. Shannon & Wilson (1976), "Geotechnical and Strong Motion Earthquake Data From U.S. Accelerograph Stations, Ferndale, Cholame, and El Centro, California, Volume 1," Shannon & Wilson, Inc. and Agbabian Associates, Seattle, Wash. and El Segundo, Calif., NVREG-0029, Vol. 1, NRC-6 (Prepared for U. S. Nuclear Regulatory Commission).
15. Woods, R.D. (1978). "Measurement of Dynamic Soil Properties," in

Earthquake Engineering and Soil Dynamics, Proc. ASCE Geotechnical Engr.
Div. Specialty Conf., June 19-21, 1978, Pasadena, Vol. I, pp. 91-178.

ACKNOWLEDGEMENTS

The earlier geophysical work and velocity correlations were done in collaboration with C. Martin Duke at the University of California at Los Angeles under the support of the National Science Foundation. I wish to thank Ron Eguchi, Jeff Johnson, Niel Malpiede, Yacoub Kharraz, Allen Chow, and Jose Paternina of UCLA for their help in collecting and analyzing these data. Most of the Down-Hole data were obtained while the author was employed by LeRoy Crandall and Associates, Los Angeles, California. I wish to thank Robert Chieruzzi, Dr. Marshall Lew, Do Mar, and Yacoub Kharraz at Crandall for their help. The support of the staff at the J. H. Wiggins Company, Redondo Beach, California is gratefully acknowledged. I want to thank Ron Eguchi for his helpful suggestions.

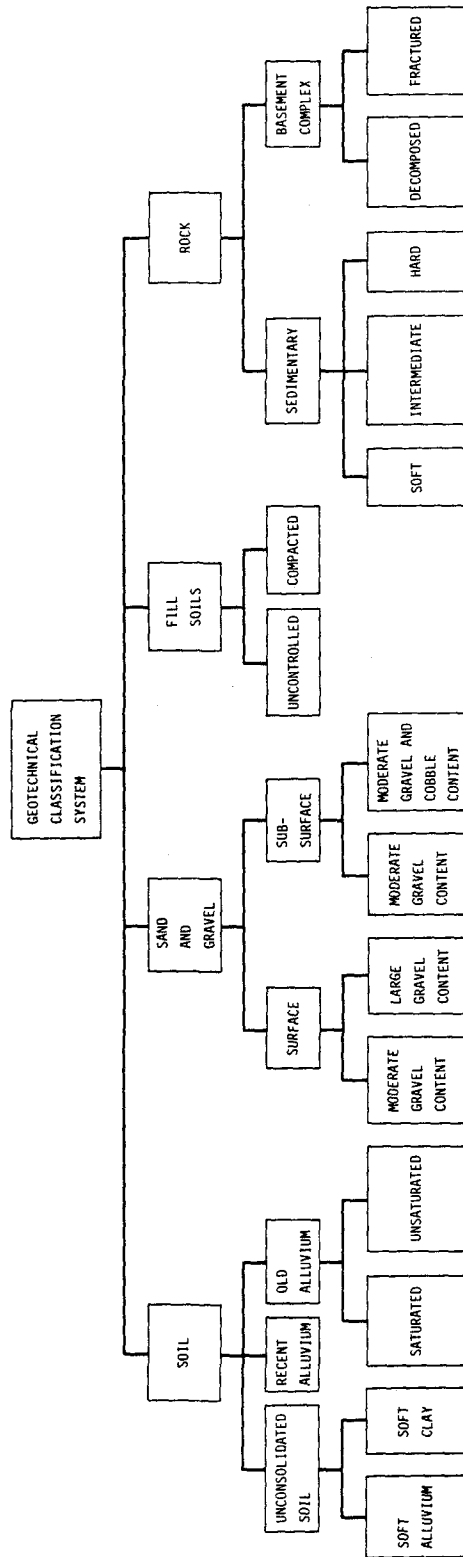


Figure 1. Diagram of The Geotechnical Classification System

Table 1. Geotechnical Classification System

GEOLOGICAL CLASSIFICATION		DESCRIPTION	DRY DENSITY (LB/CU.FT)	DEPTH (FT)	GEOLOGIC AGE	GEOLOGIC UNIT
SOIL	UNCONSOLIDATED SOIL	SOFT ALLUVIUM	<100	≥0	HOLOCENE	RECENT ALLUVIUM
		VERY RECENT RIVER, LAKE, SWAMP, ESTUARINE, AND DELTA DEPOSITS; MAY CONTAIN ORGANICS; LOW GRAVEL CONTENT				
	RECENT ALLUVIUM	SATURATED RECENT ALLUVIUM; LOW GRAVEL CONTENT	90-110	>10-15	HOLOCENE	RECENT ALLUVIUM
		LOW DENSITY SOILS; PRIMARILY FINE-GRAINED	<90	≥0	HOLOCENE	RECENT ALLUVIUM
OLD ALLUVIUM	SOFT CLAY	SOFT TO MODERATELY SOFT CLAYS AND CLAYEY SILTS; GENERALLY DARK GREY TO BLACK	<100 <80	0 >10	HOLOCENE PLEISTOCENE	RECENT ALLUVIUM OLD ALLUVIUM
		UNSATURATED ALLUVIAL DEPOSITS; LOW GRAVEL CONTENT; MAY CONTAIN MODERATE AMOUNTS OF GRAVEL (<50%) BELOW 30-50 FT.	90-110	≥0	HOLOCENE	RECENT ALLUVIUM
		SATURATED ALLUVIAL AND TERRACE DEPOSITS; UNCEMENTED; MAY CONTAIN LOW TO MODERATE (<50%) AMOUNTS OF GRAVEL	95-115	>10-15	PLEISTOCENE Eocene (SAN DIEGO CO.)	OLD ALLUVIUM SHEETWATER AND FRIARS FORMATIONS
		LOW DENSITY (UNSATURATED) ALLUVIAL AND TERRACE DEPOSITS	90-100		PLEISTOCENE Eocene (SAN DIEGO CO.)	OLD ALLUVIUM SHEETWATER AND FRIARS FORMATIONS
		UNSATURATED ALLUVIAL AND TERRACE DEPOSITS; UNCEMENTED; LOW GRAVEL CONTENT; MAY CONTAIN LOW TO MODERATE AMOUNTS OF GRAVEL (<50%) BELOW 10-20 FT.	>100	≥0	PLEISTOCENE Eocene (SAN DIEGO CO.)	OLD ALLUVIUM SHEETWATER AND FRIARS FORMATIONS
		ALLUVIAL DEPOSITS, TERRACE DEPOSITS AND COMPACTED FILL CONTAINING GRAVEL, COBBLES AND BOULDERS; PREDOMINANTLY COARSE-GRAINED	115-130	0	HOLOCENE PLEISTOCENE Eocene (SAN DIEGO CO.)	RECENT ALLUVIUM OLD ALLUVIUM STADIUM FORMATION
SAND & GRAVEL	SURFACE	MODERATE GRAVEL CONTENT				
		LARGE GRAVEL CONTENT	125-135	0	HOLOCENE PLEISTOCENE Eocene (SAN DIEGO CO.)	RECENT ALLUVIUM OLD ALLUVIUM STADIUM FORMATION
	SUBSURFACE	MODERATE GRAVEL CONTENT	115-130	5-30 (RECENT ALLUVIUM) 5-10 (OLD ALLUVIUM)	HOLOCENE PLEISTOCENE Eocene (SAN DIEGO CO.)	RECENT ALLUVIUM OLD ALLUVIUM STADIUM FORMATION
MODERATE GRAVEL AND COBBLE CONTENT		125-135		HOLOCENE PLEISTOCENE Eocene (SAN DIEGO CO.)	RECENT ALLUVIUM OLD ALLUVIUM STADIUM FORMATION	

Table 1. Geotechnical Classification System (Continued)

GEOLOGICAL CLASSIFICATION		DESCRIPTION	DRY DENSITY (LB./CU.FT)	DEPTH (FT)	GEOLOGIC AGE	GEOLOGIC UNIT
FILL	UNCONTROLLED	LOOSE OR SLIGHTLY COMPACTED MAN-MADE FILL SOILS (EXCLUDING HYDRAULIC FILL); LOW GRAVEL CONTENT	100-115	0		
	COMPACTED	MECHANICALLY COMPACTED MAN-MADE FILL OR NATURALLY-OCCURRING SOILS; LOW GRAVEL CONTENT	110-125	0		
ROCK	SEDIMENTARY	SOFT	65-90	15-50	PLIOCENE MIOCENE	FERNANDO, PICO & REPETTO FORMATIONS MODELO, PUENTE & MONTEREY FORMATIONS
		INTERMEDIATE	90-105	≥ 0	PLIOCENE MIOCENE	FERNANDO, PICO & REPETTO FORMATIONS MODELO, PUENTE & MONTEREY FORMATIONS
	HARD	>95	≥ 0	MIOCENE	MODELO, PUENTE & MONTEREY FORMATIONS	
	BASEMENT COMPLEX	DECOMPOSED		≥ 0	MESOZOIC	
		FRACTURED		0-100	MESOZOIC	

Table 2. Statistical Summary of Shear-Wave Velocity for Surface Soil and Fill Deposits (Excluding Sand and Gravel)

GEOTECHNICAL DESCRIPTION	NO. OF DATA	RANGE	S-WAVE VELOCITY (FT/SEC)		
			\bar{v}	σ	VAR
UNCONSOLIDATED SOIL	12	360-560	455	60	0.13
UNCONTROLLED FILL	12	400-550	485	50	0.10
SOFT CLAY	3	460-690	550	--	--
RECENT ALLUVIUM	23	520-790	615	80	0.13
COMPACTED FILL	18	560-940	705	110	0.16
OLD ALLUVIUM	31	735-1180	935	100	0.11

Table 3. Statistical Summary of Shear-Wave Velocity for Near Surface Sand and Gravel

GRAVEL CONTENT	DEPTH (FT)	NO. OF DATA	RANGE	S-WAVE VELOCITY (FT/SEC)		
				\bar{v}	σ	VAR
10 - 50% GRAVEL	0	7	805-1150	975	130	0.13
> 50% GRAVEL	0	6	1220-1425	1320	80	0.06
10 - 50% GRAVEL	5 TO 10-30	3	1180-1430	1310	--	--
10 - 50% GRAVEL AND COBBLES	5 TO 20-50	8	1670-1980	1780	115	0.06

Table 4. Statistical Summary of Shear-Wave Velocity for Near Surface Rock

ROCK TYPE	DEPTH (FT)	NO. OF DATA	RANGE	S-WAVE VELOCITY (FT/SEC)		
				\bar{v}	σ	VAR
SOFT AND INTERMEDIATE SEDIMENTARY ROCK	0	5	1040-1260	1160	90	0.08
HARD SEDIMENTARY ROCK	0	6	1230-1480	1360	110	0.08
SOFT SEDIMENTARY ROCK	15-50	8	1220-1500	1380	110	0.08
FRACTURED BASEMENT COMPLEX	0-100	6	3300-4610	4040	430	0.11

Table 5. Summary of Regression Analysis for V_s
 $\ln V_s = \ln K + n \ln (d+c)$

GEOTECHNICAL DESCRIPTION	REGRESSION COEFFICIENTS			CORRELATION COEFFICIENT	STANDARD ERROR OF ESTIMATE	NO. OF DATA
	Ln K	n	c			
UNCONSOLIDATED SOILS	5.665	0.296	0.30	0.93	0.16	41
RECENT ALLUVIUM AND SATURATED OLD ALLUVIUM	5.628	0.413	2.4	0.95	0.13	76
OLD ALLUVIUM (UNSATURATED)	6.251	0.349	2.0	0.93	0.13	50
INTERMEDIATE SEDIMENTARY ROCK	5.862	0.472	0.0	0.95	0.13	9
HARD SEDIMENTARY ROCK	6.607	0.405	0.0	0.87	0.15	13

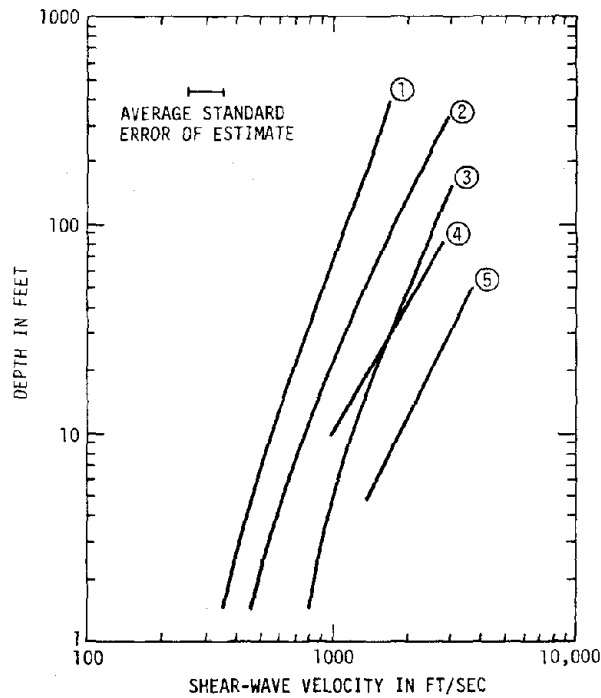


Figure 2. Comparison of Mean Regression Lines for:
 (1) Unconsolidated Soil, (2) Recent Alluvium and Saturated Old Alluvium, (3) Old Alluvium, (4) Intermediate Sedimentary Rock, and (5) Hard Sedimentary Rock

Table 6. Geotechnical and Velocity Data for Two Sites in Southern California

DEPTH (FT)	SOIL TYPE	GEOLOGY	MEASURED V_s (FT/SEC)	ESTIMATED V_s (FT/SEC)
LOS ANGELES SITE				
0 - 13	SILTY SAND	COMPACTED FILL	630	705
13 - 35	WELL GRADED SAND W/40% GRAVEL AND COBBLES	RECENT ALLUVIUM (BELOW WATER AT 25 FT.)	1770	1780
35 - 80	MASSIVE, DARK GREY SILTSTONE	FERNANDO FM. (PLIOCENE)	2180	1880
LONG BEACH SITE				
0 - 10	FINE SAND	HYDRAULIC FILL	380	420
10 - 60	FINE SAND	HYDRAULIC FILL (BELOW WATER)	550	580
60+	FINE SAND	RECENT ESTURINE DEPOSITS	1160	970

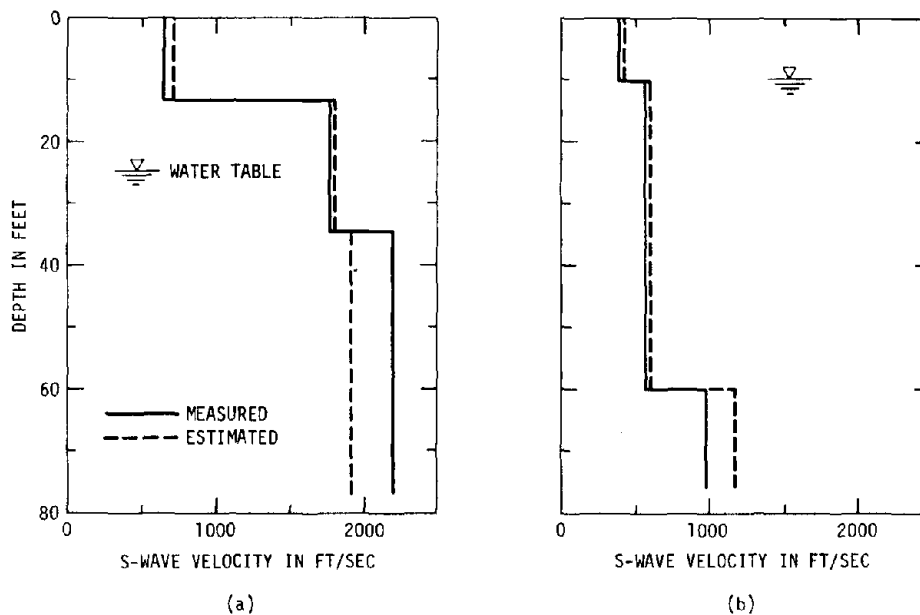


Figure 3. Estimated and Measured S-Wave Velocity Profiles for Two Southern California Sites: (a) Los Angeles Site; (b) Long Beach Site

1076

INTENTIONALLY BLANK

EFFECT OF LOCAL SITE CONDITIONS ON
SPECTRAL AMPLIFICATION FACTORSby S.D. Werner^I and H.S. Ts'ao^{II}

ABSTRACT

The effects of local site conditions on spectral amplification factors (SAFs) are studied to determine the sensitivity of these effects to the method of normalizing the spectral amplitudes and to provide comparisons with the Regulatory Guide (RG) 1.60 SAFs, which are widely used in current design practice. The study is carried out by first grouping a large ensemble of horizontal and vertical free-field records into one of three site classifications--deep soil, intermediate soil, and rock--using results from recent geotechnical investigations at accelerograph sites throughout the western United States. Then, for each site classification, statistical analyses of normalized spectral amplitudes at 91 discrete frequencies are used to develop mean and 84th percentile SAF vs. frequency curves for horizontal and vertical motions. The results show that the effects of local site conditions on the SAFs differ for high-, intermediate-, and low-frequency spectral amplitudes normalized according to peak acceleration, peak velocity, and peak displacement, respectively. Also, the RG 1.60 horizontal SAFs are seen to be most applicable to horizontal motions on the deep-soil and intermediate-soil sites, and the vertical SAFs provide extremely conservative representations of vertical motions, regardless of site conditions.

INTRODUCTION

Current seismic design practice for major structures is typically based on ground-motion criteria spectra derived from spectral amplification factors (SAFs) scaled to a suitable level of ground shaking for the site. Either site-independent or site-dependent SAFs can be used. Both are derived through statistical analyses of normalized spectral amplitudes from an ensemble of strong-motion records; however, they differ in how the ensembles of records are selected. Site-independent SAFs are derived from an ensemble selected to represent a wide range of source, regional, and local geologic parameters that could influence the ground shaking at a site (7). Site-dependent SAFs are defined in an attempt to isolate the effects of one of these sets of parameters--those related to local soil conditions. Such SAFs are developed by grouping strong-motion records into different classifications of site conditions and then statistically analyzing the SAFs from the records in each group (5, 9).

^IPrincipal Engineer, Agbabian Associates, El Segundo, California

^{II}Member of the Technical Staff, Agbabian Associates, El Segundo, California

This paper examines the applicability of site-dependent SAFs by summarizing results from a recent study of the effects of local site conditions on horizontal and vertical SAFs (12). The study has two important features. First, the grouping of the strong-motion records into various site-condition classifications is based on geotechnical investigations at accelerograph sites throughout the western United States. Prior studies of local site effects have not had the benefit of the results from these investigations, which have only recently been carried out as part of this research program (11, 13, 14, 15). Second, the study derives three different sets of SAFs for each site classification, using three different procedures for normalizing the spectral amplitudes: according to peak acceleration at high frequencies, to peak velocity in the intermediate frequency range, and to peak displacement at low frequencies. This differs from most prior studies of SAFs, which have usually been based on spectral amplitudes normalized only according to peak acceleration over the entire frequency range.

The paper describes how the strong-motion data were selected and classified according to local site conditions, and how the statistical analyses of the SAFs were carried out. The influence of local site conditions on each set of SAFs is described, and the SAFs derived from data normalized according to peak acceleration are compared to those of Regulatory Guide 1.60 (17), which are widely used in current design practice.

SITE CLASSIFICATIONS AND DATA ENSEMBLES

When strong-motion data are classified according to local site conditions, three factors should be recognized. First, the actual definition of the site classifications into which the data will be grouped is dependent to a large extent on the judgment and technical approach of the engineer performing the study. This is reflected by the large number of different site classification definitions currently in existence. Second, for any one set of site classification definitions, differences of opinion can exist among experienced engineers as to the particular classification in which to place the records from a given accelerograph station (16). These differences result not only from different interpretations of existing subsurface data at an accelerograph site, but also from the uncertainties that often exist in soil property measurements, particularly at substantial depths. Finally, grouping the data into rather broad site classifications does not represent certain details of the local site conditions which may be important, nor does it represent other factors related to the source mechanism and source-to-site transmission path which may also influence the ground shaking (4). Such factors are left as uncontrolled variables in classifications of this type (10).

The strong-motion records used in this study were measured at the accelerograph sites where the previously noted geotechnical investigations were conducted. A total ensemble of 106 record sets was thereby developed, in which each set comprises two horizontal components and one vertical component of motion. The characteristics of the ensembles for each record set are given in Table 1, where it is seen that (a) the largest ensemble of records

falls in the deep soil site classification (63 record sets) and the smallest ensemble corresponds to the rock site classification (17 record sets); (b) a large number of these records was measured during a single earthquake--the 1971 San Fernando event; and (c) the ensemble of record sets for each site classification represents a wide range of earthquake magnitudes, epicentral distances, and peak acceleration levels. These characteristics are also typical of prior examples of ensembles of records grouped only according to local site conditions (e.g., 5, 9).

TABLE 1. SITE CLASSIFICATIONS

Site Conditions	Definition	Total Number of Record sets in Ensemble ^(I)	Number of Record Sets from 1971 San Fernando Earthquake ^(I)	Range of Magnitudes	Range of Epicentral Distances, km	Range of Peak Horizontal Accelerations, g	Range of Peak Vertical Accelerations, g
Rock	20 ft or less of overburden that overlies rock-like materials (II)	17	11	5.3 to 6.4	6.6 to 70.7	0.021 to 1.171	0.007 to 0.710
Intermediate Soil	Firm soil deposits whose depth to rock-like materials ranges from 20 ft to 150 ft ^(II)	26	17	5.3 to 7.7	14.9 to 130.5	0.008 to 0.316	0.006 to 0.156
Deep Soil	Firm soil deposits whose depth to rock-like materials exceeds 150 ft ^(II)	63	25	4.0 to 7.1	9.3 to 220.3	0.002 to 0.379	0.002 to 0.210

I Each record set comprises two horizontal components and one vertical component of motion. Record sets contained in each ensemble are identified in (12).

II Rock-like material is usually defined as firm materials whose shear wave velocity exceeds 2500 fps.

ANALYSIS PROCEDURE

The basic data used to represent each record in the ensemble for each site classification were response spectrum amplitudes digitized at 91 discrete frequencies between 0.06 Hz and 25 Hz (2). The resulting SAFs developed at each frequency were based on the premise that higher-frequency motions are most directly related to the peak acceleration, while intermediate-frequency and low-frequency motions are most directly related to the peak velocity and peak displacement, respectively. Accordingly, three different types of SAFs were defined to reflect different procedures for normalizing the spectral amplitudes over high, intermediate, and low frequencies. These are as follows.

<u>Normalizing Method</u>	<u>Definition of SAF</u>	<u>Assumed Applicable Frequency Range, Hz</u>
According to peak acceleration	Ratio of spectral acceleration to peak ground acceleration	1 to 25
According to peak velocity	Ratio of spectral velocity to peak ground velocity	0.25 to 5
According to peak displacement	Ratio of spectral displacement to peak ground displacement	0.04 to 1

Once the SAFs at each frequency were defined for each record as indicated above, they were analyzed statistically to develop composite results for each site classification. The statistical analyses were carried out by assuming the ensemble of SAFs at each frequency to be lognormally distributed. The ensemble mean and standard deviation SAF values were then computed at each frequency and used to develop SAF vs. frequency curves that represent a mean and 84th percentile probability level for each site classification. Only results for 5% of critical damping were developed in this way.

COMPARISONS OF SITE-DEPENDENT SAF'S

The first set of results from this study corresponds to comparisons of horizontal and vertical SAFs for each of the three set classifications. Comparisons of the mean and 84th percentile horizontal SAFs are shown in Figures 1 and 2, and comparisons of the corresponding vertical SAFs are given in Figures 3 and 4. These comparisons are discussed separately for data normalized according to peak acceleration, peak velocity, and peak displacement.

Data Normalized According to Peak Acceleration. For this case, the horizontal and vertical SAFs for the rock sites are distinctly different from those corresponding to the two soil site classifications (Figs. 1c through 4c). At frequencies below about 4 to 5 Hz for horizontal motions and 6 Hz for vertical motions, the rock-site SAFs fall well below the SAFs for the two classes of soil sites; whereas at higher frequencies, the opposite trend occurs. There is no distinct difference between the SAFs for the two soil site classifications.

Data Normalized According to Peak Velocity. For this second case, there are some differences between the SAFs for the various site classifications; however, these differences are less distinct than those exhibited by the acceleration-normalized SAFs in that

(a) site-dependent effects are less prominent in the frequency range common to both sets of results (1 to 5 Hz), and (b) there are no strong site-dependent effects over those frequencies ranging from about 0.8 Hz to 3 Hz. Furthermore, comparisons between the SAFs for intermediate soil sites and the other two site classifications are not the same for vertical motions as they are for horizontal motions (Figs. 1b through 4b).

Data Normalized According to Peak Displacement. The SAFs that result from this final case do not exhibit clear or consistent differences among the various site classifications (Figs. 1a through 4a).

The most important feature of these trends is that the manner in which the data are normalized has a strong influence on the type and extent of local site effects on the resulting SAFs. As noted, most previous SAF definitions have been developed from data normalized only according to peak acceleration over the entire frequency range; such SAFs have been shown to exhibit prominent local site effects (9, 18), a trend supported by the present investigation for frequencies above 1 Hz. However, this normalizing approach has certain shortcomings when used to define SAFs in the low-to-intermediate frequency range. For example, peak ground accelerations can be closely related to the dynamic forces applied to high-frequency systems, but not to systems with low-to-intermediate natural frequencies. Along these lines, statistical analyses of SAFs from data normalized according to peak acceleration have shown the SAFs to have very low standard deviations at high frequencies, but markedly increasing standard deviations with decreasing frequency (3, 18, 20).

In view of this, several investigators have advocated alternative procedures that circumvent the above difficulties when developing SAFs for design purposes. For example, some studies have suggested the use of peak velocity as a normalizing parameter over the entire frequency range (3), while others have developed ground-response spectra from SAFs determined in a manner similar to that used in the present investigation; that is, spectral amplitudes in high- intermediate- and low-frequency ranges are normalized according to peak acceleration, velocity, and displacement, respectively (1, 6, 20). For such normalizing procedures, the present investigation shows that the influence of local site conditions on the resulting SAFs will be less prominent than that observed from data normalized according to peak acceleration only.

COMPARISONS WITH REGULATORY GUIDE 1.60

The SAFs defined in the Regulatory Guide (RG) 1.60 (17) are widely used in current seismic design practice for nuclear plants and other major structures as well. In view of this, RG 1.60 SAFs have been compared to the SAFs that were developed from the present investigation.

Before comparing the SAFs, it is appropriate to first consider how each set was developed. The RG 1.60 SAFs were defined from statistical analyses of spectra from 28 horizontal records and 14 vertical records (7). They are site independent in that the ensembles of records represent a wide range of geologic and local site parameters. For both horizontal and vertical motions, the RG 1.60 SAFs are defined as 84th percentile multiples of the peak *horizontal* acceleration. On the other hand, the SAFs from the present investigation differ from those of RG 1.60 in that (a) they have been developed from a larger ensemble of records; (b) they are site dependent rather than site independent; and (c) for horizontal and vertical motion, they are defined as mean and 84th percentile multiples of the peak horizontal and vertical acceleration, velocity, or displacement, depending on the frequency range.

For consistency with the RG 1.60 SAFs, only those SAFs from the present investigation that are 84th percentile multiples of the peak acceleration have been included in this comparison. Furthermore, the comparison is made only at frequencies greater than 1 Hz, which is the frequency range over which peak acceleration normalization was carried out in this study. Finally, the RG 1.60 vertical motion SAFs have been expressed as multiples of the peak vertical acceleration rather than peak horizontal acceleration, to be consistent with the vertical motion SAFs from the present investigation.*

The two sets of SAFs are compared in Figure 5. The comparisons for horizontal motions show that the RG 1.60 SAFs are reasonably similar to the SAFs from the two classifications of soil sites but differ from the SAFs from the rock sites at frequencies below about 10 Hz (Fig. 5a). This trend may be attributed in part to the fact that most of the records used to develop the RG 1.60 SAFs were measured on soil sites; in fact, only 4 of the 28 horizontal motion records that lead to RG 1.60 were measured on rock (10). The trend may also be influenced by the size of the ensemble of the horizontal rock motion records (34 records) which, as noted previously, is the smallest of any of the site classifications considered in this investigation (Table 1). This ensemble is, however, larger than the total number of records used in the development of the RG 1.60 horizontal SAFs (28 records).

For vertical motions, Figure 5b shows that the RG 1.60 SAFs substantially exceed the 84th percentile SAFs from each of the three site classifications. This trend is consistent with observations from several prior studies of vertical response spectra and spectrum shapes (e.g., 8, 19, 20) and indicates that the RG 1.60 vertical motion SAFs may be overly conservative for design applications.

*The RG 1.60 provisions for vertical motions specify that the peak vertical acceleration (which in this case corresponds to the spectral acceleration at frequencies greater than 50 Hz) is two-thirds of the peak horizontal acceleration. Therefore, the RG 1.60 vertical motion SAFs can be expressed in terms of the peak vertical acceleration by multiplying them by a factor of 1.5.

CONCLUSIONS

This investigation leads to two important sets of conclusions. First, the effects of local site conditions on the SAFs within a given frequency range are dependent on how the SAFs are normalized. Such effects are most prominent when peak acceleration is used as a normalizing parameter (applicable to higher-frequency motions) and are less prominent or nonexistent when peak velocity or displacement is used (for intermediate-frequency or low-frequency motions, respectively). Second, the applicability of the RG 1.60 SAFs at frequencies greater than 1 Hz varies according to the site conditions and the direction of motion (horizontal or vertical) being considered. The RG 1.60 SAFs are most applicable for representing horizontal motions at deep-soil or intermediate-soil sites, and are extremely conservative in their representation of vertical motions, regardless of site conditions.

ACKNOWLEDGMENTS

This study was carried out as part of a joint venture research program involving Shannon & Wilson, Inc. and Agbabian Associates and sponsored by the United States Nuclear Regulatory Commission (USNRC). The program is directed toward expanding the current understanding of the behavior of soil materials during earthquakes and the potential influence of these materials on earthquake ground motions. The authors acknowledge the contributions of M.S. Agbabian and G.A. Young of Agbabian Associates for their critical review of this paper, J.D. Radler of Agbabian Associates for her editorial assistance, and D. Clayton of Shannon & Wilson for his aid in classifying the accelerograph sites. Also, the assistance and direction of J. Harbour of USNRC, technical monitor for the joint venture, is gratefully acknowledged.

REFERENCES

1. Brady, A.G. "Estimating Response Spectra from Peak Values of Ground Motion," paper presented at the 70th Annual Meeting of the Seismological Society of America, Calif. State Univ. Los Angeles, Mar 25-27, 1975.
2. Calif. Inst. of Tech. (CIT). Strong Motion Earthquake Accelerograms, Volumes I-IV, Parts A-Y. Pasadena: CIT Earthquake Eng. Res. Lab., 1969-1975.
3. Hall, W.J.; Mohraz, B.; and Newmark, N.M. Statistical Studies of Vertical and Horizontal Earthquake Spectra, NUREG-0003. Urbana, IL: Nathan M. Newmark Consulting Eng. Services, Jan 1976. (PB 248 232)
4. Hudson, D.E. "Strong Motion Seismology," in Proc. Int. Conf. on Microzonation for Safer Construction Res. and Appl. Seattle, Nov 1972, Vol. 1, pp 29-60.

5. Mohraz, B. "A Study of Earthquake Response Spectra for Different Geological Conditions," Bull. Seismol. Soc. Amer. 66:3, Jun 1976.
6. Newmark, N.M. and Hall, W.J. "Seismic Design Criteria for Nuclear Reactor Facilities," Proc. 4th World Conf. on Earthquake Eng. Santiago, Chile, Feb 1969.
7. Newmark, N.M.; Blume, J.A. and Kapur, K.K. "Seismic Design Spectra for Nuclear Power Plants," Proc. ASCE Power Div. 99:P02, Nov 1973, pp. 287-303.
8. Rizzo, P.C.; Shaw, D.E.; and Snyder, M.D. "Vertical Seismic Response Spectra," Proc. ASCE Power Div. 102:P01, Jan 1976.
9. Seed, H.B.; Ugas, C.; and Lysmer, J. "Site Dependent Spectra for Earthquake Resistant Design," Bull. Seismol. Soc. Amer. 66:1, Feb 1976.
10. Shannon & Wilson (SW) & Agbabian Assoc. (AA). Procedures for Evaluation of Vibratory Ground Motions of Soil Deposits at Nuclear Power Plant Sites. Seattle, WA: SW & El Segundo, CA: AA, Jun 1975. (NUREG-75/072)
11. Shannon & Wilson (SW) & Agbabian Assoc. (AA). Geotechnical and Strong Motion Earthquake Data from US Accelerograph Stations: Gavilan College, Gilroy, California; Utah State University, Logan, Utah; Montana State University, Bozeman, Montana; County-City Building, Tacoma, Washington; Federal Building, Helena, Montana; Carroll College, Helena, Montana, Vol. 3. Seattle, WA: SW & El Segundo, CA: AA, Mar 1977.
12. Shannon & Wilson (SW) & Agbabian Assoc. (AA). Effects of Local Site Conditions on Earthquake Ground-Motion Parameters (draft), R-7339-4597. Seattle, WA: SW & El Segundo, CA: AA, May 1978.
13. Shannon & Wilson (SW) & Agbabian Assoc. (AA). Verification of Subsurface Conditions at Selected "Rock" Accelerograph Stations in California, NUREG/CR-0055, Vol. 1., Vol. 2 (forthcoming). Seattle, WA: SW & El Segundo, CA: AA, May 1978.
14. Shannon & Wilson (SW) & Agbabian Assoc. (AA). Data from Selected Accelerograph Stations at Wilshire Boulevard, Century City, and Ventura Boulevard, Los Angeles, California, NUREG/CR-0074. Seattle, WA: SW & El Segundo, CA: AA, Jun 1978.
15. Shannon & Wilson (SW) & Agbabian Assoc. (AA). Geotechnical and Strong Motion Data from U.S. Accelerograph Stations, NUREG-0029, 2v. Seattle WA: SW & El Segundo, CA: AA, Sep 1976 & Jun 1978.
16. Trifunac, M.D. and Brady, A.G. "On the Correlation of Seismic Intensity Scales with the Peaks of Recorded Strong Ground Motion," Bull. Seismol. Soc. Amer. 65:1, Feb 1975, pp 139-162.

17. U.S. Atomic Energy Comm. (USAEC). "Design Response Spectra for Seismic Design of Nuclear Power Plants," Regulatory Guide 1.60, Rev. 1. Washington, DC: USAEC, Dec 1973.
18. Werner, S.D. and Ts'ao, H.S. Investigation of Vertical Ground Motion Characteristics for Nuclear Plant Design, SAN/1011-108. El Segundo, CA: Agbabian Assoc., Dec 1975.
19. Werner, S.D. and Ts'ao, H.S. Correlation of Ground Response Spectra with Modified Mercalli Site Intensity, SAN/1011-113. El Segundo, CA: Agbabian Assoc., Jun 1977.
20. Werner, S.D. and Ts'ao, H.S. Study of Vertical Ground Response Spectrum Shapes, SAN/1011-114. El Segundo, CA: Agbabian Assoc., Aug 1977.

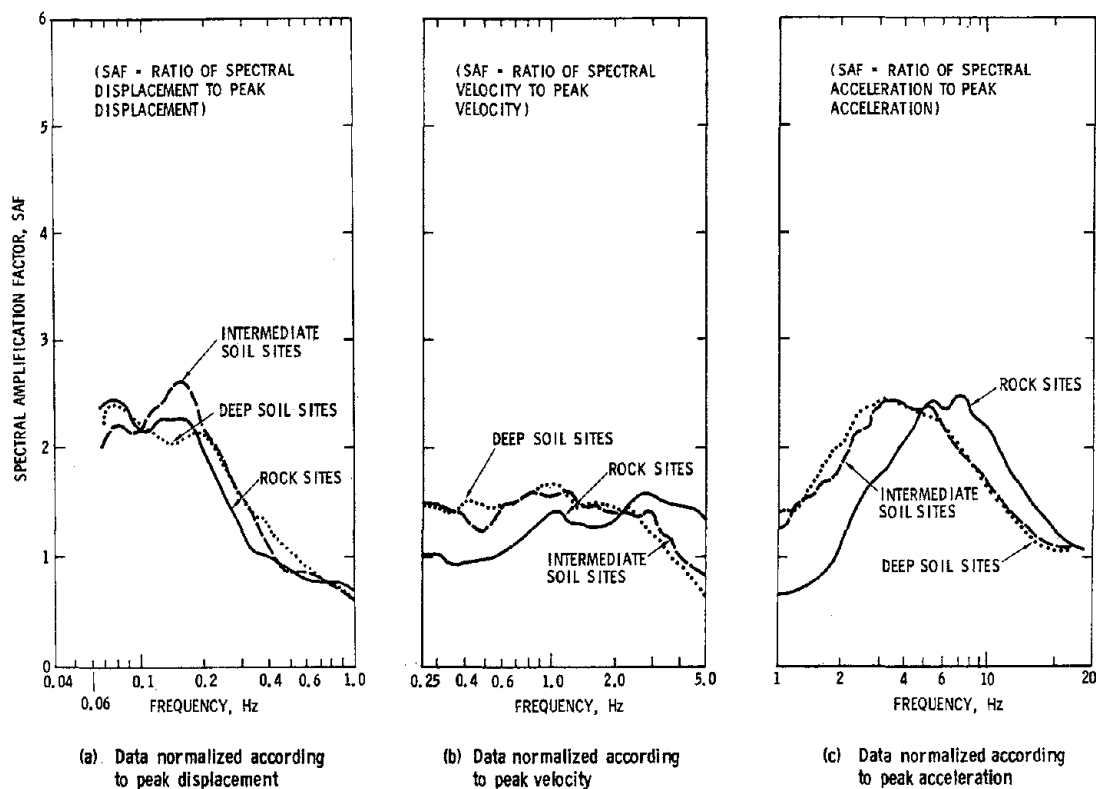


FIGURE 1. MEAN SAF'S FOR HORIZONTAL GROUND MOTIONS (DAMPING RATIO = 0.05)

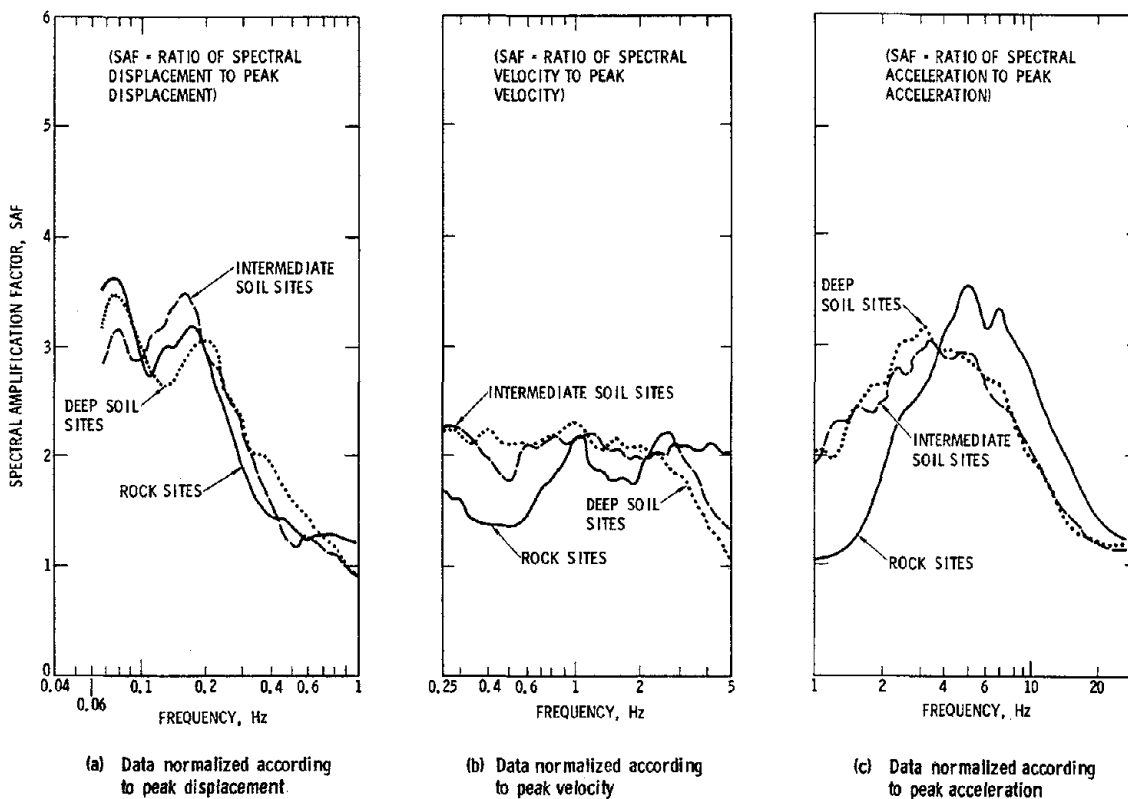


FIGURE 2. 84TH PERCENTILE SAF'S FOR HORIZONTAL GROUND MOTIONS (DAMPING RATIO = 0.05)

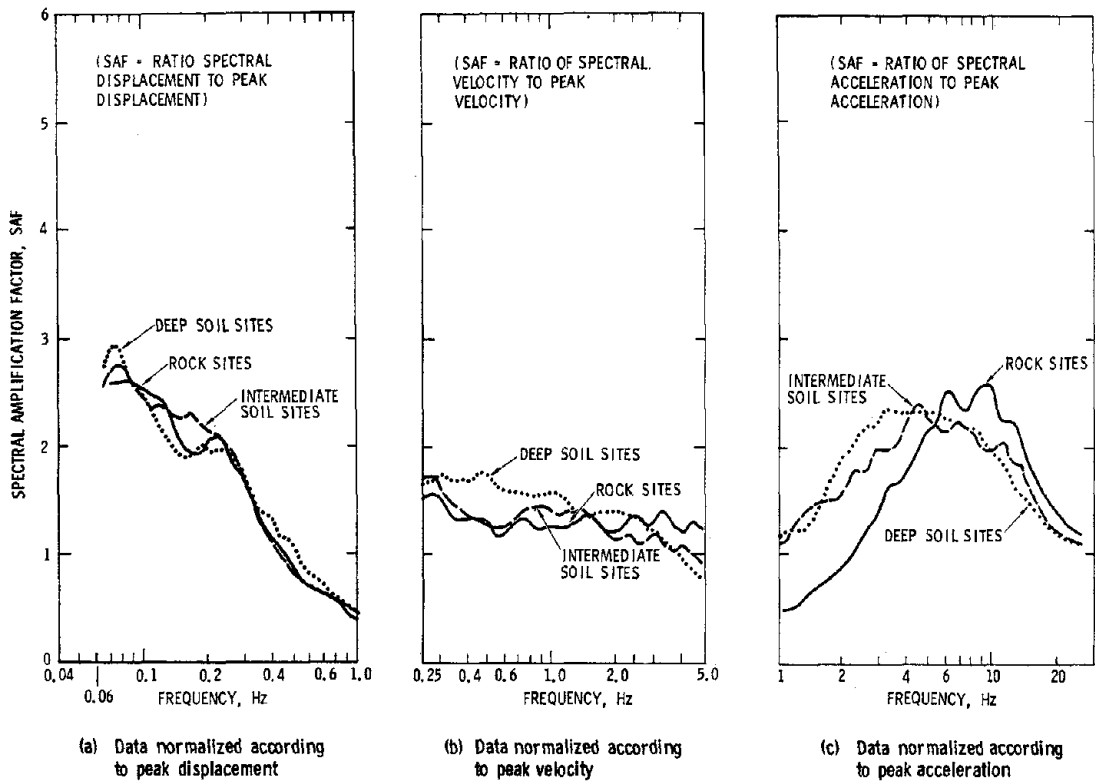


FIGURE 3. MEAN SAF'S FOR VERTICAL GROUND MOTIONS (DAMPING RATIO = 0.05)

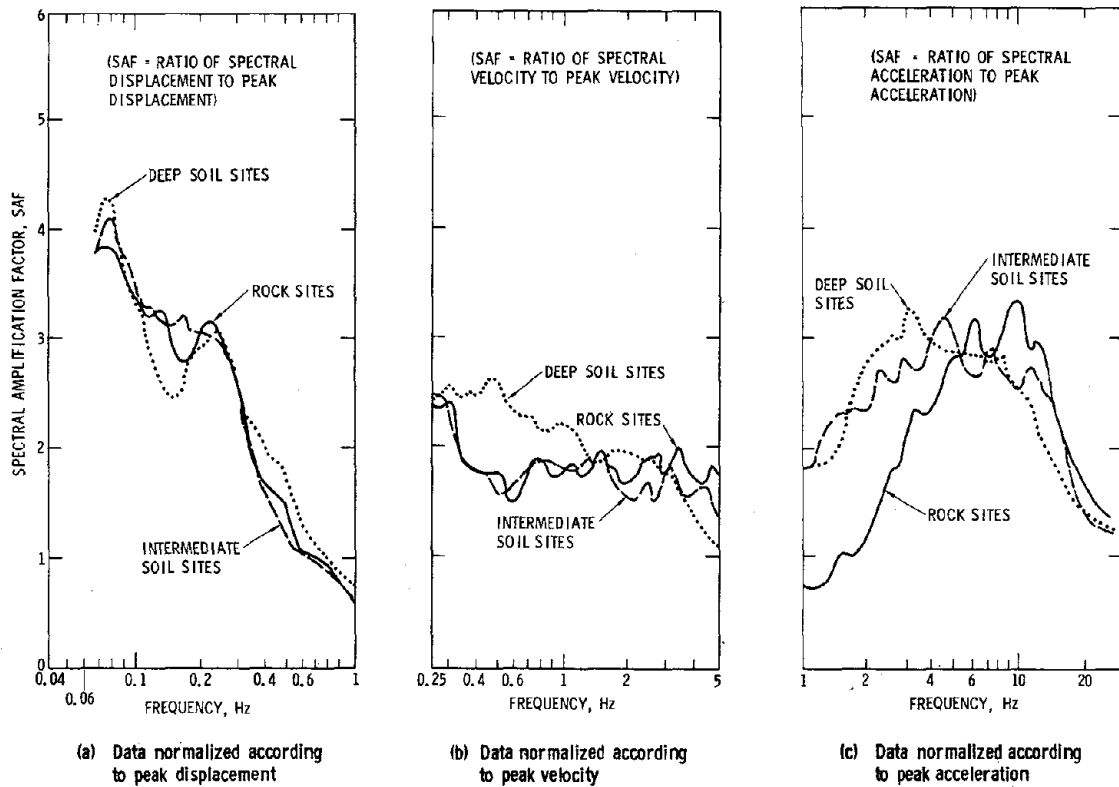
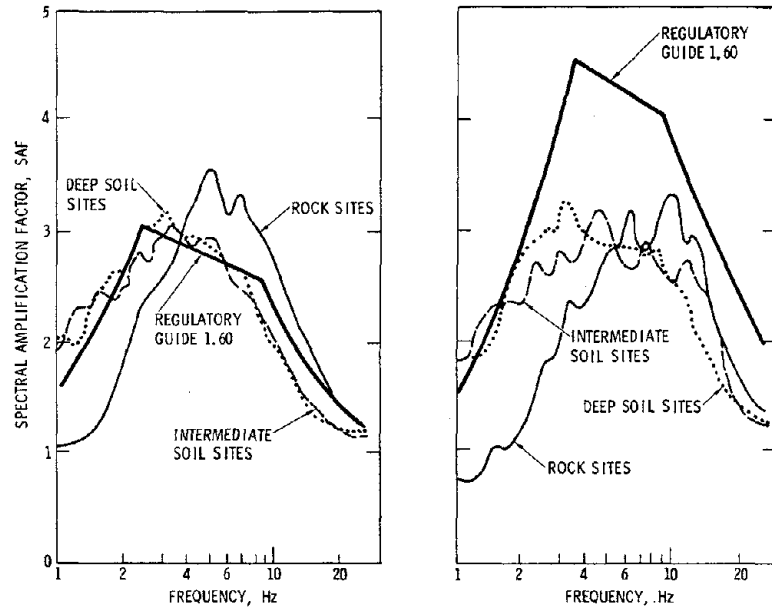


FIGURE 4. 84TH PERCENTILE SAF'S FOR VERTICAL GROUND MOTIONS (DAMPING RATIO = 0.05)

(SAF = RATIO OF SPECTRAL ACCELERATION TO PEAK ACCELERATION)



(a) Horizontal ground motions

(b) Vertical ground motions

FIGURE 5. COMPARISONS OF 84TH PERCENTILE SAF'S WITH REGULATORY GUIDE 1.60 (DAMPING RATIO = 0.05)

DETERMINATION OF SITE DEPENDENT SPECTRA
USING NON LINEAR ANALYSIS

by

Ignatius Lam^I, Chan-Feng Tsai^{II}, Geoffrey R. Martin^{III}

ABSTRACT

The significance of local site response of soft soils in modifying earthquake ground motion characteristics is examined using a non-linear one dimensional dynamic response analysis. The non-linear explicit finite difference program (DETRAN) used for these analyses, is based on a physically motivated viscous elasto-plastic soil model incorporating a failure criterion, degradation characteristics and an energy transmitting boundary. The energy transmitting boundary provides a method of ground response analysis without the need to define bedrock at a finite depth.

The analysis procedure is illustrated with reference to idealized soft soil sites underlain by more competent firm ground. Two representative firm ground earthquake acceleration time histories were defined by an outcrop surface motion, and the response of the site examined to ground motions scaled to give peak outcrop accelerations of 0.05g and 0.45g. Comparisons are made with equivalent linear SHAKE analyses, and the significance of incorporating soil yield on acceleration levels and spectral shapes is demonstrated. Spectral shapes are compared with an average smoothed spectrum available in the literature, and significant changes in shape with acceleration level are noted.

INTRODUCTION

The concept of earthquake zonation for design purposes invariably involves consideration of site soil conditions as one of the zonation parameters. With an increasing number of ground motion records available for study, several correlations between recorded surface ground motion characteristics expressed as response spectra, and site soil conditions have been made (1, 2, 3). Results from these studies are generally expressed as smoothed or mean spectra for generalized site soil conditions such as rock, deep cohesionless soils, stiff soils and soft or medium clays. As simplifications of such spectra are often adopted for zonation purposes, it is important that the potential significance of other factors influencing variations in spectral shape for a given site condition, such as site source distance and level of ground shaking be assessed. For soft sites in particular, most available records used for spectral studies have acceleration levels of the order of 0.05g. Hence the question remains as to the potential influence of stronger earthquake shaking on spectral characteristics for soft sites. For higher acceleration levels, say of the order of 0.3g or greater, it is clear that yield or failure of soft clay due to the high induced shearing stresses, could have a significant influence on recorded ground motion characteristics and indeed on the capability of such deposits in transmitting accelerations at such levels.

I Staff Engineer, Fugro, Inc., Long Beach, California

II Project Engineer, Fugro, Inc., Long Beach, California

III Senior Engineer, Fugro, Inc., Long Beach, California

In the case of site specific studies, the preferable method to develop design spectra is to utilize existing earthquake accelerograms recorded on similar sites and where magnitude, distance and regional geology are also similar. However, as noted above, few records are available for soft sites subjected to strong ground shaking. Because of the uncertainties in scaling small records to considerably higher values, it hence becomes necessary to use simplified site response analyses to examine the potential influence of local site effects on ground motion characteristics.

Perhaps the most widely recognized site response analysis method is that used by the program SHAKE (4). This program assumes site response is dominated by vertically propagating shear waves, and represents the non-linear hysteretic soil deformation properties by equivalent linear shear moduli (where shear moduli are expressed as a function of shear strain) and equivalent viscous damping coefficients. The program can input motion at bedrock level or can allow motion to be placed at a given interface at depth, provided the surface motion on the outcropping base stratum is known. Hence it becomes unnecessary to establish a bedrock level, and the response of a deep soft soil site may be studied by defining an outcropping surface input motion for a stiffer soil at a selected depth.

Whereas the equivalent linear approximation used in SHAKE provides a good approximation in most cases, the program cannot simulate the highly non-linear effects of soft sites where large deformations may occur during strong shaking. For the latter case, it is preferable to use a non-linear dynamic response procedure which incorporates a yield or failure criterion.

In this paper, a newly developed non-linear method for site response analysis is described, and is used to examine the potential influence of strong shaking on soft sites in modifying ground surface acceleration characteristics as expressed by response spectra. Although only a limited number of analyses were performed to illustrate the application of the program, the results indicate that there could be significant differences in soft site spectral shapes for low and strong shaking levels. The significant attenuation of acceleration levels by soft sites is also demonstrated.

NON LINEAR RESPONSE ANALYSES

A number of methods currently exist for estimating the earthquake response of level soil sites, where it is assumed that earthquake motion can be represented by vertically propagated horizontal shear waves. This assumption seems to provide a reasonable approximation for many sites, as demonstrated by comparisons with case histories (5, 6). Most of the different methods available were developed in the last 10 years. It is of interest to briefly summarize some of the available procedures and note some of the features of the various methods.

The program SHAKE (4), as reviewed in the introduction, is the earliest and probably the most widely used method available. It operates in the frequency domain and utilizes the equivalent linear approach (5) to take into account the strain dependent soil properties. Because of the linear nature of the solution, for a given surface control motion on a specific site, this method is the only approach which can perform a deconvolution study to derive the seismic response within a soil column beneath the surface.

The program CHARSOIL (7), uses the Ramberg-Osgood model to describe hysteretic non linear soil behavior and uses a solution in the time domain based on the method of characteristics. The main advantage of this approach is the direct use of the actual non-linear and hysteretic dynamic properties of the soils during an earthquake instead of equivalent moduli and damping. Damping is implicitly included in the hysteretic model. However, the program requires a bedrock base boundary where the input seismic motion is defined. The program DCHARM (8) was developed from CHARSOIL, and takes into account the degradation in soil stiffness arising from cyclic loading. This phenomenon may be observed in soft soils subjected to large cyclic strains, and for a soft clay site under strong seismic shaking, the effects of modulus degradation on site response can be significant.

The program NONLI3 (9) is similar to CHARSOIL in many respects, except that it is capable of solving the seismic response of a level soil site underlain by a semi-infinite elastic medium. A transmitting boundary is used to take into account the finite rigidity in the elastic substratum, and hence the need to define bedrock level is avoided. The non linear hysteretic behavior of the soil is represented by a composite of elasto-plastic subelements proposed by Iwan (10) and the time domain solution uses an explicit finite difference method. The feature of the Iwan element formulation, is that it enables any non-linear backbone curve to be simulated, such as that of the Ramberg-Osgood and hyperbolic analytical models, or actual laboratory test results. In this respect the program is very flexible. A similar non-linear formulation using elasto-plastic subelements has been described by Taylor and Larkin (11).

The program DESRA (12) is a non-linear hysteretic program similar in principle to those previously described. However, the program may also be used in an effective stress mode for analysis of pore-water pressure increases in saturated sands during earthquakes. The numerical procedure uses a hyperbolic backbone curve and the non-linear equations of motion are solved using an implicit integration scheme.

As stated in several comparative studies (8, 13, 14, 15), currently existing methods all give reasonable answers provided they are used with due regard to the assumptions and limitations inherent in each of the approaches. Naturally, there are cases where one particular approach works better than others regarding a particular aspect of the problem. Therefore, the selection of an appropriate method for a given problem should be based on an understanding of the requirements of the problem itself as well as the basics of the methods available.

Ideally, a good analytical procedure for seismic response determination of a deep soft soil site should include a realistic and flexible model which takes into account the non-linear, failure and degradation characteristics of the soils, the effects of soil stiffness below as well as above the point of control motion application, and boundary condition differences between the free surface where the control motion was recorded and the interface where the motion will be assigned in the analysis. An analytical procedure incorporating the above considerations is presented in this study. This procedure is based on the program NONLI3 with modifications to incorporate (1) modulus degradation of soft clay under cyclic loading. (2) a viscous damping option to allow refinement of implicit hysteretic damping to more closely match laboratory damping curves and to provide the means of suppression of artificial high fre-

quency oscillations induced by the numerical solution. (3) simple data input formats based on measured laboratory modulus and damping curves.

The computer program DETRAN was recently developed by Fugro as part of an "in-house" research and development program. A more detailed description of the computer program is given below.

COMPUTER PROGRAM DETRAN

As noted above, this program is based on NONLI3 with modifications to include modulus degradation, viscous damping, and simple input formats based on curve fitting to measured laboratory data. A general sketch illustrating the features of the model is shown in Fig. 1. The concept is similar to that used in SHAKE, except that a non-linear hysteretic soil model is used. Aspects of the program are noted below.

Non-linear Hysteretic Soil Model

The physically motivated Iwan model (10), is utilized in the program. The model incorporates an array of elasto-plastic elements to simulate a given non-linear backbone curve and provide hysteretic damping, while the dash-pot elements provide the means for introducing viscous damping. The main advantages of using a physical or mechanistic model are (1) the model provides the means for a non-iterative time domain solution which can be used for complicated arbitrary cyclic loading conditions such as those of earthquakes, (2) the model allows a yielding or failure criterion to be incorporated, so the seismic response of soft clay sites can be realistically studied without the need of a stress cut off to achieve yielding characteristics, and (3) any laboratory observed properties and other mathematically motivated soil models can be duplicated without difficulty. This ability not only improves the non-linear behavior modelling, but also provides a means for comparison studies which can lead to a better understanding of soil modelling. Typical hysteresis loops where a hyperbolic backbone (initial loading) curve has been modelled, are shown in Fig. 2.

Degradation Model

The degradation model proposed by Idriss, et al (8) is incorporated in the procedure. This model assumes that (a) the degradation process occurs only at the time when the stress changes sign and (b) the amount of additional degradation depends only on the amount of accumulated degradation and the maximum strain developed for the previous half cycle.

Transmitting Boundary

A boundary which can take into account the existence of soils with finite stiffness located at the base of the soil column is included in the program. In this procedure, outcrop control motion is defined at a firm ground outcrop point and the transmitting boundary combined with the soil column under consideration provides a more realistic model of a deep soil site. The boundary formulation as developed by Joyner and Chen (15), satisfies the boundary conditions on the interface for a wave vertically incident from below. Under the assumption of vertically propagating shear waves in the underlying elastic medium, the shear stress developed in the interface can be determined knowing the particle velocities of the incident wave and those on the boundary. This approach is similar to that

developed by Lysmer and Kuhlemeyer (16). Parameter studies (17), indicate that the influence of finite stiffness of soil half space on site response is quite significant in some cases. The transmitting boundary formulation has been checked against available closed form solutions as well as solutions obtained using SHAKE for 1 and 2 layer elastic systems. Identical solutions were obtained.

Formulation of Iwan Model Parameters from Laboratory Data

As mentioned earlier, any given non-linear soil properties can be simulated by the use of adequate number of elasto-plastic subelements. Laboratory determined G/G_{\max} versus strain amplitude plots can be modelled by 50 or less subelements. After matching laboratory modulus curves, damping ratio versus shearing strain amplitude curves may be computed for the implicit hysteresis damping, and compared with measured laboratory damping curves. Additional viscous damping elements may then be added to the model if necessary to more closely match the laboratory curve.

APPLICATION OF DETRAN TO SOFT SOIL PROFILES

To illustrate the application of DETRAN, an idealized soft soil site having maximum shear modulus (G_{\max}) profiles as shown in Fig. 3 was studied. Corresponding assumed maximum yield stresses (τ_{\max}) under cyclic loading are also shown on Fig. 3. In practice, these stresses could be defined by the cyclic shear stress causing a large deformation in a single cycle. The strain dependent soil properties used for the study are summarized in Fig. 4. The G/G_{\max} versus shearing strain amplitude relationship was obtained from the secant moduli of hysteretic loops with corresponding shearing strain amplitudes defined. In order to model the yielding strength of the soils, a hyperbolic type backbone curve was utilized. The implicit hysteresis damping based on Masing effects were computed as shown in Fig. 4. A very small amount of viscous damping (less than 1%) was introduced in the analyses to suppress the artificial high frequency oscillations discussed earlier.

Based on the shear strength and dynamic moduli assumed, soils at a depth of 100 feet may be considered equivalent to competent firm ground. For the study, two records obtained on deep alluvium sites were used for control outcrop motions at the 100 foot depth. These records were (1) the Orion Blvd. record of the 1971 San Fernando Valley earthquake (N-S component with recorded maximum acceleration of 0.25g), and (2) the El Centro record of the 1940 Imperial Valley earthquake (N-S component with recorded maximum acceleration of 0.35g). These two records were scaled to 0.05g and 0.45g for the representation of low and high levels of shaking, respectively.

In this study, results from DETRAN are compared with those of SHAKE, the influence of the soft site on the magnitude and shape of acceleration spectra is examined, and the effects of changes in modulus characteristics are investigated. Results of these studies are presented below.

SHAKE Comparative Study

To illustrate the relative differences between SHAKE and DETRAN, surface spectra for the two programs were compared for outcrop input motions

given by the El Centro record scaled to maximum accelerations of 0.05g and 0.45g. For the former acceleration, the two programs would be operating at low strains well below the yield criteria for the clay, while for the higher maximum acceleration, yield and degradation of the soft clay could be expected to influence the surface accelerations determined by DETRAN. The modulus and damping ratios defined by Fig. 4 for DETRAN, were also used as input for the SHAKE analysis. The "site 1" G_{max} profile shown on Fig. 3 was used for the comparative study.

Surface acceleration spectra are shown plotted in Fig. 5 for both the outcrop motion and the soft clay motion. As shown in Fig. 5, for a comparatively low maximum outcrop acceleration of 0.05g, the surface response spectra obtained from the use of SHAKE and DETRAN are almost identical. The maximum surface accelerations obtained from SHAKE and DETRAN are 0.077g and 0.071g respectively. The increased surface accelerations reflect the influence of the soft site in modifying the input outcrop accelerations, are in general agreement with expected changes noted by Seed, et al (18). For a higher level of shaking (0.45g), the computed surface response spectra were significantly different both in maximum acceleration levels and frequency content. The flatter spectrum for the DETRAN analyses may be attributed to the effects of soil yield and degradation at higher strains. Similar effects have been reported in other comparative studies (13). However, comparative analyses at higher strain levels where failure does not occur, have shown greater agreement between SHAKE and non-linear programs provided site resonant effects arising from coincidence of site and earthquake frequencies do not occur (17).

Characteristics of Soft Site Spectra

For the site under consideration, the surface response spectra derived from DETRAN analyses for the two different outcrop (firm ground) control motions (Orion Blvd. and El Centro) were determined. Spectra for the El Centro record are presented in Fig. 5 and those for the Orion Blvd. record in Fig. 6 for low (0.05g) and high (0.45g) levels of outcrop shaking. Comparing Fig. 6 with Fig. 5, it may be seen that the influence of the soft site on the Orion Blvd. record is similar to that of the El Centro record. For the 0.05g outcrop accelerations, the soft site has the effect of increasing ground accelerations and spectral accelerations. For the 0.45g outcrop accelerations, surface accelerations are reduced, and the acceleration spectra are flattened. Spectral accelerations for shorter periods are considerably reduced compared to the outcrop spectra, while for longer periods spectral ordinates for the soft soil site are increased. The influence of the soft site in modifying the input motion characteristics may also be seen by comparing the time histories for the 0.45g El Centro motion input shown in Fig. 7. Acceleration levels for the interface "within" motion are seen to be reduced compared to the outcrop motion, due to the transmitting boundary effects, while the frequency content seems much the same. Acceleration levels for the surface motion are considerably reduced, but are more uniform and have longer periods compared to the input motion.

In order to compare spectral shapes for the soft site surface motions, response spectra were normalized by dividing all ordinates of a given acceleration spectrum by the maximum surface acceleration. After normalization, the ordinates of all spectra at zero period will be one. The

normalized spectra for 0.05g and 0.45g acceleration inputs are shown on Figs. 8 and 9, respectively.

Available surface recordings (for acceleration levels 0.05g) from deep deposits of soft soils indicate that the peak ordinates of the response spectra tend to occur at relatively high period values (2, 5). An average acceleration response spectrum for the latter records reported by Seed, et al (2) is plotted on Figs. 8 and 9 for reference and comparison purposes. For the 0.05g shaking level, the average spectrum shape for shorter periods is lower than spectra corresponding to the two records used for the study, but corresponds reasonably well at larger periods. The latter spectral shapes lie generally within the mean \pm one standard deviation bounds of spectra reported by Seed, et al (2). For the 0.45g shaking level, considerable differences are noted between the average spectrum for most periods. This would suggest that considerable caution should be exercised in using an average spectral shape obtained from low levels of shaking for design at higher levels of shaking.

Influence of Site Modulus Variations

(i) Effect of Modulus Increase in Surface Layer

To illustrate the potential influence of a stiffer surface layer (arising from say overconsolidation) on response spectra, the site 2 profile shown on Fig. 3 was studied. The only difference between the site 1 and site 2 is the strength and stiffness of the top 15 feet of soils. Surface spectra were computed for the El Centro outcrop record, and compared to site 1 spectra. As shown on Fig. 10, the differences in the surface response spectra caused by the property differences are quite noticeable. If the structure under consideration has a relatively short fundamental period, the change in spectral accelerations arising from a stiff surface layer could be significant.

(ii) In-Situ Versus Laboratory Measured Modulus

Differences in stiffness of soft cohesive soils as measured by in-situ methods and by laboratory tests, have been reported in the literature (19, 20). To illustrate the potential significance of these differences, a response analysis using the Orion Blvd. outcrop motion in conjunction with site 1, but with reduced shear moduli to simulate the use of laboratory modulus data, was performed. The modulus reduction (and associated strength reduction) was achieved by adjusting G_{\max} values to the level shown on Fig. 3. The spectrum for computed surface motion is plotted on Fig. 11 for the 0.45g shaking level, and compared to the spectrum computed using the original higher modulus profile which could be assumed to be associated with in-situ conditions. The effects of reduced stiffness and strength on response may be seen to be the significant reduction of overall surface response and the slight shift of peaks due to the change of fundamental period of the site. Hence, unlike many other soil mechanics problems, the assumption of the lower strength and stiffness for a site may not necessarily lead to a conservative answer.

CONCLUSIONS

The development and use of a non-linear hysteretic one dimensional site response program (DETRAN) for evaluating earthquake response characteristics of soft soil sites has been described. The program incorporates a transmitting boundary and modulus degradation capabilities.

Using an idealized example, where two representative earthquake acceleration time histories were defined by firm alluvial outcrop motions, it has been shown that:

- (1) For low levels of ground shaking (max. outcrop accelerations about 0.05g) where soil failure does not occur, the soft site produced increased ground and spectral accelerations. Surface response spectra obtained from DETRAN and SHAKE analyses were noted to be almost identical.
- (2) For high levels of ground shaking (max. outcrop accelerations about 0.45g), the effects of soil failure and degradation resulted in reductions in ground acceleration levels. Surface acceleration spectra were "flattened" compared to outcrop spectra. Significant differences were noted between spectra computed using DETRAN and SHAKE, which could be attributed primarily to the effects of the incorporation of soil failure and degradation criterion in DETRAN.
- (3) Significant differences in the shape of surface acceleration spectra were noted for the low and high levels of outcrop ground shaking, suggesting caution in the use of average smoothed spectra obtained from soft ground earthquake records generated from low shaking levels.
- (4) The sensitivity of surface spectra to a stiffer surface layer and the magnitude of site shear moduli were noted.

ACKNOWLEDGEMENTS

The work described in this paper was supported by Fugro, Inc.'s research and development program. The assistance of William B. Joyner and Albert T. F. Chen of the U. S. Geological Survey, Menlo Park, in providing details of the program NONLI3, is gratefully acknowledged.

REFERENCES

1. Hayashi, S., H. Tsuchida, and E. Kurata (1971) "Average Response Spectra for Various Subsoil Conditions," Third Joint Meeting, U. S. - Japan Panel on Wind and Seismic Effects, UJNR, Tokyo, May 10-12, 1971.
2. Seed, H., Ugas, C., and Lysmer, J. (1976) "Site Dependent Spectra for Earthquake Resistant Design," Bull. of the Seismological Society of America, 66, pp. 221-244.
3. Mohraz, B. (1976) "A study of Earthquake Response Spectra for Different Geological Conditions," Bull. of the Seismological Society of America, 66, pp. 915-936.
4. Schnabel, P. B., Lysmer, J., and Seed, H. B. (1972) "SHAKE -- A Computer Program for Earthquake Response Analysis of Horizontally Layered Sites," Report No. EERC 72-12, Earthquake Engineering Research Center, University of California, Berkeley, December.
5. Seed, H. B. and Idriss, I. M. (1969) "Influence of Soil Conditions on Ground Motions During Earthquakes," Journal of the Soil Mechanics and Foundations Division, ASCE, Vol. 95, No. SMI, January, pp. 99-137.
6. Valera, J. E., Seed, H. B., Tsai, C. F., and Lysmer, J. (1978) "Seismic Soil, Structure Interaction Effects of Humboldt Bay Power Plant," Journal of the Geotechnical Engineering Division, ASCE, Vol. 103, Oct. 1977, pp. 1143-1161.
7. Streeter, V. L., Wylie, E. B., and Richart, F. E., Jr. (1974) "Soil Motion Computations by Characteristic Methods," Journal of the Geotechnical Engineering Division, ASCE, Vol. 100, No. GT3, pp. 247-263.
8. Idriss, I. M., Dobry, R., Doyle, E. H., and Singh, R. D. (1976) "Behavior of Soft Clays Under Earthquake Loading Conditions," Proceedings, Offshore Technology Conference, Paper No. OTC 2671, May.
9. Joyner, W. B. (1977) "A Fortran Program for Calculating Nonlinear Seismic Ground Response," U. S. Geological Survey open file report 77-671.
10. Iwan, W. D. (1967) "On a Class of Models for the Yielding Behavior of Continuous and Composite Systems," Journal of Applied Mechanics, Vol. 34, No. 3, September, pp. 612-617.
11. Taylor, P. W. and Larkin, T. J. (1978) "Seismic Site Response of Non-linear Soil Media," Journal of the Geotechnical Engineering Division ASCE, Vol. 104, March, 1978, pp. 369-383.
12. Finn, Liam W. D., Martin, G. R., and Lee, M. K. W. (1978) "Comparison of Dynamic Analyses for Saturated Sands," Proceedings of Conference on Earthquake Engineering and Soil Dynamics, Geotechnical Engineering Division, ASCE, Specialty Conference, Pasadena, June 19-21.

13. Martin, P. (1975) "Nonlinear Methods for Dynamic Analysis of Ground Response," Ph.D. Dissertation, Department of Engineering, University of California, Berkeley.
14. Larkin, T. J. (1976) "The Propagation of Seismic Waves Through Non-linear Soil Media," Ph.D. Thesis, University of Auckland, New Zealand, Sept. 1976.
15. Joyner, W. B. and Chen, A. T. F. (1975) "Calculation of Nonlinear Ground Response in Earthquakes," Bulletin of the Seismological Society of America, Vol. 65, No. 5, October, pp. 1315-1336.
16. Lysmer, J. and Kuhlemeyer, R. L. (1969) "Finite Dynamic Model for Infinite Media," Journal of Engineering Mechanics, ASCE, Vol. 95, pp. 859-877.
17. Fugro (1978) "An Evaluation of one Dimensional Non-Linear Soil Response Programs for Seismic Loading," in-house research report.
18. Seed, H. B., Murarka, R., Lysmer, J., and Idriss, I. M. (1975) "Relationships Between Maximum Acceleration, Maximum Velocity, Distance from Source and Local Site Conditions for Moderately Strong Earthquakes," EERC Report No. 75-17, University of California, Berkeley, California, July 1975.
19. Anderson, D. G. and Stokoe, K. H., II, (1977) "Shear Modulus: A Time Dependent Material Property," Symposium on Dynamic Soil and Rock Testing, ASTM, Denver, June, 1977.
20. Anderson, D. G., Espana, C., and McLamore, V. R. (1978) "Estimating In Situ Shear Moduli at Competent Sites," Proceedings of Conference on Earthquake Engineering and Soil Dynamics, Geotechnical Engineering Division, ASCE, Specialty Conference, Pasadena, June, 1978.

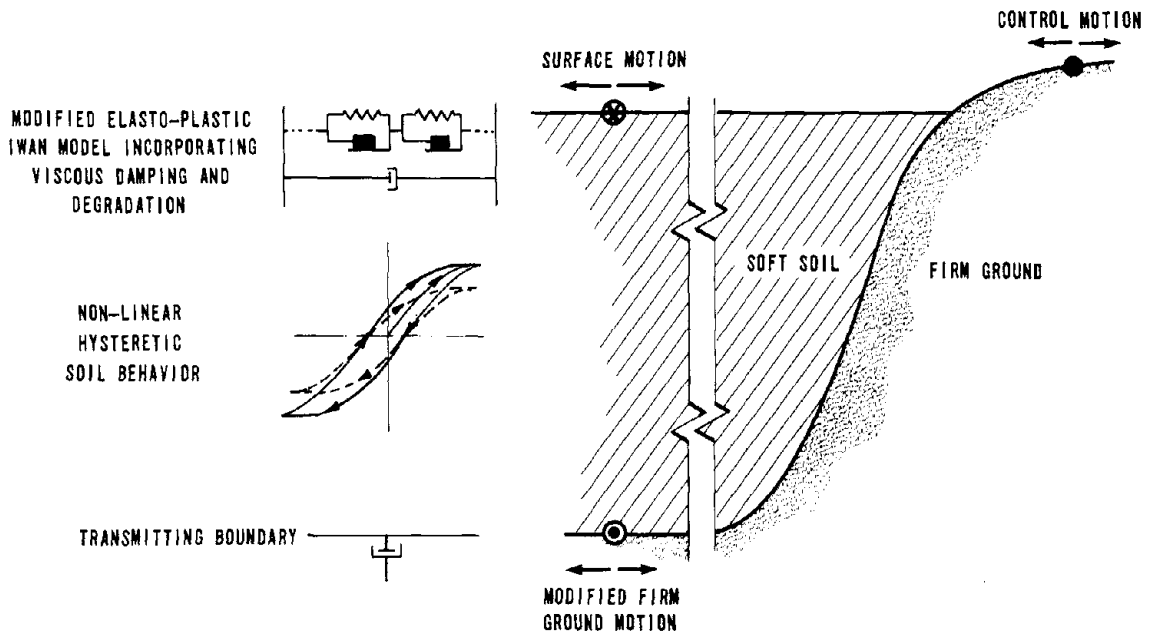


FIGURE 1 GENERAL FEATURES OF THE NON-LINEAR RESPONSE PROGRAM DETRAN

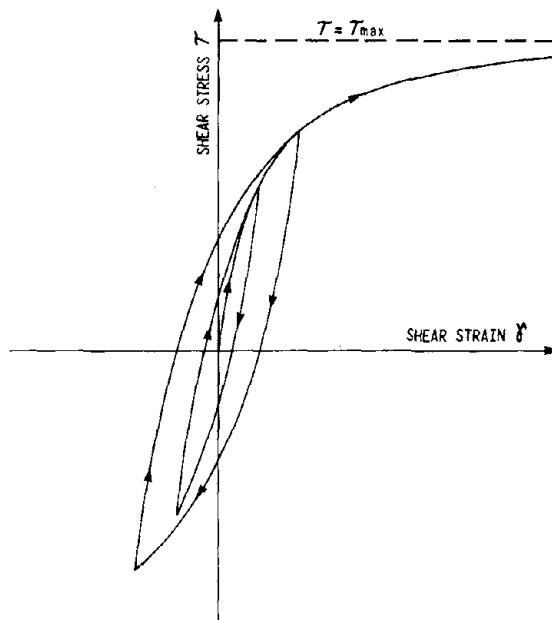


FIGURE 2 TYPICAL HYSTERESIS LOOP

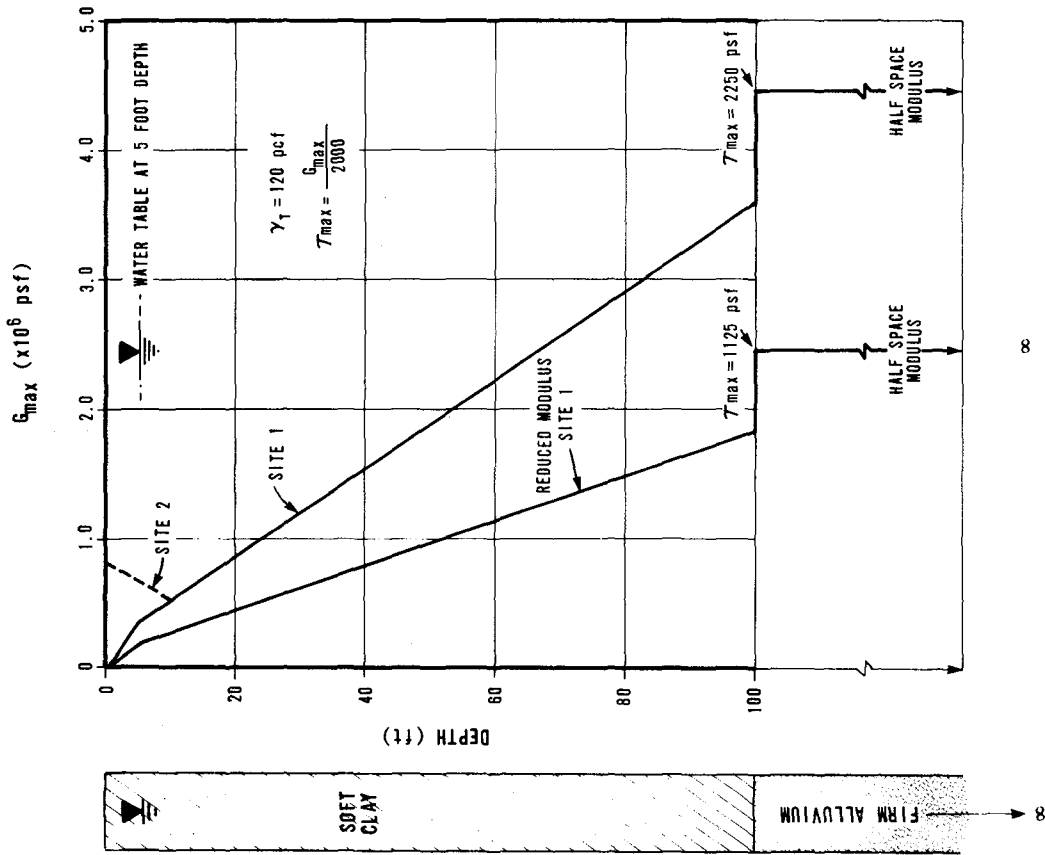


FIGURE 3 SITE PROFILE USED FOR ANALYSES.

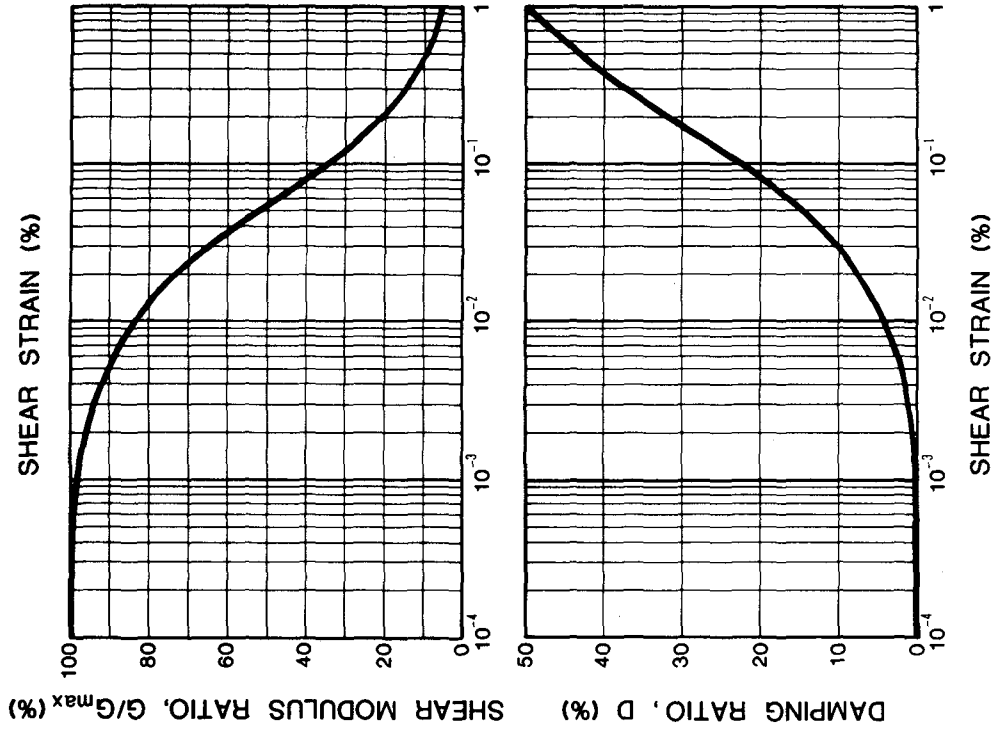


FIGURE 4 STRAIN DEPENDENT MODULUS AND DAMPING CHARACTERISTICS USED FOR ANALYSES.

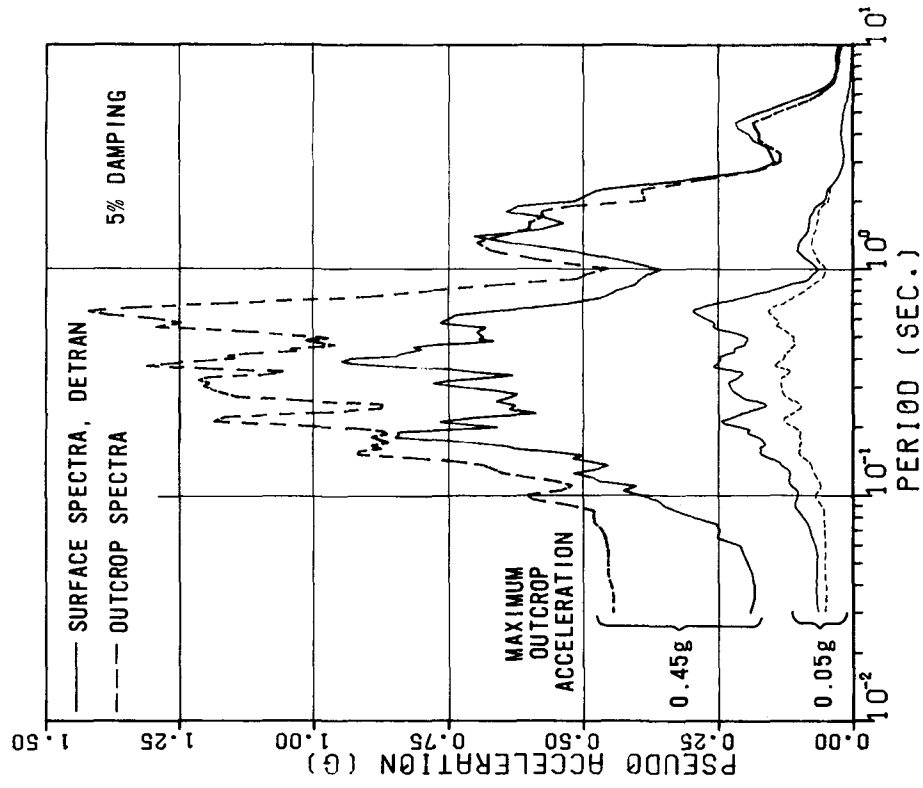


FIGURE 5 COMPARISON BETWEEN SHAKE AND DETRAN SPECTRA FOR SITE 1 (EL CENTRO OUTCROP ACCELERATIONS)

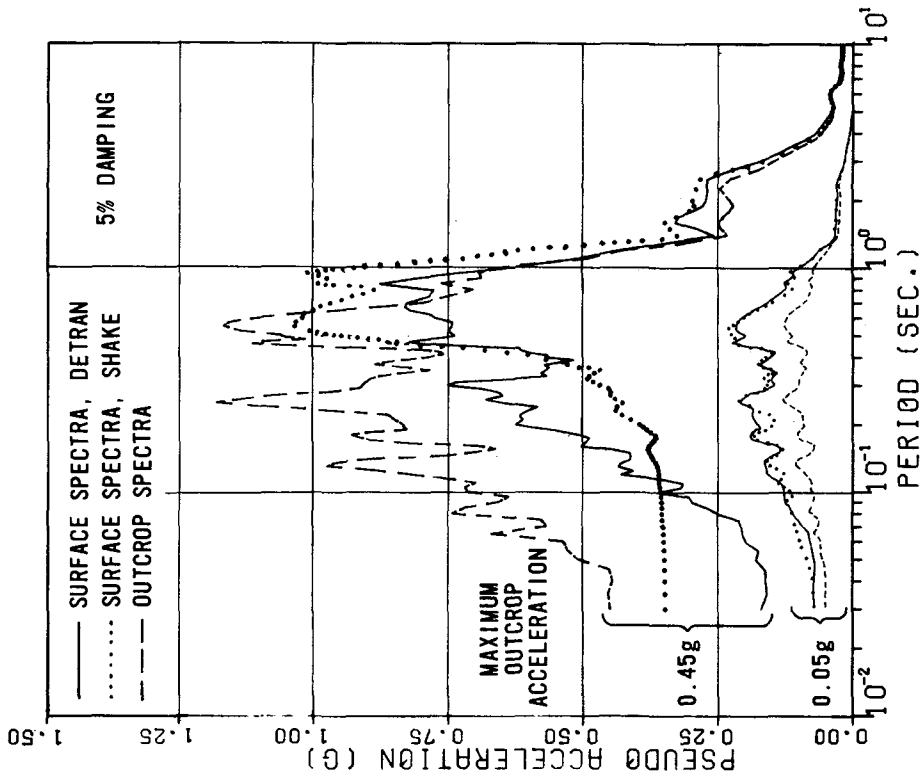


FIGURE 6 SPECTRA FOR SITE 1 (ORION BLVD. OUTCROP ACCELERATIONS)

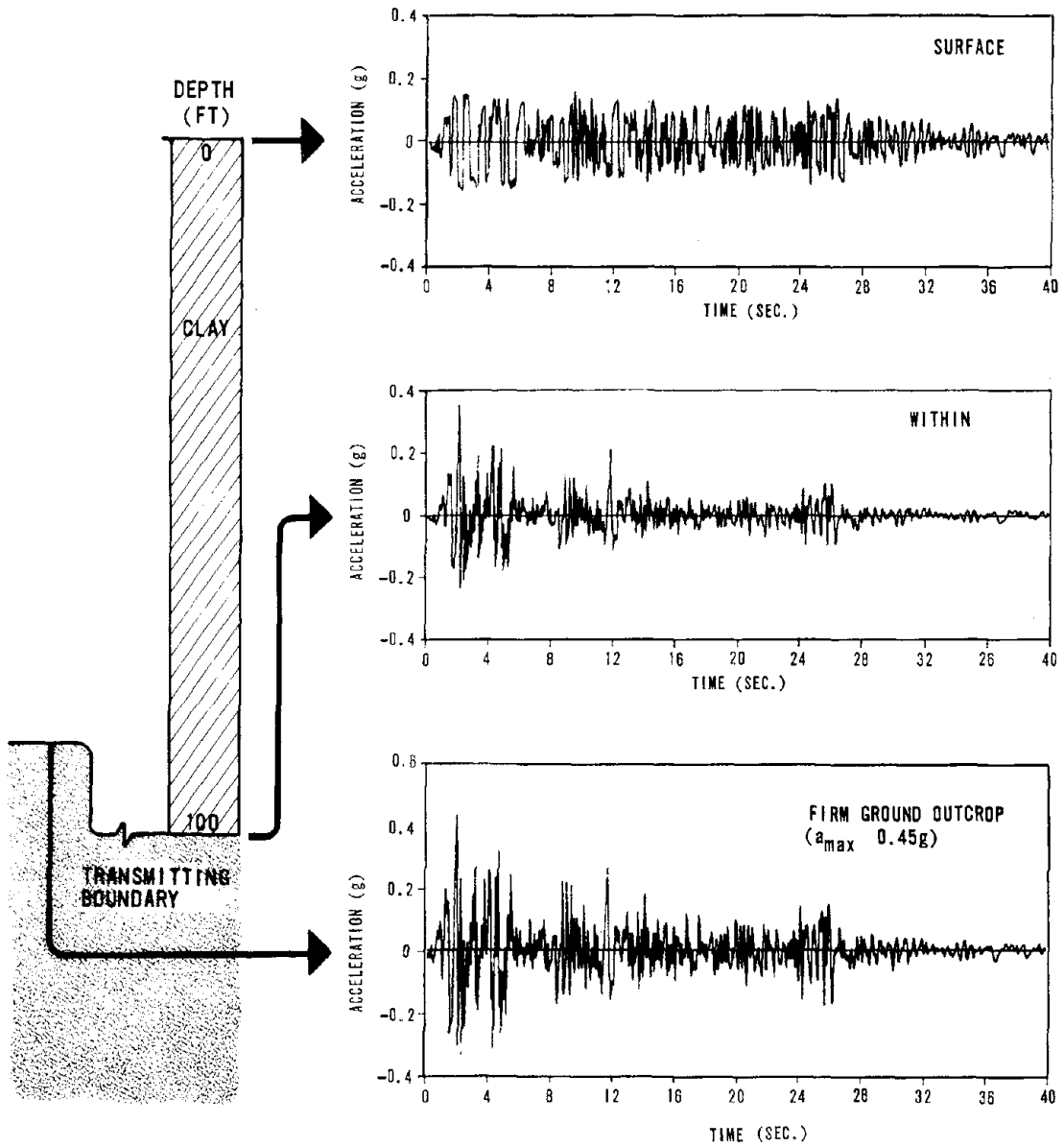


FIGURE 7 ACCELERATION TIME HISTORIES FOR SITE 1,
(EL CENTRO OUTCROP ACCELERATIONS).

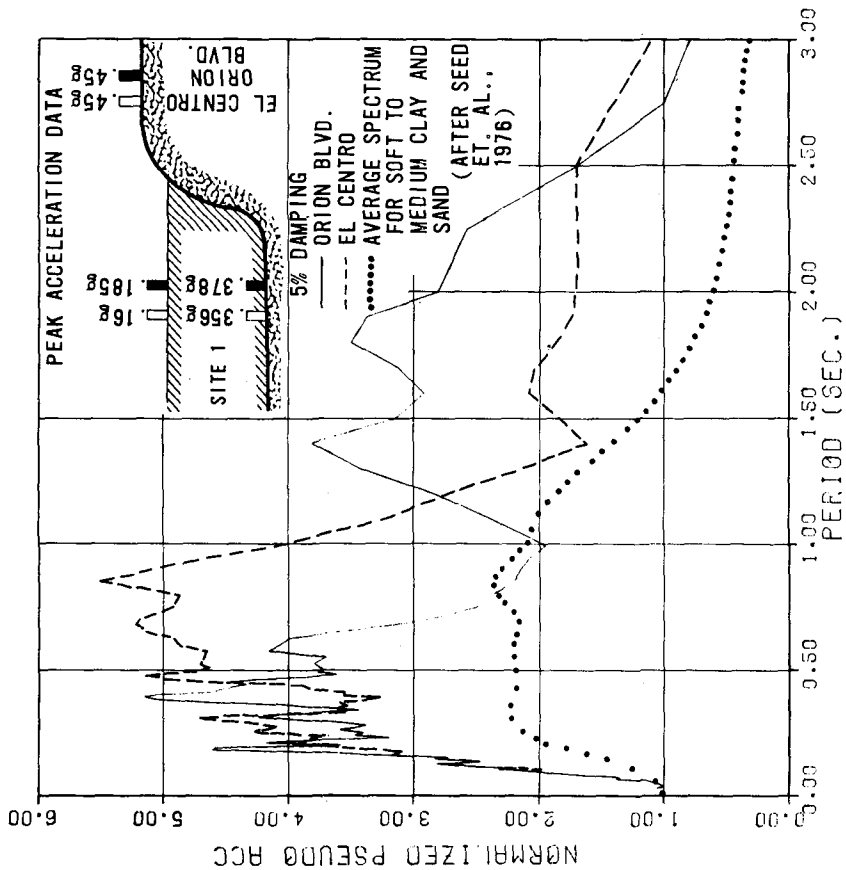


FIGURE 9 SITE SPECTRAL SHAPE COMPARISON FOR HIGH INTENSITY EXCITATION.

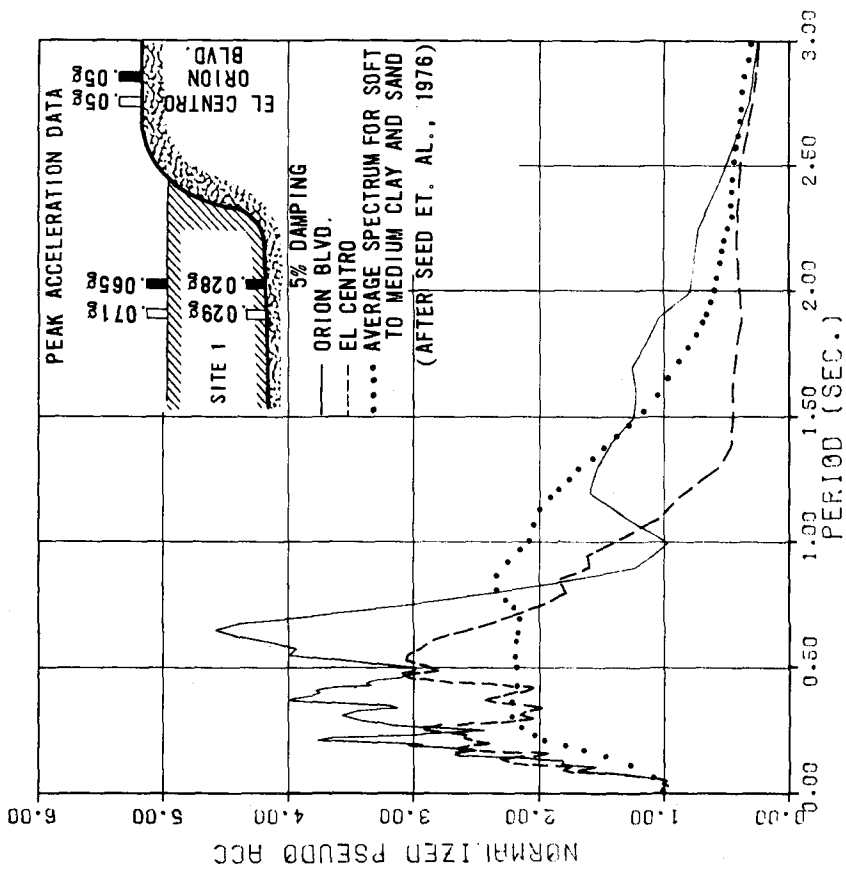


FIGURE 8 SITE SPECTRAL SHAPE COMPARISON AT LOW INTENSITY EXCITATION.

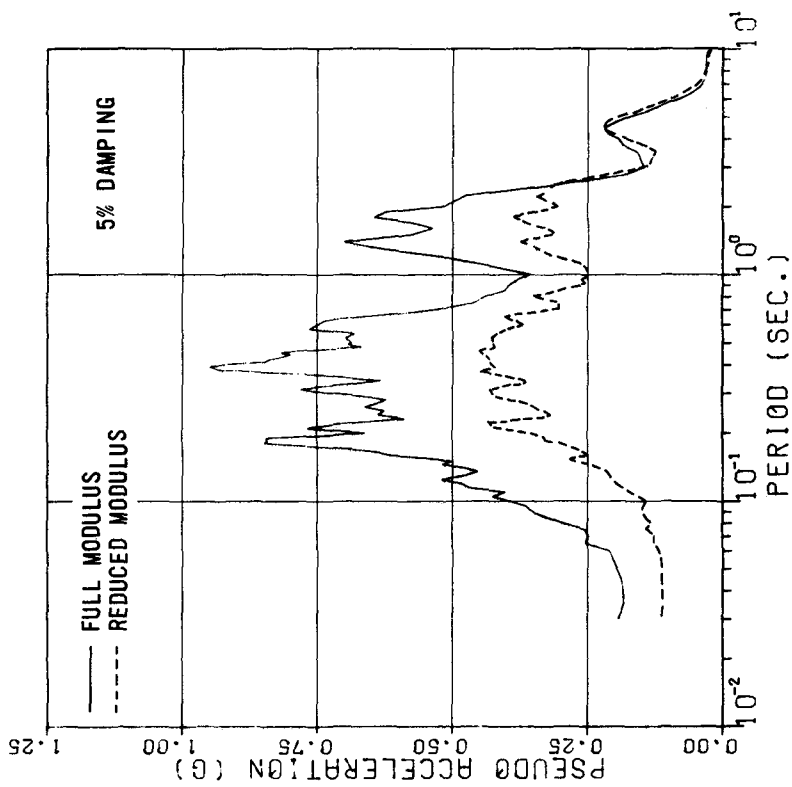


FIGURE 11 MODULUS SENSITIVITY COMPARISON, SITE 1
(ORION BLVD. OUTCROP ACCELERATIONS --
MAXIMUM ACCELERATION 0.45g)

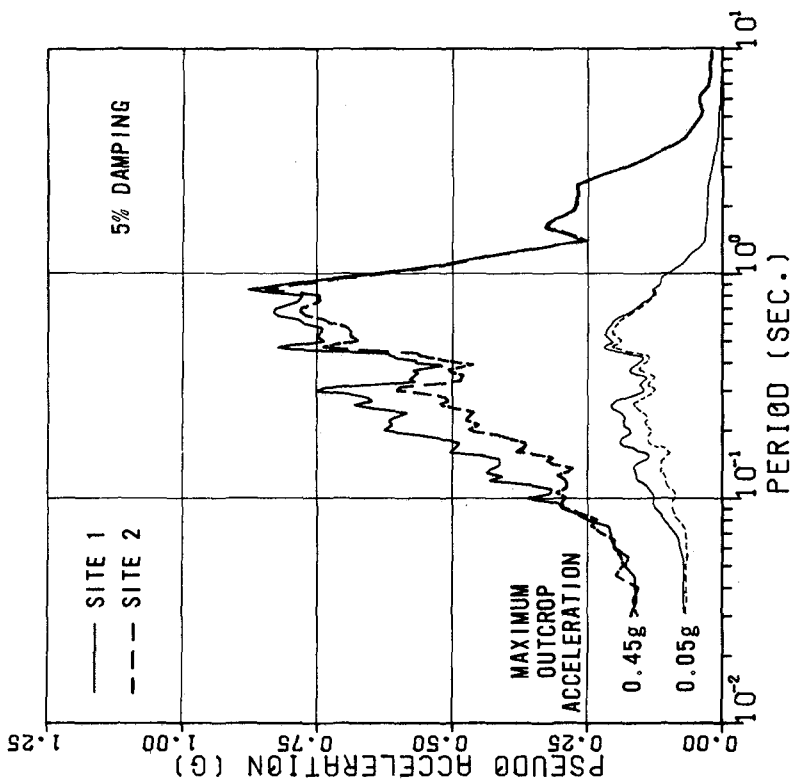


FIGURE 10 COMPARISON BETWEEN SITE 1 AND SITE 2
SURFACE SPECTRA (EL CENTRO OUTCROP
ACCELERATIONS)

EFFECTS OF SOIL INERTIA FORCES
ON DESIGN OF BURIED PIPELINES
CROSSING FAULTS

Michael L. Traubenik^I, Julio E. Valera^{II}, Wolfgang H. Roth^{III}

ABSTRACT

Current methods for seismic design of buried pipelines traversing major seismogenic strike-slip fault zones generally only consider the ultimate fault displacements postulated during fault rupture. The pipe is designed to accommodate fault displacements through axial straining of the pipe. Analyses commonly used assume that the rupture process occurs slowly enough such that the soil forces acting on the pipe can be considered to be static in nature thus neglecting any dynamic effects.

This paper suggests that design of a buried pipe for fault rupture may be unconservative if dynamic forces resulting from the acceleration produced within the fault rupture zone are ignored since they may significantly increase the normally applied static forces.

Soil inertia forces are examined for a simple hypothesized test case and are found to increase the normally predicted ultimate lateral forces, and thus, the longitudinal frictional forces acting on the pipe by approximately 30 percent.

INTRODUCTION

Large differential displacements that may result during an earthquake represent a severe hazard to a buried pipeline. Differential displacements may be the result of ground failure, such as landsliding, liquefaction or lateral spreading, or of ground rupture due to surface faulting. While in many cases it is feasible to bypass areas susceptible to landslides, liquefaction, and lateral spreading, the crossing of seismogenic fault zones usually cannot be avoided. Severe damage of a pipeline crossing an area subject to ground rupture or surface faulting can be reduced or prevented by placing the pipeline above ground or by using appropriate analyses procedures in the design of a buried pipeline.

^I Project Engineer, Dames & Moore, Los Angeles, California

^{II} Principal Geotechnical Engineer, Earth Sciences Associates, Palo Alto, California

^{III} Senior Engineer, Dames & Moore, Los Angeles, California

Buried pipelines traversing major seismogenic strike-slip fault zones must be designed to accommodate very large fault displacements. A pipeline crossing the San Andreas fault zone, for example, must be designed to withstand ultimate fault displacements of approximately 20 feet of horizontal and 5 feet of vertical (9). In current design methods, the pipe is assumed to accommodate the postulated fault displacement through axial elongation and investigators (8, 10, 12) have derived the axial strains in the pipe developed during fault rupture assuming the following conditions:

1. The pipeline undergoes only tensile strains during fault rupture.
2. Flexural strains are kept to a minimum.
3. The elongation of the pipe required to accommodate the fault displacement takes place over a significant length of pipe defined by two so-called "anchor" points and significant strain concentrations do not occur.
4. The velocity at which the fault movement takes place is such that the forces exerted on the pipe during fault rupture are essentially the same as those that would be obtained by a static displacement.

Provided the direction of the postulated fault movement can be anticipated, the criteria stated in 1 and 2 above can be met by crossing the fault zone at an appropriate angle, (Figure 1a), such that the pipe only elongates during fault displacement. The "anchor" points (Figure 1a) as assumed in condition 3 are defined as points at which the fault induced strains in the pipe are zero. The greater the distance between "anchor" points, $L_1 + L_2$, the greater the fault movement capacity of the pipeline since the elongation of the pipe is distributed over a longer pipe length. The "anchor" distance is governed by the frictional forces that exist between the pipe and the soil. Friction may be kept to a minimum by using controlled trenching and backfilling procedures.

In order to insure adequate pipeline design, it is important that the soil/pipe frictional forces be accurately determined. If the actual soil/pipe friction due to fault movement is greater than estimated, then the elongation of the pipe will take place over a smaller zone, thus increasing axial strains which could render the pipeline design inadequate. As previously stated, in current design practice frictional forces are estimated assuming static conditions

(condition 4). This may be unconservative since dynamic forces resulting from the ground acceleration within the fault rupture zone could be significant and result in an increase in the soil/pipe forces. The dynamic forces which could develop in the immediate vicinity of the rupturing fault may also cause local pinching or shearing of the pipe.

FAULTING ACCELERATION

Since a reasonable estimate of faulting acceleration is essential to evaluate the magnitude of dynamic forces suggested above, a literature review of this subject has been conducted.

The mechanism of fault rupture has been the subject of extensive investigation. Brune (3) developed a rupture model considering the effective stress available to accelerate the mass on either side of a fault. Results of Brune's study indicate that the upper limit of near-fault particle velocity is approximately 3 feet per second and the estimated upper limit for acceleration is approximately 2g at 10 Hz and is proportionally lower at lower frequencies.

Ambraseys (1) and Kanamori (7) have both suggested an upper bound particle velocity of faulting of about 3 feet per second. Ambraseys states that it is not possible to predict an upper limit of ground acceleration but considers fault rupture accelerations greater than 1g as possible. Likewise, Kanamori in a review of Japanese earthquakes states that strain release can be considered "more or less instantaneous".

Trifunac and Brady (15) suggest that for a Magnitude 7.5 earthquake, average peak particle accelerations at the fault could be on the order of 1.75g ranging from 1.2g to 2.5g. However, they warn that these values are conservative estimates and must be taken with reservation.

Hanks (4) in a study of the faulting mechanism of the San Fernando earthquake, suggested that the long period acceleration and displacement pulse occurring in the Pacoima Dam S16°E accelerogram can be interpreted as the shear radiation resulting from rupture at the focus. With this in mind, a peak acceleration of approximately 0.6g with a period of approximately 1.5 seconds could be attributed to the faulting process. However, rupture propagation characteristics may have also played a significant role in shaping the long period portion of the Pacoima Dam record.

A study by Housner and Trifunac (5) of ground motion generated by the Magnitude 5.6 Parkfield earthquake of June 27, 1966, shows that the maximum recorded ground acceleration near the fault was about 0.5g. Motion recorded transverse to the fault trace shows a maximum ground velocity of 27 inches per second and a single displacement pulse of approximately 10 inches with 1.5 seconds duration. Although the component of motion longitudinal to the fault trace was not recorded, the characteristics of the motion have been deduced. Analyses indicate that an acceleration pulse with a direction parallel to the fault of approximately 0.5g lagged behind the transverse 0.5g pulse by about one-quarter of a wave length.

Finally, personal accounts concerning the effects of the Magnitude 8+ San Andreas Fault event of 1857 indicate ground motions so severe that tree trunks located near the fault trace were actually sheared off (6).

Although the above values of faulting accelerations are mainly applicable to competent materials at depth where levels of faulting is initiated, somewhat lower but still appreciable accelerations may develop in competent materials which rupture near the ground surface.

Peak accelerations of magnitudes as described above, can be of considerable importance in the design of a buried pipe crossing a fault, if they occur simultaneously with the onset of passive lateral forces. Pipe stresses resulting from an increase in longitudinal frictional forces or concentrated shearing forces may be significant depending on the volume of soil that the pipe must displace during the rupture process.

RELATIVE MOVEMENT BETWEEN PIPE AND SOIL AT FAULT CROSSING

For the purpose of this study, it has been conservatively assumed that the fault displacement occurring during an earthquake is concentrated along a single rupture plane, rather than being distributed over a somewhat larger fault zone. Figure 1b shows a type of pipe displacement which could result from a fault rupture.

As shown in Figure 1b, a horizontal fault displacement, δ_h , causes the two hypothesized pipeline anchor points to displace a distance D_x and D_y from their initial positions. If both sides of the fault move an equal distance in opposite directions, the section of pipe located at the rupture plane can be considered "fixed". Therefore, the relative acceleration of the pipe with respect to the surrounding soil is equal to the fault acceleration.

If in addition to the horizontal fault displacement a vertical fault displacement is introduced at the same time, the pipe would tend to be effectively "locked" on the upward side of the fault due to the relatively high bearing capacity of the in situ soils. On the downward side, the pipe would tend to pull up and out of the trench and would move in the opposite direction relative to the moving ground. This type of motion would also tend to increase the forces acting on the pipe.

LONGITUDINAL SOIL/PIPE FRICTION

As a result of fault displacement the pipe must move longitudinally and laterally relative to the surrounding soil over a length defined by the "anchor" points. The lateral movement is resisted by passive earth pressure which in turn increases the soil/pipe friction resisting the longitudinal movement. Figure 2 demonstrates the development of passive earth pressure during lateral movement of the pipe. Figure 2a shows the pipe placed in a shallow trench excavated in a competent material at a fault crossing location. The trench is backfilled with a loosely placed cohesionless material to insure minimum soil resistance and soil/pipe friction. Figure 2b shows the pipe and an assumed passive failure wedge at a short time, t_1 , after the initiation of fault rupture. Time t_1 , is assumed to be the time at which full lateral passive earth pressure and therefore peak longitudinal friction is developed. The final position of the pipe and the ground surface configuration after fault rupture are shown in Figure 2c.

The longitudinal friction of the pipe has been estimated (8, 10, 12) as:

$$F_f = \pi D P_r \mu \quad (1)$$

Where P_r is the average radial pressure on the pipe around its circumference, D is the pipe diameter, and μ is the coefficient of friction between the pipe and the surrounding soil.

The average radial pressure P_r is usually calculated applying conservative estimates of the peak lateral passive earth pressure. Empirical relationships have been derived from model test results to estimate the lateral earth pressure on pipes resulting from static lateral pipe displacement. Tests have shown that the ultimate lateral soil pressure develops after a very small lateral displacement has taken place which may be conservatively estimated as:

$$\delta = 0.02 H_e \quad (2)$$

where

H_e = soil depth to the bottom of pipe.

As the lateral displacement increases, the lateral pressure decreases to approximately one-half of its peak value. However, it has been conservatively assumed by the authors and other investigators (8) that the peak lateral earth pressure is essentially constant throughout the entire fault rupture process.

INCREASE IN LATERAL FORCES DUE TO SOIL INERTIA

A cross section through a buried pipe at a fault crossing and a simplified formulation for the increase in lateral force due to soil inertia is presented in Figure 3. A trench geometry and cohesionless backfill material have been chosen for demonstration. The natural soils are assumed to be quite competent and capable of transmitting moderate to high accelerations. Furthermore, it has been assumed that the pipe displaces equally on both sides of the fault as shown in Figure 1b. With the latter assumption, a passive soil wedge is held horizontally in place by the pipe. The underlying soil moves with a horizontal acceleration a_x , causing the soil wedge to accelerate vertically upwards with an acceleration a_y . The vertical acceleration a_y creates a downward inertial force increasing the passive earth pressure P_r and thus increasing the frictional forces F_f acting on the pipe (Equation 1).

The horizontal inertial force that the pipe must exert on the soil wedge to move it out of the trench is given by:

$$F_I = W_S a_x' \quad (3)$$

where

$$\begin{aligned} W_S &= \text{weight of soil wedge} \\ a_x' &= \text{horizontal ground acceleration} \\ &\quad \text{at the fault rupture plane (g)} \end{aligned}$$

For a 30-inch-diameter pipeline buried with a soil cover of 3 feet as shown in Figure 3, the increase in passive earth pressure due to an assumed fault acceleration of 0.5g would amount to approximately 30 percent.

One could also consider the inertia force Ma_y as an apparent weight of the soil wedge. Doing so, the inertial increase in passive earth pressure can be calculated in exactly the same manner as for static conditions using a soil density multiplied by a factor; $f = a_x' \text{TAN } \theta$. Considering that the passive earth pressure is directly proportional to the soil density, the factor $f \times 100$ expresses the percentual increase in lateral earth pressure due to inertia. For the example case above, the increase would be calculated as:

$$f = a_x' \text{TAN } \theta = 0.5 \text{TAN } 30^\circ = 0.29$$

or 29% of the passive pressure.

According to Equation (2), the full static passive earth pressure for the example case considered is in effect after only 1.3 inches of lateral movement has taken place. Therefore, prudent design dictates that one assumes that both the static passive resistance plus the contribution of the inertial forces are acting concurrently over a certain duration of the fault rupture process. This additional dynamic pressure not only increases the longitudinal pipe/soil frictional forces but also increases the shearing forces the pipe must withstand at the fault crossing.

The true effects of soil inertial forces on the pipe during fault rupture obviously cannot be accurately determined by simple calculations. It is apparent, however, that the dynamics of the pipe/soil system cannot be ignored.

CONCLUSIONS

For purposes of this study, the effect of soil inertia forces were estimated for an example case in which several simplifying assumptions were made. The test case illustrates the importance of incorporating soil inertia in a dynamic analysis of a buried pipeline crossing a strike-slip fault. Inertial forces were shown to impart an additional pressure on the pipe equal to approximately 30 percent of the ultimate passive lateral earth pressure assuming a fault rupture acceleration of 0.5g. Although soil inertial forces may be cyclic in nature, they are believed to act concurrently with the passive lateral soil forces during some duration of the fault rupture process. Additional considerations indicate that soil inertia forces could be even greater if the pipe on one side of the fault "locks" due to a vertical fault movement.

This study indicates that soil inertia forces should not be ignored in pipe design. High peak accelerations that may be associated with fault movement suggest that the pipe analysis should include dynamic effects.

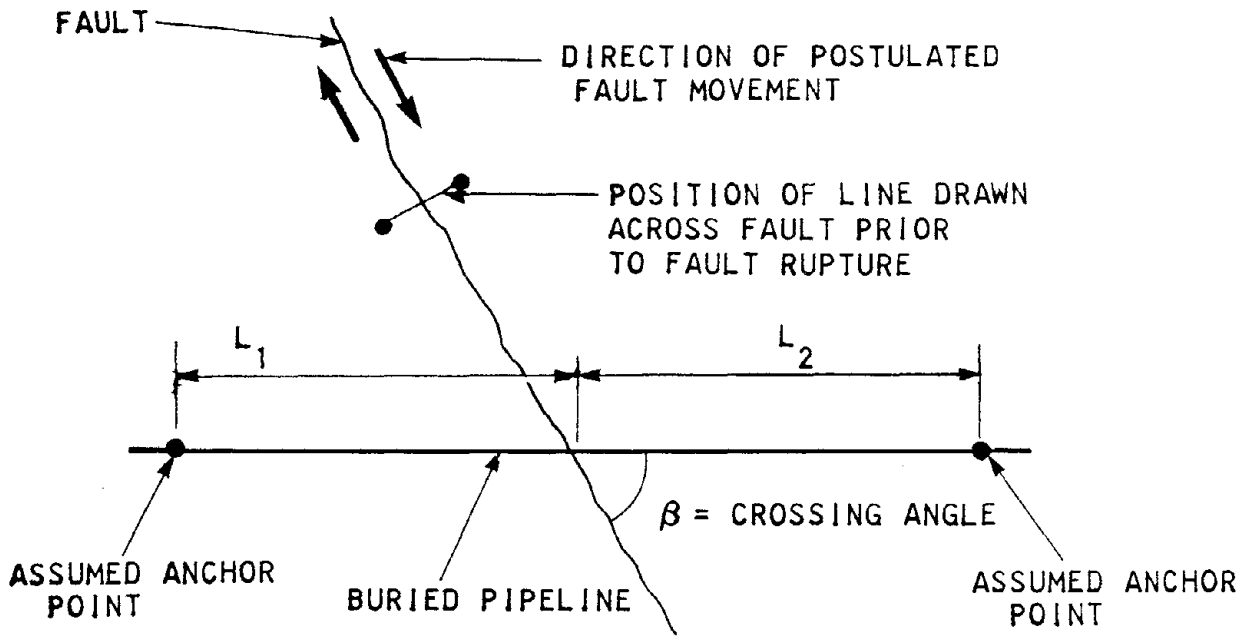


Figure 1a - Typical buried pipeline crossing seismogenic strike-slip fault

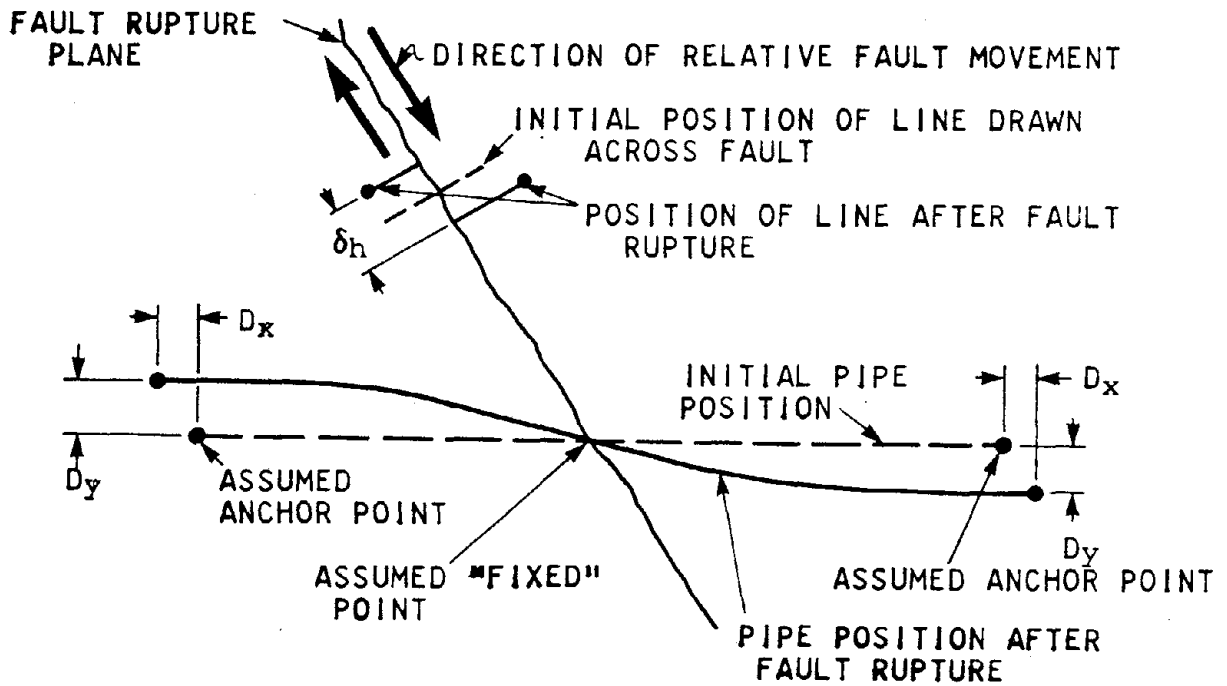


Figure 1b - Possible deformed pipeline configuration resulting from horizontal fault rupture

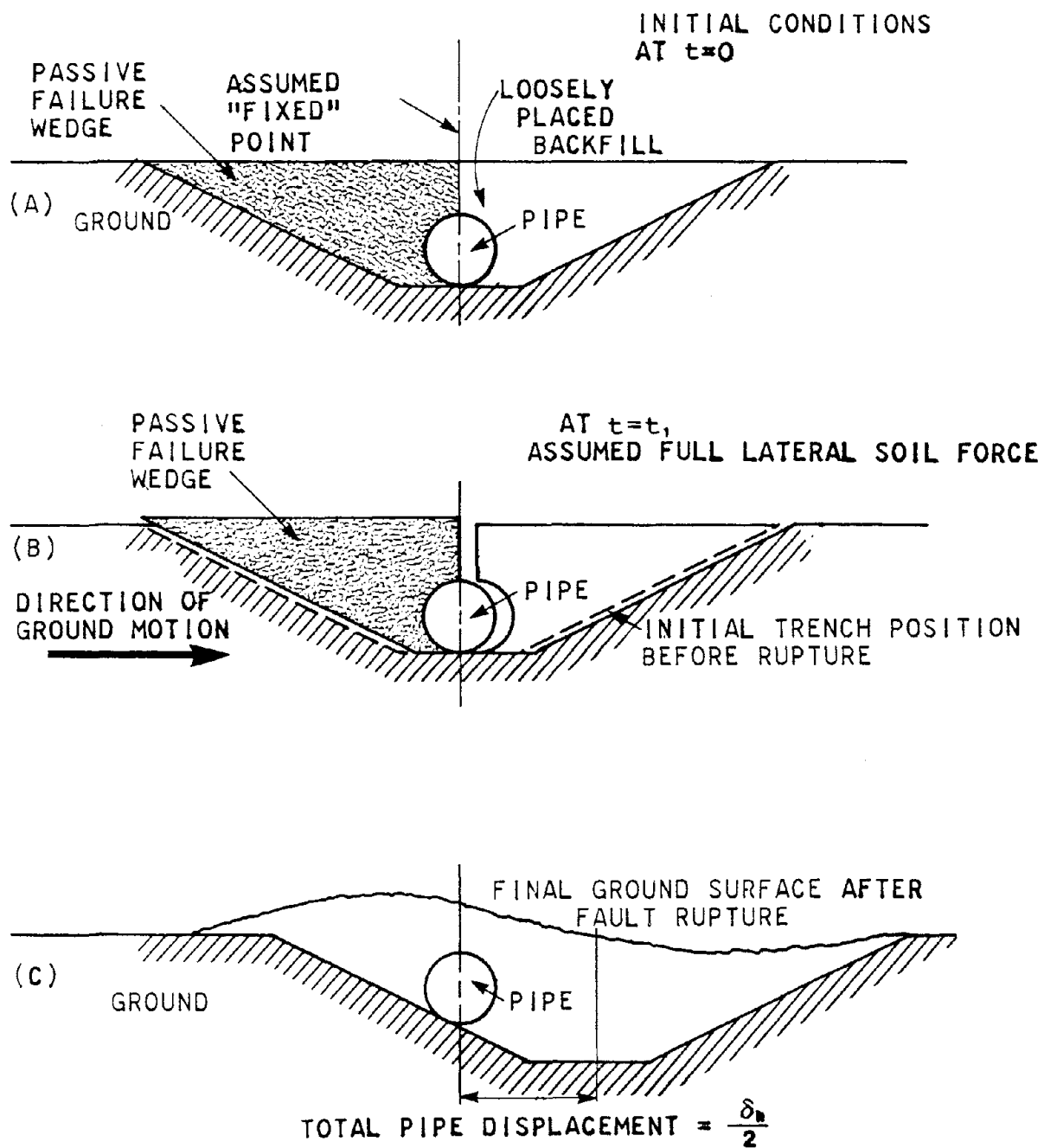
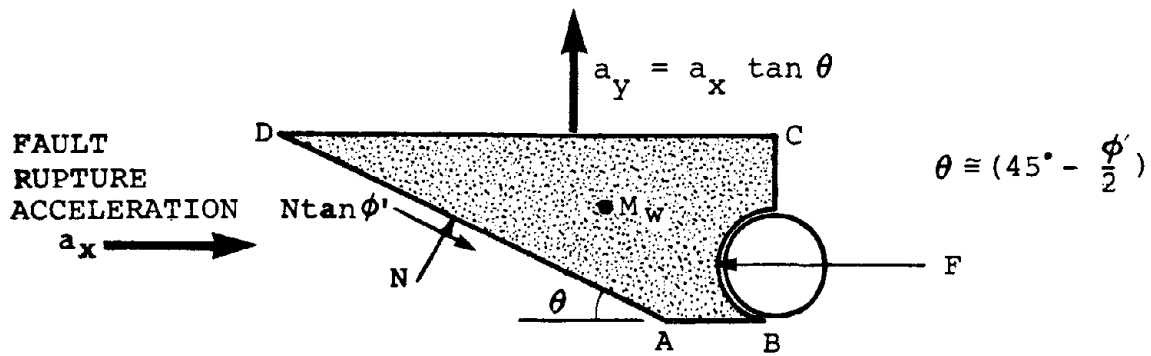


Figure 2 - Passive wedge failure and pipe motion resulting from horizontal fault movement



ASSUMPTIONS:

- (1) SOIL WEDGE (ABCD) WITH MASS M_w MOVES AS A RIGID BODY.
- (2) NO HORIZONTAL MOTION OF PIPE AND SOIL WEDGE.
- (3) PIPE AND SOIL WEDGE MOVE VERTICALLY WITH ACCELERATION

$$a_y = a_x \tan \theta \quad (\text{ft/sec}^2)$$

WHERE a_x IS THE HORIZONTAL ACCELERATION OF UNDERLYING COMPETENT MATERIAL ASSOCIATED WITH FAULT RUPTURE.

- (4) GRAVITY AND STATIC FORCES IGNORED. FORCES DERIVED ARE FOR DYNAMIC INCREMENT ONLY.
- (5) WEIGHT OF PIPE IGNORED.
- (6) FRICTION BETWEEN PIPE AND SOIL IGNORED.

EQUATIONS OF MOTION

$$\Sigma F_x = 0 \quad (\text{FROM ASSUMPTION 1 \& 2})$$

$$F - N \sin \theta - N \tan \phi' \cos \theta = 0 \quad (1)$$

$$\Sigma F_y = M_w a_y = M_w a_x \tan \theta \quad (\text{ASSUMPTION 3})$$

$$N \cos \theta - N \tan \phi' \sin \theta = M_w a_x \tan \theta \quad (2)$$

EXAMPLE CASE

SOIL PROPERTIES ASSUMED:

$$\phi' = 30^\circ, \quad C = 0, \quad \gamma = 115 \text{ pcf}$$

Solving Equation 2 for N

$$N = M_w a_x$$

Solving Equation 1

$$F = M_w a_x = W_s a'_x$$

W_s = WEIGHT OF SOIL WEDGE (ABCD)
WITH a'_x = FAULT RUPTURE ACCELERATION, IN g's

Figure 3 - Development of soil inertia

BIBLIOGRAPHY

1. Ambraseys, N.N., "Maximum Intensity of Ground Movements Caused by Faulting," Proceedings, 4th World Conference on Earthquake Engineering, Santiago, Chile, A-2, 1969, pp. 154-171.
2. Audibert, J.M.E., and Nyman, K.J., "Soil Restraint Against Horizontal Motion of Pipes," Journal of the Geotechnical Engineering Division, ASCE, vol. 103, no. GT10, proc. paper 13303, October 1977, pp. 1119-1138.
3. Brune, J.N., "Tectonic Stress and the Spectra of Seismic Shear Waves from Earthquakes," Journal of Geophysical Research, vol. 75, no. 26, September 1977, pp. 4997-5002.
4. Hanks, T.C., "The Faulting Mechanism of the San Fernando Earthquake," Journal of Geophysical Research, vol. 79, no. 8, March 1974, pp. 1215-1229.
5. Housner, G.W., and Trifunac, M.D., "Analysis of Accelerograms - Parkfield Earthquake," Bulletin of Seismological Society of America, vol. 57, no. 6, December 1967, pp. 1193-1220.
6. Johnson, J.A., Personal communications, Dames & Moore, Los Angeles, California, 1978.
7. Kanamori, H., "Mode of Strain Release Associated with Major Earthquakes in Japan," Annual Review of Earth and Planetary Sciences, vol. 1, 1973, pp. 213-239.
8. Kennedy, R.P., Chow, A.W., and Williamson, R.A., "Parametric Evaluation of Fault Movement Capacity of Buried Oil Pipeline," HN5113.7R, Holmes & Narver, Anaheim, California, August 1976.
9. Kennedy, R.P., Darrow, A.C., and Short, S.A., "General Considerations for Seismic Design of Oil Pipeline Systems," Proceedings, Technical Council on Lifeline Earthquake Engineering Specialty Conference, UCLA, Los Angeles, California, August 30-31, 1977, pp. 2-17.

BIBLIOGRAPHY (Continued)

10. Kennedy, R.P., Chow, A.W., and Williamson, R.A., "Fault Movement Effects on Buried Oil Pipeline," *Transportation Engineering Journal*, vol. 103, no. TE5, September, 1977, pp. 617-632.
11. Newmark, N.M., and Hall, W.J., "Seismic Design Spectra for Trans-Alaska Pipeline," *Proceedings 5th World Conference on Earthquake Engineering*, Rome, Italy, 1973.
12. Newmark, N.M., and Hall, W.J., "Pipeline Design to Resist Large Fault Displacements," *Proceedings of the U.S. National Conference on Earthquake Engineering*, 1975, Earthquake Engineering Research Institute, Oakland, California, June, 1975.
13. Taylor, C.L., Cluff, L.S., "Fault Displacement and Ground Deformation Associated with Surface Faulting," *Proceedings, Technical Council on Lifeline Earthquake Engineering Specialty Conference*, UCLA, Los Angeles, California, August 30-31, 1977, pp. 338-353.
14. Trifunac, M.D., "Analysis of Strong Earthquake Ground Motion for Prediction of Response Spectra," *Earthquake Engineering and Structural Dynamics*, vol. 2, 1973, pp. 59-69.
15. Trifunac, M.D., and Brady, A.G., "Correlations of Peak Acceleration, Velocity and Displacement with Earthquake Magnitude, Distance and Site Conditions," *Earthquake Engineering and Structural Dynamics*, vol. 4, 1976, pp. 455-471.

ANALYSIS OF GROUND MOTION SPECTRA

by

C. B. Crouse^I and B. E. Turner^{II}

ABSTRACT

The purpose of this investigation was to study the character of the response spectra of earthquake ground motions recorded in the western United States. Linear regression analyses of spectral ordinates with source-site distance as the independent variable were performed on data sets limited to small magnitude ranges, specific local soil conditions and component direction. The results of the study indicate that higher frequency spectral differences for records having different local soil conditions may be partially due to soil-structure interaction. The possibility of this coupling was suggested by Crouse (2), and studies of additional data lend support to this hypothesis. Attenuation rates were also noted to generally decrease with increased period for most data sets, and were generally greater for rock than soil sites. The standard errors from these regression analyses were less than those obtained by Trifunac and Anderson (14). The attenuation study also indicated that the ratio of the vertical to horizontal spectra may be independent of distance.

INTRODUCTION

The development of earthquake parameters or relationships for zonation or design purposes is often based on simplifications of more detailed studies of the characteristics of earthquake ground motion as represented by response spectra. In making such simplifications, it is important that the reasons for the differences in the computed spectra with variables such as site conditions, earthquake magnitude and site-source distance are fully understood.

The purpose of this investigation was to study the character of the response spectra of earthquake ground motions recorded in the western United States. In general the potential influence of earthquake magnitude, local soil conditions, soil-structure interaction, source-site distance, and component direction on the response spectra were examined to various degrees.

The role of local soil conditions and the possible coupling of this parameter with soil-structure interaction effects at higher frequencies were further studied in detail. This topic was discussed in a previous paper (2) and analysis of more data pertaining to the subject is presented herein. The investigation of the other variables affecting the response spectra examines to a large extent the attenuation of spectral ordinates, the scatter of these ordinates and the limitations in the basic data.

The principle method of analyzing the data was by a linear regression analysis of 2 percent damped spectral ordinates at selected periods in

I Project Engineer, Fugro, Inc., Long Beach, California

II Engineering Assistant, Fugro, Inc., Long Beach, California

the range from 0.04 sec to 4.0 sec. The equation was of the form:

$$\log Y(T) = A(T) + B(T)\log R(T) \quad (1)$$

where T is the period, Y(T) is the response spectral ordinate, R(T) is the source-site distance, and A(T) and B(T) are coefficients determined from the regression analysis.

The regression analyses were performed on data sets representative of specific recording conditions. For purposes of this study this approach was considered preferable to previously published methods of analysis (e.g. 9, 14) which lump all the data together and perform the regression analysis of all variables simultaneously. Regression analysis of this latter type cannot distinguish, for example, possible differences in rates of attenuation of ground motion for different local soil conditions, components or earthquake magnitude.

ANALYSIS OF RESPONSE SPECTRA

A total of 187 earthquake ground motion accelerograms recorded from 1933 through 1971 in the western U.S. have been systematically processed (15) and the response spectra of these records are published in Volume III of the Caltech data reports (6). Of this total 150 records plus two additional ones were selected for this study. The basic criteria for the selection of records were: (1) the location of the fault rupture of the earthquake was fairly wellknown so that a reasonable estimate of the source-site distance could be made, (2) the magnitude of the earthquake was 5 or greater, and (3) the source-site distance was greater than about 5 km. The distance from the recording station to the inferred center of energy release was used as the source-site distance. The center of energy release was generally established by examining each earthquake and selecting the location of the fault rupture that was believed to contribute significantly to the levels of shaking at the recording station. For some of the smaller earthquakes whose fault rupture dimensions are not known in detail but are presumably small, the source-site distance was measured to the epicenter provided the location of the epicenter was reasonably accurate. The recording stations were classified into categories of rock, shallow soil and deep alluvium. More detailed descriptions of these categories as well as the references used to classify the sites are found in reference (8).

The distribution of these 152 records according to a number of classifications are shown in Table 1. About three-fourths of the data are in the magnitude 6-6.9 range and most of these records are from the 1971 San Fernando earthquake. What little data exists for earthquakes in the magnitude 7-7.9 range is mostly from the 1952 Kern County earthquake and at distances greater than 40 km. With regard to local soil classification most of the data were recorded on shallow soil or deep alluvium deposits. A relatively small number of records were from rock sites. It is interesting to note that all of the rock data were recorded in small structures whereas a large portion of the alluvial records were from large structures. The possible consequences of this distribution is further examined in the first subsection below. Another significant point in Table 1 is that there were data from 23 earthquakes in the magnitude 5-5.9 range whereas there were only 9 earthquakes in the magnitude of 6-6.9 range. This large difference coupled with the fact that most of the magnitude 6-6.9 data is from the San Fernando earthquake

was thought to have a bearing on the scatter in the spectra for these two magnitude ranges. More detail on this is presented in the second subsection.

(1) Local Soil Conditions and Soil-Structure Interaction

Recent statistical analyses of response spectra by a number of authors (e.g. 8, 10, 13, 14) have shown differences in the level and shape of spectra between rock and alluvial sites. In general differences are characterized by higher spectral ordinates for rock sites at frequencies greater than about 5 cps, and higher ordinates for alluvial sites at lower frequencies. The latter differences may be attributed to local site soil conditions, regional geology or surface waves at the longer periods, and are not discussed further in this paper. Rather, attention is focused on the high frequency differences, which may be significant for the design of more rigid structures such as nuclear power plants.

The effect of local soil conditions on response spectra and the possibility that soil-structure interaction may be contributing to the differences in site-dependent spectra at high frequencies was discussed in a recent paper by Crouse (2). Briefly, the argument postulated for the possible coupling between the local soil conditions and soil-structure interaction was as follows. For data sets in previous studies (e.g. 8, 10, 13, 14) it was noted that most of the rock-site records were from small buildings or sheds; whereas, a significant amount of the alluvial records were from large multi-story buildings. Evidence from ground motions recorded at the Hollywood Storage site in Los Angeles and at a site in Japan (16) suggests that large buildings tend to filter higher frequency motions. Regression analyses of spectral ordinates (8, 9, 14) have shown that the rock spectra are greater than the alluvial spectra at high frequencies. A linear regression analysis of rock and alluvial data sets in the magnitude 6-6.9 range was recently performed and site-dependent spectra were computed at a distance of 18 km (8). Differences in the rock and alluvial spectra were approximately the same as the spectral differences between the motions recorded in the free field and the basement of a large building at the Hollywood Storage site during the San Fernando earthquake at about the same distance. Therefore, the tentative conclusion was that differences in site-dependent spectra at high frequencies previously attributed local soil conditions may be due in part to soil-structure interaction (2). This possibility is further explored below.

A linear regression analysis of spectral ordinates (Equation (1)) was performed on rock and deep alluvium data sets in the magnitude 6-6.9 range (Table 1). From this analysis mean spectra were computed at a distance of 100 km (Fig. 1). As shown in this figure the rock spectra are about 50 percent greater than the deep alluvial spectra for periods between about 0.08 sec and 0.2 sec. Similar differences are seen in approximately this period range for the response spectra of accelerograms recorded in the free field and basement of the Hollywood Storage site during the 1952 Kern County earthquake (Fig. 2). The distance from the earthquake source to this site was on the order of 100 km. This similarity in the differences in the spectra shown in Figures 1 and 2 supports the hypothesis advanced above that soil-structure interaction may be causing part of the differences between rock and alluvial spectra in this high frequency range.

Additional comparisons of site-dependent spectra were made by regression analysis of deep alluvium records in the magnitude 5-5.9 range using

Equation (1). The mean and mean \pm one standard deviation levels were computed at the distances of the rock records in this magnitude range and compared to those rock spectra (Fig. 4). The basic trends seen in this figure were also noted by LADWP (8) for site-dependent spectra in the magnitude 6-6.9 range at a distance of 18 km, i.e. the rock spectra are greater than the alluvial spectra at high frequencies and the opposite trend is observed at long periods. Table 1 reveals that all of the rock records were from small structures and over one-half of the deep alluvium records were from large structures in the magnitude 5-5.9 range. Therefore, part of the differences in the deep alluvial and rock spectra at high frequencies in Figure 4 could be due to soil-structure interaction.

Further analyses were performed to obtain an indication of how much influence the soil-structure interaction phenomena might have on the results of regression analyses discussed above. The deep alluvium data (Table 1) in the magnitude 6-6.9 range were separated into two data sets, one for small structures (17 records) and another for large structures (40 records). Regression analyses were run on these two data sets and mean spectra were computed at a distance of 25 km. The results, shown in Figure 3, indicate that the response spectra for the small structures are up to 50 percent greater than the spectra for the large structures at high frequencies. These differences are not as great as the differences of 100 percent and greater between the basement and free-field response spectra from the Hollywood Storage site for the San Fernando earthquake at about the same distance. This may be due to the fact that the differences in the sizes of the structures in the two categories are not as great as the size differential between the Hollywood Storage building and the small shed nearby which housed the "free-field" instrument. Most of the accelerograms from the rock sites were recorded in structures that were generally of the size of the shed at the Hollywood Storage site.

Exactly how much soil-structure interaction has biased site-dependent spectral estimates at high frequencies probably cannot be quantified with the available data. However, there is reasonable evidence to suggest that this coupling is present.

(2) Attenuation of Response Spectra

This subsection examines the distribution of response spectral ordinates (pseudovelocities at 2 percent damping) with respect to distance for different soil conditions, magnitude ranges and component direction. Quantitative estimates of attenuation rates and scatter in the data were derived from simple regression analyses (equation (1)) applied to data sets with a sufficient amount of data that were fairly uniformly distributed over large distance ranges. These analyses were performed for the shallow soil and deep alluvium data in the magnitude 5-5.9 and 6-6.9 ranges and rock data in the magnitude 6-6.9 range. The data in other categories in Table 1 were thought to be too limited for meaningful regression analysis.

The data in Table 1 can be visually examined in Figures 5 and 6, which show the effects of local soil conditions and magnitude, respectively, for three periods. Each period (T) intends to represent the low, intermediate, and high periods. Basic trends in the data at these periods are generally similar to trends at other periods close to these three. Figure 5 shows that the rock data are generally greater than the alluvial data at $T=0.08$ sec and

that this trend reverses for $T=3.0$ sec. The differences between the shallow soil and the deep alluvium data do not appear to be as great for all three periods. Some of the differences between the rock and alluvial data at $T=0.08$ sec may be due to soil-structure interaction as discussed in the last subsection.

The data in Figure 5 along with the additional data in the magnitude 7-7.9 range were plotted in Figure 6 to show the effects of earthquake magnitude. In general the differences in the data with respect to magnitude become greater as the period increases. This phenomenon has been observed by McGuire (9) and Trifunac and Anderson (14) as a result of their simultaneous regression analyses mentioned earlier. It is probably due to the general increase in duration of ground motion with magnitude as a result of the general increase in the source dimensions (e.g. 14) and the ability of bigger magnitude events to generate large surface waves. The extent of the magnitude differences at $T=0.8$ sec are reasonable and reflect the definition of the local Richter magnitude, which is basically a number linearly related to the logarithm of a relative displacement spectral ordinate at the same period and damping of about 80 percent (7, 12).

Differences in the deep alluvium data between the magnitude 6-6.9 and 7-7.9 ranges are more obvious (Fig. 6) at a period of $T=0.8$ sec than at $T=3.0$ sec. This observation may be partly due to limitations of the data base since most of the data in the magnitude 6-6.9 range are from the San Fernando earthquake. The deep alluvium spectra from this earthquake were amplified in the period range from about 3 to 5 sec and this was believed to be caused by surface waves propagating through the Los Angeles basin (5).

There do not appear to be any obvious differences in the effects of magnitude as a function of soil conditions from a visual examination of Figure 6. Comparable differences between the levels of the spectra exist for the magnitude 5-5.9 and 6-6.9 ranges independent of the soil classification. The lack of rock data precludes a generalization of this observation.

A quantitative measure of the attenuation rates and scatter in the data was obtained by the regression analyses discussed in the introduction of this subsection. Equation (1) was considered appropriate for the regression analyses based on the linear trends of the data with distance as indicated in Figures 5 and 6. The coefficients $B(T)$ and the standard errors, which indicate the attenuation and scatter, respectively, are shown in Figure 7. With the two exceptions of the magnitude 5-5.9 deep alluvium and magnitude 6-6.9 rock data sets, the rates of attenuation generally decrease with increasing period. This type of frequency-dependent attenuation has been observed by Berrill (1) and McGuire (9) for Fourier Amplitude Spectra but not by Trifunac and Anderson (14) to any significant extent for response spectra. The two exceptions to this trend noted in Figure 7 may be the result of a small amount data confined to relatively narrow distance ranges rather than representing a real phenomenon.

The rates of attenuation generally decrease in going from rock to shallow soil to deep alluvium for all periods. For the low periods in the magnitude 6-6.9 range some of the differences between the rock and alluvium attenuation may be due to the effects of soil-structure interaction discussed earlier. It was noted that high frequency filtering due to soil-structure interaction appeared to be more pronounced at the shorter distances. This

would tend to lower the rate of attenuation for the alluvial data at the low periods since most of the alluvial sites were from large buildings that could permit filtering at these periods.

The attenuation is less for the alluvial data in the magnitude 5-5.9 range than for the corresponding soil data in the magnitude 6-6.9 range (Fig. 7). There is no known physical reason for this phenomena although it may be related to possible increases in the strain-dependent material damping of the soil with increasing amplitudes of ground motion from larger magnitude events. The possible significance of this trend is certainly obscured by the limitations of the data bases.

The standard errors from the regression analysis (Fig. 7) show no major differences with respect to soil classification, but they are higher for the magnitude 5-5.9 data than the magnitude 6-6.9 data. This latter point is likely the result of two characteristics of the data in these magnitude ranges: (1) the magnitude 6-6.9 data is predominately from the San Fernando earthquake whereas the magnitude 5-5.9 data comes from many earthquakes, and (2) the magnitude of earthquakes in the 5-5.9 range cover a wider range of values. Therefore, the scatter in the magnitude 6-6.9 data is essentially due to the San Fernando earthquake and part of the scatter in the magnitude 5-5.9 data may be due to magnitude. The standard error of about 0.2 for the magnitude 6-6.9 data is virtually the same as the standard deviations reported by Donovan (4) for peak acceleration data from the San Fernando earthquake.

In the magnitude 6-6.9 range the attenuation and scatter of the data of the vertical and horizontal components (Fig. 7) are generally similar. A comparison of the attenuation rates of the vertical and horizontal data in this magnitude range is shown in Figure 8 for the three soil classifications. The attenuation rates for these components are quite similar for the alluvial data but differ by up to about 40 percent for the rock data. These differences for the rock data probably are due to the limited number (15 records) of vertical spectral ordinates in this data set. The fact that the vertical and horizontal attenuation rates are similar for the alluvial data suggests that the ratio of vertical and horizontal spectra on the average are independent of distance. The value of this ratio and its possible variation with period has not been investigated in this study, but results have been reported by others (e.g. 11, 14) using broader, less restrictive data sets.

SUMMARY AND CONCLUSIONS

Further evidence is presented in this paper to substantiate the coupling between the soil-structure interaction and local soil conditions at high frequencies suggested previously. High frequency filtering of seismic waves by the foundations of large buildings seems responsible for some of the differences in site-dependent spectra previously attributed to local soil conditions. This conclusion is supported in this paper and in a previous study (2) by comparisons of the Hollywood Storage free-field and basement spectra from the 1952 Kern County and 1971 San Fernando earthquakes with rock and deep alluvium spectra derived from regression analyses at similar source-site distances. The differences in the two groups of spectra were similar at high frequencies; i.e., the rock spectra were greater than the alluvial spectra by about the same amount that the free-field spectra were greater than the basement spectra. Since, in the regression analysis, most

of the alluvial data were from large buildings and the rock data were from small buildings or sheds, the differences in these site-dependent spectra may be partly due to soil-structure interaction. A similar conclusion was reached when comparisons were made between rock spectra and deep alluvial spectra from regression analyses of data in the magnitude 5-5.9 range. Another indication of how much influence large buildings have in affecting response spectra levels at high frequencies was seen in Figure 3. Spectra from two sets of magnitude 6-6.9 records, those obtained in small and large structures, were predicted by regression analyses. The small-structure spectra were greater than the large-structure spectra by up to 50 percent for high frequencies. It was noted, however, that many of structures classified as small were larger than most of the instrumented structures at the rock sites which could be considered more representative of free-field conditions. Had the small structures been the size of the structures on rock, the spectral differences in Figure 3 at high frequencies might have been greater.

The study suggests that any empirical method to determine free-field, site-dependent spectra using western U.S. strong motion data should consider the possible effects of soil-structure interaction at high frequencies. Selection of records from large buildings should be kept to a minimum or at least recognized in setting the level of the spectra for design or analysis purposes. The elimination of these data altogether is not recommended as it would severely limit the amount of available data.

Table 1 revealed other limitations in the western U.S. data besides the problems with the majority of the data coming from large buildings, and some of these were mentioned in the introduction. Because of these limitations the attenuation studies by the method of regression analyses were conducted only for a few of the data sets in Table 1, and as a result many generalized conclusions could not be made.

The decrease in rates of attenuation with increasing period was not observed for all data sets. However, the exceptions had the least amount of data and, therefore, the results for them may not be particularly significant. Part of the differences in attenuation rates for high frequencies between the rock and alluvial data in the magnitude 6-6.9 range again may be due to soil-structure interaction.

The attenuation rates for the vertical and horizontal components of the magnitude 6-6.9 alluvial data were similar indicating that on the average the ratio of vertical to horizontal spectra are independent of distance. There is some reservation in generalizing this conclusion since most of these alluvial data were from the San Fernando earthquake.

The standard errors from the regression analyses of the data were generally less than those from multiple regression analyses performed simultaneously on a number of independent variables such as magnitude, distance, and soil-conditions (e.g. 14). This difference could have significant impact on the determination of site-dependent spectra if confidence levels other than the mean are chosen for the design spectral level.

Finally, it is recommended that the data base for regression analyses and other empirical procedures used to determine design spectra for important structures should be examined closely for any possible biases or limitations such as those discussed in this paper.

ACKNOWLEDGMENTS

Comments and suggestions from Geoff Martin, Jim Hileman, Ricardo Guzman and Paul Jennings were appreciated. Portions of the study were extensions of work for the San Joaquin Nuclear Project of the Los Angeles Department of Water and Power. The financial support of Fugro, Inc., is gratefully acknowledged.

BIBLIOGRAPHY

1. Berrill, J.B. (1975), A Study of High-Frequency Strong Ground Motion from the San Fernando Earthquake, Ph.D. thesis, California Institute of Technology.
2. Crouse, C.B. (1978), Prediction of Free-Field Earthquake Ground Motions, Earthquake Engineering and Soil Dynamics, Proc. ASCE Geotech. Eng. Div., June, pp. 359-379.
3. Crouse, C.B. and Jennings, P.C. (1975), Soil-Structure Interaction During the San Fernando Earthquake, Bull. Seism. Soc. Am., vol. 65, no. 1, pp. 13-36.
4. Donovan, N.C. (1973), A Statistical Evaluation of Strong Motion Data Including the February 9, 1971, San Fernando Earthquake, Proc. Fifth World Conf. Earthquake Eng., Rome, Italy.
5. Hanks, T.C. (1975), Strong Ground Motion of the San Fernando, California, Earthquake: Ground Displacements, Bull. Seism. Soc. Am., vol. 65, no. 1, pp. 193-226.
6. Hudson, D.E., Trifunac, M.D., Brady, A.G., Nigam, N.C., Vijayaraghavan, A., and Udawadia, F.E. (1969-1975), Analyses of Strong Motion Earthquake Accelerograms, California Institute of Technology, vols. I-IV.
7. Kanamori, H., and Jennings, P.C. (1978), Determination of Local Magnitude, M_L , from Strong-Motion Accelerograms, Bull. Seism. Soc. Am., vol. 68, no. 2, pp. 471-486.
8. Los Angeles Department of Water and Power (LADWP, 1977), Early Site Review Report, San Joaquin Nuclear Project, Amendment 19, Appendix R, pp. 2.5R-42 to 2.5R-67.
9. McGuire, R.K. (1978), A Simple Model for Estimating Fourier Amplitude Spectra of Horizontal Ground Acceleration, Bull. Seism. Soc. Am., vol. 68, no. 3, pp. 803-822.
10. Mohraz, B. (1976), A Study of Earthquake Response Spectra for Different Geological Conditions, Bull. Seism. Soc. Am., vol. 66, no. 3, pp. 915-936.
11. Newmark, N.M., Consulting Engineering Services, (1976), Statistical Studies of Vertical and Horizontal Earthquake Spectra, NUREG 003, WASH 1255, U.S. Nuclear Regulatory Commission, 128 p.

BIBLIOGRAPHY (Continued)

12. Richter, C.F. (1958), Elementary Seismology, W. H. Freeman & Co., 768 p.
13. Seed, H.B., Ugas, C., Lysmer, J. (1976), Site Dependent Spectra for Earthquake-Resistant Design, Bull. Seism. Soc. Am., vol. 66, no. 1, pp. 221-244.
14. Trifunac, M.D., and Anderson, J.G. (1977), Preliminary Empirical Models for Scaling Absolute Acceleration Spectra, Report No. CE77-03, Univ. of So. Calif., 141 p.
15. Trifunac, M.D., and Lee, V. (1973), Routine Computer Processing of Strong-Motion Accelerograms, EERL 73-03, California Institute of Technology.
16. Yamahara, H. (1970), Ground Motions During Earthquakes and the Input Loss of Earthquake Power to an Excitation of Buildings, Soils and Foundations, vol. 10, no. 2, Tokyo, Japan, pp. 145-161.

TABLE 1 DISTRIBUTION OF STRONG MOTION DATA IN WESTERN UNITED STATES
USED IN THIS STUDY

MAGNITUDE RANGE	SOIL CLASSIFICATION	NUMBER OF RECORDS				NUMBER OF		RANGE OF RECORDING DISTANCES (KM)
		TOTAL	1971 SAN FERNANDO EARTHQUAKE	SMALL STRUCTURE	LARGE STRUCTURE	EARTHQUAKES	SITES	
5 - 5.9	ROCK	6	-	6	0	4	6	9 - 19
	SHALLOW SOIL	16	-	11	5	10	12	5 - 113
	DEEP ALLOUVIUM	11	-	5	6	9	9	6 - 56
6 - 6.9	ROCK	15	15	15	0	1	15	26 - 82
	SHALLOW SOIL	39	36	9	30	3	37	21 - 224
	DEEP ALLOUVIUM	57	44	17	40	5	46	10 - 230
7 - 7.9	ROCK	-	-	-	-	-	-	---
	SHALLOW SOIL	1	-	1	0	1	1	42
	DEEP ALLOUVIUM	7	-	5	2	3	7	48 - 109

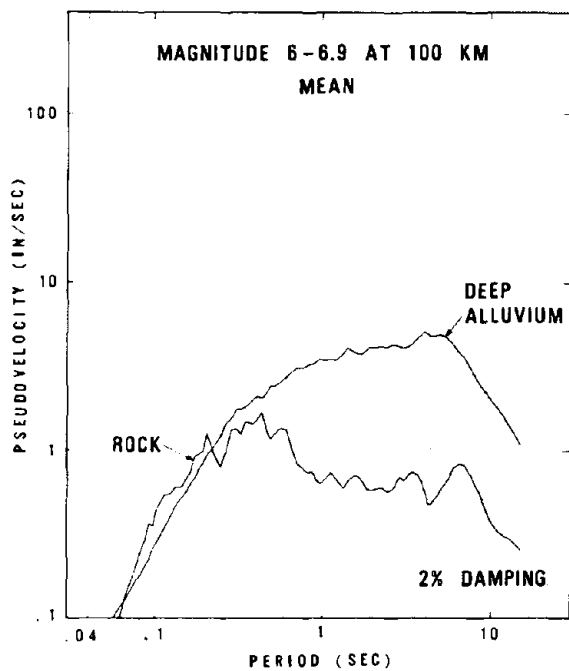


FIGURE 1. SITE DEPENDENT SPECTRA FROM REGRESSION ANALYSIS

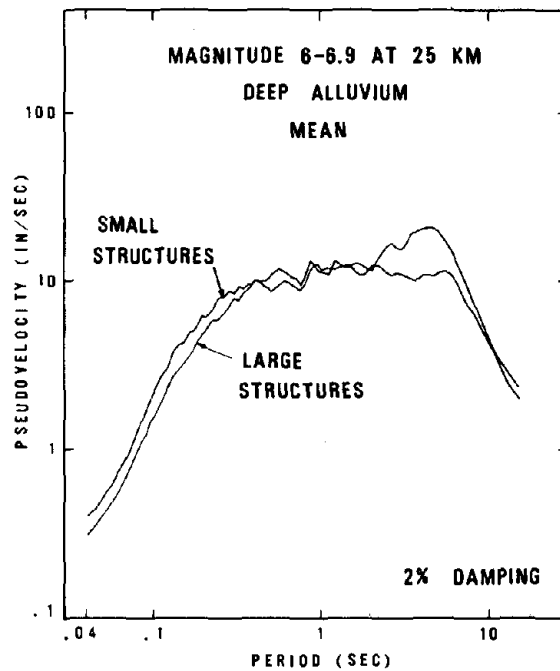


FIGURE 3. SPECTRA FROM REGRESSION ANALYSIS OF DATA RECORDED IN LARGE AND SMALL STRUCTURES

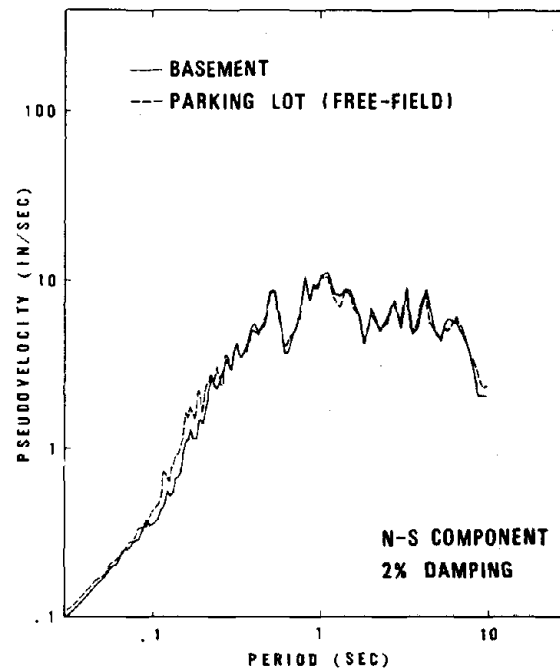
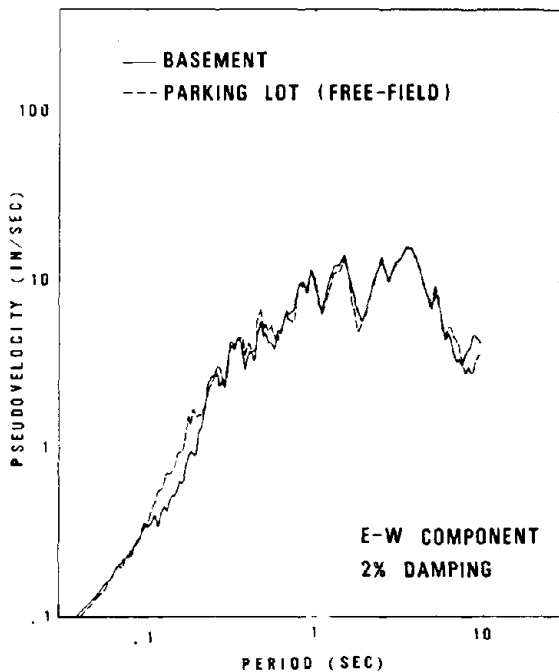


FIGURE 2. RESPONSE SPECTRA AT HOLLYWOOD STORAGE SITE. 1952 KERN COUNTY EARTHQUAKE.

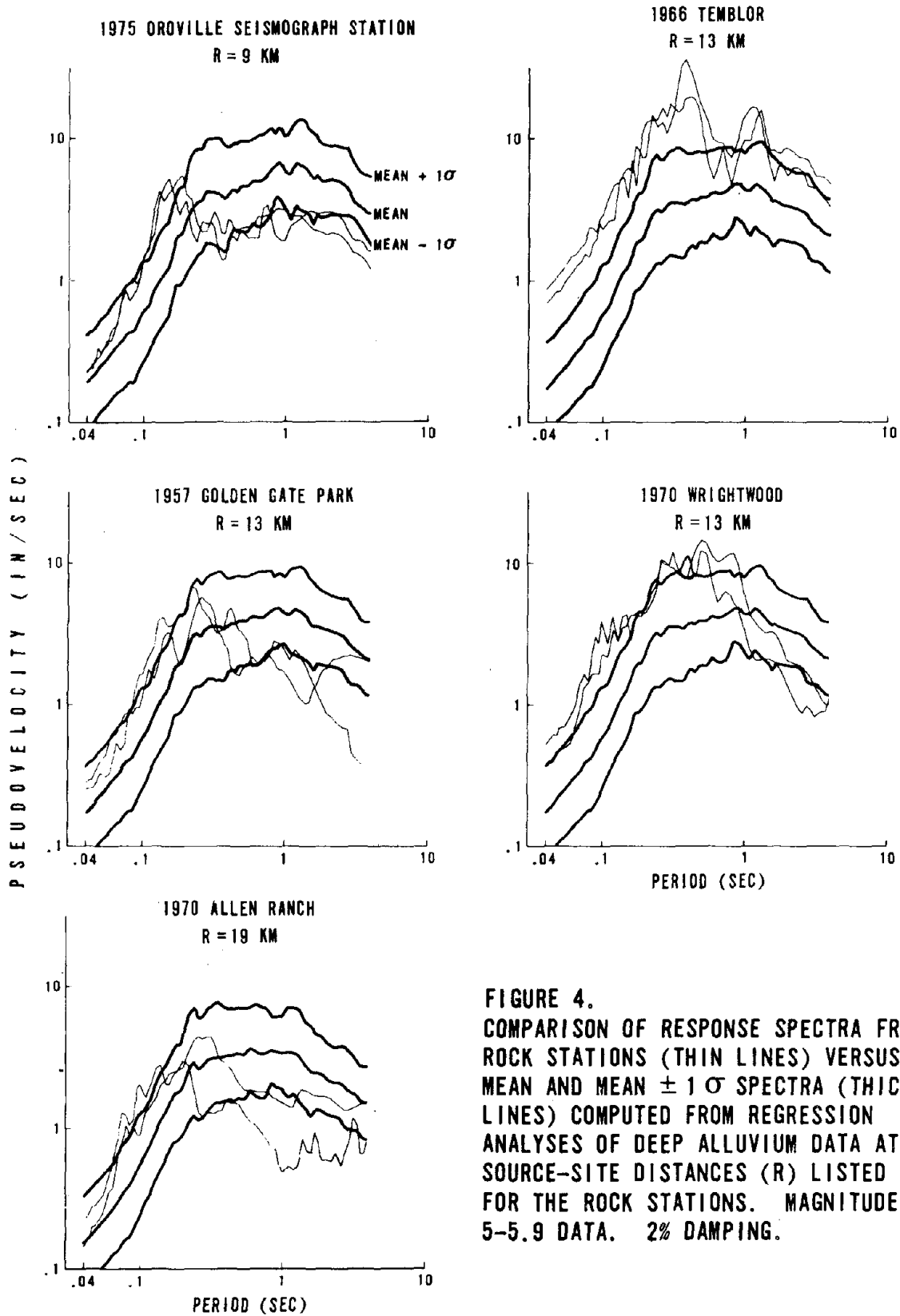
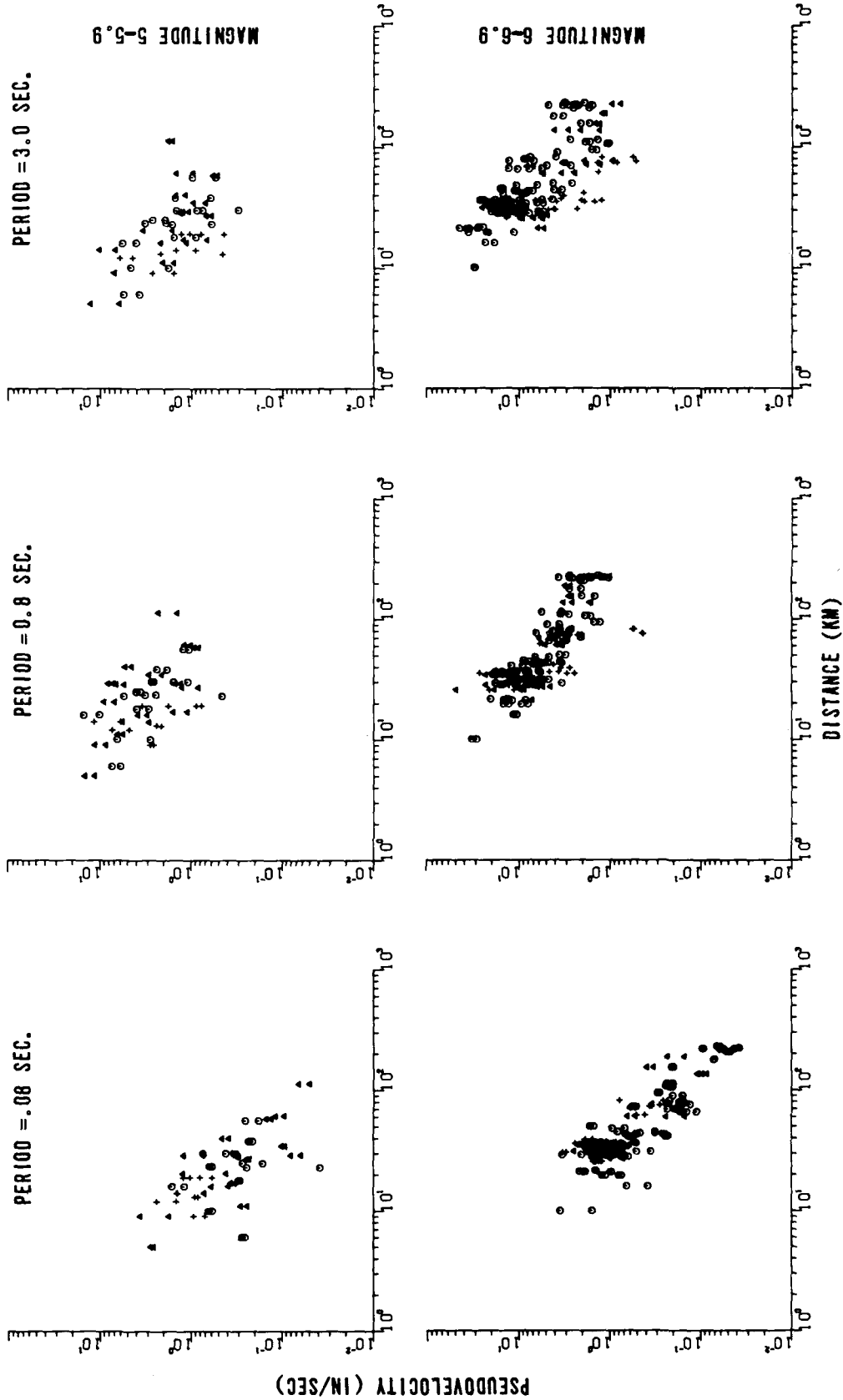
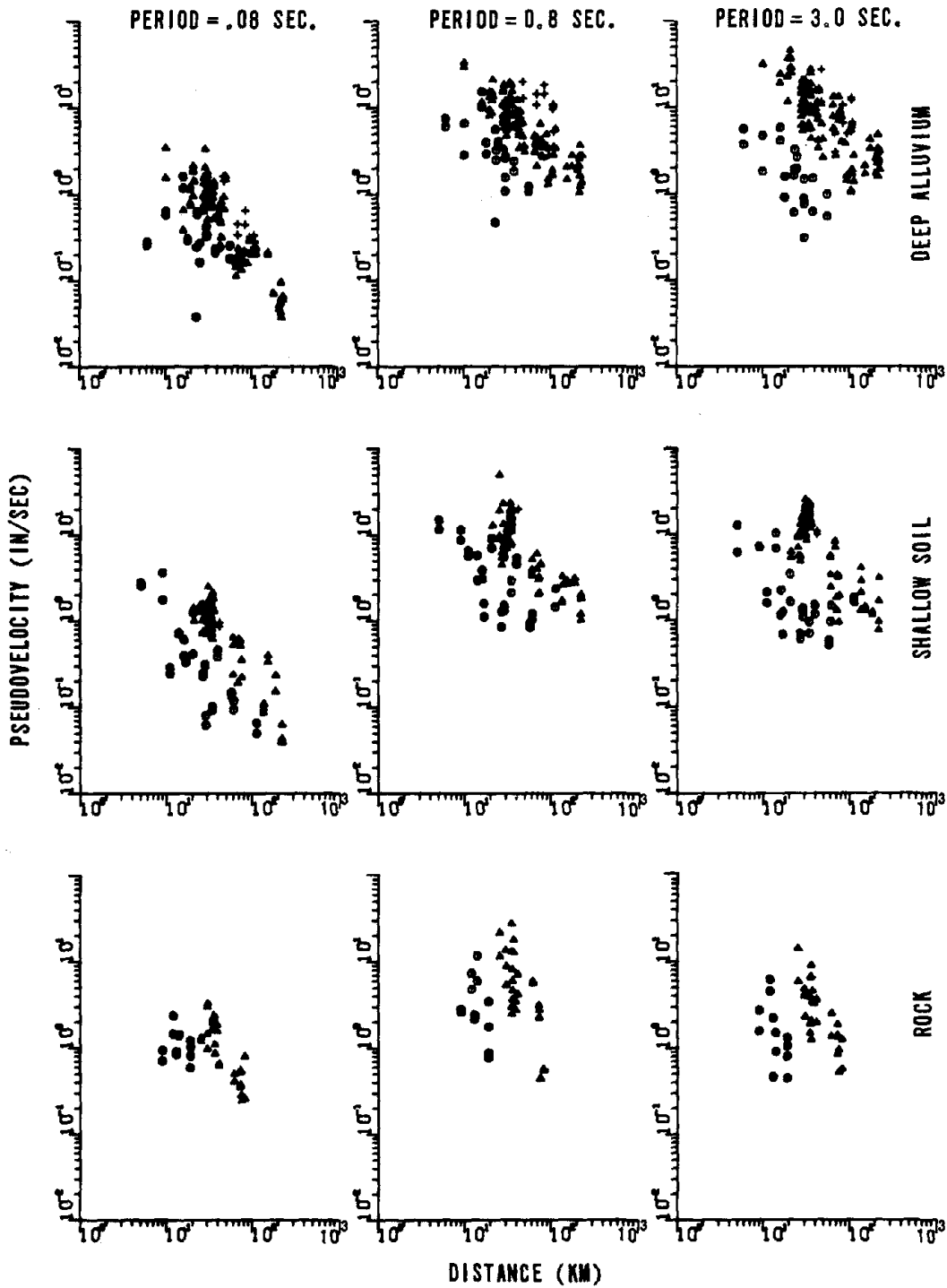


FIGURE 4.
COMPARISON OF RESPONSE SPECTRA FROM
ROCK STATIONS (THIN LINES) VERSUS
MEAN AND MEAN $\pm 1\sigma$ SPECTRA (THICK
LINES) COMPUTED FROM REGRESSION
ANALYSES OF DEEP ALLUVIUM DATA AT
SOURCE-SITE DISTANCES (R) LISTED
FOR THE ROCK STATIONS. MAGNITUDE
5-5.9 DATA. 2% DAMPING.



SYMBOLS: ○ DEEP ALLUVIUM ▲ SHALLOW SOIL + ROCK

FIGURE 5. EFFECT OF LOCAL SOIL CONDITIONS ON SPECTRAL ORDINATES FOR THREE PERIODS AND TWO MAGNITUDE RANGES. 2% DAMPING



SYMBOLS: ○ MAGNITUDE 5-5.9 ▲ MAGNITUDE 6-6.9 + MAGNITUDE 7-7.9

FIGURE 6. EFFECT OF EARTHQUAKE MAGNITUDE ON THE SPECTRAL ORDINATES FOR THREE PERIODS AND SITE CLASSIFICATIONS. 2% DAMPING

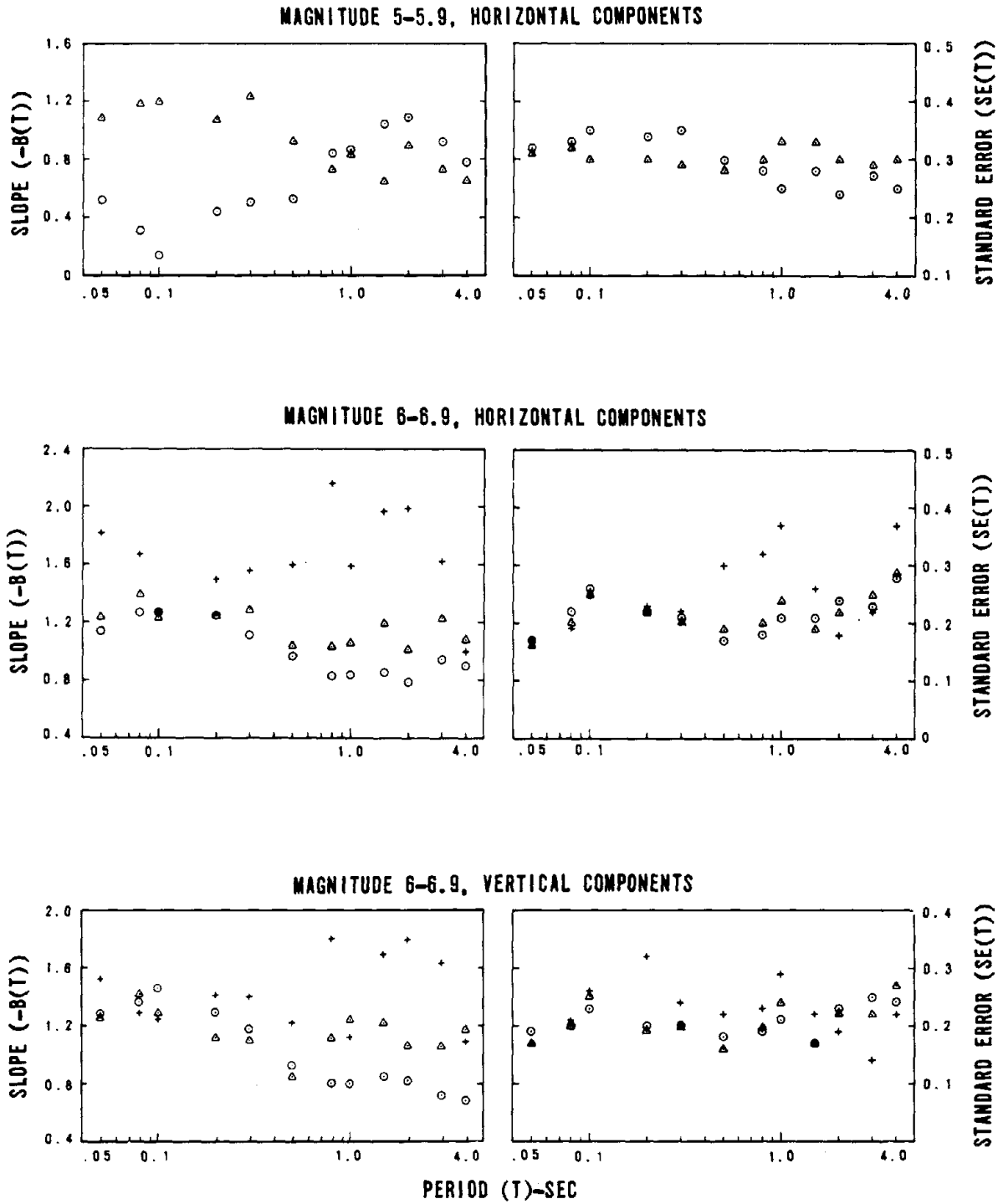


FIGURE 7. COEFFICIENTS, $B(T)$, AND STANDARD ERRORS, $SE(T)$, DETERMINED FROM REGRESSION ANALYSIS OF ROCK (+), SHALLOW SOIL (Δ), AND DEEP ALLUVIUM (\odot) DATA SETS.

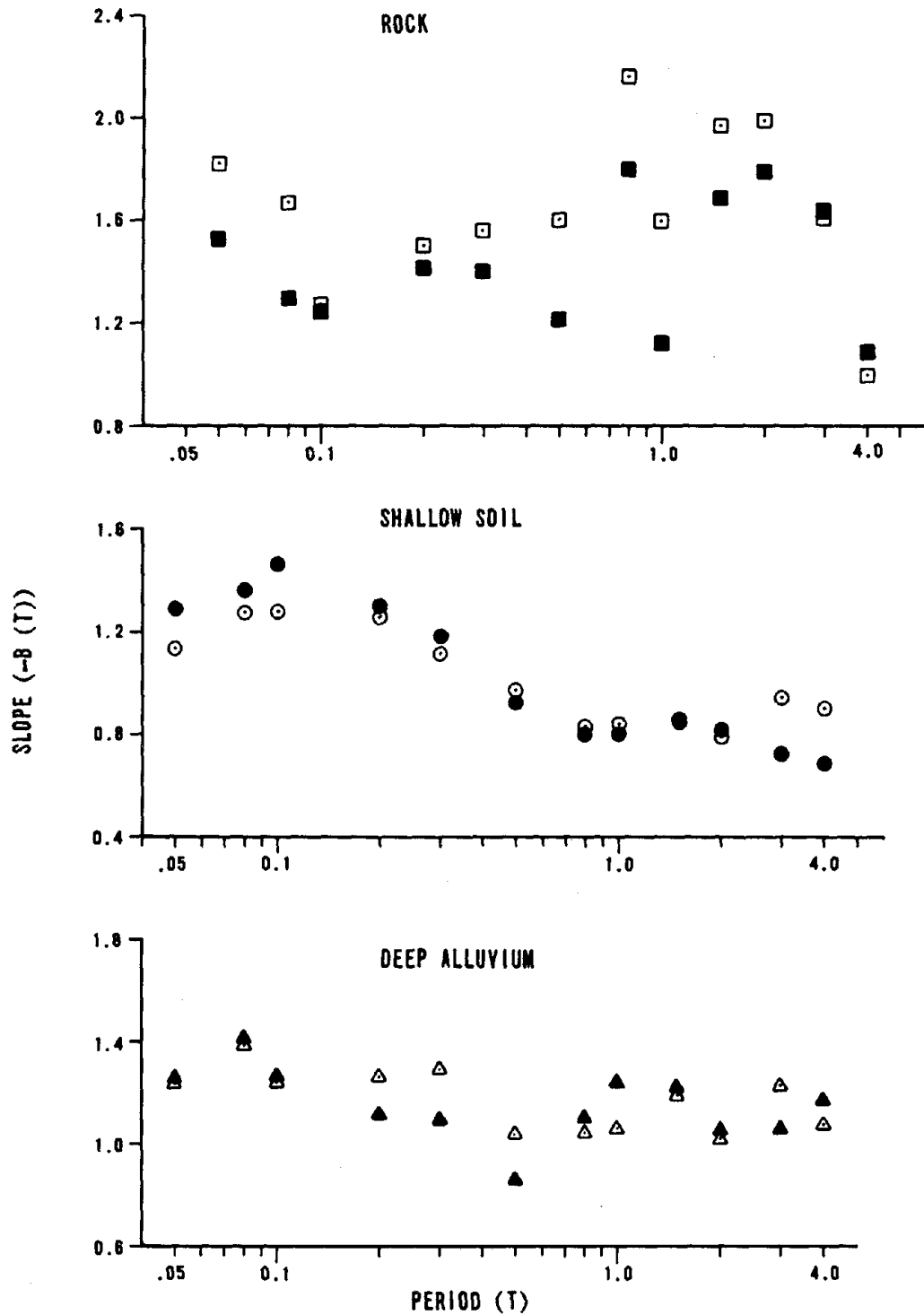
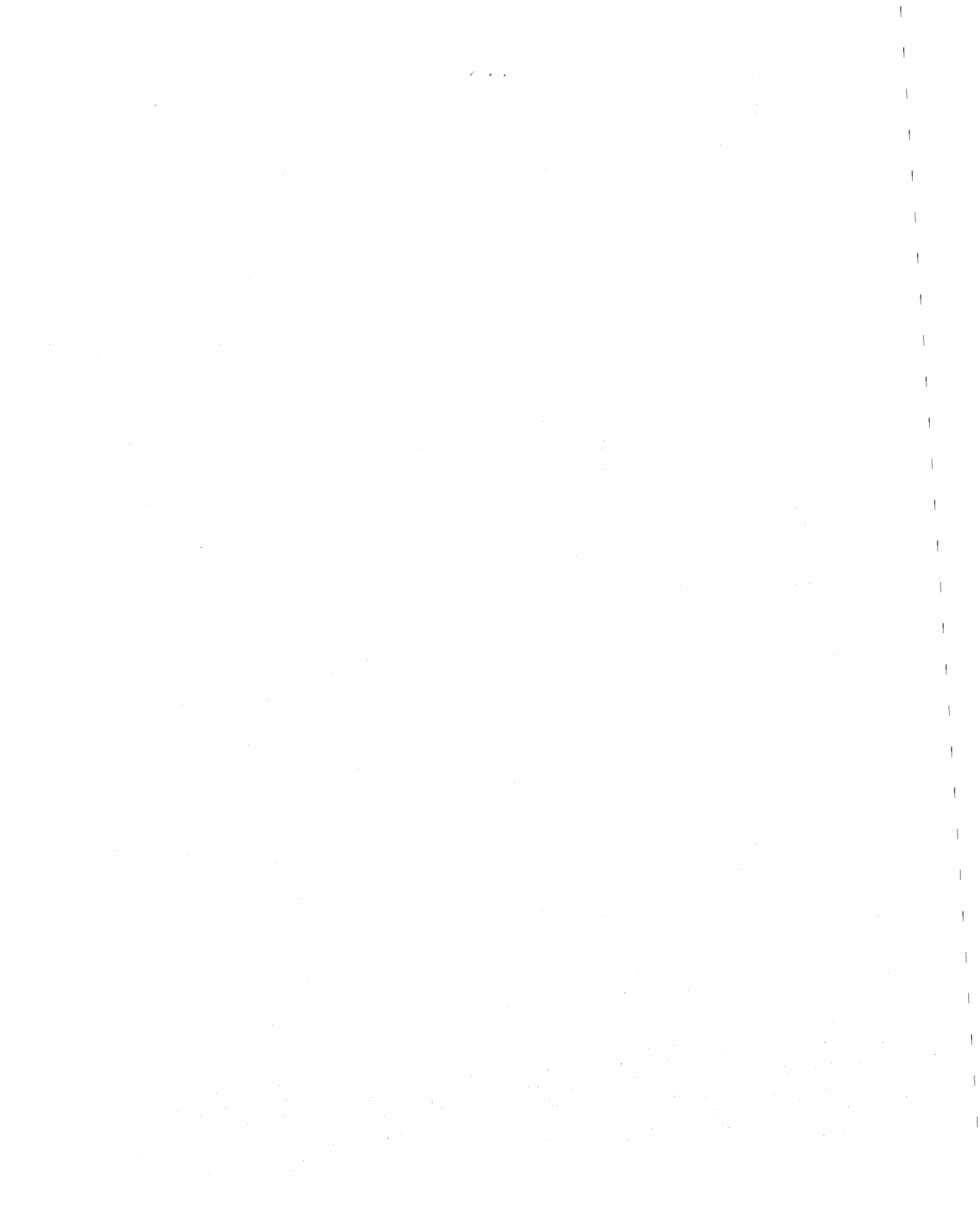


FIGURE 8. COMPARISON OF COEFFICIENTS, $B(T)$, FOR HORIZONTAL (OPEN SYMBOLS) AND VERTICAL (SOLID SYMBOLS) COMPONENTS IN MAGNITUDE 6-6.9 RANGE.



INDEX OF AUTHORS

- Abdel-Ghaffar, A.M.II-1037
 Abolafia, M.III-1489
 Acharya, H.K.I-379
 Alarcón, E.II-921
 Aki, K.II-1051
 Akky, M.R.III-1307
 Algermissen, S.T.I-291, 497
 Alonso, J.L.I-523
 Alt, J.N.II-669
 Anderson, J.G.I-559
 Apsel, R.II-693
 Arango, I.II-983
 Archuleta, R.J.I-255
 Arya, A.S.II-865

 Ballard, R.F. Jr.II-1013
 Bazán, E.II-657
 Bea, R.G.III-1307
 Bell, E.J.I-471
 Bell, J.W.I-471
 Benjamin, J.R.III-1369
 Bertero, V.V.III-1145
 Bhatia, S.K.II-839
 Bolt, B.A.II-617
 Boore, D.M.I-255; III-1447
 Borchardt, R.D.I-229, 241
 Botsai, E.E.I-193
 Brabb, E.E.I-229, 303
 Brune, J.II-1051
 Byrd, R.C.III-1409

 Campbell, K.W.II-1063
 Chandrasekaran, A.R.III-1157
 Chen, J.H.III-1169
 Chen, P.C.III-1169
 Clayton, D.N.II-983
 Cluff, L.S.I-135, 457, 535;
 II-669; III-1281
 Cochrane, H.C.III-1511
 Cooper, S.S.II-1013
 Crouse, C.B.II-1117

 Delfosse, G.C.III-1223
 Deza, E.I-341
 Dezfulian, H.II-873
 Dobry, R.II-945
 Dominguez, J.II-921
 Donovan, N.C.I-55
 Doyle, E.H.III-1433
 Duke, C.M.II-1025

 Eguchi, R.T.III-1341
 England, R.II-813
 Eskijian, M.L.III-1257
 Esteva, L.II-657

 Finn, W.D.L.II-839
 Fischer, J.A.I-329; III-1329
 Frazier, G.A.II-693
 Fumal, T.E.I-241
 Furuya, T.II-1001

 Gardner, W.S.II-945
 Gibbs, J.F.I-241
 Glass, C.E.I-509
 Goto, N.II-793
 Grant, W.P.II-983

 Hadjian, A.H.III-1199
 Hall, W.J.III-1235
 Harp, E.L.I-279, 353
 Hart, E.W.II-635
 Hart, G.C.III-1135
 Hasselman, T.K.III-1341
 Hattori, S.I-421
 Hayes, R.A.III-1383
 Hays, W.W.I-497; II-753
 Helmberger, D.V.I-27
 Herd, D.G.I-231
 Herrera, I.II-813
 Hisada, T.III-1187
 Hutton, J.R.I-179

 Idriss, I.M.I-457; III-1281
 Isenberg, J.II-911
 Ishibashi, I.I-81
 Ishihara, K.II-897
 Iwasaki, T.II-705, 885; III-1211
 Iwasaki, Y.T.I-445

 Jaén, H.I-341
 Jennings, P.C.I-27
 Joyner, W.B.I-255

 Kafka, A.L.III-1489
 Kagami, H.II-793
 Kallaby, J.III-1459
 Kao, C.S.I-367
 Kappler, H.III-1399
 Katayama, T.I-606; II-705
 Kawashima, K.II-705; III-1211
 Keefer, D.K.I-279, 353
 King, E.J.I-267
 King, J.II-1051
 King, K.W.I-497
 Kircher, C.III-1369
 Kisslinger, C.I-3
 Kobayashi, H.I-588; II-825
 Kockelman, W.J.I-303
 Kogan, J.I-341
 Kudo, K.II-765

- Kuribayashi, E.III-1499
 Kuroiwa, J.I-341

 Lagorio, H.J.I-193
 Lam, I.II-1089
 Liang, G.C.II-1025

 Mahin, S.A.III-1145
 Mândrescu, N.I-399
 Marcuson, W.F. IIIII-1013
 Mardiross, E.II-739
 Martín, A.II-921
 Martin, G.R.II-1089
 Matthews, R.A.III-1531
 Mau, S.T.I-367
 McWhorter, J.G.I-329
 Midorikawa, K.I-547
 Midorikawa, S.I-588; II-825
 Miletì, D.S.I-179
 Miller, R.D.I-497
 Milne, W.G.I-323
 Miranda, J.C.III-1223
 Mitchell, W.W.III-1459
 Moazami-Goudarzi, K.I-391
 Mohraz, B.III-1257
 Morgan, J.R.III-1235
 Moriwaki, Y.III-1433
 Mukerjee, S.II-865
 Murakami, S.I-547
 Murphy, V.J.I-153

 Nair, D.III-1383
 Nandakumaran, P.II-865
 Negmatullaev, S.Kh.II-681
 Nemat-Nasser, S.II-957
 Nersesov, I.II-1051
 Newmark, N.M.III-1235
 Nichols, D.R.III-1531
 Nishi, M.II-971
 Noda, T.II-971
 Nowack, R.L.I-485

 Ogawa, K.II-897
 Ohsaki, Y.III-1187
 Ohta, T.III-1187
 Ohta, Y.II-793
 Okahara, M.II-1001
 Olson, R.A.III-1475
 Oweis, I.S.II-777

 Packer, D.R.I-457
 Page, W.D.II-669
 Parhikhteh, H.I-391
 Paris, F.II-921
 Patwardhan, A.S.I-485, 535;
 III-1281, 1291
 Paul, D.K.III-1157

 Perkins, D.M.I-267
 Perkins, J.B.I-315
 Petrovski, J.I-413; III-1269
 Ploessel, M.R.II-647
 Power, M.S.II-801
 Prager, S.R.II-873
 Preston, R.F.I-267
 Prothero, W.II-1051
 Puri, V.K.II-865

 Remmer, N.S.I-215
 Rogers, A.M.II-753
 Rojahn, C.II-681; III-1135
 Roth, W.H.II-1105

 Sabina, F.A.II-813
 Sadigh, K.II-801
 Saeki, M.II-705
 Sánchez-Sesma, F.J.II-729
 Savage, W.U.II-669
 Schell, B.A.I-571
 Schuëller, G.I.III-1399
 Schwartz, D.P.I-457
 Scott, R.F.II-1037
 Seleznyov, G.S.II-681
 Self, G.II-1051
 Selzer, L.A.III-1341
 Seo, K.I-588
 Shakal, A.F.II-717
 Sherif, M.A.I-81
 Shibata, H.I-612
 Shima, E.I-433
 Shioi, Y.II-1001
 Shokooh, A.II-957
 Shpilker, G.II-1051
 Simpson, D.W.II-681
 Singh, R.D.II-945
 Spiker, C.T.III-1329
 Steinbrugge, K.V.I-203, 291
 Sugimura, Y.II-933
 Swan, F.H. IIII-457
 Swanger, H.J.III-1447
 Sweet, J.II-693

 Tai, M.I-445
 Tanimoto, K.II-971
 Tatsuoka, F.II-885
 Tazaki, T.III-1499
 Themptander, R.III-1525
 Tillson, D.D.I-485
 Tinsley, J.C.I-267
 Tocher, D.II-669
 Tohno, I.I-600
 Tokida, K.II-885
 Tokimatsu, K.I-600; II-853
 Toksöz, M.N.II-717
 Traubenik, M.L.II-1105

Trexler, D.T.I-471
Trifunac, M.D.I-559
Tsai, C.F.II-1089
Ts'ao, H.S.II-1077
Tucker, B.II-1051
Tuel, D.G.I-279
Turner, B.E.II-1117

Urbina, L.I-523

Vaid, Y.P.II-839
Valera, J.E.II-1105
Vaughan, D.K.II-911
Veletsos, A.S.I-111

Watabe, M.III-1187
Watt, B.J.III-1409
Webster, F.A.III-1369
Weichert, D.H.I-323
Weidler, J.B.III-1383
Werner, S.D.II-1077
Whitman, R.V.III-1247
Wieczorek, G.F.I-279, 353
Wiggins, R.A.II-693
Wilson, R.C.I-353
Wu, F.T.II-701

Yasuda, S.II-885
Yoshikawa, S.I-445
Yoshimi, Y.I-600; II-853
Youd, T.L.I-267
Youngs, R.R.II-801





